Dissertation

submitted to the

Combined Faculties for the Natural Sciences and for Mathematics

of the Ruperto-Carola University of Heidelberg, Germany

for the degree of

Doctor of Natural Sciences

Put forward by

Elke Hebisch, MSc.

Born in: Berlin

Oral examination: February 8, 2017

STED microscopy of cardiac membrane nanodomains

Referees: **Prof. Dr. Stefan W. Hell**
Prof. Dr. Rainer H. A. Fink

Für meine Eltern und meinen Bruder

Abstract

Heart muscle cells (cardiomyocytes) have to fulfill a demanding task. They have to ensure continuous and regular heartbeat and maintain their integrity despite undergoing constant mechanical stress during muscle contraction. To accomplish this, they feature a characteristic membrane architecture: the Transverse-Axial Tubular System (TATS), a network of membrane invaginations – the Transverse Tubules (TT) – which allows the fast translation of an electrical stimulus into a mechanical response. Further, specialized membrane protein complexes ensure membrane flexibility and stability during cycles of contraction and relaxation. Structural alterations of the TATS and the membrane protein complexes are linked to cardiac pathologies.

This thesis presents the subdiffraction image based investigations of the cardiac membrane architecture and membrane nanodomains using STimulated Emission Depletion (STED) microscopy of mouse ventricular cardiomyocytes (VM). Experimental and analytical methods comprising single- and multicolor, one- and two-photon-excitation STED microscopy are developed and applied. Special focus is laid on the three-dimensional (3D) TATS topology, on the membrane lipids Cholesterol (Chol) and Ganglioside GM1 (GM1), and on the membrane associated proteins Caveolin-3 (Cav-3) and Dystrophin (Dyst).

Novel fluorescent Chol analogs are characterized and established as a class of membrane labels with superior properties for STED microscopy of living VM. These dye compounds allow the visualization of the TATS with an unprecedented lateral resolution of below 35 nm and can be used for both membrane bulk staining and labeling of nanoscopic membrane compartments.

Using a custom-built two-photon-excitation-STED (2P-Exc-STED) microscope, the new Chol dyes enable the acquisition of 3D subdiffraction images of the TATS of living VM. These 3D images reveal that TT bud from Chol rich membrane domains and that these Chol rich domains can also form shallow membrane invaginations which are hypothesized to be caveolae.

The signal patterns of the caveolae-associated protein Cav-3 and of Chol are comparatively investigated and their similarities quantitatively evaluated. The dramatic effect of membrane Chol depletion on the nanoscopic Cav-3 signal

distribution is assessed. The correlation between the Cav-3 and Chol membrane patterns is further supported by two-color STED microscopy of VM labeled for Cav-3 and GM1, and Chol and GM1.

Finally, the spatial association between Cav-3 and the cytoskeletal protein Dyst is studied in detail. For this, two- and three-color STED imaging protocols and image analysis procedures are developed. To determine the molecular orientation of the Dyst protein with respect to Cav-3 and with respect to the cardiac membrane, a multicolor "intra-protein" labeling protocol is developed that is based on immunofluorescence staining using different primary antibodies that target specific epitopes along the Dyst protein.

A cardiac membrane nanodomain model summarizing the presented observations and findings is derived, validated, and discussed in detail.

Zusammenfassung

Herzmuskelzellen (Kardiomyozyten) müssen einer sehr anspruchsvollen Aufgabe gerecht werden. Sie müssen für einen kontinuierlichen und wohlgetakteten Herzschlag sorgen und gleichsam unversehrt bleiben trotz konstanter auf sie wirkender Scherkräfte während der Muskelkontraktion. Aufgrund dieser Anforderungen weisen Kardiomyozyten eine charakteristische Membranarchitektur auf: das Transversal-Axiale Tubuläre System (TATS), ein verzweigtes Netzwerk gebildet von Einstülpungen der Zellmembran, den Transversen Tubuli (TT), welches die rasche Umsetzung eines elektrischen Reizes in eine mechanische Reaktion ermöglicht. Desweiteren erhalten spezielle Membranprotein-Komplexe sowohl die Flexibilität, als auch die Stabilität der Zellmembran während der immerwährenden Abfolge von Zellkontraktion und Relaxation. Strukturelle Veränderungen des TATS und der Membranprotein-Komplexe stehen in Verbindung mit herzspezifischen Krankheitsbildern.

In dieser Doktorarbeit werden die Membranarchitektur und Membran-Nanodomänen in ventrikulären Kardiomyozyten aus der Maus (VM) mithilfe der nicht durch die Beugung limitierten "STimulated Emission Depletion" (STED) Mikroskopie untersucht. Experimentelle und analytische Methoden für die Ein- und Mehrfarben-, Ein- und Zwei-Photonen-Anregungs-STED Mikroskopie werden entwickelt und angewendet. Besonderes Augenmerk wird auf die dreidimensionale (3D) Topologie des TATS gelegt, sowie auf die Membranlipide Cholesterin (Chol) und GM1-Gangliosid (GM1) und die mit der Zellmembran in Verbindung stehenden Proteine Caveolin-3 (Cav-3) und Dystrophin (Dyst).

Neuartige fluoreszente Chol-Derivate werden beschrieben und als Membranindikatoren mit hervorragenden Eigenschaften für die STED Mikroskopie von lebenden VM etabliert. Diese Farbstoffverbindungen ermöglichen die Visualisierung des TATS mit nie zuvor dagewesener lateraler Auflösung von unter 35 nm und können sowohl für die Markierung der gesamten Membran, als auch für die Markierung einzelner nanoskopischer Membran-Kompartimente eingesetzt werden.

Die Verwendung der neuen Chol-Farbstoffe zusammen mit einem im Rah-

men dieser Doktorarbeit aufgebauten und detailliert beschriebenen Zwei-Photonen-Anregungs-STED Mikroskop ermöglicht die Aufnahme von hochaufgelösten 3D-Bildern des TATS in lebenden VM. Diese 3D-Bilder zeigen, dass TT aus mit Chol angereicherten Strukturen entlang der zellulären Oberflächenmembran entspringen und dass ein Teil dieser mit Chol angereicherten Strukturen flachere Einstülpungen der Membran markiert. Es wird hypothetisiert, dass diese flacheren Einstülpungen den Caveolae der Zellmembran entsprechen.

Die Signalmuster des mit den Caveolae assoziierten Proteins Cav-3 und des Membranlipids Chol werden vergleichend untersucht und ihre Übereinstimmungen quantifiziert. Der dramatische Effekt, den die Extraktion von Membran ansässigem Chol auf das nanoskopische Cav-3 Signalmuster hat, wird herausgearbeitet. Die Korrelation zwischen dem Cav-3 und dem Chol Membranmuster wird zusätzlich bestätigt durch Zweifarben-STED mikroskopische Aufnahmen von VM-Proben, in denen jeweils GM1 und Cav-3, sowie GM1 und Chol fluoreszent markiert sind.

Abschließend wird die räumliche Anordnung von Cav-3 und dem mit dem Zytoskelett verbundenen Protein Dyst im Detail untersucht. Dafür werden Protokolle für Bildaufnahmen mit Zwei- und Dreifarben-STED Mikroskopie und zugehörige Strategien der Bildanalyse entwickelt. Um die molekulare Orientierung des Dyst Proteins bezüglich Cav-3 und entlang der kardialen Zellmembran zu bestimmen, wird ein Protokoll für die mehrfarbige “Intra-Protein”-Markierung etabliert. Dieses Protokoll basiert auf der indirekten Immunfluoreszenz-Markierung verschiedener Domänen des Dyst Proteins mithilfe unterschiedlicher epitopspezifischer Primärantikörper.

Ein herzspezifisches Membran-Nanodomänen Modell, welches die in dieser Doktorarbeit gemachten Beobachtungen und die daraus gewonnenen Erkenntnisse zusammenfasst, wird abgeleitet, überprüft und im Detail diskutiert.

List of Abbreviations

Note: the most frequently used abbreviations are listed here. Less frequently used abbreviations are introduced in place in the respective sections.

2P-Exc	Two-photon excitation
2P-Exc-CWSTED	Two-photon-excitation-continuous-wave-STED
3D	Three-dimensional
AF594	Alexa Fluor 594 (fluorescent dye)
AP	Action potential
Cav-3	Caveolin-3
Chol	Cholesterol
Chol depl.	Cholesterol depletion
Chol-KK114	Fluorescent Chol analog (PEG-linker; dye: KK114)
Chol-OG488	Fluorescent Chol analog (PEG-linker; dye: Oregon Green 488)
CtB	Cholera toxin subunit B
CtB-AF594	Fluorescent recombinant CtB (dye: AF594)
CVD	Cardiovascular disease
Dyst	Dystrophin
ECC	Excitation-contraction coupling
F-Actin	Filamentous Actin
GM1	Ganglioside GM1
HAd	Human adipocyte (derived from adipose heart tissue)
KK114	Fluorescent dye
M-β-CD	Methyl-β-cyclodextrin
NND	Nearest neighbor distance
OG488	Oregon Green 488 (fluorescent dye)
PEG	Polyethylene glycol
SR	Sarcoplasmic reticulum
STAR635P	Fluorescent dye (Abberior STAR 635P)
STED	Stimulated emission depletion
TATS	Transverse-axial tubular system
TT	Transverse tubule
ViPSC	Ventricular induced pluripotent stem cell
VM	Mouse ventricular cardiomyocyte

Contents

List of Tables

List of Figures

1. Introduction

1.1. The cardiac membrane system

The heart is undoubtedly the most romanticized and stylized organ in the body and is perhaps the most recognizable pictogram throughout the world. Even if hidden and well-sheltered in the chest, it readily comes back to mind; beating tirelessly - directly heard and felt at any time. The heart is a symbol. It has almost become an independent-minded, autonomously acting personality.
The heart is also an organ. It is part of the machinery which is responsible for maintaining the necessary order defined as life. And as part of this machinery, it is clocked by the basic principles of science: cause and effect. This is the actual magic which provokes fascination and makes the heart one of the organs studied in greatest detail across all life sciences ranging from physiology to biology and physics.
The average human heart is made up of about 2 to 3 billion individual heart muscle cells - the cardiomyocytes - that share the space with other 3 to 6 billion cells of other types [1]. The cardiomyocytes are connected with each other at the intercalated disc and embedded in a wickerwork of extracellular matrix. Together, these cells form the four chambers of the mammalian heart: the left and the right atrium, and the left and the right ventricle. Arriving at the right atrium, deoxygenated blood is directed to the right ventricle, and to the lungs to be oxygenated. The oxygenated blood re-enters the heart via the left atrium to the left ventricle, and from there pumped into the bloodstream to supply the organism's cells with fresh oxygen for the maintenance of cellular homeostasis [2].
Being at the node of an organism's oxygen distribution, the heart is a veritable working horse. Under normal conditions, i.e. 60 to 70 heart beats per minute, the human heart - assuming it to be a mechanical pump - has to generate about 2 W of power - and this for a whole lifetime. Under extreme conditions, the

power output demand of the heart can even rise up to about 10 W [3]. Thus, even under normal conditions, the heart consumes a lot of oxygen: 20 times more than skeletal muscle at rest (normalized to tissue mass) [4]. To meet this high demand in oxygen, the heart has an oxygen extraction level of between 70 and 80 %.
Impairment of the cardiac function results in a cascade of consequences: the systemic oxygen demand cannot be met any more - and this holds true for all organs, including the heart itself. This is the onset of heart failure which is defined as the progressive and typically lethal syndrome being the common consequence of CardioVascular Diseases (CVD) arising from various underlying origins [5, 2].
The vital importance of proper heart function manifests itself in the fact that since data is collected on the statistics of mortality, CVD ranks top as the underlying cause of death. Based on the 2013 mortality data, one third of all deaths in the United States are caused by CVD with about 2200 Americans dying of CVD every day - which is equal to 1 death every 40 seconds. On a global scale, over 17 million deaths in 2013 were of CVD. Additionally, CVD related diseases pose a tremendous financial burden regarding prevention, treatment, and aftercare [6]. Basic research investigating the molecular changes involved in CVD and aiming at translating findings into clinical studies is hence of great importance.

To ensure regular, robust, and continuous heartbeat, cardiomyocytes have to contract and relax with precise timing. The initial triggering signal for contraction is electrical: the depolarization of the cardiomyocyte plasma membrane (the sarcolemma) by a propagating action potential (AP) [2, 7]. Unlike skeletal muscle, the heart muscle as a whole does not need external stimulation to rhythmically initiate its AP. This ability is know as cardiac automaticity and is mediated by pacemaker cells situated in a region of the right atrium known as the sinoatrial node. These pacemaker cells constantly have a higher transmembrane potential than other cardiomyocytes and can undergo spontaneous depolarization [8, 9]. Since all cardiomyocytes are electrically coupled, an AP in one cell will dominantly cause all neighboring cells to depolarize and generate a propagating AP. Along the sarcolemma, this propagating AP induces the opening of membrane resident voltage-gated Calcium ion channels ($Ca_v1.2$),

resulting in an influx of Calcium ions (Ca^{2+}) into the sarcoplasm (i.e. the cytosol). This Ca^{2+} influx leads to an increase in the permeability of the Sarcoplasmic Reticulum (SR) to Ca^{2+} - a process mediated by the Ryanodine Receptors type 2 (RyR2) which are SR resident Ca^{2+} release channels and which open upon Ca^{2+} influx through $Ca_v1.2$ [10]. The SR is the cell's main store of Ca^{2+} and the opening of RyR2s leads to the release of the stored Ca^{2+} from inside the SR into the sarcoplasm. Thus, the Ca^{2+} concentration inside the cell is potentiated. This cascade is called Calcium Induced Calcium Release (CICR) [11, 12, 13, 14]. Ca^{2+} will reach the myofibrils via diffusion. There, long filamentous Tropomyosin proteins lie on two sides of the Actin myofilament, covering up the sites where the Myosin can bind. Globular Troponin proteins are attached to the Tropomyosin. When Ca^{2+} binds to Troponin, the protein undergoes a conformational change and moves the Tropomyosin. This again uncovers the Myosin binding sites on the Actin, allowing Myosin heads to bind and form cross-bridges which results in the movement of Myosin along the Actin filaments and thus in muscle contraction [15, 2].

The translation between AP, i.e. electrical stimulus, and contraction, i.e. mechanical response, is called Excitation-Contraction Coupling (ECC). The ECC in cardiomyocytes must be reliable, synchronous, repetitive and - most of all - fast. In this context, it is important to note that cardiomyocytes are rather large cells: e.g. mouse ventricular cardiomyocytes (VM) measure about $20\,\mu\text{m} \times 20\,\mu\text{m} \times 80\,\mu\text{m}$. A rough estimate assuming a cardiomyocyte to be a cuboid yields a surface area of 7200 μm^2 and a volume of 32,000 μm^3. The propagating AP has a velocity of about $v_{\text{AP}} \approx 50$ m/s [16, 17] while the diffusion constant of Ca^{2+} in the sarcoplasm amounts to about $D \approx 2 \times 10^{-7}\,\text{cm}^2/\text{s}$ [18]. In this "gedankenexperiment", we will assume that the initial AP at the most has to cover the distance along one of the short axes of the cell and along the long axis because in a cascade, the AP triggers membrane depolarization along its way. Thus, it would take the AP a time of $t_{\text{AP}} \approx 2 \times 10^{-6}\,\text{s} = 2\,\mu\text{s}$ to travel across the cell surface once and open the membrane resident $Ca_v1.2$ channels. For the Ca^{2+} released from the SR, we will assume that it has to traverse (at least) the cuboid cell's diagonal $d = 7200\,\mu\text{m}$ by diffusion. Making use of Einstein's approximation equation [19], the time it will take the Ca^{2+} to diffuse across this area amounts to $t_{Ca^{2+}} \approx ((7200\,\mu\text{m})^2)/(2 \times 2 \times 10^{-7}\text{cm}^2\text{s}^{-1}) \approx$

1.3×10^6 s. This is equivalent to 15 days that it would take the Ca^{2+} to reach every myofibril to initiate contraction of the whole cell. Even when taking into account that there is an accelerating effect on the stimulus conduction by the Ca^{2+} concentration amplifying and Ca^{2+} distributing function of SR, this is still much too slow. The human heart beats about 65 times per minute, ECC can obviously not rely on intracellular diffusion of Ca^{2+} alone.
Hence, in order to meet the demand of fast ECC, cardiomyocytes feature a specialized membrane architecture: the Transverse-Axial Tubular System (TATS) [20]. The TATS is a cell wide network or membrane invaginations - the so called Transverse Tubules (TT). The basic functionality of TT is to connect regions buried deep inside the large cells with the extracellular space, thus providing for a cell spanning spatial association between the electrically excitable cell membrane and the SR inside the cell. The TATS of a VM is visualized in Fig. 1.1.
Fig. 1.1 **A** shows a widefield image of a living, resting VM of typical size with evenly spaced sarcomeres of a length of about 2 µm. In Fig. 1.1 **B**, a living VM was fluorescently stained with the membrane dye Cholesterol-PEG-OG488 and imaged using two-photon-excitation microscopy to obtain a whole-cell three-dimensional image. Both images were obtained in the course of this thesis (see also section 3.4). The highly interconnected TATS is to the biggest extent composed of tubules oriented parallel to the short (transverse) cell axes. These TT are evenly spaced corresponding to the sarcomere lengths of about 2 µm. There are also, albeit fewer, longitudinal tubules. From two-photon-excitation microscopy of rat cardiomyocytes, the average TT diameter was estimated to be about 250 nm [21] while recent subdiffraction STED microscopy of the fluorescently labeled TATS of VM determined the average TT diameter to be about 198 nm [22, 23] and electron microscopy based studies found the TT diameter to be between 70 and 100 nm [24] in rat cardiomyocytes.
Although the TATS is structurally formed by invaginations of the surface sarcolemma, it has been found that the density and distribution of proteins - predominantly those proteins involved in Calcium in- and efflux - differ between the surface sarcolemma and the TT membrane composing the TATS [25, 26, 27]. The $Ca_v1.2$ channels, for example, occur in higher abundance at the TT membrane than at the surface sarcolemma [28]. On the other hand, in the absence of

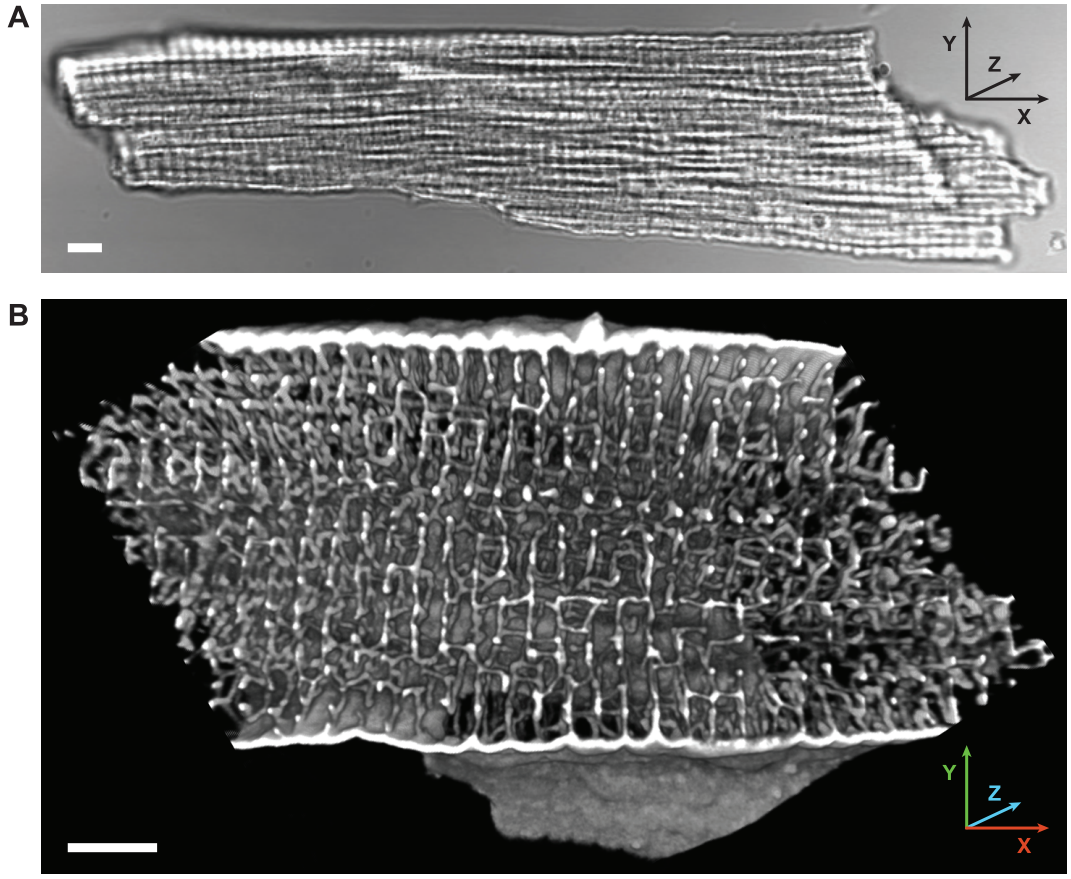

Figure 1.1.: Micrographs of living mouse ventricular cardimyocytes (VM). Coordinate systems indicate the longitudinal cell axis (X) and the transverse cell axes (Y and Z), respectively. **A** Widefield image of a living VM. **B** two-photon-excitation microscopy image of the Transverse-Axial Tubular System (TATS) of a living VM stained with the fluorescent membrane dye Cholesterol-PEG-OG488 (see section 3.4). Scale bars: 5 µm.

TT, the β-adrenergic pathway was found to stay functional and that the phosphorylation of Phospholamban, a protein involved in the initiation of muscle relaxation, was not changed upon loss of TT [29, 30].

Further, the membrane capacitance is assumed to be lower for the TT membrane than for the surface sarcolemma [28] - an effect which might be due to the specific membrane content of Cholesterol and caveolae (see also sections 1.1.1, 1.1.2, and 3.3).

Changes of surface sarcolemma and TT membrane architecture are linked to cardiac pathophysiology. Heart failure is linked to cardiac hypertrophy, especially an increase in mass and wall thickness of the left ventricle [2, 31]. The size of VM increases as well and, with it, the area of the surface sarcolemma [23]. This results in morphological changes of the surface sarcolemma, predominantly flattening of the surface and loss of the typical "Z-grooves" at the

cardiomyocyte surface [32] which has been shown to lead to reduction in cardiomyocyte contraction amplitudes [33]. Further, combined atomic force microscopy and electron microscopy studies of a mouse model of myocardial infarction revealed a loss of sarcolemmal stiffness already in the early stages of heart failure [34].
In several animal disease models and also based on biopsies from diseased and healthy human hearts, the loss and geometric rearrangement of TT structures has been reported. In animal models of heart failure a loss of TT and a concomitant loss in $Ca_v1.2$ channels has been reported [35, 36]. There, the TT depletion led to a loss of between 28 and 41 % of TT membrane area [37, 38]. Based on a computational model, structural changes of the TT architecture in cells depleted of TT resulted in AP propagation inhibition [39]. In the failing human heart, a loss of the rectangular arrangement, an increase in the number of longitudinally oriented TT, and an increase in TT diameter was observed [40, 41]. These pathological changes were have also been confirmed in a mouse model of myocardial infarction using subdiffraction STED microscopy [22].
Consequently, it is likely that the surface sarcolemma and the TT membrane serve different - yet equally important - functions that are specifically tailored for different processes of cell excitation and signaling events. After all, the total cardiomyocyte membrane area is composed of the surface sarcolemma and the TT membrane in roughly equal shares [42, 43].
Concluding, the sarcolemma of cardiomyocytes can essentially be divided into two parts based on their structure and molecular composition: the surface sarcolemma and the TT membrane. These two components feature some characteristics that make them distinguishable. Throughout this thesis, for simplicity, the surface sarcolemma will be referred to as the sarcolemma while the TT membrane will be addressed as such. Both sarcolemma and TT membrane have an equally important impact on cardiac electrophysiology, signaling and cellular integrity. The specific electro- and biomechanical demands on cardiac myocytes and the therefrom arising distinct cellular membrane topology motivates the worthwhile closer look at the concept of the “cell membrane” itself.

When in the mid-seventeenth century the English polymath Robert Hooke first looked at the microscopic structure of thinly cut slices of cork, he was immediately reminded of the small dwellings of Italian cenobites, the cells. With

this catchy term that he established in his bestselling book *Micrographia* [44], he stressed one of the most important and defining properties of these elementary biological building blocks: the existence of a cell wall. A cell wall that defines the "inside" and "outside" of a cell and thus identifies a self-contained unit. In eukaryotes, the development of a cell membrane - i.e. a selectively permeable and flexible cell boundary - can be considered to be a tremendously advantageous evolutionary step beyond the concept of the stiff and impermeable cell wall found in plant cells, bacteria, and other prokaryotes [45]. Cell membranes create a Ca^{2+} gradient of roughly a factor of 10,000 between the extra- and the intracellular space [46]. Since the tight control of intracellular Ca^{2+} concentration is key for cell homeostasis, the integrity and functionality of the eukaryotic membrane are vital. This is especially the case for terminally differentiated cells like cardiomyocytes which don't have high self-renewal capability and hence need tightly regulated mechanisms of membrane maintenance and repair [47].

A characteristic feature of the eukaryotic cell membrane is the assembly of phospholipids, glycolipids, cholesterol and membrane proteins that together form a bilayer sheet of about 5 - 6 nm thickness [48] covering the entire cytosol - and sometimes, in the case of striated muscle cells, even penetrating the complete cellular volume in a network-like fashion and thus letting regions normally buried deep inside the cell come into close contact with the extracellular space [21]. The lipid bilayer sheet provides cellular membranes with unique properties. First, the cell membrane is plastic and flexible, thus allowing the cells to change shape according to its momentary functional need, e.g. the necessity to reversible contract and relax as is the case in a muscle cell [49]. Second, the eukaryotic cell membrane is both permeable and impenetrable, thus providing the cell with protection against possibly harmful molecules or organisms while at the same time allowing control over chemical gradients and the uptake of nutrients to maintain cellular homeostasis. Indeed, the cellular membrane is more than a pragmatic or minimalist evolutionary approach to simply delimit intracellular vs. extracellular territory: the cell membrane of eukaryotes is made up of far more different kinds of lipids than would be necessary to form a basic bilayer [50]. It is this surplus complexity and sophistication in lipid structure which enables the opening of

various pathways for differently-natured exchange and signaling mechanisms across the cellular membrane. And there are many different transmembrane pathways - based on a broad variety of principles and mechanisms - that cells utilize to communicate with their "outside world": endocytosis [51], exocytosis [52], caveolae [53, 54] (see also section 1.1.2), pits [55], tubules [56, 57, 49], protrusions [58, 59, 60], and channels [61, 62, 63], just to name a few prominent examples. Given this plethora of specific tasks that a functional cellular membrane can perform - and has to perform - it is hardly surprising that the cellular membrane is not a chemically isotropic sheet but features a very heterogeneous and complex arrangement of different lipids and proteins in various stoichiometries and assemblies. For a long time, the predominant focus had been laid on the investigation of the distribution and the therefrom deduced functionality of membrane proteins. The membrane lipid composition, however, albeit being an ever present parameter in every investigation of the functional implications of a certain membrane organization, was much less in the spotlight [64]. After the 1980s, more and more studies started recognizing the influence of lipids in cellular signaling processes and the spatial interaction of lipids and proteins [65, 66, 67], hence commencing the field of lipid biochemistry. The observation that there is an asymmetry of the lipid composition at the apical vs. the basolateral membrane of polarized epithelial cells lead to the proposition that this asymmetry helps in the precise shipment and sorting of function-specific lipids and proteins from the Golgi complex to select locations in the cellular membranes (i.e. either the apical or basolateral membrane where different functional requirements have to be met) and from there to the proposition of membrane microdomains featuring a specific heterogeneous composition that would define their functionality [68]. These heterogeneous, function-specific membrane microdomains laid the foundation of the concept of "lipid rafts" which was first proposed and propagated by *Simons and Ikonen* in 1997 [69]. According to their "raft hypothesis", sphingolipids and Cholesterol assemble into membrane domains (the "rafts") along the lipid bilayer and float laterally in a "sea" of phospholipids. The postulate of lipid rafts immediately triggered profound excitement in the scientific community - in fields ranging from biochemistry over biophysics to molecular medicine. Studies regarding the visualization and characterization of lipid

rafts and their properties - sometimes quite contradictory studies - accumulated (for review see [70, 71, 72]), soon demanding a generalized definition of what a lipid raft actually is - *if* it actually is. In the "Keystone Symposium on Lipid Rafts and Cell Function" in 2006 - about 10 years after the proposition of the lipid raft principle - the terminology of membrane rafts (note that the expression "lipid raft" was abandoned in favor of the more general "membrane raft") was established as follows: "Membrane rafts are small (10 - 200 nm), heterogeneous, highly dynamic, sterol- and sphingolipid-enriched domains that compartmentalize cellular processes. Small rafts can sometimes be stabilized to form larger platforms through protein-protein and protein-lipid interactions" (cf. [73]). This formalism was intentionally broadly and carefully defined since the corresponding area of lipid research was and is still developing. The existence of membrane rafts has been met with support [74, 75, 76] - and it has been questioned [77, 78]. Albeit the fact that it is quite an appealing concept that provides explanations of many robust and specific cellular transport and signaling processes [79, 80, 81, 82], the controversy still remains. This is mostly because membrane rafts have not yet been directly and unequivocally detected or visualized. And such a visualization remains a challenging task - because of three of the main defining properties of membrane rafts: 1.) they are small, 2.) they are dynamic, and 3.) they are heterogeneous. To unravel the heterogeneity of a small and fast object, a probing mechanism with both a spatially and temporally sufficient resolution is necessary - otherwise, the object will appear homogeneous and its structural and functional uniqueness cannot be pinpointed. There are many different approaches to detect and characterize membrane rafts. Regarding biochemical methods, there is for example the determination of the molecular content of membrane domains that survive the solubilizing effects of certain detergents (e.g. Triton X-100 or Saponin) [83, 84, 85] - typically resulting in the classification of the insoluble protein and lipid fraction to be membrane raft associated. However, it has been argued that detergent insolubility of a specific protein or lipid does not necessarily indicate its association to membrane rafts [86, 87]. Microscopic approaches like electron microscopy or Atomic Force Microscopy (AFM) suffer from an unphysiological sample preparation or from the necessary reductionist approach of studying artificially prepared model membranes [88, 89, 90].

Microscopic approaches like confocal fluorescence microscopy or Fluorescence Correlation Spectroscopy (FCS) suffer from their diffraction limited spatial resolution [91, 92, 93, 94, 72]. Further, there is always the issue of the experimental bias introduced by a specific lipid or protein marker needed for molecular labeling - cross-linking effects caused by standardly used toxin or antibody based lipid markers can lead to the misinterpretation of the actual degree of lipid or protein clustering [95, 96, 97].
Recent advances in subdiffraction fluorescence light microscopy - namely STimulated Emission Depletion (STED) microscopy (see section 1.2) and STED-FCS - in conjunction with novel techniques to fluorescently label specific lipids have, however, revitalized the search for membrane rafts and extended the scope of lipid biochemistry [98, 99, 100, 101, 72]. So far, the majority of the conducted subdiffraction investigations of the properties of membrane domains are based on STED-FCS, i.e. inferring the size of these membrane domains from the diffusion behavior of fluorescently labeled proteins or lipids. Yet, diffusion based measurements are not the definite answer to the question about the existence of lipid rafts and their properties because the diffusion properties of cellular membranes are certainly not restricted to the clustering of membrane lipids [102] but are likely influenced and mediated by membrane associated proteins, e.g. cytoskeletal structures [100]. Hence, the explicit visualization and characterization of subdiffraction membrane clusters and domains is of great interest to accompany and complement the so far available data on the nature of membrane domains.

This thesis focuses on cardiac membrane nanodomains, their spatial association and the therefrom arising functional implications. Four key players associated with the cardiac sarcolemma and the TT membrane will be investigated using STED microscopy: the lipid Cholesterol, the membrane assciated protein Caveolin-3, the glyocsphingolipid Ganglioside GM1, and the cytoskeletal protein Dystrophin. These four molecules and their relevance for cardiac function will be introduced in the next sections.

1.1.1. Cholesterol

Cholesterol ($C_{27}H_{46}O$; in the following abbreviated as Chol) is a lipid molecule - a sterol - that is both endogenously synthesized and internalized via receptor mediated endocytosis by all eukaryotic cells in a ratio of about 2:1 [103, 104]. Chol is an essential component of the lipid bilayer sheet of eukaryotic membranes and is the precursor of bile salts [105], vitamin D, and all steroid hormones [106, 107].

Since its discovery in 1815 by the French chemist M. E. Chevreul who isolated Chol from human gallstones [108], it has been subject to extended research across many scientific fields, earning H. O. Wieland the Nobel Prize in Chemistry in 1927 for pioneering studies in deciphering its chemical structure, earning K. Bloch and F. Lynen the Nobel Prize in Physiology or Medicine in 1964 for elucidating the processes of the Chol metabolism, and earning M. S. Brown and J. L. Goldstein the Nobel Prize in Physiology or Medicine in 1985 for clarification of the regulation of the Chol metabolism. Chol has by now become one of the pets of popular science. Most prominently, Chol is widely known - and dreaded - for its connection to arterial plaques and cardiovascular disease [109, 110, 111]. But despite Chol's somewhat bad reputation, proper function of eukaryotic cells is not possible without it because of its vital role in diverse cellular processes.

Chol is an integral component of the plasma membrane of eukaryotes, accounting for 20 - 50 mol% of the membrane's lipid content [112, 113, 76]. It is thus the most abundant molecule in the plasma membrane - and this applies to all eukaryotes [76]. Just like the development of the eurkaryotic cell membrane (see section 1.1), the cellular synthesis of Chol as the "sterol of choice" [114] was a concomitant evolutionary process towards the improvement of membrane functionality under the pressure of selection [115, 116].

Chol features a rather small hydrophilic polar domain that consists of merely one -OH headgroup which is facing either the extracellular or the cytosolic space (shaded in pink in Fig. 1.2 **A**), and a hydrophobic domain that is buried between the hydrocarbon chains of the membrane phospholipids and that consists of a steroid nucleus and a hydrocarbon side chain (shaded in blue in Fig. 1.2 **A**) [117, 118, 119]. Chol provides for membrane stiffness, reducing membrane permeability [116], increasing membrane viscosity [120], reducing the

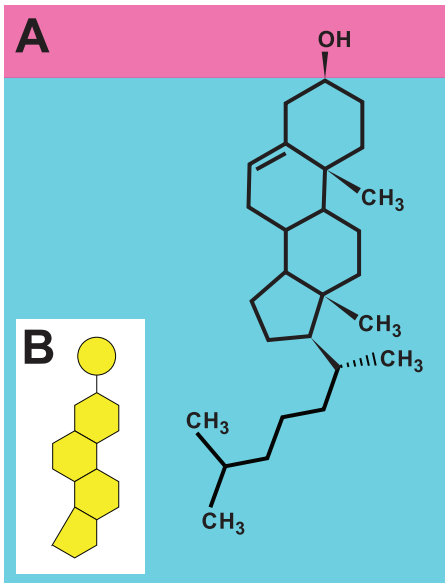

Figure 1.2.: Schematic of the structure of Cholesterol (Chol). **A** The hydrophilic, polar -OH headgroup that is facing either the extracellular or the cytosolic space is shaded in pink; the hydrophobic tail that inserts itself in-between the hydrocarbon chains of the membrane phospholipids and that consists of a steroid nucleus and a hydrocarbon side chain is shaded in blue. **B** Pictographic illustration of Chol as it will be used throughout this thesis.

lateral diffusion along the membrane [121], and decreasing the membrane's compressibility [122]. Additional to these Chol dependent biophysical properties of cell membranes, Chol is involved in many biochemical processes such as cellular transport [123], cell signaling [124, 125], and gene expression [126, 127] (also well reviewed in [128]). In fact, Chol plays such a crucial role in cellular homeostasis that its concentration in different cellular organelles is very sensitively and precisely regulated by the interplay of many proteins that allow a "switch-like" control of cellular Chol levels [129, 130, 131].

Further, Chol tends to induce and organize sphingolipid and Chol rich domains along the membrane bilayer - the so called "membrane rafts" (see section 1.1 and [69]). The existence and precise nature of membrane rafts are still unanswered questions whose elucidation will require the unequivocal visualization of the rafts and a consensus about the specific interactions between Chol and other membrane lipids. There are three major models that were proposed to describe and explain these interactions: 1.) the "Condensed Complex Model, 2.) the "Superlattice Model", and 3.) the "Umbrella" Model. The Condensed Complex Model hypothesizes Chol-lipid complexes that are so densely packed that they together would occupy smaller areas in the bilayer than the individual components of the complex would - an effect caused by the lower free energy of the complex [132]. The Superlattice Model hypothesizes that sterols in membranes maximize their inter-molecular spacing by forming long range superlattices of different geometries [133]. The Umbrella Model hypoth-

esizes that since Chol's hydrophilic -OH headgroup is too small to shield its bulky hydrophobic steroid nucleus and hydrocarbon side chain from the aqueous phase, Chol tends to "seek shelter" under the larger hydrophilic headgroups of glycosphingolipids - e.g. sphingomyelin and Ganglioside GM1 (see also section 1.1.3) [134, 135]. The glycosphingolipids thus provide an "umbrella" for Chol's sterol group. The Umbrella Model can adequately - probably most adequately of the three here introduced models - explain the formation of Chol/glycosphingolipid clusters in the membrane [136] and also predicts that a cluster of only Chol would result in an inward bend of the membrane as a result of the preferred reduction of the interface area with the aqueous phase to which Chol's hydrophobic tail would be exposed [135].

Indeed, due to the size difference between the hydrophilic headgroup and the hydrophobic tail, Chol has a reported highly negative intrinsic curvature [137, 138, 118, 139], featuring a spontaneous curvature of about -0.45 nm^{-1} (at 20 °C) and about -0.5 nm^{-1} (at 35 °C) which is about at least a factor 2 more negative than that of phosphatidylcholines [139]. Chol thus tends to form inwardly curved membrane structures, i.e. concave formations that bend away from the aqueous phase and cause dents or pits in the membrane. A very prominent example of such Chol enriched pits along the membranes of many cell types are caveolae [140, 54] which will be discussed in detail in the next section (section 1.1.2), thereby focusing on the association of Chol and the muscle cell specific caveolae scaffolding protein Caveolin-3 (Cav-3) which will be one of the main subjects of investigation of this thesis. This is because the Chol rich caveolae are abundant in cardiomyocytes and are assumed to serve as a membrane surface area reservoir to enable the reversible geometrical changes of the cardiomyocyte sarcolemma during the cycles of contraction and relaxation [141, 142] (see also section 1.1).

Here, a brief outline of the functional relevance of Chol in cardiomyocytes shall conclude this introductory section about Chol. Especially the membrane of cardiomyocytes features high amounts of free Chol (note that free Chol - opposed to esterified Chol - is mobile and accessible in the respective cell organelles and not confined to and stored in lipid droplets [143]). When estimating the Chol content in the cardiac membrane system and its influence on the properties of cardiomyocytes, three factors should be taken into account. First, in

cultured rat cardiomyocytes, the free Chol content of the whole sarcolemma (i.e. surface sarcolemma and Transverse tubule (TT) associated membranes) was determined to amount to about 53 % of the total cellular Chol content [144]. Note here that according to the terminological convention used in this thesis, i.e. generally referring to the surface sarcolemma as "sarcolemma" vs. the TT membranes (see section 1.1), this means that about half the cellular Chol content is distributed among the sarcolemma and the TT membrane. Second, the fraction of the TT membrane area is estimated to amount to about 50 % of the total cardiac membrane area [21, 42]. And third, from data obtained from skeletal muscle, it was found that the TT membrane contain an about 2 fold higher amount of Chol than the sarcolemmal membrane [145]. Conclusively, this means that the cardiac membrane contains high amounts of Chol and that there is a difference in Chol content between the TT associated membrane and the sarcolemmal membrane which shapes the functional properties of these two specific types of cardiac membrane.

Regarding the electrophysiological properties of cardiomyocytes, an increase in Chol content is assumed to decrease the specific membrane capacitance due to the increase in membrane thickness caused by the additional insertion of Chol [42]. For example, Chol depleted cultured rat cardiomyocytes showed a faster rate of depolarization than controls (which might again indicate an increase in Calcium influx during depolarization) [146]. Since TT membranes contain higher levels of Chol, it is assumed that they feature a lower capacitance than the sarcolemma [42] (for example, it has been shown that the capacitance of cardiomyocytes proportionally depends on the developmental stage of the cells which correlates with their degree of tubulation [147]). Thus, Chol content in the cardiac membrane influences its specific capacitance.

Further, studies about the influence of the acute alteration of cellular Chol levels on the intracellular Ca^{2+} ion concentration $[Ca^{2+}]_i$ showed the significant effect of Chol concentration - yet, the results were very contradictory, either stating a positive dependence between Chol levels and $[Ca^{2+}]_i$ [144, 148], or a negative one [149].

Regarding the structural properties and the integrity of cardiomyocytes, Chol is involved in cardiac membrane repair mechanisms: upon rupture of the plasma membrane, the Chol that is release from the site of membrane injury triggers

the relocation of the repair protein MG53 to the site of membrane rupture [46]. The initiation of repair mechanisms is especially important in cardiomyocytes because they are terminally differentiated cells that have only minimal possibilities for self-renewal [47]. In addition, lowering of Chol content has been reported to lead to a loss of TT integrity in cultured mouse ventricular cardiomyocytes [150]. However, these findings could not be reproduced in the experiments conducted in this thesis using freshly isolated mouse ventricular cardiomyocytes (see section 3.5.1) and showing that Chol depletion did not compromise the cardiac TT architecture. This discrepancy could be explained by the fact that upon culture, mouse cardiomyocytes tend to lose TT structures which has been reported oftentimes in the literature [151, 152, 153, 32].
Finally, on a clinical scale, the influence of Chol on health and longevity remains controversial. Some studies indicate that lower levels of serum Chol correlate with a lower risk of arterosclerotic cardiovascular disease [154, 111] (although the decrease of blood Chol levels also correlated with a higher risk of diabetes [154]). Then again, some studies report that low levels of serum total Chol correlate with and increased risk of heart failure [155, 156]. Also, in meta-analysis of 40 Chol associated studies, dietary Chol intake could not be found to be statistically significantly linked to a number of cardiovascular diseases [110]. Further, unbiased clinical trials accompanied by new insights from molecular biology will be needed to resolve the decade old question whether Cholesterol is “good or bad for you”.
In this thesis, I will not try to make a statement regarding this ongoing debate. Rather, I will concentrate on the association between Chol and membrane caveolae since many of the Chol dependent cellular processes - generally in many cell types and specifically in cardiomyocytes - can be traced back to caveolae that seem to provide membrane-resident signaling hubs, reservoirs of membrane surface area, and stores of membrane integral proteins. The next section will thus introduce the muscle specific caveolae scaffolding protein Caveolin-3 (Cav-3) and discuss its functional connection to Chol.

1.1.2. Caveolin-3

Caveolin-3 (Cav-3) is a 21 kDa protein [157] and was identified as the muscle specific isoform of the caveolin protein family [158, 159]. The caveolins - i.e.

Caveolin-1, Caveolin-2, and Cav-3 - are the major scaffolding proteins of membrane caveolae [160, 140]. Accordingly, Cav-3 is the caveolae forming protein of sarcolemmal caveolae in muscle cells and is highly expressed in cardiac myocytes [161].

Cav-3 consists of 151 amino acids (aa) that can be classified into an amino terminus (N-terminus or "N", aa 1-73), a hydrophobic transmembrane domain (aa 75-106, assumed to form a hairpin loop), and a carboxyl terminus (C-terminus or "C", aa 107-151) [162, 163, 164]. The N-terminus contains a scaffolding domain (aa 55-74) that is known to bind various signaling proteins [165]; the C-terminus contains three palmitoylation sites [166]. Fig. 1.3 schematically depicts the estimated structure and conformation and its location in the membrane lipid bilayer. The shown schematic structure of Cav-3 summarizes the possible appearance and membrane association of Cav-3 that are proposed in [167, 168, 169, 170, 140, 164, 166]. Cav-3 has been shown to be

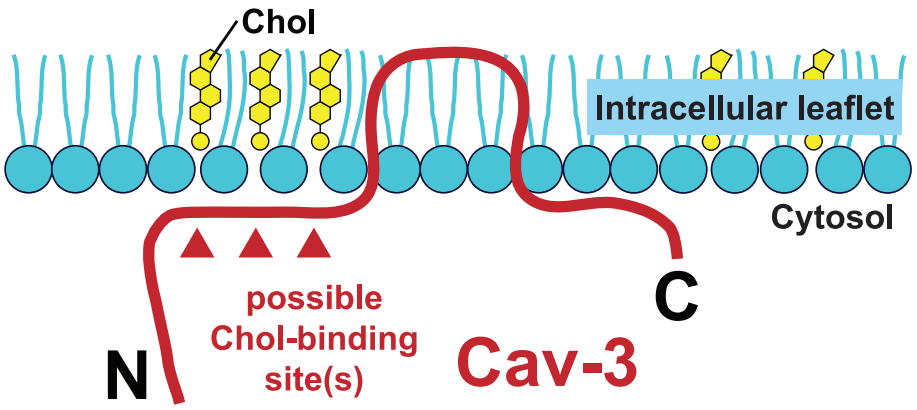

Figure 1.3.: Schematic of the protein Caveolin-3 (Cav-3). The depiction summarizes the assumed structure and membrane location of Cav-3 that are proposed in [167, 168, 169, 170, 140, 164, 166]. Abbreviations: C - carboxyl terminus; Chol - Cholesterol; N - amino terminus. Red triangles indicate possible Chol binding site(s).

a Cholesterol (Chol) binding protein and supposedly binds tightly to Chol in a ratio of at least 1:1 lipid:protein [171, 172]. A study involving the artificial expression of caveolin in a cell system normally lacking caveolae, however, showed that the additional caveolin expression led to a Chol enrichment by a factor of $\geq$ 2 [173]. The exact binding site (or binding sites) of Chol along the Cav-3 protein is not yet unequivocally determined but it is most likely located within the scaffolding domain of the N-terminus [170]. This scaffoldinig region is supposed to bind to the membrane via electrostatic and hydrophobic interactions [167]. In Fig. 1.3, three possible Chol binding sites along the Cav-3

protein are indicated by red triangles.
The Chol binding properties of Cav-3 predict the promotion of Cav-3 protein oligomerization [171]. Indeed, Cav-3 has been shown - based on transmission electron microscopy and single particle analysis - to form nonamers with a radial symmetry (similar to a cartwheel with the C-termini at the axle, the transmembrane domains forming the spokes, and the N-termini forming the wheel's rim) [164]. The Cav-3 nonamers partly reside in the intracellular leaflet of the lipid bilayer, are $\approx$ 16.5 nm in diameter and $\approx$ 5.5 nm in height, with the C-terminus and the N-terminus extending about 1.8 nm and 2.8 nm into the cytosol, respectively.
Many Cav-3 molecules (i.e. between 100 and 200 molecules per caveola [174, 175]) assemble to form (sarcolemmmal) membrane caveolae. Caveolae are shallow membrane invaginations that were first discovered in the 1950s in electron micrographs of blood capillaries and epithelial tissue [176, 177]. After synthesis, Cav-3 oligomerizes in the sarcoplasmatic reticulum, is transported to the Golgi apparatus, then interacts with Chol - eventually, the thus prepared Cav-3/Chol assembly is transported to and integrated into the plasma membrane (being stabilized, among other proteins, by cavin) [178, 179, 180]. Caveolae are very characteristic and easily recognizable membrane structures: they are omega-shaped pits with their neck region featuring a diameter of about 45 nm and their bulbous body being between about 60 - 80 nm in diameter [170]. Both the arrangement of single caveolae that are either in close proximity or that fuse together to form "grape-like" structures have been reported based on electron micrographs and fluorescence microscopy [175, 140] (see also section 3.5 and the Appendix K). Further, regarding striated muscle cells, caveolae are assumed to be the precursor structures for Transverse Tubules (TT) in developing muscle cells [20, 181]. In adult skeletal muscle fibers, Cav-3 has been shown to be present at the TT membrane although the protein is most abundant at the surface sarcolemma [182] and Cav-3 predominantly occurs at the neck regions of TT [183] which might indicate that in mature myocytes the generation of new TT is already terminally concluded.
Caveolae are strongly involved in many specific cellular signaling processes. For example (and especially interesting regarding cardiomyocytes), caveolae are involved in Calcium signaling [184, 185] and endothelial and neuronal Ni-

tric Oxide Synthase (eNOS and nNOS, respectively) signaling [186, 187] (also well reviewed in [165, 188]).
The connection of caveolae to many cellular signaling events is in unison with the enrichment of caveolae with Chol and Chol also being a well-known regulative molecule for signaling processes. Since each Cav-3 molecule tightly binds to one or more Chol molecules, caveolae feature high concentrations of Chol. As mentioned in the last section (section 1.1.1), the highly negative spontaneous curvature of Cholesterol (Chol) causes clusters of Chol to form membrane invaginations, e.g. caveolae. Cav-3 then serves as a scaffolding protein to maintain the integrity of the Chol rich caveolae. Interestingly, in vascular epithelial tissue, the portion of free (i.e. unesterified) Chol that is associated to caveolae (amounting to about 2-5 % of the entire free Chol in the plasma membrane) is exclusively contained in the extracellular leaflet of the lipid bilayer [160] (cf. section 3.1, Fig. 3.2).
The enrichment of Chol in caveolae is typically shown by using a standard protocol for the extraction of Chol from membranes: Chol depletion by Methyl-β-Cyclodextrin [189, 190] (see also section 3.5.1). Chol depletion leads to a disruption of caveolar structures [191] (and other Chol rich membrane structures, e.g. clathrin coated pits [192]) and flattening of the caveolae and thus of the plasma membrane [193, 194]. This effect of caveolar flattening was reported to be reversible by the addition of exogenous Chol [193]. Hence, there is reason to believe that the Chol enriched caveolae at the cellular plasma membrane serve as a membrane (and Chol) reservoir providing additional surface area to allow the cell to expand as a fast response to an external stimulus such as membrane tension caused by cell stretching or cell swelling [195, 142]. This is of particular interest in the study of cardiomyocytes that undergo constant contraction and relaxation cycles. Indeed, caveolae have been shown to be crucially involved in mechanosensation and mechanoprotection, i.e. regulatory mechanisms triggered by the geometrical alteration of a cell's surface [196, 188].
Likewise, membrane repair mechanisms are also potentially mediated by caveolae. In mechanically injured muscle cells, it seems that there is a subsarcolemmal abundance of vesicles that strongly resemble assemblies of fused caveolae [197]. This motivates the hypothesis that myocytes contain an intracellular reservoir of caveolae associated proteins that can be mobilized fast upon in-

cidents of mechanical injury [198, 199]. Since many incidents of heart failure can essentially be traced back to hypertrophy of cardiomyocytes and thus an increased demand of membrane extensibility, caveolae and the proteins and lipids they contain are interesting starting points for therapeutic targeting in the field of molecular medicine [142].
Finally, both over- and under-expression of Cav-3 and thus surplus or lack of caveolae are involved in many pathologies: in cardiac arrhythmias [200, 201] (although cardiac specific overexpression of Cav-3 could also show potential for cardiac protection [202, 203]) and, most prominently, in muscular dystrophies [204, 205, 206, 188]. Regarding muscular dystrophies, an upregulation of Cav-3 expression and an increase in abundance of caveolae have been reported [207, 208, 209]. A fraction (not all) of the cellular Cav-3 content has been shown to co-purify with Dystrophin [204], a product of the Duchenne Muscular Dystrophy gene. Further, (probably also only a fraction of the total) Cav-3 is part of the Dystrophin-Glycoprotein Complex (DGC) [206]. In dystrophic myocytes, the interaction between Cav-3 and the DGC is compromised [208]. The eponymous protein involved in muscular dystrophies, Dystrophin, its connection to Cav-3 and Chol and its association to the cardiac sarcolemma will be introduced in detail in section 1.1.4, together with the most common forms of muscular dystrophies, i.e. Duchenne and Becker Muscular Dystrophy - DMD and BMD, respectively - and their phenotypes.
In the next section, another typically raft-associated lipid shall be introduced first: Ganglioside GM1 (GM1). In the scope of this thesis, to show the association between Chol and Cav-3 nanostructures at the cardiac sarcolemma, an association that has so far been shown mostly biochemically (see this section and section 1.1.1), I will make use of the visualization of GM1 in two-color imaging protocols together with Chol and Cav-3, respectively. Therefore, focus shall be laid first on this lipid which will be called on for the combined sarcolemmal localization of Cav-2 and Chol later on (see also section 3.6).

1.1.3. Ganglioside GM1

Ganglioside GM1 (monosialotetrahexosylganglioside, $C_{77}H_{139}N_3O_{31}$; in the following abbreviated as GM1) is a $\approx$ 1.6 kDa [210] glycosphingolipid, i.e. featuring a hydrophilic oligosaccharide headgroup and a hydrophobic ceramide

tail [211]. Gangliosides were first isolated from ganglion cells of the human brain by the German biochemist Ernst Klenk [212]. Brain tissue is abundant in gangliosides (about 1 - 2 g per kg of brain tissue [213]) but also other types of mammalian cells feature gangliosides as general and intergral part of their plasma membrane [214, 215]. GM1 is considered the "parent" or "prototype" ganglioside because most of the various types of different gangliosides can be chemically derived from GM1 [216, 217]. GM1 is resident in the extracellular leaflet of the mammalian membrane bilayer [218, 219, 220, 221]. From there, its charged polar sugar headgroup protrudes about 2.5 nm into the extracellular space, creating an electric potential with a Debye length of about 1 nm [222, 223]. Fig. 1.4 **A** schematically depicts the chemical structure of GM1 with its hydrophilic oligosaccharide headgroup facing the extracellular space (highlighted in pink) and its hydrophobic ceramide tail that is buried within the plasma membrane (highlighted in blue). A pictographic illustration of GM1 is given in Fig. 1.4 **B**; this illustration will be used to conceptually and schematically visualize GM1 in the specific cardiac membrane models proposed in this thesis (see e.g. section 1.4). Together with other glycolipids

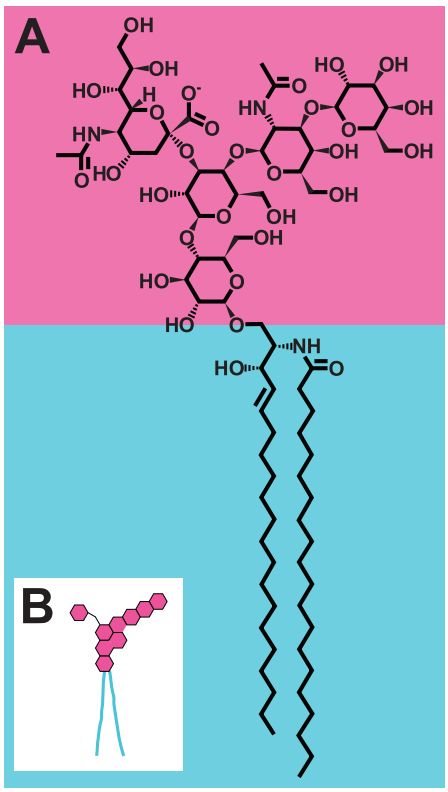

Figure 1.4.: Schematic of the structure of Ganglioside GM1 (GM1). **A** The hydrophilic, polar oligosaccharide headgroup that is facing the extracellular space is shaded in pink; the hydrophobic ceramide tail is shaded in blue. **B** Pictographic illustration of GM1 as it will be used throughout this thesis.

and glycoproteins, GM1 contributes to the formation of the cellular glycoca-

lyx - a nanometer thick coat surrounding many cell types and presenting a unique and cell type specific composition [223, 212]. The glycocalyx of a cell functions like a cellular fingerprint and allows the specialized mutual recognition and the communication between cells. A variety of these communication and signaling processes are mediated by membrane clusters that contain large fractions of GM1 and Cholesterol. These clusters - generally enriched in sphingolipids and Cholesterol [91] and oftentimes referred to as lipid rafts (see also section 1.1) - contribute to the heterogeneous distribution of lipids and proteins along the membrane bilayer and associate to the liquid ordered phase of the lipid bilayer. Effectively, GM1 clusters that associate with the membrane liquid ordered phase summarize highly functional units that are involved in the binding of hormones [224, 225], lectins [88, 226, 212], monoclonal antibodies [227, 228, 215] - but also viruses [229] and toxins [230] (also well summarized in [214]). Specifically, GM1 is the natural receptor of the Choleratoxin [231]: each one of the pentameric Choleratoxin subunit B (CtB) binds with high specificity and affinity [232, 233] to two sugars of the GM1 oligosaccharide headgroup (i.e. sialic acid and galactose [234, 235, 236]). Effectively, one molecule of CtB can bind five molecules of GM1 [97, 221]. Using CtB - in some cases in conjunction with an anti-CtB antibody - is the most common procedure to label membrane GM1, e.g. for immuno-electron microscopy [237] or Atomic Force Microscopy (AFM). As an example, AFM studies of the assembly of GM1 crosslinked by CtB could show that GM1 forms raised domains of 30 - 200 nm diameter in experimental systems of supported lipid bilayers of controlled lipid compositions [89, 90]. Analogous GM1 clustering could be visualized using fluorescence light microscopy via the standard protocol of labeling GM1 by using fluorescently tagged recombinant, i.e. non-toxic, CtB (in combination with an anti-CtB antibody) [92, 219, 95]. Yet, due to the diffraction limited resolution of this imaging approach, the lower limit of the observed GM1 cluster size was typically found to be ≈ 300 nm.

In this thesis, however, the application of subdiffraction STED microscopy of GM1 clusters labeled with fluorescent CtB, revealed variously shaped GM1 clusters at the sarcolemma of living and fixed mouse ventricular cardiomyocytes (VM). These clusters ranged in size between 70 nm up to 1 µm and showed a distinct substructure. Note that although GM1 is typically consid-

ered to be a marker of the liquid ordered membrane phase, it has been proposed that only upon binding of CtB to GM1, the GM1 is redistributed from the liquid disordered phase to the liquid ordered phase [95, 238]. This might be due to the above mentioned cross-linking effect induced by the combination of CtB and anti-CtB for fluorescence tagging of GM1. Nevertheless, since CtB alone can only crosslink GM1 to form at most pentamers, there is reason to assume that the observed > 100 nm large GM1 membrane clusters require a certain degree of pre-existing GM1 clustering - an assembly that is likely Cholesterol mediated [239, 240]. This again would reconstitute the association of GM1 to the Cholesterol rich liquid ordered phase. Further, within the scope of this thesis, fluorescence labeling of GM1 via CtB will be used as a strategy to identify regions of the densely packed Cholesterol rich liquid ordered phase at the sarcolemma of living and fixed VM. Hence, the question whether GM1 naturally resides in the liquid ordered or liquid disordered phase is thus neither directly relevant nor challenging the reliability of the localization of the sarcolemmal liquid ordered phase. Additionally, studies based on immunogold labeling electron microscopy and total internal reflection microscopy have shown that GM1 is concentrated in membrane caveolae [241, 242, 243] (see section 1.1.2). This association of GM1 to both Cholesterol rich membrane domains and caveolae makes the fluorescent GM1-CtB complex a preferred reporter to motivate similarity of Cholesterol clusters in living cardiomyocytes to Caveolin-3 clusters in fixed cardiomyocytes (see section 3.6).

1.1.4. Dystrophin

Dystrophin (Dyst) is a large cytoskeletal and membrane associated protein of 427 kDa which constitutes about 0.002 % of the total protein in striated muscle cells [244, 245]. Dyst is the 3685 amino acid (aa) protein product of the Duchenne Muscular Dystrophy (DMD) gene which is located at band Xp21 on the short arm of the X chromosome and which - with 2.5 Mb - is the largest human gene [246, 245, 247]. Dyst is assumed to be of an elongated, flexible rod shape with an approximate folded contour length of 150 nm [245, 248].
Fig. 1.5 schematically shows the Dyst protein how it is currently perceived in the scientific field. The schematic summarizes the specific protein domains and structure proposed in [245, 249, 250, 251, 247, 252, 253, 254].

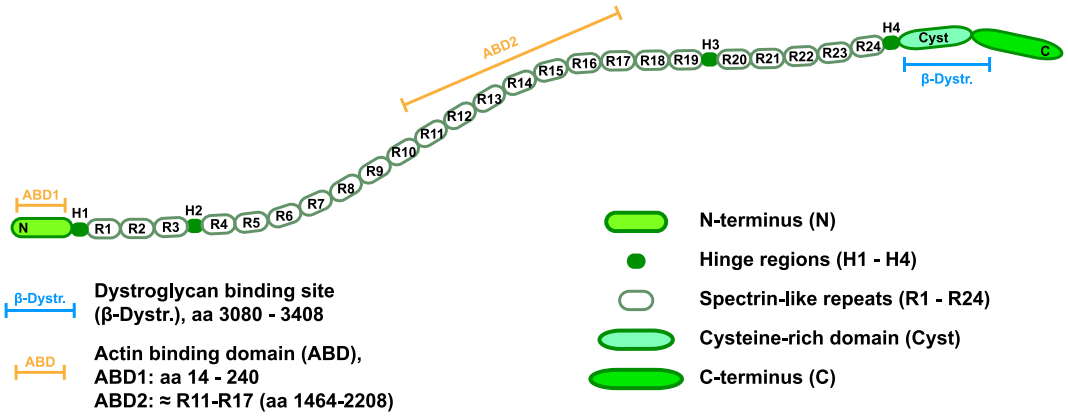

Figure 1.5.: Schematic of the protein Dystrophin (Dyst) summarizing the specific protein domains and structure proposed in [245, 249, 250, 251, 247, 252, 253, 254]. The specific protein domains and binding motifs are denoted in the figure key.

Dyst can be structurally subdivided into four major domains:

1.) The amino terminus (N-terminus or N in Fig. 1.5) comprising aa 1-240 [245] and featuring an (F-)Actin Binding Domain (ABD1) in the region of aa 14-240 [255].

2.) The central rod domain (H1-H4 and R1-R24 in Fig. 1.5) approximately comprising aa 253-3112 and featuring 24 triple helical repeats that resemble the protein Spectrin (R1-R24) [245, 253]. In between the Spectrin like repeats, 4 hinge regions (H1-H4) are distributed: H1 right in front of R1; H2 between R3 and R4; H4 between R19 and R20; H4 behind R24. These hinge regions are assumed to provide the flexibility of the Dyst protein along the region of the rather rigid 24 helical repeats [256]. A second Actin Binding Domain (ABD2) is located along R11-R17 and is supposed to bind Filamentous Actin (F-Actin) monomers in a stoichiometry of 1:24 Dyst:F-Actin - ABD2 is thought to bind F-Actin with a lower affinity than ABD1 in the N-terminus [250, 257, 251, 253]. Further, the Spectrin like repeats R16 and R17 are supposed to bind Nitric Oxide Synthase (NOS) and anchor it to the sarcolemma [258], possible via the interaction of NOS with Caveolin-3 (Cav-3) which is assumed to interact with both endothelial NOS (eNOS) and neuronal NOS (nNOS) [259, 260, 261] and which resides in the intracellular leaflet of the sarcolemma (see section 1.1.2). Note that both eNOS and nNOS are expressed in cardiomyocytes [262, 263]. Further, the Dyst rod domain presents a possible binding motif for mi-

crotubules. This motif is assumed to lie between R20 and H4 but has also been proposed to extend as far as the Cystein rich Dyst domain (see 3.)) [264, 265, 253, 266]; generally, the microtubule binding site(s) can be assumed to lie somewhere between aa 2471-3092.

3.) The Cystein rich domain (Cyst in Fig. 1.5) approximately comprising aa 3080-3360 and carrying a structural motif that binds to β-Dystroglycan of the Dystroglycan complex that resides in the sarcolemma [267, 268]. β-Dystroglycan is connected, via its α domain, to Laminin-2 - an extracellular matrix protein - that in turn binds Collagen. Thus, the Cyst rich domain is anchoring Dyst to the sarcolemma and from there to the extracellular matrix.

4.) The carboxy-terminus (C-terminus or C in Fig. 1.5) approximately comprising aa 3361-3685 and featuring an α_1-Syntrophin and a β_1-Syntrophin binding site [269, 268]. α_1-Syntrophin is assumed to bind NOS [270, 271] which in turn is supposed to interact with Cav-3 (see also 2.).

Summarizing, by binding F-Actin and binding to the Dystroglycan complex, Dyst connects the muscle cytoskeleton to the sarcolemma and, from there, to the extracellular matrix. This makes Dyst an important protein of the costamere - a large protein complex that connects the myofibrils to the plasma membrane [272, 273, 274]. Dyst thus helps provide the transmission of contractile forces originating in the myofibrils to the sarcolemma and is vital for sarcolemmal stability.

Malexpression of Dyst leads to the class of pathologies that gave the protein its name: the (muscular) dystrophies, i.e. muscle-wasting diseases. The most severe form, Duchenne Muscular Dystrophy (DMD), is caused by a complete absence of Dyst expression. DMD affects about 1 in 3,500 newborn boys (since the disease is linked to the X chromosome) [275, 276], leading to confinement of patients to a wheelchair by the age of about 13 and death by the age of about 20 (typically due to respiratory or cardiac failure) [277, 278]. A less pronounced form of muscular dystrophy - Becker Muscular Dystrophy (BMD) - is caused by the expression of smaller, truncated Dyst variants. BMD affects about 1 in 12,000 newborn boys and shows many different pathological phenotypes with varying severity of the disease [279, 280]. Typically, affected individuals show

first symptoms around the age of 17 and have almost average life expectancies [268]. Myocardial pathologies emerge for the majority of both DMD and BMD patients and most often manifest themselves as dilated cardiomyopathy, predominantly left-ventricle dilation [281, 282, 283, 284, 285].
The localization of the DMD gene on the X chromosome was of tremendous importance for the muscular dystrophy research [269]. For both DMD and BMD many possible mutation sites along the DMD gene have now been identified [286, 268]. Investigating the effect of these specific mutations on the Dyst protein functionality is a powerful starting point for the prevention and treatment of muscular dystrophy. Generally, studies of Dyst related pathologies are complicated by the unusually large size of the DMD gene. The pathological effects of Dyst malexpression are typically studied by partial deletion or mutation of specific regions of the gene [254, 287]. Widely used animal models are for example the *mdx* mouse strains that feature different mutations of the DMD gene ([288], see also sections 2.3.4 and 3.8).
Studies of this kind have revealed that there is a relatively large margin of the extent of Dyst expression regarding the proper functionality of the resulting protein product albeit being a truncated variant of the full-length Dyst protein. These findings have opened a fruitful approach to gene therapy based on the generation (and induced cellular expression) of "mini-" and "micro-Dystrophins" that - despite not mimicking the complete Dyst protein (explicitly, they are missing a portion of the Spectrin like repeats) - are capable to adopt the function of Dyst. In mouse models, these Dyst variants have been shown to potentially alleviate dystrophic phenotypes by compensating for the Dyst deficiency [289, 290, 291, 254, 287]. However, such gene therapy might require the introduction of adeno-associated viral vectors to the dystrophic organism in order to deliver the mini-Dystrophin encoding genes (this introduction would be performed by intramuscular injection) [292] - a procedure that could not only result in a profound immune response [293] but would also require tight ethical control.
Further, it is estimated that exon skipping would offer possible gene therapy because although it would result in the expression of truncated (yet, still functional) Dyst variants, it would reconstitute the reading frame of the DMD gene [292]. Other, pharmacological, interventions that have shown some success

to compensate for Dyst malexpression included administration of Gentamicin to patients with mutations in the Dyst gene based on premature stop codons [294], and the pharmacological prevention of the loss of Nitric Oxide which is typically involved in DMD [295].
In addition to Dyst, it has been reported that also the membrane resident protein Cav-3 (see section 1.1.2) is associated with muscular dystrophies. In both DMD patients and in mice of the *mdx*, i.e. dystrophic, strains, Cav-3 is expressed in surplus [207, 296, 209]. This Cav-3 upregulation is assumed to distort the connection between Dyst and the sarcolemma interrupting the sarcolemmal Dyst distribution [205]. On the other hand, however, different muscular dystrophies are associated with a downregulation of Cav-3, e.g. Limb Girdle Muscular Dystrophy Type 1C [297, 298]. All in all, the proper expression of the Dyst protein and the tight regulation of Cav-3 expression seem to be essential for the functional Dyst mediated connection between the myofibrils and the sarcolemma.

In this thesis, the spatial association between Dyst and Cav-3 will be investigated using STED microscopy. The reported association between Dyst and NOS - either via direct binding or mediated by α_1-Syntrophin - and the interaction of Cav-3 and NOS serves as the starting point for the here presented nanoscopic investigations of the mutual spatial arrangement of Dyst and Cav-3 along the cardiac sarcolemma (see also Fig. 1.10 in section 1.4). It has been shown that Dyst is localized to plasma membrane caveolae [208] and recently, Dyst has evolved from being considered to have merely mechanical function in myocytes to actually comprise signaling function as well [271]. This motivates the association of Dyst and sarcolemmal caveolae which are assumed to be cellular signaling hubs. Yet, Cav-3 has also been reported to interact with other membrane associated proteins, e.g. with β-Dystroglycan [299, 300]. The fact that there are different populations of Cav-3 present at the sarcolemma that can be discriminated by the spatial association with certain proteins will be discussed in section 3.7. Finally, this work will present and discuss a possible strategy to visualize the molecular orientation of the Dyst protein along the cardiac sarcolemma by immunofluorescence labeling of different protein domains using specific primary antibodies directed against distinct amino acid sequences of the Dyst protein.

At the end of the day, many questions about the cardiomyocyte-specific, nanoscopic spatial arrangement of the two prominent membrane-associated proteins Cav-3 and Dyst, and the two membrane lipids Chol and GM1 remain. Biochemical methods, for example co-immunoprecipitation (and Western blotting) or mass spectrometry (e.g. SILAC [301]), are precise and powerful techniques to detect *that* specific molecules are associated - but not *how* this association is actually structured and oriented in the cell. Neither do these methods supply information if there is one or more bridging molecules that mediate a certain protein protein association. Thus, biochemical analysis is not enough to shed light on questions about the architecture and topology of associated protein and lipid complexes. Answers will only be found using a combined approach together with imaging, i.e. microscopy, techniques. There exist many different types of microscopy, each of them having their advantages and disadvantages. Generally, for the investigation of membrane domains in living cardiomyocytes, fluorescence light microscopy is the method of choice. This is because fluorescence microscopy is live-cell compatible, can cover large fields of view in all three dimensions, and is highly target-specific when used together with immunolabeling. However, the seemingly perfect match of biological specimen and far-field fluorescence microscopy has a major drawback: resolution. The object resolution that can be achieved using confocal fluorescence microscopy - which is, so far, the sharpest lens-based, and thus diffraction-limited, method in light microscopy - lies roughly at about 200 nm, depending on the wavelengths of fluorescence excitation and detection. This is insufficient to reveal the details of the mosaic of the proteins and lipids that line and shape the cardiac sarcolemma.

As mentioned, the proteins and lipids within and along the cardiac sarcolemmal membrane are nanoscopic, and partially highly dynamic, complexes: a single molecule of Chol has a hydrodynamic radius $R \approx 5\,\text{Å}$ [302], an area of about 32 Å^2 [303, 304] when crystallized, and forms aggregates of $R \approx 10\,\text{Å}$ when at 35 °C at a concentration of 400 mM which corresponds to the standard concentration of ≈ 30 mol % of Chol in the plasma membrane [302]. GM1 micelles have a hydrodynamic radius of about 6 nm [305, 306] and, in supported lipid bilayers, form domains of ≈ 100 nm diameter [90]. Cav-3 is supposed to form nonamers of 16.5 nm diameter [164]. And Dyst, quite large with its

molecular weight of 427 kDa [307], is assumed to have a folded contour length of $\approx$ 150 nm [245, 248].

Yet, abandoning far-field optical microscopy in favor of methods with a much higher resolution but with much harsher sample preparation steps, for example electron microscopy or near-field microscopy, is a great sacrifice for the study of the dynamic and diverse processes in a living cell.

Until the early 1990s, this dilemma remained. A new class of fluorescence-based microscopes made its appearance thereafter. These novel microscopes moved on from the previous endeavors of pushing the diffraction barrier by solely working with its fundamental physical parameters - wavelength, angle of incidence, and index of refraction. In what from the purely physical point of view might almost seem like a hack coming from chemistry, their concept was to exploit the molecular states of fluorophores - "bright" vs. "dark" - by photophysically switching between them and thus markedly reducing the volume of the effective detectable fluorescence, and thereby locating single fluorophores with much higher precision. The principle fundamentally challenged the diffraction barrier - until it crumbled, giving way to unprecedented fluorescence image resolution and coining the term "nanoscopy". By 2014, these former "underdog" methods of super-resolved microscopy had established themselves in the scientific community, had been broadly commercialized and had earned their major developers - Stefan W. Hell, William E. Moerner, and Eric Betzig - the Nobel Prize in Chemistry. Pioneering the field, one of the methods was STimulated Emission Depletion (STED) microscopy which is based on the targeted silencing of excited fluorophores. Since STED microscopy makes use of the most basic molecular transition, i.e. from the ground state to the excited state, it is compatible with many organic fluorophores, fluorescent proteins, and with standard immunofluorescence protocols - without the need for any special sample preparation or treatment with detrimental chemicals. In this thesis, the nanoscopic cardiac membrane composition will be investigated using STED microscopy. The next section will give a detailed introduction to diffraction-limited and subdiffraction fluorescence light microscopy and demonstrate how the field of optical microscopy was revolutionized by subdiffraction imaging techniques, with STED microscopy leading the way.

1.2. STED microscopy

Understanding biological processes and relationships has always relied on visualization. From the depiction of organisms (of the size of $\approx$ 1 m - 1 cm) and cells ($\approx$ 1 µm) to eventually modeling the various shapes of proteins ($\approx$ 1 nm), the scale of biological considerations became smaller and smaller. This extension of the accessible length scales naturally happened in synergy with the technical advancement of the possibilities at hand to image and map, i.e. the resolving power of the available microscopes. By better design, more careful engineering, and more precise manufacturing, the resolving power of optical microscopes could historically be improved more and more.
This is because the resolution of all microscope systems that depend on interrogating the structure of a sample by a focused beam of electromagnetic waves is fundamentally limited by diffraction. Diffraction summarizes the complex alterations of the spatial and frequency pattern of the incident light that occur upon its interaction with an obstacle [308]. Even a small point light source (e.g. a laser beam), after hitting an obstacle, will form a diffraction pattern that will contain additional information about the obstacle - the light source will hence not be point-like any more. Every aperture, lens, mirror etc. within an optical microscope system is such an obstacle. Due to diffraction, it is thus impossible to focus light to an infinitesimally small spot within the investigated sample. Likewise, the signal stemming from an ideal point-like object within the sample will not reach the microscope's signal detecting unit (e.g. the eye, a camera, an avalanche photodiode) as an ideal point-like object be but will smear out in all three dimensions and appear larger than it actually is. The specific three-dimensional diffraction pattern that a point-like object displays when being imaged by a microscope is called the Point Spread Function (PSF). The PSF is a microscope's characteristic response function. In the lateral imaging plane (i.e. the X-Y plane), the PSF corresponds to a circular Airy diffraction image whose central intensity maximum is called the Airy disk. Now, if two equally bright point objects within the imaged sample are very close together, the overlap of their Airy disks at the microscope's detector can result in the two objects to appear as a single one. According to the Rayleigh criterion for minimum resolvable detail [309, 310], a microscope can resolve only those individual features that are at a distance from each other of at least the radius of

the Airy disk.
This immutable barrier that diffraction imposes on the possible resolution of a microscope was formulated by the German physicist Ernst Abbe in 1873 [311]. In 1866, Ernst Abbe had been hired by the entrepreneur and optical manufacturer Carl Zeiss to formulate a theoretical framework, a recipe, how to design and build the highest quality light microscope [312]. In addition to being very successful at his assigned task, he came up with a fundamental law that - admittedly - would nowadays be considered to have "low advertising appeal" for the microscope industry: Abbe's diffraction limit. In a nutshell, it states that two objects can only be discerned by a microscope if they are further apart than about half the wavelength of the particle (including photons) that they are examined with. Explicitly formulated, the approximate lateral resolution Δx and Δy, respectively, and the axial resolution Δz of a microscope are subject to the following relations:

$$\begin{aligned} \Delta x, \Delta y &\approx \frac{\lambda}{2 \cdot n \cdot \sin(\alpha)} \\ \Delta z &\approx \frac{\lambda}{2 \cdot n \cdot \sin^2(\alpha)}. \end{aligned} \tag{1.1}$$

Therein, Δx and Δy denote the full width at half maximum (FWHM) of the two lateral directions, i.e. the directions spanning the focal plane, and Δz denotes the FWHM along the axial direction, i.e. the direction of the propagation of the illuminating light. λ denotes the wavelength of the light used for the investigation of the sample, n is the refractive index of the immersion medium between the objective lens and the sample, and α refers to half of the angular aperture of the objective. In practice, the specific ability of the objective to collect light is given by its Numerical Aperture (NA) which is defined as $NA = n \sin(\alpha)$.
Examining Abbe's formulation of the diffraction limit, two parameters can be optimized to achieve better resolution. First, maximization of the numerical aperture NA: the value of NA depends on the refractive index of the immersion medium. The immersion media with the highest refractive indices available are immersion oils reaching $n \approx 1.51$ which would lead to $NA \approx 1.3$ and thus not a profound increase in resolution compared to a dry objective (with $NA \approx 0.95$). Note that the concept of 4Pi-microscopy introduced by *S. W. Hell* in 1990 [313] which achieves an effective doubling of the numerical aperture by

mounting the sample between two opposing objectives can yield a profound increase of the axial resolution Δz by making use of the interference pattern of the detected signal stemming from the sample. The lateral resolution, however, is not significantly improved in this approach. Second, minimization of the wavelength λ of the employed light. Using short wavelengths, e.g. 400 nm UV light would, under ideal conditions (i.e. $NA \approx 1.3$), lead to a possible object resolution of $d \approx 150$nm - this is not sufficient to resolve subcellular features. Also, for living biological systems, this UV light would be extremely detrimental. Further, UV light needs special optical components to ensure high transmission along the microscope's beam paths.

Also based on the reduction of the sample interrogation wavelength, a major step in increasing image resolution was the introduction of Electron Microscopy (EM) by Ernst Ruska in 1931 [314, 315]. Electrons feature a de Broglie wavelength of about 2.5 pm when accelerated by about 200 keV. And despite the fact that focusing electron beams by electrostatic and electromagnetic lenses results in very small numerical apertures ($NA \approx 10^{-2}$ in transmission electron microscopy), a resolution of about 0.1 nm can be achieved with EM; this is imaging on the atomic scale. Yet, sample preparation for EM includes treatments that are very harsh for the biological system, e.g. fixation with glutaraldehyde, then ultra-thin slicing (cf section 2.10.3) - hence, imaging conditions in EM are certainly no longer physiological. Further, in electron microscopy, image contrast is based on the density of the scattering electrons within the sample. Thus, targeting and highlighting specific structures is not possible. A solution to this is immunoelectron microscopy [316] which is, however, a rather expensive and definitely challenging technique that requires a lot of effort regarding protocol optimization and control experiments.

For completeness, a third strategy to increase the resolution shall be mentioned here: scanning near-field optical microscopy (SNOM) [308]. SNOM is based on avoiding the effect of diffraction by placing the probe (i.e. the light source or a force sensor) closer to the sample surface than half the wavelength. That way, effectively creating the focus next to the structure, there is not enough space for the light waves to spread out due to diffraction and no diffraction pattern is created. However, since they depend on the almost direct contact to the sample, near field methods are restricted to surface sampling and need very

complicated feedback controls to keep the distance from the sample constant. Conclusively, there are very powerful approaches available that can achieve much higher detail resolution than diffraction-limited light microscopy. Nevertheless, (far-field) light microscopy is still the most frequently used imaging modality to study biological systems. With the development of stable running and powerful laser sources, especially fluorescence light microscopy has established itself firmly in the life sciences. This has many convincing reasons:

- Light microscopy is minimally invasive to the sample and thus allows imaging living, dynamic systems.
- Light microscopy is easy to implement at ambient conditions (i.e. temperature, pressure etc.).
- Using fluorescence microscopy in conjunction with fluorescent proteins allows the visualization of specifically tagged proteins in living systems.
- Using fluorescence microscopy in conjunction with immunolabeling allows the visualization of specifically targeted proteins.
- Using fluorescence microscopy allows the simultaneous imaging of different structures in multi-color assays.

Nowadays, one of the most advanced systems in light microscopy - the laser-scanning confocal fluorescence microscope - can almost standardly be found in most life science laboratories. The principle of fluorescence microscopy makes use of the properties of fluorescent dyes (fluorophores): they can be excited with a certain laser wavelength, they will fluoresce at a more red-shifted wavelength which can be detected, and this cycle of excitation and fluorescence can be repeated multiple times.
With the invention of the general concept of immunofluorescence by *Coons et al.* [317, 318] in 1941 which is based on coupling fluorescent dyes to protein specific antibodies to achieve the targeted fluorescent readout of the respectively labeled proteins, fluorescence microscopy quickly became a widely used imaging technique for diagnostics and in the basic research of protein localization and interactions.
Another pioneering advancement in the field was the introduction of the scanning confocal microscope by Marvin Minsky in 1957 [319, 320, 310]. Together

with the appearance of high performance, highly focused laser systems and precise, stable beam and sample stage scanning devices, Minsky's prototype of the confocal microscopy evolved to the phenotype that is predominantly used today and that is displayed schematically in Fig. 1.6. In laser-scanning

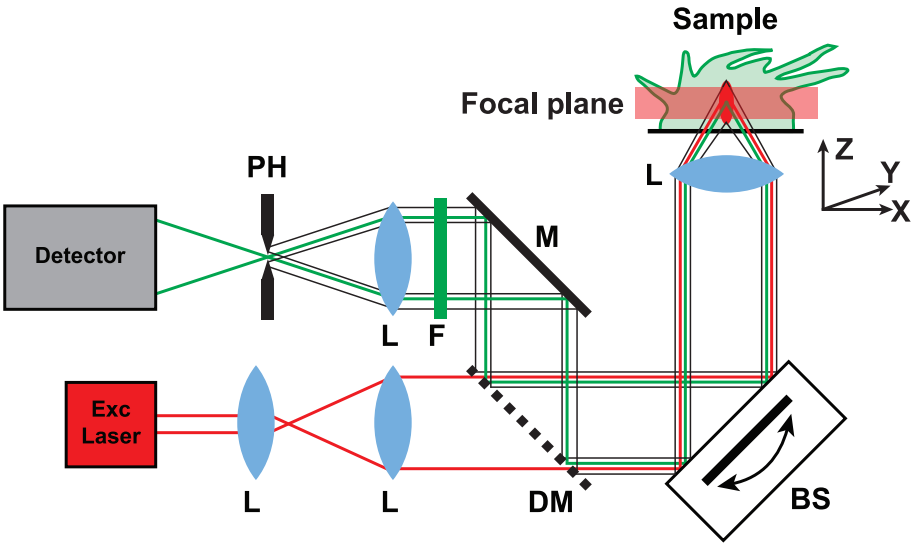

Figure 1.6.: Schematic of a laser-scanning confocal microscope. Abbreviations (in alphabetical order): DM - Dichroic Mirror; Exc - Excitation; F - Filter; L - Lens; PH - Pinhole; BS - Beam Scanner. The fluorescently labeled sample is scanned and excited by a focused laser beam (red beam path) and fluorescence is collected by a detector (green beam path). Fluorescence signal stemming from the out-of-focus regions (black beam paths) are rejected before they enter the aperture of the detector by a pinhole placed in a plane conjugate to the focal plane within the sample. The depicted coordinate system respectively indicates the lateral (X and Y) and axial (Z) directions within the sample with respect to the optical axis.

confocal fluorescence microscopy, the fluorescently labeled sample is scanned and excited by a focused laser beam (displayed in red in Fig. 1.6). The focal spot in the sample is diffraction-limited. Thus, fluorescence signal stemming from both the ideally focused plane (displayed in green in Fig. 1.6) as well as from out-of-focus planes (displayed in black in Fig. 1.6) will propagate towards the detector. However, the confocal pinhole (PH) before the detector in a plane conjugate to the focal plane within the sample, will reject every fluorescence signal stemming from out-of-focus regions. This readily provides for optical sectioning. The procedure of scanning the laser beam over the sample (or moving the sample through the laser focus by stage-scanning, respectively) allows for the pixel based readout of the sample's fluorescence signal.

In summary, the advantages of the labeling specificity, the possibility to image living systems, and the relatively easy implementation make laser-scanning confocal fluorescence microscopy the preferred method to image biological

samples. Of course, it is just as diffraction-limited as every other thus far discussed microscopic technique. But the stated advantages justify why the scientific field was and is so eager to refine fluorescence microscopy to its full potential. Since knowledge is power, it is vital to understand the principles of fluorescence excitation and emission in order to design the optimal fluorescence microscope. After all, it was the knowledge about the energy levels of fluorescent dyes and the knowledge how the transition between these levels can be provoked that, 120 years after Abbe's formulation of the diffraction limit, would give optical microscopy another boost at nanometer resolution.

There exist three basic processes describing the possible interactions between light and atoms or molecules: 1.) absorption, 2.) spontaneous emission, and 3.) induced (or stimulated) emission. These three concepts were formulated within the framework of quantum theory by Einstein in 1916 [321]. In each of the three cases, the energetic state of the atom or molecule is changed, resulting, because of the conservation of energy, in the "consumption" or "production" of photons. When a photon is emitted by a molecule due to its radiative transition from a higher (excited) energy level to a lower energy level, one speaks of photoluminescence. Fluorescence is a special case of photoluminescence in which the radiative transitions occur between molecular energy levels of the same spin multiplicity [308]. Typical organic fluorophores generally make an electronic transition between their singlet ground state and their first excited singlet state when absorbing a photon [322] - and then make a transition back from the first excited singlet state to the singlet ground state via spontaneous emission of a photon, known as fluorescence. Another possible process causing the fluorophore to transition from its first excited singlet state back to its singlet ground state is by stimulated emission.
Fig. 1.7 schematically displays the basic principle of photon absorption (i.e. excitation), spontaneous emission (i.e. fluorescence) and stimulated emission. To demonstrate these principles, a simplified model of a fluorescent molecule is shown consisting of two energy levels: the dark ground state (the molecular "Off" state) $\mathbf{S}_0$ and the fluorescent first excited state (the molecular "On" state) $\mathbf{S}_1$. The ground and the first excited state are both accompanied by higher energy vibrational levels (S_0^{vib} and S_1^{vib} in Fig. 1.7, respectively). The energy difference between the ground state $\mathbf{S}_0$ and its corresponding vibrational lev-

els S_0^{vib} is very small. Likewise, the energy difference between the first excited state $\mathbf{S}_1$ and its corresponding vibrational levels S_1^{vib} is very small as well. The fluorescent molecule can thus transition between S_0^{vib} and $\mathbf{S}_0$ (and between S_1^{vib} and $\mathbf{S}_1$, respectively) via nonradiative relaxation - a process called "internal conversion". This typically happens on a time scale on the order of a few picoseconds [323]. In Fig. 1.7, the nonradiative relaxation is indicated by black arrows.

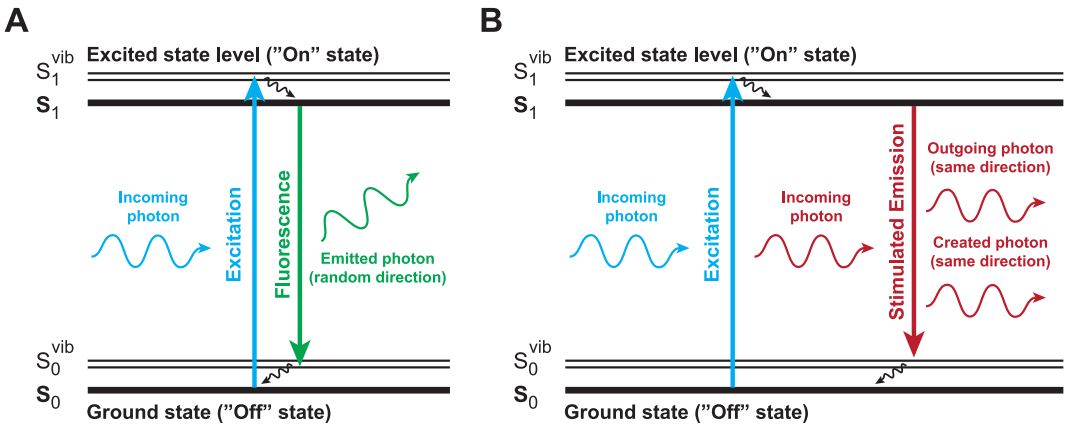

Figure 1.7.: Schematic energy level diagram of the processes of excitation, fluorescence and stimulated emission. The schematic shows the simplified model of a fluorescent molecule assumed to comprise two (singlet) energy levels. $\mathbf{S}_0$ and S_0^{vib} denote the ground state and higher vibrational levels of the ground state, respectively. $\mathbf{S}_1$ and S_1^{vib} denote the first excited state and higher vibrational levels of the first excited state, respectively. Black arrows indicate nonradiative relaxation. **A** The principles of molecular excitation (in blue) and fluorescence (in green). **B** The principles of molecular excitation (in blue) and stimulated emission (in red).

Fig. 1.7 **A** summarizes one complete excitation-emission duty cycle of a fluorescent molecule. First, via absorption of a photon, the molecule is excited and transitions from its ground state $\mathbf{S}_0$ to one of the short-lived vibrational levels of the first excited state, i.e. to S_1^{vib}. In this process (shown in blue in Fig. 1.7 **A**), the energy of the absorbed photon matches the energetic gap between $\mathbf{S}_0$ and S_1^{vib}. After the fast nonradiative relaxation from S_1^{vib} to $\mathbf{S}_1$, the molecule will spontaneously and radiatively transition from $\mathbf{S}_1$ back to one of the vibrational levels of the ground state, i.e. to S_0^{vib}. This transition comprises the process of fluorescence in which bridging the energy gap between $\mathbf{S}_1$ and S_0^{vib} results in the emission of a photon carrying this energy difference. The photon is emitted in a random direction (depicted in green in Fig. 1.7 **A**). Since the energy gap between $\mathbf{S}_1$ and S_0^{vib} is smaller than that between $\mathbf{S}_0$ and S_1^{vib}, the fluorescence photon has a longer wavelength than the initial, exciting photon. From the state S_0^{vib}, the fluorescent molecule will now - again via nonradiative relaxation

- return to its ground state $\mathbf{S}_0$ and is in princinple ready to be excited again. The fluorescence life time of a typical organic fluorophore, i.e. the characteristic time it takes for an excited molecule to emit the fluorescence photon, is generally on the order of 2 - 10 ns [308].
The number of possible duty cycles that a fluorophore can perform is limited by the process of photobleaching. Photobleaching occurs when the population of fluorophores that can return to the energetic ground state is decimated by permanent photochemical destruction of individual fluorescent molecules [324]. Photochemical destruction can happen to the molecule from one of its excited singlet energy levels and also from one of its excited triplet energy level (which is usually reached by a molecule in the excited singlet state via intersystem crossing). Photochemical destruction will not happen to fluorophores in the energetic ground state. After photobleaching, fluorescent molecules are irreversibly excluded from the excitation-emission cycle. Thus, for fluorescence microscopy, the number of duty cycles that a fluorescent molecule can undergo before it succumbs to photobleaching is an important sign of quality: the more often a dye can be excited - and thus emit fluorescence and thus yield fluorescence signal - the better suited it is for imaging.
To complete the set of the three possible optical transition processes that Einstein described in 1916, Fig. 1.7 **B** schematically displays the process of stimulated emission. In stimulated emission, the interaction of a photon within an already excited molecule results in the induced transition of that molecule back into its energetic ground state. For stimulated emission to happen, the molecular system has to be already prepared to be in the excited state. That is after excitation from $\mathbf{S}_0$ to S_1^{vib} and after nonradiative relaxation from S_1^{vib}, the molecule is prepared in the state $\mathbf{S}_1$. Now, instead of spontaneously returning back from $\mathbf{S}_1$ to S_0^{vib}, the transient interaction with another photon can instantaneously induce this transition. In this case, the photon needs to have the necessary energy to bridge the gap between $\mathbf{S}_1$ and S_0^{vib}. Then, if the additional photon transiently interacts with the molecule, the molecule will return to S_0^{vib}, thereby emitting a photon of the energy that matches the energetic gap between the states $\mathbf{S}_1$ and S_0^{vib}. Explicitly, the emitted photon will be of the same wavelength as the one that initialized the process of stimulated emission. Since the emission stimulating photon only transiently interacts with the

molecule, it will leave the molecule along the same direction of propagation along which it arrived. The photon emitted by the molecule will be coherent to the incident photon and propagate in the same direction. In Fig. 1.7 **B**, the process of stimulated emission is displayed in red. Effectively, one will be left with two coherent photons that propagate in the same direction: stimulated emission is the underlying working principle of a laser.
These are the three basic tools at hand to harvest the chemical properties of fluorescent molecules for light microscopy: excitation, fluorescence, and stimulated emission. Ingeniously combining these three tools to manipulate and influence the energy state that a dye is in during the time of fluorescence read-out by a microscope lead to the clever *de facto* circumvention of the diffraction limit and to the advent of superresolution optical microscopy.

In 1994, *Hell and Wichmann* envisioned using the process of stimulated emission to design a fluorescence microscope that would eventually break Abbe's diffraction barrier - not by bending the laws of Physics but by employing the basic chemical properties of fluorescent molecules: the fact, that they can be switched "On" and "Off" [325]. The idea of the targeted photoswitching of fluorophores resulted in the concept of STimulated Emission Depletion (STED) microscopy.
STED microscopy is a special case of the concept of Reversible Saturable Optical Fluorescence Transition (RESOLFT) microscopy [326, 327]. As the name implies, the principle of RESOLFT microscopy is based on the reversible saturation of one of the specific energy levels of the fluorophores in a specimen. The molecular energy level can correspond to a dark state (the "Off" state) or a state from which a radiative transition would be possible (the "On" state). In any case, the saturated molecular state is externally induced while the depleted state serves as the information read-out channel. Typically, the molecular dark state is saturated [328, 329, 330, 331, 332] because saturation of the excited state [333, 334] is more vulnerable to increased levels of noise.
In essence, by the controlled saturation of specific molecular states, the concept of RESOLFT allows the targeted preparation of the ensemble of fluorophores in a specimen into a portion that is "Off" and a portion that is "On" - like a light switch. The degree of saturation of the molecular state - i.e. the effectiveness of the light switch - depends on the energy that is added to or taken from the

molecular system. This energy can be controlled by adjusting the power of the illuminating light sources that can induce specific state transitions, i.e. by the intensity of the laser light with which the sample is irradiated. Further, the region in which the optical state transitions are induced can be controlled by spatially modulating the illumination pattern.

STED microscopy is the first and the most straightforward implementation of RESOLFT type microscopy. In STED microscopy, the molecular ground state (i.e. the dark state) of a fluorophore is saturated by making use of the principle of stimulated emission. A STED microscope is basically an enhanced laser-scanning confocal microscope (see Fig. 1.6). Because to achieve the saturation of the molecular dark state, an additional laser beam (hereafter referred to as the STED laser) is overlaid with the excitation laser beam of the confocal microscope, both laser beams are focused into the sample, and the sample is scanned. The circularly polarized STED laser features a spatially modulated light pattern: a helical phase ramp from 0 to 2π, typically created by a vortex phase plate placed in the STED laser beam path, shapes the lateral intensity distribution of the STED laser into a ring with an intensity zero in the center. This characteristic intensity distribution is the so-called STED "doughnut" - an expression that has gained some popularity and which will be used hereafter as well to describe the specific appearance of the STED laser beam (in the lateral direction).
Fig. 1.8 shows the calculated PSFs for a typical STED microscope featuring a helical phase ramp from 0 to 2π in the STED laser beam path. The PSFs are displayed in the lateral plane (X-Y-plane) and in one of the axial planes (X-Z-plane), respectively. Fig. 1.8 **C** shows the ideal spatial alignment of the excitation and STED laser beam in all three dimensions that is generally pursued when building and aligning a STED microscope.
Both the excitation and the STED laser beam PSFs are diffraction-limited. However, aligning excitation and STED laser beam and simultaneously scanning the fluorescent sample with both focused lasers results in an effective STED PSF that is diffraction-unlimited. The effective STED PSF is displayed in Fig. 1.8 **D** and features a FWHM of about 40 nm, i.e. a factor 6 smaller than in the confocal case.
This remarkable increase in resolution beyond Abbe's diffraction limit (see

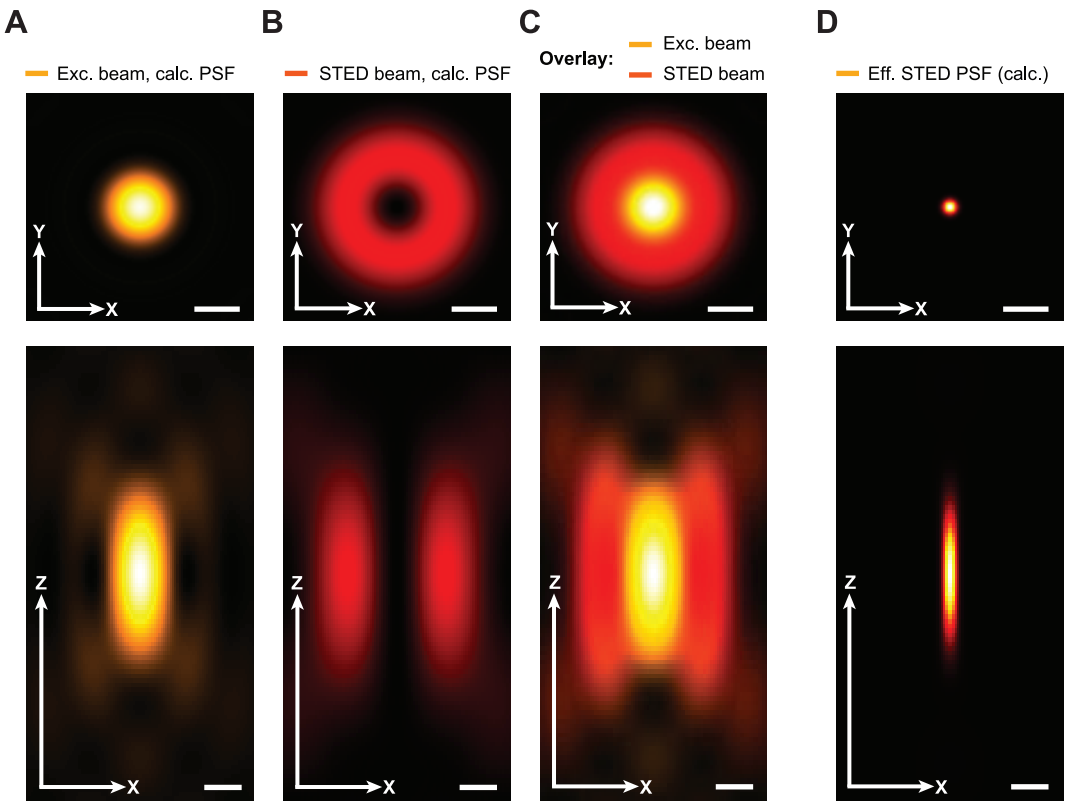

Figure 1.8.: Calculated Point Spread Functions (PSF) for a STED microscope featuring a helical phase ramp from 0 to 2π in the STED laser beam path, i.e. a doughnut shaped light distribution in the lateral imaging plane (X-Y-plane). The calculated PSFs in the lateral plane (X-Y-plane) and in one of the axial planes (X-Z-plane) are displayed, respectively. The PSFs are radially symmetrical along the axial direction. **A** The calculated PSF of the Gaussian shaped excitation laser beam, assuming an excitation wavelength of 532 nm. **B** The calculated PSF of the initially Gaussian shaped, circularly polarized STED laser beam, assuming a wavelength of 775 nm. **C** Overlay of the excitation and STED laser beams from **A** and **B**. **D** Effective PSF of the STED microscope, assuming fluorescence detection at 580 nm, a numerical aperture of the objective of $NA \approx 1.2$ and a saturation factor of $\zeta = 50$. Scale bars: 200 nm.

Eqs. 1.1) stems from the forced optical transition from the excited to the ground state of those fluorophores within the diffraction limited focal spot of the excitation laser that are at the same time (in fact, within a certain time frame after the arrival of the excitation laser pulse at the sample) illuminated with the STED laser beam. A portion of the fluorophores in the "On" state will be switched into the "Off" state - and another portion of fluorophores will not be switched off and thus stay in the "On" state. The efficiency of the switch-off depends on the STED laser intensity: The higher the intensity of the STED laser light, the higher is the probability of stimulated emission and the more fluorophores will be switched off. Since the STED doughnut features an intensity zero at its center, no fluorophores will be switched off there - those fluorophores are the ones recorded by the fluorescence detection; those fluorophores are the

ones that yield the effective information for the image acquisition.
Thus, the combination of two diffraction-limited focused laser beams results in the STED laser intensity dependent reduction of the sample volume contributing to the fluorescence signal. Summarizing, the effective lateral resolution of a STED microscope (along the X-direction) can be expressed by [335]

$$\Delta x_{\mathrm{STED}} \approx \frac{\Delta x}{\sqrt{1+(\Delta x)^2 a^2 (I_{\mathrm{STED}}/I_{\mathrm{Sat}})}} = \frac{\Delta x}{\sqrt{1+(\Delta x)^2 a^2 \zeta}} \tag{1.2}$$

where Δx_{STED} is the FWHM along the X-direction in STED illumination mode, Δx is the FWHM along the X-direction in confocal mode (see also Eqs. 1.1), and a is the steepness of the intensity distribution between the doughnut rim and the doughnut zero along the X-direction. I_{STED} denotes the intensity of the STED laser beam in the sample and I_{Sat} denotes the effective saturation intensity, i.e. the STED laser intensity that is necessary to switch off half of the fluorophores in an ensemble (I_{Sat} is an intrinsic property of a given fluorophore; a low I_{Sat} typically results in a favorable switch-off behavior of a dye for STED microscopy applications). These two figures can be summarized by the saturation factor $\zeta = I_{\mathrm{STED}}/I_{\mathrm{Sat}}$. In Fig. 1.8 **D**, the effective STED PSF was calculated for an assumed saturation factor $\zeta = 50$. For large saturation factors, Δx_{STED} becomes independent of Δx and one can write [335]:

$$\Delta x_{\mathrm{STED}} \approx \frac{1}{a\sqrt{\zeta}}. \tag{1.3}$$

As can be seen from Eq. 1.2, the achievable lateral resolution in STED microscopy is in principle unlimited. Factors influencing the achievable resolution in reality are the switch-off behavior of the used fluorophores, the available STED laser intensities, the photobleaching behavior of the fluorophores, and the steepness of the pattern used for spatial light modulations - but none of these factors pose a fundamental limit. Regarding the STED laser source, using STED lasers operated in both pulsed mode [330, 336] and continuous wave (CW) mode [337, 338] has resulted in high quality subdiffraction images. Typically, to achieve the same spatial resolution, the laser power in CW mode has to be larger by about a factor of 3 than the time-averaged power in pulsed mode (assuming a laser repetition rate of about 80 MHz and a pulse length of 250

ps) [337, 339, 340]. Both the application of pulsed and CW STED lasers has its advantages and disadvantages: CW STED lasers are easier to implement in an optical setup, are easier to maintain, and offer larger flexibility regarding available wavelengths. Pulsed STED lasers on the other hand typically yield better image resolution at lower time-averaged intensities and are thus less invasive with respect to photobleaching of fluorophores and heat induced damage to the specimen. The implementation of fluorescence time gating for CW STED applications has, however, proven to be a very feasible strategy to achieve high resolution at lower STED powers [338, 341]. The principle and implementation of fluorescence time gating for CW STED microscopy is described in more detail in section 1.3.

Beside the choice of the STED laser source, many other successful approaches to optimize the implementation of STED microscopy have been and are being investigated across various scientific areas, i.e. the development of refined imaging setups [342], new fluorophores [343, 344], and staining protocols [345]. So far, the focus has been on the explicit improvement in lateral resolution in STED microscopy. Note that by using a helical phase ramp, the axial resolution of the STED microscope is not enhanced but equals that of the corresponding confocal image. A 3D STED "doughnut" is typically realized by splitting the STED beam into two perpendicularly polarized beams using a polarizing beam splitter [339, 346, 347]. One beam is then directed through a vortex phase plate, the other beam is directed through an axial phase plate which features a layer of mineral (typically cryolite) of a certain thickness that causes a phase shift of the STED beam along the optical axis. After passing the respective phase plates, the two STED beams are recombined by another polarizing beam splitter. The resulting STED beam profile has an intensity zero both in the lateral plane and along the optical axis. The combination of the lateral and the axial phase plates results in a trade-off between achievable lateral and axial resolution since the intensity of the initial STED beam has to be split between the lateral doughnut and the axial doughnut. This splitting can be adjusted by a half-wave retarder plate in front of the first polarizing beam splitter to tune the ratio of the intensity of the vertically and the horizontally polarized portion of the STED laser beam. The optimal intensity distribution is about 70 % vs. 30 % for helical phase plate vs. axial phase plate [348]. An alternative approach to

achieve a 3D STED effect included the implementation of adaptive optics for wave front shaping [349].

Apart from the targeted read-out approach in STED microscopy, there are also other types of subdiffraction optical microscopy.
One alternative relies on the stochastic read-out of fluorophores or subdiffraction proteins. Here, the superresolution is achieved by "thinning out" the population of simultaneously emitting fluorophores. This is done by using only low light intensities to excite the fluorophores such that only a fraction of the whole ensemble of possible emitters transitions to the excited energy state. The cycle of partial activation and read-out is repeated until every fluorophore is terminally photobleached. The final image is then reconstructed by considering the signal from every cycle of excitation and read-out and assigning every detected signal per cycle a location within the field of view. Thus, the achievable resolution with these techniques depends on the accuracy of the localization of individual fluorescent molecules and hence on the number of duty cycles a fluorophore can undergo before photobleaching, i.e. on the number of emitted photons per molecule. Examples of these stochastic approaches are PhotoActivated Localization Microscopy (PALM) invented by *Betzig et al.* in 2006 [350], STochastic Optical Reconstruction Microscopy (STORM) developed by *Rust et al.* in 2006 [351], and (GSDIM) introduced by *Hell et al.* in 1995 [352, 353]. As opposed to STED microscopy which is a direct imaging technique, the stochastic read-out methods have the drawback that in addition to a quite extended image acquisition time, they require algorithm based image post-processing to reconstruct the image.
Finally, another option of subdiffraction optical microscopy, the concept of saturated structured illumination (SSIM), put forward by *Gustafsson* in 2005 [333], shall be mentioned here in brief. Here, the fluorophores in the sample are illuminated with a spatially modulated light pattern in the wide-field mode and tuning the excitation to the level of fluorophore excitation. The overlay of the actual sample structure and the patterned illumination will lead to Moiré fringes between the two structures that encode higher spatial frequencies, i.e. structural detail. The direct image read-out is the outline of the sample structure (a "negative" image) which then has to be deconvolved to yield the actual sample structure. While this concept has the advantage of not relying on fo-

cused light and hence being a parallelized method, it also has the drawback of necessary algorithm-based image post-processing.

Just like the above mentioned subdiffraction imaging methods, STED microscopy has now officially arrived in the scientific community as well as in the industrial sector. There is no longer the need to simultaneously show a STED image with its confocal counterpart to justify the data's scientific reliability or to stress the increase in object resolution. The coming of age of STED microscopy is ushering in a new era of formulating new biological questions - and of revisiting already decade old ones - under the light of subdiffraction resolution and the possibilities that it brings about. Some very impressive and biologically relevant results arising from STED microscopy investigations shall be mentioned in the following.
In the field of virology and the basic research on the Human Immunodeficiency Virus type 1 (HIV-1), the application of STED microscopy unraveled that upon maturation, the viral envelope glycoprotein will cluster, thereby augmenting the capability of the virus to invade the host cell [354].
In structural biology, the eight fold symmetry of proteins of the cellular Nuclear Pore Complex (NPC) could be visualized [336], thus enabling the protein targeted structure resolution of the NPC in unison with and to accompany studies based on, for example, cryoelectron tomography, X-ray crystallography, and Nuclear Magnetic Resonance (NMR) spectroscopy [355, 356, 357].
In structural neuroscience, the striped arrangement of axonal Actin structures in living cultured rat neurons could be revealed [345, 358], an arrangement that had so far only been shown in fixed cells [359] or could only be hypothesized based on electron micrographs [360].
In live-organism neuroscience, STED microscopy could be applied to visualize the structurally dynamic behavior of dendritic spines and the rearrangement of Actin structures in the brain of living mice in real time [361, 362, 363].
Of special importance for this thesis, in the field of cardiovascular research, STED microscopy was successfully applied to study the remodeling of Transverse Tubules in living mouse ventricular cardiomyocytes in a disease model of myocardial infarction [22, 23] (see also section 1.1 for more detail).
Note that this is by far not a comprehensive listing since many new insights made possible by STED microscopy are constantly being published.

Further, STED microscopy has been successfully combined with other powerful imaging techniques such as Atomic Force Microscopy (AFM) [364, 365], Electron Microscopy (EM) [366], Fluorescence Correlation Spectroscopy (FCS) [98, 367] (see also section 1.1), and Two-Photon-Excitation (2P-Exc) microscopy [368, 369].
Hence, with an ingenious and basically more and more refinable underlying principle, a rapidly evolving field of convincing and impressive applications, and the possibility to match and control experimental findings with other powerful imaging approaches, STED microscopy has established itself firmly among the staple techniques of biological imaging.
In this thesis, the subdiffraction imaging and study of membrane lipid and membrane protein clusters in cardiomyocytes were of particular interest. The conducted studies brought about new labeling, imaging and image analysis techniques. The advantages of 2P-Exc microscopy in conjunction with STED microscopy were explored and utilized to achieve three-dimensional (3D) imaging of membrane structures in living mouse ventricular cardiomyocytes (see also sections 3.4 and 3.4.3).

1.3. Two-Photon-Excitation-STED microscopy

The theoretical foundation of two-photon excitation dates back to 1931 when the physicist Maria Göppert-Mayer in her doctoral dissertation theoretically predicted that in one quantum event, a molecule could absorb two photons, thereby being excited to an energy level which is the sum of the energy of the two photons. Göppert-Mayer gave her thesis the wonderful title - here freely translated from German - "About elementary processes with two quantum leaps" [370].
In Fig. 1.9, the principle of Two-Photon Excitation (2P-Exc) and the ensuing process of fluorescence (i.e. spontaneous emission) are schematically depicted for a fluorescent molecule comprising two energy levels: the dark ground state level ($\mathbf{S}_0$, the molecular "Off" state) and the fluorescent first excited state ($\mathbf{S}_1$, the molecular "On" state). S_0^{vib} and S_1^{vib} denote the higher vibrational levels of the ground state and the first excited state, respectively. The 2P-Exc process is depicted in red, the process of fluorescence is depicted in green, and black ar-

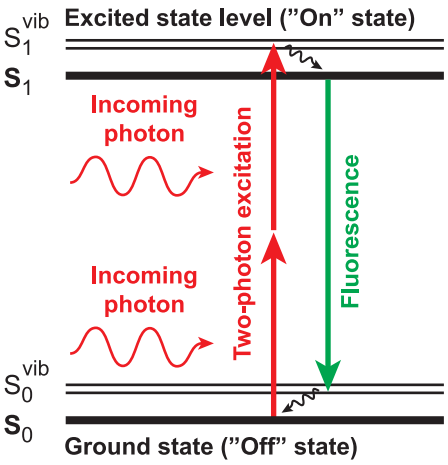

Figure 1.9.: Schematic energy level diagram of the process of Two-Photon Excitation (2P-Exc) and the ensuing fluorescence relaxation of a fluorescent molecule. A two-level energy system was assumed for the fluorescent molecule. $\mathbf{S}_0$ and S_0^{vib} denote the single ground state and higher vibrational levels of the singlet ground state, respectively. $\mathbf{S}_1$ and S_1^{vib} denote the singlet first excited state and higher vibrational levels of the singlet first excited state, respectively. The 2P-Exc process is displayed in red, the fluorescence process (i.e. spontaneous emission) is depicted in green; black arrows indicate vibrational energy relaxation.

rows indicate vibrational energy relaxation from higher vibrational levels back to the first excited state or back to the ground state, respectively. For the fluorophore transition from the ground state to the excited state, the two simultaneously absorbed photons have to deliver an energy of

$$\Delta E = E_{\mathbf{S}_1} - E_{\mathbf{S}_0} \approx 2\frac{hc}{\lambda_{2P}} \tag{1.4}$$

with $E_{\mathbf{S}_1}$ and $E_{\mathbf{S}_0}$ being the first excited state and ground state energy, respectively, h being Planck's constant, c being the speed of light, and λ_{2P} being the wavelength of each of the two photons absorbed in the 2P-Exc process.
In a microscope setup making use of 2P-Exc, the following relationship for the number of absorbed photons per fluorophore per laser pulse, N_{abs} would apply [371, 372]:

$$N_{abs} \approx \frac{P_0^2 \delta}{\tau_P f_P^2} \left(\frac{\pi (NA)^2}{hc\lambda_{2P}} \right)^2 \tag{1.5}$$

with P_0 being the average laser intensity, δ being the fluorophore's two-photon absorption cross section at the 2P-Exc wavelength λ_{2P}, τ_P and f_P being the pulse duration and the repetition rate of the excitation laser source, respectively, and NA being the numerical aperture of the microscope's objective lens. h and c are Planck's constant and the speed of light, respectively. From equation 1.5, it follows that in 2P-Exc microscopy, the intensity of the emitted fluorescence of a dye molecule depends quadratically on the excitation intensity [373].

The simultaneity of the two-photon absorption process requires the two photons to be absorbed during the Heisenberg uncertainty principle time of $\approx 10^{-16}$ s. Thus, efficient 2P-Exc requires very high photon densities of about $10^{32}/\text{cm}^2$ [374]. For practical fluorescence imaging applications, this puts a vital demand on the illumination source: providing extremely high peak powers per sample area - typically in the range of about 10 GW/cm² [375] - while at the same time avoiding damage of the sample. Pulsed lasers with pulse lengths in the region of $\approx$ 100 fs and $\approx$ 80-100 MHz repetition rate (e.g. Titanium:Sapphire lasers) can supply the necessary peak powers without delivering the detrimental thermal load to the samples.
Therefore, the application of the proposed principle of 2P-Exc for fluorescence microscopy needed to await the advent of bright and stable laser sources supplying the necessary photon density to achieve a sufficient two-photon absorption cross section [374]. Then, in 1990, combining laser scanning microscopy and a femtosecond pulsed laser, *Denk, Strickler, and Webb* first applied the technique of two-photon laser scanning fluorescence microscopy to image DNA in living pig kidney cells [371].
Since then, Two-Photon Excitation (2P-Exc) microscopy has become widely used and favored in the life sciences, especially for 3D imaging deep inside living cells. This is due to the three major advantages of 2P-Exc microscopy:

1.) In 2P-Exc microscopy, the optical sectioning effect which in confocal microscopy can only be achieved via the confocal pinhole (see section 1.2), comes for free since the quadratic dependence of the fluorescence signal on the excitation intensity substantially decreases the effectively fluorescing sample volume. Hence, background signal from out-of-focus planes is eliminated without having to sacrifice precious fluorescence signal [376].

2.) Second, due the "virtual pinhole" inside the focal plane caused by the 2P effect, also those fluorescence photons that are scattered within the specimen on their way back through the objective lens can be detected and are not rejected by a physical confocal pinhole [376]. This is particularly useful for imaging deep within thick and strongly scattering samples, e.g. biological tissues, and additionally supported by the longer illumination

wavelengths used in 2P-Exc applications because the degree of scattering is inversely proportional to the wavelength.

3.) Third, photobleaching of the used fluorophores and photodamage to the specimen are reduced because longer wavelengths are used for fluorophore excitation and because the region of laser light absorption is confined to the focal plane since only there, at the excitation laser focus, the absorption cross section is large enough to provide fluorophore excitation [371].

Of course, the concept of fluorophore excitation by the simultaneous absorption of multiple photons can and has already been extended to three-photon absorption processes for biological imaging [377, 378] and even four-photon absorption [379], although the latter has so far remained rather exotic but may prove useful for the investigation of the properties of semiconductors.
Regarding the usable fluorophores for 2P-Exc microscopy applications, basically all dyes that are standardly used for one-photon excitation microscopy can be used under 2P-Exc conditions - of course, more or less efficiently, depending on their 2P absorption efficiency, i.e. the 2P cross section of the respective dye. While the emission spectra of fluorophores are essentially unchanged under one-photon vs. 2P-Exc conditions, the absorption spectra can show profound blue-shifts in the 2P-Exc case compared to one-photon excitation [380, 381, 382]. It can thus not be readily assumed that the optimal 2P-Exc wavelength for a given fluorophore whose one-photon absorption spectrum is known simply corresponds to twice the wavelength of the one-photon absorption maximum. The optimal 2P-Exc wavelength for a given fluorophore in a given specimen thus has to be determined experimentally.

2P-Exc microscopy could successfully be applied to visualize and unravel astonishing biological relations [383, 384]. Especially in the neurosciences, 2P-Exc microscopy is a staple method for imaging all the intricate details deep inside the brain - partly even in live, freely moving animals [385, 386, 387, 388]. But also in developmental biology [389, 390, 391] and in materials science [392, 393, 394] 2P-Exc microscopy are now a standard method.
However, it has to be kept in mind that the resolution of a 2P-Exc microscope is about the same as that of a standard "perfect" (i.e. pinhole $\ll$ one Airy

Unit diameter) confocal microscope. In fact, 2P-Exc microscopy features even worse resolution because of the necessary application of longer wavelengths for fluorophore excitation (see also the equations 1.1 in section 1.2). If an object cannot be resolved by a confocal microscope, then the 2P-Exc microscope will not resolve it either. Nevertheless, because of the above mentioned three major advantages of 2P-Exc microscopy, it is still better suited than confocal microscopy for imaging specific biological samples.
Note also that the excitation power densities necessary for a sufficient absorption cross section are significantly higher for 2P-Exc than for one-photon excitation, corresponding to $\approx$ 10 GW/cm^2 as compared to $\approx$ 1 MW/cm^2 [373] (also observed from one-photon excitation vs. 2P-Exc experiments of the same specimen conducted in this thesis). This can undo the benefits of reduced sample bleaching in out-of-focus planes and, in the worst case, lead to increased photobleaching and photodamage. Several studies have thus investigated the effect of the relatively high 2P illumination intensities on the sample quality, especially cell/organism longevity in live-cell experiments using 2P-Exc microscopy. Generally, the parameters that actually define the fitness or quality of a biological sample have to be determined very specifically with respect to the specimen under consideration and then lay the foundation for appropriate control experiments. For example, examining the continued normal development of mammalian embryos, *Squirrell et al.* could show that repetitive sample scanning with 2P-Exc even over a period of 24 h did not compromise the developmental stages - opposed to analogously performed one-photon excitation scanning which lead to the inhibition of embryo development already after 8 h [395]. Likewise, the unimpaired function of pancreatic islets [396] and the viability of cultured cells [397] in 2P-Exc imaging experiments could be verified. However, 2P-Exc processes are assumed to be the major cause of photodamage to a specimen scanned with laser radiation within the wavelength range between 700 and 1000 nm [398]. All in all, it is important to find the lowest 2P-Exc illumination power that yields both a sufficiently high signal-to-noise ratio and at the same time limits damage to the biological system - typically employed 2P-Exc powers ($\approx$ 5 mW measured right at the sample) can fulfill both these prerequisites [399]. And since the fluorophores in the out-of-focus sample planes do not interact with the 2P-Exc light, they are spared the detrimental

effects of photobleaching and possible photodamage. This will be of particular importance when combining 2P-Exc microscopy and STED microscopy which will be discussed next.

Regarding the further improvement of spatial resolution in 2P-Exc microscopy, several successful approaches have been demonstrated. For example, 2P-Exc microscopy has been combined with structured illumination microscopy (SIM) and thus achieved an improvement in the lateral resolution by a factor of ≈ 2 [400]. In 2009, the combination of 2P-Exc and STED microscopy (from here on referred to as 2P-Exc-STED) was first reported by *Moneron et al.* who could show lateral structure resolutions down to 80 nm in fixed mammalian cells immunofluorescently labeled for the protein complex NF-κB [368]. This corresponds to an improvement in lateral resolution by a factor of 4 compared to conventional 2P-Exc microscopy. Also in 2009, 2P-Exc-STED imaging of pyramidal neurons identified within hippocampal brain slices, loaded with a fluorescent dye solution, and recorded at an imaging depth of between 45 and 80 µm, *Ding et al.* could show lateral structure resolutions of $\approx$ 280 nm, corresponding to a 3-fold resolution improvement over 2P-Exc microscopy [369]. Further, 2P-Exc-STED could be shown to also be used in conjunction with fluorescent proteins. In 2009, *Li et al.* tagged the protein Caveolin-1 in Chinese Hamster Ovary cells with the green fluorescent protein derivative EGFP and, using 2P-Exc-STED, achieved a structural resolution of about 70 nm [401].
Since these first applications of 2P-Exc-STED microscopy in biological imaging, 2P-Exc-STED microscopy has been successfully applied predominantly to visualize topological features in the mammalian brain: axons, dendrites, pyramidal neurons - all under physiological conditions [402, 403, 404].
When designing a 2P-Exc-STED microscope, the researcher can typically make a choice whether to use a STED laser operated in pulsed or continuous wave (CW) mode. Deciding for a pulsed STED laser has the advantage that it provides a higher signal-to-noise ratio and leads to a more confined focal spot in which fluorescence is still possible compared to using a CW STED laser [348]. This effectively results in a more efficient fluorescence switch-off of the dye molecules and thus comparatively lower illumination intensities focused into the sample in the case of a pulsed STED laser as compared to a CW STED laser (see also section 1.2). However, pulsed lasers are more expensive than

CW lasers. Further, incorporating a pulsed STED laser in a 2P-Exc microscope can be quite challenging since both the laser pulses stemming from the 2P-Exc source as well as the STED laser pulses have to be temporally synchronized, a procedure that has to be performed as a part of the daily microscope alignment. Also, the optimal synchronization depends on factors like the lifetime of the used dye in a specific sample - a property that is influenced by the dye environment, i.e. the sample medium or the sample substrate, resulting in having to adjust the proper laser pulse synchronization using the actual sample; at least when wanting to ensure optimal sample imaging conditions [402].
In contrast, the technical realization of combining 2P-Exc and STED microscopy using a CW STED laser (an imaging modality from here on referred to as 2P-Exc-CWSTED) is very straightforward: starting from a standard designed 2P-Exc microscope, an additional CW STED laser featuring the distinct "doughnut-shape" (see section 1.2) is coaligned with the 2P-Exc laser and the sample simultaneously scanned with the two focused laser beams (see also section 2.1.1 for the 2P-Exc-CWSTED system custom-built in this thesis). However, as mentioned in section 1.2 and in the last paragraph, using a STED laser operated in CW mode results in having to apply higher illumination powers to the sample compared to the case of using a pulsed STED laser to achieve the same gain in resolution. Additionally, the recorded images feature a lower signal-to-noise ratio [341].
Therefore, it has been found that time gating of the detected fluorescence signal stemming from the scanned sample brings about a tremendous improvement in both image resolution and background noise suppression [405, 338, 406, 341, 407] - and this applies to both one-photon-excitation-CW-STED as well as 2P-Exc-CWSTED applications. In brief, the concept of time gating makes use of the fact that the effective excited-state life time of a dye molecule depends on its position within the STED "doughnut's" illumination pattern, i.e. on the intensity of the light that leads to stimulated emission. The higher the STED laser intensity "seen" by the fluorophore, the longer its effective excited-state life time. Accordingly: the closer a fluorophore is located to the center of the STED laser, the longer its effective excited-state life time. Selecting for the long-lived excited-state dye molecules for fluorescence recording means selecting for the dye molecules close to the center of the STED beam - thus spatially confin-

ing the spot from which the fluorescence is recorded and thereby enhancing resolution (and decreasing unspecific background signal). In principle, a fluorescence time gate is implemented by first setting the time of arrival of the excitation laser pulses as a relative and periodic reference point for the fluorescence photons recorded by the detection device. With respect to this reference point, only those photons that were detected after a certain time T_{Gate} (the "gate delay") after the excitation laser pulse are accepted to contain information for image acquisition. The photons that arrive before T_{Gate} are rejected. Note here that fluorescence time gating will sacrifice a portion of the detected fluorescence photons. It is therefore important and highly advisable to adjust the fluorescence time gate precisely . This is typically done by aiming to set the time gate such that optimal image resolution and signal-to-noise ratio are achieved. The gate delays for many of the organic fluorophores in this thesis that have proven to be suitable for 2P-Exc-CWSTED are within the range of 2 - 3 ns (see also section 3.4.2).
Finally, regarding the choice of suitable fluorophores for 2P-Exc-CWSTED, no comprehensive studies stating the ideal 2P-Exc wavelength and illumination conditions, and the performance under 2P-Exc-CWSTED conditions of standard used STED microscopy compatible dyes has been conducted until now - a shortcoming that will be remedied in this thesis (see section 3.4.2).

Conclusively, 2P-Exc-CWSTED microscopy is also a promising approach to image living isolated cardiomyocytes in 3D. First, because cardiomyocytes are quite large cells, e.g. mouse ventricular myocytes measure about $20\,\mu\text{m} \times 20\,\mu\text{m} \times 80\,\mu\text{m}$ – 3D imaging of whole cardiomyocytes thus necessarily results in deep-tissue imaging. Second, because cardiomyocytes feature their Transverse-Axial Tubular System (TATS, see section 1.1) that basically presents channels that are filled with aqueous culture medium, and because they also feature an abundance of mitochondria. This results in many interfaces inside the cells at which scattering events are very likely. These limitations regarding image quality are best compensated for by the 2P-Exc-CWSTED imaging protocol. Based on the known facts as well as the hypotheses about the distinct cardiac membrane organization and based on the two types of STED microscopy techniques (i.e. STED and 2P-Exc-CWSTED) that have here been introduced in brief, the overall aim of this thesis shall be formulated in the next section.

1.4. Aim of this thesis

The aim of this thesis is the generation of a comprehensive cardiac sarcolemmal membrane model localizing and structurally relating Cholesterol (Chol), Caveolin-3 (Cav-3), Ganglioside GM1 (GM1), and Dystrophin (Dyst), thereby focusing on the specific membrane architectures and sarcolemmal nanopatterns that these lipids and proteins form - individually and mutually associated. The generation of this cardiac membrane model is based on, will be investigated with and verified by single- and multi-color STED and 2P-Exc-CWSTED microscopy.

The here proposed cardiac sarcolemmal membrane model is summarized in Fig. 1.10. This model comprises the cardiac membrane structures of caveolae and Transverse Tubules (T-Tubules) as well as the possible mutual arrangement of Chol, Cav-3, GM1, and Dyst at the sarcolemma. Note that the model is not drawn to actual proportions nor correct stoichiometry. The enrichment of Chol and GM1 at the membrane of caveolae lined by Cav-3 is schematically depicted; possible binding sites for Chol along the Cav-3 protein are indicated by red triangles (see also sections 1.1.1, 1.1.2, and 1.1.3). The location of possible F-Actin, Nitric Oxide Synthase (NOS), Dystroglycan (including the α and β subunit), and Syntrophins (Syntr., including α_1- and β_1-Syntr.) binding sites along the Dyst protein are shown based on the information presented in section 1.1.4. Note here that in this model, NOS comprises both endothelial NOS as well as neuronal NOS since they are both expressed in cardiac tissue (see section 1.1.4). The possible association between Dyst and Cav-3 mediated via interaction with NOS and located to the Dyst rod domain and the Dyst C-terminus (C) are suggested (question marks). The potential binding sites for microtubules at different locations long the Dyst protein (see section 1.1.4) are depicted (question marks) but will not be investigated within the scope of this thesis. Finally, the following molecular orientation of the Dyst molecule is proposed and displayed in the model: a) the Cystein rich and the C-terminal protein domains are located closest to the sarcolemma (and to Cav-3), b) there is a possible close proximity between the rod domain (at the Spectrin like repeats R17-R18, i.e. the potential NOS binding site, see section 1.1.4) and Cav-3 at the sarcolemma, and c) the N-terminus (N) of the Dyst protein is located further away from the sarcolemma (and the therein residing Cav-3).

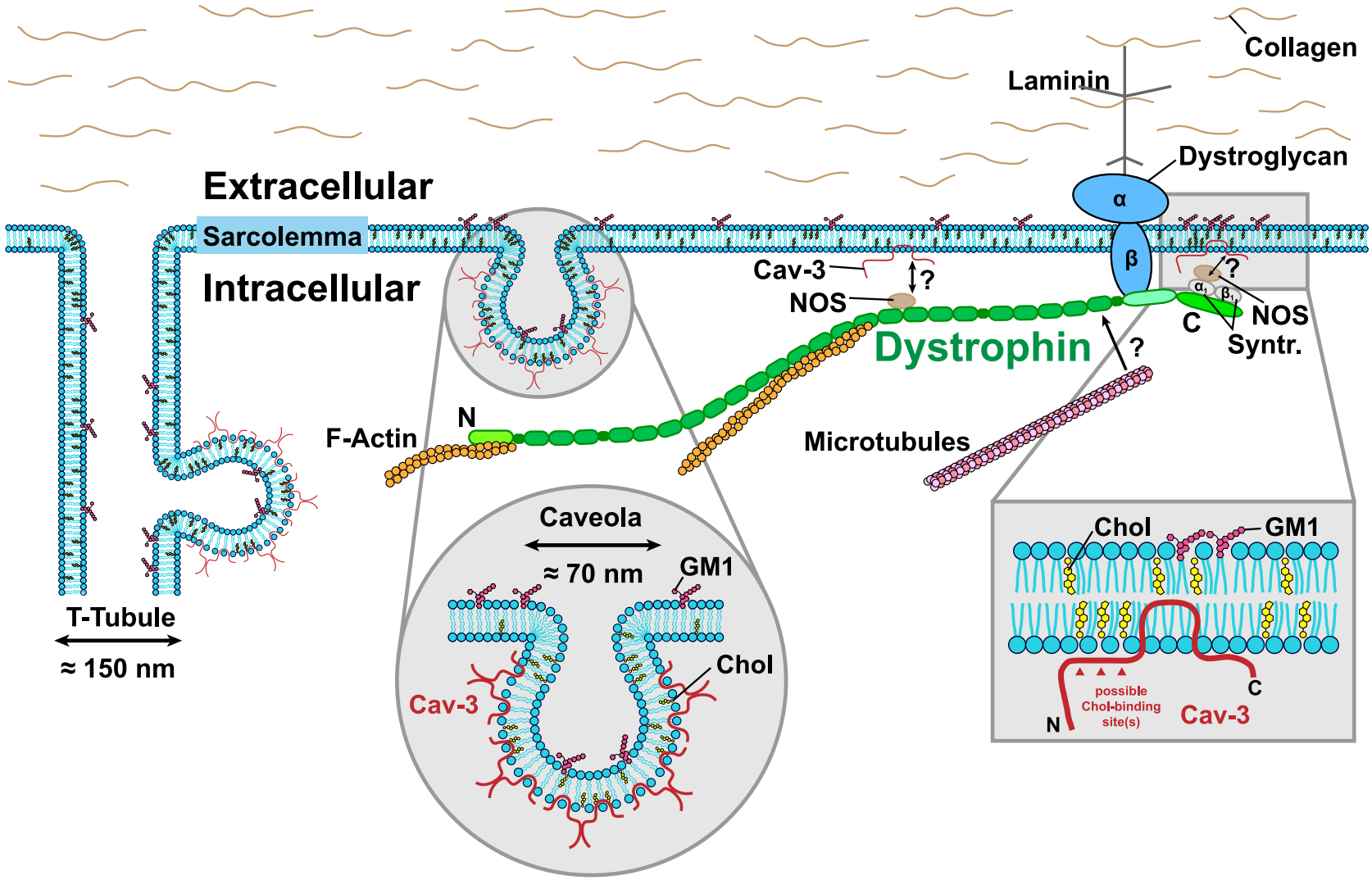

Figure 1.10.: The cardiac membrane nanodomain model proposed in this work. This membrane model is focusing on the two sarcolemmal lipids Cholesterol (Chol) and Ganglioside GM1 (GM1), and on the two sarcolemma-associated proteins Caveolin-3 (Cav-3) and Dystrophin (Dyst). Question marks indicate so far unknown association or interaction. Additional abbreviations: C - Dyst C-terminus; F-Actin - Filamentous Actin; N - Dyst N-terminus; NOS - Nitric Oxide Synthase; Syntr. - Syntrophins (α_1 and β_1, respectively); T-Tubule - Transverse Tubule. Neither drawn to actual proportions nor with correct stoichiometry.

In summary, this thesis will address the following topics and present strategies for their investigation:

1.) To allow fluorescent labeling of Chol rich membrane nanodomains for STED and 2P-Exc-CWSTED microscopy imaging, a new class of variously colored fluorescent Cholesterol analogs will be introduced and a general protocol for cardiomyocyte labeling will be established.

2.) To enable three-dimensional subdiffraction imaging of whole mouse ventricular cardiomyocytes (VM), the design and construction of a 2P-Exc-CWSTED microscope will be outlined together with an overview of suitable fluorophores.

3.) To relate the sarcolemmal signal structures of the associated proteins and lipids Chol/GM1, Cav-3/GM1, and Cav-3/Dyst, two-color imaging protocols for STED microscopy will be established and analyzed quantitatively.

4.) To develop a model for the molecular orientation between Cav-3 and Dyst, and to resolve the molecular orientation of the complete Dyst protein along the sarcolemma, three-color imaging protocols for STED microscopy with a single STED laser wavelength will be established based on the targeted labeling of specific protein epitopes via different primary antibodies.

2. Experimental methods and techniques

For providers and order numbers of used chemicals, equipment, and antibodies, please refer to Appendix A. Appendix B contains a comprehensive, tabular overview over all the images presented throughout this thesis; the table explicitly summarizes which microscopes were used and which parameters were set for image acquisition.

2.1. Microscope setups

2.1.1. Custom-built Two-Photon-Excitation-CW-STED (2P-Exc-CWSTED) microscope

The following experiments were conducted using a Two-Photon-Excitation-CW-STED (2P-Exc-CWSTED) microscope setup that was custom-built within the scope of this thesis:

- Investigation of the effect of the repetition rate (rep rate) of the 2P-Exc laser on the photobleaching behavior of fluorophores in 2P-Exc and 2P-Exc-CWSTED applications (specifically: 1 GHz vs. 800 MHz rep rate, see section 3.4.1).

- Screening and evaluation of organic fluorophores for their suitability in Two-Photon-Excitation-CW-STED microscopy applications (see section 3.4.2).

- Three-dimensional (3D) imaging of membrane and Cholesterol structures in living mouse ventricular cardiomyocytes (VM) (see section 3.4.3).

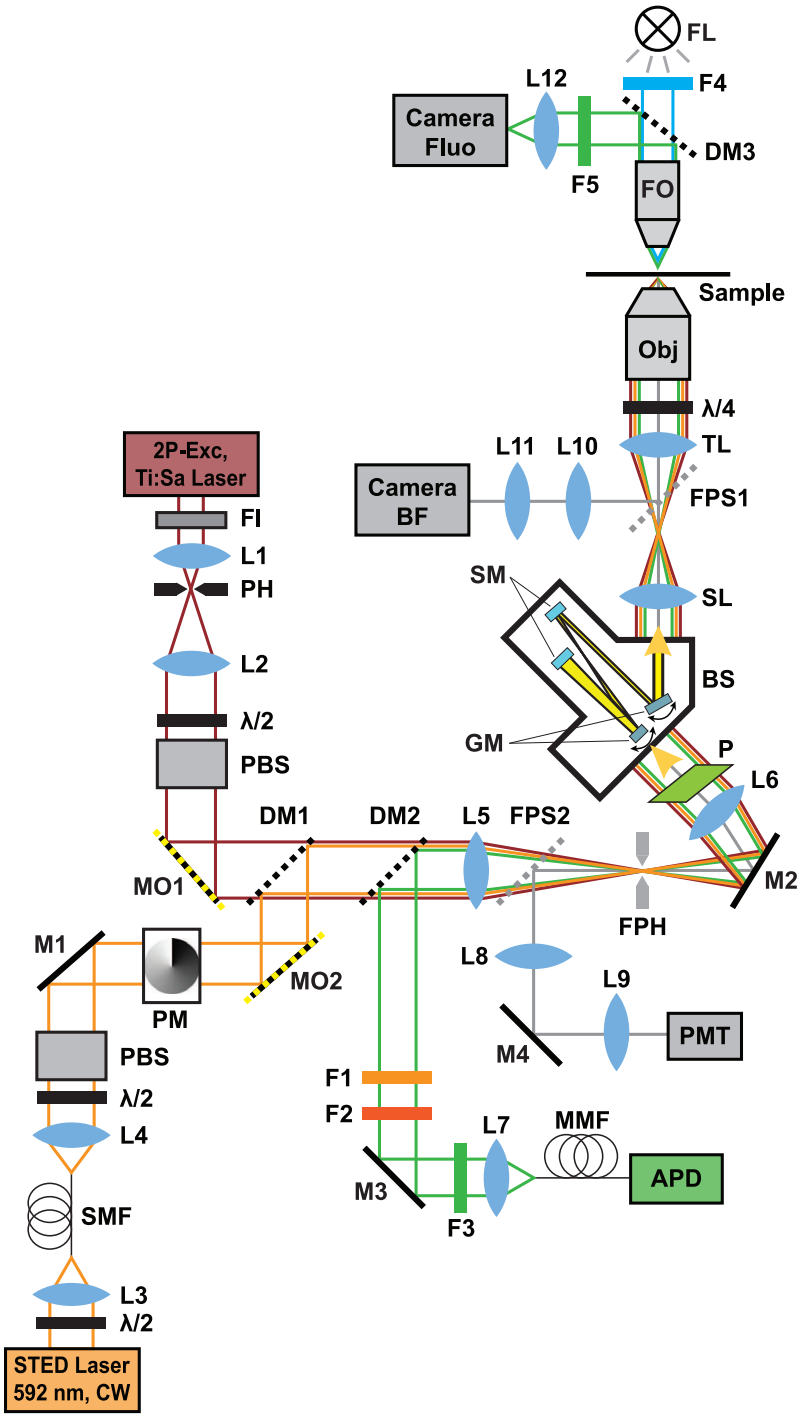

Figure 2.1.: Scheme of the custom-built, Two-Photon-Excitation-CWSTED (2P-Exc-CWSTED) microscope (see also section 3.4.3). Abbreviations (in alphabetical order): 2P-Exc - Two-Photon-Excitation; APD - Avalanche Photo Diode; BF - Bright Field; BS - Beam Scanner; DM - Dichroic Mirror; F - Filter; FI - Faraday Isolator; FL - Fluorescence Lamp; Fluo - Fluorescence; FO - Fluorescence Objective; FPH - Flippable Pinhole; FPS - Flippable Pellicle Beam Splitter; GM - Galvanometer Mirror; λ /2 - Half-Wave Retarder Plate; λ /4 - Quarter-Wave Retarder Plate; L - Lens; M - Mirror; MMF - Multi Mode Fiber; MO - Mirror for beam Overlay; Obj - Objective; P - Periscope; PBS - Polarizing Beam Splitter Cube; PH - Pinhole; PM - Phase Mask; PMT - Photomultiplier Tube; SL - Scan Lens; SM - Spherical Mirror; SMF - Single Mode Fiber (polarization maintaining); Ti:Sa - Titanium Sapphire; TL - Tube Lens.

The 2P-Exc-CWSTED microscope is schematically depicted in Fig. 2.1 and described in the following, making implicit use of the nomenclature and abbreviations introduced in the scheme.
The setup was built from scratch and designed to meet the specific requirements imposed by live cardiomyocyte imaging for biological studies. Special attention was paid to the provision of fast workflow for the experimenter. This was done to ensure optimal cell quality within the physiologically relevant time window of approximately 5 hours after cardiomyocyte isolation (see section 2.3.1), and to achieve high throughput of investigated cells per prepared sample. Further, the 2P-Exc-CWSTED setup comprised both bright field as well as fluorescence widefield imaging channels that could be operated simultaneously. This allowed direct feedback to control the cardiomyocyte quality: regular striations and sharp cell edges could be confirmed in the bright field channel, and even distribution of the membrane stain and the absence of vesicle formation could be confirmed in the fluorescence widefield channel. Both the bright field and the fluorescence widefield channels were realized by focusing the light from a fluorescence lamp (FL, Leica EL6000 LQ-HXP 120, Leica Microsystems, Wetzlar, Germany) into the sample in an upright fashion using a 10x, 0.25 NA air objective (FO, 038712, Spindler & Hoyer, now Qioptiq Photonics GmbH, Goettingen, Germany). For the bright field channel, after passing the microscope objective (Obj), a portion of the light was reflected onto a CCD camera chip (Camera BF) via a flippable pellicle beam splitter (FPS1, BP145B1, Thorlabs, Munich, Germany). For the fluorescence widefield channel, the light from the fluorescence lamp first passed a bandpass filter (F4, 488/50 BrightLine HC, F39-486, AHF Analysentechnik, Tuebingen, Germany) and a short pass dichroic beam splitter (DM3, T500SPXR, F48-499, AHF Analysentechnik, Tuebingen, Germany) before entering the air objective. The fluorescence from the sample was collected by the air objective and reflected by the above mentioned dichroic beam splitter (DM3). The fluorescence light then passed a bandpass filter (F5, ET535/70m, Chroma Technology, Bellows Falls, VT, USA) and was focused onto a CMOS camera (Camera Fluo, DMK 72BUC02, The Imaging Source GmbH, Bremen, Germany). With both the bright field and the fluorescence widefield channels, intact cells could be found fast and positioned coarsely using a motorized XY-translation stage for inverse microscope setups

(SCAN IM 130 × 100-1 mm with TANGO controller, 00-24-546-0000 and 00-76-150-1802, Maerzhaeuser Wetzlar GmbH, Wetzlar, Germany).

The 2P-Exc-CWSTED microscope setup was designed as an inverse microscope. Two-Photon Excitation (2P-Exc) was provided by a tunable, mode-locked Titanium:Sapphire laser (2P-Exc Laser Ti:Sa, Mai Tai, Newport Spectra-Physics, Darmstadt, Germany) with a pulse width of 100 fs and a repetition rate of 80 MHz. The total of all optical components in the laser beam path introduced positive group velocity dispersion and thus resulted in pulse spreading. Therefore, the 2P-Exc laser pulse width was controlled right before entering the microscope objective with an autocorrelator (pulseCheck, APE Angewandte Physik & Elektronik GmbH, Berlin, Germany) and amounted to 300 fs which provided a sufficient two-photon absorption cross section. The laser was operated within the wavelength range of 730 - 850 nm. A Faraday Isolator (FI, FI-820-5SV-BB, Linos via Qioptiq Photonics GmbH, Goettingen, Germany) was placed in front of the laser output aperture to avoid back reflections into the laser head. The 2P-Exc laser light was operated in a free beam mode to provide the high illumination peak powers necessary for efficient 2P-Exc. Hence, the beam profile was laterally cleaned up with a 100 µm mechanical pinhole (PH) positioned at the focus of a telescope lens system (L1 and L2) and controlled to have a Gaussian profile using a CCD camera beam profiler (BC106N-VIS/M, Thorlabs, Munich, Germany). Vertical linear polarization of the 2P-Exc laser beam as well as laser power control was provided by a combination of a half-wave retarder plate ($\lambda/2$, RAC 4.2.15, B. Halle Nachfl. GmbH, Berlin, Germany) and a polarizing beam splitter (PBS, PTW 1.20, B. Halle Nachfl. GmbH, Berlin, Germany). The 2P-Exc laser beam could be precisely aligned with the STED laser beam using a dielectric mirror positioned in a conjugated plane of the focus of the microscope objective (conjugated planes are indicated by dashed yellow lines in Fig. 2.1).

The STED light was provided by a continuous wave visible fiber laser at a wavelength of 592 nm (STED Laser 592 nm CW, 2RU-VFL-P-1500-592, MPB Communications Inc., Montreal, Quebec, Canada). The polarization of the STED laser beam was adjusted with a half-wave retarder plate ($\lambda/2$, RAC 3.2.15, B. Halle Nachfl. GmbH, Berlin, Germany) before being coupled into a polarization maintaining single mode fiber (SMF, P3-488PM-FC-2, Thorlabs,

Munich, Germany). After the fiber, the beam was collimated by an achromatic lens (L4). Vertical linear polarization and and laser power control were provided by a combination of a half-wave retarder plate (λ /2, RAC 3.2.15, B. Halle Nachfl. GmbH, Berlin, Germany) and a polarizing beam splitter (PBS, PTW 20, B. Halle Nachfl. GmbH, Berlin, Germany). The STED beam then passed a vortex phase plate (PM, VPP-A1, RPC Photonics, Rochester, NY, USA) which generated the typical toroidal lateral intensity distribution used in STED microscopy (the so-called "STED Doughnut"). The STED laser beam could be precisely aligned with the 2P-Exc laser beam using a dielectric mirror positioned in a conjugated plane of the focus of the microscope objective (conjugated planes are indicated by dashed yellow lines in Fig. 2.1). The STED laser beam was coupled into the common beam path with the 2P-Exc beam by a dichroic mirror (DM1, DCLP660DCXR, F25-660, AHF Analysentechnik, Tuebingen, Germany).

The spatial alignment of the 2P-Exc and the STED beam was performed on a daily basis prior to an experiment as described in section 2.10.1. In brief, a calibration sample of ⌀ 80 nm gold beads was illuminated with the two laser beams and the back-scattered signal from an individual bead recorded with a photomultiplier tube (PMT, H10723-20, Hamamatsu, Herrsching am Ammersee, Germany). To that end, a flippable pellicle beam splitter (FPS2, BP145B1, Thorlabs, Munich, Germany) was placed in the reflection path of the optical setup and the gold bead signal focused onto the PMT. The aligned 2P-Exc and STED beam passed another telescope lens arrangement (L5 and L6) and were vertically shifted by a custom-built mirror periscope (P) to enter the input aperture of the beam scanning unit (BS, YANUS IV, Till Photonics via FEI Munich, Graefelfing, Germany) without angular tilt. The beam scanning unit deflected the beams in two directions using two galvanometer mirrors (GM). The two galvanometer mirrors and two additional spherical mirrors (SM) were arranged in a 4f-configuration inside the beam scanner. The galvanometer mirrors are thus imaged onto each other which prevents a lateral shift of the laser beams during scanning. After the beam scanning unit, a matched pair of a scan and a tube lens (obtained from Leica Microsystems, Wetzlar, Germany), and the microscope objective were positioned such that the second galvanometer mirror of the beam scanning unit is imaged into the back aperture of the objective.

Circular polarization of both beams was adjusted with a quarter-wave retarder plate ($\lambda/4$, 4.4.15, B. Halle Nachfl. GmbH, Berlin, Germany) right in front of the microscope objective. The circular laser beam polarization, especially for the STED laser beam, was checked with a polarization analyzer (SK010PA-VIS, Schaefter + Kirchhoff GmbH, Hamburg, Germany) positioned in the backfocal plane of the objective. The 2P-Exc laser beam and the STED laser beam were focused into the sample by a water immersion objective equipped with a correction collar (HCX PL APO 63x/1.20 W Corr CS, Leica Microsystems, Wetzlar, Germany). The correction collar was adjusted for the # 1.0 coverslips on which the ventricular mouse cardiomyocytes were typically plated for imaging (see sections 2.3 and 2.10.1). Coarse axial positioning of the objective was provided by a custom-built socket equipped with a micrometer screw. For axial fine positioning and axial scanning of the sample, the objective was mounted into a (MIPOS 100 SG, piezosystem jena GmbH, Jena, Germany).
The fluorescence signal from the sample was collected by the objective and reversely passed through the above described laser beam path, thus being descanned by the beam scanning unit, and was coupled out of the beam path by a dichroic mirror (DM2, DCXR580DCXRU, on request, Chroma Technology, Bellows Falls, VT, USA). A notch filter and a shortpass filter were placed in the fluorescence signal path to filter possible residual laser light stemming from STED and/or excitation beam (F1, 612/SP, F37-612, and F2, F40-593, AHF Analysentechnik, Tuebingen, Germany). After passing a fluorescence bandpass filter (F3) that could be adjusted according to the respectively used fluorescent dye in the sample, the fluorescence signal was focused into a multi mode optical fiber (MMF, M42L01, Thorlabs, Munich, Germany) that was connected to an avalanche photo diode (APD, SPCM-AQRH-13-FC, Perkin Elmer, Fremont, CA, USA) for detection. The fluorescence signal was recorded using time gated detection (see section 1.3). For the realization of the time gated detection, a home-built constant fraction discriminator (CFD) was triggered by a reflection of the pulsed 2P-Exc laser beam directly at the laser output, thus picking up the temporal information about the 2P-Exc pulse arrival time. The temporal information from the CFD served as a reference input signal for a home-built time delay unit. The time delay unit was installed downstream of the APD output signal, i.e. the detected fluorescence photons. Thus, the

time delay unit imposed a time gate on the fluorescence signal that could be adjusted regarding both the time delay with respect to the 2P-Exc pulses, and the width of the time gate. For the coarse adjustment of the appropriate time gate settings, the fluorescence signal from a dye solution (Alexa Fluor 488, see section 2.5.2) was detected and visualized by a Time-Correlated Single Photon Counting (TCSPC) system (PicoHarp 300, PicoQuant, Berlin, Germany) and set to a time delay of approximately 1.5 ns and a gate width of 9 ns. The fine adjustment of the gated detection was performed for each respective experimental sample and is stated explicitly in the corresponding sections.

2.1.2. Custom-built fast scanning STED microscope

The following experiments were carried out using a custom-built, fast scanning STED microscope setup:

- STED imaging of sarcolemmal Cholesterol structures in living VM (see section 3.5).
- STED imaging of sarcolemmal Caveolin-3 structures in fixed VM (see section 3.5).
- Two-color STED imaging of Caveolin-3 and Dystrophin structures in fixed VM (see section 3.7).

This fast scanning microscope setup has, in its basics, been first described in [408, 330, 409]. For this thesis, the setup was equipped with an additional excitation laser with a wavelength of 532 nm, as well as with an additional fluorescence detection channel covering the wavelength range of (630 ± 20) nm. Also, the wavelength range of the de-exciting STED pulses was extended to an effectively usable region of 740 to 800 nm provided by a tunable, mode-locked Titanium:Sapphire (Ti:Sa) laser. These changes were made to enable two-color STED imaging of Caveolin-3 and Dystrophin structures in fixed cardiomyocytes labeled with spectrally appropriate organic dyes via indirect immunofluorescence as described in detail in section 2.3.3. This modified STED setup described in the following is schematically illustrated in Fig. 2.2.
All lasers in the setup were operated in the pulsed mode and their pulse trains synchronized using the STED laser pulses as trigger signals by recording their

reflection with a fast photo diode (s5973-01, Hamamatsu, Herrsching am Ammersee, Germany), converting the laser signals into NIM (Nuclear Instrumentation Module Standard) signals, and sending them to a custom-built electronic delay module with a time resolution of 10 ps. The electronic delay was adjusted such that the de-exciting STED pulses would follow the excitation laser pulses immediately to ensure most efficient photophysical switching of fluorescent molecules. The delay adjustment was performed separately for each excitation laser and for each fluorescent dye used in the respective experimental sample using a sample of a fluorescent dye in solution (a so-called "dye sea") within the daily microscope alignment routine described in section 2.10.1.
Excitation laser beams at wavelengths of 635 nm and 532 nm, respectively, were provided by triggerable laser diodes with pulse durations of 120 ps (LDH-P-635 and LDH-P-FA-530XL, respectively, PicoQuant, Berlin, Germany). The STED laser pulses stemmed from a tunable Ti:sapphire laser with a repetition rate of 80 MHz and a 120 fs pulse duration (Chameleon, Coherent LaserSystems GmbH, Dieburg, Germany). For one- and two-color STED imaging of the biological samples, the STED laser was operated at a wavelength of 750 nm which was found to yield the highest image quality; optimization of the STED laser wavelength was performed within a wavelength range of $730 - 780$ nm.
After passing a Faraday Isolator (FI, FR 500/1100, Linos, Goettingen, Germany) to avoid back reflections into the laser cavity, the STED laser pulses were stretched to a duration of 300 ps by coupling the STED beam into a 100 m polarization maintaining single mode optical fiber (SMF1, PM-S630-HP, Thorlabs GmbH, Munich, Germany) after guiding the beam through 30 cm of SF6 (dense flint) glass rods in order to prevent nonlinear effects in the fiber. The linear polarization of the STED laser beam was appropriately adjusted with a half-wave retarder plate ($\lambda/2$, AHWP05M-90, Thorlabs, Munich, Germany) for maximum output before the laser was coupled into the single mode fiber. After the fiber, the STED beam was collimated and its wavelength cleaned up using a bandpass filter (F1, F49-755, AHF Analysentechnik, Tuebingen, Germany) with a transmission wavelength range of 755 ± 25 nm. The STED beam then passed a vortex phase plate (PM, VPP-A1, RPC Photonics, Rochester, NY, USA) which generated the typical toroidal lateral intensity distribution used in STED microscopy (the so-called STED "doughnut").

The 635 nm excitation laser (also referred to as the "red" excitation) passed through an electronically adjustable liquid crystal variable retarder (VR1, Meadowlark Optics, Frederick, CO, USA) followed by a Glan-Thompson polarizing prism (GT, PGT 2.10.0, B. Halle Nachfl. GmbH, Berlin, Germany) to allow both laser power control as well as linear polarization of the laser beam before coupling it into the optical fiber. The red excitation laser wavelength spectrum was cleaned up by a dielectric filter (F2, z633/10, AHF Analysentechnik, Tuebingen, Germany) and the spatial mode profile of the laser was adjusted to optimal Gaussian shape by coupling the laser beam into a single mode polarization maintaining optical fiber (SMF2, P1-630PM-FC-2, Thorlabs, Munich, Germany). After the fiber, the beam was collimated and passed through a half-wave retarder plate ($\lambda/2$, AHWP05M-600, Thorlabs, Munich, Germany) to ensure vertical linear polarization. The red excitation laser beam was then combined with the STED laser beam path by a dichroic mirror (DM1, zt 647 rdc-xxrxt, F48-649, AHF Analysentechnik, Tuebingen, Germany).
The 532 nm excitation laser (also referred to as the "green" excitation) passed through an electronically adjustable liquid crystal variable retarder (VR2, Meadowlark Optics, Frederick, CO, USA) followed by a polarizing beam splitter (PBS, PTW15, B. Halle Nachfl. GmbH, Berlin, Germany) to allow both laser power control as well as linear polarization of the laser beam before coupling it into the optical fiber. The green excitation laser wavelength spectrum was cleaned up by a dielectric filter (F3, ZET 532/10, F49-532, AHF Analysentechnik, Tuebingen, Germany) and the spatial mode profile of the laser adjusted to optimal Gaussian shape by coupling the laser beam into a single mode polarization maintaining optical fiber (SMF3, P1-488PM-FC-2, Thorlabs, Munich, Germany). After the fiber, the beam was collimated by a lens (L6) and passed through a half-wave retarder plate ($\lambda/2$, AHWP05M-600, Thorlabs, Munich, Germany) to ensure vertical linear polarization. The green excitation laser beam was then combined with the STED (and the red excitation) laser beam path by a dichroic mirror (DM2, HCBS R594, F38-594, AHF Analysentechnik, Tuebingen, Germany). The two excitation laser beams and the STED beam, being axially aligned, then passed a resonant beam scanner (as previously described in [409]) and, with access from the bottom, was led through the modified headpiece of an inverted microscope (IRB, Leica, Heidelberg, Germany)

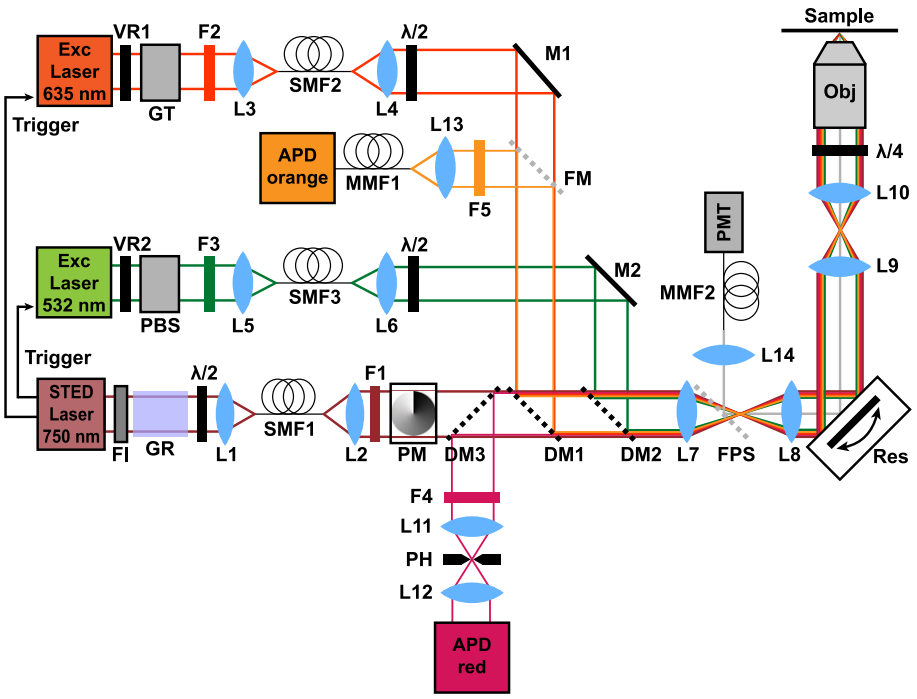

Figure 2.2.: Scheme of the custom-built, fast scanning STED microscope used for select experiments as indicated in section 2.1.2. Abbreviations (in alphabetical order): APD - Avalanche Photo Diode; DM - Dichroic Mirror; Exc - Excitation; F - Filter; FI - Faraday Isolator; FM - Flip Mirror; FPS - Flippable Pellicle Beam Splitter; GR - Glass Rods; GT - Glan Thompson Polarizer; λ/2 - Half-Wave Retarder Plate; λ/4 - Quarter-Wave Retarder Plate; L - Lens; M - Mirror; MMF - Multi Mode Fiber; Obj - Objective; PBS - Polarizing Beam Splitter Cube; PH - Pinhole; PM - Phase Mask; PMT - Photomultiplier Tube; Res - Resonant Scanning Mirror; SMF - Single Mode Fiber (polarization maintaining); VR - Variable Retarder.

equipped with an oil immersion objective (Obj, HCX PL APO 100x/1.4-0.7 Oil CS, Leica Microsystems GmbH, Wetzlar, Germany). All three beams were circularly polarized before passing through the objective by an adjustable quarter-wave retarder plate ($\lambda/4$, WPH05M-670, Thorlabs, Munich, Germany) that was installed close to the back aperture of the objective and whose position was set to ensure optimal circular polarization, especially of the STED beam. The biological sample was imaged laterally by resonantly scanning it in one spatial dimension (the X-axis), and by stage scanning it along the other spatial dimension (the Y-axis) with a piezo stage (733-3DD and E-710, Physik Instrumente GmbH, Karlsruhe, Germany).

The fluorescence signal of the "red" color channel (i.e. of the respective fluorophores with an absorption maximum close to the 635 nm laser line of the "red" excitation laser) passed through the objective, was descanned and eventually coupled out of the common laser beam path by a dichroic mirror (DM3, zt670 rdc-xxrxt, F48-677, AHF Analysentechnik, Tuebingen, Germany). The

fluorescence signal of the red channel was cleaned up by a bandpass filter (F4, 675/67 BrightLine HC, F39-674, AHF Analysentechnik, Tuebingen, Germany) that removed unwanted scattered light. Confocal detection of the red fluorescence signal was achieved by imaging the sample plane onto a pinhole with a diameter of 100 µm (PH, custom-built part) and then collecting the signal with a free-beam avalanche photo diode (APD red, SPCM-AQRH-13 20220, Perkin Elmer, Fremont, CA, USA).
The fluorescence signal of the "green" color channel (i.e. of the respective fluorophore with an absorption maximum close to the 532 nm laser line of the "green" excitation laser) was, after being descanned, coupled out of the common laser beam path by the dichroic mirror DM1. It then passed a flippable mirror (FM) and a bandpass filter (F5, 630/38 BrightLine HC, F39-633, AHF Analysentechnik, Tuebingen, Germany). Confocal detection was achieved by focusing the green channel fluorescence signal into a multi mode fiber with a core diameter of 62.5 $\pm$ 2.5 µm (MMF1, M31L01, Thorlabs, Munich, Germany). The multi mode fiber was attached to an avalanche photo diode (APD orange, SPCM-AQRH-13-FC, Perkin Elmer, Fremont, CA, USA).
For further improvement of achievable image resolution, the fluorescence signals of both the "red" color channel (detected by "APD red") and the "green" color channel (detected by "APD orange") in STED imaging mode was time-gated using the STED laser pulses as internal trigger signals. To this end, the two APDs were each connected to custom-built time gating electronics which recorded the fluorescence signal following the individual STED laser pulses (cf. [410, 405]). The ranges of the time gates for the respectively used fluorescent dyes were optimized to yield the best STED images.
Since the green channel fluorescence signal was coupled out of the common beam path with the red excitation laser via a flippable mirror, the two color channels (i.e. the "red" and the "green" color channels) could only be recorded in consecutive scans. Yet, as the resonant scanner of this STED microscope setup provided very fast image scanning, effects of sample drift could be neglected when overlaying the two-color images for analysis. This procedure was controlled and justified after imaging samples that were labeled with the respective fluorophores coupled to two primary antibodies against the same biological structure and finding complete colocalization when performing sam-

ple scans in an analogous fashion as for the actual investigated samples.
As part of the daily microscope alignment routine to ensure proper beam alignment, proper synchronization of the excitation and STED pulses, and optimal illumination of the detection devices (see section 2.10.1), the setup also comprised a Photomultiplier Tube (PMT, MD 963CPM D, Perkin Elmer, Fremont, CA, USA) as a diagnostic unit. The PMT was used to record the backscattered light from a sample of $\varnothing$ 80 nm gold beads (see section 2.5.1). To this end, the reflected light from the gold beads scanned with the respective laser beam was coupled out of the common laser beam path via a flippable pellicle beam splitter (FPS, BP145B1, Thorlabs, Munich, Germany) and focused with a lens (L14) onto a multi mode fiber (MMF2, M31L01, Thorlabs, Munich, Germany) to which the PMT was attached.

2.1.3. STED microscope Leica TCS SP8 STED 3X

The following experiments were conducted using the commercially available STED microscope system Leica TCS SP8 STED 3X (Leica Microsystems GmbH, Wetzlar, Germany):

- STED imaging of human adipocytes and ventricular induced pluripotent stem cells stained with Cholesterol-PEG-KK114 (employing a live-cell labeling protocol, see section 3.2) and respectively stained for Caveolin-1 and Caveolin-3 (via indirect immunofluorescence, see section 3.5).

- Two-color STED imaging of living VM stained with Chol-KK114 and either Di-8-ANEPPS or Cholesterol-BODIPY (see sections 2.3.2 and 3.3).

- Two-color STED imaging of Cholesterol and Ganglioside GM1 structures in living VM labeled with the dye conjugates Chol-KK114 and Cholera Toxin Subunit B (see sections 2.3.2 and 3.6).

- Three-color STED imaging of fixed VM stained for Dystrophin and/or Caveolin-3 at different epitopes along the respective proteins via indirect immunofluorescence (see section 3.8).

The STED microscope was equipped with a white light laser source operated in pulsed mode (78 MHz repetition rate) for fluorophore excitation and two STED

lasers for fluorescence inhibition: one STED laser with a wavelength of 775 nm operated in pulsed mode with pulse trains synchronized to the white light laser pulses, and one continuous-wave STED laser with a wavelength of 592 nm. Excitation wavelengths between $470 - 670$ nm were selected from the white light laser emission spectrum via an acousto-optical beam splitter (AOBS). All laser beams were focused into the cell sample with a wavelength corrected, 1.40 numerical aperture oil immersion objective (HC PL APO 100x/1.40 OIL STED WHITE). The samples were scanned using the field-of-view beam scanner at a scanning rate of 600 lines per second, resulting in a pixel dwell time of 0.4 µs, and within a scan format of (1024×1024) pixels, and a pixel size of (22.73×22.73) nm^2. The fluorescence light emitted from the samples was detected by the two built-in GaAsP hybrid detectors set to the respective detection windows appropriate for the fluorescent dyes used in the samples. For imaging three-color samples (see section 3.8), a photomultiplier tube (PMT) was additionally used to record the third color channel. The recorded fluorescence signal in the STED imaging mode was time-gated using the white light laser pulses as internal trigger signals. The fluorescence images were obtained with 16-fold line averaging but no frame accumulation.
The explicit imaging parameters used for individual samples - especially excitation wavelengths, detection channels, and time gating windows - are specified in the sections discussing the respective experiments.

2.1.4. STED microscope Abberior 2C STED 775 QUAD Scan

The following experiments were conducted using the commercially available STED microscope system Abberior 2C STED 775 QUAD Scan (Abberior Instruments GmbH, Goettingen, Germany):

- STED imaging of living culture cell lines (U2OS, HeLa, HEK-293, Vero) stained with Cholesterol-PEG-KK114 (Chol-KK114) (see section 3.2).
- STED imaging of living HeLa cells overexpressing a Caveolin-3-SNAP construct and stained with the dye compound SiR-SNAP (see sections 2.4.1 and 3.5).

- Two-color STED imaging of living HeLa cells overexpressing a Caveolin-3-SNAP construct and stained with the dye compound 580CP-BG(SNAP) and Chol-KK114 (see sections 2.4.1 and 3.5).

The microscope was built around an Olympus IX83 microscope stand (Olympus Deutschland GmbH, Hamburg, Germany) and was used in a configuration employing excitation lasers with wavelengths of 561 nm (LightUp561, Abberior Instruments GmbH, Goettingen, Germany) and 640 nm (PiL063X, Advanced Laser Diode Systems GmbH, Berlin, Germany), respectively, as well as a pulsed STED laser at a wavelength of 775 nm (Nanosecond pulsed fiber laser, MPB Communications Inc., Pointe-Claire, Canada). All three lasers were operated in pulsed mode at a repetition rate of 40 MHz. Lasers were focused into the sample plane by a 1.40 numerical aperture oil immersion objective (UPlanSApo 100x/1.40 Oil 8/0.17/FN26.5, Olympus Deutschland GmbH, Hamburg, Germany). Fluorescence of the respective color channels was detected with avalanche photo diodes (APD, SPCM-AQRH, Excelitas Technologies Corp., Fremont, CA, USA). The red fluorescent color channel (i.e. for the dyes Chol-KK114 and SiR-SNAP) was recorded within a detection window of (685 $\pm$ 35) nm; the green fluorescent color channel (i.e. the dye compound 580CP-BG(SNAP)) was recorded within a detection window of (615 $\pm$ 10) nm. Samples were scanned using the Abberior QUAD beamscanner with a constant pixel size of of (20×20) nm^2 and a typical pixel dwell time of 30 µs. Two-color STED images (see section 3.5) were recorded in pixel interleaved mode with a pixel dwell time of 40 µs and 20 µs for the green and the red color channel, respectively. The recorded fluorescence signal in the STED imaging mode was time-gated using the STED laser pulses as internal trigger signals. The time gates for the respectively used fluorescent dyes were optimized to yield the best STED images and could be set explicitly in the microscope's software. For the detection of Chol-KK114 signals, the time gate was optimized to a delay of 2.813 ns and a width of 5.391 ns. For the detection of SiR-SNAP signals, the time gate was optimized to a delay of 3.438 ns and a width of 5.859 ns. For the detection of 580CP-BG(SNAP) signals, the time gate was optimized to a delay of 2.656 ns and a width of 8.047 ns.

2.2. Synthesis of fluorescent Cholesterol analogs

Fluorescent Cholesterol analogs were prepared by coupling the respective fluorescent dye compound to a Cholesterol-Polyethylene Glycol (Chol-PEG) derivative. 1.0 mg of the NHS ester of the dye compound were solved in 50 µl of dry N,N-dimethylformamide (DMF). A solution of 3 mg (2.9 µmol) of Chol-PEG(1k)-amine (PG2-AMCS-1k, Nanocs via Scholz GmbH, Neubiberg, Germany) in 50 µl dry DMF and 2 µl triethylamine was added gradually in an argon atmosphere and stirred overnight at room temperature. The reaction was controlled by thin-layer chromatography (TLC). The volatile components were removed under vacuum. The product was purified by flash column chromatography ($CHCl_3$/MeOH/(H_2O+1% AcOH), 80:20:2) and stored as a solid.
For the preparation of stock solutions, the solid fluorescent Cholesterol analog was dissolved in methanol to arrive at a concentration of 2 mg/ml. The solution was vortexed and was stored air-tight and protected from light at -20 °C.
For the preparation of working solutions, the methanol was evaporated from the stock solution using N_2. Phosphate-Buffered Saline (PBS, pH 7.4) was added to arrive at a concentration of 2 mg/ml. The working solution could be stored air-tight and protected from light at 8 °C for several months without loss in quality.

2.3. Mouse ventricular cardiomyocyte samples

All animal procedures were carried out in accordance with the German animal welfare act (TierSchG) and in agreement with the animal welfare committee at both the Max Planck Institute for Biophysical Chemistry, and the University Medicine Goettingen. During every procedure performed on the animals, i.e. sacrifice for tissue and organ harvesting, the individuals carrying out the procedures took greatest care to ensure the humane treatment and use of laboratory animals and to ensure the greatest possible avoidance of harm to the animals.

	MW [g/mol]	Final concentration [mM]
10 × Perfusion buffer		
NaCl	58.4	120.4
KCl	74.6	14.7
KH_2PO_4	136.1	0.6
$Na_2HPO_4 \times 2H_2O$	177.99	0.6
$MgSO_4 \times 7H_2O$	246.5	1.2
Na−HEPES	238.31	10
Ad. H_2O; adjust pH to 7.4 at 37 °C with NaOH [1M]		
1 × Perfusion buffer		
$NaHCO_3$	84	4.6
Taurin	125.1	30
2, 3-Butanedione monoxime	101.1	10
Glucose	180.2	5.5
Ad. 10 × Perfusion buffer (diluted 1:10 in H_2O)		
	Concentration	**Final concentration**
Digestion buffer		
Collagenase Type II	340 units/mg	2 mg/ml
$CaCl_2$	100 mM	40 µM
Ad. 1 × Perfusion buffer		
Stopping buffer		
Bovine Calf Serum (BCS)	100%	10%
$CaCl_2$	100 mM	12.5 µM
Ad. 1 × Perfusion buffer		
Blocking buffer		
Bovine Calf Serum (BCS)	100 %	10 %
Triton X-100	10 %	0.2 %
Ad. Phosphate-Buffered Saline (PBS, pH 7.4)		

Table 2.1.: Perfusion buffer, digestion buffer, and stopping buffer for isolation of mouse ventricular cardiomyocytes as described in section 2.3.1; blocking buffer for blocking and permeabilization of fixed mouse ventricular cardiomyocytes as described in section 2.3.3. Providers and order numbers of the used chemicals are given in the Appendix A.1.

2.3.1. Isolation of mouse ventricular cardiomyocytes

The isolation of adult mouse ventricular cardiomyocytes was performed according to the protocol published by *Wagner et al.* [22, 23, 411]. In brief, mice were anesthetized with Isoflurane (3 % in O_2) and sacrificed by cervical dislocation. Hearts were extracted and their proximal aorta connected to a 21 gauge cannula (clipped to about 0.5 mm in length and roughened around its outer surface). Cannulas were connected to a modified Langendorff perfusion system [412] and the cannulated hearts were perfused with Ca^{2+}-free perfusion buffer (see Table 2.1) for 4 min at 37 °C and at a flow rate of 4 ml/min. The perfusion buffer was then replaced by digestion buffer (see Table 2.1) containing 2 mg/ml Collagenase Type II and 40 µM $CaCl_2$. Hearts were perfused with the digestion buffer for 8 min at 37 °C and at a flow rate of 4 ml/min. After 5 min of perfusion with digestion buffer, about 2 ml of the digestion buffer that had passed through the heart was collected in a Petri dish. After 8 min of perfusion, hearts were cut off the perfusion cannula below the atria, the ventricles collected in the Petri dish and manually dissected. Possibly remaining blood clots were removed. Digestion was stopped by adding to the Petri dish 5 ml of perfusion buffer containing 10 % Bovine Calf Serum (BCS) and 12.5 µM $CaCl_2$ (see "Stopping buffer" in Table 2.1). The entire content of the Petri dish was transferred to a 15 ml conical centrifuge tube and was left to sediment very briefly. The supernatant was transferred into another tube and filled to a final volume of 10 ml with stopping buffer. The isolated ventricular cardiomyocytes were left to sediment for 8 min, then washed with 10 ml of fresh stopping buffer and left to sediment for another 8 min. The supernatant was then discarded and the cell pellet was resuspended in fresh perfusion buffer. For staining and imaging experiments, the cell pellet was split to ensure a cell density of about 1500 cells/cm^2 when plating on ⌀ 42 mm laminin coated glass cover slips (#1.0, MARI011199039234, VWR International GmbH, Darmstadt, Germany). Imaging experiments of living mouse ventricular cardiomyocytes were conducted within 5 h after isolation. High cell quality was ensured by verifying the following traits of intact living cardiomyocytes: rod shape, even/sharp cell edges, regular striations, no signs of aberrant contractions, and no membrane blebs.

2.3.2. Live cardiomyocyte samples

Staining with fluorescent Cholesterol analogs

Cholesterol rich membrane domains within the extracellular leaflet of the plasma membrane of living isolated mouse ventricular cardiomyocytes (VM) were stained with the fluorescently labeled Cholesterol constructs Cholesterol-PEG-KK114 (Chol-KK114) [100], Cholesterol-PEG-DY380XL (Chol-DY380XL), Cholesterol-PEG-AF488 (Chol-AF488), Cholesterol-PEG-STAR488 (Chol-STAR488), and Cholesterol-PEG-OG488 (Chol-OG488) (see also section 2.2 for the synthesis of the respective fluorescent Cholesterol analogs). For labeling VM, ⌀ 42 mm glass cover slips were coated with mouse laminin (2 mg/ml, 354232, BD Biosciences, Heidelberg, Germany) diluted 1:10 in perfusion buffer. The coated cover slips were either placed inside an open cell imaging chamber (POC-R2, PeCon GmbH, Erbach, Germany) for immediate experiments or placed inside disposable Petri dishes that were then sealed with Parafilm and set aside for later use. Freshly isolated living cardiomyocytes were resuspended in Ca^{2+} free perfusion buffer and sedimented by gravity for 10 min. The supernatant was carefully removed and the cells were resuspended in perfusion buffer with added Chol-KK114 in different concentrations, specified in the corresponding sections, and ranging from 5 µM to 25 mM. Cells were incubated in the dye solution for 8 min while sedimenting by gravity. The supernatant was then carefully removed and the cells were resuspended in perfusion buffer and transferred onto the coated cover slips mounted inside the cell chamber. Cells were left to attach to the coated cover slips for 5 min, then washed three times to remove excess dye. Cells were covered with perfusion buffer and imaged inside the imaging chamber using one of the respective STED microscope systems (see section 2.1.1). For labeling living VM with the fluorescent Cholesterol analog Cholesterol-BODIPY (Chol-BODIPY, 810255, Avanti Polar Lipids, Inc., Alabaster, AL, USA), a Chol-BODIPY working solution was prepared. To that end, 10 µl Chol-BODIPY from a 0.3125 mM stock were dried under N_2. A solution of 40 mg Methyl-β-Cyclodextrin and 1 mg Bovine Serum Albumine (BSA) in 2 ml Phosphate-Buffered Saline (PBS) was prepared and added to the dried Chol-BODIPY. The mixture was continuously shaken for 5 min. Freshly isolated living cardiomyocytes were resuspended in perfusion buffer with added

Chol-BODIPY working solution at a concentration of 1:20. The ensuing incubation and plating procedure was the same as for labeling with Chol-KK114 (as described in this section). Double stains of living VM with both Chol-KK114 and Chol-BODIPY were prepared by simultaneously labeling cells with the two fluorescent analogs following the protocols described in this section. Confocal images of these double stains are presented in section 3.3, Fig. 3.8. Double stains were recorded using the STED microscope Abberior 2C STED 775 QUAD Scan, operated in confocal mode. The Chol-BODIPY signal was excited at a wavelength of 485 nm and detected within a region of (525 $\pm$ 25) nm. The Chol-KK114 signal was excited at a wavelength of 640 nm and detected within a region of (685 $\pm$ 35) nm. The pixel size was set to (20 $\times$ 20) nm^2; the pixel dwell time was set to 0.05 ms.

Staining with Di-8-ANEPPS

The plasma membrane of living isolated cardiomyocytes was stained with the voltage-sensitive membrane marker dye Di-8-ANEPPS [413, 414] (D-3167, Molecular Probes, Life Technologies, Darmstadt, Germany). For this, $\varnothing$ 42 mm glass cover slips were coated with mouse laminin (2 mg/ml, 354232, BD Biosciences, Heidelberg, Germany) diluted 1:10 in perfusion buffer. The coated cover slips were either placed inside an open cell imaging chamber (POC-R2, PeCon GmbH, Erbach, Germany) for immediate experiments or placed inside disposable Petri dishes that were then sealed with Parafilm and set aside for later use. Freshly isolated living cardiomyocytes were resuspended in Ca^{2+} free perfusion buffer and sedimented by gravity for 10 min. The supernatant was carefully removed and the cells were resuspended in perfusion buffer with added Di-8-ANEPPS in a 50 µM concentration. The mixture of cells and dye-containing perfusion buffer was transferred onto the coated cover slips and incubated for 15 min at room temperature and in the dark. Cells were washed three times with perfusion buffer, then the imaging chamber was filled with 1 - 2 ml perfusion buffer and cells were imaged using the Leica TCS SP8 STED 3X (see section 2.1.3).

For dual-labeled living cardiomyocyte samples stained with Di-8-ANEPPS and Cholesterol-PEG-KK114 (Chol-KK114), cells were resuspended in perfusion buffer containing both Di-8-ANEPPS (50 µM) and Chol-KK114 (5 µM), trans-

ferred into the imaging chamber and incubated for 15 min, then washed three times and imaged in perfusion buffer using the Leica TCS SP8 STED 3X STED microscope.

Staining with fluorescence labeled Choleratoxin B

Ganglioside GM1 (Monosialotetrahexosylganglioside) within the outer membrane leaflet of living mouse ventricular cardiomyocytes was stained using recombinant Cholera Toxin Subunit B fluorescently labeled with the dye Alexa Fluor 594 (CtB-AF594, C34777, Molecular Probes via ThermoFisher Scientific, Dreieich, Germany; see Appendix A.3). For this, freshly isolated mouse ventricular cardiomyoctes (see section 2.3.1) were slowly cooled down to 10 °C. The dye-labeled CtB conjugate (1.0 mg/ml stock solution prepared following the supplier instructions) was diluted 1:500 in perfusion buffer (see Table 2.1) containing 2 % Bovine Calf Serum (BCS) and cooled to 10 °C. Cells were resuspended in the CtB-AF594 solution and incubated for 20 min at 10 °C, inverting the solution twice manually during incubation to gently mix the cells with the dye solution. Cells were resuspended in cooled (10 °C) perfusion buffer containing 2 % BCS and left at 10 °C for another 2 min before being resuspended in cooled (10 °C) perfusion buffer. Cells were plated on ⌀ 42 mm laminin coated cover slips placed inside an open cell imaging chamber and left to warm up to room temperature for 5 min. Cells were imaged using the Abberior 2C STED 775 QUAD Scan microscope with the specific imaging parameters described in section 2.1.4.

For dual-labeled living cardiomyocyte samples stained with both CtB-AF594 and Cholesterol-PEG-KK114 (Chol-KK114), cells were incubated with Chol-KK114 at a concentration of 2.5 µM as described in section 2.3.2 prior to incubation with CtB-AF594. Dual-labeled samples were imaged using the Abberior 2C STED 775 QUAD Scan microscope (see section 2.1.4).

2.3.3. Fixed cardiomyocyte samples

Immunofluorescence-labeling of cardiomyocytes

For immunofluorescence stains, freshly isolated mouse ventricular cardiomyocytes were plated on laminin coated glass cover slips (10 µM laminin per ⌀ 18 mm cover slip from a 2 mg/ml stock solution, diluted 1:10 in perfusion buffer) for 30 min prior to fixation with 4 % Paraformaldehyde (PFA, in PBS, pH 7.4) for 10 min at room temperature. PFA was removed and cells were covered with blocking buffer containing 0.2 % Triton X-100 and 10 % bovine calf serum (see Table 2.1) for blocking and permeabilization (1 h at 4 °C). Primary antibodies were diluted 1:500 in blocking buffer and cells incubated with the primary antibody overnight at 4 °C. Cells were washed three times with PBS (twice for 1 min, once for 10 min). Secondary antibodies were diluted 1:1000 in blocking buffer and cells incubated with the secondary antibody for 2 h in the dark at room temperature. Cells were washed three times with PBS (twice for 1 min, once for 10 min) and samples mounted on coverslides (631-1551, VWR International GmbH, Darmstadt, Germany) in polyvinyl alcohol (Mowiol 4-88, Sigma-Aldrich, Taufkirchen, Germany) containing 2.5 % DABCO (see Appendix A.1). Samples were left to dry in the dark overnight, sealed with clear nail polish, and used for respective microscopic imaging. An overview of the respectively used primary and secondary antibodies can be found in the Appendix A.3.

Staining with fluorescence labeled Choleratoxin B

To stain for Ganglioside GM1 (Monosialotetrahexosylganglioside) within the outer membrane leaflet of fixed mouse ventricular cardiomyocytes, freshly isolated cardiomyocytes were incubated with CtB-AF594 as described in section 2.3.2. Cells were then plated on glass cover slips, fixed, blocked, permeabilized, and mounted on coverslides as described in section 2.3.3.
For fixed cardiomyocyte samples dual-labeled with CtB-AF594 and Caveolin-3-STAR635P (see section 3.6), cardiomyocytes were incubated with CtB-AF594 as described in section 2.3.2, then fixed and further stained via indirect immunofluorescence as described in section 2.3.3. Dual-labeled samples were

imaged using the Abberior 2C STED 775 QUAD Scan microscope with the specific imaging parameters described in section 2.1.4.

Cholesterol depletion with Methyl-β-Cyclodextrin

For the treatment of freshly isolated mouse ventricular cardiomyocytes (VM) with Methyl-β-Cyclodextrin (M-β-CD), VM were typically incubated in VM culture medium (see Table 2.2) in a humidified incubator (37 °C, 5 % CO_2).

	Final concentration
VM culture medium	
HEPES	10 mM
2, 3-Butanedione monoxime	10 mM
Penicillin-Streptomycin (PenStrep):	
Penicillin	100 units/ml
Streptomycin	100 µg/ml
Bovine Serum Albumin (BSA)	0.2 %
Insulin-Transferrin-Sodium Selenite supplement (ITS):	
Recombinant human insulin	10 µg/ml
Human transferrin	5.5 µg/ml
Sodium selenite	5 ng/ml
Ad. 1 × Minimum Essential Medium (MEM)	

Table 2.2.: Culture medium for mouse ventricular cardiomyocytes (VM). Providers and order numbers of the used chemicals are given in Appendix A.1.

VM were treated with M-β-CD to investigate the cardiac membrane architecture as well as sarcolemmal Caveolin-3, and Dystrophin protein arrangements upon extraction of Cholesterol (Chol) from the membrane (see section 3.5.1).
To this end, mouse ventricular cardiomyocytes (VM) were isolated as described in section 2.3.1. Reintroduction of Calcium (Ca^{2+}) to the suspension of isolated VM in stopping buffer (see Table 2.1) was performed in the following four steps. First, the Ca^{2+}-free cell suspension was left to sediment for 8 min, the supernatant discarded, and the cell pellet resuspended in stopping buffer containing 12.5 µM Ca^{2+}. Next, the cell suspension was left to sediment for another 8 min, the supernatant discarded, and the cell pellet resuspended in perfusion buffer (see Table 2.1) containing 100 µM Ca^{2+}. This step was repeated

two more times with resuspension in perfusion buffer containing 400 µM Ca^{2+}, and 900 µM Ca^{2+}, respectively.
After Ca^{2+} reintroduction, cells were resuspended in VM culture medium (see Table 2.2) to which M-β-CD was added at a concentration of 5 mM. VM were incubated in this solution in a humidified incubator for 1 h, carefully mixing the solution by manually turning it upside-down every 20 min.
For staining Cav-3 and Dyst structures in Chol-depleted fixed VM via indirect immunofluorescence, cells were removed from the incubator, the supernatant discarded and the fixation and staining protocol was carried out as described in section 2.3.3.
For the visualization of membrane structures in Chol-depleted living VM, cells were stained with Di-8-ANEPPS according to the protocol described in section 2.3.2 (with the slight alteration that 900 µM Ca^{2+} containing perfusion buffer was used instead of Ca^{2+}-free perfusion buffer for incubation).
For reintroduction of Chol ("Cholesterol-repletion") and simultaneously staining Chol structures in Chol-depleted living VM, VM were incubated at very high concentrations of the membrane marker Cholesterol-PEG-KK114 (Chol-KK114). To this end, cells were removed from the incubator, the supernatant discarded and the cells resuspended in perfusion buffer containing 900 µM Ca^{2+} and 1 µM Chol-KK114, and incubated at room temperature for 10 min. Cells were washed twice with Ca^{2+}-containing perfusion buffer, plated on laminin-coated coverslips placed inside an open cell imaging chamber for 5 min, washed once more with Ca^{2+}-containing perfusion buffer, and imaged using the custom-built fast scanning STED microscope described in section 2.1.2.

2.3.4. The *mdx 5cv* mouse model of muscular dystrophy

Mice of the Dystrophin (Dyst) deficient strain B6Ros.Cg-$Dmd^{mdx\text{-}5Cv}$/J [288] were purchased from The Jackson Laboratory, Bar Harbor, ME, USA. The strain was maintained and cared for in the animal facility of the University Medicine Goettingen according to the German animal welfare act (TierSchG) and in agreement with the animal welfare committee at the University Medicine Goettingen. Male mice at an age ranging from 12 to 16 weeks were used. Male wild-type C57BL/6N mice at a similar age served as control.

2.4. Samples of culture cell lines

2.4.1. U2OS, HeLa, HEK-293, and Vero cells

U2OS, HeLa, HEK-293 (referred to as HEK), and Vero cell lines were cultured on glass cover slips in immortal cell line culture medium (see Table 2.3) and typically seeded one day prior to further experiments (i.e. transfection and/or staining for STED imaging); all incubation protocols were carried out in a humidified incubator (37 °C, 5 % CO_2). For STED imaging, adherent cells were covered with colorless immortal cell line imaging medium (see Table 2.3).
For staining living culture cells with Cholesterol-PEG-KK114 (Chol-KK114), cells were freshly seeded one day before being incubated with imaging medium containing 5 µM Chol-KK114. After three washing steps with imaging medium, imaging was performed using the commercial STED microscope Abberior 2C STED 775 QUAD Scan (see section 2.1.4).
For staining living HeLa cells overexpressing a human-Caveolin-3-SNAP construct (see Appendix C, and [415, 416]) and stained, via SNAP-tagging, with either the dye Silicon-Rhodamine (SiR, S9102S, New England Biolabs, Ipswich, MA, USA), or the dye compound 580CP-BG(SNAP) (the dye 580CP [344] was conjugated to a SNAP-tag and kindly provided by Dr. A. Butkevich from the MPICBPC in Göttingen, Germany; see also section 3.5), HeLa cells were seeded one day prior to being transfected. For transfection, serum-free DMEM medium (see Table 2.3) containing 0.7 µg/ml DNA of the Caveolin-3-SNAP construct, and 1.5 % transfection agent (TurboFect, R0531, ThermoFisher Scientific, Dreieich, Germany) was left to incubate at room temperature for 20 min before being added to the cells. Cells were incubated for 24 h. For staining with SiR or 580CP-BG(SNAP), respectively, cells were incubated with imaging medium (see Table 2.3) containing 1 µM of the respective fluorescent SNAP-dye for 30 min. After three short washing steps with imaging medium, cells were used for STED imaging with the STED microscope Abberior 2C STED 775 QUAD Scan (see section 2.1.4).
For two-color stains of living HeLa cells overexpressing the aforementioned human-Caveolin-3-SNAP construct and stained with the dye compound 580CP-BG(SNAP) and with Chol-KK114 (see section 3.5), HeLa cells were seeded, transfected, and incubated with 580CP-BG(SNAP) as described in the last para-

graph. Cells were stained with Chol-KK114 according to the protocol described in section 2.3.2 and used for STED imaging with the STED microscope Abberior 2C STED 775 QUAD Scan (see section 2.1.4).

	Concentration	Final concentration
Immortal cell line culture medium		
Fetal Bovine Serum (FBS)	100 %	10 %
Sodium pyruvate	100 mM	1 mM
Penicillin-Streptomycin (PenStrep):		
Penicillin	10,000 units/ml	100 units/ml
Streptomycin	10,000 µg/ml	100 µg/ml
Ad. DMEM (4.5 mg/ml Glucose, Glutamax, Phenol red)		
Immortal cell line imaging medium		
HEPES	–	10 mM
Penicillin-Streptomycin (PenStrep):		
Penicillin	10,000 units/ml	100 units/ml
Streptomycin	10,000 µg/ml	100 µg/ml
Ad. DMEM (4.5 mg/ml Glucose, no Phenol red)		

Table 2.3.: Culture and imaging media for U2OS, HeLa, HEK, and Vero cells. Providers and order numbers of the used chemicals are given in Appendix A.1.

2.4.2. Ventricular induced pluripotent stem cells

Human induced pluripotent stem cells (iPSC, cell line: iWT.D2.1o) were maintained under feeder-free and serum-free culture conditions with E8 medium (A1517001, Gibco via ThermoFisher Scientific, Dreieich, Germany) on plates coated with Geltrex (12760021, ThermoFisher Scientific, Dreieich, Germany). Directed ventricular cardiomyocyte differentiation of iPSC was initiated at confluence of $90-100$ % via Wingless-related integration site (Wnt) signaling modulation with cardio differentiation medium. The cardio differentiation medium consisted of RPMI 1640 medium that was modified with HEPES and Glutamax (72400021, Gibco via ThermoFisher Scientific, Dreieich, Germany) as well as 0.5 mg/ml human recombinant albumin (A9731, Sigma-Aldrich, Taufkirchen, Germany), and 0.2 mg/ml L-ascorbic acid 2-phosphate (A8960, Sigma-Aldrich, Taufkirchen, Germany). Cells were progressively treated with 4 µM

CHIR99021 (SML1046, Sigma-Aldrich, Taufkirchen, Germany) for 48 h (inhibiting Glycogen Synthase Kinase 3) and with 5 µM IWP-2 (I0536, Sigma-Aldrich, Taufkirchen, Germany) for an additional 48 h (inhibiting Wnt production). The medium was changed to cardio culture medium at day 10 after initiation of differentiation. Cardio culture medium consisted of RPMI 1640 medium containing 2 % B-27 serum-free supplement (17504001, Gibco via ThermoFisher Scientific, Dreieich, Germany). Metabolic cardiomyocyte selection was performed using cardio selection medium for 5 days. Cardio selection medium consisted of Glucose-free RPMI 1640 medium (11879020, Gibco via ThermoFisher Scientific, Dreieich, Germany) and 4 mM Lactate (L7022, Sigma-Aldrich, Taufkirchen, Germany). Cardiomyocytes were cultured in cardio culture medium for 60-120 days after initiation of differentiation to enhance maturation. Differentiated iPSC will now be referred to as Ventricular iPSC (ViPSC). ViPSC were trypsinated and seeded on ⌀ 25 mm glass cover slips coated with basement membrane matrix, growth factor reduced, Phenol Red-free (BD Matrigel, BD 356231, BD Biosciences, Heidelberg, Germany), and cultivated for 10 days before being used for the fluorescence staining techniques described in the following.
For staining ViPSC with Cholesterol-PEG-KK114 (Chol-KK114), the adherent ViPSC growing on ⌀ 25 mm glass cover slips were mounted in an open cell imaging chamber, incubated with Phenol Red-free cardio culture medium containing 5 µM Chol-KK114 for 10 min at room temperature, and washed three times with PBS before being imaged using the Leica TCS SP8 STED 3X STED microscope with the specific imaging parameters described in section 2.1.3.
For staining α-Actinin (α-Act), Caveolin-3 (Cav-3) and Dystrophin (Dyst) structures in ViPSC, adherent ViPSC growing on ⌀ 25 mm glass cover slips were fixed with 4 % Paraformaldehyde (PFA, in PBS, pH 7.4) for 5 min at room temperature. PFA was removed, cells were washed twice with blocking buffer (see Table 2.1) and incubated in blocking buffer for blocking and permeabilization (2 h at room temperature). The primary antibodies for each α-Act, Cav-3, and Dyst were respectively diluted 1:500 in blocking buffer and ViPSC incubated with the primary antibodies overnight at 4 °C. ViPSC were washed twice (once with PBS, pH 7.4, for 5 min, once with blocking buffer for 1 h). The secondary antibodies, respectively coupled to the fluorescent dyes Abberior STAR635P and Abberior STAR488, were diluted 1:1000 in blocking buffer and ViPSC in-

cubated with the secondary antibodies for 2 h in the dark at room temperature. Cells were washed three times (once with PBS, pH 7.4, for 5 min, once with blocking buffer for 1 h, and once with PBS, pH 7.4, for 5 min) and samples mounted on coverslides (631-1551, VWR International GmbH, Darmstadt, Germany) in an antifade reagent (ProLong Gold P36934, Molecular Probes via ThermoFisher Scientific, Dreieich, Germany). Samples were left to dry in the dark overnight, sealed with clear nail polish and imaged using the Leica TCS SP8 STED 3X STED microscope with the specific imaging parameters described in section 2.1.3.
An overview of the used primary and secondary antibodies can be found in Appendix A.3.

2.4.3. Human adipocytes

Cryopreserved human preadipocytes (HPAd) derived from human heart adipose tissue were purchased from Cell Applications (802hK-05a, Cell Applications Inc., San Diego, CA, USA) and cultured according to the supplier instructions. In brief, cryopreserved HPAd were thawed and cultured in Preadipocyte Growth Medium (811-500, Cell Applications Inc., San Diego, CA, USA) in a 37 °C, 5 % CO_2 humidified incubator, changing the growth medium every other day. For differentiation, HPAd were trypsinated and seeded on ⌀ 32 mm glass cover slips (in a 6-well culture plate) and on ⌀ 18 mm glass cover slips (in a 12-well culture plate), respectively. To facilitate the adhesion of HPAd [417, 418], the glass cover slips were coated with basement membrane matrix, growth factor reduced, Phenol Red-free (BD Matrigel, BD 356231, BD Biosciences, Heidelberg, Germany) diluted in PBS at a protein concentration of 10 mg/ml. When cells reached 100 % confluency after about 1-2 days, the Preadipocyte Growth Medium was replaced by Adipocyte Differentiation Medium (811D-250, Cell Applications Inc., San Diego, CA, USA) and cultured in a 37 °C, 5 % CO_2 humidified incubator for about 15 days, changing to fresh Adipocyte Differentiation Medium every 3 days. Fully differentiated human adipocytes will be referred to as HAd throughout this work.
For staining living HAd with Cholesterol-PEG-KK114 (Chol-KK114), adherent adipocytes growing on ⌀ 32 mm glass cover slips were mounted in an open cell imaging chamber, incubated with PBS (pH 7.4) containing 5 µM Chol-KK114

for 10 min at room temperature, and washed three times with PBS before being imaged using the Leica TCS SP8 STED 3X STED microscope with the specific imaging parameters described in section 2.1.3.

For staining Caveolin-1 (Cav-1) structures in differentiated fixed HAd, adherent adipocytes growing on ⌀ 18 mm glass cover slips were fixed with 4 % Paraformaldehyde (PFA, in PBS, pH 7.4) for 10 min at room temperature. PFA was removed, cells were washed twice with adipocyte blocking buffer (PBS pH 7.4 containing 0.1 % Saponin and 10 % Bovine Calf Serum (BCS)), and incubated in adipocyte blocking buffer for 30 min at room temperature. The primary antibody for Cav-1 was diluted 1:500 in adipocyte blocking buffer and cells incubated with the primary antibody overnight at 4 °C. HAd were washed three times with adipocyte blocking buffer (twice for 1 min, once for 10 min). The secondary antibody coupled to the fluorescent dye Abberior STAR635P was diluted 1:500 in adipocyte blocking buffer and cells incubated with the secondary antibody for 1.5 h in the dark at room temperature. HAd were washed three times with PBS (twice for 1 min, once for 10 min) and samples mounted on coverslides (631-1551, VWR International GmbH, Darmstadt, Germany) in an antifade reagent (ProLong Gold P36934, Molecular Probes via ThermoFisher Scientific, Dreieich, Germany). Samples were left to dry in the dark overnight, sealed with clear nail polish and imaged using the Leica TCS SP8 STED 3X STED microscope with the specific imaging parameters described in section 2.1.3.

An overview of the used primary and secondary antibodies can be found in Appendix A.3.

To control for proper cell differentiation, human preadipocytes and HAd were stained with the lysochrome diazo dye Oil Red O (ORO, $C_{26}H_{24}N_4O$). ORO is a well-established marker of triglycerides and neutral lipids [419]. The prevalence of lipid droplets indicates the full differentiation of preadipocytes into mature adipocytes [420]. Staining was carried out similarly to the protocol described in [421]. Explicitly, adherent preadipocytes and adipocytes respectively growing on ⌀ 18 mm glass cover slips were washed twice with 1 × Dulbecco's Phosphate-Buffered Saline (DPBS, no Calcium, no Magnesium, 14200-067, Life Technologies via ThermoFisher Scientific, Dreieich, Germany) prior to fixation with 4 % Paraformaldehyde (PFA, in PBS, pH 7.4) for 30 min at room tempera-

ture. A 3 % stock solution of ORO was prepared by dissolving 300 mg ORO powder (O0625-25G, Sigma-Aldrich, Taufkirchen, Germany) in 100 ml 99 % Isopropanol. A working solution of ORO was prepared by adding 1.5 parts of the ORO stock solution to 1 part of deionized water, letting the solution stand at 4 °C for 10 min and filtering it through a grade 4 paper filter (pore size ca. 25 µm). PFA was removed from the cells, the cells were washed once with deionized water and once with 60 % Isopropanol for 3 min prior to incubation with the ORO working solution for 5 min. Cells were then washed with deionized water until the formerly red supernatant became clear. Samples were mounted on coverslides (631-1551, VWR International GmbH, Darmstadt, Germany) in an antifade reagent (ProLong Gold P36934, Molecular Probes via ThermoFisher Scientific, Dreieich, Germany), left to dry in the dark overnight, sealed with clear nail polish and confocal images were obtained using the Leica TCS SP8 STED 3X STED microscope (see section 2.1.3). The obtained ORO control stains of undifferentiated vs. differentiated human adipocytes, as well as the specific imaging settings, are presented in Appendix D.2.

2.5. Calibration samples

2.5.1. Gold beads

Gold bead samples were used to control for the proper alignment of the excitation and STED laser beams both during the first stages of microscope construction as well as within the daily microscope alignment routine (see section 2.10.1). While stirring and heating to 50 °C, 1.5 g polyvinyl alcohol (Mowiol 4-88, Sigma-Aldrich, Taufkirchen, Germany) was diluted in 10 ml distilled water. A colloid of gold nanoparticles of 80 nm diameter suspended in water (BBinternational, Cardiff, UK) was sonicated for 10 min. A volume of 10 µl of the gold colloid was diluted with 100 µl of the Mowiol 4-88 solution and 100 µl of the dispersion was pipetted onto (22×22) mm^2 glass coverslips of thickness #1.5 (i.e. $(0.16 - 0.19)$ mm thickness; 631-0125, VWR International GmbH, Darmstadt, Germany)). The coverslips were spincoated for 30 s at 4000 rpm, covered, and left to dry for 30 min. The coverslips were mounted onto a glass microscope coverslide (631-1551, VWR International GmbH, Darmstadt, Ger-

many) in immersion oil appropriate for our imaging system (immersion oil type F, Leica Biosystems, Nussloch, Germany). The sample was left to dry for 5 min and sealed with nail polish.

2.5.2. Fluorescent Dye Solutions

Fluorescent dye solutions (dye seas) were prepared to control the proper alignment of the signal detecting Avalanche Photo Diodes (APD) within the daily microscope alignment routine (see section 2.10.1) as well as for screening for proper dyes for use in the Two-Photon-Excitation-CW-STED microscope that was built within the scope of this thesis (see sections 2.1.1 and 3.4.2). About 20 µg of the respective dye compound in the NHS−ester modification was solvated in 30-60 µl methanol. The less a dye would dissolve in methanol, the more methanol was applied, yet never exceeding 60 µl. The mixture of dye in methanol was vortexed vigorously and then filled up with purified water (Milli-Q, Merck Chemicals GmbH, Darmstadt, Germany) to a final volume of 500 µl. In case the dye was poorly dissolved, the mixture was centrifuged shortly and only the supernatant used for further sample preparation. Square ((22×22) mm^2; thickness # 1.5) glass coverslips (631-0125, VWR International GmbH, Darmstadt, Germany) were moved slowly across a single-well glass coverslide (5861, GT Vision Ltd, Stansfield, Suffolk, UK) while pipetting about 100 µl of the dye solution into the well avoiding the formation of air pockets underneath the coverslip. Excess liquid was dabbed off carefully and the samples sealed with clear nail polish. An overview of the used fluorescent dye compounds can be found in Appendix A.4.

2.5.3. Fluorescent Beads

Fluorescent bead samples were prepared for use as a benchmark determination of the image resolution achievable with the used "open" (i.e. user accessible) microscope systems (see sections 2.1.1 and 2.1.2) and measured prior to every imaging experiment within the daily microscope alignment routine (see section 2.10.1), thus providing the validation of reproducible microscope performance. For imaging with the Two-Photon-Excitation-CW-STED setup (see section 2.1.1), $\varnothing$ 40 nm yellow-green fluorescent beads (FluoSpheres, F8795,

Molecular Probes via ThermoFisher Scientific, Dreieich, Germany) were used. For imaging with the custom-built fast scanning STED setup (see section 2.1.2), ⌀ 20 nm crimson fluorescent beads (FluoSpheres, F8782, Molecular Probes via ThermoFisher Scientific, Dreieich, Germany) were used. Square glass coverslips ((22×22) mm^2; thickness #1.5, 631-0125, VWR International GmbH, Darmstadt, Germany) were covered with Poly-L-lysine (0.1 % (w/v) in H_2O, P8920-100ML, Sigma-Aldrich, Taufkirchen, Germany) for 10 min, then the excess Poly-L-lysine was rinsed off with deionized water and blown dry with compressed air. Fluorescent beads were vortexed and diluted 1:1000 in purified water (Milli-Q, Merck Chemicals GmbH, Darmstadt, Germany), and the solution vortexed prior to sonication for 8 min. The bead solution was pipetted onto the coated coverslips (about 80 µl per coverslip, forming a roughly ⌀ 1 cm circle) and left for 10 min, then rinsed off with deionized water and blown dry with compressed air. The coverslips were mounted onto glass coverslides (631-1551, VWR International GmbH, Darmstadt, Germany) in polyvinyl alcohol (Mowiol 4-88, Sigma-Aldrich, Taufkirchen, Germany) containing 2.5 % DABCO. Samples were left to dry for 1 h and sealed with clear nail polish.

2.5.4. Standardly prepared fluorescent cell samples

Samples of Vero cells fluorescently labeled for the cytoskeletal protein Tubulin via indirect immunofluorescence served as standardly prepared specimens for comparative studies of different fluorescent dyes regarding their spectroscopic properties and their bleaching behavior. For fluorescence staining, cultured Vero cells (see section 2.4.1) grown on glass cover slips were fixed with ice-cold methanol for 4 min. To block unspecific binding, cover slips were washed three times (for 5 min per step) in 2 % Bovine Serum Albumine diluted in pH 7.4 PBS (BSA/PBS) at room temperature. The primary antibody against α-Tubulin (mouse monoclonal, T6074, Sigma-Aldrich, Taufkirchen, Germany) was diluted 1:50 in 2 % BSA/PBS and cells were incubated with it for 1 hour in a wet chamber at room temperature, then washed three times (for 5 min per step) in 2 % BSA/PBS. The secondary antibody, decorated with the respective fluorescent dye, was diluted 1:50 in 2 % BSA/PBS and cells were incubated with it for 1 hour in a wet chamber at room temperature, then washed three fast times in PBS. Samples were mounted in polyvinyl alcohol (Mowiol

4-88, Sigma-Aldrich, Taufkirchen, Germany) containing 2.5 % DABCO (see Appendix A.1), were left to dry, and sealed with clear nail polish. An overview of the used primary and secondary antibodies can be found in Appendix A.3.

2.6. Image analysis

2.6.1. General image processing

All acquired images were visualized, processed and analyzed using the software package ImSpector [422], Fiji (`http://imagej.net/Fiji`, [423]), Origin (OriginLab, Northhampton, MA, USA), and MATLAB (The MathWorks, Inc., Natick, Massachusetts, United States).
Image smoothing was performed with the ImSpector software using a low-pass Gaussian filter with a width of 1.5 times the respective image pixel size (typically corresponding to 30 nm). If a smoothing step has been applied to the images, it is stated explicitly in the corresponding figure caption.
Image deconvolution was performed with the ImSpector software using an experimentally obtained point spread function (from fluorescent bead measurements, see section 2.10.1) of 40 nm full width at half maximum and performing two iterations of a two-dimensional (2D) Richardson-Lucy deconvolution [424, 425]; if a deconvolution step has been applied to the images, it is stated explicitly in the corresponding figure caption.
Images were corrected for background signal with the software Fiji typically using a rolling ball radius of 30 px, and contrast was enhanced to a saturated pixel ratio of typically 0.4 %, unless stated otherwise. If a background correction or contrast enhancement has been applied to the images, it is stated explicitly in the corresponding figure caption. In general, the two image processing steps of background correction and contrast enhancement were only used for reasons of better visibility.
Three-dimensional (3D) images were obtained from Z-stacks, i.e. successive scans along the axial direction of two-dimensional (2D) images scanned laterally along the imaging plane parallel to the cover slip. 3D image rendering was performed with the software AMIRA 6.0 (FEI Visualization Sciences Group, Mérignac, France). For rendering, raw data images were smoothed with the

software ImSpector using a two-dimensional Gaussian filter with a width of 1.5 pixels and exported to the binary double format. The exported files were read in with AMIRA 6.0 and displayed in the "Voltex" or "Volren" rendering modes with adjusted brightness thresholds. Cell sections were obtained by cutting the rendered 3D images using the "OrthoSlice" mode.
Two-color images were converted to a color map comprising zero signal in black, the first color channel in cyan, the second color channel in magenta, and overlap of the first and the second color channel in yellow. The color channel brightness was normalized to its respective minimum and maximum.
Three color images (see section 3.9, Fig. 3.40) were smoothed using a two-dimensional Gaussian filter with a width of 1.5 pixels using the software Imspector. Image brightness normalized to the respective minimum and maximum, and converted to an RGB color map using Fiji. This color map comprises zero signal in black, the first color channel in red, the second color channel in green, and the third color channel in blue. Overlap of two color channels results in a cyan, magenta, or yellow signal; overlap of all three color channels results in a white signal. A summarizing color key is given in the figure.

2.6.2. Determination of image resolution

For the determination of the STED image resolution, I followed a protocol similar to the one that I have established, employed and described elsewhere (e.g. in [426, 427, 343]). For circular signals and structures (e.g. fluorescent beads or single Caveolin-3 and Dystrophin domains, respectively), a box of between (200×200) nm^2 and (400×400) nm^2 was drawn around a single structure in the raw data image. The signal intensity was added up along the X-axis of this box and then graphically displayed against the Y-axis of the boxed region. For elongated signal structures (e.g. transverse tubules), a line of a width of at least 5 pixels (typically corresponding to 100 nm) was drawn to perpendicularly cross a selected elongated structure in the raw data image. The signal intensity was added up parallel to the structure and was displayed against the position along the drawn line. These plotting procedures for circular and elongated structures, respectively, were performed using the software package ImSpector. The signal intensity graphs were exported to the software Origin. Since the shape of the point spread function (PSF) of a STED microscope de-

pends on whether the STED laser was operated in pulsed mode or continuous wave (CW) mode [348], a case differentiation was made for determining the image resolution depending on the respective STED laser used. Hence, the signal intensity was normalized and the Origin built-in Lorentzian peak function was fit to the data if the data was recorded using a STED laser operated in CW mode, i.e. using the custom-built 2P-Exc-CWSTED setup (see section 2.1.1). A Gaussian function was fit to the data if the data was recorded using a STED laser operated in pulsed mode, i.e. using the custom-built fast scanning STED setup (see section 2.1.2), or one of the commercial STED microscope systems (see sections 2.1.3 and 2.1.4). The upper limit for image resolution was extracted from these fits as the full width at half maximum of the Lorentzian or Gaussian curve, respectively. The estimates of the resolution of both circular and elongated structures that are given in this thesis were obtained from the arithmetic mean of several such Lorentzian or Gaussian fits of different structures; the type of the used curves for fitting along with the total number of evaluated signal structures is denoted explicitly in the sections discussing the corresponding results.

2.6.3. Determination of bleaching constants

Bleaching under STED imaging conditions of samples fluorescently labeled with various dye compounds followed a protocol I established and previously reported in [427]. This protocol is based on the study of bleaching of a sample under the same image acquisition conditions that are also employed in the actual imaging experiment. I found this procedure to be the most suitable because it emulates the bleaching of the actual sample's region of interest on a different region in the same sample and thus provides the most realistic assessment of the bleaching process with all its underlying, and, in part, not well-understood, details. Further, the bleaching constant was determined in units of imaged frames. The frames were recorded with imaging parameters specific to the regarding sample. I chose this unit for representation because, in my experience, when imaging a sample in STED microscopy, the imaging parameters are set such that the best possible STED image is obtained. This procedure is hardly comparable across different samples and different microscope setups. Therefore, the most useful measure of bleaching is the number of reasonably

bright images (i.e. the sample structure must be clearly identifiable) that can be recorded of a single sample region under optimal imaging conditions. This, admittedly, very qualitative number should then be compared among samples where the same structure is labeled with different fluorescent dyes and imaged using the same microscope. In brief, 20 subsequent frames per sample spot were obtained under optimized imaging conditions for the respective fluorescent dye in the sample, i.e. 2P-Exc wavelength, detection window, 2P and STED illumination powers, and time gating of the fluorescence signal. The pixel size was kept at 20 nm for all samples and the sample scanning rate was set to a pixel dwell time of 0.05 ms. The total signal of each acquired frame was determined, thereby excluding pixels at the image borders as they could add to an increase in signal over time due to sample drift and therefore detection of signal stemming from an unbleached sample area. Pixel intensities were plotted against the number of acquired frames. The resulting curves were normalized to their maximum value and plotted in one graph for comparison of the bleaching rates. Bleaching rate constants were extracted as the nominal image frame at which the total fluorescence signal had dropped to half of its initial/maximum value. The bleaching rate constant was always rounded down to the next smaller integer. For the characterization of the bleaching behavior of selected dyes under 2P-Exc-CWSTED conditions, the decrease in fluorescence intensity was fit to mono- and biexponential decay functions using the software Origin. The regular residuals per fit function were compared to each other to evaluate the goodness of fit; this is discussed in Appendix G.3.

2.6.4. Determination of surface signal densities

For the determination of the surface signal densities in filopodia of U2OS, HeLa, HEK, and Vero cells (see e.g. section 3.3), recorded STED images were processed with the software Fiji to enhance the contrast (2 % saturated pixels) and to subtract the background (rolling ball radius: 30 pixels). Filopodial structures in the images were carefully identified as elongated protrusions from the basement membrane that showed a fluorescent signal only along their outlines. Filopodia were outlined manually using the freehand selection tool. The pixel values outside the outlines were set to zero (Fiji command: “clear outside”) and the images of the filopodial outlines were saved as separate files and further

processed in MATLAB. A custom-written MATLAB routine was used to threshold and binarize the images of filopodial outlines. Thresholding was based on evaluating the value of each pixel in the image and on the comparison of each pixel with its directly adjacent, and its diagonally neighboring pixels. To binarize the image, a pixel was set to "1" (positive signal) if its value was 40 % above the mean image brightness and if it was surrounded by both directly adjacent and diagonally neighboring pixels of values at least equal to the mean image brightness. The values defininig the binarization thresholds were chosen by iteratively setting different threshold values and examining by eye how well they would capture the filopodial structures of the original images. The binarized images were then inverted and further processed, again using Fiji. The "Analyze Particles" plugin was used to determine the area of positive signal within the filopodial region of interest (ROI), denoted as A_{signal} and given in pixel. In the "Analyze Particles" plugin, the minimum acceptable particle size was set to 10 pixel to avoid artifacts of falsely positively categorized signal stemming from the binarization protocol. In a next step, to arrive at the total area of the filopodial structure, the binarized filopodial ROI was processed using the Fiji built-in functions 1.) "Dilate", 2.) "Close", and 3.) "Open"; this procedure extends the binary signal in the filopodial ROI to encompass the complete filopodial structures. Using the "Analyze Particles" plugin on this dilated and filled binary image of the filopodial ROI yields the total area, denoted as A_{total} and given in pixel. From the values of A_{signal} and A_{total}, the surface signal density in filopodia ρ_{Filo} was calculated as

$$\rho_{Filo} = \frac{A_{signal}}{A_{total}}$$

ρ_{Filo} is standardly presented as a percentage. The above described procedure for the determination of ρ_{Filo} is visualized exemplarily in the Appendix F.
For the determination of the surface signal densities at the basement membrane of culture cell lines, and at the sarcolemma of primary mouse ventricular cardiomyocytes (VM, see e.g. section 3.3), recorded images were processed with Fiji to enhance the contrast (0.4 % saturated pixels) and to subtract the background (rolling ball radius: 30 pixels). Regions of interest for surface density analysis were carefully selected according to the following criteria. For culture

cell lines featuring filopodia, only membrane regions that did not show filopodial structures were selected. Additionally, in all investigated cell types, regions of cell borders were not considered for analysis because they are usually oriented perpendicularly to the focal plane and labeled structures thus tend to stack on top of each other along the axial direction leading to a fluorescence signal add-up and thus yielding a disproportionally bright signal compared to the signal brightness along the "flat" cell membrane. This would compromise the accuracy of the image binarization algorithm based on pixel brightness values. Moreover, it was made sure that the analyzed area of cellular basement membrane was the same for each cell type to justify comparability of the calculated surface signal densities. The selected image regions that fulfilled these criteria were saved as separate files and further processed in MATLAB. A custom-written MATLAB routine was used to threshold and binarize the image regions following a similar procedure as stated above for binarization of images of filopodial structures. Explicitly, for the binary thresholding of signal structures along the cellular basement membrane, pixel brightness was considered "positive signal" if its value was at least 60 % of the mean image brightness and if it was surrounded by directly adjacent pixels of at least 40 % of the mean image brightness, and diagonally neighboring pixels of at least 30 % of the mean image brightness. The binarization algorithm then counted all the pixels considered to have "positive signal", divided it by the total amount of pixels in the selected image and gave out the thus obtained surface signal density ρ_{Surf}. ρ_{Surf} is standardly presented as a percentage. The above described procedure for the determination of ρ_{Surf} is visualized exemplarily in the Appendix F.

2.6.5. Determination of single domain sizes

For the analysis of single Cholesterol (Chol) and Caveolin-3 (Cav-3) signal domains (defined and discussed in section 3.5) at the sarcolemma of mouse ventricular cardiomyoctes (VM), recorded STED images were processed with MATLAB. Single signal domains were carefully identified by eye and were outlined manually. Within this chosen outline, the single signal distribution was approximated by fitting a Gaussian profile (in case of pulsed STED laser illumination), or a Lorentzian profile (in case of CW STED laser illumination)

in the X- and the Y-direction, respectively. The full width at half maximum (FWHM) in the X-direction ($FWHM_x$) and in the Y-direction ($FWHM_y$) was denoted. This procedure was carried out for several identified single domains per image (with one image corresponding to one VM), thereby making sure that the same amount of single domains per image was evaluated. For each image the arithmetic mean and the standard deviation of both $FWHM_x$ and $FWHM_y$ was calculated to yield the diameter of single signal structures within one cell. This evaluation was repeated for all obtained STED images of VM. Finally, the arithmetic mean and the standard deviation of the average domain diameter obtained from each image was calculated and defined as the overall single domain size.

2.6.6. Determination of ring structure diameters

For the analysis of ring shaped Caveolin-3 and Cholesterol signal structures at the sarcolemma of mouse ventricular cardiomyocytes and at the basement membrane of living HeLa cells (see section 3.5), recorded STED images were processed with the software Fiji to enhance the contrast (2 % saturated pixels) and to subtract the background (rolling ball radius: 30 pixels). Individual ring structures in the images were carefully identified by eye and were outlined manually. The pixel values outside the outlines were set to zero (Fiji command: "clear outside"), and the images of single, isolated ring structures were saved as separate files and further processed in MATLAB. A custom-written MATLAB routine was used to smooth the images with a low-pass Gaussian filter with a width of 2 times the image pixel size (corresponding to 40 nm). Signal intensity peaks along the ring structures were identified with a threshold set to 0.4 times the maximum image brightness. The signal peaks were localized to a single pixel coordinate. A circle was fit to the positions of all determined signal peaks using the MATLAB built-in function "circfit.m", and the corresponding diameter extracted from the fit.

2.6.7. Determination of contour densities

To quantify the observed effect of the dissociation of sarcolemmal Caveolin-3 (Cav-3) signal clusters upon Cholesterol depletion of mouse ventricular cardiomyocytes (VM) by incubation with Methyl-β-CycloDextrin (M-β-CD, see sections 3.5.1 and 2.3.3), I developed an algorithm that extracted the contour densities of Cav-3 signal structures from the according STED images as explained in the following. I defined the signal contour density Γ as the ratio of the number of boundaries between pixels showing a positive Cav-3 signal vs. pixels showing no Cav-3 signal, and the total number of possible pixel boundaries within the image. Γ thus describes the extent of clustering of a signal structure in an inverse fashion, meaning: the bigger Γ, the less clustered is the spatial distribution of the signal. The algorithm thresholds and binarizes the STED images analogous to the procedure described in section 2.6.4. In the binarized images, pixels are categorized into having "positive signal" if their brightness is above the binarization threshold and "negative signal" (i.e. background signal) if their brightness is below the binarization threshold. For every pixel, the algorithm compares the pixel value with the value of the adjacently neighboring pixels. If there is a transition from positive to negative signal (or vice versa) between two pixels, this transition is counted as one signal boundary. The number of the recorded boundaries is halved for the actual analysis to avoid double counting of redundant boundaries, thus yielding the number of signal transition boundaries B_{trans}. Additionally, a 1-pixel wide border is defined along the edges of each image. Transition boundaries are not counted for pixels of this border to avoid signal artifacts. The total number of possible pixel boundaries B_{tot} is given by

$$B_{\text{tot}} = 2 \cdot A_{\text{tot}} - (R + C)$$

where A_{tot}: total area of the image (in pixels), R: number of rows in the image matrix, and C: number of columns in the image matrix. These three input parameters were extracted from the image from which the border mentioned above was already subtracted. The signal contour density is determined by the ratio

$$\Gamma = \frac{B_{\text{trans}}}{B_{\text{tot}}}.$$

Three exemplary cases of signal distribution and their description by Γ are schematically sketched in Fig. 2.3 **A** - **C**, respectively. Therein, the red boxes symbolize pixels with a positive signal, the white boxes symbolize pixels with a negative signal, and the grey boxes define the 1-pixel wide image border. Blue dots mark the counted pixel boundaries upon a transition between a positive signal pixel to a negative signal pixel. The total area of the signal is the same

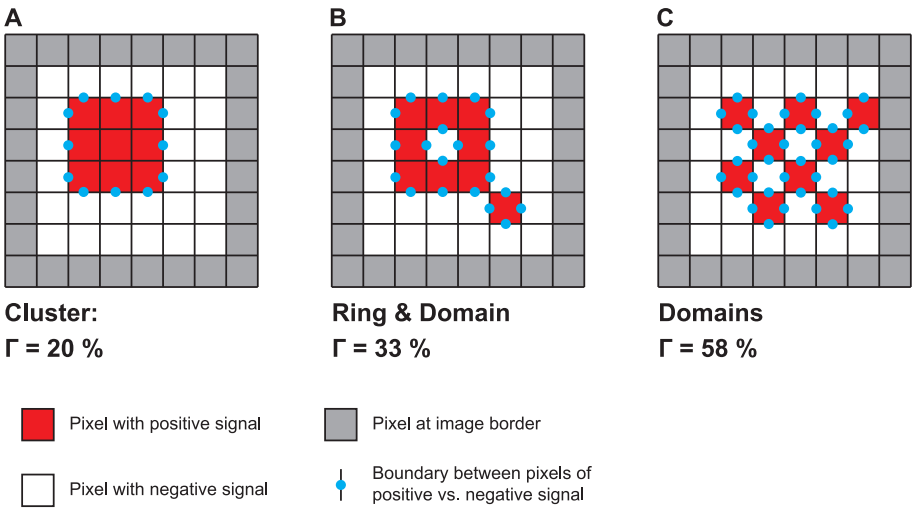

Figure 2.3.: Schematic of the definition of the contour density Γ

in Fig. 2.3 **A** - **C**, yet its spatial distribution is different. Fig. 2.3 **A** illustrates a totally clustered signal structure, **B** a ring and a small, singular signal entity (a "single domain"), and **C** a completely dispersed signal only consisting of single domains. The contour density Γ gradually increases for these three cases of signal distribution. A complete dissociation of a clustered signal into single domains, albeit of constant signal area, is here characterized by an increase in Γ by a factor of almost 3. Γ is typically given in % of the total number of possible pixel boundaries.

2.7. Colocalization analysis

For the colocalization analysis of sarcolemmal Cholesterol (Chol) and Ganglioside GM1 (GM1) clusters in living cardiomyocytes (for sample preparation see section 2.3.2) as well as sarcolemmal Caveolin-3 (Cav-3) and GM1 clusters in fixed cardiomyocytes (for sample preparation see section 2.3.3), two-color STED images of the respective samples were obtained as described in sections

2.3.2 and 2.3.3. Equally sized regions of interest were extracted from images of individual cells and used for analysis. The two-color STED images were binarized as described in section 2.6.4. The respective signal in the binarized images was then converted to a false color scale with one color channel displayed in magenta (for the Chol and the Cav-3 signal, respectively) and the other color channel displayed in cyan (for the GM1 signal). Binarized and color-converted images from the same sample scan were overlaid and the overlap of the two color channels displayed in yellow. The number of pixels featuring the respective colors magenta, cyan, and yellow were counted. The relative colocalization (in %) of the first color channel (e.g. Chol in magenta) with the second color channel (e.g. GM1 in cyan) was determined by dividing the number of yellow pixels by the total number of pixels in the respective first color channel (i.e. all magenta pixels in the image). This relative colocalization thus describes the ratio of the signal of the first color signal colocalizing with the second color signal with respect to the total signal of the first color channel (e.g. the percentage of all Chol clusters that colocalize with GM1 clusters). Results are given and discussed in section 3.6.
An analogous colocalization analysis was performed to determine the effect of Chol depletion on the spatial association between Dystrophin (Dyst) and Cav-3 signals in VM (see e.g. section 3.7.1).

2.8. Determination of nearest neighbor distances

To extract the peak-to-peak Nearest Neighbor Distance (NND) from multicolor STED images (see section 3.7), images were processed and analyzed using a custom-written routine in MATLAB. Images were smoothed using a two-dimensional Gaussian filter with a width of 1.5 pixels (corresponding to 30 nm as all analyzed images were acquired with a pixel size of 20 nm). Local signal maxima in the smoothed images were identified via a pixel by pixel comparison of a central pixel with its directly adjacent and diagonally neighboring pixels if they were above a threshold value of about 25 % of the maximum image brightness. Coordinates of the found maxima were extracted and indexed for each color channel of the multicolor images. NND between nearest neighbors from different color channels were determined using the MATLAB built-in

function “knnsearch”.
Note that the determined NNDs have a directionality, i.e. there is a distinct distribution of NNDs between A and B vs. between B and A. In this thesis, the determination of the distribution of the peak-to-peak NND between a population A and a population B means that for a fixed signal spot in A the nearest signal spot from the whole set of all signals in B is identified; then the distance to A is extracted and enters the NND distribution. Accordingly, the NND between B and A means that for every B, the distance to the nearest neighbor in A is determined and denoted.

2.9. Statistics

Statistical significance of all the obtained quantitative data throughout this work was tested using the two-sided Mann-Whitney-Wilcoxon U test (MWW) [428, 429]. Statistical significance testing was performed for all possible permutations of pairs of two sample groups within each complete data set per assessed descriptive quantity. The following properties of the quantitative data sets presented in this work justify the choice of the two-sided MWW:

- The independent variable, i.e. one of the two sample groups, is categorical and can only take on two values: e.g. “cell type 1” vs. “cell type 2”.
- The dependent variable, i.e. the assessed descriptive quantity, is continuous and ordinal.
- The two sample groups, i.e. the two compared cell types, are independent: all descriptive quantities were assessed in individual experiments.
- The ordering of the data for each considered sample group is random.
- The sample sizes per sample group differ and are not paired.
- The data within each sample group are not assumed to be normally distributed, i.e. the sample data are nonparametric.
- The variances of the data within each sample group are not assumed to be equal nor homogeneously distributed.

- There is no initial hypothesis about the nominal direction along which the data sets of each sample group differ from each other. Thus, a two-sided MWW is performed.

The U statistic of the MWW was determined by first assigning ranks to all ordinal sample data and, second, determining the sum of ranks for all data stemming from sample group 1 and all data stemming from sample group 2, respectively. The U statistic for each sample group (i.e. U_1 for sample group 1 and U_2 for sample group 2) is then calculated via

$$U_1 = n_1 n_2 + \left(\frac{n_1 (n_1 + 1)}{2} \right) - R_1$$

and

$$U_2 = n_1 n_2 + \left(\frac{n_2 (n_2 + 1)}{2} \right) - R_2$$

where n_1 and n_2 are the sample data size and R_1 and R_2 are the sum of ranks of sample group 1 and sample group 2, respectively. I determined the defining parameters n_i and U_i for each pair of sample groups and therefrom the p-value of statistical significance of the MWW using the MATLAB script "mwwtest.m" [430]. The difference between data from different sample groups was considered statistically significant for $p \leq 0.01$ (marked with (*)), highly statistically significant for $p \leq 0.001$ (marked with (**)) and not significant for $p \geq 0.01$ (marked with "n.s.").
The explicit MWW U statistics for the data sets presented in this PhD work are summarized and displayed in the Appendix I.

2.10. Additional experimental techniques

2.10.1. Daily microscope alignment routine

The performance of the custom-built microscope systems used within the scope of this thesis - i.e. the two-photon-excitation-CW-STED microscope (see section 2.1.1) and the fast scanning STED microscope (see section 2.1.2) - was controlled on a day-to-day basis using standardized calibration samples (see sections 2.5.1, 2.5.2 and 2.5.3). To this end, a three-step system alignment procedure was performed as described in the following.

First, the mutual spatial alignment of the excitation and STED laser beams was monitored and adjusted by scanning a sample of $\varnothing$ 80 nm gold beads (see section 2.5.1) with the respective laser beam and recording the point spread function (PSF) of an individual bead with a PMT in the path of the backscattered light. The excitation laser beams were aligned to the STED beam as the reference to achieve maximal overlap of both lateral and axial PSFs, respectively.
Second, the optimal alignment of the fluorescence detection units was adjusted using a fluorescent dye sea sample (see section 2.5.2) that was illuminated with the respective excitation laser beam. The sample was scanned axially and the fluorescence signal at the edge of the dye sea was monitored with the APD of the respective color channel. The illumination of the APD was optimized by maximizing the fluorescence signal stemming from the dye sea sample. Additionally, for the fast scanning STED microscope (see section 2.1.2) with pulsed excitation lasers, the dye sea fluorescence signal was used to synchronize excitation and STED laser pulses. To this end, the dye sea was illuminated with both excitation and STED laser light (at very low intensities) and the time delay between the two laser pulse trains was adjusted such that the recorded signal became minimal (i.e. resulting in a maximal switch-off effect).
Third, to have a comparative standard for the achievable STED image resolution on the day of a specific experiment using either the fast scanning STED microscope setup (see section 2.1.2) or the Two-Photon-Excitation-CW-STED (2P-Exc-CWSTED) microscope (see section 2.1.1), images of spectrally appropriate fluorescent beads (see section 2.5.3) were recorded in both STED and confocal mode. Based on the obtained images, the achievable object resolution was determined as is described in section 2.6.2. Experiments were conducted only if the thus determined resolution reached an acceptable value. If this criterion of image quality could not be met, the system was checked and re-aligned until appropriate performance was guaranteed. The measured diameter of sample beads served as a control value for the achievable resolution. The 2P-Exc-CWSTED setup provided a standard lateral bead diameter of ≤ 50 nm (see section 3.4.1); the custom-built fast scanning STED setup provided a standard lateral bead diameter of ≤ 40 nm .
Further, for image acquisition with the 2P-Exc-CWSTED setup (see section 2.1.1), the correction collar of the used water immersion objective was adjusted

to match the thickness of the cover slips on which the samples were plated and/or mounted (typically a thickness of 0.13 - 0.16 mm, i.e. cover slips of type #1.0). To this end, fluorescent beads were axially scanned and the correction collar was iteratively adjusted to yield the smallest axial point spread function free of spherical aberrations. An axial resolution of 450 nm was achieved using yellow-green fluorescent beads featuring an emission maximum at 515 nm (see section 2.5.3). The optimal position of the correction collar was controlled from time to time at an appropriate interval.

2.10.2. Western blots

Caveolin-3 (Cav-3) protein expression in mouse ventricular cardiac tissue and in Cav-3 overexpressing HeLa cells (via the transfection protocol described in section 2.4.1) was determined by Western Blotting.
To this end, hearts from four 12-week-old, male C57Bl/6N mice (Charles River, Sulzfeld, Germany) were excised and the left ventricles were dissected. Left ventricles were homogenized in 1 ml homogenization buffer (HB, see Table 2.4) using a disperser (Ultra-Turrax, IKA-Werke GmbH, Staufen, Germany). Tissue homogenates were incubated in an overhead shaker for 30 min at 4 °C prior to being centrifuged at 5,000 g for 10 min in a centrifuge cooled to 4 °C. Homogenates of Cav-3 overexpressing HeLa cells were obtained analogously after collecting cells from the culture dish with a cell scraper, discarding the supernatant of culture medium and pelleting the cells at 600 g at 4 °C for 5 min.
For the determination of protein concentrations, 3 µl of the supernatant of the respective homogenate was diluted in 57 µl H_2O (1:20 dilution) and used in a standard protein detection kit (Pierce BCA Protein Assay Kit, 23227, ThermoFisher Scientific, Dreieich, Germany) following the manufacturer's instructions. The specific protein concentrations in tissue and cell homogenates are given in the Appendix, see Table L.1. For the gel preparation, a 12 % Acrylamide separating gel (see Table 2.5) was mixed and poured, covered with water-saturated butanol. The gel was polymerized at room temperature until the aqueous phase between the gel and the butanol became clearly visible. The butanol was discarded, the separating gel was rinsed with distilled water and dried with filter paper. The 4 % Acrylamide stacking gel (see Table 2.5)

	MW [g/mol]	Final concentration
Homogenization buffer (HB)		
HEPES	238.31	10 mM
Sucrose	342.30	300 mM
NaCl	58.44	150 mM
EGTA	380.35	1 mM
$CaCl_2$	110.98	2 mM
Adjust to pH 7.4 at 37 °C with NaOH [1M]		
Triton X-100	647	1 % (v/v)
Phosphate inhibitor cocktail (PhosSTOP)	–	1 tablet/10 ml
Protease inhibitor cocktail, EDTA free (cOmplete)	–	1 tablet/10 ml
Ad. H_2O		
4 × Laemmli sample buffer (SB)		
Glycerol	92.09	47 % (v/v)
EGTA	380.35	16 mM
Tris/HCl (pH 6.8)	121.14	240 mM
SDS	288.37	4 % (w/v)
Bromophenol blue	669.96	0.05 % (w/v)
TCEP	286.65	10 % (w/v)
Ad. H_2O		
Transfer buffer (TB)		
Tris	121.14	65 mM
Glycine	75.07	380 mM
Methanol	32.04	20 % (v/v)
Ad. H_2O		
Tris-buffered saline with Tween 20 (TBST)		
Tris	121.14	10 mM
NaCl	58.44	170 mM
Tween 20	1227.54	0.05 % (v/v)
Ad. H_2O; adjust pH to 7.5		

Table 2.4.: Buffers for Western blot analysis. Providers and order numbers of the used chemicals are given in Appendix A.1.

was poured on top and the comb was inserted immediately. The gel was polymerized at room temperature for 1 h. Protein samples were brought to 90 µg

	Absolute amount
12 % Acrylamide separating gel, 15 ml total volume	
H_2O	5.25 ml
Acrylamide/Bis-acrylamide (30 %/0.8 % w/v)	6.0 ml
1.5 M Tris-HCl, pH 8.8	3.75 ml
10 % (w/v) SDS	150 µl
TEMED	7.5 µl
10 % APS	75 µl
4 % Acrylamide stacking gel, 15 ml total volume	
H_2O	9 ml
Acrylamide/Bis-acrylamide (30 %/0.8 % w/v)	1.98 ml
0.5 M Tris-HCl, pH 6.8	3.78 ml
10 % (w/v) SDS	150 µl
TEMED	15 µl
10 % APS	75 µl

Table 2.5.: Gels for Western blot analysis. Providers and order numbers of the used chemicals are given in Appendix A.1.

protein in 45 µl 1x Laemmli sample buffer (SB, see Table 2.4). A prestained molecular weight marker (Protein-Marker V, 27-2210, Peqlab via VWR International GmbH, Darmstadt, Germany) was used as a size standard. Samples were loaded on the gel and electrophoresis was performed at 70 V for approximately 15 min, then the voltage was increased to 150 V and electrophoresis was continued until the first weight marker band reached the bottom of the gel.
For blotting, PVDF membranes were soaked in transfer buffer (TB, see Table 2.4) for 1 min. Proteins were blotted to PVDF membranes in a wet blotting apparatus consisting of two layers of filter paper, the PVDF membrane, the protein gel, and another two layers of filter paper. The wet blotting apparatus was filled with 1× TB (see Table 2.4), put on ice, and blotting was performed at 100 V for 1 h. After blotting, the membrane was stained in a solution of 0.1 % Ponceau in 5 % acetic acid (P7170, Sigma-Aldrich, Taufkirchen, Germany) for 5 min to confirm uniform protein transfer onto the membrane. The membrane was then washed thoroughly with H_2O and transferred to Tris-buffered saline

with Tween 20 (TBST, see Table 2.4) containing 5 % milk powder and blocked for 1 h to avoid artifacts due to unspecific binding.
The $\approx$ 36 kDa enzyme Glyceraldehyde 3-phosphate dehydrogenase (GAPDH) was used as a loading control. Primary antibodies were diluted in TBST containing 5 % milk powder in the following concentrations: 1:80,000 for mouse anti-GAPDH (5G4 Mab 6C5, Biotrend, Cologne, Germany) and 1:1,000 for rabbit anti-Cav-3 (ab2912, Abcam, Cambridge, UK). After blocking, the membranes were incubated with the primary antibodies overnight at 4 °C. Membranes were washed three times (for 10 min per washing step) with TBST. The secondary antibodies ECL-HRP-linked sheep anti-mouse for GAPDH detection, and ECL-HRP-linked donkey anti-rabbit for Cav-3 detection (Enhanced Chemiluminescence Horse Radish Peroxidase, NA9310/NA9340, GE Healthcare, Munich, Germany) were diluted 1:15,000 in TBST containing 5 % milk powder. Membranes were incubated with the secondary antibodies for 1 h at room temperature, and were washed four times (for 10 min per washing step) with TBST.
For detection, the chemiluminescense reagents were mixed at a ratio of 1:1 Luminol:Peroxide solution (Immobilon Western HRP Substrate, WBKLS0500, Merck Millipore, Darmstadt, Germany), pipetted onto the membrane while tilting it gently in an amount to completely cover the membrane. After a short incubation time, chemiluminescence was recorded using an appropriate imaging station (Kodak Image Station 4000R Pro, Carestream Health Inc., Rochester, NY, USA).
One of the obtained Western blots is exemplarily shown and thoroughly discussed in section 3.5. The complete set of Western blots that were prepared is shown and described in Figure L.1 in Appendix L.

2.10.3. Electron microscopy

Cardiac samples for electron microscopy

Adult mouse ventricular cardiomyocytes were isolated as described in section 2.3.1.
For electron microscopy (EM) imaging of single cells, isolated cells were carefully plated in perfusion buffer on $\varnothing$ 13 mm ACLAR® foil punch-outs (10501-

10, Plano GmbH, Wetzlar, Germany) for at least 30 min. The supernatant was carefully pipetted off and replaced by fixative solution consisting of 2.5 % Glutaraldehyde (G5882, Sigma-Aldrich, Taufkirchen, Germany) in 0.1 M Sodium cacodylate buffer (pH 7.5, C4945, Sigma-Aldrich, Taufkirchen, Germany). Cells were fixed overnight at 4 °C before being processed further as described in section 2.10.3.
For EM imaging of cell pellets, i.e. of cells in a loose cell complex, isolated cells suspended in perfusion buffer were left to sediment for 10 min to form a visible cell pellet. For immobilization of the cell pellet, the supernatant was carefully pipetted off and the pellet resuspended in 4 % warm (max. 60 °C to avoid damage to the sample) Agarose (A9539, Sigma-Aldrich, Taufkirchen, Germany) and centrifuged immediately. After the Agarose had hardened, the mixture of cell pellet and Agarose was dissected into small pieces and incubated in fixative solution for 30 min. Ensuingly, the samples were fixed overnight at 4 °C before being further processed as described in section 2.10.3.
For EM imaging of tissue sections, mouse hearts were extracted, their proximal aorta connected to a 21 gauge cannula, and cannulas were connected to a modified Langendorff perfusion system (see section 2.3.1) placed in a fume cupboard. The cannulated hearts were perfused with perfusion buffer (see Table 2.1) for 4 min at 37 °C and at a flow rate of 4 ml/min. Perfusion buffer was replaced by fixative solution and the hearts perfusion-fixed for 10 min at a flow rate of 4 ml/min (total volume of throughput: 40 ml). The hearts were then transferred into a Petri dish coated with Silicone and filled with fixative solution. *Trabeculae carnae* from the left ventricle were excised and transferred into an Eppendorf cup filled with fixative solution and further processed for EM sample preparation.

Sample preparation for electron microscopy

After fixation, cell and tissue samples (see section 2.10.3) were washed thoroughly with 0.1 M sodium cacodylate buffer (three times for 5 min each). Samples were transferred into 0.1 M sodium cacodylate buffer containing 1 % OsO_4 (75633, Sigma-Aldrich, Taufkirchen, Germany) and incubated on ice for 1 h. OsO_4 containing buffer was removed thoroughly and samples washed several times with H_2O. Samples were transferred into 1 % uranyl acetate (in H_2O) and

incubated in the dark at room temperature for 20 min. For dehydration, samples were washed according to the following scheme: twice with 30 % ethanol for 5 min each; three times with 50 % ethanol for 5 min each, three times with 70 % ethanol for 5 min each; three times with 100 % ethanol for 5 min each; twice with 100 % ethanol for 10 min each; and twice with 100 % propylene oxide (110205, Sigma-Aldrich, Taufkirchen, Germany) for 5 min each (closed lid). Samples were incubated in a 1:1 mixture of Epon 812 (45345, Sigma-Aldrich, Taufkirchen, Germany) and propylene oxide for 30 min (closed lid). Samples were incubated in pure Epon 812 for 60 min (closed lid). Epon 812 was replaced and samples were incubated overnight on a platform shaker. Samples were let to polymerize in flat embedding molds at 60 °C for 48 h. Samples of cell pellets and cardiac tissue embedded in Epon 812 were cut into 70 nm thin slices using an ultramicrotome (Ultracut UCT, Leica Microsystems GmbH, Wetzlar, Germany) equipped with a 35° ultra diamond knife (Diatome, Hatfield, PA, USA). All samples were counterstained with 1 % methanolic uranyl acetate (incubation for 20 min followed by thorough washing with distilled water). Samples were investigated using a BioTwin CM120 transmission electron microscope (Philips/FEI, Graefelfing, Germany) equipped with a TemCam F416 CMOS camera (TVIPS GmbH, Gauting, Germany). Images were taken in a format of (4000×4000) pixels without binning.

3. Results and discussion

3.1. Cholesterol-PEG-KK114: a novel live-cell membrane marker for STED microscopy

As mentioned in the introduction (see section 1.1), cardiomyocytes feature an intricate and complex network of cell-wide membrane invaginations: the Transverse-Axial Tubular System (TATS). The specific architecture of the TATS and the vast set of proteins and lipids that are associated with it are vital for physiological cell function. Deviations from size, regularity, and molecular composition of the TATS have been shown to be indicative of cardiac pathophysiology. Thus, visualizing the TATS of living cardiomyocytes in different models of cardiac disease using appropriate membrane labels for optical microscopy is an important experimental approach to complement and control biochemical data.
Finding and selecting a suitable membrane label for living cells, especially very sensitive cells like cardiomyocytes, and specifically for the application in STED microscopy demand certain basic requirements. These requirements comprise, but are not restricted to, the following key points:

1. The label must be non-toxic, i.e. it must not cause cell death, cell rounding, or membrane blebbing. Specifically, for STED imaging of cardiomyocytes, the labeled cells must stay quiescent during the illumination cyle and the fluorescence read-out. Therefore, the appropriate membrane label must not only be non-toxic but also show no signs of possibly illumination induced toxicity, the so-called “phototoxicity” [431, 432, 433].

2. The staining protocol must be fast and physiological.

3. The membrane label must be cell- and membrane-specific.

4. Cellular internalization must be slow to ensure a membrane-specific, stable fluorescence signal over the course of the whole experiment.

5. The fluorophore of the membrane label must be compatible with STED applications, i.e. the fluorophore must have a high quantum yield when emitting fluorescence light, and at the same time be efficiently switched into a dark state by the STED laser. Also, the fluorophore must be both photophysically (i.e. it must have a low rate of photobleaching) and photochemically stable (i.e. it must retain its spectral properties even after multiple cycles of excitation and depletion). Preferably, the fluorophore would have absorption and emission peaks in the near-infrared spectral region to reduce imaging artifacts due to intracellular scattering, cellular autofluorescence, and to achieve higher sample penetration depth. In short, the fluorophore must provide bright STED images with the highest possible resolution.

A well-established class of dyes that is typically used for fluorescence microscopy of cellular membranes is potentiometric (i.e. voltage-sensitive) membrane markers. Widely used examples of these potentiometric dyes are Aminonaphthylethenylpyridinium (ANEP) dyes, such as Di-4-ANEPPS [434, 435] and Di-8-ANEPPS [414, 413], the latter being used as the current "gold standard" for labeling cardiomyocyte and skeletal myocyte membrane structures and visualizing their action potentials [436, 437, 438, 439, 440]. However, phototoxicity [441, 442, 443] has been reported for Di-8-ANEPPS. And although Di-8-ANEPPS has been used in STED microscopy studies of the membrane topology of cardiomyocytes [22], its spectroscopic properties make it less than ideal for STED applications. Di-8-ANEPPS features a very broad excitation range between 420 nm and 510 nm paired with a similarly broad emission range between 560 nm and 720 nm [444, 445, 446]. For one, these broad excitation and emission spectra of Di-8-ANEPPS make it rather unsuited for multicolor imaging applications employing other fluorescent live-cell labels, such as fluorescent proteins whose most prominent and most often used representatives cover a similar spectral region as that of Di-8-ANEPPS, e.g. Green Fluorescent Protein (GFP) and its spectrally similar, mutation-derived variations [447, 448, 449]. For the other, Di-8-ANEPPS shows a high rate of photobleaching in STED microscopy of living cardiomyocytes. This could be due to an

appreciable overlap between the dye's stimulated emission spectrum and its excited state absorption spectrum [450, 451]. The non-negligible photobleaching is paired with a relatively low lateral diffusion time [17] between 0.2 $\mu m^2/s$ [452] and 0.5 $\mu m^2/s$ [453] along the extracellular leaflet of the membrane. This restricts the applicability of Di-8-ANEPPS for three-dimensional (3D) STED microscopy to static and rather time-consuming imaging schemes. Specifically, after having acquired a single two-dimensional image of a live cardiomyocyte stained with Di-8-ANEPPS, and thus having bleached the dye within the focal volume, it takes several minutes before enough of the membrane probe has diffused back into the bleached region before another image at a different axial position can be acquired with a sufficiently high signal-to-noise ratio. Therefore, dynamic and video-rate STED image acquisition is not feasible using Di-8-ANEPPS.

A highly promising alternative to Di-8-ANEPPS is the novel membrane label Cholesterol-PEG-KK114 (Chol-KK114), a fluorescent lipid compound first presented by *Honigmann et al.* in 2014 [100] and which has up to now been mostly used in STED-FCS applications [100, 454, 455], and for experiments regarding cholesterol partitioning in specially prepared lipid vesicles [456] or supported lipid bilayers [457]. So far this dye compound has not been exploited to its full potential in actual subdiffraction cellular membrane structure imaging. Therefore the motivation was to demonstrate the applicability and versatility of Chol-KK114 for STED microscopy of membrane structures in living cells. I will show this applicability and quantify the observed nanometric membrane patterns for a set of widely used culture cell lines and extend it to primary mouse ventricular cardiomyocytes with their complex and sophisticated TATS membrane architecture.

Chol-KK114 features the membrane lipid cholesterol (Chol) labeled with the organic dye KK114 [458] via a 1 kDa large PolyEthylene Glycol (PEG) linker molecule. The molecular structure of Chol-KK114 is schematically depicted in Fig. 3.1 **A**. The spectroscopic properties of the organic dye KK114 decorating the Chol-PEG complex in water are displayed in Fig. 3.1 **B**. The dye has its absorption and emission maximum around 638 nm and 655 nm, respectively. KK114 is switched off most efficiently with a STED wavelength between 750 and 800 nm [427]. Regarding the requirements for an optimal STED-compatible

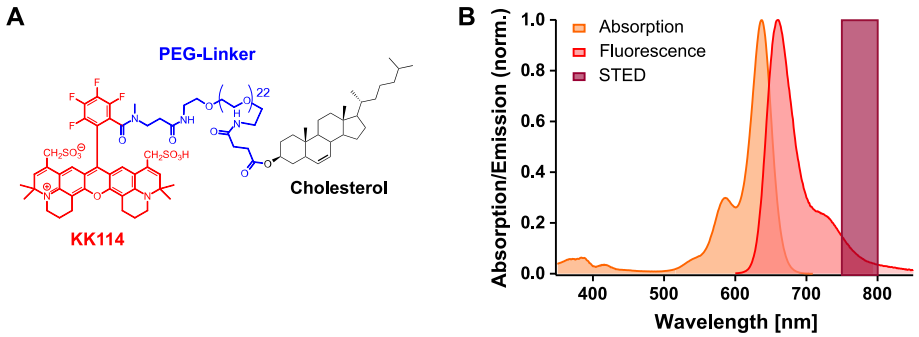

Figure 3.1.: Structure of Cholesterol-PEG-KK114 (Chol-KK114), and absorbance/emission spectra of the dye KK114. **A** Schematics of the molecular structure of the dye compound Cholesterol-PEG-KK114. The fluorescent dye KK114 is displayed in red, the PolyEthylene Glycol (PEG) linker is displayed in blue (the number 22 indicates the number of repeats of the structure motif in parentheses), and the lipid Cholesterol is displayed in black. The drawing was adapted with permission from [100]. **B** Normalized absorbance and emission spectra of the fluorescent dye KK114 [458], and the spectral region of suitable STED laser wavelengths for efficient fluorescence switch-off (indicated by the dark red bar).

live-cell membrane label identified above, Chol-KK114 proves most suitable due to its specific chemical and structural composition. Considering the enumeration of criteria introduced above, and explicitly comparing Chol-KK114 and Di-8-ANEPPS as membrane labels for living cardiomyocytes, it can be summarized that:

1. Membrane labeling with Chol-KK114 according to the herein established staining protocol (see section 2.3.2) enabled long-term STED imaging experiments without observing any signs of toxicity to cells, i.e. cell rounding, membrane blebbing, or, in the case of living cardiomyocytes, cell contraction. Living cardiomyocytes could be used for STED imaging for up to 4 hours without signs of compromised cell viability. This is at least twice as long as a reliable physiological STED imaging session using cardiomyocytes labeled with Di-8-ANEPPS.

2. Membrane labeling with Chol-KK114 does not rely on any special treatment of the living cell samples (e.g. temperature changes or additional chemicals for marker delivery). It is thus as physiological as possible. Further, it is fast: the general staining protocol requires only 1 to 3 min of incubation with the dye solution followed by a maximum of three washing steps. Compared to the standard Di-8-ANEPPS staining routine, this speeds up the sample labeling by at least a factor of 5.

3. Chol-KK114 shows highly cell-specific membrane signals for different culture cell lines as well as for primary mouse ventricular cardiomyocytes.

The distinct nanometric membrane patterns will be presented and discussed in detail in the following sections (see sections 3.2 and 3.3).

4. Chol-KK114, as compared to other fluorescently labeled lipids, features a very slow rate of internalization into the cell. This is most likely due to the size of the PEG-linker which - with 1 kDa - is rather bulky and is thus causing the labeled Cholesterol to "get stuck" in the extracellular leaflet of the lipid bilayer [459, 100, 460] (cf. Fig. 3.2). Due to steric hindrance, this suppresses events of flip-flopping [460, 461, 462] or cellular transport processes [463, 464, 465] of the labeled Cholesterol from the extra- to the intracellular leaflet. Along that line, no indication of diffusion-mediated internalization of Chol-KK114 in any of the long-term experiments was observed. Label internalization was always coupled to endocytotic processes with clearly identifiable inclusion bodies. Before any signs of Chol-KK114 internalization would be observable, investigated cells would rather start forming vesicles. This would, admittedly, impair the physiological validity of a live-cell sample but never compromise image quality.

5. The possibility of attaching different organic fluorophores to the Chol-PEG compound creates a spectrally diverse set of fluorescent membrane labels that allow optimal STED imaging performance and that fit the respective need of the experiment. The dye compound KK114 [458] has proven to be one of the most suited fluorescent dyes for STED applications, enabling the acquisition of images with superior resolution of down to 20 nm [336]. The spectral properties of Chol-KK114 (see Fig. 3.1) make it ideal for STED imaging in the red spectral region, thus further reducing phototoxicity, cellular autofluorescence, and scattering within thick samples. By labeling living mouse ventricular cardiomyocytes with Chol-KK114, a resolution of membrane compartments down to 35 nm was achieved (see section 3.3).

An additional and future-oriented advantage of the dye compound KK114 is that it can be effectively switched off with STED laser wavelengths ranging from $750 - 800$ nm (see Fig. 3.1 **B**) as we previously investigated and reported in [427]. The possible application of STED laser wavelengths in the spectral

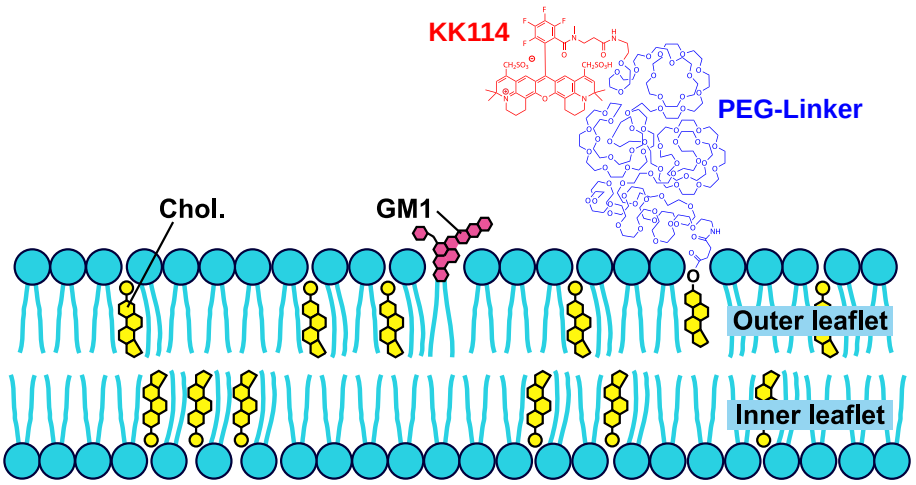

Figure 3.2.: Sketch of the insertion of Chol-KK114 into the cellular membrane. The schematic membrane model is based on the one introduced in section 1.4. The labeled Cholesterol (in yellow) inserts itself into the outer leaflet of the lipid bilayer (drawn in light blue). The bulky PEG-linker (in dark blue) prevents the lipid-dye compound from cellular internalization and keeps the fluorescent dye KK114 (in red) in the extracellular space (see also Fig. 3.1 **A**). Abbreviations: Chol. - Cholesterol; GM1 - Monosialotetrahexosylganglioside; PEG - PolyEthylene Glycol. Not drawn to scale.

region farther red than the 775 nm laser line that is implemented in most commercial STED microscopes is a promising future direction for the improvement of STED image quality regarding increase of image resolution, decrease of sample bleaching, and suppression of background signal. This is because, as stated above, the scattering inside thick specimen and photobleaching are reduced at longer STED laser wavelengths. Further, the use of a fluorescent lipid analog for live-cell membrane staining instead of a voltage-sensor like Di-8-ANEPPS has advantages that effectively manifest themselves as brighter and more stable detectable fluorescence signals. These advantages are that the lateral diffusion along the cell membrane is faster by a factor of 10 to 50 for lipid-raft associated fluorescent lipid analogs such as Chol-KK114 than it is for Di-8-ANEPPS [466, 467]. Also, the above mentioned flexibility in choosing the organic dye that is coupled to the Chol-PEG construct allows the selection of fluorophores that offer high photostability and high quantum yields. This enables the quick acquisition of images either at a fixed spot in the sample or while scanning through the sample, thus facilitating the recording of videos or 3D stacks, respectively. In the following, I will justify the possibilities for live-cell membrane imaging using Chol-KK114 in different cell systems and present its excellent applicability in subdiffraction topological investigations of the Transverse-Axial Tubular System (TATS) of living cardiomyocytes.

3.2. Cell-specific Cholesterol nanopatterns

To assess the suitability of Chol-KK114 for live-cell STED imaging and the specificity of membrane labeling, I prepared samples of culture cell lines derived from various tissue types. I stained them with Chol-KK114 and used them for STED imaging under optimized imaging conditions. These select culture cell lines were: U2OS, HeLa, HEK, Vero (see section 2.4.1, respectively), ventricular induced pluripotent stem cells (ViPSC, see section 2.4.2), and human adipocytes (HAd, from adipose heart tissue, see section 2.4.3). For U2OS, HeLa, HEK, and Vero cells labeled with Chol-KK114, Figure 3.3 shows exemplary overview images and magnifications of regions of interest (ROI) marked by the yellow boxes therein. U2OS (derived from human osteosarcoma can-

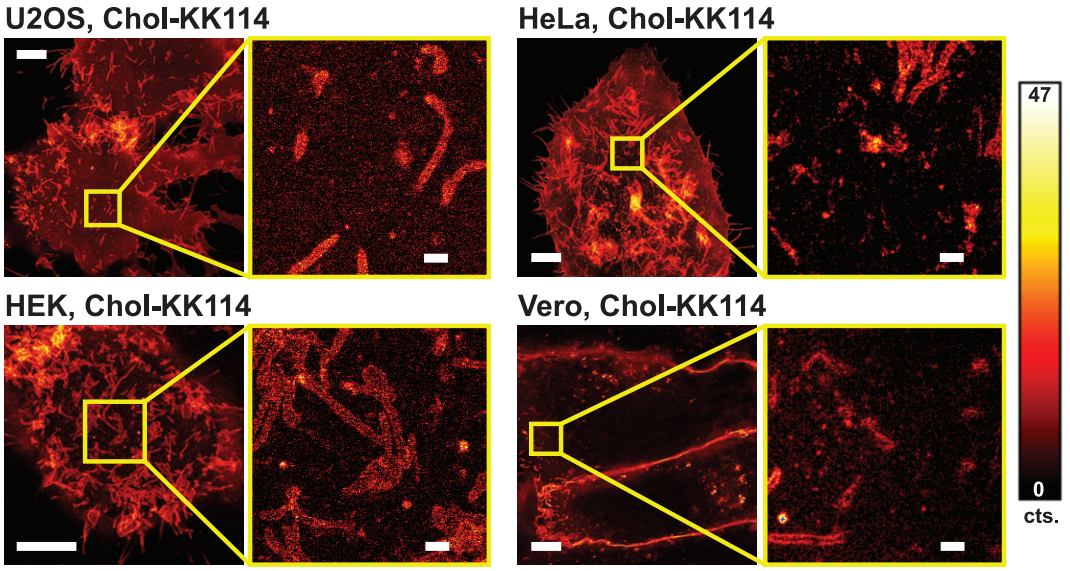

Figure 3.3.: STED images of the cell-specific Cholesterol-PEG-KK114 (Chol-KK114) nanopattern at the basement membrane of living culture cells. The following four culture cell lines were stained with 5 µM Chol-KK114 for STED microscopy as described in section 2.4.1: U2OS, HeLa, HEK, and Vero. Overview images and magnifications corresponding to the indicated yellow boxed regions are displayed. Scale bars in overview images: 5 µm; scale bars in magnified insets: 500 nm. Images were smoothed using a two-dimensional Gaussian filter with a width of 1.5 pixels. Image brightness was adjusted in the magnified insets for visibility. The color bar indicates the respective image brightness of the magnified images in photon counts (cts.); for the overview images, the same color code was used but ranging from 0 to 132 cts.

cer), HeLa (derived from human cervical cancer), HEK (Human Embryonic Kidney cells), and Vero (epithelial cells from African Green Monkey) are cells that typically feature filopodia. Filopodia are elongated, cytoplasmic membrane protrusions that are involved in cell adhesion, cell migration, and cell sensing [468, 469]. Filopodia are highly enriched in Cholesterol (Chol) [470] as has been shown by fluorescence microscopy [471] and immunoelectron mi-

croscopy [472]. By labeling the extracellular leaflet of the lipid bilayer of the above mentioned four cell lines with Chol-KK114 for STED microscopy, the assembly of Chol nanodomains mainly along filopodial structures could be demonstrated (see Fig. 3.3, top and middle row). With STED microscopy of the Chol-KK114 membrane label it was possible to precisely outline filopodia in living cells and show the compartmentalization of Chol alongside the outer membrane leaflet of these protrusions. To quantify these Chol nanodomain assemblies in filopodial structures, I determined the Chol-KK114 signal density ρ as described in section 2.6.4. In Fig. 3.4, the obtained values of ρ in filopodia are displayed in percent of the total filopodial area for each cell line. As can

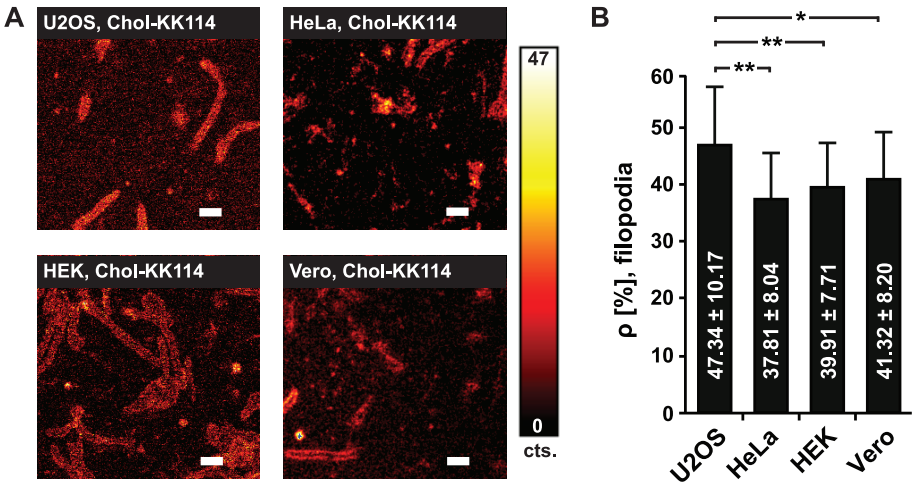

Figure 3.4.: Comparison of the Cholesterol-PEG-KK114 (Chol-KK114) signal density ρ in filopodia of the cultured cell lines U2OS, HeLa, HEK, and Vero. **A** STED images of the culture cell lines labeled with Chol-KK114, corresponding to the magnified insets presented and described in Fig. 3.3. Images were smoothed using a two-dimensional Gaussian filter with a width of 1.5 pixels. The color bar indicates the respective image brightness in photon counts (cts.). Scale bars: 500 nm. **B** Bar graph representation of the Chol-KK114 surface signal density ρ in filopodia. ρ was determined as described in section 2.6.4, is given in % of the total filopodial area, and is presented as mean $\pm$ standard deviation. Number of analyzed cells: U2OS - 13; HeLa - 8; HEK - 24; Vero - 13. Statistical significance is denoted as $p > 0.01$; $(*)$: significant, $p < 0.01$; $(**)$: very significant, $p < 0.001$ (see also section 2.9 and Appendix I, Table I.1)

be seen in Fig. 3.4, the Chol-KK114 signal density in filopodia is significantly different between cell types (see also Appendix I, Table I.1). Notably, the density of Chol-KK114 structures in filopodia of U2OS, HeLa, HEK, and Vero cells is profoundly higher (by a factor of 100) than the Chol-KK114 signal density along the cellular basement membrane (see Fig. 3.7). The mentioned cell lines show from little to no Chol-KK114 membrane domains that are not associated to filopodia. An increase in the concentration of Chol-KK114 used for membrane labeling above 5 µM did not increase the amount of Chol-KK114 signal

at the basement membrane of the cells indicating that with 5 µM Chol-KK114 the labeling saturation concentration is reached. There has so far only been one study involving subdiffraction imaging of Chol clusters in the cell membrane: *Mizuno et al.* [473] used PhotoActivation Localization Microscopy (PALM) to visualize nanoscopic Chol enriched membrane domains in fixed HeLa cells and could confirm the prevalence of Chol signal in filopodia. In their publication however, Chol signal could only be observed at the apical membrane of the cells and in addition to the filopodial Chol signal, there were circular Chol structures along the membrane. These findings could not be reproduced here using Chol-KK114. Yet, *Mizuno et al.* conducted subdiffraction imaging experiments using fixed HeLa cells fluorescently labeled via the C-terminal domain of θ-toxin. Thus, the additionally observed Chol cluster signal at the apical membrane and the absence of Chol clusters at the basement membrane might be fixation artifacts. Also, the fluorescent θ-toxin label might either be internalized by the cells or transferred to the cytosolic membrane leaflet by flip-flopping, resulting in a possible tagging of Chol structures along the intracellular leaflet.

The here observed preferred assembly of Chol-KK114 in filopodia, as opposed to along the basement membrane, might be interpreted in two ways. Either that the cellular basement membrane is fully and stably packed with endogenous Chol which results in a highly reduced possibility of exogenous Chol insertion into the outer leaflet. Or that there is a general absence of large-scale Chol clusters along the extracellular leaflet of the basement membrane resulting in a homogeneous distribution of single Chol-KK114 monomers (or only small Chol-KK114 assemblies) with an overall brightness that would be too dim to be detectable by fluorescence recording.

For future studies, an in-depth investigation of the Chol distribution in filopodia of living cells would be of great interest, especially because malformation of filopodia is associated with many pathologies most prominently in the fields of cancer [474, 475, 476] and neurological disorders [477, 478]. Using Chol-KK114 together with STED microscopy would definitely be a very valuable method supporting such research.

Contrary to the above findings in the immortal cell lines, other cell types labeled with Chol-KK114 and that typically do not feature filopodia, showed a

distinct Chol-KK114 signal along their basement membrane with a high degree of signal clustering. Specifically, I used Chol-KK114 to label and image cultured ventricular induced pluripotent stem cells (ViPSC, see section 2.4.2) and human adipocytes (HAd, from adipose heart tissue, see section 2.4.3). I

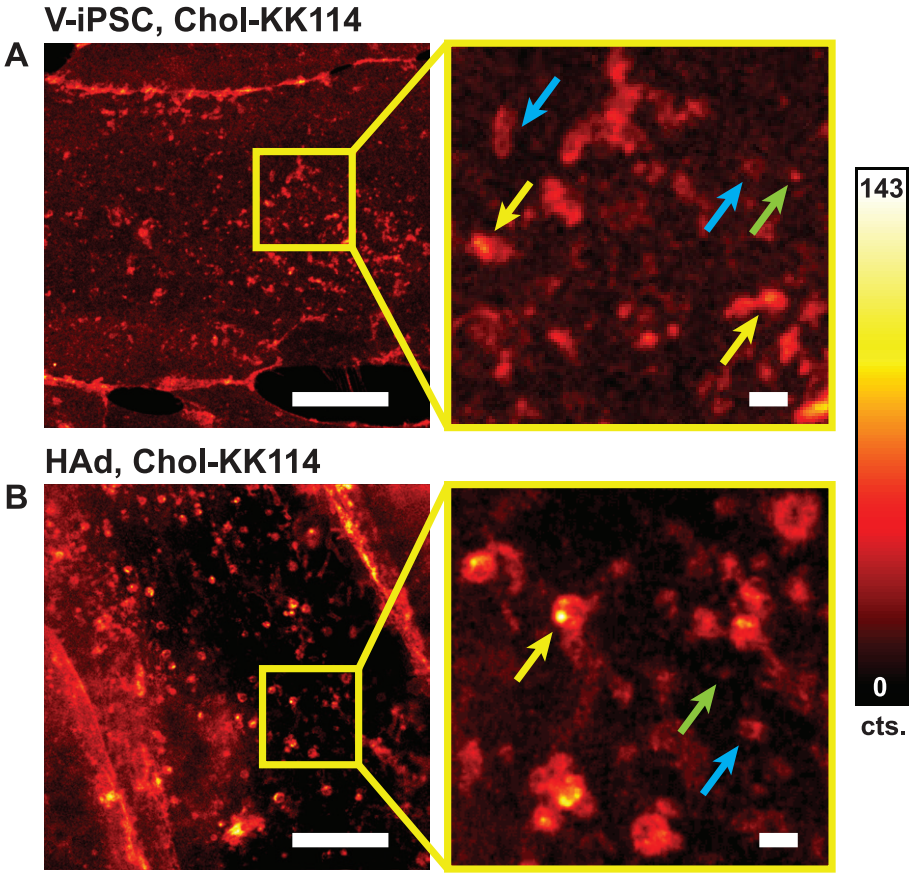

Figure 3.5.: STED images of the cell-specific Cholesterol-PEG-KK114 (Chol-KK114) nanopattern at the basement membrane of living ventricular induced pluripotent stem cells (ViPSC, displayed in **A**) and living human adipocytes (HAd, from adipose heart tissue, displayed in **B**). ViPSC and HAd were stained with 5 µM Chol-KK114 for STED microscopy as described in section 2.4.1. Overview images and magnifications corresponding to the indicated yellow boxed regions are displayed. Green arrows point out single Cholesterol domains; yellow arrows point out exemplary bunchy clusters of Cholesterol; blue arrows point out Cholesterol ring structures. Images were smoothed using a two-dimensional Gaussian filter with a width of 1.5 pixels. Image brightness was adjusted in the magnified insets for visibility. The color bar indicates the image brightness in photon counts (cts.). Scale bars in overview images: 5 µm; scale bars in magnified insets: 500 nm.

chose to label Chol-rich membrane domains in ViPSC because these cells are often used as a model system to study molecular mechanisms of cardiac disease [479, 480]. This is due to the fact that it is much easier to obtain, cultivate, and control ViPSC than it is for primary living cardiomyocytes [481, 482, 483]. Additionally, ViPSC offer the possibility to study patient-specific diseases and their potential therapies - recently, they have even been cultured to serve as

grafts repairing injured, fibrotic hearts [484]. There have been many critical reviews regarding the aptness of ViPSC as a model system [485, 486]. Most of these studies conclude that ViPSC should be used with caution and always in combination with necessary control experiments. To justify the quantitative comparison of the Chol arrangement at the basement membrane of ViPSC and at the sarcolemma of mouse ventricular cardiomyocytes (VM), I selected only those ViPSC for image evaluation that were of a similar size and shape as VM. Further, I assessed the degree of differentiation of the imaged ViPSC by immunofluorescence staining for α-Actinin which is a cardiomyocyte marker protein [487, 481, 482, 488]. Exemplary images of these control stains that confirm the virtually population-wide differentiation of ViPSC can be found in the Appendix D.1. As shown in the overview and magnified images of Chol-KK114 labeled ViPSC in Fig. 3.5, the cells show a dense and characteristic pattern of Chol clusters at their basement membrane. The quantitative evaluation of the Chol-KK114 surface signal density will be discussed in detail in section 3.3. There, it will also be explicitly compared to the Chol-KK114 signal structure and density in living VM. Note that along the basement membrane of living ViPSC, the Chol-KK114 signal partitions into single domains (see Fig. 3.5 **A**, green arrow), into ring structures with a diameter between approximately 100 and 200 nm (see Fig. 3.5 **A**, blue arrows), and into bunchy clusters of variable shapes and sizes of several hundred nanometers (see Fig. 3.5 **A**, yellow arrows). Further, there are regions devoid of any Chol-KK114 signal.

Finally, as another example to motivate the use of Chol-KK114 in cardiomyocytes and compare the resulting membrane structures and patterns, I chose to label and image Chol domains in human adipocytes (HAd), derived from adipose heart tissue. The study of Chol domains in cardiac membranes could benefit significantly from the assessment of the nanoscale distribution of Chol in HAd. First, because HAd contain large amounts of Chol that predominantly accumulate inside lipid droplets which are organelles that are formed to a great extent by HAd [489, 490]. Second, various clinical studies have shown the connection between obesity and cardiovascular disease [491, 492]. Both the size as well as the Chol content in adipocytes has been proportionally associated with the risk of cardiac pathologies [493, 494, 495]. Fig. 3.5 displays the obtained STED images of the basement membrane of Chol-KK114 labeled

living HAd. Interestingly, the incubation of HAd with Chol-KK114 did not result in obviously visibly stained lipid droplets as is typically known from other Chol stains of adipocytes, e.g. by indirect labeling using filipin [496] or NBD cholesterol [497]. Typical signal of lipid droplets could not be detected in neither the confocal nor the STED images of Chol-KK114 labeled HAd. In general, upon the addition of free Chol to the cell membrane, Chol is quickly recognized by the low-density lipoprotein (LDL) receptor. Together with the LDL receptor, Chol is endocytosed and, if in excess, either stored in the lipid droplets, or transported back across the cell membrane [489]. The absence of lipid droplet labeling could be due to Chol-KK114 not penetrating the cellular basement membrane but inserting itself stably into the extracellular leaflet and thus not reaching the lipid droplets via endocytosis. Hence, the Chol-KK114 signal in HAd observed here does not contradict the lipid droplet signal seen when labeling with filipin or NBD cholesterol because the latter two cholesterol probes are specific to the cytosolic membrane leaflet. Compared to the Chol-KK114 signal observed in ViPSC, HAd show a similar arrangement of basement membrane Chol-KK114. Again, the Chol-KK114 signal partitions into the above mentioned three characteristic pattern motifs: single domains (see Fig. 3.5 **B**, green arrow), ring structures of between 100 and 200 nm in diameter (see Fig. 3.5 **B**, blue arrow), and variably shaped bunchy clusters of several hundred nanometers in size (see Fig. 3.5 **B**, yellow arrow). Regions devoid of Chol-KK114 signal can also be observed.

Up to now, there are no reports involving live-cell subdiffraction imaging of Chol structures at the basement membrane and/or in filopodia of the above investigated cell lines, although Chol-KK114 has been proposed to be very feasible for such applications [457]. Chol-KK114 has so far been used in STED-Fluorescence-Correlation-Spectroscopy (STED-FCS) studies of Chol partitioning and Chol trapping in cell membranes [100, 460]. Further, Chol-KK114 has been applied to study Chol partitioning in Giant Unilamellar Vesicles (GUVs) and Giant Plasma Membrane Vesicles (GPMVs) [456, 457]. Comparative reviews of different fluorescent Chol analogs as reporters for Chol distribution in both artificial and cellular membrane systems, especially regarding their normal insertion, partitioning, and diffusion behavior, have emphasized Chol-KK114 (and similarly constructed fluorescent Chol-PEG analogs) to be among

the most suitable labels for the visualization of Chol assemblies in the extracellular leaflet [460, 457]. Further, there have been several studies on the fluorescent Cholesterol analog Cholesterol-BODIPY (Chol-BODIPY [498], commercially distributed by Avanti Polar Lipids, Inc., Alabaster, AL, USA) proving this compound to behave very similarly to free Chol [499, 500]. Hence, to examine if Chol-KK114 inserts itself into the extracellular membrane in a similar fashion as Chol-BODIPY, I prepared samples of living VM double-labeled with Chol-KK114 and Chol-BODIPY for confocal fluorescence imaging. These double stains are presented in section 3.3 and show that, indeed, the Chol-KK114 and the Chol-BODIPY signals colocalize. This signal overlap served as an indirect verification that Chol-KK114, just like Chol-BODIPY, can be assumed to behave like a quasi-physiological membrane lipid probe. Apart from being a membrane marker, Chol-KK114 is thus also suitable for image-based investigations of the assembly of exogenous free Chol along the outer leaflet of the lipid bilayer. These control studies and the high quality, cell-specific, and quantifiable STED images above confirm the applicability of Chol-KK114 as a trustworthy exogenous membrane marker for living cells.

When attempting to interpret the observed Chol-KK114 signal patterns at the basement membrane of U2OS, HeLa, HEK, and Vero cells versus that in ViPSC and HAd, it should be noted that according to the lipid raft hypothesis, exogenous Chol would preferentially insert itself into those regions of the extracellular leaflet that are enriched with saturated phospholipids and sphingolipids [501, 502, 503]. The assumption of assemblies of saturated lipids that are heterogeneously distributed along the cell membrane and that bind large amounts of Chol could explain the Chol-KK114 signal structures in ViPSC and HAd, but cannot explain the absence of basement membrane Chol-KK114 signal in U2OS, HeLa, HEK, and Vero cells. A further possibility would be the association of the exogenous Chol-KK114 with another membrane compartment that is more often found in ViPSC and HAd than in the other four immortal cell lines. This membrane compartment could be caveolae (see also section 1.1) that might form more complex three-dimensional structures at the basement membrane of ViPSC, HAd, and most importantly - as will be shown in the next section - at the sarcolemma of cardiomyocytes than in the immortal cell lines where caveolae might be smaller, more solitary, and less branched

structures. Based on the one- and two-photon-excitation-STED images of Chol structures in living cardiomyocytes that will be presented in the following sections, I will motivate this possible direct association between the presented fluorescent Chol analogs and caveolae. This could make the family of organic dye labeled Chol-PEG markers an indicator of sarcolemmal caveolae in living cardiomyocytes. In the following, the unique pattern of Chol nanodomains in cardiomyocytes is presented.

3.3. Cholesterol nanopatterns in living cardiomyocytes

The Chol nanopattern at the sarcolemma (i.e. the basement membrane of myocytes) of living mouse ventricular cardiomyocytes (VM) is very distinct. Fig. 3.6 shows a living VM labeled with 5 µM Chol-KK114 as described in section 2.3.2 and imaged using the custom-built fast scanning STED microscope setup (see section 2.1.2). The additionally shown bright field image of the labeled VM (Fig. 3.6 **B**) confirms the cell fitness regarding even striations, no membrane blebbing, and no cell rounding, and thus validates that the STED image shows Chol structures under physiological conditions. In the STED image, it can be seen that the sarcolemmal Chol signal is highly clustered and that it does not align with the cellular striations. The three reoccurring membrane motifs that had already been encountered when looking at Chol-KK114 stained ViPSC and HAd (see last section) are conserved in VM: single Chol domains (Fig. 3.6 **B**, green arrow), bunchy Chol clusters of variable sizes (Fig. 3.6 **B**, yellow arrow), and Chol ring structures (Fig. 3.6 **B**, blue arrow).
When quantitatively evaluating the Chol-KK114 surface signal density ρ at the basement membrane (see section 2.6.4) and comparing it between the here investigated seven cell types, the expected formation of two groups is confirmed. The obtained per cent values of ρ are presented in Fig. 3.7. On the one hand, the immortal cell lines U2OS, HeLa, HEK, and Vero show only a minor Chol-KK114 signal at the basement membrane. The area of the Chol-KK114 signal amounts to less than 1 % of the total basement membrane area and is thus negligible. On the other hand, the terminally differentiated cells ViPSC, HAd, and VM show a significantly more abundant Chol-KK114 surface sig-

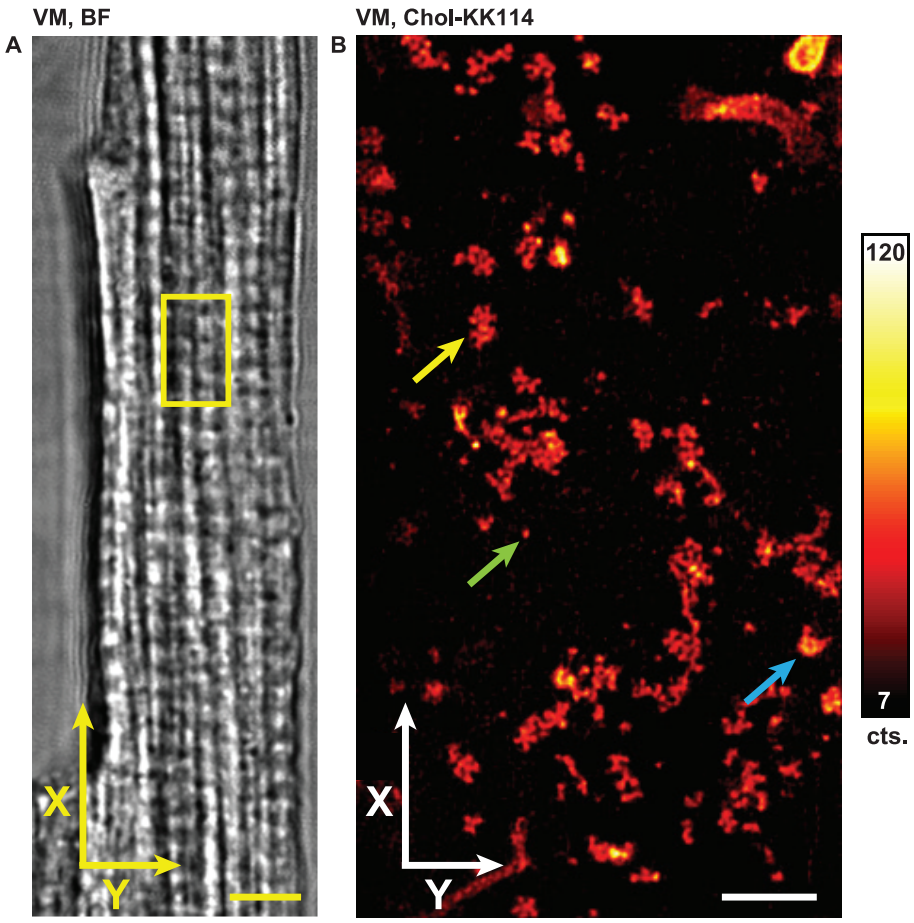

Figure 3.6.: The distinct Cholesterol-PEG-KK114 (Chol-KK114) nanopattern at the sarcolemma of living primary mouse ventricular cardiomyocytes (VM). VM were stained with 5 µM Chol-KK114 as described in section 2.3.2. The coordinate system indicates the longitudinal (X) and the transverse (Y) cell axes. **A** bright field (BF) image of a living primary VM, scale bar: 5 µm. **B** STED image of the sarcolemma of the same VM stained with Chol-KK114 within the field of view indicated by the yellow box in the bright field image. Three distinct membrane motifs can be distinguished: single Chol domains (green arrow), Chol ring structures (blue arrow), and bunchy clusters of Chol (yellow arrow). The STED image was smoothed using a two-dimensional Gaussian filter with a width of 1.5 pixels. The color bar indicates the image brightness in photon counts (cts.). Scale bar: 1 µm

nal that comprises almost 20 % of the cellular basement membrane. Further, the Chol-KK114 surface signal density does not differ significantly between ViPSC, HAd, and VM (see Appendix I, Table I.2 for a detailed statistical analysis). Across ViPSC, HAd, and VM, the complexity and abundance of Chol structures at the basement membrane is conserved.

Summarizing the above findings, as opposed to U2OS, HeLa, HEK, and Vero cells, the VM, ViPSC, and HAd show both the Chol membrane motifs of single domains, bunchy clusters, and ring structures, as well as a significantly high surface signal density of Chol clusters at the basement membrane. VM, ViPSC, and HAd seem to feature a complex, probably three-dimensional, arrangement

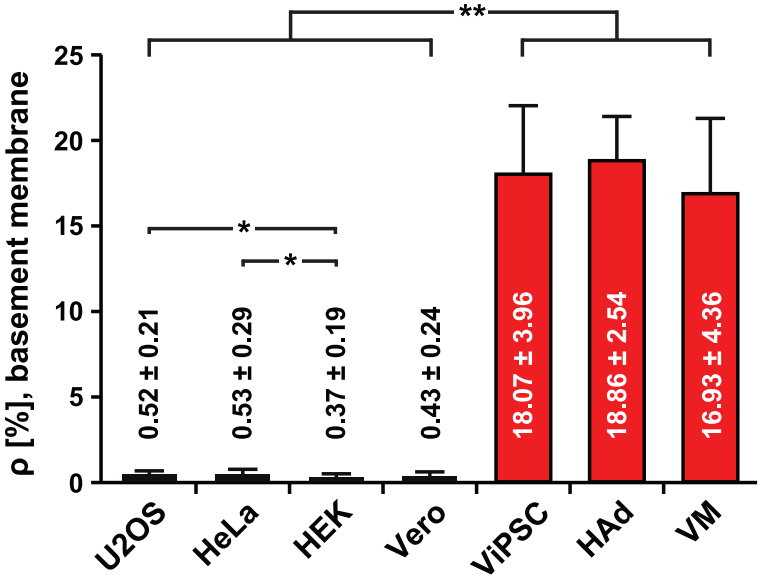

Figure 3.7.: Comparison of the Cholesterol-PEG-KK114 (Chol-KK114) signal density ρ at the basement membrane of different cell types. Cell lines: U2OS, HeLa, HEK, Vero, ventricular induced pluripotent stem cells (ViPSC), human adipocytes (HAd, from adipose heart tissue), mouse ventricular cardiomyocytes (VM). ρ was determined along the basement membrane of the cell body of cultured and primary cells as described in section 2.6.4, is given in % of the total area of the basement membrane, and is presented as mean $\pm$ standard deviation. Statistical significance is denoted as $p > 0.01$; $(*)$: significant, $p < 0.01$; $(**)$: very significant, $p < 0.001$ (see also section 2.9 and Appendix I, Table I.2). Number of analyzed cells: U2OS - 13; HeLa - 8; HEK - 24; Vero - 13; ViPSC - 16; HAd - 37; VM - 55. STED images of the basement membranes of the mentioned cells labeled with Chol-KK114 are respectively shown in Fig. 3.3, Fig. 3.5, and Fig. 3.6.

of Chol-rich membrane regions. According to the working model of the cardiac sarcolemma that wa proposed in this thesis (see section 1.4), the arrangement of Chol could be mediated by caveolar structures at the cell membrane. In VM, there is a highly abundant sarcolemmal signal of the caveolae forming protein Caveolin-3 (Cav-3). This is similar to the abundant signal of Cav-3 and Caveolin-1 (Cav-1) at the basement membrane of ViPSC and HAd, respectively. For these three cell types, the mentioned complex Chol-KK114 membrane pattern motifs could be observed. These motifs might coincide with similarly arranged caveolar structures that could potentially organize and shape the Chol structures into branched three-dimensional membrane indentations. This possible association between the membrane structures labeled by Chol-KK114 and the Caveolin proteins will be investigated in more detail in section 3.5. The validation of Chol-KK114 as a physiological membrane label for living VM and its superior performance for subdiffraction STED imaging will be shown below.
Since the membrane labeling procedure with Chol-KK114 involves the introduction of a surplus of exogenous Chol to the cell, it has to be controlled that

Chol-KK114 does not disturb the native membrane arrangement and properties. To that end, I prepared samples of living cardiomyocytes and labeled them with both Chol-KK114 and Chol-BODIPY (as described in section 2.3.2). Chol-BODIPY has been shown to conserve many properties of free Chol upon insertion and partitioning in the cell membrane [499, 500]. The colocalization of the Chol-KK114 and the Chol-BODIPY signal would thus verify that Chol-KK114 alters the physiological membrane composition as minimally as Chol-BODIPY. The overlap of the Chol-KK114 signal with that of Chol-BODIPY had to be verified using confocal microscopy. It was not possible to use Chol-BODIPY in STED image acquisition because Chol-BODIPY shows an unfortunate additional absorption peak at 590 nm which coincides with the STED wavelength used for the BODIPY color channel; using a STED wavelength between 750 - 800 nm did not result in a significant switch-off of the fluorophore. The inapplicability of Chol-BODIPY for STED imaging with a 592 nm STED wavelength is discussed in more detail in the Appendix E. Nevertheless, the confocal inves-

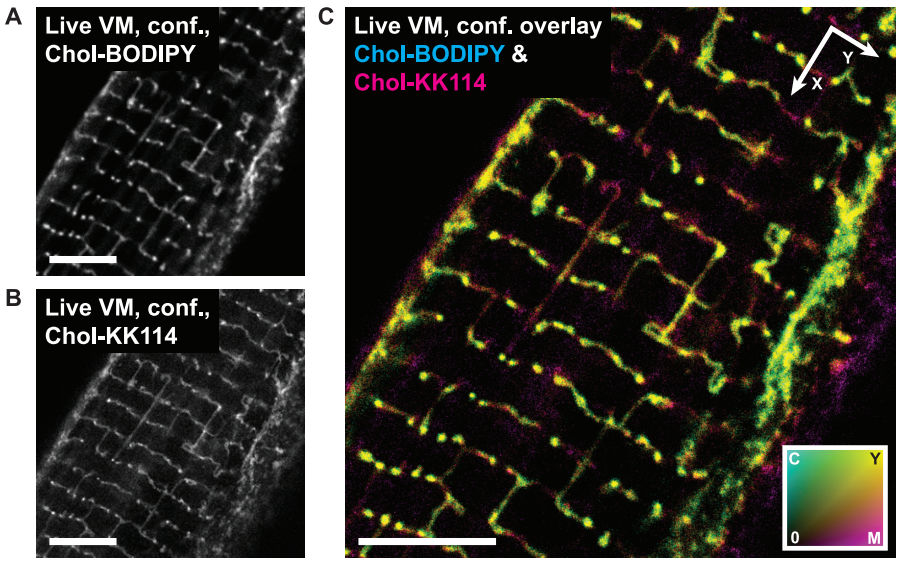

Figure 3.8.: Confocal images of living mouse ventricular cardiomyocytes (VM) double labeled with Cholesterol-PEG-KK114 (Chol-KK114) and Cholesterol-BODIPY (Chol-BODIPY), see section 2.3.2. **A** Single color channel image of the Chol-BODIPY color channel. **B** Single color channel image of the Chol-KK114 color channel. **C** Overlay of the two color channels with the Chol-BODIPY channel displayed in cyan (C) and the Chol-KK114 channel displayed in magenta (M), yellow signal (Y) indicates signal overlap of the color channels. The corresponding color map is displayed in the image (bottom right); images were transformed to this color map as described in section 2.6.1. White arrows indicate the longitudinal (X) and the transverse (Y) cell axes, respectively. Images were smoothed using a two-dimensional Gaussian filter with a width of 1.5 pixels. Scale bars: 5 µm.

tigation of the colocalization of the Chol-KK114 and the Chol-BODIPY signals reveals the significant signal overlap of the two membrane markers. This is

demonstrated in Fig. 3.8 which shows the single color channels (Fig. 3.8 **A** and **B**, respectively) and the overlay thereof (Fig. 3.8 **C**) with the Chol-BODIPY signal color-coded in cyan and the Chol-KK114 signal color-coded in magenta. The abundant yellow signal indicates a profound color channel overlap and thus confirms that the two Chol analogs label the same structures. This validates that Chol-KK114 is behaving similarly to Chol-BODIPY and is hence potentially mimicking the behavior of free Chol quite well when inserting itself into the membrane.

As another control that Chol-KK114 is an apt membrane probe, especially for cardiomyocytes, it had to be compared with the "gold standard" of cardiomyocyte membrane labels: Di-8-ANEPPS. When comparing the Chol-KK114 to the Di-8-ANEPPS membrane signal in living VM, one should again expect significant colocalization of the two labels since both dye compounds exclusively label the outer leaflet of the plasma membrane (see section 3.1 and [504]). To verify this, I prepared samples of living VM and dually labeled them with both Chol-KK114 and Di-8-ANEPPS following the staining protocols described in section 2.3.2. These two-color samples were imaged both in confocal and in STED mode using the commercial STED microscope Leica TCS SP8 STED 3X (see section 2.1.3) with an excitation wavelength of 490 nm at 10 % laser power, a detection window of $(510 - 630)$ nm, and a fluorescence time gate of $(2.80 - 6.30)$ ns for the Di-8-ANEPPS color channel. For the Chol-KK114 color channel, an excitation wavelength of 640 nm at 10 % laser power, a detection window of $(670 - 720)$ nm, and a fluorescence time gate of $(2.00 - 6.00)$ ns was used. Both color channels were imaged in STED mode using the 775 nm STED laser. This justifies that the two color channels, although obtained in two consecutive scans, can be directly overlaid without an additional image registration procedure because the use of a single STED beam localizes the signal stemming from each color channel to the same subdiffraction sized spot. The spectral crosstalk between the two color channels was negligibly low. Fig. 3.9 **A** shows the significant signal overlap of the Di-8-ANEPPS and the Chol-KK114 color channels, both in confocal as well as in STED mode. Especially the signal overlap in the STED images confirms that Chol-KK114 labels the same structures as Di-8-ANEPPS. Additionally, using the Chol-KK114 and Di-8-ANEPPS two-color VM sample, I could directly evaluate the improved STED image res-

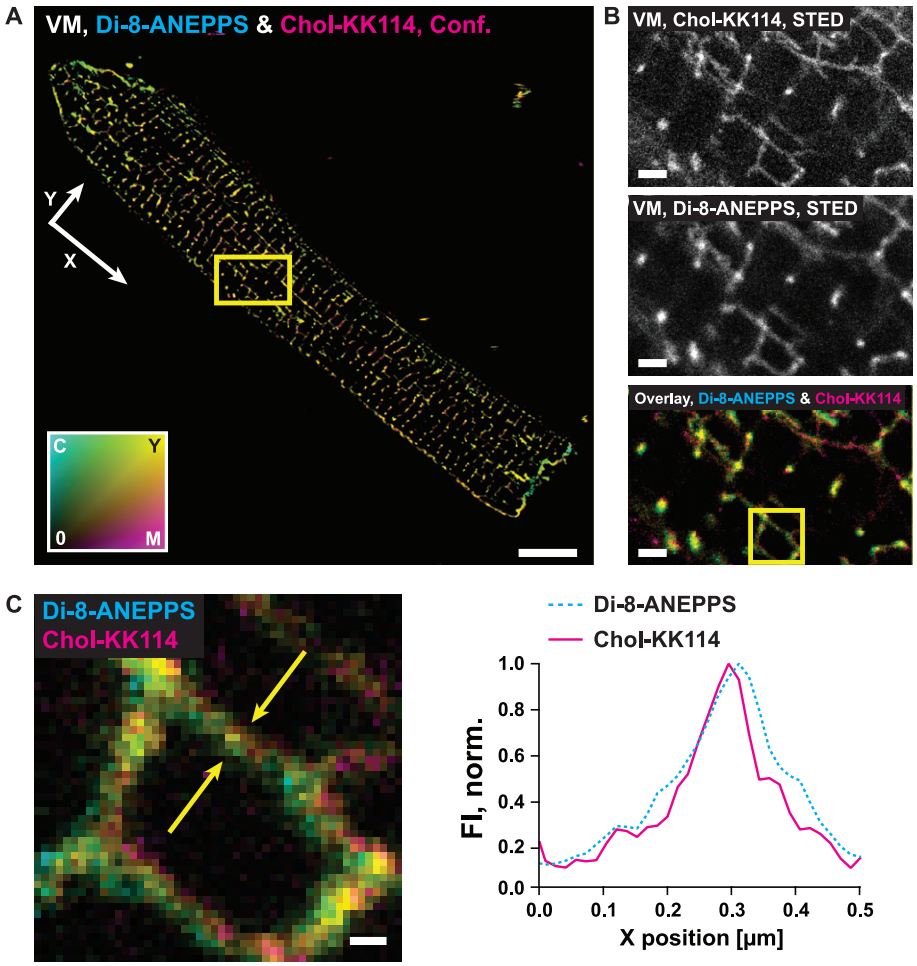

Figure 3.9.: Two-color images of living primary ventricular mouse cardiomyocytes (VM) labeled with the membrane markers Cholesterol-PEG-KK114 (Chol-KK114, at the saturation labeling concentration of 5 µM) and Di-8-ANEPPS (at a concentration of 50 µM). Images were taken inside the cell, at least 3 µm beneath the sarcolemma. Images were smoothed using a two-dimensional Gaussian filter with a width of 1.5 pixels. The used color map is depicted in **A**, bottom left. Images were transformed to this color map as described in section 2.6.1. **A** Confocal overview image of a VM dual-labeled with Chol-KK114 (color-coded in magenta) and Di-8-ANEPPS (color-coded in cyan); the highly abundant yellow signal indicates the significant overlap of the Chol-KK114 and the Di-8-ANEPPS signal. White arrows indicate the longitudinal (X) and transverse (Y) cell axes, respectively. Scale bar: 10 µm. **B** STED images of the region of interest marked by the yellow box in the confocal overview image. From top to bottom: single-color Chol-KK114 STED image, single-color Di-8-ANEPPS STED image, and overlay of the two color channels with the Chol-KK114 signal in magenta, the Di-8-ANEPPS signal in cyan and the yellow signal indicating spatial overlap of the magenta and cyan color channels. Scale bars: 1 µm. **C** Graphical depiction of the averaged and normalized fluorescence intensity profile (FI, norm.) of both the Chol-KK114 and the Di-8-ANEPPS STED signal obtained from a line profile through a dual-labeled tubular membrane structure (depicted in the left panel and corresponding to the yellow boxed region in the overlay image in **B**; scale bar: 200 nm). Image resolution was determined as the full width at half maximum (FWHM) of the tubular membrane structure (see section 2.6.2) and amounts to 100 nm in the Chol-KK114 color channel, and 150 nm in the Di-8-ANEPPS color channel.

olution achievable with the Chol-KK114 stain mentioned in 3.1. Fig. 3.9 **B** displays a highly magnified region of the two-color STED image and the T-Tubule membrane structure for which the image resolution was determined as described in section 2.6.2 (indicated by the two yellow arrows). The determined

resolution of the T-Tubule structure amounts to 100 nm in the Chol-KK114 color channel, and 150 nm in the Di-8-ANEPPS color channel. This increase in image resolution of 30 % demonstrates the improved photophysical properties of Chol-KK114 compared to Di-8-ANEPPS. Regarding image resolution, it has to be considered, however, that the apparent size of the here measured signal structures is a convolution of the microscope point spread function (PSF) with the size of the labeled structure, i.e. the diameter of the T-Tubule (including the size of the respective membrane label). When looking at smaller signal structures, the actually achievable image resolution using Chol-KK114 as a membrane label for STED microscopy is far better than the above-mentioned 100 nm for T-Tubule cross sections. This is nicely demonstrated when looking at single Chol domains that assemble along the T-Tubular membrane. Such single Chol domains can be visualized when decreasing the labeling concentration of Chol-KK114 well below the saturation concentration of 5 µM which results in the distinct labeling of Chol-rich cardiac membrane compartments. This membrane compartmentalization is exemplified in Fig. 3.10 which shows an inner-cell (i.e. at least 3 µm beneath the sarcolemma) STED image of a living VM labeled with Chol-KK114 at a concentration of 500 nM. At this concentration, single Chol-domains can be identified (see magnified inset in Fig. 3.10, corresponding to the yellow boxed region in the overview image) and their resolution can be determined by fitting a Gaussian curve to the signal intensity distribution of the Chol domain (see section 2.6.2; the images in Fig. 3.9 were obtained using a pulsed STED laser, see also Appendix B). Based on the evaluation of single Chol domains, the image resolution that is possible with the Chol-KK114 membrane marker then amounts to ≤ 35 nm.

Additionally to this remarkable achievable object resolution, the low concentration labeling strategy presented in Fig. 3.10 already suggests another advantage: the high versatility of Chol-KK114 for biological studies. Depending on the Chol-KK114 concentration used in the staining protocol, it can serve both as a membrane bulk label as well as a membrane nanodomain label. Fig. 3.11 displays these two possible applications of Chol-KK114 for living VM: for one, the thorough bulk staining of the membrane at high concentrations of Chol-KK114 (Fig. 3.11 **A**), and, for the other, the exclusive staining of Cholesterol rich membrane nanodomains at very low concentrations, resulting in a

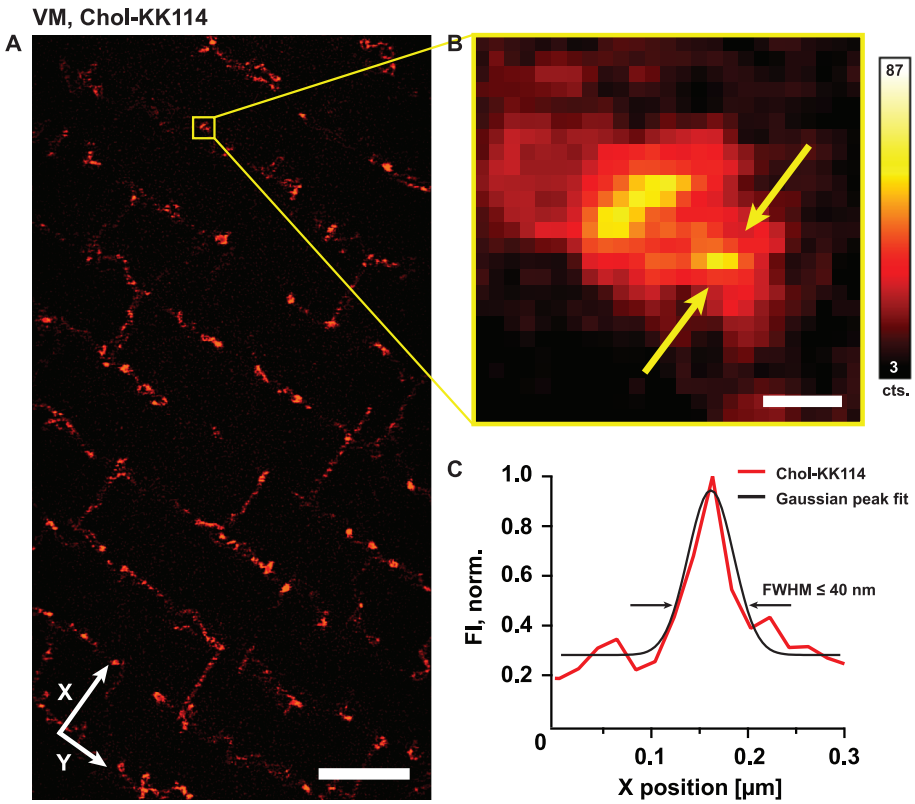

Figure 3.10.: Inner-cell STED image of a ventricular mouse cardiomyocyte (VM) labeled with Chol-KK114. **A** Overview STED image. Scale bar: 2 µm. **B** Image magnification corresponding to the yellow boxed region in the overview image. The color bar indicates the respective image brightness of the magnified images in photon counts (cts.); for the overview images, the same color code was used but, there, ranging from 0 to 115 cts. Images were smoothed using a two-dimensional Gaussian filter with a width of 1.5 pixels. Scale bar: 100 nm. **C** Graphical depiction of the averaged and normalized fluorescence intensity profile (FI, norm.) of the Chol-KK114 single domain signal structure indicated by the two yellow arrows. The structure resolution was determined as the Full Width at Half Maximum (FWHM) of the circular Chol-KK114 signal structure, obtained as described in section 2.6.2, and amounts to $\leq$ 40 nm.

compartmentalized membrane signal (Fig. 3.11 **B**). A thorough staining of the Transverse-Axial Tubular System (TATS, see section 1.1) was achieved using the membrane saturating concentration of $\approx$ 5 µM (Fig. 3.11 **A**; the saturating concentration was experimentally identified in a series of Chol-KK114 titrations that I tested for staining living VM). The resulting membrane signal is bright, stable and shows the typical continuous rectangular arrangement of evenly spaced T-Tubule structures as it is known from comparable bulk and solution stains, such as immersion stains with dextran-linked fluorescein [21], or topographical near-field imaging of T-Tubules, such as Scanning Ion Conductance Microscopy (SICM, [32]). This possibility of labeling the cardiac membrane system as an entity proves highly useful for studies of the cardiac membrane architecture, for example to investigate topological changes

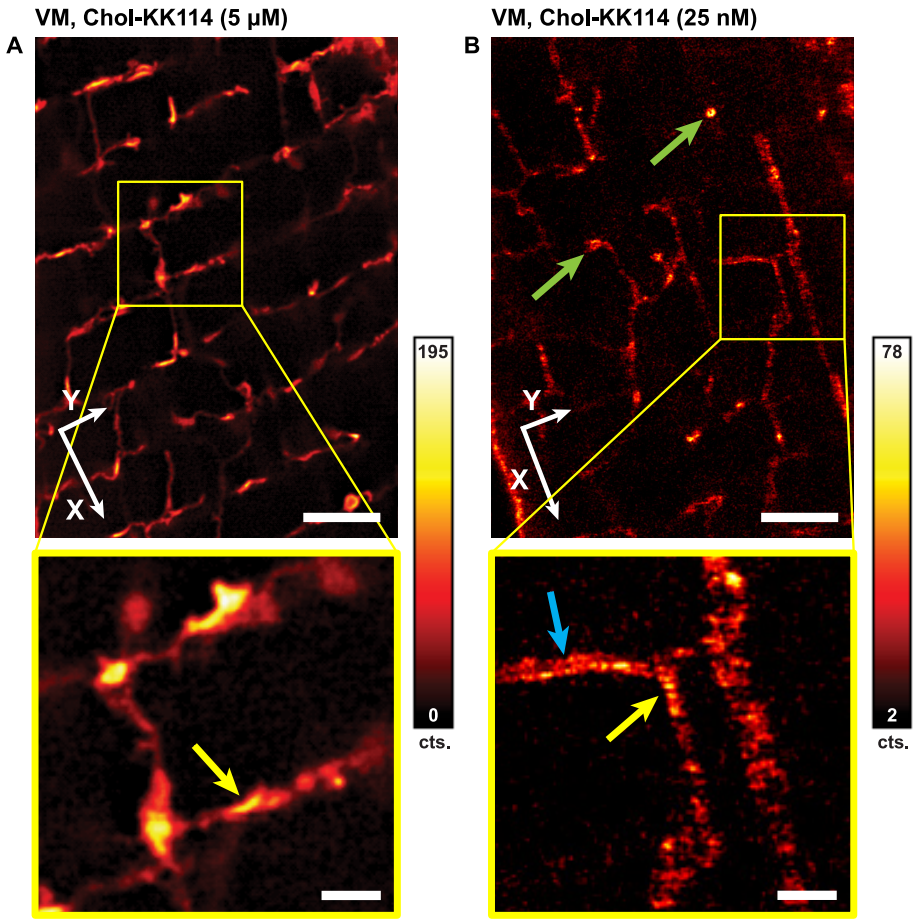

Figure 3.11.: Chol-KK114 serves as a bulk or compartment specific membrane label in living mouse ventricular cardiomyocytes (VM), depending on the used labeling concentration. The white arrow coordinate system indicates the longitudinal (X) and the transverse (Y) cell axes, respectively. STED images of inner-cell regions in living VM labeled at different concentrations of Chol-KK114. Images were obtained with the custom-built fast scanning STED microscope described in section 2.1.2. Images were smoothed using a two-dimensional Gaussian filter with a width of 1.5 pixels. Scale bars in overview images: 2 µm; scale bars in magnifications: 500 nm. **A** Inner-cell STED overview image of a living VM labeled with Chol-KK114 at the saturation concentration of 5 µM. Image magnification corresponding to the yellow boxed region in the overview image; the yellow arrow indicates a region of very dense signal not associated to a perpendicular T-Tubule cross section. The color bar indicates the respective image brightness in photon counts (cts.). **B** Inner-cell STED overview image of a living VM labeled with Chol-KK114 at the low concentration of 25 nM; green arrows indicate perpendicular cross sections of T-Tubules. Image magnification corresponding to the yellow boxed region in the overview image; the yellow arrow indicates a region of Chol-rich compartments along the membrane; the blue arrow indicates a longitudinal section of a T-Tubule. The color bar indicates the respective image brightness of the magnified images in photon counts (cts.); for the overview images, the same color code was used but, there, ranging from 0 to 103 cts.

of membrane arrangements in disease models [22, 505, 440], especially in combination with high resolution STED imaging. And with the new membrane label, these studies are not restricted to only lateral sample recordings but can be readily extended to a three-dimensional imaging scheme, an application in which once again the advantages of slow label internalization, high lateral diffusion rate and high photostability offered by Chol-KK114, are of great impor-

tance. Looking more closely at the saturated Chol-KK114 signal distribution, there are regions with increased signal brightness. These signal structures are unlikely to be cross-sections of T-Tubules branching off (magnification of Fig. 3.11 **A**, yellow arrow). The bright-signal regions might be interpreted as overlapping, highly clustered Chol domains accumulating along the TATS. And indeed, when applying the very low concentration of 25 nM Chol-KK114 to label living VM, such label-saturated bright-signal regions appear to actually be an assembly of smaller sized, Chol-rich membrane compartments (see magnification of Fig. 3.11 **B**, yellow arrow). Since Chol-KK114 inserts itself stably into the extracellular membrane leaflet and since the lipid raft hypothesis postulates the heterogeneous distribution of Chol-rich domains along this extracellular leaflet, the here shown nanometric Chol signal patterns could be a first visualization of Chol islands in the intact cardiac membrane. Further, at the 25 nM Chol-KK114 labeling concentration, perpendicular cross sections of T-Tubules could be resolved as hollow ring-like structures (Fig. 3.11 **B**, green arrows). The membrane signal stemming from longitudinal sections of T-Tubules could be resolved as the expected two parallel lines (see magnification of Fig. 3.11 **B**, blue arrow).

Finally, the slow rate of cellular internalization of Chol-KK114, as stated in section 3.1, makes Chol-KK114 so valuable for labeling cardiac membrane structures since the fast internalization of membrane and lipid labels into cardiomyocytes is a common problem that has been reported before [23]. To qualitatively confirm Chol-KK114 to have one of the slowest internalization times, I screened a non-exhaustive set of fluorescently labeled lipids and assessed their suitability for cardiomyocyte membrane labeling. Chol-KK114 proved to be the most satisfactory marker among the tested lipid labels (cf. Appendix E for an overview of the tested lipid labels).

Conclusively, the fluorescent Chol analog Chol-KK114 is a trustworthy membrane label for living cardiomyocytes that yields signal structures that are analogous to well-established membrane probes. So far, Chol-KK114 is the best performing cardiac membrane stain for live-cell STED microscopy. Further, by choosing the labeling concentration of Chol-KK114, one can flexibly adjust to the specific biological questions underlying the experiment. In the next section, the aim is to realize subdiffraction three-dimensional whole cardiomyocyte

staining of membrane structures. The concept of the fluorescent Chol-PEG derivative Chol-KK114 as a cardiomyocyte membrane label will be expanded to obtain fluorescent Chol analogs that are compatible with Two-Photon-Excitation-CW-STED (2P-Exc-CWSTED) microscopy. I will introduce a custom-built 2P-Exc-CWSTED microscope system and elaborate on the necessary criteria to find suitable fluorophores for such a system. I will present the novel compound Chol-PEG-OregonGreen488 as the best fluorescent Chol probe for 2P-Exc-CWSTED and show the three-dimensional membrane architecture of living cardiomyocytes labeled with Chol-OG488 and imaged via 2P-Exc-CW-STED.

3.4. Two-Photon-Excitation-STED microscopy of the cardiac membrane system

3.4.1. Characterization of the custom-built Two-Photon-Excitation-CW-STED microscope for live cardiomyocyte imaging

As shown in the previous sections, STED microscopy (with one-photon-excitation) yields superior subdiffraction images of Cholesterol structures in standard as well as sophisticated live-cell systems. Two-Photon (2P) microscopy has the benefits of deeper tissue penetration due to the near-infrared excitation wavelengths used and thus less scattering events, and decreased photobleaching of out-of-focus layers in the sample because of the smaller axial focal volume stemming from the quadratic dependence of the emitted fluorescence intensity on the excitation intensity (see section 1.3). To reap the benefits of these two microscopy methods and use them to visualize the complex three-dimensional and Cholesterol rich membrane system deep inside living cardiomyocytes while at the same time reducing cellular stress and photobleaching, I designed and built a microscope setup featuring pulsed two-photon-excitation and a continuous wave (CW) STED laser. This two-photon-excitation-CW-STED (2P-Exc-STED) setup is schematically depicted and described in detail in section 2.1.1.

Important for 2P-Exc-CWSTED imaging deep inside cells, the microscope was equipped with a water immersion objective with an adjustable correction collar to compensate for the spherical aberrations. This measure maintained the quality of the STED PSF, thus yielding a significant image resolution improvement along the whole extent of live cardiomyocytes in aqueous solutions. Further, the high numerical aperture (NA) of the water immersion objective (NA = 1.20) reduced the focal volume, thereby increasing the 2P-Exc efficiency and collecting more emitted photons from the sample.
As already mentioned in the introduction (see section 1.3), for 2P-Exc-CWSTED, it is vital to temporally clean up the detected fluorescence signal by time gating. Setting up a proper time gate for the detected fluorescence signal relies on two parameters. First, the time delay (T_{Gate}) of the accepted fluorescence signal with respect to the incoming 2P-Exc laser pulses. Second, the width of the time gate (W_{Gate}) defining the duration of recording fluorescence starting from T_{Gate}. The delay and width of the fluorescence time gate should be optimized for an individual sample regarding the highest achievable image quality considering the most favorable trade-off between image brightness and image resolution in the 2P-Exc-CWSTED mode. Typically, the time gate settings do not differ profoundly between similar samples. Yet, important properties of fluorescent dyes, such as fluorescence lifetime [506], quantum yield [507], and rate of photobleaching [508, 509], depend on the specific configuration and environment in which a dye is used, like for example if conjugated to an antibody or a lipid analog, or if used for indirect immunofluorescence or for live-cell labeling approaches. Therefore, special attention should be paid on adjusting the respective fluorescence time gate for individual samples. The optimal settings for T_{Gate} and W_{Gate} are mentioned where appropriate. Unless stated otherwise, all 2P-Exc-CWSTED images were obtained with an optimally set fluorescence time gate. The highly enhanced image resolution that is achievable when setting up a time gate for 2P-Exc-CWSTED is demonstrated in the Appendix G.1 for both fluorescent bead samples (yellow-green, 40 nm diameter) as well as for a sample of fixed Vero cells with immunofluorescently labeled Tubulin.
Additionally, I explored the effect of the 2P-Exc laser's repetition rate on the photobleaching rate of the organic fluorophores in 2P-Exc-CWSTED applications. In a preliminary configuration of the 2P-Exc-STED microscope, I used

a Ti:Sa laser that provided laser pulses with a repetition rate of 1 GHz (GigaJet TWIN 20c/20c, Laser Quantum, Konstanz, Germany) for 2P-Exc. This was to test if there is an effect of reduced photobleaching in the case of 2P-Exc with very high repetition rates (quasi CW excitation). A number of published studies point towards such a reduction in photobleaching [510, 511, 368]. For example, at higher repetition rates, the peak intensities can be reduced while maintaining the same 2P-Exc efficiency. However, repetition rates above 100 MHz are assumed to counteract the main strength of 2P-Exc, namely the reduction in the fluorescing sample volume due to an increased fluorophore duty cycle [380]. Further, repetition rates above 1 MHz are assumed to transfer too much thermal load into the specimen [512]. In my studies, I could observe a profound advantageous reduction of fluorophore bleaching when performing 2P-Exc with 1 GHz instead of 80 MHz repetition rate. A 1 GHz repetition rate for 2P-Exc yielded a significant improvement in photobleaching in both 2P-Exc mode as well as in 2P-Exc-CWSTED mode. Fig. 3.12 summarizes these results. The shown bleaching curves were obtained as described in section 2.6.3 using a test sample of Vero cells stained for Tubulin via indirect immunofluorescence using the dye compound STAR 488 (see Appendix A.4). All image acquisition parameters except for the repetition rate of the 2P-Exc laser were kept constant in the course of the bleaching experiments. The 2P-Exc wavelength was tuned to 790 nm and the 2P-Exc power set to 10 mW (measured in the back-focal plane of the objective); the 592 nm CW-STED illumination power was set to 240 mW and the sample scanned with a 0.05 ms pixel dwell time and a pixel size of 20 nm. To ensure direct comparability, the fluorescence signal was not time gated in case of 2P-Exc at 80 MHz repetition rate. In the 2P-Exc mode (Fig. 3.12 **A**), the fluorophore bleaching is reduced by approximately a factor of 10; in the 2P-Exc-CWSTED mode (Fig. 3.12 **B**) the fluorophore bleaching is reduced by approximately a factor of 5 when employing a 2P-Exc laser with a repetition rate of 1 GHz instead of 80 MHz. Notably, in both imaging modes, the fluorophore bleaching behavior at 1 GHz 2P-Exc laser repetition rate follows a mono-exponential decay (fit shown in red in Fig. 3.12 **A** and **B**). In contrast, the bleaching behavior at 80 MHz repetition rate is best modeled by a bi-exponential decay (curve fit shown in blue in Fig. 3.12 **A** and **B**). A mono-exponential bleaching behavior typically indicates that the fluorophore

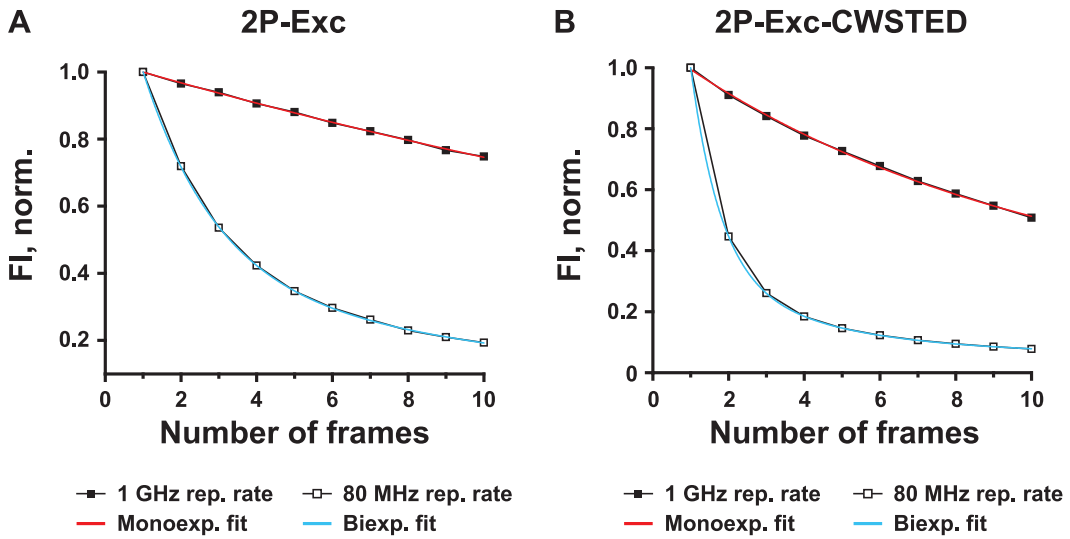

Figure 3.12.: Photobleaching in two-photon excitation (2P-Exc, in **A**) and two-photon-excitation-CW-STED (2P-Exc-CWSTED, in **B**) microscopy at a 2P-Exc laser repetition rate (rep. rate) of 1 GHz (filled squares) vs. 80 MHz (open squares). Bleaching curves were obtained as described in section 2.6.3 using a sample of fixed Vero cells immunolabeled with the dye Abberior STAR 488. The normalized fluorescence intensity (FI, norm.) is plotted against the number of successively acquired image frames. Bleaching curves were fit to either mono-exponential (in red) or bi-exponential (in blue) decays.

transitions from a defined excited state into the terminally bleached dark state at a constant rate [513, 514]. A bi- or even multiexponential decay might be explained by additional, also multi-photon, absorption processes that lead into the bleached molecular state [515, 516]. The modeling and interpretation of photobleaching is discussed in more detail later (see e.g. Fig. 3.14) where the bleaching behavior of suitable dyes for 2P-Exc-CWSTED is further explored. However, laser pulse repetition rates of 1 GHz pose a profound disadvantage for 2P-Exc-CWSTED because such a high repetition rate makes fluorescence time gating impossible since we were not in possession of fast electronics to pick up the 2P-Exc laser pulses with a time resolution of < 1 ns and provide them as a reference signal. Hence, the ungated 2P-Exc-CWSTED images from the configuration with 2P-Exc at 1 GHz repetition rate showed only minor to no resolution improvement compared to the corresponding 2P-Exc images (see Appendix G.2). It was thus not feasible to employ a 2P-Exc laser with 1 GHz repetition rate in 2P-Exc-CWSTED microscopy although the high repetition resulting in lower peak intensities significantly reduces fluorophore bleaching. Equipped with the 2P-Exc laser at a repetition rate of 80 MHz and the possibility for fluorescence signal time gating, the here described 2P-Exc-CWSTED microscope system could reliably provide a point spread function (PSF) with a

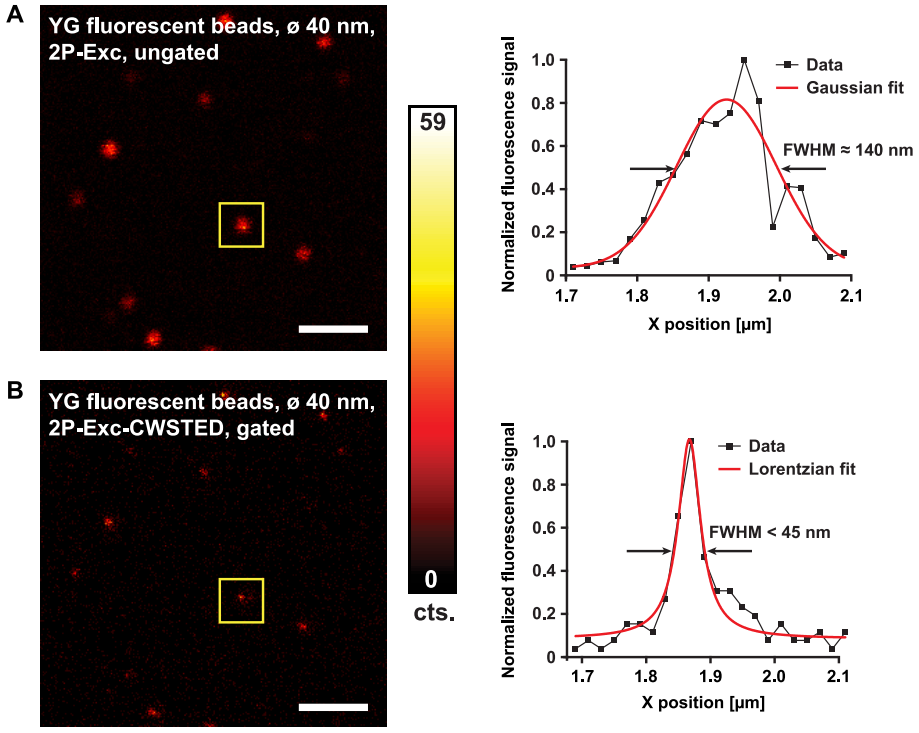

Figure 3.13.: Achievable image resolution with the custom-built two-photon-excitation-CW-STED (2P-Exc-CWSTED) microscope setup. Images show yellow-green (YG) fluorescent beads with an excitation and emission maximum at 505 nm and 515 nm, respectively, and a diameter of 40 nm. Beads were optimally 2P-excited at 757 nm and detected at (525 ± 25) nm. Graphs show the normalized fluorescence signal summed up over the X direction within the image region marked by the yellow box. Image resolution was determined as the full width at half maximum (FWHM) of the respective fit curve to the fluorescence signal profile (see section 2.6.2). **A** Ungated 2P-Exc image of YG fluorescent beads and corresponding normalized fluorescence signal profile of the bead inside the image region marked by the yellow box. The fluorescence profile was fit to a Gaussian curve; the thereof extracted image resolution amounts to 140 nm (FWHM). **B** Gated 2P-Exc-CWSTED image of YG fluorescent beads with a time gate delay at 3.74 ns, time gate width at 9.88 ns, and corresponding normalized fluorescence signal profile of the same bead as in **A** as marked by the yellow box. The fluorescence profile was fit to a Lorentzian curve; the therefrom extracted lowest measured bead diameter amounts to < 45 nm (FWHM). Images show unprocessed raw data. The color bar indicates the image brightness in both **A** and **B** in photon counts (cts.). Scale bars: 1 µm.

full width at half maximum (FWHM) of below 50 nm in the 2P-Exc-CWSTED mode. The system's intrinsic image resolution was controlled prior to each experiment by recording yellow-green fluorescent beads (with excitation and emission maxima at 505 nm and 515 nm, respectively) of 40 nm diameter and determining their apparent size in both 2P-Exc as well as 2P-Exc-CWSTED modes. The obtained 2P-Exc and 2P-Exc-CWSTED PSFs are shown in Fig. 3.13. There, a fluorescent bead of apparent size of 140 nm in the 2P-Exc mode (Fig. 3.13 **A**) could be resolved to its actual size of below 45 nm in the 2P-Exc-CWSTED mode (Fig. 3.13 **B**).

3.4.2. Screening and evaluation of fluorescent dyes for 2P-Exc-CWSTED

The one-photon-excitation and -emission spectra of commercially available fluorescent dyes are usually very well-documented and readily communicated by the respective suppliers. However, the naive assumption of just doubling the wavelength of a dye's absorption maximum to arrive at the ideal wavelength for Two-Photon-Excitation (2P-Exc) does not necessarily apply. It is known from the literature that the absorption spectra of many dyes can show mild to very profound blue-shifts under 2P-Exc conditions [381, 383, 517, 382]. In my attempts to find suitable fluorophores for Two-Photon-Excitation-CW-STED (2P-Exc-CWSTED) microscopy, I could qualitatively observe and confirm this quite unpredictable blue-shift for various organic fluorophores in my experiments. Further, combining 2P-Exc with CW-STED is a balancing act between two main prerequisites. First, the necessity of efficient two-photon excitation leading to a sufficiently high molecular state inversion of the fluorophores between the ground state and the excited state. Second, reducing photobleaching to its minimum, especially when keeping in mind that both the 2P-Exc laser as well as the STED laser are operated at high intensities and thus increase the probability of permanent fluorophore bleaching, and also transfer a high thermal load into the specimen. It is therefore necessary to identify the optimal wavelength for 2P-Exc of a given fluorophore to obtain the most efficient state inversion and thus the highest possible fluorescence signal at the lowest possible 2P-Exc power. Conveniently, the emission spectra of fluorescent molecules stay the same under one-photon- and two-photon-excitation conditions [381] and are neither dependent on the 2P-Exc wavelength nor on the 2P-Exc power [518]. The disclosed one-photon emission spectra of commercially available dyes can thus be readily assumed when searching for suitable dyes for a given STED laser wavelength. The stimulated emission cross section of many fluorophores is typically only slightly red-shifted with respect to the dye's emission spectrum [329]. This would, in a first approximation, motivate choosing fluorescent dyes with emission spectra close to the employed STED wavelength to achieve the most efficient effect of stimulated emission. In most applications of STED microscopy, however, the best performing fluorophores are typically those for which the STED wavelength is located at the red tail of the emission

spectrum. Such a configuration reduces unwanted fluorescence background signal stemming from fluorophore re-excitation due to the residual absorption cross section at the STED laser wavelength (known as anti-Stokes-excitation [519, 520]). Also, that way, the largest portion of the fluorescence signal can be collected without overlap with the STED laser line. Although there have been implementations of STED microscopy with STED wavelengths close to the maxima of the fluorophores' emission spectra [520, 521], these approaches require additional image acquisition and processing steps that reduce the signal brightness, possibly increase photobleaching due to a decreased sample scanning speed, and add complexity and possible sources of artifacts. For completeness, I investigated fluorophores with emission spectra close to the employed 592 nm STED laser wavelength - for example the dyes ATTO 542, Alexa Fluor 555, and DY 555 with emission maxima at 562 nm, 565 nm, and 572 nm respectively. These dyes, however, proved highly unsuitable in the 2P-Exc-CWSTED setup as they showed the expected anti-Stokes-excitation effect that outweighed the desired fluorophore switch-off by stimulated emission.
Based on the above mentioned reasons and prerequisites, I screened a reasonably large subset of fluorescent dyes that I anticipated to fulfill the following five criteria:

1.) The fluorophore needs to show a sufficiently large two-photon excitation cross section when illuminated within the available excitation wavelength range of 740 - 850 nm provided by the Ti:Sa-laser in the 2P-Exc-STED system.

2.) The fluorophore's stimulated emission spectrum needs to peak close to the used STED laser wavelength of 592 nm. That way, the fluorophore, being in the excited state, returns to its ground state with a high probability via stimulated emission. This effect of photoswitching by stimulated emission will be referred to as "switch-off".

3.) The fluorophore's absorption coefficient needs to be very low in the vicinity of the used STED laser wavelength of 592 nm to avoid excitation and re-excitation [522, 329] by the STED laser.

4.) The fluorophore has to be efficiently switched-off by the STED laser. In essence, this criterion summarizes the premises 1.), 2.) and 3.) as it re-

lies on a high efficiency of the inversion between the excited state and the ground state and thus depends on each the two-photon absorption spectrum, the stimulated emission spectrum, and the STED wavelength absorption spectrum.

5.) The fluorophore needs to be photostable to withstand both the high-peak-power 2P-excitation beam as well as the high-power CW-STED-beam without bleaching.

In a first round of screening fluorescent dyes for their suitability for 2P-Exc-STED, I restricted my investigation to criteria 1.) - 4.), i.e. omitting photobleaching. I decided to do so because photobleaching of dyes is a complex process with many underlying mechanisms. This complexity is observed in the two fields of 2P-Exc microscopy [371, 523, 516] and STED microscopy [524, 329], and becomes even more complex for 2P-Exc-STED as a combination of the two methods [368, 402, 525]. Hence, I chose to decouple the evaluation of the spectral properties of fluorophores from their bleaching behavior to narrow down the vast amount of possible dyes to a few, most promising candidates. For this subset of selected dyes, I performed a more in-depth evaluation of their bleaching behavior which will be presented later in this section.
To assess the fluorescent dyes with optimal spectral properties for the 2P-Exc-STED microscope setup, I prepared solutions of various fluorophores (so-called "dye seas", see section 2.5.2) which I selected based on their available one-photon-absorption spectra. A comprehensive list of the tested dyes and their ordering information is given in the Appendix A.4. Due to fast diffusion of the fluorescent molecules within the dye sea, effects of photobleaching are negligible. Since the fluorophores are dissolved in purified water, the fast flow of molecules into and out of the focal volume can reasonably be assumed to be similar to the self-diffusion rate of water. For example, the self-diffusion rate of the dye fluorescein in water has been determined to be 760 $\mu m^2/s$ [526]. Principally, the dye seas with their high diffusion rate and their subordinate photobleaching might be a more suitable model system than the widely used fixed cell samples stained via indirect immunofluorescence if the aim is to fast and conveniently mimic the behavior of a fast-diffusing fluorescent lipid analog. However, the lateral diffusion rate of fluorescent lipid analogs in the cell membrane is still two orders of magnitude lower than that of the freely diffus-

ing dye in solution. Therefore, having identified suitable dyes for 2P-Exc-STED applications, additional studies of the bleaching behavior were performed in a second round of dye screening and are presented further below.
For the characterization of the spectral properties under 2P-Exc-STED conditions, the 2P-Exc and the STED laser beams were axially focused to the edge of the respective fluorescent dye sea, i.e. the transition between the cover slip and the solution, and the fluorescence signal recorded with the Avalanche Photo Diode (APD) in the fluorescence detection path. For simplicity, the phase mask was removed from the STED laser path and the focused STED beam had a Gaussian intensity profile. A bandpass filter was installed in front of the APD that could be easily interchanged to cover the appropriate wavelength range of the emission spectrum of the fluorophore. The fluorescence photon counts of the respective dye sea under different illumination conditions were recorded with a pixel dwell time of 3 ms; this setting was kept constant for all tested dyes for reasons of comparability. The fluorescence time gate of the APD signal was globally set for all investigated dye seas. The gate had a time delay of 1.5 ns with respect to the 2P-Exc laser pulses and a width of 9 ns. The APD dark counts were taken into consideration by subtraction from the recorded fluorescence photon counts. For comparative quantification of the fluorescence response of the tested dyes, I defined three parameters that are described in the following.

- The ratio α describes the switch-off efficiency of the fluorophore by the STED laser and is calculated by

$$\alpha = \min\left(\frac{C_{\text{2P-Exc-STED}}(P_{\text{STED}})}{C_{\text{2P-Exc}}}\right)$$

  with $C_{\text{2P-Exc-STED}}$ being the detected fluorescence photon counts under illumination with both the excitation and the STED laser, $C_{\text{2P-Exc}}$ being the detected fluorescence photon counts under illumination with the excitation laser only, and P_{STED} being the power of the 592 nm STED laser. Note that the value of $C_{\text{2P-Exc-STED}}$ depends on P_{STED}. The smaller the obtained α, the more efficient is the switch-off by the STED laser. If $\alpha \geq 1$, then the STED laser does not switch off the fluorophore but is, instead, exciting it in addition to the excitation laser. When determining α, I optimized the

2P-Exc wavelength for a given dye within the range of 740 - 850 nm at a respective laser power of 50 mW. P_{STED} was tuned in the range of 10 - 240 mW. Both laser powers were measured in the backfocal plane of the objective. If not stated otherwise in Table 3.1, the maximum STED laser power of 240 mW yielded the denoted value for α.

- The term β describes the amount of re-excitation of the fluorophore by the STED laser and is calculated by

$$\beta = 1 - \left(\frac{C_{\text{STED}}}{C_{\text{2P-Exc-STED}}} \right)$$

with C_{STED} being the detected fluorescence photon counts under illumination with the STED laser, and $C_{\text{2P-Exc-STED}}$ being the detected fluorescence photon counts under illumination with both the excitation and the STED lasers. Generally, it can be stated that the bigger the β, the lower is the amount of re-excitation by the STED laser and thus the more suitable is the dye. Optimally, β will become 1. β was determined for the optimal 2P-Exc wavelength for the respective dye at an 2P-Exc power of 50 mW and for the STED laser power that yielded the best switch-off (see the evaluation of α). β is defined in the above fashion to prevent it from becoming 0 in case of no re-excitation. This is because the goodness factor η that is defined next, and which relates α and β to one another, should not become 0 either so as to not obscure the impact of α.

- The ratio η is a compound expression relating α and β to one another and is calculated by

$$\eta = \frac{\beta}{\alpha}.$$

This definition of η gives a quick and qualitative estimate of the suitability of the spectral properties of a fluorophore. Generally, the bigger the η, the more promising is the dye.

A comprehensive overview of the dyes tested and evaluated for their applicability in 2P-Exc-STED microscopy is given in Table 3.1. The tested dyes are listed in order of ascending emission wavelengths. The names of the dye compounds are abbreviated, more detailed information about the tested dyes can be found in the Appendix A.5. Table 3.1 displays the wavelengths of maximum

absorption and emission (Abs/Em), respectively in nm, and the fluorescence lifetimes in ns as provided by the manufacturer, except in the case of the compounds DY 380XL and DY 375XL whose lifetimes were measured in-house for the dye in solution (PBS, pH 7.4), marked as (*), and for the dye labeling Tubulin in Vero cells via indirect immunofluorescence, marked as (**). For each dye, I optimized the region of fluorescence detection (Det.) and the 2P-Exc wavelength (opt. λ_{2P}) for the highest measured signal and determined the descriptive parameters α, β, and η for these settings. To qualitatively assess the brightness of a given dye, I also recorded the maximum signal brightness as detected by the APD; this maximum brightness (max. bright.) is displayed in Table 3.1 and denoted in photon counts. The column "Comments" summarizes the observed dye performance regarding switch-off and re-excitation (re-exc.) behavior as well as the detected signal brightness and additional noteworthy remarks for evaluation, e.g. if the dye sea shows any signs of photobleaching. The spectroscopic suitability of the dye for 2P-Exc-STED is then qualitatively rated according to: (++) - very suitable; (+) - potentially suitable; (-) - not recommended; (--) - not suitable.

Based on the mentioned criteria defined above, the following seven dyes could be identified as being the most promising for application in 2P-Exc-STED: ATTO 390, ATTO 425, DY 380XL, AF 488, ATTO 488, STAR 488, and OG 488. For these compounds, I conducted a more in-depth study of optimal 2P-Exc-STED imaging conditions and the resulting photobleaching behavior. To fulfill the high photostability mentioned above in criterion 5.), the fluorophore needs to provide a large fluorescence signal in the STED imaging mode at a reasonable sample scan rate (i.e. a pixel dwell time between 0.05 and 0.6 ms). Additionally, the fluorophore needs to be photostable to enable the acquisition of multiple images of the same lateral region of interest along different axial depths for three-dimensional reconstruction imaging. As stated above, the specific properties of a fluorophore regarding its photostability cannot be quantified using a dye solution because due to diffusion of dye molecules the solution is not subject to photobleaching. Hence, for completeness, I evaluated the bleaching behavior of those dyes that I had identified to fulfill the above stated criteria 1.) - 4.). I used standard prepared samples of Methanol fixed Vero cells in which the cytoskeletal protein Tubulin was labeled with the respective fluorophore via in-

Dye	Abs/Em [nm]	Lifetime [ns]	Det. [nm]	α (opt. λ_{2P})	β	$\eta = \frac{\beta}{\alpha}$	Comments	Rating
ATTO 390	390/479	5	(490 ± 20)	0.19 (760 nm)	0.92	4.84	good switch-off, medium re-exc.	(+)
ATTO 425	436/484	3.6	(490 ± 20)	0.23 (810 nm)	0.96	4.17	medium switch-off, low re-exc.	(+)
ATTO 465	453/508	5	(500 ± 20)	0.47 (810 nm)	0.70	1.49	bad switch-off, high re-exc.	(-)
DY 380XL	381/510	$3.16^{(*)}$; $1.77^{(**)}$	(525 ± 25)	0.10 (760 nm)	0.99	9.90	very good switch-off, very low re-exc.	(++)
STAR 440SXP	436/515	3.3	(525 ± 25)	0.49 (850 nm)	0.72	1.47	bad switch-off, high re-exc., low absolute signal	(-)
Chromeo 488	488/517	n.s.	(525 ± 25)	0.28 (800 nm)	0.93	3.32	medium switch-off, medium re-exc., low absolute signal	(-)
AF 488	496/519	4.1	(530 ± 20)	0.14 (760 nm)	0.94	6.71	very good switch-off, low re-exc.	(++)
ATTO 488	501/523	4.1	(530 ± 20)	0.10 (800 nm)	0.92	9.20	very good switch-off, medium re-exc.	(++)
STAR 488	501/524	3.9	(530 ± 20)	0.14 (790 nm)	0.91	6.50	very good switch-off, medium re-exc.	(+)
OG 488	498/526	4.1	(530 ± 20)	0.14 (800 nm)	0.86	6.14	very good switch-off, medium re-exc.	(+)
ATTO 495	495/527	1	(530 ± 20)	0.44 (830 nm)	0.73	1.66	bad switch-off, high re-exc.	(--)
DY 505	505/530	n.s.	(530 ± 20)	0.17 (810 nm)	0.87	5.12	good switch-off, high re-exc., dye sea bleaches!	(-)
STAR 512	512/530	4.1	(530 ± 20)	0.15 (810 nm)	0.74	4.93	good switch-off, high re-exc.	(-)
DY 375XL	376/543	$2.90^{(*)}$; $2.62^{(**)}$	(530 ± 20)	0.20 (850 nm)	0.82	4.10	good switch-off, high re-exc.	(-)
ATTO 430LS	433/547	4	(550 ± 20)	0.22 (850 nm)	0.49	2.23	medium switch-off, very high re-exc.	(-)
ATTO 532	532/553	3.8	(550 ± 20)	0.84 (800 nm)	0.33	0.39	$P_{STED} \overset{!}{\leq} 25$ mW, bad switch-off, high re-exc.	(--)
AF 532	532/553	2.5	(550 ± 20)	$\geq 1 \; \forall \; \lambda_{2P}$	(see α)	(see α)	no switch-off possible!	(--)
DY 500XL	505/555	n.s.	(550 ± 20)	0.89 (810 nm)	0.17	0.19	$P_{STED} \overset{!}{\leq} 25$ mW; very bad switch-off, very high re-exc., dye sea bleaches!	(--)
DY 490XL	486/556	n.s.	(550 ± 20)	$\geq 1 \; \forall \; \lambda_{2P}$	(see α)	(see α)	no switch-off possible!	(--)

Table 3.1.: Evaluation of the dyes tested for their suitability for two-photon-excitation-STED (2P-Exc-STED) microscopy regarding their spectral properties. Denoted parameters are explained and discussed in the text (section 3.4.2). (*) - life time of the dye (measured in-house) in solution (PBS, pH 7.4); (**) - life time of the dye (measured in-house) in a cell sample stained via indirect immunofluorescence (see section 2.5.4). A comprehensive overview of the tested dyes (and their abbreviated names) is given in Appendix A.5.

direct immunofluorescence (see section 2.5.4). I recorded bleaching curves of the respective fluorophores by consecutively scanning one spot in the cell samples with a pixel dwell time of 0.05 ms and a pixel size of 20 nm. The resulting pixel intensity was summed up over each frame and normalized to its maximal value. It was then plotted against the number of acquired image frames (see section 2.6.3). The resulting bleaching curves for the above mentioned seven dye compounds are shown in Fig. 3.14.

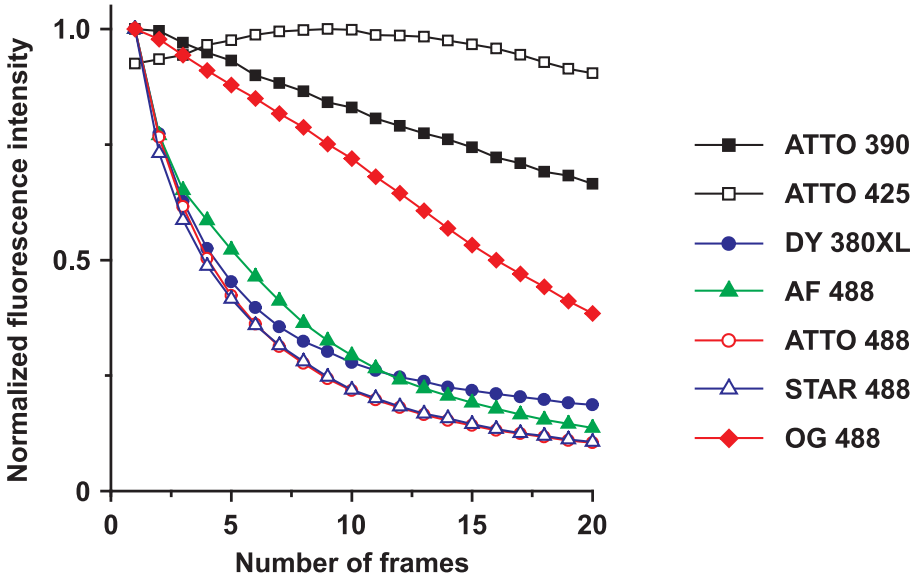

Figure 3.14.: Bleaching curves of selected dyes for Two-Photon-Excitation-STED (2P-Exc-STED) microscopy. The investigated dyes were selected after a first round of dye screening regarding the 2P-Exc-STED behavior, see Table 3.1, and used for staining the cytoskeletal protein Tubulin in Vero cells via indirect immunofluorescence, see section 2.5.4. The bleaching curves were obtained as described in section 2.6.3 and are evaluated and discussed in section 3.4.2 and in Table 3.2.

For the dyes DY 380 XL, AF 488, ATTO 488, and STAR 488, the bleaching behavior is best described by a bi-exponential decay. I explored both the goodness of fit of a mono-, bi- and higher order exponential decays to model the bleaching behavior under 2P-Exc-STED conditions. The residuals of these different fit functions (see Appendix G.3) clearly show that a bi-exponential decay is the most adequate model. This bi-exponential decay in fluorescence intensity is the typical bleaching behavior for most dyes under one-photon-excitation [513], and two-photon-excitation [516], respectively. A mono-exponential decay in fluorescence intensity would usually indicate that photobleaching is a single-photon-absorption process and can be described as the transition of the fluorescent molecule from the excited state to a dark state with a constant rate [513, 514]. For one-photon-excitation-STED, such a mono-exponential decay

has been reported [346]. The here observed bi-exponential decay under 2P-Exc-STED conditions motivates a more complex model of photobleaching comprising multiple photon absorption pathways that can lead to photobleaching [515, 516].
Performing a similar analysis on the bleaching behavior of the dyes ATTO 390 and OG 488 reveals that there a mono-exponential decay is the most adequate model for photobleaching. Although I could verify that the excitation of these two fluorophores followed a two-photon absorption process, i.e. there was a quadratic dependence of the fluorescence signal on the illumination intensity (data not shown), the photobleaching behavior of ATTO 390 and OG 488 resembles that of fluorophores under one-photon-excitation-STED conditions [346]. This hints towards a single photobleaching process with a constant transition rate into the terminally bleached molecular state. It is beyond the scope of this work to investigate the underlying processes of photobleaching for different dyes in detail. The important observation is that ATTO 390 and OG 488 essentially show a much slower rate of photobleaching than the above mentioned four investigated dyes and are thus promising candidates for use in 2P-Exc-STED microscopy of Cholesterol rich membrane structures in cardiomyocytes.
The time development of the fluorescence of the dye ATTO 425 features a gradual increase in total fluorescence intensity before showing signs of photobleaching. This somewhat deviant behavior is most likely attributable to self-quenching of the fluorophores [406, 527, 528], a phenomenon also known as concentration-quenching. Due to the self-quenching effect, the fluorescence of ATTO 425 first increases in each image frame since more and more fluorophores are photobleached and thus the concentration of still excitable fluorescent molecule decreases, counteracting the suppression of fluorescence signal introduced by self-quenching. As soon as photobleaching has irreversibly reduced the fluorophore concentration necessary for effective self-quenching, the effect of photobleaching prevails and a monotonous decrease in fluorescence signal is observed. For ATTO 425, this is the case starting at about image frame 8. Although the effect of self-quenching effectively delays the disadvantageous photobleaching of the dye ATTO 425, self-quenching is an undesirable property of a dye for STED microscopy in general and for gated 2P-Exc-STED

microscopy specifically. This is because the fluorescence switch-off caused by the STED laser becomes anisotropic depending on the fluorophore concentration within the sample. Additionally, in essence, self-quenching creates several subpopulations of the same dye that feature different fluorescence lifetimes [406]. This profoundly compromises the advantageous setting of a fluorescence detection time gate that is necessary for optimal image resolution. For these reasons, and although the fluorescence signal of ATTO 425 does not nearly drop to half of its maximal value after 20 acquired frames, ATTO 425 was classified as unsuitable for gated 2P-Exc-STED applications. This is especially the case for the finally intended imaging of Cholesterol rich membrane structures in living cardiomyocytes because Cholesterol is a raft-associated lipid and, as we have seen in section 3.3, partitions into local membrane clusters. Any concentration dependent alterations of dye properties should thus be avoided.
It is important to note that I conducted the bleaching study for optimized imaging parameters for each dye compound. I identified these optimal settings by iteratively adjusting them during scanning of the actual sample to arrive at the highest quality STED images before performing the actual bleaching scans. This qualitative assessment of appropriate imaging conditions provides more comparability between different dyes than an experiment with constant imaging settings for each fluorescent compound. This is because the best image is the result of the interplay of several underlying factors that cannot be categorized isolated but must be customized for individual fluorophores. Admittedly, the choice of the test sample for a certain study also has a significant impact on the photophysical behavior of a fluorophore. I therefore chose to image Tubulin structures because such specimen are standardly used in the literature in proof-of-principle applications [529, 530, 531], and because the sample preparation protocol is highly reproducible. While keeping the image scan rate and pixel size constant, I explored several image acquisition parameters (summarized in Table 3.2) to achieve the highest quality images of the test sample. First, the appropriate detection filter was chosen to efficiently collect the majority of the fluorescence stemming from a given fluorophore. As mentioned previously, the emission spectra of a fluorophore for one-photon- and two-photon-excitation are the same. Therefore, the choice of detection window per dye was readily made according to its disclosed emission spectrum. Nevertheless, hav-

ing adjusted all the other imaging parameters, I went back and tested different detection regions for fluorescence recording, namely (490 $\pm$ 20); (525 $\pm$ 25); (530 $\pm$ 20), to validate my initial choice. Conclusively, the detection windows chosen based on the one-photon-emission spectra were already optimal for detection which confirms the reported observation of unaltered emission spectra of most dyes under 2P-illumination conditions.
Second, the optimal 2P-Exc wavelength was identified within the range of 740 - 850 nm by gradually adjusting the excitation wavelength while scanning the sample in two-photon mode to achieve the highest fluorescence signal. The thus found 2P-Exc wavelengths corresponded to those that I could identify previously for in the dyes in solution (see Table 3.1). This hints towards the dyes' unaltered 2P-absorption spectra in solution vs. as antibody conjugate.
Third, the 2P-Exc and the STED laser powers were adjusted simultaneously while scanning the sample. Illumination powers were measured in the back focal plane of the objective. 2P-Exc powers were tested within a range of 1 - 50 mW. Although the 2P-Exc laser was capable of providing even higher illumination powers, any increase beyond 50 mW would result in instantaneous sample bleaching rendering the search for an appropriate region of interest for scanning impossible. STED illumination powers were tested within a range of 10 - 240 mW, optimized for a given 2P-Exc power, and the resulting images were mutually compared for the different combinations of 2P-Exc and STED powers. In summary, the dye compounds were most efficiently two-photon-excited for powers in a range of 7 - 20 mW; fluorescence depletion was most favorable for STED illumination powers in a range of 150 - 240 mW.
Fourth, the time gating of the fluorescence signal detected by the APD was optimized for each dye individually while scanning the test sample in 2P-Exc-STED mode. Both the time delay with respect to the 2P-Exc laser beam pulses as well as the width of the time gate were adjusted and could be fine-tuned with a temporal resolution of 40 ps.

For reasons of comparability between the bleaching curves of the different dyes, I chose to describe the bleaching behavior by the parameter $F_{Bleach;\,0.5}$ being the number of image frames taken before the summed fluorescence signal had decreased to half of its initial/maximal value. Defining this qualitative parameter circumvents having to make an assumption about the underlying

Dye	Abs/Em [nm]	Lifetime [ns]	Det. [nm]	opt. λ_{2P} [nm]	opt. $P_{2P\text{-}Exc}$ [mW]	opt. P_{STED} [mW]	T_{Gate} [ns]	W_{Gate} [ns]	$F_{Bleach;\,0.5}$	Rating
ATTO 390	390/479	5	(490 ± 20)	760	20	150	3.42	8.00	> 20	(+)
ATTO 425	436/484	3.6	(490 ± 20)	810	7	240	0.86	9.92	>> 20†	(-)
DY 380XL	381/510	3.16$^{(*)}$; 1.77$^{(**)}$	(525 ± 25)	760	7	200	0.86	9.92	5	(+)
AF 488	496/519	4.1	(530 ± 20)	760	10	200	2.78	10.56	6	(+)
ATTO 488	501/523	4.1	(530 ± 20)	800	15	150	2.14	10.56	4	(-)
STAR 488	501/524	3.9	(530 ± 20)	790	10	150	0.86	9.92	4	(-)
OG 488	498/526	4.1	(530 ± 20)	800	10	150	2.42	9.80	16	(+)

Table 3.2.: Evaluation of the bleaching behavior of select dyes for Two-Photon-Excitation-CW-STED (2P-Exc-CWSTED) microscopy. The investigated dyes were selected after a first round of dye screening regarding their spectral suitability for 2P-Exc-CWSTED, see Table 3.1, and used for staining the cytoskeletal protein Tubulin in Vero cells via indirect immunofluorescence, see section 2.5.4. The corresponding bleaching curves are shown in Fig. 3.14. Denoted fluorescence lifetimes are adopted from the supplier and were typically determined from dye solutions in MeOH or PBS (pH 7.4), except for the compound DY 380XL where: (*) - life time of the dye (measured in-house) in solution (PBS, pH 7.4); (**) - life time of the dye (measured in-house) in the Vero-Tubulin cell sample. The bleaching behavior was characterized as described in section 2.6.3. Bleaching curves were determined for optimal imaging conditions adjusted for each respective dye, i.e. fluorescence detection (Det.), optimal 2P-Exc wavelength (opt. λ_{2P}), illumination powers ($P_{2P\text{-}Exc}$ and P_{STED}, measured in a back focal plane of the objective, respectively), and fluorescence time gating (with T_{Gate} denoting the time delay with respect to the 2P-Exc laser pulse and W_{Gate} denoting the width of the set time gate). $F_{Bleach;\,0.5}$ denotes the bleaching constant defined as the number of acquired image frames after which the total fluorescence signal had dropped to half of its initial/maximum value. † - the bleaching behavior is likely due to self-quenching of the fluorophore (see also the corresponding bleaching curve in Fig. 3.14). Qualitative rating: (+) - promising for 2P-Exc-STED microscopy; (-) - not promising for 2P-Exc-STED microscopy. A comprehensive overview of the dyes (and their abbreviated names) is given in the Appendix A.5

model of fluorescence decay and takes into account the optimized image settings for each dye. $F_{Bleach;\,0.5}$ is listed in Table 3.2.

In addition to the evaluation of the dye suitability for 2P-Exc-CWSTED based on the photobleaching behavior, I tested the image quality achievable with each of the above mentioned seven dye compounds. To this end, I recorded 2P-Exc-CWSTED images of fixed Vero cells stained for the cytoskeletal protein Tubulin (see section 2.5.4). I focused on the following three criteria to assess image quality: signal specificity and highest image resolution at a sufficient signal-to-noise ratio. Looking at the obtained images, the dyes ATTO 390 and ATTO 425, showed very poor performance in both 2P-Exc and 2P-Exc-CWSTED imaging as the signal seemed very unspecific (in case of ATTO 425), the signal-to-noise ratio was low, and the image resolution was not notably increased in 2P-Exc-CWSTED mode as compared to 2P-Exc mode. Images that were obtained using ATTO 390 and ATTO 425 are shown in the Appendix G.4 and demonstrate the unsuitability of these dye compounds for 2P-Exc-CWSTED. For the dye compounds that were found to be very suitable for 2P-Exc-CWSTED (i.e. DY 380XL, AF 488, ATTO 488, STAR 488, and OG 488), Fig. 3.15 gives an overview of the 2P-Exc-CWSTED images obtained with the respective dyes and the corresponding image resolutions. For comparability, similar spots were recorded within the sample, i.e. Tubulin structures close to the apical cell membrane and imaged through the nucleus at an imaging depth of approximately 5 µm. This region of interest (ROI) was chosen, for one, to demonstrate the achievable 2P-Exc-CWSTED image quality deep inside a specimen. For the other, such an ROI facilitates the visualization of 2P-Exc-CWSTED image resolution since Tubulin is less densely arranged around the nucleus.

All five dye compounds showed superior image resolution between 77 nm (AF 488) and 44 nm (OG 488) which corresponds to an increase in resolution by a factor of 2 up to 3, respectively, when compared to 2P-Exc microscopy. Especially the dye compounds DY 380XL, AF 488, and OG 488 show high image resolution while also exhibiting high signal specificity and low background signal. The dye STAR 488 shows some unspecific labeling artifacts which might stem from antibody clustering. Nevertheless, STAR 488 provided a standardly high enough signal-to-noise ratio to allow reliable data evaluation. The dye ATTO 488 provided images with an unfavorably low signal-to-noise ratio, resulting

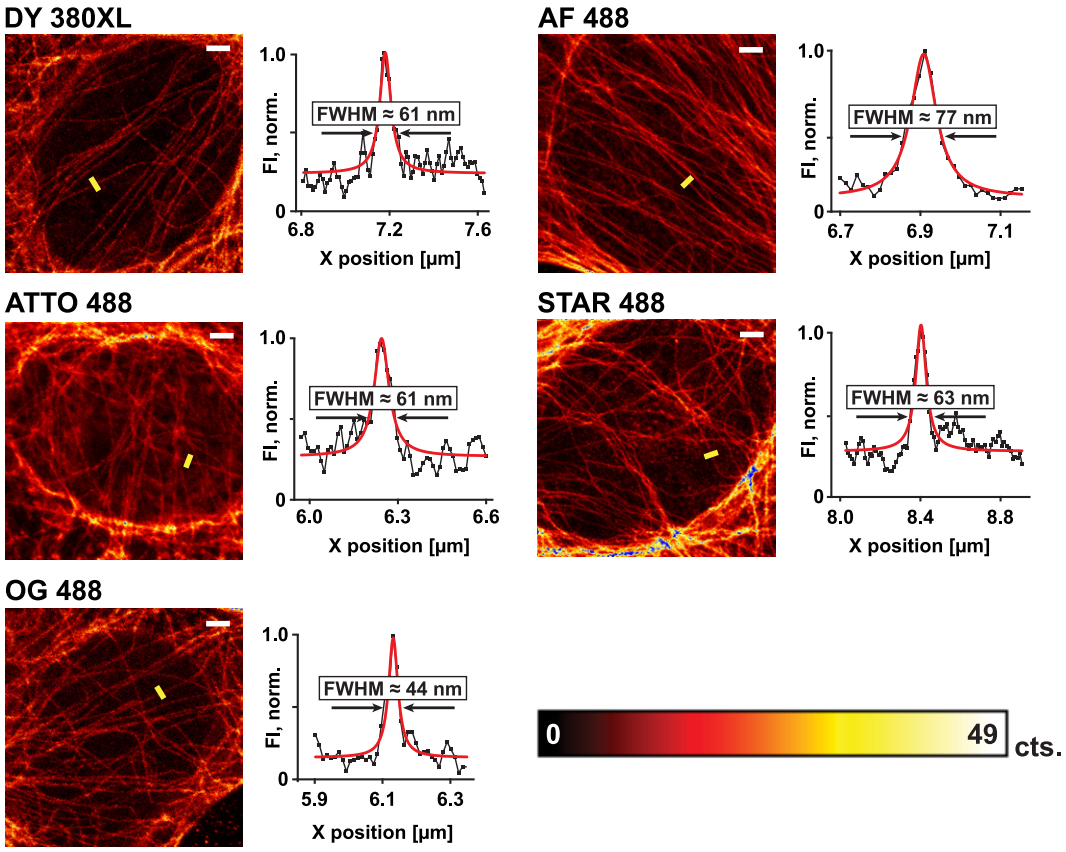

Figure 3.15.: Two-photon-excitation-CW-STED (2P-Exc-CWSTED) images of fixed Vero cells labeled for the cytoskeletal protein Tubulin via indirect immunofluorescence. Tubulin was decorated with the antibody-coupled dye compounds DY 380XL, AF 488, ATTO 488, STAR 488, and OG 488, respectively. Image settings were adjusted to yield optimal 2P-Exc-CWSTED images; fluorescence time gates were set individually for each dye compound and correspond to the ones stated in Table 3.2. Graphs next to the corresponding images show the normalized fluorescence signal intensity averaged over a width of 5 pixels and obtained from line profiles along the yellow bars. Image resolution was extracted from the profiles by fitting them to a Lorentzian curve (red line, see section 2.6.2); image resolution is displayed as the full width at half maximum (FWHM). Images show raw data with adjusted brightness to facilitate visualization. The color bar indicates the image brightness in photon counts (cts.). Scale bars: 1 µm.

in blurred sample features. It was thus excluded from further investigations. Altogether, for membrane labeling of living cardiomyocytes via a fluorescent Cholesterol analog, the following four dyes showed the highest potential: DY 380XL, AF 488, STAR 488, and OG 488 (ordered by ascending emission wavelength). These four dyes were coupled to Chol-PEG derivatives as described in section 2.2. I will hereafter refer to the obtained Chol-PEG-dye compounds as Chol-DY380XL, Chol-AF488, Chol-STAR488, and Chol-OG488.

I used the obtained Chol-PEG-dye compounds to stain living mouse ventricular cardiomyocytes (VM) and assessed the compounds' suitability for application in 2P-Exc-CWSTED microscopy. For this suitability assessment, I aimed at achieving the highest quality membrane specific 2P-Exc-CWSTED image

stacks - i.e. fast 3D image acquisition with a high signal-to-noise ratio and superior spatial resolution - while at the same time avoiding unspecific background signal, and cellular stress due to phototoxicity and thermal energy transfer into the specimen because of high laser powers.
Employing the four fluorescent lipid analogs Chol-DY380XL, Chol-AF488, Chol-STAR488, and Chol-OG488 for 2P-Exc-CWSTED imaging of cardiac membrane structures, Chol-OG488 proved to be the most suitable due to slow cellular internalization, low phototoxicity and reasonably high photostability.
Unfortunately, labeling cardiomyocytes with Chol-DY380XL yielded a diffuse and unspecific fluorescence signal. This signal unspecificity seemed to stem from either a very high degree of cellular internalization, and/or a high affinity of the Chol-DY380XL compound to cardiac mitochondria. Both Chol-AF488 and Chol-STAR488, on the other hand, showed slow cellular internalization, a membrane-specific signal, and a very good switch-off behavior in STED mode while maintaining a high signal-to-noise ratio. However, both membrane labels subjected the cells to stress, resulting in membrane blebbing and cell contraction soon after staining. Additionally, Chol-AF488 had a seemingly high potential for phototoxicity as cells could neither sustain extended laser illumination nor an increase in illumination intensity when they were stained with Chol-AF488. Similar illumination protocols were far less critical for the cells when being stained with the other prepared fluorescent Cholesterol analogs. To demonstrate the unsuitability of Chol-DY380XL, and the less than optimal performance of Chol-AF488 and Chol-STAR488, an overview of the images obtained with these membrane markers (as negative examples) is given in the Appendix G.5.
Conclusively, I could identify the membrane marker Chol-OG488 as the optimal probe for the visualization of the membrane system of living cardiomyocytes with the novel approach of 2P-Exc-CWSTED microscopy using a fluorescent Cholesterol analog. The results are presented in the next section.

3.4.3. 2P-Exc-CWSTED of membrane structures in living cardiomyocytes

The images of living mouse ventricular cardiomyocytes (VM) labeled with the fluorescent Cholesterol (Chol) analog Cholesterol-PEG-OG488 (Chol-OG488)

presented below were obtained under standardized conditions after optimization of both the staining protocol and the image acquisition parameters. The cells were stained with 5 µM Chol-OG488 according to the protocol described in section 2.3.2.

Images of living VM in 2P-Exc mode were obtained with an optimized 2P-Exc wavelength at 760 nm and with an illumination power of 10 mW measured in the back focal plane of the objective. The 2P-Exc images were acquired with a pixel size of $(40 \times 40 \times 200)$ nm³ in $(X \times Y \times Z)$ with a pixel dwell time of 0.02 ms, and without fluorescence time gating. The images of living VM in 2P-Exc-CWSTED mode were obtained with 2P-Exc at 760 nm at 10 mW illumination power and a STED beam at 592 nm with illumination power between 50 mW and 100 mW (the illumination powers were measured for the 2P-Exc and for the STED laser, respectively, i.e. appropriately gauged to the respective laser wavelength). The fluorescence signal in 2P-Exc-CWSTED mode was time gated with an optimized gate delay T_{Gate} = 2.42 ns and an optimized gate width W_{Gate} = 9.80 ns. The 2P-Exc-CWSTED images were acquired with a pixel size of $(20 \times 20 \times 200)$ nm³ in $(X \times Y \times Z)$ and with a pixel dwell time of 0.05 ms. All deviations from the above stated imaging conditions will be stated explicitly in the corresponding figure captions. Three-dimensional images of labeled VM were rendered using the software AMIRA 6.0 (see section 2.6.1) and are always presented such that the side of the VM with which they attach to the cover slip (i.e. the basement membrane) is seen at the bottom of the image and the apical membrane is seen at the top.

Fig. 3.16 displays whole-cell 3D renders obtained from 2P-Exc microscopy imaging of a living VM labeled with Chol-OG488. A volume of $(20 \times 20 \times 15)$ µm³ along $(X \times Y \times Z)$ was scanned within $\approx$ 6 min using the above mentioned imaging parameters; image acquisition had no detrimental effects on the cell fitness which was assessed based on the bright field images of the respective cell before and after the 2P-Exc scan. As can be seen in Fig. 3.16 **A**, using Chol-OG488 enables thorough staining of both the cellular surface sarcolemma and the complete Transverse-Axial Tubular System (TATS). Transversely and longitudinally oriented tubules of the TATS and the junctions between them can be identified. This characteristic rectangular network of the TATS is shown in more detail in Fig. 3.16 **B**, which displays a top view of a lateral cross section of

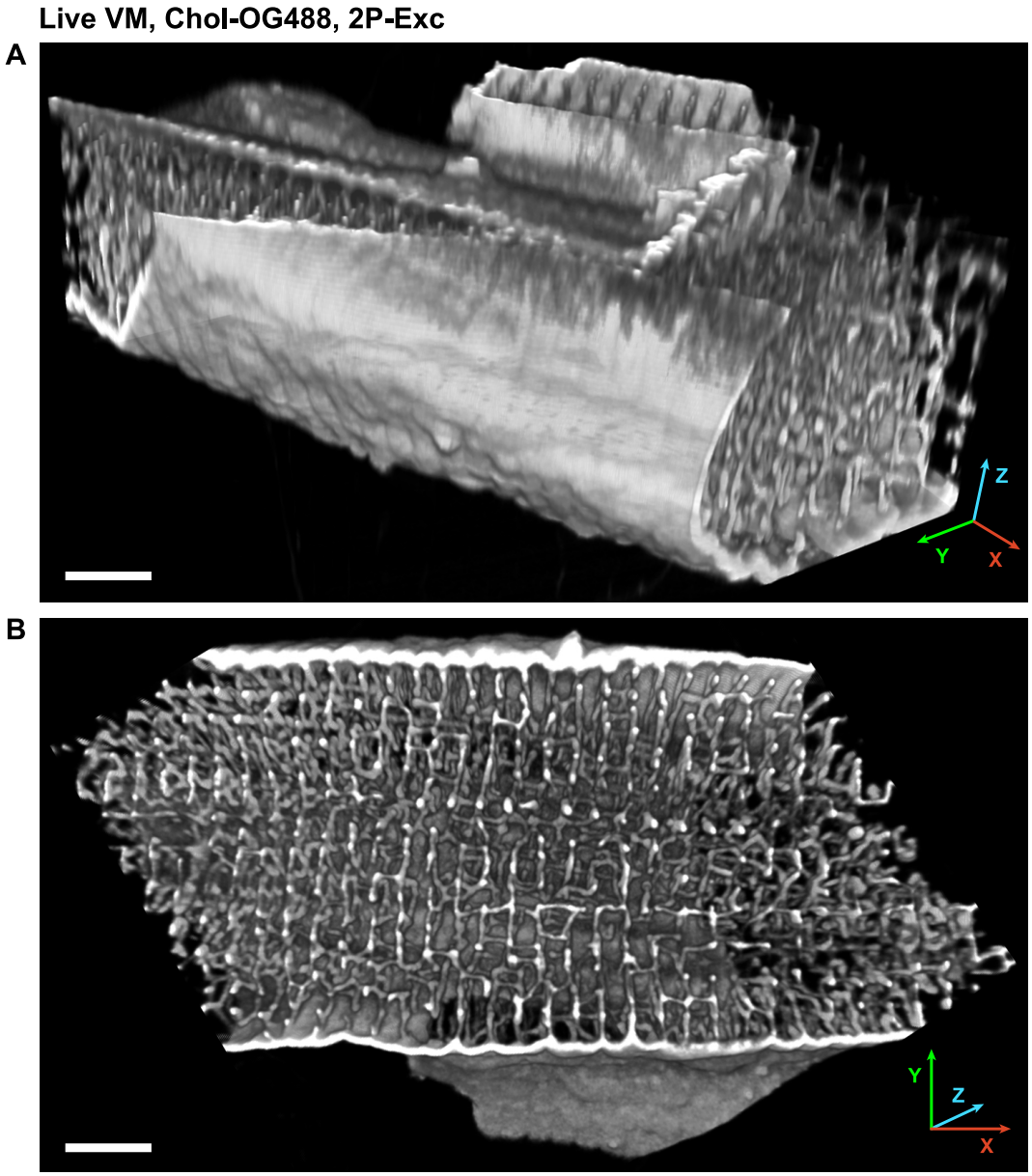

Figure 3.16.: Three-dimensional (3D) two-photon excitation (2P-Exc) image renders of a living mouse ventricular cardiomyocyte (VM) labeled with Chol-OG488. VM were stained as described in section 2.3.2, imaging was performed as described in this section, and 3D image renders were obtained as described in section 2.6.1. **A** 3D render of a VM section with the dimensions of $(20 \times 20 \times 15)$ µm³ with the basement membrane seen in the lower part of the image and the apical membrane seen in the top part. **B** Rotated view of the same cell in top view from the basement membrane (which was cut off in the render for visual assessment of the cell interior). The inserted coordinated systems indicate the longitudinal (X) and the transverse (Y) cell axes (also defining the imaging plane parallel to the cover slip), and the Z axis corresponding to the optical axis. Scale bars: 5 µm.

the same cell as in Fig. 3.16 **A**. The Transverse Tubule (TT) structures are regularly spaced at a distance of about 2 µm; transversely oriented TT are much more frequently observed that longitudinally oriented TT.

The whole-cell 3D renders that are presented in Fig. 3.16 and 3.17 visualize

the complex structure of the TATS in living VM and reveal that the extracellular leaflet of the TATS membrane is rich in Chol. The 3D TATS structure in living ventricular cardiomyocytes (from rat) had first been shown in a pioneering study by *Soeller and Cannell* in 1999 [21] who had used fluorescein-linked dextran as a solution stain for 2P-Exc microscopy. This study showed the cell-wide network of membrane invaginations in intact cardiomyocytes, a ramified arrangement of both transverse and longitudinal tubules as can also be seen here in Fig. 3.16 and 3.17. *Soeller and Cannell* showed that the surface openings where the TT join the cellular surface sarcolemma (the so-called "ostia") are arranged in a rectangular grid-like fashion across the cardiomyocyte surface sarcolemma. This arrangement of the ostia was reproduced in a similar follow-up study by *Savio-Galimberti et al.* in 2008 [532] who used fluorescein-linked dextran and a fluorescent Wheat-Germ Agglutinin (WGA) conjugate for 3D confocal fluorescence microscopy.

Here, using the fluorescent Chol analog Chol-OG488, I find that the ostia correspond to Chol rich patches at the surface sarcolemma. The budding of these Chol rich sarcolemmal patches into TT is shown in more detail in Fig. 3.17 wherein VM cross sections are displayed. In Fig. 3.17 **C**, two exemplary TT that each bud from a Chol rich assembly at the surface sarcolemma are marked by pink arrows. Very interestingly, when looking closely at the 3D image renders of Chol-OG488 labeled VM, another peculiarity becomes apparent - not every Chol rich patch at the surface sarcolemma buds into a TT. Examining the intracellular side of the surface sarcolemma, little "bumps" can be observed. These bumps are only small membrane invaginations that vary in diameter and elongation, extend not more than a few hundred nanometers into the cell, and are distributed irregularly. Note also that longitudinally oriented TT structures are observed only at positions at least 2 µm (i.e. at least one sarcomere length) away from the surface sarcolemma. This indicates that longitudinally oriented TT typically develop from the rectangular branching of transversely oriented TT and are not formed directly at the surface sarcolemma. The pink arrow head in Fig. 3.17 **C** marks such an event of several transversely oriented TT branching out; the branches then fuse to form an elongated longitudinally oriented TT. Another characteristic of the TATS is the bifurcation of transversely oriented TT into two branches that then continue to extend along the same di-

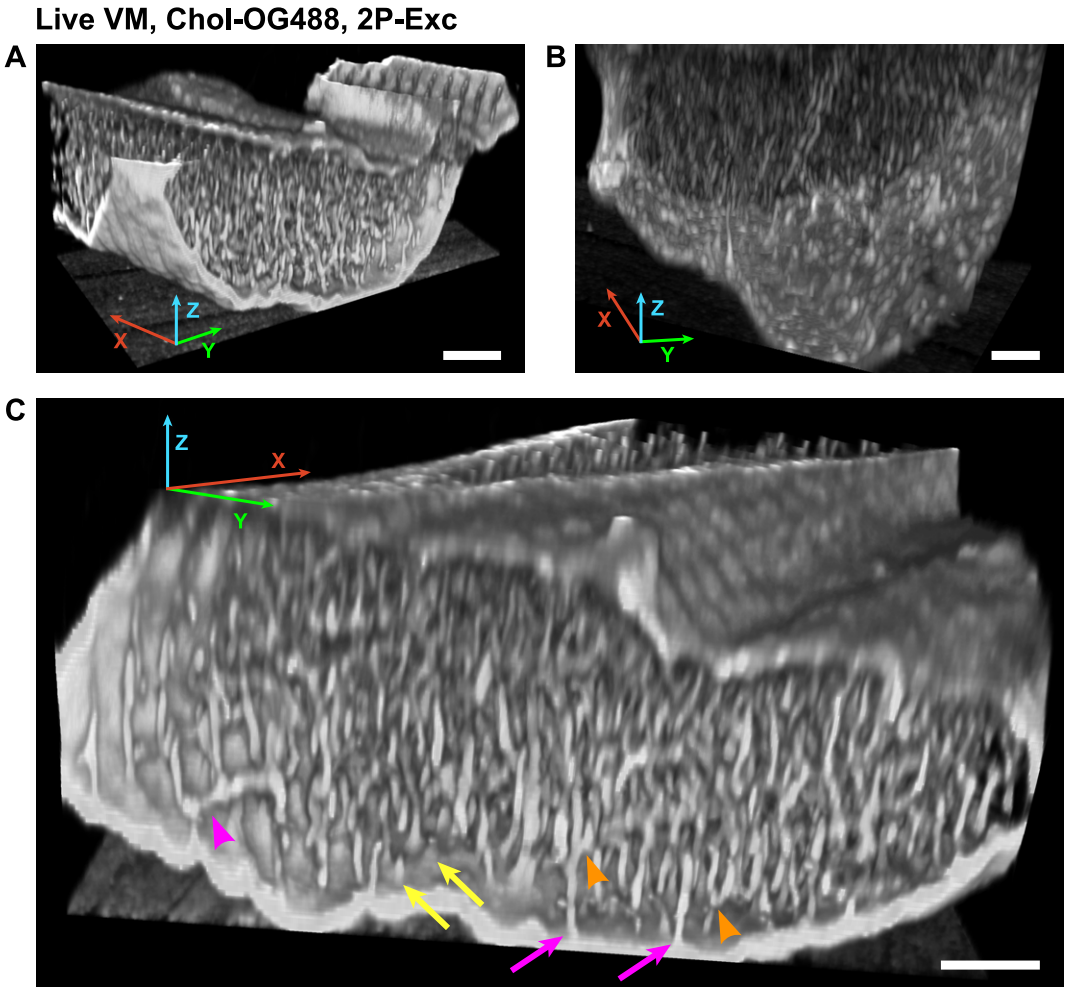

Figure 3.17.: Three-dimensional (3D) Two-Photon-Excitation (2P-Exc) image renders of a living mouse ventricular cardiomyocyte (VM) labeled with Chol-OG488. VM were stained as described in section 2.3.2, imaging was performed as described in this section, and 3D image renders were obtained as described in section 2.6.1. The basement membrane of the VM is seen in the lower part and the apical membrane is seen in the top part of the respective images. The inserted coordinate systems indicate the longitudinal (X) and the transverse (Y) cell axes (also defining the imaging plane parallel to the cover slip), and the Z axis corresponding to the optical axis. Scale bars: 5 µm. **A** 3D render of a VM section displayed in solid mode. **B** 3D render of the same VM as in **A** with adjusted signal transparency to allow for better visibility of membrane structures inside the VM. **C** Rotated view of the same cell in top view from the basement membrane (which was cut off in the render for visual assessment of the cell interior). T-Tubules (TT, pink arrows) and smaller membrane invaginations (yellow arrows) bud from Chol rich patches at the sarcolemma. Branching of TT into longitudinally oriented tubules (pink arrow head) and bifurcation of TT (orange arrow heads) is observed only inside the VM at least 2 µm away from the sarcolemma.

rection as the initial TT (marked by the orange arrow heads in Fig. 3.17 **C**). Similarly to the branching of TT to form longitudinal structures, such a bifurcation of TT was only observed at distances at least about 2 µm away from the surface sarcolemma.

In summary, using Chol-OG488 in a 2P-Exc imaging configuration is excellently suited to highlight the architecture of the TATS throughout whole living VM. The TT network and its distinct topological features, i.e. bifurcation of

TT and branching of TT to form longitudinal TT structures, can thus be well visualized and studied.

However, to investigate the above mentioned sarcolemmal "bumps" which are shallow sarcolemmal membrane invaginations and which bud from Chol rich patches along the sarcolemma but never develop into TT, it was necessary to look at the membrane architecture in the vicinity of the basal sarcolemma with a much higher resolution. This is because the two questions that come to mind first are: 1.) Which structural factor decides whether a Chol rich sarcolemmal patch buds into a full TT or remains a more shallow membrane invagination? and: 2.) What is the composition of these shallow membrane invaginations? To shed light on these questions, I recorded 2P-Exc-CWSTED images of living VM labeled with Chol-OG488, thereby focusing on the region starting from the basal sarcolemma (i.e. where Chol rich patches were observed) and extending about 4 µm deep into the cell (i.e. where a clear distinction between TT and shallow membrane invaginations could be made).

As a first control experiment to demonstrate the ability of 2P-Exc-CWSTED to resolve the subdiffractional features of the membrane architecture in Chol-OG488 labeled living VM, I recorded image stacks in 2P-Exc-CWSTED mode, assessed the effect of the imaging procedure on the cell fitness, and determined the achievable structure resolution. The intrinsic property of fast diffusion of the dye compound Chol-OG488 together with the intrinsic property of 2P-Exc of reduced photobleaching in out-of-focus layers within the scanned sample proved to be a very favorable combination enabling the fast acquisition of high quality 3D 2P-Exc-CWSTED scans.

Regarding cell viability in the 2P-Exc-CWSTED imaging scheme, it was possible to consecutively scan a cellular volume of about (20 $\times$ 20 $\times$ 5) µm^3 in (X $\times$ Y $\times$ Z) direction with a corresponding pixel size of (20 $\times$ 20 $\times$ 200) nm^3, a pixel dwell time of 0.02 ms, and employing a 2P-Exc and STED illumination power of 10 mW and of 50 - 100 mW, respectively (these settings were identified to yield optimized images with respect to resolution, signal to noise ration and signal bleaching). 2P-Exc-CWSTED scans with longer duration of acquisition and/or higher illumination powers (of either the 2P-Exc laser or the STED laser) would lead to a fast deterioration of cell fitness. This deterioration would typically manifest itself in a bulging of the cell very locally around

the scanned region. Heat generation due to laser light absorption within the cell might be the main explanation for this observed detrimental effect during prolonged scanning of the same region of interest within the cell. Yet, when imaging the cells using the above stated parameters, no adverse effects on the cell fitness were observed when monitoring the cells in widefield images after 2P-Exc-CWSTED scanning.

Regarding the achievable lateral image resolution in 2P-Exc-CWSTED images of Chol-OG488 labeled living VM, the upper limit of the possible lateral resolution of elongated membrane structures (i.e. longitudinal cross sections of TT) could be determined to be about 65 nm. For circular membrane structures (i.e. transverse cross sections of TT), this upper limit of achievable lateral resolution was found to be about 83 nm. The individual frames of an exemplary image stack of a living VM labeled with Chol-OG488 and the therefrom obtained respective structure resolutions are shown in Fig. 3.18. Therein, the VM was scanned over an axial region extending from 2.0 µm to 0.4 µm below the sarcolemma.

The achievable lateral resolution of individual elongated and circular membrane structures was determined by fitting a Lorentzian peak function to extracted signal intensity profiles as described in section 2.6.2. Ensuingly, the Z-stacks of labeled VM obtained from scanning lateral image frames at different depths within the cell as shown in Fig. 3.18 were processed with the software AMIRA 6.0 (see section 2.6.1) and yielded high-detail 3D image renders that capture the subsarcolemmal architecture of the TATS in living VM with sub-diffraction resolution. Fig. 3.19 shows such 3D renders of 2P-Exc-CWSTED images of a single VM seen from two perspectives: first, in a top view looking from the basement sarcolemma (i.e. at the cover slip) into the inside of the cell (displayed in Fig. 3.19 **A**) and second, in a top view looking from the inside of the cell towards the basement sarcolemma (displayed in Fig. 3.19 **B**). Both Fig. 3.18 **A** and **B** feature magnifications of selected regions in the corresponding overview 3D renders. In these magnifications, pink arrows indicated Chol rich patches at the sarcolemma that bud into TT while yellow arrrows mark those Chol rich sarcolemmal patches that remain such shallow membrane invaginations which had been observed in the 2P-Exc 3D renders and which were demonstrated in Fig. 3.17 **C**). The fact that the Chol rich sarcolemmal patches

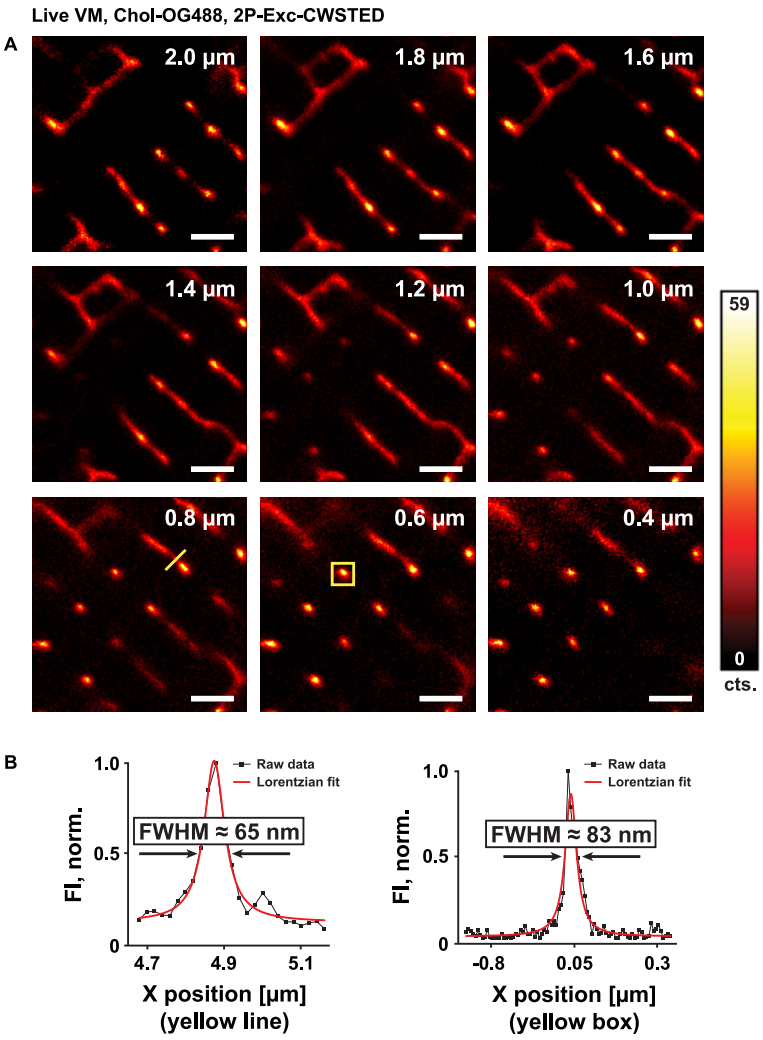

Figure 3.18.: Two-Photon-Excitation-CW-STED (2P-Exc-CWSTED) images of a living mouse ventricular cardiomyocyte (VM) stained with Cholesterol-PEG-OregonGreen488 (Chol-OG488). VM were stained as described in section 2.3.2 and imaged at different depths within the cell. **A** 2P-Exc-CWSTED depth scan through a living VM. The imaging depth is indicated in the image frames, refers to µm beneath the sarcolemma and ranges from 0.4 µm to 2.0 µm beneath the sarcolemma. Images were smoothed using a two-dimensional Gaussian filter with a width of 1.5 pixels. The color bar indicates the image brightness in photon counts (cts.). Scale bars: 1 µm. **B** Normalized fluorescence intensity profiles (FI, norm.) that were obtained from the yellow line (for the left graph) and yellow box (for the right graph, obtained from the addup of fluorescence signal along the Y-direction) indicated in the respective image frames (of the raw data) and marking transverse tubular cross sections. The resolution of transverse tubule structures is denoted as the full width at half maximum (FWHM) extracted from fitting the intensity data to a Lorentzian curve (see also section 2.6.2). The resolution was determined using the raw data images that are explicitly displayed in the Appendix H.1, Fig. H.1.

are either associated with TT or with regions of membrane curvature that protrude far less deeply into the inside of the VM is illustrated once more in Fig. 3.20. Therein, a 3D 2P-Exc-CWSTED image render of a Chol-OG488 labeled VM is displayed and, on one side, orthogonally sliced which results in a 2D cross section of the cell (indicated by the dashed blue box in Fig. 3.20). Again, pink arrows exemplarily mark Chol rich sarcolemmal regions that develop into

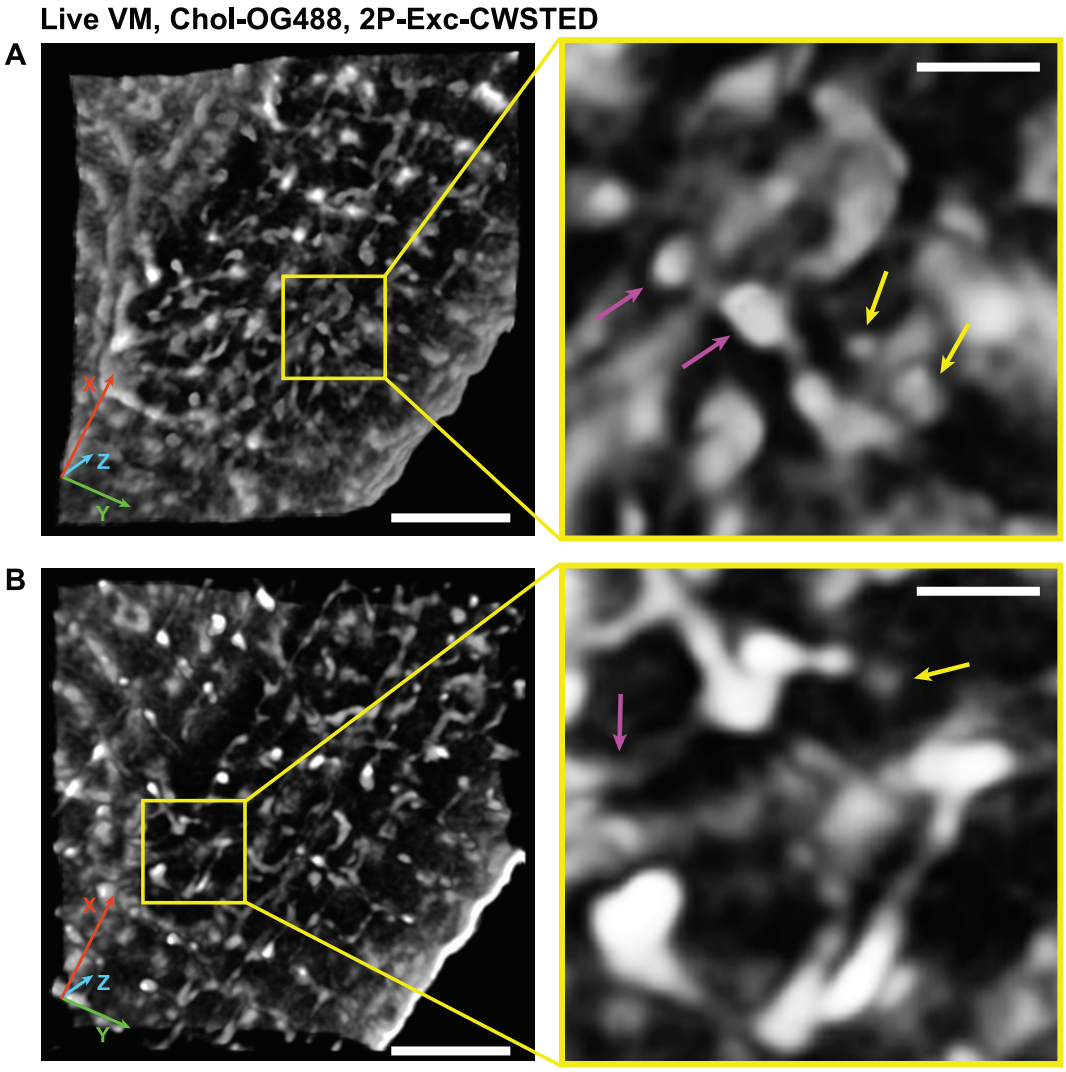

Figure 3.19.: Three-dimensional (3D) Two-Photon-Excitation-CW-STED (2P-Exc-CWSTED) image renders of living mouse ventricular cardiomyocytes (VM) labeled with Chol-OG488. VM were stained as described in section 2.3.2, imaging was performed as described in this section, and 3D image renders were obtained as described in section 2.6.1. The inserted coordinate systems indicate the longitudinal (X) and the transverse (Y) cell axes (also defining the imaging plane parallel to the cover slip), and the Z axis corresponding to the optical axis. **A** Top view into VM, looking from the basement sarcolemma into the inside of the cell. Magnification corresponding to the yellow boxed region with pink arrows indicating Chol rich sarcolemmal patches that bud into transverse tubules and yellow arrows indicating Chol rich sarcolemmal patches that are associated with shallow membrane invaginations at the sarcolemma. **B** Top view out of the same VM as in **A**, looking from inside the cell out towards the sarcolemma. Magnification corresponding to the yellow boxed region with the pink arrow indicating a Chol rich sarcolemmal patch that buds into a transverse tubule and the yellow arrow indicating Chol rich sarcolemmal patches that are associated with shallow membrane invaginations at the sarcolemma. Scale bars in overview 3D renders: 5 µm; scale bars in magnifications: 1 µm.

TT while yellow arrows mark shallow Chol rich membrane invaginations. All in all, the 3D renders of Chol structures in living VM revealed that there are two populations of Chol rich patches at the sarcolemma: one that is TT associated and one that is not. More stringently, it can be stated that every TT buds

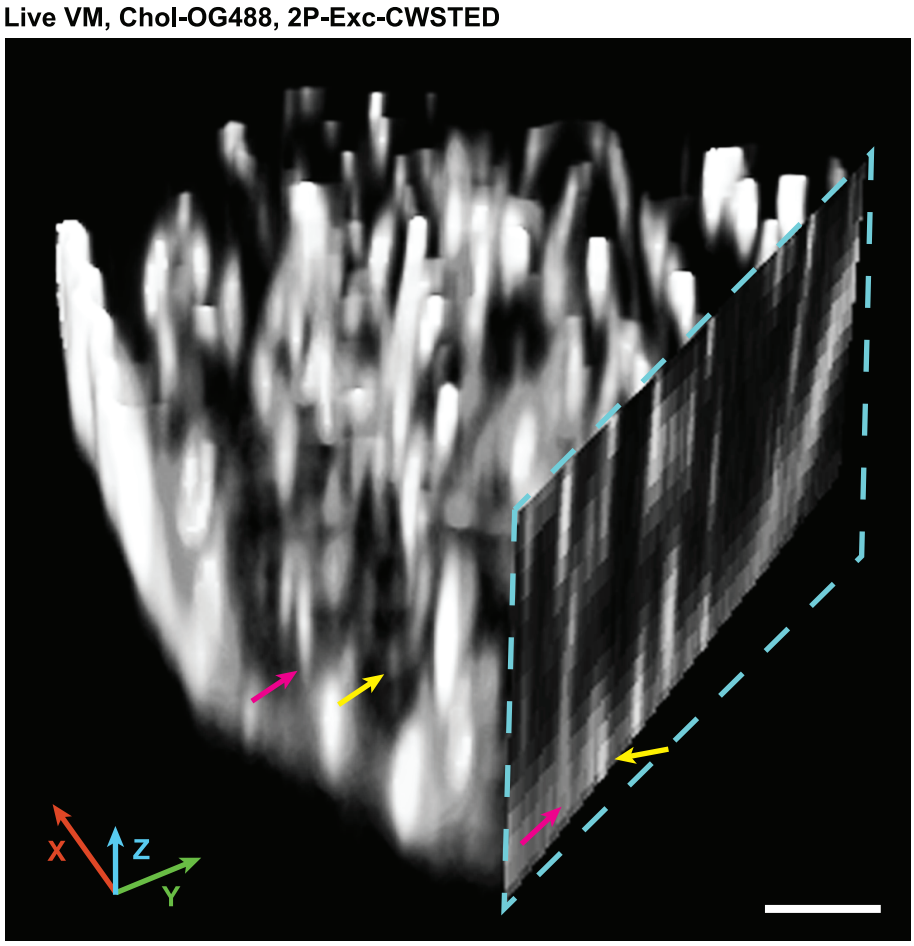

Figure 3.20.: Three-dimensional (3D) Two-Photon-Excitation-CW-STED (2P-Exc-CWSTED) image renders of a living mouse ventricular cardiomyocyte (VM) labeled with Chol-OG488 (see section 2.3.2). Imaging was performed as described in this section and 3D image renders were obtained as described in section 2.6.1. The inserted coordinate systems indicate the longitudinal (X) and the transverse (Y) cell axes (also defining the imaging plane parallel to the cover slip), and the Z axis corresponding to the optical axis. The image shows a tilted 3D render of the VM. The dashed blue box indicates an orthogonal slice along the Y-Z-plane. In both the 3D render and the planar slice, some Cholesterol rich sarcolemmal domains bud into Transverse Tubules (TT, indicated by pink arrows) and some domains develop into less deeply penetrating membrane invaginations (indicated by yellow arrows). The image was oversaturated in brightness to facilitate the identification of the different Chol signal patterns indicated by the respectively colored arrows. Scale bar: 5 µm.

from a Chol rich sarcolemmal patch but not every Chol rich sarcolemmal patch develops into a TT. Trying to find a general structural principle that decides whether a Chol rich patch at the sarcolemma turns into a TT or not, I looked at the size distribution of Chol patches and the shape distribution of Chol patches and compared the obtained distributions between TT associated Chol patches and not TT associated Chol patches. To categorize the patches into TT associated and not TT associated, I tracked the continuity of the fluorescence signal of the Chol patches over several consecutive lateral 2P-Exc-CWSTED image frames within an axial range starting right at the sarcolemma of a respective

VM and ending about 4 µm deep within the cell. If a Chol signal was clearly traceable over a range of more than 2 µm, it was considered TT associated. If a Chol signal was lost after about 500 nm within the cell, it was considered not TT associated. If a signal could not be clearly classified regarding its continuity, the corresponding sarcolemmal Chol rich patch was not considered for analysis. Note that I initially planned to also evaluate the spacing between Chol rich sarcolemmal patches to investigate whether the distance between patches had an influence on the extent of Chol associated membrane invaginations. Yet, since not every signal of Chol rich patches could definitely be classified as TT associated or not, such an analysis of the distance between patches was not feasible because a significant portion of the sarcolemmal Chol signal had to be excluded from the analysis. The remaining, categorized sarcolemmal Chol rich patches were evaluated regarding their size and shape after a binarization step of the 2P-Exc-CWSTED images obtained in the sarcolemmal plane (i.e. single 2D image frames). Image thresholding for binarization was performed in a procedure analogous to the one described in section 2.6.4. The binarized images were evaluated using the software FiJi. The built-in "Analyze Particles" plugin was used which allowed the distinct numbering of particles in the binarized image so that the previously classified Chol rich patches (i.e. TT associated or not) could be identified, addressed, and characterized individually regarding their shape and size by comparing the enumerated particles in the binarized image with the original raw data images and the therein categorized Chol rich patches. The shape of Chol rich sarcolemmal patches was analyzed by determination of the circularity of individual patches: a circularity of 1 would indicate a completely circular object while a circularity of 0 would indicate a line. The circularity *Circ* is defined as $Circ = 4\pi \times [Area] \,/\, [Perimeter]^2$. The size of the Chol rich sarcolemmal patches was analyzed by determination of the area of the individually identified patches.

The determined Chol patch shape and size, respectively showed a very high variation. This variation was observable for both TT associated Chol rich sarcolemmal patches and for Chol patches associated to shallow membrane invaginations. The difference between the distributions of patch shape and patch size was not significant when comparing the two populations of Chol rich sarcolemmal patches.

The patch circularity ranged predominantly between about 0.2 and close to 1.0 meaning that most patches were either of elliptical or circular shape. The area size of the patches ranged between about 1800 nm² up to about 150,000 nm² which corresponds to object diameters of about 50 nm up to about 440 nm, respectively, when assuming a roughly circular object shape. The circular patches could mostly be identified as those patches which were close to the smallest object size that was resolvable by the 2P-Exc-CWSTED microscope system, i.e. about 50 nm in diameter. The most often observed patch area size for both TT as well as shallow invagination associated Chol patches was at about 4500 nm², corresponding to a roughly circular object of about 75 nm in diameter. All in all, while a typical patch size could be identified, neither a typical patch circularity (i.e. patch shape) nor a characteristic difference between those Chol patches that bud into TT and those Chol patches that do not was found. Thus, a clear distinction between Chol rich sarcolemmal patches that were associated to TT and Chol patches that were associated to shallow invaginations could not be made based on the obtained distributions of patch shape and patch size, respectively. The obtained results for the distribution of the area sizes of Chol rich sarcolemmal patches are presented in the Appendix H.2. There, a bar graph plots displays the area sizes determined for TT associated patches vs. patches associated to shallow membrane invaginations.
The high variation in shape and size of the sarcolemmal Chol signal is demonstrated in Fig. 3.21 for two individual VM that were labeled with Chol-OG488 and imaged in 2P-Exc-CWSTED mode in the plane of the basement sarcolemma. In both Fig. 3.21 **A** and **B**, pink arrows exemplarily indicated Chol rich sarcolemmal patches that are TT associated while yellow arrows mark Chol rich sarcolemmal patches that are not TT associated. As can be seen from Fig. 3.21 **A** and **B**, the Chol rich sarcolemmal patches present themselves with a highly variant distribution in patch shape and patch size. Both circular and elongated patches, as well as patches with a small area size (about 1800 nm², i.e. corresponding to a diameter of about 50 nm when assuming a roughly circular object shape) and patches extending over larger areas (up to about 150,000 nm², i.e. corresponding to a diameter of about 440 nm when assuming a roughly circular object shape) can either bud into TT or remain associated to shallow membrane invaginations, respectively. It is hence not readily predictable from

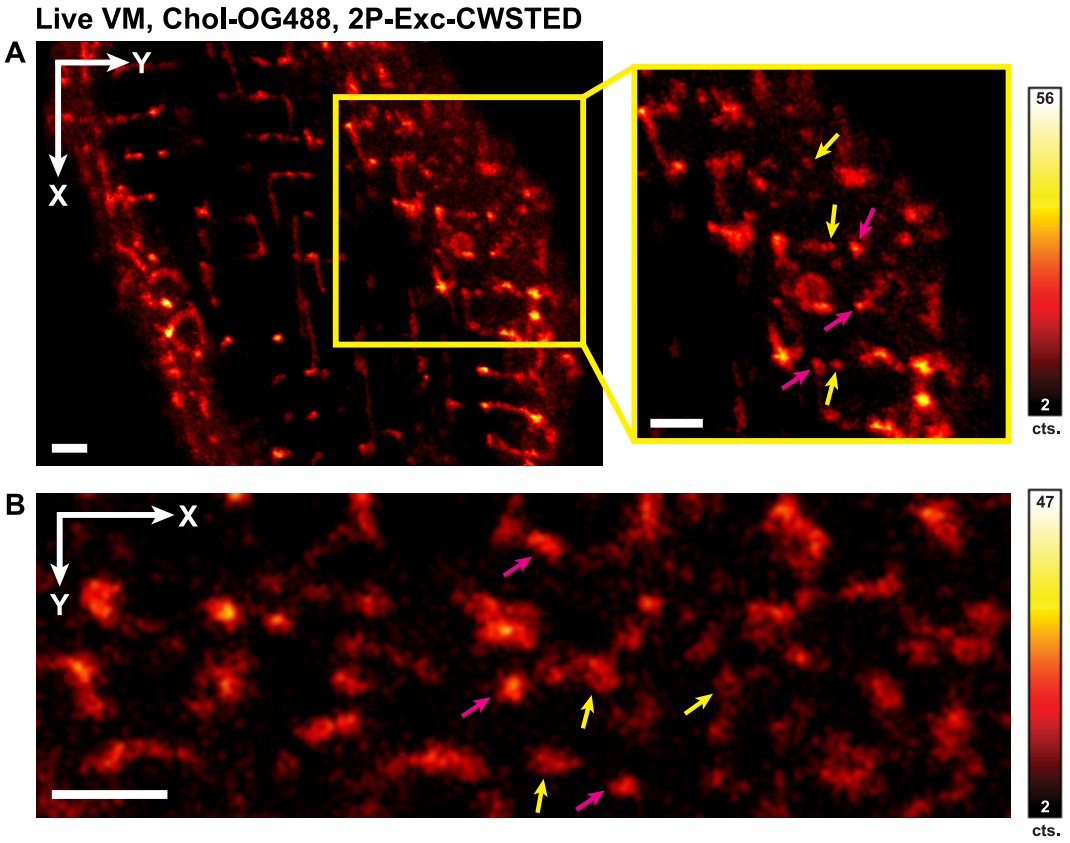

Figure 3.21.: Highly clustered nanoscopic sarcolemmal Cholesterol (Chol) structures visualized by Two-Photon-Excitation-CW-STED (2P-Exc-CWSTED) imaging of a living mouse ventricular cardiomyocyte (VM) labeled with Cholesterol-PEG-OregonGreen488 (Chol-OG488). VM were stained as described in section 2.3.2, images were taken at the sarcolemma. White arrows indicate the longitudinal (X) and transverse (Y) cell axes, respectively. Images were smoothed using a two-dimensional Gaussian filter with a width of 1.5 pixels. **A** Overview image of sarcolemmal Chol-OG488 signal in a living VM; image magnification corresponding to the yellow boxed region. **B** Sarcolemmal Chol-OG488 signal in a living VM. In both **A** and **B** pink arrows indicated Chol rich sarcolemmal patches that bud into transverse tubules while yellow arrows indicate Chol rich sarcolemmal patches that are associated to shallow membrane invaginations at the sarcolemma. The color bars indicate the image brightness in each **A** and **B** in photon counts (cts.). Scale bars: 1 µm.

the heterogeneous appearance where TT mouth into/from the sarcolemma and where shallow membrane invaginations are located. This confirms the findings of the analysis of the shape and size distribution of Chol rich sarcolemmal patches. Thus, no general principle could be derived that would allow an inference from the determination of the shape or size of a Chol patch to whether it is TT associated or not. However, when looking at the ensemble of all Chol rich sarcolemmal patches, reoccurring patterns could be observed. The distinct arrangement of Chol rich sarcolemmal clusters is a mosaic composed of three basic structural elements:

1.) Small single Chol domains,

2.) Ring structures formed by these single domains,

3.) Bunchy clusters of various sizes also featuring a substructure of single domains.

These three here-defined "membrane motifs" will be elucidated and discussed in detail in the next section.
Concluding, using 2P-Exc-CWSTED microscopy to image living VM labeled with the novel fluorescent Chol analog Chol-OG488, the 3D architecture of the Chol rich cardiac membrane system with a lateral resolution of about 65 nm and an axial resolution of about 450 nm could be visualized. This allowed the visualization of the complex transverse-axial tubular system (TATS) inside the living VM in relation to a distinct arrangement of Chol rich patches at the sarcolemma (a signal pattern that had been shown before using Chol-KK114, see section 3.3). Further, it could be shown that TT emerge from/into sarcolemmal membrane regions that are highly enriched in Chol. Chol provides for membrane stiffness and induces membrane curvature [137, 120]. Specifically, Chol, with its large hydrophobic tail in proportion to its small hydrophilic head group, has a high intrinsic negative curvature [95, 138, 118, 139]. Hence, enrichment of Chol at the membrane is typically indicative of concave (i.e. inwardly curved) membrane regions.
The Chol enrichment of sarcolemmal regions that bud into TT was thus to be expected. Interestingly, however, the Chol rich patches at the sarcolemma of VM could actually be categorized into two distinct populations. One portion of Chol rich patches buds into transverse tubules (TT) which eventually branch out and/or fuse together to form TATS - the most characteristic and integral membrane architecture of VM. The other portion of Chol rich patches at the sarcolemma does not add to the TATS but forms shallow membrane invaginations that do not protrude further than about 500 nm into the inside of the VM - they probably protrude much less than 500 nm into the inside given the axial resolution limit of $\approx$ 450 nm of the microscope. A general principle regarding the size or shape of the individual sarcolemmal Chol patches from which it could be predicted whether they form either TT or shallow invaginations could not be derived unequivocally. There might be a tendency that the sarcolemmal

Chol clusters need a certain minimal size to develop into TT. However, spatially very extended Chol patches that did not form TT but remained rather flat along the sarcolemma were also observed.
Two additional facts about the distinct sarcolemmal pattern of Chol rich patches were revealed by successively scanning multiple frames of the same region of interest along the sarcolemma:

1.) Globally, the Chol rich structures seem to be anchored within the membrane and the Chol signal pattern is temporally stable and conserved;

2.) Locally, there are dynamic fluctuations of influx and efflux of Chol signal around these invariant Chol rich structures.

Note that the image acquisition procedure can be defined as "quasi-dynamical" given the pixel dwell time of at least 0.02 ms that is necessary for sufficient signal brightness. Hence, scanning was possible with a frame rate on the order of tens of seconds.
It can hence be stated that there are local dynamics of Chol around fixed sarcolemmal Chol rich structures. This might indicate a transient recruitment and release of Chol by these spatially highly localized and temporally stable Chol rich membrane compartments. These specific Chol signal dynamics were observed for both those Chol rich sarcolemmal patches that bud into TT as well as for those Chol rich patches that remain more shallow membrane invaginations.
So, what are these Chol rich shallow membrane invaginations? It has been proposed that a large curvature in a membrane bilayer requires a higher concentration of lipids with a negative intrinsic curvature (like Chol) in the extracellular vs. the intracellular membrane leaflet [533]. This difference in concentration would probably have to be a protein-mediated process. The most likely membrane compartments that could match the Chol rich shallow membrane invaginations would be caveolae. Caveolae are omega-shaped pits at the cellular membrane. They are about 70 nm in size at their neck regions and can fuse together, thus summarizing sophisticated, branched membrane structures [140]. Caveolae are highly enriched in the protein family of the Caveolins that line the caveolae along their cytosolic side. The myocyte-specific isoform of the caveolins is the protein Caveolin-3 (Cav-3) which is also the most strongly expressed Caveolin in these cell types. Cav-3 features an intermembrane do-

main, resides at the intracellular membrane leaflet and presents distinct Chol binding sites. For a more detailed description of Cav-3, its properties, and its relation to Chol, please refer to section 1.1.2.
The most obvious next step would thus be the investigation of the possible association between the observed sarcolemmal Chol structures and the myocyte caveolae forming protein Cav-3. For this purpose, the ideal specimen would be living primary cardiomyocytes from a genetically engineered mouse model in which the Cav-3 is co-expressed together with a fluorescent protein. Unfortunately, such a mouse model was not readily available within the scope of this thesis. Visualizing the nanoscopic sarcolemmal arrangement of Cav-3 using STED microscopy was thus only possible in fixed VM that were stained for Cav-3 via indirect immunofluorescence. The fluorescent Chol analogs, however, were not compatible with immunofluorescence protocols since the therein used necessary membrane permeabilization step led to the internalization of the Chol labels. This resulted in an unspecific fluorescence signal throughout the whole cell. In the following, I therefore indirectly validated the structural association of Chol clusters with caveolae. My studies included carefully designed control experiments based on both established and novel control systems. I quantitatively characterized the sarcolemmal Chol signal in living VM and compared it to the sarcolemmal Cav-3 signal in fixed VM that were labeled via immunofluorescence. I could observe a distinct nanoscopic signal pattern for both Chol and Cav-3. This signal pattern was also found in Ventricular induced Pluripotent Stem Cells (ViPSC) and in Human Adipocytes (HAd, derived from heart tissue). Further, the artificial expression of Cav-3 in transfected living HeLa cells led to the formation of the above mentioned signal patterns of both Chol and Cav-3. Such signal patterns were not seen in the corresponding control cells. The dependence of Chol clusters and nanopatterns on the expression of Cav-3 was thus confirmed. On the other hand, Chol depletion of VM led to the dissociation of Cav-3 clusters and to the loss of sarcolemmal nanopatterns. Finally, the two-color STED imaging of Chol structures together with the extracellular leaflet associated glycosphingolipid Ganglioside GM1 (GM1) in living VM showed significant co-clustering on a nanometric scale. Two-color STED images of Cav-3 and GM1 in fixed VM showed similar arrangements. These images are presented in the following.

3.5. Association of Caveolin-3 and Cholesterol membrane domains at the sarcolemma of living cardiomyocytes

In a first step to study the association of sarcolemmal Chol structures with sarcolemmal caveolae, and vice versa, STED images of the sarcolemma of living VM labeled with Chol-K114 and of fixed VM labeled for Cav-3 via indirect immunofluorescence were acquired, respectively. Since the focus was laid on STED imaging of the basement sarcolemma, i.e. of the outer membrane close to the cover slip, the investigated samples could be simplified to being quasi two-dimensional. Hence, instead of using 2P-Exc-CWSTED, I decided to conduct the experiments using one-photon-excitation (pulsed) STED microscopy with excitation and depletion lasers in the red spectral region. I prepared the samples accordingly using Chol-KK114 to label Chol rich membrane structures in living VM, and using the antibody coupled dye Abberior STAR635P to visualize Cav-3 structures in fixed VM. Using such microscope and sample configurations had several major advantages. First, without the immediate necessity to acquire 3D images, photobleaching of out-of-focus imaging planes is a minor issue. In a one-photon-excitation configuration, the reduction of the lateral PSF size due to the shorter wavelength that is used and the highly reduced intensity that is needed for efficient fluorescence excitation thus outweigh the benefit of the quadratic dependence of the fluorophore excitation on the illumination intensity in a 2P-Exc configuration which essentially provides a pinhole in the sample plane. Second, using Chol-KK114 in a STED microscope configuration with synchronized pulsed excitation and pulsed STED lasers yielded images with the highest resolution. This was an empirical finding which might be attributable to the properties of Chol-KK114 and/or the nature of fluorophore off-switching by the pulsed STED laser which is more efficient than with a CW STED laser [348]. Therefore, the in the following presented and analyzed STED images were acquired using either the custom-built, fast scanning STED setup (see section 2.1.2), or the STED microscope system Leica TCS SP8 STED 3X (see section 2.1.3), or the STED microscope system Abberior 2C STED 775 QUAD Scan (see section 2.1.4).

The obtained STED images revealed that both the Chol and the Cav-3 signals

are highly clustered at the cardiac sarcolemma and that both the Chol and the Cav-3 clusters show a distinct nanopattern that can be categorized into three re-occurring membrane motifs: 1. single domains of an average diameter of about 70 nm, 2. ring structures of an average diameter of about 240 nm, and 3. bunchy clusters of variable sizes. Fig. 3.22 shows exemplary overview images and corresponding magnifications of the mentioned membrane motifs at the sarcolemma of living VM labeled with Chol-KK114 and of fixed VM labeled with the dye STAR635P via indirect immunofluorescence. The sarcolemmal

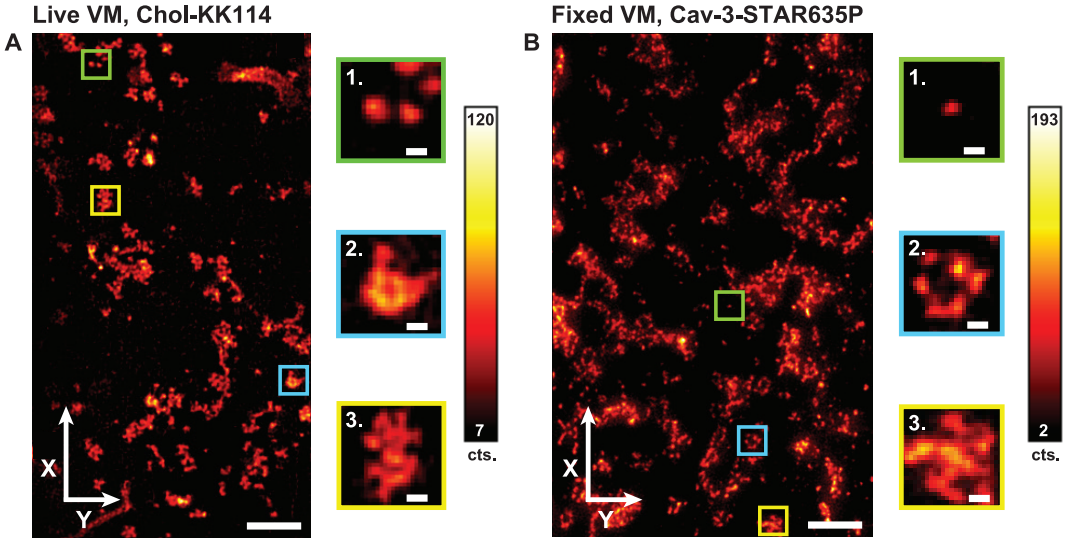

Figure 3.22.: STED images of **A** living mouse ventricular cardiomyocytes (VM) labeled for Cholesterol (Chol) with Chol-KK114, and **B** fixed VM labeled for Caveolin-3 (Cav-3) via indirect immunofluorescence using the antibody-coupled fluorescent dye Abberior STAR635P (see Appendix A.4). Demonstration of the similarity of the following three re-occurring sarcolemmal Cholesterol (Chol) and Caveolin-3 (Cav-3) pattern motifs in mouse ventricular cardiomyocytes (VM): 1. single domains, 2. ring structures, and 3. bunchy clusters. Following this enumeration, representative magnifications of exemplary motifs as indicated by the boxed regions in the overview images are displayed to the right of the corresponding images. Images were smoothed using a two-dimensional Gaussian filter with a width of 1.5 pixels. The color bars indicate the image brightness in each **A** and **B** in photon counts (cts.). White arrows indicate the longitudinal (X) and the transverse (Y) cell axes, respectively. Scale bars in the overview images: 1 µm; scale bars in the magnifications: 100 nm.

signal density ρ, the diameter of single domains, and the diameter of ring structures of the Chol and Cav-3 signal, respectively, were quantified as described in sections 2.6.4, 2.6.5, and 2.6.6; the obtained results are summarized in Fig. 3.23. The quantitative assessment of the sarcolemmal signal density ρ showed that about one sixth (16.93 %) of the sarcolemma of living VM is covered by the Chol rich clustered structures that could be detected using Chol-KK114 as a probe. Regarding the sarcolemmal signal density of the Cav-3 signal in fixed VM, almost one quarter (24.13 %) of the sarcolemma is covered by Cav-3 structures. The difference between the sarcolemmal signal densities of Chol and Cav-3 is

very significant. Assuming that Chol-KK114, due to its bulky PEG linker, is confined to the extracellular membrane leaflet (see section 3.1) and knowing that Cav-3 is an intermembrane protein that resides at the intracellular leaflet (see section 1.1.2), this discrepancy in ρ might indicate that the sarcolemmal membrane shows a very high density of the inwardly curved caveolar structures that create regions of highly negative curvature along the extracellular leaflet. In these regions, the resident endogenous membrane lipids might move closely together and thus might prevent the exogenous fluorescenent Chol-KK114 from inserting itself into the membrane. Chol-KK114 might thus not be able to detect the "bulbous" body of the flask-shaped caveolar structures. However, at the caveolar neck region, there should be two kinks in the extracellular membrane leaflet that stem from the inward bend. Here, the endogenous membrane lipids could be arranged further apart from each other, facilitating the insertion of Chol-KK114. Regarding the association between Chol and Cav-3 signal structures, Chol-KK114 might hence be a marker of the caveolar neck region which has a smaller cross section than the body of the caveolus. In essence, due to the still limited resolution in the obtained images and due to the finite size of the Chol-KK114 probe, the precise location of Chol with respect to an individual caveolus cannot be identified. Yet, this consideration of the effect of the membrane curvature caused by caveolae might be one possible reason for the lower Chol-KK114 signal density compared to that of Cav-3. On the intracellular side, the membrane curvature provided by the caveolae might lead to a more spread distribution of the polar headgroups of intracellular membrane lipids and and would thus allow more space for cytosolic intramembrane proteins, including more Cav-3 proteins, to assemble along the intracellular leaflet. Of course, it cannot be assumed that the Chol-KK114 and the Cav-3 signals would be associated in a 1:1 ratio since there are many other Cav-3-independent membrane structures that are rich in Chol. However, this would rather fuel the expectation that the observed Chol-KK114 signal density is significantly higher than the Cav-3 signal density.

With the sarcolemmal signal density a rather global figure for comparison, the Chol and Cav-3 signal structures are also very similar on a local scale. Both signal structures form a specific nanopattern comprising the following three basic motifs that shall be discussed in detail:

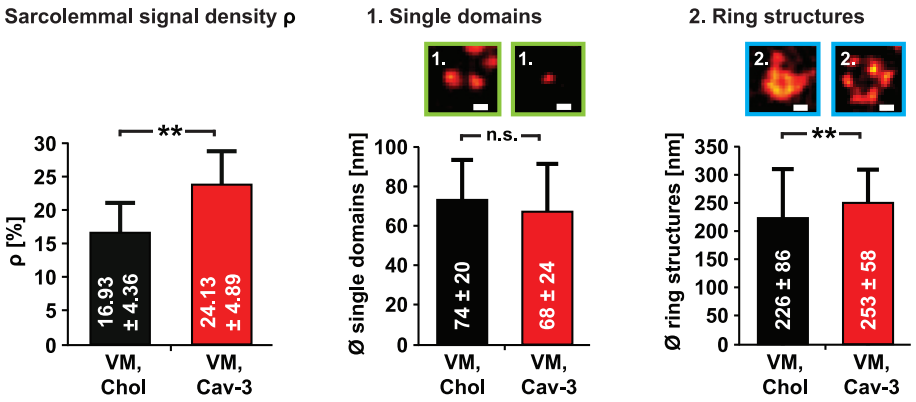

Figure 3.23.: Quantification of the signal density ρ, the diameter ($\varnothing$) of single domains, and the diameter of rings structures of Cholesterol (Chol) and Caveolin-3 (Cav-3) signals at the sarcolemma of living and fixed mouse ventricular cardiomyocytes (VM), respectively. ρ and the diameters of single domains and ring structures were determined as described in sections 2.6.4, 2.6.5, and 2.6.6. Values are presented as mean $\pm$ standard deviation. Statistical significance was tested using the two-sided Mann-Whitney-Wilcoxon U test as described in section 2.9 (the explicit parameters of the statistical test are presented in Appendix I, Tables I.3, I.4, and I.5) and is given as: (**) - very significant ($p < 0.001$), and (n.s.) - not significant ($p > 0.01$). Number of analyzed cells for determination of ρ: 55 (Chol), 44 (Cav-3). Number of analyzed single domains for diameter determination: 182 (Chol), 2397 (Cav-3). Number of analyzed ring structures for diameter determination: 404 (Chol), 80 (Cav-3). The image insets reproduce the respective magnifications presented in Fig. 3.22. Scale bars: 100 nm.

1. Single domains. As indicated in Fig. 3.22 (green boxes), both the Chol and Cav-3 signals feature separate, small circular signal entities along the sarcolemma. These entities shall here be referred to as "single domains" because they can be seen as the basic building blocks of all higher order structural assemblies observed for the Chol and Cav-3 signals. Quantification of the single domains - as described in section 2.6.5 and as shown in Fig. 3.23 - yielded an average diameter of about 74 nm (Chol) and 68 nm (Cav-3). The difference between the diameters of the Chol and the Cav-3 single domains was not significant. Since the obtained diameter sizes of both Chol and Cav-3 single domains is well above the resolution of 40 nm that was achievable with the used STED microscope, it can be assumed that the actual object forming such a single domain would have a diameter of roughly 50 to 60 nm (note that the size of the fluorescent label has to be considered and adds to the detected single domain size). Thus, the single domains observed here might be single caveolae because caveolae have been reported to be of similar sizes as those determined here and because, as we will see in the following, several caveolae tend to assemble to form more complex shapes [140]. To verify that the observed sarcolemmal Cav-3 single domains were not attributable to artifacts of antibody clustering [534], samples with a fragment antigen-binding (Fab) fragment instead of the

full length secondary antibody were prepared as a control (cf. [354]). The Fab fragment was also conjugated to the dye STAR635P and the immunolabeling protocol was conducted analogous to the one described in section 2.3.3. The images obtained from the use of the fluorescent Fab fragment are not shown here since they were of much lower signal brightness and thus less instructive. However, an image of fixed VM labeled for Cav-3 via a Fab-fragment coupled to STAR635P is shown in the Appendix J; the image shows Cav-3 single domains of about 65 nm in diameter and thus confirms that the here described single domains are not artifacts stemming from antibody clustering.

2. Ring structures A very peculiar membrane motif is the observed Chol and Cav-3 ring structures. These ring structures are typically formed by the assembly of between 4 to 8 single domains of Chol and Cav-3, respectively (data not shown). These rings are exemplarily shown in Fig. 3.22 and the quantification of their diameters is graphically displayed in Fig. 3.23. The average diameter of Chol and Cav-3 ring structures was assessed as described in section 2.6.6 and amounts to about 226 nm (Chol) and 253 nm (Cav-3). The difference between the diameters of the Chol and Cav-3 ring structures is very significant. A possible explanation for the larger diameter of the Cav-3 ring structures compared to the Chol-KK114 ring structures - in addition to the above discussed consideration that membrane labeling using Chol-KK114 might only have access to the caveolar neck regions - could be that the Cav-3 antibody construct is of a larger size than Chol-KK114 and thus increases the size of the detected structure. It has been shown that the antibody-dye constructs used in an immunofluorescence assay increases the detected size of a target protein by about 30 nm [535]. However, such a profound difference in size has not been seen for the diameters of single domains (see above) which might indicate that Chol-KK114 and the antibody-based label for Cav-3 do not drastically differ in size. Therefore, the actual difference in size of the two labels becomes more obvious for the assembly of many single domains in a ring than for an isolated single domain.

3. Bunchy Clusters The third membrane motif covers a rather broad range of possible assemblies of Chol and Cav-3 single domains into higher-order signal structures: bunchy clusters of various sizes. Such clusters are exemplarily

shown in Fig. 3.22. Although these bunchy clusters feature a high variety of shapes and sizes, they can clearly be identified as arrangements of individual single domains in close proximity which gives the clusters a distinct appearance that might best be described as botryoidal (i.e. "grape like"). The tendency of individual caveolae (i.e. the here defined "single domains") to fuse and form higher-order complexes of two or more single caveolae has been reported [175, 140] (see also section 1.1.2) which supports the assumption that the here observed bunchy clusters of Cav-3 and Chol structures are caveolar super-complexes. I could confirm that two or more single, omega-shaped, caveolae would fuse to form branched complexes using Electron Microscopy (EM). I prepared samples for EM of single VM, VM in a loose cell complex (cell pellet) and tissue sections from excised papillary muscle. In all of these samples, I could observe caveolae being in close proximity to each other and somtimes fusing to form higher-order complexes. I could find these fused assemblies most often in the prepared tissue sections, possibly because this kind of sample preparation provided the most physiological analogy to living cells. An exemplary overview of the obtained EM images is given in the Appendix K. It is interesting to note that the here proposed caveolar super-complexes are very frequently seen in the STED images - much more frequently than has been reported based on EM. The here observed super-complexes extend over very large interconnected regions across the sarcolemma. This observation holds true for both the Cav-3 clusters in fixed VM and for the Chol clusters in living VM. The high abundance of bunchy Chol clusters, i.e. possible caveolar super-complexes, in intact VM might indicate that these assemblies are a physiological characteristic of VM. As mentioned in section 1.1.2, one function of caveolae is most likely that they serve as reservoirs for membrane proteins, similar to storage rooms. Additionally, they could serve as reservoirs for cellular surface area and thus a cell's capability to stretch (reviewed e.g. in [188]). Especially cells like VM that undergo constant strain and stress due to contraction and relaxation need a high degree of elasticity which could be provided by a dynamically adjustable sarcolemmal surface area. Caveolae and the high Chol levels associated with them could likely serve the purpose to ensure the elasticity of VM.

Based on the above findings, the next question was whether the distinct membrane patterns of Chol and Cav-3 structures and their mutual association found for VM could also be observed in cell types with similar protein expression profiles and/or cell types that feature similar physiological demands. To address this question, I prepared samples of Ventricular induced Pluripotent Stem Cells (ViPSC) and Human Adipocytes (HAd, derived from adipose heart tissue) analogous to the ones of VM. I chose to look at ViPSC because they have a similar protein expression profile as VM and because they ought to perform similar physiological tasks, i.e. contraction (see also section 3.2). Additionally, I decided to look at HAd because, although these cells do not express Cav-3, HAd express very high amounts of the protein Caveolin-1 (Cav-1, [536, 537]) which was the first identified isoform of the Caveolin protein family and also forms caveolae. Further, HAd also need an elastic membrane since their function is to store triglycerides. Thus, to compare Chol and Caveolin nanoscopic signal structures at the basement membrane of the respective cell types, I prepared samples of living ViPSC and HAd labeled with 5 µM Chol-KK114 and samples of fixed ViPSC and HAd labeled for Cav-3 and Cav-1, respectively, via indirect immunofluorescence. All samples were imaged using the STED microscope system Leica TCS SP8 STED 3X (see section 2.1.3). The STED images are shown in Fig. 3.24. In ViPSC and HAd, the signal structure of both Chol and Cav-3 is highly clustered at the cellular basement membrane. In both cell types, the distinct membrane motifs that had been identified in VM could be observed as well. In Fig. 3.24, green arrows point out single domains, blue arrows indicate ring structures, and yellow arrows mark bunchy clusters. The qualitative comparison of Chol vs. the Cav-3 (or Cav-1, respectively) membrane motifs again shows similarities, although they are not as obvious as it was in the case of VM. Nevertheless, the association of Chol clusters along the extracellular membrane leaflet and Cav-3 clusters along the intracellular membrane leaflet seems to follow a more general principle that is not exclusive for VM. Note here that HAd show a distinct Chol signal at their basement membrane although they do not endogenously express the protein Cav-3. Still, HAd express high levels of the caveolae forming protein Cav-1 [536, 537] which is likely to have the same role in the assembly of Chol clusters as does Cav-3 in VM and ViPSC. Yet, as has been shown in section 3.2, HEK cells do not fea-

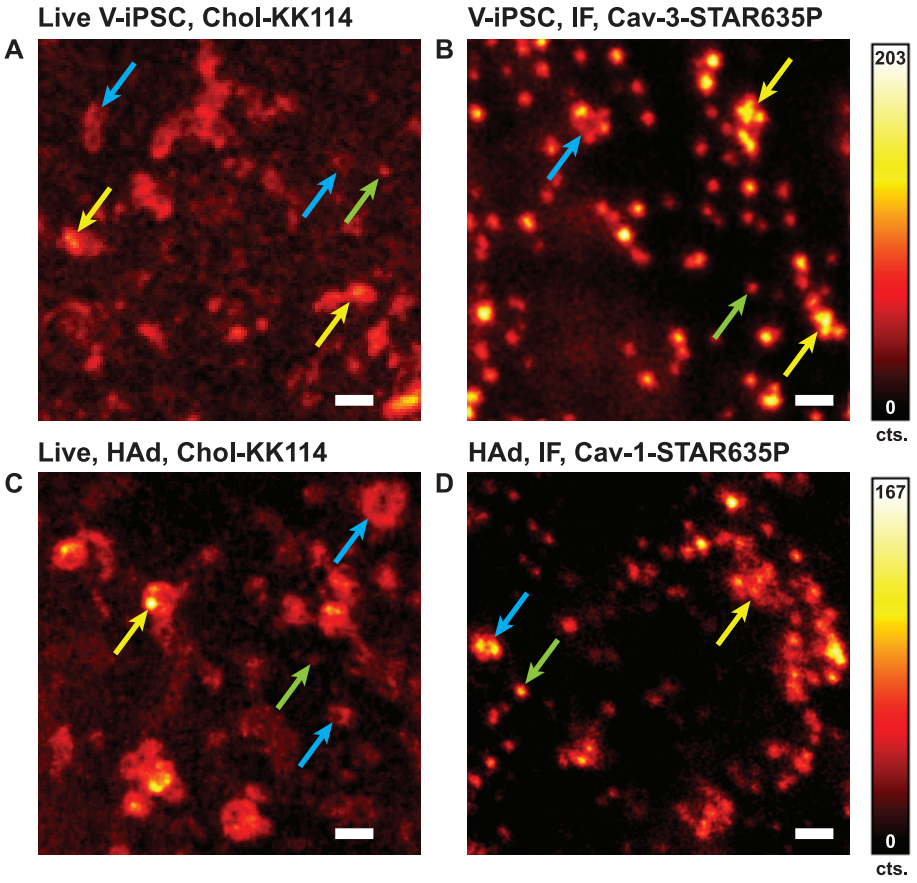

Figure 3.24.: STED images of the basement membrane of ventricular induced pluripotent stem cells (ViPSC) and human adipocytes (HAd). **A** and **C** Live ViPSC and live HAd, respectively, labeled with 5 µM Chol-KK114 as described in sections 2.4.2 and 2.4.3. **B** and **D** Fixed ViPSC and fixed HAd stained for Caveolin-3 (Cav-3) and Caveolin-1 (Cav-1), respectively, via indirect immunofluorescence (see sections 2.4.2 and 2.4.3). Arrows indicate distinct membrane pattern motifs of the respectively labeled lipid or protein: Green arrows - single domains; blue arrows - ring structures; yellow arrows - bunchy clusters. Images were smoothed using a two-dimensional Gaussian filter with a width of 1.5 pixels. The color bars indicate the image brightness in each **A** and **B**, and **C** and **D** in photon counts (cts.). Scale bars: 500 nm.

ture Chol clusters at their basement membrane when labeled with Chol-KK114 although HEK cells, being epithelial cells, are known to express Cav-1 very strongly [538]. Thus, in HAd, additional factors are most likely necessary for the formation of Chol clusters. These factors, be they proteins or special physical conditions at the membrane, i.e. curvature or mechanical tension, remain to be elucidated.

Having shown that clustered Chol signals and analogous Cav-3 signals can also be found at the basement membrane of cell types other than VM, I was interested in investigating if a cell system which does not endogenously express Cav-3 and does not show clustered Chol structures at its basement membrane could be manipulated to form Chol clusters - and probably even form

the described distinct membrane motifs - upon overexpression of Cav-3. I chose HeLa cells as the experimental cell system to study the effects of such an intervention. Opposed to VM and ViPSC, HeLa cells which do not endogenously express Cav-3 show neither clustered Chol structures nor distinct Chol membrane motifs (see section 3.2). This might indicate that the expression of Cav-3 (and, in the case of HAd, a significantly high expression level of Cav-1 [536, 537]) is necessary 1. for the general clustering of Chol structures at the cellular basement membrane and 2. for the formation of the specific arrangement of Chol structures into the nanoscopic membrane motifs that were observed. To address this hypothesized dependence of the nanoscopic Chol arrangement on the cellular Cav-3 protein levels, living HeLa cells were transfected with a Cav-3-SNAP construct to induce simultaneous overexpression of the protein Cav-3 together with a SNAP tag (see section 2.4.1). The transfected living HeLa cells were stained with either Chol-KK114 or with the fluorescent compound Silicon Rhodamine SNAP (SiR-SNAP). Live-cell STED imaging of Chol or Cav-3 structures at the cellular basement membrane was performed using the Abberior 2C STED 775 QUAD Scan microscope (see section 2.1.4 and the therein specified imaging parameters). The obtained results are summarized in Fig. 3.25.

As a first control to validate that (a) HeLa cells do not endogenously express Cav-3 and (b) overexpression of the Cav-3-SNAP construct leads to significant levels of Cav-3 expression in living HeLa cells, protein expression levels were assessed by Western blot analysis of homogenates of control vs. Cav-3 overexpressing HeLa cells. The preparation of Western blots is described in detail in section 2.10.2 and in the Appendix L. The exemplary Western blot shown in Fig. 3.25 **A**, left panel, displays the Cav-3-SNAP bands in four individual samples of Cav-3-SNAP overexpressing HeLa cells (L5-L8; shown in green); an antibody directed against Cav-3 (anti-Cav-3) was used for protein detection. Note that the expressed Cav-3-SNAP construct has a molecular weight of ≈ 40 kDa, a value stemming from the simultaneous expression of the Cav-3 protein (at ≈ 20 kDa) and the SNAP tag (at ≈ 20 kDa, see also [539]). Therefore, the green Cav-3 protein band in samples of the Cav-3-SNAP overexpressing HeLa cells is detected at 40 kDa. Lane 9 (L9) shows the protein signal of a sample of control HeLa cells, i.e. not overexpressing the Cav-3-SNAP construct; here, no Cav-3 band is detected which confirms that HeLa cells do not endogenously

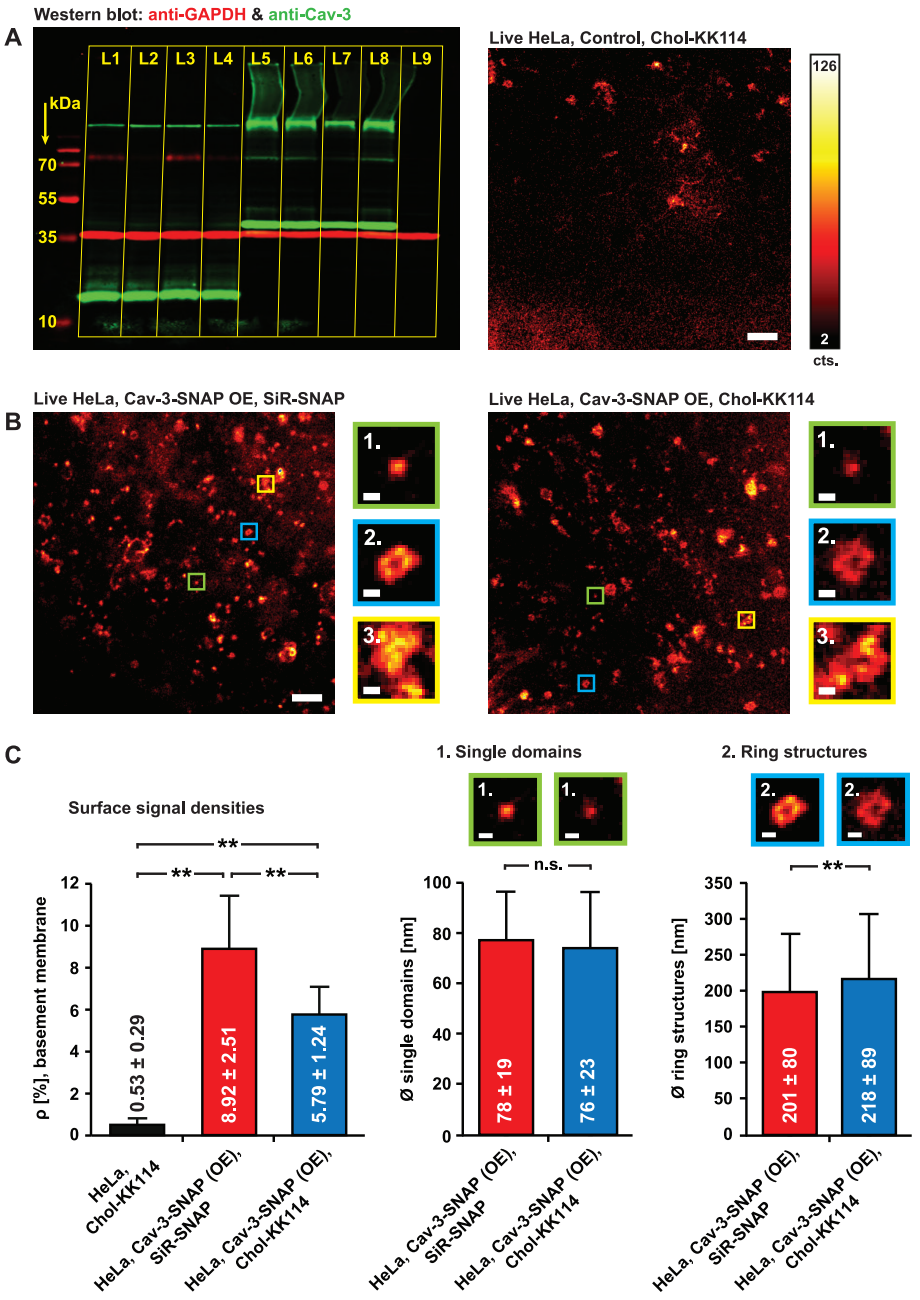

Figure 3.25.: STED images of Cholesterol (Chol) and Caveolin-3 (Cav-3) structures at the basement membrane of control vs. Cav-3-overexpressing living HeLa cells (Cav-3-SNAP OE). **A**, left panel: Exemplary Western blot of HeLa cells overexpressing the Cav-3-SNAP construct (lanes L5 - L8), and of control HeLa cells (lane L9); see also section 2.10.2 and the Appendix L. Lanes L1 - L4 additionally show Cav-3 protein bands of samples of heart homogenates from the left ventricle excised from four mice. The Cav-3 band detected by an anti-Cav-3 antibody is shown in green. GAPDH was used as a load control; the signal form the anti-GAPDH antibody is shown in red. Yellow grid lines and labels are added to facilitate the identification of individual lanes and of the molecular weight marks in the blot; image brightness was deliberately overshot to facilitate identification of the fluorescent bands. Right panel: STED image of living control HeLa cells labeled with 5 µM Chol-KK114. **B**, left panel: Cav-3 signal structure at the basement membrane of living HeLa cells overexpressing a Cav-3-SNAP construct and labeled with a Silicon Rhodamine SNAP tag (SiR-SNAP). Right panel: Chol-KK114 signal structure at the basement membrane of living HeLa cells overexpressing a Cav-3-SNAP construct. Image magnifications show the distinct membrane motifs: 1. single domains; 2. ring structures; 3. bunchy clusters. **C** Bar graph representation of the quantitative analysis of the surface signal densities ρ (in %), the diameter ⌀ of single domains (in nm), and the diameter ⌀ of ring structures (in nm) of Cav-3 and Chol-KK114 signals, respectively. ρ and ⌀ are given as mean ± standard deviation; statistical significance was assessed using a Mann-Whitney-Wilcoxon U test (see section 2.9) and is displayed as: n.s. - not significant; ** - very significant ($p < 0.01$). Detailed statistics including sample sizes are given in the Appendix I, Tables I.6, I.7, and I.8. Images were smoothed using a two-dimensional Gaussian filter with a width of 1.5 pixels. The color bar in **A** indicates the image brightness for every fluorescence image in **A** and **B** in photon counts (cts.). Scale bars in overview images: 1 µm; scale bars in magnifications: 100 nm.

express Cav-3. GAPDH was used as a load control (shown in red) and confirms the even distribution of protein in the samples. For comparison, lanes 1-4 show the Cav-3 expression levels in heart tissue (protein bands shown in green and detected by the same antibody used also for the samples of HeLa cells). Samples of heart tissue homogenates were obtained from left ventricles excised from four mice, see also section 2.10.2 and Appendix L) and validate that Cav-3 is endogenously expressed in VM. Note that in the heart tissue samples, the protein bands of endogenously expressed Cav-3 are located at $\approx$ 20 kDa since here the protein is not coupled to a SNAP tag.

Fig. 3.25 **A**, right panel, shows an exemplary STED image obtained at the basement membrane of control HeLa cells, i.e. not overexpressing the Cav-3-SNAP construct that were labeled with 5 µM Chol-KK114. In the control HeLa cells, no significant Chol-KK114 signal was observed. This finding has been discussed previously in sections 3.2 and 3.3 where it could be shown that living HeLa cells feature high amounts of Chol-KK114 signal along filopodial structures but little to no Chol-KK114 signal at their basement membrane.

Transfected HeLa cells overexpressing the Cav-3-SNAP construct, however, feature a membrane architecture that is completely different from that of the control cells. As can be seen in the STED images in Fig. 3.25 **B**, overexpression of Cav-3 leads to a profound signal of Cav-3 as well as Chol-KK114 at the basement membrane of living HeLa cells. Both the Cav-3 and the Chol structures are highly clustered. Such Chol clusters are not seen in the control cells (see Fig. 3.25 **A** vs. **B**, and also section 3.3). The surface signal density ρ of the Cav-3 clusters amounts to 8.92 % (see Fig. 3.25 **C**). This means that almost one tenth of the cellular basement membrane is covered by Cav-3 rich clusters. The density of the Chol-KK114 signal at the basement membrane of living HeLa cells overexpressing Cav-3 amounts to 5.79 % and is thus larger by a factor of 10 compared to the signal density of 0.53 % at the basement membrane of control HeLa cells (see Fig. 3.25 **C**).

Further, STED images of living HeLa cells overexpressing the Cav-3-SNAP construct and labeled with SiR-SNAP or Chol-KK114 show the three distinct nanoscopic membrane motifs, i.e. 1. single domains, 2. ring structures, and 3. bunchy clusters of various sizes (see Fig. 3.25 **B**) that have also been observed in VM, ViPSC, and HAd. Magnifications of the STED images presented

in Fig. 3.25 **B** exemplarily show these three re-occurring patterns. Again, just like in VM, the Cav-3 and Chol membrane motifs resemble each other strongly - qualitatively and quantitatively. Quantification of the diameter of the Cav-3 and Chol single domains (see section 2.6.5 and Fig. 3.25 **C**) yielded average diameters of 78 nm (Cav-3) and 76 nm (Chol). Hence, the Cav-3 and Chol single domains do not differ significantly in size. Interestingly, the single domains of Cav-3 and Chol in HeLa cells overexpressing the Cav-3-SNAP construct have a similar diameter as the corresponding domains in VM, albeit in HeLa cells they are slightly larger; in VM the single domains had an average diameter of 68 nm (Cav-3) and 74 nm (Chol). Assessment of the average diameter of the Cav-3 and Chol ring structures featured by the Cav-3-SNAP overexpressing living HeLa cells (see section 2.6.6 and Fig. 3.25 **C**), yielded average diameters of 201 nm (Cav-3) and 218 nm (Chol). Again, these ring structure diameters in living HeLa cells are similar, although somewhat smaller than the corresponding ring structure diameters in VM where they amounted to 253 nm (Cav-3) and 226 nm (Chol). From the statistical analysis using the Mann-Whitney-Wilcoxon U test for the comparison of the datasets of the acquired Cav-3 and Chol ring diameters, it was found that the size difference between the ring diameters is very significant (see also Appendix I). The significant difference between the measured ring diameters might again be attributable to the size of the used fluorescence labels, as it might have been the case for VM (see the discussion further above). The SNAP tag has a molecular weight of about 20 kDa [539] and the Silicon Rhodamine SNAP construct has a molecular weight of 720 Da [540]. Since the exact physical dimension of the Chol-KK114 membrane label is not know, the SiR-SNAP construct might be smaller than Chol-KK114, resulting in the smaller observed diameter of Cav-3 ring structures compared to that of Chol-KK114 ring structures.

From the above findings, two things can be concluded. First, the overexpression of Cav-3 in a cell type that does not endogenously express Cav-3 induces the formation of Cav-3 assemblies at the cellular basement membrane; these Cav-3 assemblies qualitatively and quantitatively resemble those assemblies seen in VM, ViPSC, and HAd (note that VM and ViPSC endogenously express Cav-3 and that HAd express very high amounts of Cav-1 [536, 537]). Second, the Cav-3 structures that form upon Cav-3 overexpression assemble Chol into

similar arrangements at the basement membrane; these Chol arrangements, again, qualitatively and quantitatively resemble those in VM, ViPSC, and HAd. This could mean that it is an intrinsic property of Cav-3 to cluster and form a very specific nanopattern at the basement membrane. Further, the expression of the protein Cav-3 may be necessary to induce the clustering of Chol into specific assemblies that resemble those formed by Cav-3.

Having established the experimental system of Cav-3 overexpressing living HeLa cells and having observed the emergence of both Cav-3 and Chol structures that resemble those observed in cell types that endogenously express Cav-3, I could simultaneously label Cav-3 and Chol in living HeLa cells and perform two-color STED imaging. To this end, living Cav-3 overexpressing HeLa cells were labeled for Cav-3 with the fluorescent SNAP-tag 580CP-BG-(SNAP) and for Chol with Chol-KK114 following the protocol described in section 2.4.1. Images were acquired using the STED microscope system Abberior 2C STED 775 QUAD Scan (see section 2.1.4). The two color channels were simultaneously recorded via laser scanning and fluorescence detection in interleafed mode. The same STED laser at the wavelength of 775 nm was applied so that registration of the color channels was not required. Fig. 3.26 exemplarily shows one of the obtained two-color STED images of living HeLa cells. As can be seen in Fig. 3.26 **A**, the Chol-KK114 signal (displayed in magenta) predominantly accumulates along filopodial structures of the cells (see also section 3.2). However, a profound Chol-KK114 signal is also seen at the basement membrane and in close association with found Cav-3 structures (displayed in cyan). Both the Cav-3 as well as the Chol-KK114 signal are highly clustered. The image magnifications displayed in Fig. 3.26 **B** and **C** reveal a mosaic-like arrangement of Cav-3 and Chol clusters. There are regions of structural colocalization (displayed in yellow; e.g. in Fig. 3.26 **B**, yellow arrow heads), but also singular Chol-KK114 and Cav-3 clusters, respectively (see Fig. 3.26 **C**, red arrow heads). Further, there are regions of separate, variously shaped Cav-3 and Chol clusters in close mutual proximity that are arranged in an intermeshed fashion - a patterning which shall here be referred to as “para-localization” (see Fig. 3.26 **C**, white arrow heads). The two types of close association between Cav-3 and Chol-KK114 clusters at the basement membrane - i.e. colocalization and para-localization - are the most frequently observed structural patterns. Since Cav-3

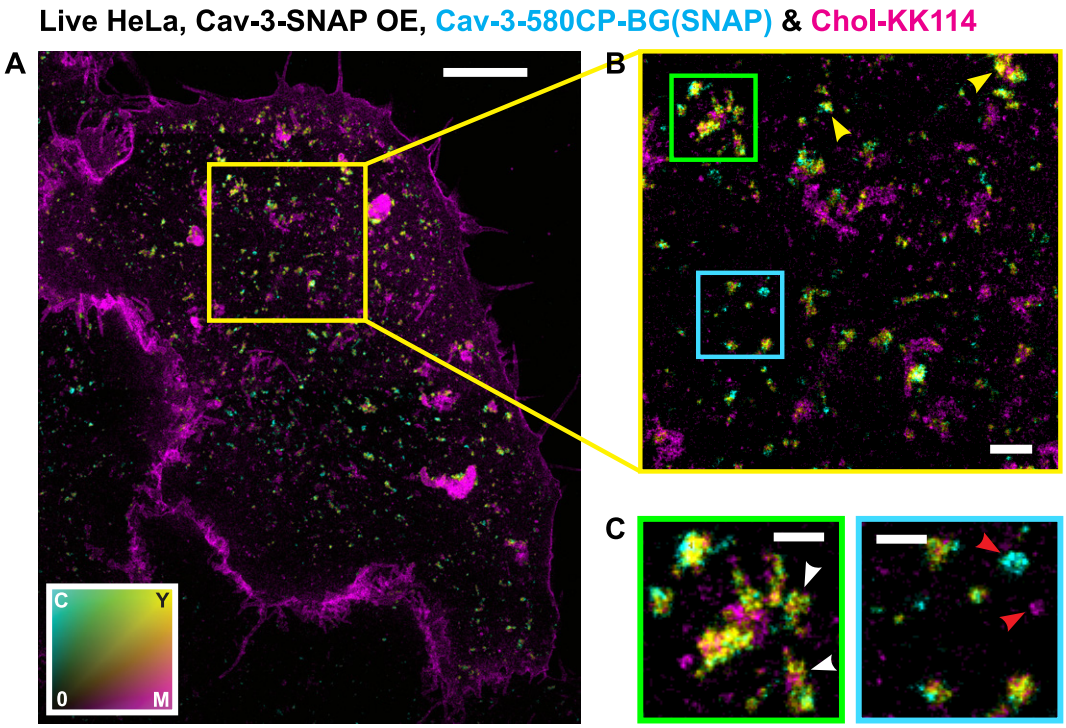

Figure 3.26.: Two-color STED images of a living HeLa cell overexpressing the Cav-3-SNAP construct and double-labeled with the fluorescent SNAP tag 580CP-BG(SNAP) (Cav-3-580CP-BG(SNAP), see section 2.4.1 and Chol-KK114. HeLa cells were transfected and stained as described in section 2.4.1. The Cav-3-580CP-BG(SNAP) color channel is displayed in cyan (C), the Chol-KK114 color channel is displayed in magenta (M), yellow signal (Y) indicates the overlap of the two color channels. **A** Overview image of a living HeLa cell overexpressing the Cav-3-SNAP construct and labeled with 580CP-BG(SNAP) and Chol-KK114. Scale bar: 5 µm. **B** Magnification of the yellow boxed region in **A**. Yellow arrow heads indicate regions of structural colocalization. Scale bar: 1 µm. **C** Zoom-Ins to the green and blue boxed regions, respectively, in **B**. White arrow heads indicate regions of para-localization. Red arrow heads indicate separate Cav-3 and Chol clusters, respectively. Images were smoothed using a two-dimensional Gaussian filter with a width of 1.5 pixels and transformed to the color map depicted in **A** as described in section 2.6.1. Scale bar: 500 nm.

is anchored within the intracellular membrane leaflet and since Chol-KK114 due to its bulky PEG-linker most likely inserts itself specifically in the extracellular leaflet, the observed prevalent co- and para-localization of Cav-3 and Chol-KK114 suggest that Chol-KK114 is an indirect label of Cav-3 rich membrane clusters - and vice versa. From this, it is arguable that Cav-3 clusters and Chol rich clusters might mutually influence and mediate each other's localization to and positioning in the same membrane regions. Hence, the data presented in Fig. 3.26 support the assumption that cluster formation at the plasma membrane is a cooperative process between both membrane leaflets which has also been suggested in earlier studies [132]. For completeness, note that not all observed Cav-3 and Chol-KK114 signals were associated with each other. The two-color STED images show that, albeit Cav-3 and Chol clusters are closely

associated at the cellular basement membrane, there is no 1:1 mapping of their signal patterns (see Fig. 3.26 **C**, red arrow heads). The observation of stand-alone Cav-3 signal that is not associated to Chol-KK114 structures could be due to a partial retention of the overexpressed Cav-3-SNAP construct in the Golgi apparatus. The membrane permeable dye compound 580CP-BG(SNAP) labeling the overexpressed Cav-3-SNAP construct would still access this portion of Golgi associated Cav-3 proteins and due to the limited axial resolution of the microscope such structures that are not incorporated into the cellular membrane would still yield a detectable signal in the imaging plane right at the basement membrane. This would, however, most likely only explain those observed solitary Cav-3 clusters that are low in signal brightness. Further, there is only little evidence that wild-type, i.e. not mutated, Cav-3 shows a high colocalization with Golgi markers [541]. The more likely conclusion derived from the observed Cav-3 and Chol signal patterns in Cav-3 overexpressing living HeLa cells is that the Cav-3 signal does not completely colocalize with the Chol-KK114 signal because Cav-3 partly resides in the intracellular leaflet of the plasma membrane while Chol-KK114 is most probably exclusively inserted in the extracellular membrane leaflet. The solitary, i.e. not Chol associated, portion of the detected Cav-3 proteins might hence reside in regions along the cellular membrane that would not be readily accessible for Chol-KK114 with its bulky PEG-linker which could possibly be due to steric hindrance in regions with high negative membrane curvature (as it is also discussed for VM at the beginning of this section). In addition, some Cav-3 rich membrane clusters may have bound sufficient amounts of endogenous Chol so that these membrane areas are already saturated in Chol when Chol-KK114 is exogenously added to the membrane; and assuming a possibly slow interchange rate between the fluorescent Chol analog and the resident endogenous Chol associated to those Cav-3 clusters, colocalization would not be expected there. On the other hand, Cav-3 is certainly not the only protein that binds Chol [542] and caveolae are thus likely not the only Chol rich membrane domains [543, 544] - caveolae independent Chol clustering in the outer cellular leaflet would hence explain the solitary Chol signal clusters.

Concluding, it could be shown that Chol structures in the extracellular leaflet and of structures of the intramembrane protein Cav-3 at the intracellular leaflet

feature highly similar, distinct nanoscopic arrangements at the sarcolemma of VM. These sarcolemmal arrangments feature three reoccurring motifs: 1. single domains of $\approx$ 70 nm in diameter, 2. ring structures of $\approx$ 240 nm in diameter, and 3. bunchy clusters of variable sizes. ViPSC and HAd show an analogous arrangement of Chol and Cav-3 structures, or Chol and Cav-1 structures, respectively, at their basement membrane. Further, the overexpression of Cav-3 in HeLa cells - which do not express endogenous Cav-3 and which, under physiological conditions, do not show Chol clusters at their basement membrane (see also section 3.3) - led to the formation of the above-mentioned distinct basement membrane Chol motifs, i.e. single domains, ring structures, and bunchy clusters. In two-color STED images of living HeLa cells overexpressing Cav-3 and labeled for both Cav-3 and Chol, a close spatial association between Cav-3 and Chol clusters could be observed at the cellular basement membrane. However, there was no 1:1 mapping of the protein and lipid clusters but rather a mosaic-like arrangement. Hence, since Cav-3 and Chol show similar nanopatterns at the sarcolemma of VM, and since the amount of Cav-3 present at the cellular basement membrane influences the assembly of Chol clusters, in a next step, the influence of the Chol content at the sarcolemma of VM on the nanopattern of Cav-3 structures was investigated to verify if there is a mutual dependence between the sarcolemmal Cav-3 and Chol content. To this end, living VM were depleted of Chol, then labeled for Cav-3, and imaged using STED microscopy. The resulting profound changes in the sarcolemmal Cav-3 arrangements are presented in the next section.

3.5.1. Cholesterol depletion leads to the dissociation of sarcolemmal Caveolin-3 clusters

Cholesterol depletion by the treatment of cells with Methyl-β-Cyclodextrin (M-β-CD) is a well-established protocol to achieve disruption of caveolar structures [190]. Further, apart from caveolae, the extraction of Chol from the cellular membrane using M-β-CD has been shown to cause the dissociation of the respective complexes of many other typically clustered proteins [545, 546, 454]. M-β-CD features an oligosaccharide ring composed of seven glucose monomers and is of a toroidal structure with a central cavity. The central cavity of M-β-CD is hydrophobic, the outer surface is polar. When in dimeric

form, M-β-CD transiently binds to the membrane and can extract membrane Chol by binding to it with high affinity followed by desorption of the resulting Chol/M-β-CD complex [547]. Note that M-β-CD does not permanently bind to the membrane and does not insert itself into the membrane [548].
Here, to extract membrane Chol from the sarcolemma of mouse ventricular cardiomyocytes (VM), living VM were treated with 5 mM M-β-CD as described in section 2.3.3. Control cells and M-β-CD cells were fixed and labeled for Cav-3 via indirect immunofluorescence (see section 2.3.3). STED images of Cav-3 signal structures at the sarcolemma of control vs. Chol depleted fixed VM were obtained using the custom-built fast scanning STED microscope that is described in section 2.1.2. Cell fitness was assessed prior to imaging (i.e. only intact cells featuring regular striations and no signs of blebbing or contraction were chosen). Additionally, the used concentration of 5 mM of M-β-CD is well below the concentration of M-β-CD at 20 mM for which an onset of cell toxicity has been reported [549]. Upon Chol depletion, the clustered Cav-3 signal that was described in detail in the last section changes dramatically. Fig. 3.27 exemplarily shows STED images of control vs. M-β-CD treated fixed VM labeled for Cav-3 via indirect immunofluorescence using the antibody coupled dye STAR635P. As can be seen, the highly clustered sarcolemmal Cav-3 pattern is lost in Chol depleted cells. Upon Chol depletion, all higher-order structural arrangements of Cav-3 single domains dissociate which leads to an almost isotropic distribution of Cav-3 single domains along the sarcolemma. Accordingly, the membrane motifs of bunchy clusters and ring structures are no longer observed in Chol depleted cells. The effect of Chol depletion on the sarcolemmal Cav-3 signal structure was quantitatively assessed by the determination of three descriptive figures: 1. the diameter of single domains of Cav-3 $\varnothing$ (see section 2.6.5), 2. the Cav-3 signal contour density Γ (see section 2.6.7), and 3. the sarcolemmal Cav-3 signal density ρ (see section 2.6.4). These figures are displayed in bar graph notation in Fig. 3.27 for control vs. Chol depleted VM. From the determination of $\varnothing$, Γ, and ρ, three major and very interesting observations can be made.
First, the diameter of sarcolemmal Cav-3 single domains remains unchanged upon Chol depletion: for control cells, the Cav-3 single domains are about 68 nm in diameter, in Chol depleted cells the diameter of single domains amounts

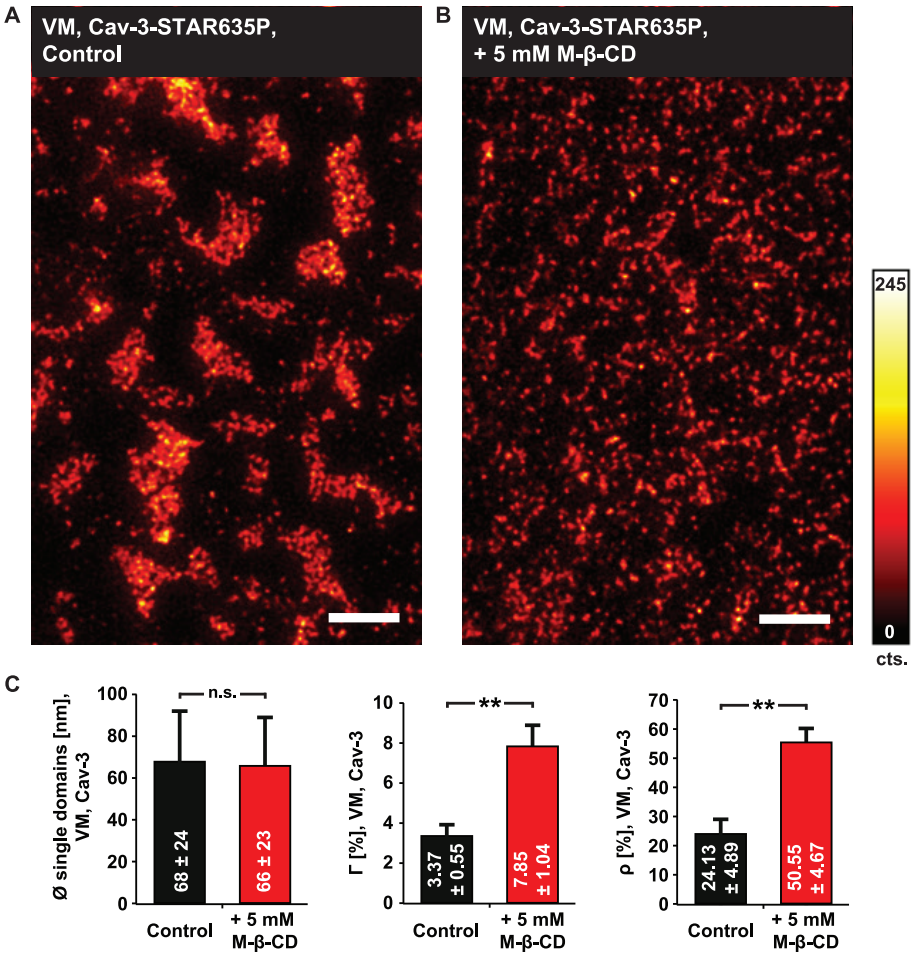

Figure 3.27.: Effect of membrane Cholesterol (Chol) depletion on the Caveolin-3 (Cav-3) signal structure at the sarcolemma of fixed mouse ventricular cardiomyocytes (VM). Membrane Chol was depleted by incubation of living VM with Methyl-β-Cyclodextrin (M-β-CD) at a concentration of 5 mM prior to fixation and staining for Cav-3 (see section 2.3.3). **A** STED image of a fixed, untreated VM (Control) labeled for Cav-3 (marker dye: STAR635P). **B** STED image of a fixed, Chol depleted VM (+ 5 mM M-β-CD) labeled for Cav-3 (marker dye: STAR635P). Images were smoothed using a two-dimensional Gaussian filter with a width of 1.5 pixels. The color bar in indicates the image brightness for **A** and **B** in photon counts (cts.). Scale bars: 1 µm. **C** Bar graph representation of quantitative measures describing the Cav-3 signal structures. Left graph: the diameter (⌀) of single Cav-3 domains (see section 2.6.5) in untreated VM (Control, in black) vs. Chol depleted VM (+ 5 mM M-β-CD, in red); diameters are given in nm and presented as mean ± standard deviation. Middle graph: the Cav-3 signal contour density Γ (see section 2.6.7) in untreated VM (Control, in black) vs. Chol depleted VM (+ 5 mM M-β-CD, in red); Γ is given in % of the total number of possible pixel boundaries and presented as mean ± standard deviation. Right graph: the Cav-3 surface signal density ρ (see section 2.6.4) in untreated VM (Control, in black) vs. Chol depleted VM (+ 5 mM M-β-CD, in red); ρ is given in % of the total sarcolemmal area and presented as mean ± standard deviation. Statistical significance of the variation of the diameter of single domains, the variation of ρ and the variation of Γ (see section 2.9 and Appendix I, Tables I.9, I.10, and I.11) between control and Chol depleted VM is displayed as : (n.s) - not significant ($p > 0.01$), and (**) - very significant ($p < 0.001$). Number of analyzed single Cav-3 domains for diameter determination: Control - 2397; + 5 mM M-β-CD - 2360. Number of analyzed cells for determination of Γ: Control - 44; + 5 mM M-β-CD - 38. Number of analyzed cells for determination of ρ: Control - 44; + 5 mM M-β-CD - 38.

to 66 nm. This minor difference in the single domain diameters is not statistically significant. Based on this, it can be stated that the identified membrane motif of single domains which was found to be the main "building block" of

all higher order sarcolemmal Cav-3 patterns (see section 3.5) is not influenced by the sarcolemmal Chol content. This "survival" of small membrane protein clusters has been reported previously [454] and could be attributed to mechanisms that stabilize the clusters and that are independent or Chol.
Second, the Cav-3 signal contour density Γ significantly increases by a factor of ≈ 2.6 upon Chol depletion: while control cells showed a mean Γ of about 3 %, in Chol depleted cells Γ amounted to about 8 %. Since Γ is a measure of the degree of clustering of an assembly of individual structural entities (see section 2.6.7), the doubling in Γ quantitatively describes the dissociation of Cav-3 clusters into their main building blocks (i.e. single domains) upon Chol depletion. As a consequence, the area of interconnected sarcolemmal regions that do not show a Cav-3 signal (i.e. black regions in the STED images in Fig. 3.27 **A** and **B**, from here on referred to as "Cav-3-negative" regions) is reduced. This indicates that in a Chol depleted VM there are more "borders" between Cav-3-positive and Cav-3-negative regions at the sarcolemma. A molecule diffusing along the sarcolemma of a Chol depleted VM would thus encounter Cav-3 rich regions more frequently than a molecule diffusing along the sarcolemma of a VM with a physiological Chol content. An effective slowed down molecule diffusion upon Chol depletion has been reported [546].
Third, the surface signal density ρ significantly increases by a factor of ≈ 2 upon Chol depletion: while in a control VM about one quarter of the sarcolemma is covered by Cav-3 signal ($\rho \approx 24\%$), the Cav-3 signal covers about half of the sarcolemma of a Chol depleted VM ($\rho \approx 51\%$). The doubling of ρ indicates that upon Chol depletion, Cav-3 signal is added to the sarcolemma. This raises the question about where this additional signal is coming from. One possible explanation could be that the additional Cav-3 signal is coming from the dissociation of Cav-3 clusters that consisted of several densely packed Cav-3 single domains which could not be resolved individually. The cluster dissociation would lead to a spatial spreading of these single domains until their individual resolution would be possible. This case shall here be referred to as a "lateral increase" in signal. Another possible explanation of the additional Cav-3 signal could be that upon Chol depletion, Cav-3 domains from layers deeper below the sarcolemma might be freed from their connection to the sarcolemma-bound Cav-3 domains and "swim to the surface". This

case shall here be referred to as an "axial increase" in signal. This explanation seems possible because one should also consider that the axial resolution of the used microscope system is limited to confocal resolution ($\approx$ 700 nm for the dye STAR635P, see section 1.2), single Cav-3 domains cannot readily be discerned if they overlap along the axial direction.

Taken together, the sarcolemmal membrane Chol content is not only important for the lateral assembly and arrangement of Cav-3 structures, i.e. clustering and formation of higher-order membrane motifs, but also for the axial Cav-3 arrangement at the sarcolemma, i.e. 3D structures that extend perpendicularly to the sarcolemma. The integrity of such 3D Cav-3 structures seems to be dependent on the available sarcolemmal Chol content and it is possible that Chol depletion flattens the sarcolemma by disruption of these 3D arrangements. This would effectively result in a loss of the cellular "surface area reservoir" that might be formed by extended caveolar structures.

For completeness, another possible factor shaping the sarcolemmal Cav-3 signal arrangement upon Chol depletion shall be critically discussed here: it has been reported that Chol depletion leads to a loss of Transverse Tubule (TT) structures in cardiomyocytes [150]. Hence, the increase in Cav-3 signal at the sarcolemma of Chol depleted VM might stem from Cav-3 domains that were formerly associated with TT and lost their confinement to these TT when the TT were lost/altered due to Chol depletion. However, in the mentioned study, cultured VM were incubated with M-β-CD for 48 h before being stained with Di-8-ANEPPS and imaged for characterization of their TT. The observed loss of TT might be an artifact of the cell culture: it has been reported in many studies that the cell culturing process itself leads to a loss of cardiac TT [151, 152, 153, 32]. To control if the here observed change in sarcolemmal Cav-3 clustering upon Chol depletion was actually an effect of a loss of TT, I compared the Transverse-Axial Tubular System (TATS) signal architecture in living control VM to that of living Chol depleted VM (following the herein used Chol depletion protocol, see section 2.3.3) by labeling those cells with Di-8-ANEPPS. No alterations of the TATS in Chol depleted VM could be observed. Further, I replenished the Chol content of Chol depleted living VM by labeling them with Chol-KK114. Again, when compared to Chol-KK114 labeled control VM, no alterations of the TATS was observed. The conducted control experiments and the obtained

images are presented in detail in the Appendix M. The Chol depletion induced dissociation of sarcolemmal Cav-3 clusters is thus unlikely caused by a loss in the TATS integrity.
In summary, the presented image-based comparison between the sarcolemmal Chol and Cav-3 signal patterns points towards the direct structural association of outer leaflet Chol and inner leaflet Cav-3 domains. However, there remains an unfortunate factor impairing the experimental verification of this direct association: Chol-KK114 is a feasible fluorescent marker only in living VM with intact membranes - and without access to genetically modified animals expressing a fluorescent version of Cav-3, Cav-3 can only be imaged via immunolabeling, i.e. by fixing and permeabilizing the VM. The straightforward approach of simply dual-labeling a living (or fixed) VM to simultaneously detect Chol-KK114 and Cav-3 was hence not possible. I therefore chose another, more indirect approach to further motivate the specific connection of the observed sarcolemmal Chol-KK114 and Cav-3 motifs. In this approach, I made use of the properties of Ganglioside GM1 (GM1, see section 1.1) which is a commonly used marker of the liquid ordered phase in the extracellular membrane leaflet [89]. GM1 offers the great advantage that it can be fluorescently labeled both for live-cell as well as fixed cell imaging applications. It was thus possible to simultaneously label Chol and GM1 in the intact cardiac membrane, resulting in the first two-color STED images of living VM. Further, a two-color immunofluorescence assay tagging GM1 and Cav-3 for STED microscopy enabled additional colocalization studies. The results are presented in the following section.

3.6. Association of sarcolemmal Cholesterol, Caveolin-3, and Ganglioside GM1 domains

This section is focusing on the spatial association and colocalization of Cholesterol (Chol) and Ganglioside GM1 (GM1) clusters at the sarcolemma of living mouse ventricular cardiomyocytes (VM), and of Caveolin-3 (Cav-3) and GM1 clusters at the sarcolemma of fixed VM. The image based evaluation of the sarcolemmal mosaic-like membrane lipid and membrane protein nanopatterning, specifically comparing the two experimental cell systems (i.e. living vs. fixed

VM) will be presented qualitatively and quantitatively. As a quick recapitulation, Fig. 3.28 schematically shows the possible arrangement and association of Chol, Cav-3 and GM1 along the cardiac sarcolemma, as proposed in the introduction (see section 1.4, Fig. 1.10). With respect to the model presented in

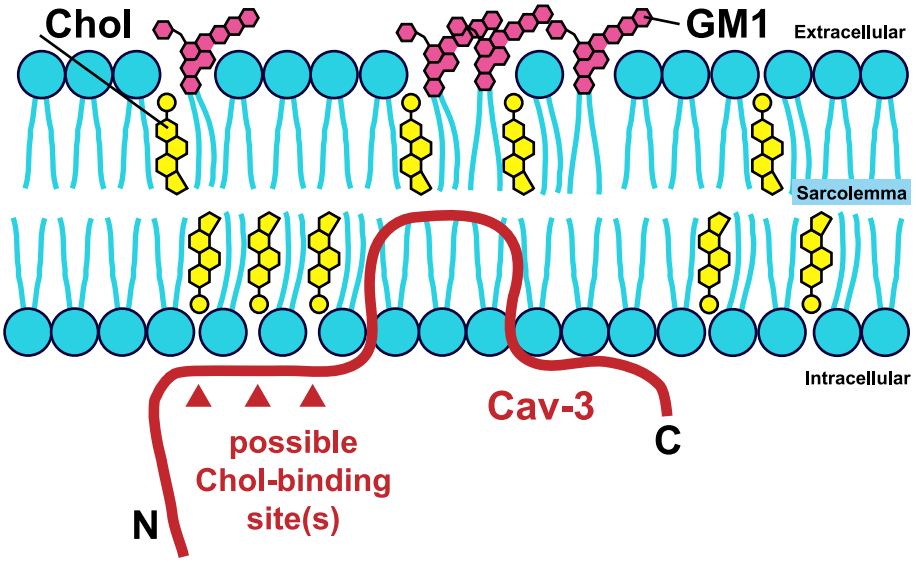

Figure 3.28.: Schematic of the postulated association of the membrane lipids Cholesterol (Chol), Ganglioside GM1 (GM1), and the membrane associated protein Caveolin-3 (Cav-3). The intramembrane domain of Cav-3 resides within the lipid bilayer, while its amino-terminus (N) and its carboxyl-terminus (C) face the cytosol. Approximate sites of possible Chol-binding domains are marked by (+). The scheme does not provide the correct stoichiometry of the lipid and protein distribution (because it is not precisely known). Neither drawn to actual proportions nor with correct stoichiometry. See also section 1.4.

Fig. 3.28, three important aspects shall be noted here. First, GM1 resides in the extracellular leaflet of the lipid bilayer [219, 220, 240] with its sugar group protruding about 2.5 nm into the extracellular space [222, 223] and thus, amongst other glycolipids and glycoproteins, constituting the glycocalyx [223]. Second, while Chol is abundantly present within both the extracellular and the intracellular sarcolemmal leaflet, the portion of possible Chol insertion sites into the membrane that can be assessed using Chol-KK114 as a membrane marker is most likely exclusive to the extracellular leaflet (see also section 3.1). Third, the amino-terminus (N) and the carboxyl-terminus (C) of Cav-3 are in the cytosol while its hairpin-like transmembrane region is anchored within the intracellular membrane leaflet. Further, Cav-3 features Chol-binding motifs near its N-terminus that suggest the connection between Cav-3 and intracellular leaflet Chol molecules (the Chol-binding motifs have been discussed in detail in the introduction, section 1.1). Following this membrane model, it can be seen that there is a Chol/Cav-3 complex along the cytosolic side of the sarcolemma, and

a possible Chol/GM1 complex along the extracellular sarcolemmal membrane leaflet. It has been reported that a change in lipid composition of the extracellular leaflet concomitantly changes the lipid composition of the intracellular leaflet [132, 550]. According to this, lipid and/or protein structures along the intracellular membrane leaflet can serve as interdependent sensors of the specific lipid content in the extracellular leaflet, specifically, the content of Chol and/or GM1 in the extracellular leaflet. For example, caveolae associated proteins (such as the members of the Caveolin protein family) along the intracelluar leaflet indicate Chol and GM1 rich domains at the opposing extracellular leaflet whereas certain prenylated proteins at the intracellular leaflet indicate the liquid disordered phase at the opposing extracellular leaflet [551, 552]. Transitively, this suggests the use of Chol-KK114 as a marker of caveolar structures in living VM, a possible application which is supported by the findings presented in section 3.5, i.e. the highly similar sarcolemmal nanopatterning of cardiac Chol and Cav-3 signals. This possible and very useful correlation between the cardiac Cav-3 and Chol-KK114 signal motivates the use of GM1 as an indirect marker to control for the spatial association of Chol at the extracellular leaflet and Cav-3 along the cytosolic side of the membrane.

First, in search of the above proposed possible outer leaflet Chol/GM1 complex, I incubated living VM with Chol-KK114 and fluorescenctly labeled recombinant Choleratoxin subunit B (CtB-AF594) to tag GM1 as described in section 2.3.2. The dual-labeled samples were imaged using the STED microscope Leica TCS SP8 STED 3X (see section 2.1.3). Specifically, the choice of the fluorescent dyes KK114 and AF594 for the labeling of the respective membrane constituents allowed the use of the same STED laser wavelength (at 775 nm) so that the emergence of the recorded fluorescence signal from each color channel was confined to the same subdiffractional focal spot (i.e. to the vicinity of the center of the toroidally shaped STED beam). Thus, both color channels could be recorded simultaneously and could be readily overlaid for colocalization analysis without the need of image post processing steps regarding color channel registration. Figure 3.29 shows the STED image of the sarcolemma of a living VM dually labeled with Chol-KK114 and CtB-AF594. Considering the single color channels, i.e. the Chol-KK114 and the CtB-AF594 channel, separately (see Fig. 3.29 **C**), signal clustering of both Chol and GM1 can be observed. The

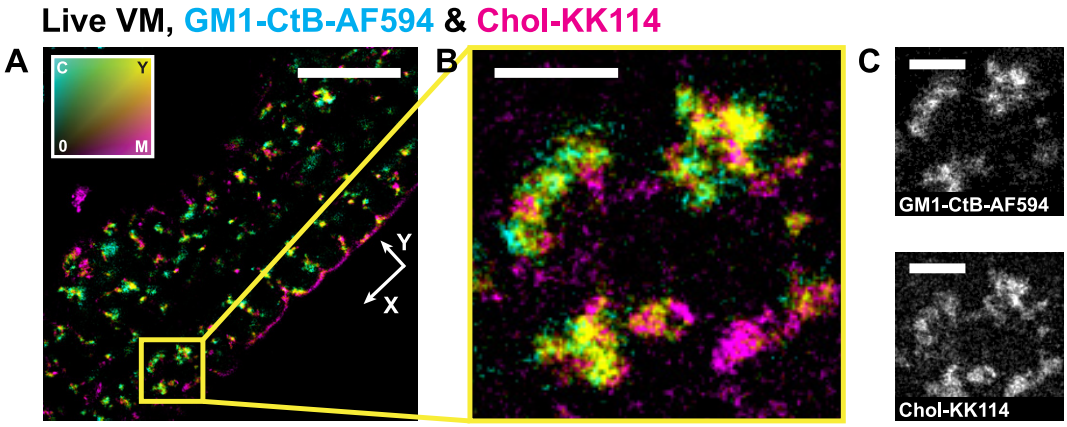

Figure 3.29.: Two-color STED image of a living mouse ventricular cardiomyocyte (VM) labeled for Ganglioside GM1 (GM1) via Choleratoxin subunit B coupled to the dye Alexa Fluor 594 (CtB-AF594) and with Chol-KK114. VM were stained as described in sections 2.3.2 and 2.3.3. **A** Two-color overview STED image of the VM. The two color channels are color coded with the GM1-CtB-AF594 channel displayed in cyan (C) and the Chol-KK114 channel displayed in magenta (M); yellow signal (Y) indicates signal overlap of the color channels. The corresponding color map is displayed in the top left corner. White arrows indicate the longitudinal (X) and the transverse (Y) cell axes, respectively. Scale bar: 5 µm. **B** Magnification of the STED overview image corresponding to the yellow boxed region. Scale bar: 1 µm. **C** Single color images of the respective GM1-CtB-AF594 and Chol-KK114 signal channels corresponding to the image magnification shown in **B**. Images were smoothed using a two-dimensional Gaussian filter with a width of 1.5 pixels and converted to the displayed color map as described in section 2.6.1. Scale bar: 1 µm.

respective Chol and GM1 signal clusters appear in various shapes and sizes, with the largest clusters being up to 1 µm in diameter (when approximately assuming a roughly circular cluster shape) and with the smallest clusters being approximately 60 - 70 nm in diameter. These smallest clusters resemble the previously described smallest Chol and Cav-3 signal entities that were defined as "single domains" (see section 3.5). Note that most larger cluster arrangements can readily be identified as consisting of a substructural arrangement of Chol and GM1 single domains. Regarding the overlay images of the two color channels, it can be seen from Fig. 3.29 **A** and **B** that GM1 is very tightly associated with Chol but the two signal structures do not entirely overlap. Both the colocalization and the gap arrangement (i.e. para-localization, see section 3.5) of Chol- and GM1-rich sarcolemmal domains were observed. However, GM1 and Chol signals are always in close proximity to each other - within a distance that hardly ever exceeds about 500 nm. Areas devoid of any signal from either color channel made up the remaining sarcolemmal space between the labeled domains. The subdiffraction Chol/GM1 double stains thus reveal the intra-leaflet registration of Chol and GM1 domains at the sarcolemma of living VM, i.e. the spatial association of Chol and GM1 structures within the same membrane leaflet (here, the extracellular leaflet). This is in agreement with previ-

ously reported Atomic Force Microscopy (AFM) based observations that GM1 preferentially partitions into the Chol rich liquid ordered phase when added in physiological concentrations to artificially prepared supported membranes of controlled lipid compositions [89, 90, 96]. In their AFM studies of the GM1 distribution in supported monolayers and bilayers of ternary lipid mixtures, *Yuan et al.* [90] found irregularly shaped GM1 rich aggregates that formed patches of about 40 - 150 nm in size in monolayers and about 100 - 400 nm size in bilayers. Attempts using conventional fluorescence microscopy have been made to support these data acquired with near-field microscopy [132, 92, 219], but could not visualize the assembly of Chol and GM1 clusters along the membrane with such a level of detail shown in the AFM measurements due to limited achievable feature resolution. The here presented STED images (see Fig. 3.29), however, reliably reproduce the AFM images of the specific arrangement of GM1 clusters that preferentially assemble in close proximity to Chol clusters (i.e. in the liquid ordered phase of the sarcolemmal membrane). Further, the possible visualization of small GM1 domains (i.e. < 100 nm and thus in the range of the unlabeled GM1 aggregates detected using AFM) also motivates the use of fluorescent CtB as a fluorescent lipid marker that does not necessarily induce additional - and unphysiological - structural clustering. In summary, the two-color STED images of the Chol-KK114 and GM1-CtB-AF594 signal at the sarcolemma of living VM indicate that:

1.) Both Chol and GM1 form spatially closely associated clusters at the sarcolemma of living VM;

2.) The Chol and GM1 clusters show an intra-leaflet registration along the extracellular sarcolemmal leaflet motivating the use of the fluorescent GM1 signal as a marker of analogously shaped Chol rich regions in living VM;

3.) Both Chol and GM1 clusters are highly variable in size ranging from small single domains of about 60 - 70 nm in diameter to variously shaped clusters of up to 1 µm in diameter;

4.) The here observed Chol/GM1 complexes show an arrangement that is very similar to the one reported from AFM studies of GM1 rich assemblies associated to the liquid ordered phase (i.e. Chol rich) in supported lipid bilayers.

In a next step, I investigated the arrangement of Cav-3 and GM1 structures at the sarcolemma of fixed VM that were labeled for Cav-3 and GM1 via indirect immunofluorescence. The antibody coupled dye compound STAR635P was used to label Cav-3 and, like in the two-color stains of Chol and GM1 in living VM, CtB-AF594 was used to label GM1 (see section 2.3.3). Two-color STED images were obtained using the STED microscope Leica TCS SP8 STED 3X (see section 2.1.3). As was the case for the Chol-KK114 and GM1-CtB-AF594 double stains of living VM, the same STED laser at 775 nm could be used for imaging, thus enabling the direct overlay of color channels without post-acquisition image registration. The obtained STED images are shown in Fig. 3.30. When

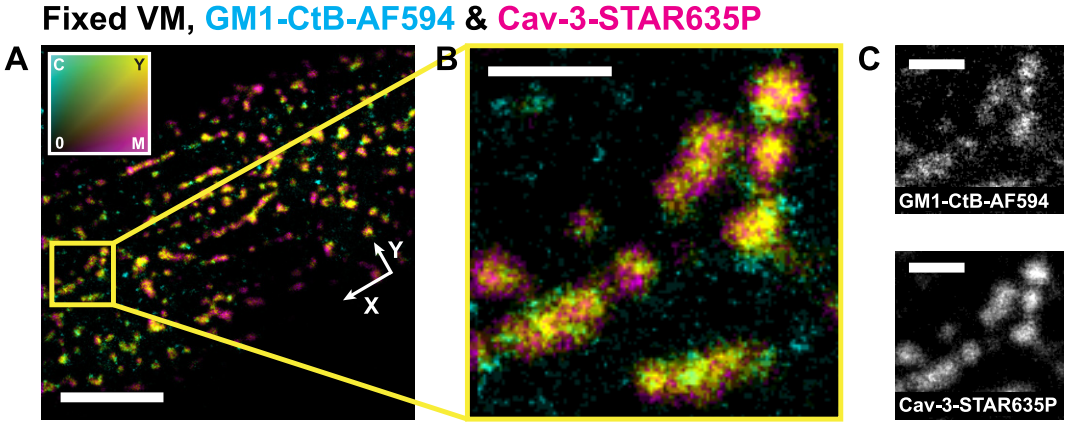

Figure 3.30.: Two-color STED image of a fixed mouse ventricular cardiomyocyte (VM) labeled for Ganglioside GM1 (GM1) via Choleratoxin subunit B coupled to the dye Alexa Fluor 594 (GM1-CtB-AF594) and labeled for Caveolin-3 (Cav-3) via indirect immunofluorescence using the dye STAR635P (Cav-3-STAR635P). VM were stained as described in sections 2.3.3 and 2.3.2. **A** Two-color overview STED image of the VM. The two color channels are color coded with the GM1-CtB-AF594 channel displayed in cyan (C) and the Cav-3-STAR635P channel displayed in magenta (M); yellow signal (Y) indicates signal overlap of the color channels. The corresponding color map is displayed in the top left corner. White arrows indicate the longitudinal (X) and the transverse (Y) cell axes, respectively. Scale bar: 5 µm. **B** Magnification of the STED overview image corresponding to the yellow boxed region. Scale bar: 1 µm. **C** Single color images of the respective GM1-CtB-AF594 and Cav-3-STAR635P signal channels corresponding to the image magnification shown in **B**. Images were smoothed using a two-dimensional Gaussian filter with a width of 1.5 pixels and converted to the displayed color map as described in section 2.6.1. Scale bar: 1 µm

looking at the single color channel images displayed in Fig. 3.30 **C**, the clustering of both the sarcolemmal Cav-3 and GM1 signal becomes obvious. Again, similarly to what has been observed in the double stains using Chol-KK114 and GM1-CtB-AF594 in living VM, the single-color images of immunofluorescently labeled Cav-3 and GM1-CtB-AF594 in fixed VM reveal typical cluster sizes of between 60 - 70 nm up to 1 µm. The smallest respective Cav-3 and GM1 clusters of about 60 - 70 nm diameter are circular and strongly resemble the membrane motif of "single domains" that has been defined for Chol-KK114 and Cav-3

clusters in section 3.5. The larger clusters are of various sizes and shapes, yet, they show an underlying substructure and can be identified as assemblies of single domains. Note also that the general appearance of the GM1 clusters in both living VM and fixed VM is very similar. This serves as a valuable control which confirms that the membrane clustering of GM1 is conserved despite the cell fixation process and therefore supports the assumption that immunofluorescence imaging of GM1 domains in fixed cells can capture the actual physiological composition of the liquid ordered phase at the sarcolemma of living VM. This strengthens the here conducted strategy of relating Chol-KK114 signal structures in living VM with Cav-3 signal structures in fixed VM using the GM1 signal as a mediator. The color channel overlay images in Fig. 3.30 **A** and **B** demonstrate that, analogously to the Chol-KK114/GM1-CtB-AF594 pattern, the Cav-3 and the GM1 signal are always in close proximity and feature an either colocalized or para-localized arrangement. With Cav-3 rich structures residing at the intracellular membrane leaflet and GM1 rich clusters being located at the extracellular leaflet, it can be stated from the here obtained sub-diffraction two-color STED images that Cav-3 and GM1 show an inter-leaflet registration along the cardiac sarcolemma, i.e. there is a specific spatial association between regions facing each other at the intra- and extracellular leaflets. This means that the observation of a GM1 rich region along the extracellular leaflet is likely indicative for a Cav-3 rich region of similar spatial extent at the opposing intracellular leaflet. In summary, the two-color STED images of the Cav-3-STAR635P and GM1-CtB-AF594 signal at the sarcolemma of fixed VM indicate that:

1.) Both Cav-3 and GM1 form spatially closely associated clusters at the sarcolemma of fixed VM;

2.) The Cav-3 and GM1 clusters show an inter-leaflet registration between the extracellular and the opposing intracellular leaflet of the sarcolemma motivating the use of the fluorescent GM1 signal as a marker of analogously shaped Cav-3 rich regions in fixed VM;

3.) Both Cav-3 and GM1 clusters are highly variable in size ranging from small single domains of about 60 - 70 nm diameter to variously shaped clusters of up to 1 µm diameter;

4.) The here observed GM1 clusters (i.e. in fixed VM) are of similar size, shape and substructure as the GM1 clusters observed in living VM and are thus likely to represent the physiological arrangement of GM1 in VM despite the cell fixation process.

The above enumeration was intentionally structured in accordance with the enumeration for the conclusions drawn from the two-color STED images of simultaneously labeled Chol and GM1 clusters in living VM. That way, a direct comparison of the results obtained from the two experimental schemes, i.e. Chol/GM1 STED imaging in living VM vs. Cav-3/GM1 STED imaging in fixed VM, is possible. It reveals the profound similarity of the structure and the specific relationship of Chol and GM1 clusters in living VM, and Cav-3 and GM1 clusters in fixed VM.
All in all, the here presented two-color STED images of sarcolemmal Chol-KK114 and GM1 clusters in living VM and of sarcolemmal Cav-3 and GM1 clusters in fixed VM reveal a very distinct mosaic-like nanopattern of membrane constituents belonging to the liquid ordered phase. This nanopattern was shown here for the first time using subdiffraction optical microscopy. Chol-KK114 and GM1 clusters in living VM show an intra-leaflet registration while Cav-3 and GM1 clusters in fixed VM show an inter-leaflet registration. Fluorescently labeled GM1 is a highly potent marker of Chol rich regions at the extracellular membrane leaflet in living VM and, likewise, a highly potent marker of Cav-3 rich regions at the intracellular membrane leaflet in fixed VM. This further supports the possible application of Chol-KK114 as a direct marker of caveolae in living VM.
In addition to the mostly qualitative conclusions drawn from the two-color STED images of cardiac membrane lipid and membrane protein domains that were presented in the last paragraphs, the spatial association of Chol and GM1 clusters in living VM, and Cav-3 and GM1 clusters in fixed VM was quantitatively characterized and evaluated. To this end, I developed a protocol for the colocalization analysis of these clusters. It evaluates the relative overlap of the signal from corresponding single-color channel STED images after image binarization via pixel based thresholding (see section 2.7). A conceptually similar overlap based colocalization analysis procedure has been presented by *Lachmanovich et al.* [553]. This approach was initially developed for the analysis

of antibody-mediated protein "co-patching" experiments based on diffraction limited fluorescence microscopy images (cf [91, 554, 555, 556]). In these experiments, signal clusters are typically assumed to be homogeneous and not possessing any sophisticated substructures. Further, the determination of the degree of colocalization is based on the coincidence of the center of mass of a cluster from one population and the area occupied by a cluster from the other population. Thus, the algorithms employed by *Lachmanovich et al.* for image binarization use *ab initio* input parameters such as the estimated patch (i.e. cluster) size which cannot be readily determined for STED images since here, the possibility of resolving clusters of subdiffractional size that form higher-order cluster superstructures render the average cluster size an imprecise figure. Hence, to adequately treat and analyze the here obtained two-color STED images, I employed an image thresholding procedure relying on the relative signal intensity of each defined pixel and its close proximity. The thus binarized images of corresponding single-color channels were overlaid and the number of overlapping pixels was determined and evaluated in relation to the total number of pixels belonging to the signal in the binary single color image. This resulted in the abstracted display of the mosaic-like arrangement of Chol clusters (or Cav-3 clusters) and GM1 clusters at the cardiac sarcolemma. In these abstract membrane lipid and membrane protein mosaics, four distinct membrane areas were thus clearly distinguishable: 1.) membrane areas only containing Chol-KK114 or Cav-3 signal; 2.) membrane areas containing only GM1 signal; 3.) membrane areas containing both Chol-KK114 (or Cav-3) signal and GM1 signal; 4.) membrane areas devoid of any Chol-KK114, Cav-3 or GM1 signal. The obtained membrane lipid and membrane protein mosaics are displayed in Fig. 3.31 together with a bar graph representation of the relative colocalization of respective clusters that were determined as described in section 2.7 and which are discussed in the following. In the image overlays in Fig. 3.31 **A** and **B**, the mosaic-like arrangement of the sarcolemmal Chol and GM1 clusters in living VM, and of the Cav-3 and GM1 clusters in fixed VM is respectively visualized. Therein, the Chol and Cav-3 signal is displayed in magenta, the GM1 signal is displayed in cyan and spatial overlap of the signal from the two different color channels is displayed in yellow. In course of the image binarization, thresholding and the overlap based image analysis, the sarcolemmal signal density of

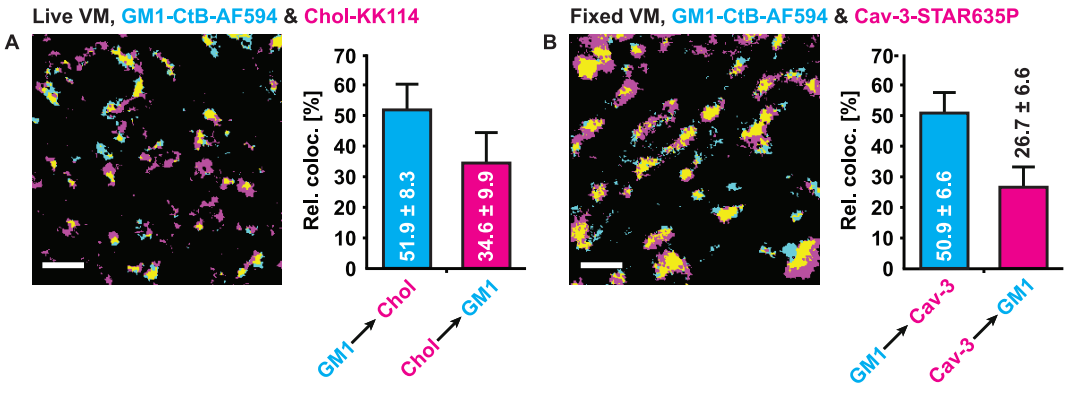

Figure 3.31.: Colocalization analysis of sarcolemmal GM1 and Chol-KK114 clusters in living VM as well as GM1 and Cav-3 clusters in fixed VM. Living VM were dual-labeled for Ganglioside GM1 (GM1) via labeled CtB-AF594 coupled to the dye Alexa Fluor 594 (GM1-CtB-AF594) and with Chol-KK114 (see section 2.3.2). Fixed VM were dual-labeled for GM1 (via GM1-CtB-AF594) and for Cav-3 via indirect immunofluorescence using the dye STAR635P (Cav-3-STAR635P) (see section 2.3.3). STED images of the respectively labeled VM samples were binarized and the colocalization of signal structures was analyzed as described in section 2.7. **A** Binarized STED image of the sarcolemma of a living VM dual-labeled with GM1-CtB-AF594 (in cyan) and with Chol-KK114 (in magenta); the signal overlap is displayed in yellow. Bar graph representation of the relative colocalization (Rel. col., in % of the total signal of the respective color channel) of GM1 clusters with Chol clusters (GM1 → Chol) and of Chol clusters with GM1 clusters (Chol → GM1). **B** Binarized STED image of the sarcolemma of a living VM dual-labeled with GM1-CtB-AF594 (in cyan) and with Cav-3-STAR635P (in magenta); the signal overlap is displayed in yellow. Bar graph representation of the relative colocalization of GM1 clusters with Cav-3 clusters (GM1 → Cav-3) and of Cav-3 clusters with GM1 clusters (Cav-3 → GM1). The relative colocalization is presented as mean ± standard deviation. Number of analyzed cells: GM1-Chol double stains - 38; GM1-Cav-3 double stains - 47. Scale bars: 1 µm.

the Chol and Cav-3 signal structures was respectively determined as a control and was found to match the signal densities obtained from the respective single color samples (i.e. living VM exclusively labeled with Chol-KK114 as well as fixed VM exclusively labeled via Cav-3-STAR635P as presented in sections 3.3 and 3.5). The sarcolemmal signal density of the Chol signal was determined to be about 14 % (cf. $\approx$ 17 % in living VM samples single-labeled with Chol-KK114, see section 3.3) and the sarcolemmal density of the Cav-3 signal was determined to be about 22 % (cf. $\approx$ 24 % in fixed VM samples single-labeled via Cav-3-STAR635P, see section 3.5). Likewise, the sarcolemmal signal density of the GM1 signal was determined for both the living VM samples (i.e. when dual-labeling with Chol-KK114 and via GM1-CtB-AF594) and for the fixed VM samples (i.e. when dual-labeling via Cav-3-STAR635P and GM1-CtB-AF594). My expectation was to find approximately the same GM1 signal density for the living as well as for the fixed VM samples. There was, however, a minor difference between the determined mean sarcolemmal GM1 signal densities that laid just outside the respective error margins: in living VM (double-stain with Chol-KK114), the GM1 signal density amounted to about 7 $\pm$ 2 % while in

fixed VM (double-stain with Cav-3-STAR635P), it was determined to be about 11 ± 2 %. This slight discrepancy could be attributable to the process of cell fixation and permeabilization which might cause minor and so far unknown imaging artifacts. Further, the addition of the primary antibody against Cav-3 could induce additional cross-linking of GM1 molecules and thus increase the GM1 cluster size and eventually their fluorescence brightness directly manifesting itself in the recorded images and the ensuing analysis steps that were based on relative pixel brightness. However, the mentioned difference in GM1 signal densities found in living vs. fixed VM samples was merely marginal and very likely not profound enough to influence the performed determination of the relative colocalization of signal clusters. The relative colocalization of Chol-KK114 clusters with GM1 clusters (and vice versa) and of Cav-3 clusters with GM1 clusters (and vice versa) was determined as described in section 2.7. At the sarcolemma of living VM, the relative colocalization of Chol clusters with GM1 clusters was determined to be about 34.6 % while the relative colocalization of GM1 clusters with Chol clusters amounts to about 51.9 %. This means that about one third of all Chol-KK114 clusters is spatially associated with GM1 clusters while more than half of all GM1 clusters is associated with Chol-KK114 clusters. At the sarcolemma of fixed VM, the relative colocalization of Cav-3 clusters with GM1 clusters is found to be about 26.7 % and the relative colocalization of GM1 clusters with Cav-3 clusters is at about 50.9 %, meaning that while roughly only one quarter of all Cav-3 clusters colocalize with GM1 clusters, half of all GM1 clusters are spatially associated with Cav-3 clusters.

Comparing these relations between sarcolemmal Chol and GM1 clusters in living VM and sarcolemmal and Cav-3 and GM1 clusters in fixed VM, it can be seen that a profound amount of GM1 colocalizes with Chol or Cav-3, respectively. Thus, with a 50 % probability, one would find a Chol (or Cav-3) signal where there is a GM1 signal. Considering that the determination of the relative colocalization is based on the pixel-by-pixel comparison of the signal distribution from the two color channels, it is a rather strict approach and gives a potential lower limit for the degree of colocalization between, in this case, GM1 and Chol (or Cav-3). The GM1 signal can thus arguably be used as a reporter for colocalized or spatially associated Chol or Cav-3 signal. In conjunction with

the observation that the spatial relation between Chol and GM1 and the spatial relation between Cav-3 and GM1 share similar features, the use of GM1 as a reporter matching the live VM Chol signal with the fixed VM Cav-3 signal is an arguably valid approach - at least for qualitative and comparative investigations. In any case, here, I could show that there exists a specific type of sarcolemmal nanodomain that is enriched in Chol, GM1, and Cav-3 and which is heterogeneously distributed across the cardiac membrane.

Concluding, Cav-3 and Chol both share a similar spatial arrangement with respect to GM1. Since Chol and Cav-3 are associated to the same membrane domains as GM1, it is thus probable, that Chol and Cav-3 also reside in the same sarcolemmal domains. The use of Chol-KK114 to stain sarcolemmal Chol rich clusters could hence be a strategy to label Cav-3 clusters in living VM without having to establish a transgenic mouse line that expresses a fluorescent Cav-3 analog. Accordingly, the Cav-3 signal in fixed VM could be used to indicate Chol rich sarcolemmal regions and relate them to other membrane associated proteins to determine their spatial orientation along the sarcolemma and their dependence on the sarcolemmal Chol content. The next section will take such an approach to study the positioning of the protein Dystrophin (Dyst, see section 1.1.4) along the sarcolemma with respect to Cav-3 and depending on the membrane Chol abundance.

3.7. Association of sarcolemmal Caveolin-3 and Dystrophin domains at the sarcolemma of cardiomyocytes

Based on the cardiac membrane model that was proposed in section 1.4, this section will elucidate the association between the membrane associated protein Caveolin-3 (Cav-3) and the cytoskeletal protein Dystrophin (Dyst). To this end, one-, two- and three-color STED images of immunofluorescently labeled mouse ventricular cardiomyocytes (VM) will be analyzed to extract the mutual spatial arrangement of sarcolemmal Dyst and Cav-3 signal structures. The effect of Cholesterol (Chol) depletion on the sarcolemmal Dyst/Cav-3 arrangement will be investigated. Further, the molecular orientation of Dyst and Cav-

3, and of the entire Dyst protein at the sarcolemma will be studied. For this, Dyst was simultaneously fluorescently labeled using different primary antibodies that target specific protein domains.

In a first step, for the visualization and quantification of the sarcolemmal Dyst arrangement, VM were stained via indirect immunofluorescence (see section 2.3.3) using the primary antibody ab7163 which recognizes the amino acids (aa) $\approx$ 1400-1505, i.e. the central rod domain. Fig. 3.32 **A** shows an exemplary STED images of the obtained VM samples. The sarcolemmal Dyst signal pattern is highly clustered and reproduces the three distinct membrane motifs that have already been described for Chol and Cav-3 at the sarcolemma: 1.) single domains, 2.) ring structures, and 3.) bunchy clusters of various sizes. Ring structures and bunchy clusters could be identified as higher-order arrangements of individual single clusters; ring structures were typically composed of 5 ± 2 single clusters (data not shown). Quantitative analysis of the diameters of single domains and ring structures (see sections 2.6.5 and 2.6.6) reveals that single sarcolemmal Dyst domains have an average diameter of about 67 nm, while ring structures have an average diameter of about 211 nm. In Fig. 3.32 **B**, the obtained values for single domain diameters and ring structure diameters are compared between the Dyst and the Cav-3 signal (see also section 3.5). There is no significant difference between the single domain sizes for Dyst vs. Cav-3. For the Cav-3 single domains, it can be assumed that they correspond to single caveolae, i.e. assemblies of up to 200 Cav-3 molecules. For the Dyst single domains, however, since the Dyst protein has an estimated contour length of about 150 nm, the single domains probably correspond to individual Dyst molecules or to Dyst clusters that are attached via their rod domains. The sarcolemmal Dyst pattern shown in Fig. 3.32 **A** thus corresponds to the spatial arrangement of the Dyst rod domain.
The diameter of the sarcolemmal ring structures was found to be 211 nm for Dyst and 253 nm for Cav-3. The statistical difference between the ring structure diameters of the two protein signals was very significant. This could on the one hand be due to the size of the specific antibodies used for labeling Dyst and Cav-3. On the other hand, this difference in size could be indicative for the specific mutual arrangement of Dyst and Cav-3 (i.e. caveolae) along the cardiac sarcolemma. The findings of the structural similarities of the Dyst and

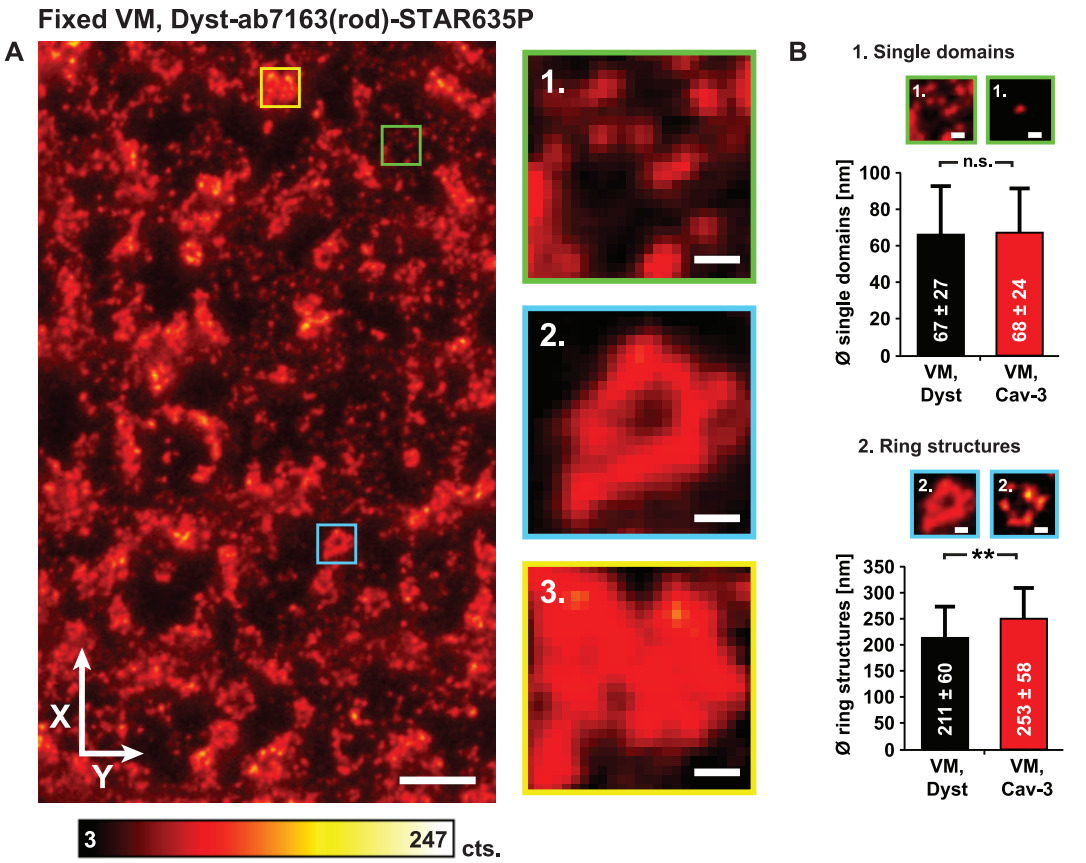

Figure 3.32.: STED image of the Dystrophin (Dyst) signal pattern at the sarcolemma of a fixed mouse ventricular cardiomyocyte (VM) and quantitative analysis of Dyst vs. Caveolin-3 (Cav-3) membrane motifs. **A** STED image of fixed VM labeled for Dyst via indirect immunofluorescence using the primary antibody ab7163 targeting the Dyst rod domain (see section 2.3.3 and Appendix A.3, and the antibody-coupled fluorescent dye Abberior STAR635P (see Appendix A.4). Image magnifications are indicated by the colored boxes and show the three reoccurring sarcolemmal Dyst pattern motifs: 1. single domains, 2. ring structures, and 3. bunchy clusters. **B** Bar graph representation of the quantification of the diameter ⌀ of single domains and ring structures, respectively, of the sarcolemmal Dyst signal compared to the corresponding Cav-3 membrane motifs (see section 3.5). Statistical significance was tested as described in section 2.9 with the explicit parameters of the statistical test given in Appendix I, Tables I.12 and I.13, and is denoted as: (n.s.) - not significant ($p > 0.01$) and (**) - very significant ($p < 0.001$). Number of analyzed single domains for diameter determination: 2947 (Dyst), 2397 (Cav-3). Number of analyzed ring structures for diameter determination: 121 (Dyst), 80 (Cav-3). White arrows indicate the longitudinal (X) and the transverse (Y) cell axes. Images were smoothed using a two-dimensional Gaussian filter with a width of 1.5 pixels. The color bar indicates the image brightness in measured photon counts (cts.). Scale bar in overview image: 1 µm; scale bar in magnifications: 100 nm.

the Cav-3 - and also the Chol - signal pattern led to the question if Dyst and Cav-3 are associated to the same sarcolemmal nanodomains.

To investigate the mutual spatial arrangement of Dyst and Cav-3, two-color STED images of VM labeled fo Dyst and Cav-3 via indirect immunofluorescence were acquired and are presented in Fig. 3.33. Regions of both colocalization and para-localization of Dyst and Cav-3 clusters were observed. Further, there were Dyst single domains that were remote from Cav-3 signal and

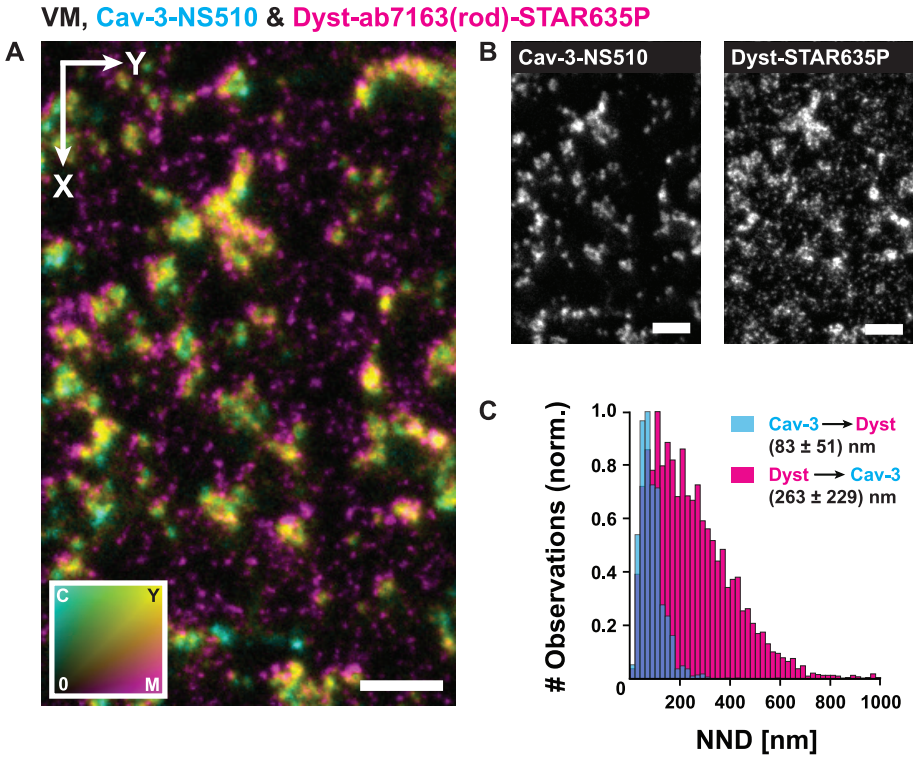

Figure 3.33.: Two-color STED image of Dystrophin (Dyst) and Caveolin-3 (Cav-3) at the sarcolemma of a fixed mouse ventricular cardiomyocyte (VM) and quantification of the peak-to-peak nearest neighbor distance (NND) between Dyst and Cav-3 (and vice versa). Primary antibodies against Dyst (ab7163) and Cav-3 were decorated with the fluorescent dye compounds Abberior STAR635P and NS510, respectively (see also Appendix A.3 and A.4). **A** Two-color STED image of the sarcolemmal Dyst and Cav-3 signal color coded in magenta and cyan, respectively. Yellow signal indicates signal overlap. **B** Single color channel images corresponding to the overlay in **A**. **C** Bar graph representation of the normalized distribution of the peak-to-peak nearest neighbor distance (NND) between Dyst and Cav-3 signal structures (in magenta), and the Cav-3 and Dyst signal structures (in cyan). The purple shaded regions of the bar graph representation indicate overlap of the respective NND data. NNDs were determined as described in section 2.8, are given in nm and are presented as mean ± standard deviation. Images were smoothed using a two-dimensional Gaussian filter with a width of 1.5 pixels and converted to the displayed color map as described in section 2.6.1. White arrows indicate the longitudinal (X) and the transverse (Y) cell axes. Scale bars: 1 µm.

seemed to be unassociated with it. Bunchy clusters of Dyst always colocalized or para-localized with Cav-3 clusters. The majority of the Cav-3 signal (single domains, rings and bunchy clusters) colocalized or para-localized with Dyst structures. The two-color STED images thus reveal that while almost every Cav-3 signal cluster is in close proximity to a Dyst signal structure, there are two distinct populations of Dyst: one population in the vicinity of Cav-3 signal and one population remote from Cav-3 signal. The population that is spatially associated with Cav-3 consists mostly of assemblies of single domains of Dyst signal. The population that is not associated with Cav-3 consists mostly of single Dyst domains. To quantify this distinct distribution of the sarcolemmal Dyst and Cav-3 pattern, I determined the peak-to-peak nearest neighbor dis-

tances (NND) between Dyst and Cav-3 signal structures and vice versa. NNDs were determined as described in section 2.8. The obtained results are graphically displayed Fig. 3.33 **C**. The average NND between a Cav-3 signal peak and a Dyst signal peak amounts to about (83 $\pm$ 51) nm. This very well describes the observations made from the two-color STED image in Fig. 3.33 **A**: Cav-3 structures either colocalize with Dyst within the limits of the achievable maximum resolution of the microscope or they are in close proximity to Dyst - not further away than about 130 nm which would still lie within the approximate length of the Dyst molecule and could thus still be considered a distance in which direct molecular interactions would be possible. On the other hand, the average NND between a Dyst signal peak and a Cav-3 signal peak amounts to (263 $\pm$ 229) nm, i.e. the NND is very broadly distributed. This also captures the observations made from Fig. 3.33 **A**: there exist both Dyst structures closely associated to Cav-3 structures as well as Dyst structures far away from the next Cav-3 signal, in part much further away than the approximate length of a Dyst molecule. Hence, there is a large population of Dyst molecules for which, based on spatial association, a direct interaction with Cav-3 is not to be expected. In summary, it can be stated that while every Cav-3 signal at the sarcolemma has a neighboring Dyst signal in close proximity, not every Dyst structure is spatially associated with a Cav-3 structure. This is in contrast to the observations made by *McNally et al.* in 1998 [204] who found that in skeletal muscle, there is one fraction of Cav-3 that co-purifies with Dyst, while another does not. They concluded that Cav-3 is not exclusively associated with Dyst. Note that in their studies *McNally et al.* were considering both the sarcolemmal and the intracellular Cav-3, i.e. also newly expressed protein that would still be associated to the Golgi apparatus and would not yet have been recruited to the sarcolemma. In the image based studies in this thesis, the Dyst signal inside cardiomyocytes was found to be very low, almost not present (data not shown). This might explain the Cav-3 fraction that is not associated with Dyst. Of course, it has to be kept in mind that in the here shown STED images, a small fraction of sarcolemmal Cav-3 that was not spatially associated with Dyst could also be identified. Generally, however, the obtained data from two-color STED images of sarcolemmal Dyst and Cav-3 structures in VM show that the majority of Cav-3 clusters is closely associated with Dyst. And, refining this

statement: since the antibody ab7163 was used in this two-color imaging protocol, the data suggest that the spatial association caveolae and Dyst can be localized to the central rod domain of the Dyst protein.
To further investigate the association of sarcolemmal Cav-3 and Dyst signal patterns, more precisely: whether the alteration of caveolar integrity changes the Dyst pattern or the mutual arrangement of Cav-3 and Dyst structures, VM were depleted of membrane Chol by treatment with Methyl-β-Cyclodextrin as described in section 2.3.3 (see also section 3.5.1). Chol depleted VM were labeled for Dyst and Cav-3 and two-color STED images of the samples were acquired. The results are presented in the next section.

3.7.1. Cholesterol depletion alters the mutual sarcolemmal Dystrophin/Caveolin-3 association

Chol depletion disrupts caveolae and thus selectively alters the spatial distribution of Cav-3 clusters at the sarcolemma (see section 3.5.1). In section 3.7, the similarities between the sarcolemmal Dyst and Cav-3 nanopatterns and their partial spatial overlap have been shown. It was hence of great interest to know if the depletion of membrane Chol would alter the sarcolemmal Dyst structure. Since for immunofluorescence labeling of Dyst the primary antibody ab7163 targeting the Dyst central rod domain was used (see also Appendix A.3), the two possible effects of Chol depletion on the Dyst nanopattern could be hypothesized to have the following implications: a) If Chol depletion led to a dissociation of higher order Dyst arrangements, then a close spatial association between the Dyst central rod domain and sarcolemmal caveolae would be expected, i.e. only few intermediate proteins should be assumed to be involved in the mediation of the Dyst–Cav-3 interaction. b) If Chol depletion had no effect on the sarcolemmal Dyst nanopattern, then a more or less direct interaction between Dyst and caveolae cannot be assumed - at least not at the site of the Dyst central rod domain.
STED images of control and Chol depleted VM labeled for both Dyst and Cav-3 are presented in Fig. 3.34 **A** and **B**.
While the dissociation of sarcolemmal Cav-3 clusters in Chol depleted VM - as it has also been shown in section 3.5.1, Fig. 3.27 - is clearly visible, Chol depletion has no distinct effect on the sarcolemmal Dyst pattern. However, the

dissociation and redistribution of the Cav-3 clusters leads to an altered spatial association between Cav-3 and Dyst signal structures. With the Cav-3 single domains (i.e. potential single caveolae) being more isotropically distributed in Chol depleted VM, the population of Dyst single domains that in control VM is remote from Cav-3 signal structures (see section 3.7) is lost. There is a profound decrease in the distance between Dyst and Cav-3. I could quantify this effect in two ways: by determining the peak-to-peak nearest neighbor distances (NND) between Dyst and Cav-3 signals (and vice versa), and by evaluation of the relative colocalization of Cav-3 with Dyst (and vice versa). Fig. 3.34 **C** shows a comparison between the respective distributions of the peak-to-peak NND between the Cav-3 and the Dyst signals, and between the Dyst and the Cav-3 signals for control vs. Chol depleted VM. NNDs were determined as described in section 2.8, the bar graph representation of the NND for control cells in Fig. 3.34 **C** is a reproduction of Fig. 3.33 **C**. Upon Chol depletion, the NND between the Cav-3 and the Dyst signal increases only slightly regarding mean and standard deviation: from (83 $\pm$ 51) nm in control VM to (89 $\pm$ 59) nm in Chol depleted VM. However, the NND between the Dyst and the Cav-3 signal changes dramatically upon Chol depletion, decreasing profoundly regarding both mean and standard deviation: from (263 $\pm$ 229) nm to (134 $\pm$ 89). Thus, the average NND decreases by a factor of about two, while the standard deviation of the NND decreases by a factor of about 2.5. Another more global figure confirming the increase in proximity between Dyst and Cav-3 signals is the relative colocalization of Cav-3 signal with Dyst signal and vice versa in the two cases of control vs. Chol depleted VM. The relative colocalization was determined after image binarization as described in section 2.7 and is displayed in Fig. 3.34 **D**. The relative colocalization indicates which fraction of the total signal of one species (i.e. Dyst or Cav-3) directly colocalizes with the other species based on the comparison of the pixel values of the binarized images from the two color channels. As can be seen from Fig. 3.34 **D**, about 30 % of the total Cav-3 signal maps 1:1 to the Dyst signal - a ratio which is basically constant between control and Chol depleted VM. On the other hand, only 7 % of the total Dyst signal maps to a coinciding Cav-3 signal in control cells, yet this ratio changes by a factor of 2 in Chol depleted VM where about 15 % of the total Dyst signal colocalizes with Cav-3 signal. The here shown decrease

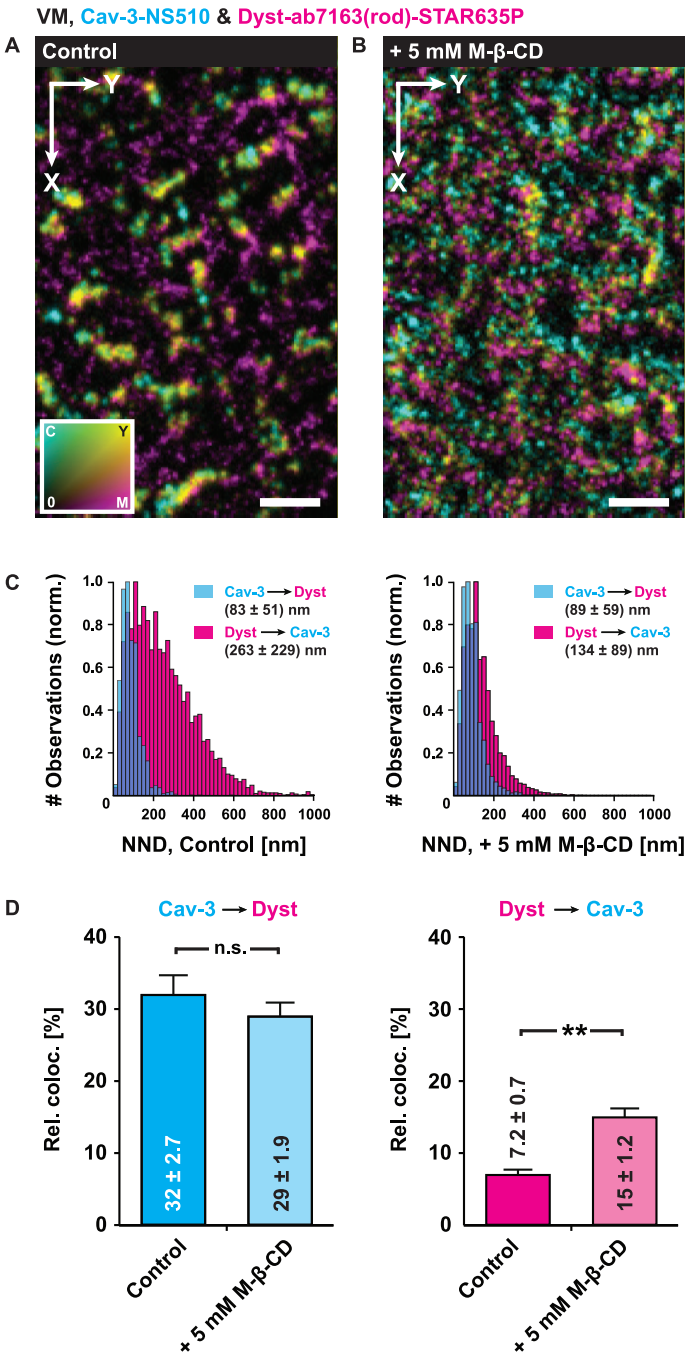

Figure 3.34.: Effect of Cholesterol (Chol) depletion on the spatial association of sarcolemmal Dystrophin (Dyst) and Caveolin-3 (Cav-3) signal structures. VM were fluorescently labeled as described in section 2.3.3; Dyst was labeled using the primary antibody ab7163 targeting the Dyst rod domain (see section A.3). Chol depletion was performed by treatment of VM with 5 mM Methyl-β-CycloDextrin (M-β-CD, see section 2.3.3). **A** STED image of Dyst and Cav-3 signal at the sarcolemma of control VM. **B** STED image of Dyst and Cav-3 signal at the sarcolemma of Chol depleted VM. **C** Bar graph representation of the normalized distribution of the peak-to-peak nearest neighbor distance (NND) between Dyst and Cav-3 signal structures (please refer to Fig. 3.33 **C** for a more detailed description). **D** Bar graph representation of the relative colocalization (rel. coloc.) of Dyst and Cav-3 signal structures (please refer to the main text of section 3.7.1 for a more detailed description). Statistical significance was tested as described in section 2.9 with the explicit parameters of the statistical test given in Appendix I, Tables I.14 and I.15, and is denoted as: (n.s.) - not significant ($p > 0.01$) and (**) - very significant ($p < 0.001$). Number of analyzed cells: 57 (Control); 41 (+ 5 mM M-β-CD). Images were smoothed using a two-dimensional Gaussian filter with a width of 1.5 pixels and converted to the displayed color map as described in section 2.6.1. The image color map is displayed in **A**: Dyst signal is displayed in magenta; Cav-3 signal is displayed in cyan; signal overlap is indicated in yellow. White arrows indicate the longitudinal (X) and the transverse (Y) cell axes, respectively. Scale bars: 500 nm.

in the mean and standard deviation of the NND between Dyst and Cav-3 signals (while the mean and standard deviation of the NND between Cav-3 and Dyst signal stays roughly constant) as well as the increase of the relative colocalization of Dyst signal with Cav-3 signal (while the relative colocalization of the Cav-3 signal with the Dyst signal stays roughly constant) reflect the two structural changes that are obvious from the STED images in Fig. 3.34 **A** and **B**: 1.) Dyst and Cav-3 move closer together (with the Cav-3 signal actually approaching the Dyst signal) and 2.) a clear distinction between single Dyst domains in close proximity to or remote from Cav-3 clusters can no longer be made. Not that the changes in the mutual arrangement of Dyst and Cav-3 both arise from the dispersion of caveolae across the sarcolemma. The sarcolemmal Dyst pattern is not directly altered.

Concluding, the absence of an effect of Chol depletion on the sarcolemmal Dyst distribution indicates that there is no direct spatial association between the Dyst central rod domain and sarcolemmal caveolae. However, the nominal increase of Dyst and Cav-3 structures that are in close proximity may have functional consequences. These consequences may include additional attachment of the Dyst rod domain to sarcolemmal caveolae, potentially mediated by several intermediate proteins. This might result in an additional stabilization between the myofibrils and the sarcolemma but also to a loss in flexibility of the Dyst molecule.

The potential lack of a direct connection between caveolae and the Dyst central rod domain led to the question about the actual orientation of the Dyst molecule with respect to Cav-3 and, generally, with respect to the sarcolemma. An attempt to elucidate this question is made in the next section.

3.8. Molecular orientation of Dystrophin and Caveolin-3 at the cardiac sarcolemma

As mentioned in section 1.1.4, the Dyst protein has an estimated contour length of about 150 nm. Using subdiffraction STED imaging with a standard lateral resolution of about 40 nm should allow to resolve different domains along the protein when labeling them with different fluorescent dyes.

In order to be able to 1.) identify and characterize the spatial association be-

tween Cav-3 and different domains of the Dyst protein and 2.) simultaneously label different domains of the Dyst protein in a multicolor immunofluorescence assay and thus investigate the molecular orientation of the Dyst protein along the sarcolemma using STED microscopy, I tested a set of different anti-Dyst primary antibodies targeting specific epitopes. Fig. 3.35 gives an overview of these tested primary antibodies and the approximate epitopes to which they bind. Detailed information about the antibodies, including host species and order information, can be found in Appendix A.3.

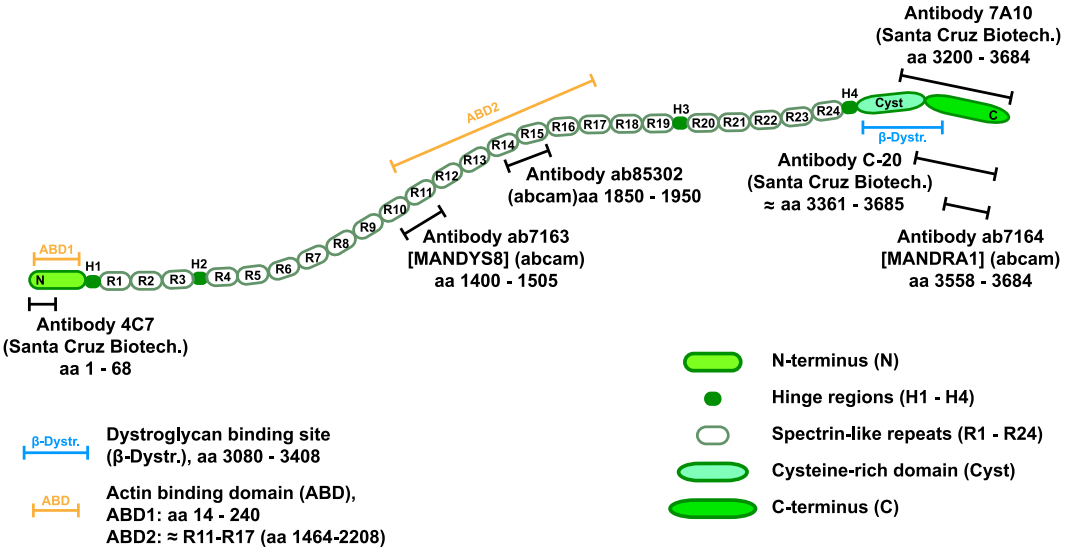

Figure 3.35.: Schematic depiction of the Dystrophin (Dyst) protein and a selection of commercially available primary antibodies and the epitopes they are binding to. These antibodies were tested in this thesis (see also Appendix N). Antibody name, distributor, and the approximate amino acid (aa) sequence of the targeted protein epitope are shown. For a description of the Dyst protein structure, please refer to section 1.1.4. Information about all tested primary antibodies can be found in Appendix A.3.

I chose the following three antibodies for use in this thesis:

1.) 4C7 (host species: mouse), targeting the Dyst N-terminus (≈ aa 1-68),

2.) ab85302 (host species: rabbit), targeting the Dyst central rod domain (≈ aa 1850-1950),

3.) C-20 (host species: goat), targeting the Dyst C-terminus (≈ aa 3361-3685).

I made this choice because these three antibodies - derived from three different host species and targeting three different protein domains - would eventually allow three-color immunofluorescence staining of the Dyst protein, i.e. intra-protein labeling and imaging (see section 3.9).

To control for the labeling specificity of the antibodies, I prepared single-color immunofluorescence samples of VM from control mice, i.e. from the wild type C57BL/6N strain, and from Dyst deficient mice, i.e. from the *mdx 5cv* strain (see section 2.3.4), using each of the three chosen antibodies. I imaged these samples in the region of the sarcolemma using STED microscopy. The used primary antibodies were decorated with different fluorescent dye compounds (coupled to a secondary antibody): 4C7 was decorated with the dye compound STAR635P, ab85302 was decorated with the dye compound NS510, and C-20 was decorated with the dye compound STAR580. I chose this set of fluorescent dyes because of their favorable spectral properties for the three-color STED imaging protocol using only one STED wavelength (three-color images are shown and discussed in section 3.9). For detailed information about primary antibodies, secondary antibodies, and the used dye compounds, please refer to Appendix A.3 and Appendix A.4.

So, what is to be expected from the prepared control samples? An antibody that specifically labels Dyst would not yield a fluorescence signal in VM of the dystrophic *mdx 5cv* mice while it would yield a fluorescence signal in control mice. Fig. 3.36 summarizes the obtained STED images of these samples.

For the primary antibodies ab85302 (central rod domain, see Fig. 3.36 **A**) and C-20 (C-terminus, see Fig. 3.36 **B**), the expected fluorescence signal was observed: little to no sarcolemmal signal in VM of *mdx 5cv* mice and a distinct sarcolemmal signal pattern in VM of control mice. For the primary antibody 4C7 (N-terminus, see Fig. 3.36 **C**), however, a characteristic signal can be observed in VM of both *mdx 5cv* and control mice. The observed signal pattern shows a dotted structure but also lines along the transverse cell axis. These lines are evenly spaced at a distance of about 2.1 µm in control VM and at a slightly shorter distance of about 1.8 µm in *mdx 5cv* VM. The striped signal pattern hence strongly resembles that of costameres - protein assemblies characteristic for striated muscle cells. Costameres are adjacent and parallel to the Z-lines and comprise protein assemblies that connect the sarcomeres to the sarcolemma [557, 558]. When taking a closer look at the *mdx 5cv* mouse model the signal similarity to the control mouse strain can be explained. The *mdx 5cv* mouse model was introduced by *Chapman et al.* in 1989 [288] and was generated via an N-ethylnitrosourea (ENU) chemical mutagenesis. This muta-

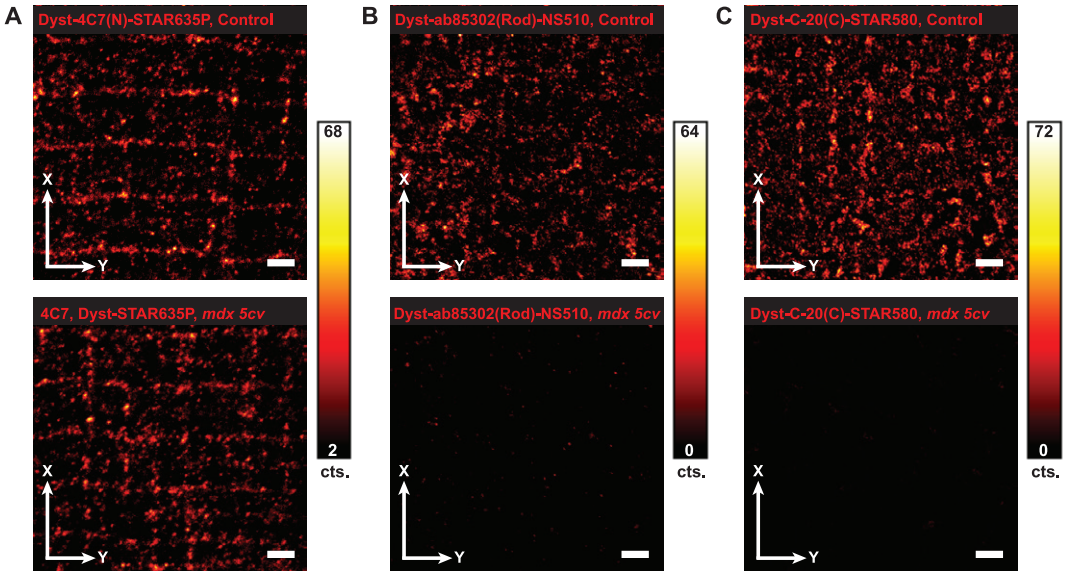

Figure 3.36.: STED images of VM from control (wild type C57BL/6N) vs. *mdx 5cv* mice labeled each with one of the three antibodies 4C7, ab85302, or C-20. Please refer to Appendix A.3 and Appendix A.4 for detailed information about the used antibodies and fluorescent dye compounds. **A** STED images of VM from control (top) vs. *mdx 5cv* (bottom) mice immunofluorescence labeled with the primary antibody 4C7 targeting the N-terminus (N) of the Dyst protein. The primary antibody was decorated with the dye compound STAR635P. **B** STED images of VM from control (top) vs. *mdx 5cv* (bottom) mice immunofluorescence labeled with the primary antibody ab85302 targeting the central rod domain (Rod) of the Dyst protein. The primary antibody was decorated with the dye compound NS510. **C** STED images of VM from control (top) vs. *mdx 5cv* (bottom) mice immunofluorescence labeled with the primary antibody C-20 targeting the C-terminus (C) of the Dyst protein. The primary antibody was decorated with the dye compound STAR580. Images were smoothed using a two-dimensional Gaussian filter with a width of 1.5 pixels. Color bars indicate the respective image brightness in photon counts (cts.). White arrows indicate the longitudinal (X) and transverse (Y) cell axes, respectively. Scale bars: 1 µm.

genesis causes the Dyst protein synthesis to stop at base 1416 of the full length wild type Dyst [559]. The remaining truncated Dyst "stump" comprises aa 1-381 and has a molecular weight of $\approx$ 43.7 kDa. Since the N-terminal F-Actin binding domain of Dyst protein is assumed to be located along aa 14-240 (see section 1.1.4 and Fig. 3.35), the expressed truncated Dyst is still attached to the costamere by binding F-Actin. The observed signal pattern of the primary antibody 4C7 in VM of *mdx 5cv* is hence to be expected and confirms the specificity of the antibody for the Dyst N-terminus.

In summary, it can be stated that, although the primary antibody 4C7 yields a fluorescence signal in VM of both control and *mdx 5cv* mice, the antibody still shows very high specificity because it reproduces the expected costamere regularity. All three here chosen anti-Dyst primary antibody are thus specific and suitable for fluorescence labeling of distinct Dyst protein domains.

Being equipped with three specific primary antibodies that respectively target the N-terminus, the central rod domain, and the C-terminus of the Dyst pro-

tein, I prepared VM samples dual-labeled for Cav-3 and one of the three Dyst protein regions. Hence, in order to investigate the spatial association between Cav-3 and different domains of the Dyst protein, I could compare two-color STED images of the following three combinations:

1.) Cav-3 and the Dyst N-terminus (N),

2.) Cav-3 and the Dyst central rod domain (Rod),

3.) Cav-3 and the Dyst C-terminus (C).

For reasons of comparability, the anti-Cav-3 primary antibody was always decorated with the dye compound STAR580 and the used anti-Dyst primary antibody was always decorated with the dye compound STAR635P. In Fig. 3.37, STED images of each of the above combinations are shown. The Cav-3 color channel is displayed in cyan, the respective Dyst color channel is displayed in magenta, and overlap of the two color channels is indicated by yellow signal.
For all three two-color combinations (see Fig. 3.37 **B**, **D**, and **F**), both the Cav-3 and the Dyst signal stemming from the particular protein regions show the familiar sarcolemmal structures of single domains and bunchy clusters (see e.g. Fig. 3.22 and Fig. 3.32).
Fig. 3.37 **B** displays the overlay image of the sarcolemmal Cav-3 signal with the sarcolemmal signal of the N-terminus (N) of the Dyst protein that was labeled using the antibody 4C7. The distinct Dyst N-terminal signal resembling the costameres which had already been shown in the antibody control stains displayed in Fig. 3.36 is reproduced. Interestingly, there are only few regions of yellow signal, i.e. only little overlap between Cav-3 and N-terminal Dyst structures. Still, the two populations of Dyst - one close to Cav-3 signal and one further away - can be identified in accordance with the data shown and discussed in section 3.7.
Fig. 3.37 **D** presents the overlay image of the sarcolemmal Cav-3 signal with the sarcolemmal signal of the Dyst central rod domain (Rod) that was labeled using the antibody ab85302. This two-color combination is already known from Fig. 3.33 and Fig. 3.34. There are clearly identifiable regions of signal overlap between the two color channels. Both colocalization and para-localization of the signal structures can be observed. The two Dyst populations that were defined with respect to their distance to the Cav-3 signal are again visible.

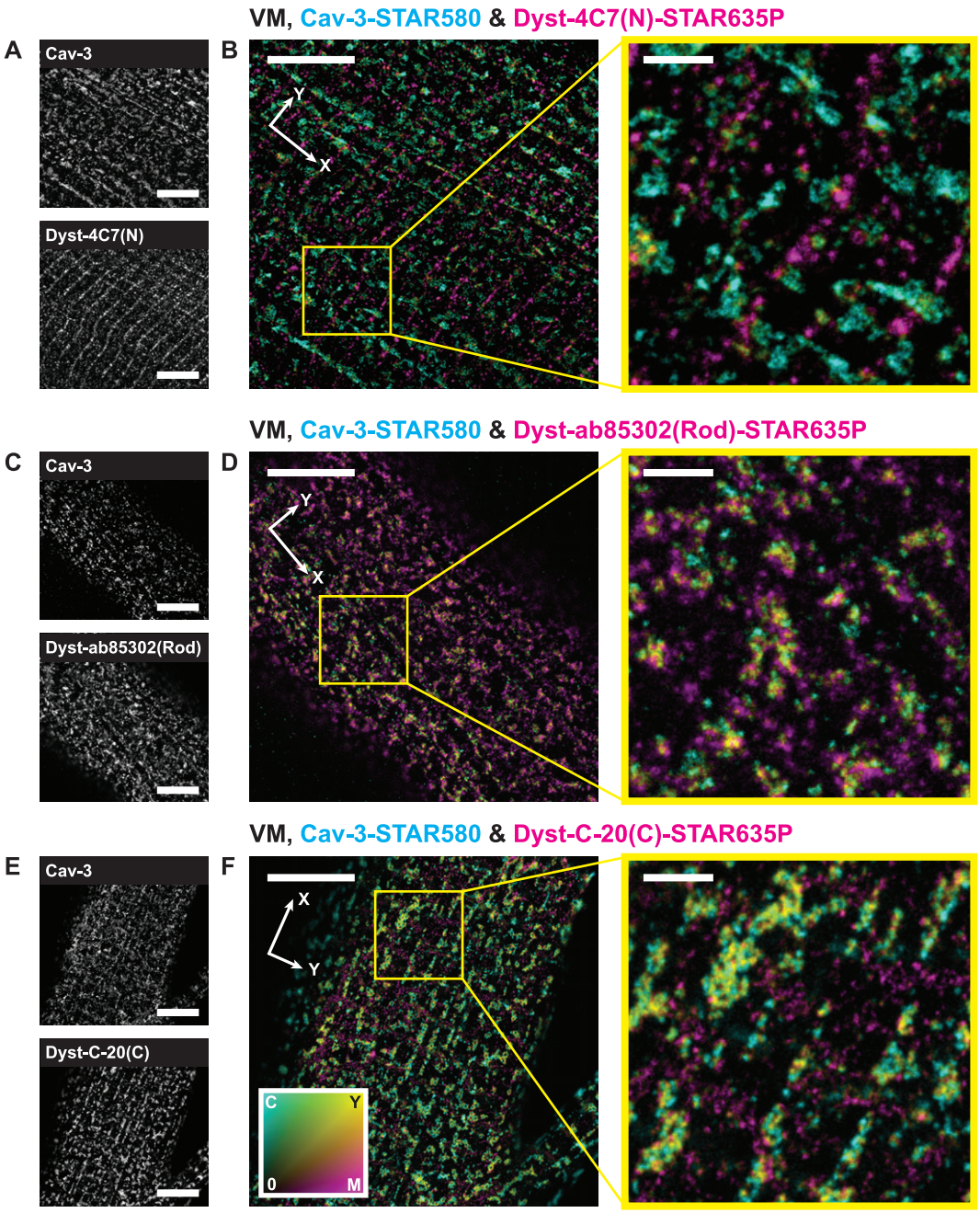

Figure 3.37.: Two-color STED images of the sarcolemma of mouse ventricular cardiomyocytes (VM) immunofluorescence labeled for Caveolin-3 (Cav-3) and the Dystrophin(Dyst) N-terminus (N), central rod domain (Rod), or C-terminus (C), respectively. Cav-3 was decorated with the dye compound STAR580 and is displayed in cyan; Dyst domains were decorated with the dye compound STAR635P and are displayed in magenta. The respectively labeled Dyst protein domains and the used primary antibodies are denoted in the corresponding image panels; detailed information about the used antibodies and dye compounds can be found in Appendix A.3 and Appendix A.4. **A**, **C** and **E** Single color channel images of the Cav-3 signal and the Dyst N-terminus (N), central rod domain (Rod), or C-terminus (C), respectively. **B**, **D**, and **F** Two-color overlays of the corresponding single color channels in **A**, **C** and **E** (see image captions). Magnifications correspond to the yellow boxed regions in the overview images. The image color map is displayed in **F**: Cav-3 signal is displayed in cyan; Dyst signal is displayed in magenta; signal overlap is indicated in yellow. Raw data images were smoothed using a two-dimensional Gaussian filter with a width of 1.5 pixels and converted into the two-dimensional color map as described in section 2.6.1. White arrows indicate the longitudinal (X) and the transverse (Y) cell axes, respectively. Scale bars in overview images: 5 µm; scale bars in magnifications: 1 µm.

In Fig. 3.37 **F**, the sarcolemmal Cav-3 signal in combination with the sarcolemmal signal of the Dyst C-terminus (C, labeled using the antibody C-20) is shown. Extended regions of overlapping Cav-3 and C-terminal Dyst structures can be identified. The combination of Cav-3 and C-terminal Dyst seems to show the largest fraction of signal colocalization of all three tested two-color combinations. At the same time, a profound area fraction of the sarcolemma is occupied by free-standing C-terminal Dyst signal that is mostly composed of single domains. More clustered Dyst signal appears to be mainly associated to nearby larger Cav-3 clusters.

From the qualitative comparison between Fig. 3.37 **B**, **D**, and **F**, it can be stated that the spatial association between Cav-3 and the Dyst depends on the respective region along the Dyst protein that is considered. More precisely, the degree of colocalization between Cav-3 and Dyst signal structures appears to be much higher for the two-color combinations of Cav-3 and the Dyst central rod domain, and Cav-3 and the C-terminal Dyst domain than for Cav-3 and the N-terminal Dyst domain. When comparing Figs. 3.37 **D** and **F**, the signal overlap for the two-color combination of Cav-3 and the C-terminal Dyst domain seems to be slightly higher than the signal overlap for the combination of Cav-3 and the Dyst central rod domain.

For the quantitative evaluation of the above findings, I analyzed the peak-to-peak nearest neighbor distance (NND) and the relative colocalization between the Cav-3 signal and the signal stemming from a particular Dyst protein domain. Note that I decided not to analyze the peak-to-peak NND nor the relative colocalization between a particular Dyst domain and Cav-3 (as it was done in section 3.7; cf. Fig. 3.33). This is because of the two populations of Dyst that were identified in section 3.7 when labeling the Dyst central rod domain: one Dyst population in close proximity to and one Dyst population remote from Cav-3. These two populations could also be identified when labeling the N-terminus and the C-terminus of the Dyst protein (see Fig. 3.37). The existence of the two Dyst populations introduces a large variance to the obtained values of the relative colocalization and the peak-to-peak NND between the Dyst domains and Cav-3 and thus render these two figures rather unsuited for comparative studies.

The peak-to-peak NND between Cav-3 and the Dyst N-terminus, central rod

domain, or C-terminus was determined as described in section 2.8; the relative colocalization was determined as described in section 2.7. For clarity, the relation between Cav-3 and the particular Dyst protein domains shall here be referred to as Cav-3⟶Dyst(N) (in case the Dyst N-terminus was labeled), Cav-3⟶Dyst(Rod) (in case the Dyst central rod domain was labeled), and Cav-3⟶Dyst(C) (in case the Dyst C-terminus was labeled), respectively. In Fig. 3.38, a bar graph representation of the obtained results is displayed.

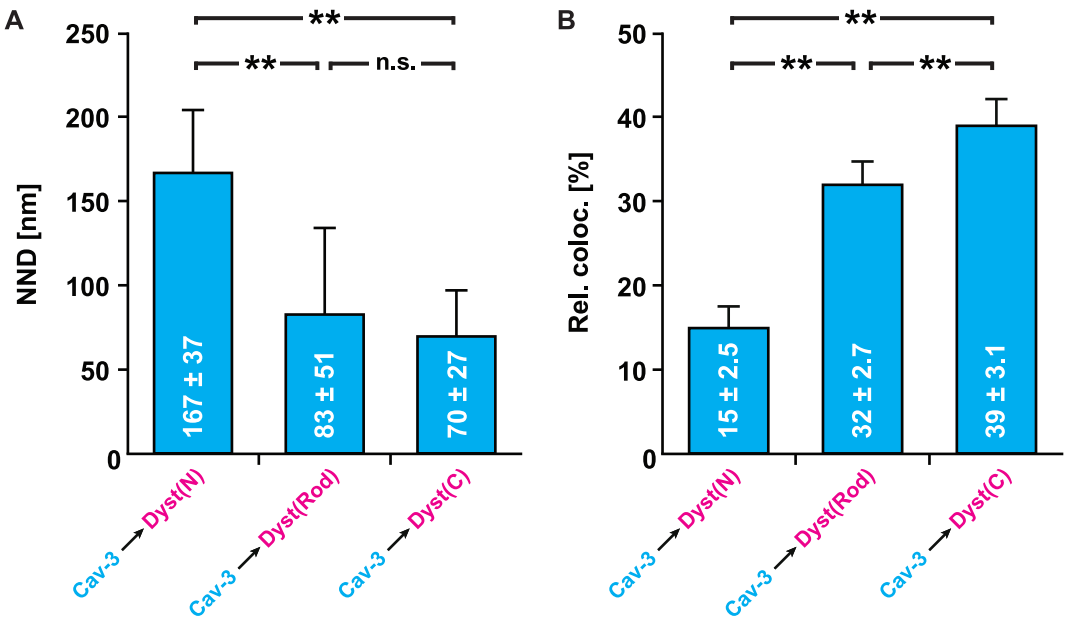

Figure 3.38.: Bar graph representation of the determined peak-to-peak nearest neighbor distance (NND, in nm) and the relative colocalization (rel. coloc., in % of the total Cav-3 signal) between the sarcolemmal Cav-3 signal and the Dyst N-terminus (Dyst(N)), central rod domain (Dyst(Rod)), and C-terminus (Dyst(C)) signal, respectively. The displayed figures were obtained as described in sections 2.8 and 2.7 and summarize the two-color STED images presented in Fig. 3.37. **A** NND between the Cav-3 signal and each Dyst(N), Dyst(Rod), and Dyst(C). **B** Rel. coloc. between the Cav-3 signal and each Dyst(N), Dyst(Rod), and Dyst(C). NND and rel. coloc are presented as mean ± standard deviation. Statistical significance was tested as described in section 2.9 with the explicit parameters of the statistical test given in Appendix I, Tables I.16 and I.17, and is denoted as: (n.s.) - not significant ($p > 0.01$) and (**) - very significant ($p < 0.001$). Number of analyzed cells: Cav-3–Dyst(N): 47; Cav-3–Dyst(Rod): 43; Cav-3–Dyst(C): 51.

Both the determination of the NND and of the relative colocalization reproduce the qualitative conclusions that could be extracted from Fig. 3.37 **B**, **D**, and **F**. Fig. 3.38 **A** shows that there is a very significant decrease between Cav-3⟶Dyst(N) and Cav-3⟶Dyst(Rod) (from about 167 nm to about 83 nm), and between Cav-3⟶Dyst(N) and Cav-3⟶Dyst(C) (from about 167 nm to about 70 nm). There is also a decrease in NND between Cav-3⟶Dyst(Rod) and Cav-3⟶Dyst(C), yet it is not statistically significant.

Likewise, from Fig. 3.38 **B**, it can be seen that the relative colocalization be-

tween Cav-3 and the particular Dyst domains very significantly increases from Cav-3⟶Dyst(N) over Cav-3⟶Dyst(Rod) to Cav-3⟶Dyst(C) (from ≈ 15 % to ≈ 32 % to ≈ 39 %). The relative colocalization denotes the percentage the total observed Cav-3 signal that colocalizes with a Dyst signal. Since the relative colocalization is obtained from binarized raw data, it captures the one-to-one pixel overlap of the two considered fluorescence signals. Such a pixel based approach to evaluate the fluorescence signal overlap is very sensitive and very strict since it demands a precision of one px (i.e. 20 nm for the here acquired images). Therefore, the concise values of the percental signal overlap may be lower than it would be expected when looking at the two-color STED images presented in Fig. 3.37.
Nevertheless, from the obtained two-color STED images (see Fig. 3.37) and the found comparative increase in relative colocalization in conjunction with the observed decrease in NND from Cav-3⟶Dyst(N) to Cav-3⟶Dyst(Rod) to Cav-3⟶Dyst(C), the following possible conclusions can be drawn:

1.) Both Cav-3 and the Dyst C-terminus, and Cav-3 and the Dyst central rod domain share a closer spatial association than Cav-3 and the Dyst N-terminus.

2.) The spatial association between Cav-3 and the Dyst C-terminus is slightly higher than between Cav-3 and the Dyst central rod domain.

3.) The fluorescence signal of each the Dyst N-terminus, central rod domain, and C-terminus show the existence of two distinct Dyst populations of which one is close to and one remote from the Cav-3 signal.

In summary, regarding the cardiac membrane nanodomain model that I proposed in section 1.4, the here presented data and the therefrom derived conclusions confirm the postulated orientation of the Dyst protein along the sarcolemma with respect to the membrane resident Cav-3: the Dyst N-terminus is located further away from the sarcolemma than the central rod domain and the C-terminus and does probably not interact with Cav-3. Both the central rod domain and the C-terminus show a higher degree of spatial association with Cav-3 and thus seem to be located closer to the sarcolemma, arguably within a distance of 30-120 nm, and with the C-terminus potentially more strongly associated to Cav-3 and the sarcolemma than the central rod domain. As has been

shown in section 3.7.1, Cholesterol (Chol) depletion and thus dissociation of caveolae does not alter the sarcolemmal arrangement of the Dyst central rod domain. This might hint towards an only indirect interaction between Cav-3 and the Dyst central rod domain, possibly mediated by one or more intermediate proteins (e.g. Nitric Oxide Synthase). The here found closer spatial association between Cav-3 and the Dyst C-terminus could indicate a more direct interaction between the two proteins at this particular Dyst domain. A similar study investigating the effect of Chol depletion on the sarcolemmal nanopattern of the particular Dyst domain signal distribution with respect to the caveolar arrangement would elucidate the questions if and how different Dyst domains associate with the sarcolemma (see also section 4).

To conclude the studies on the spatial orientation of the Dyst protein along the cardiac sarcolemma, the next section will present and discuss so-called "Dyst intra-protein labeling" approaches that allow the simultaneous fluorescence tagging of different protein domains in order to relate their specific arrangement with respect to each other and identify their similar and different structural - and thus potentially functional - properties.

3.9. Intra-protein immunofluorescence labeling of Dystrophin

Using the three distinct anti-Dyst primary antibodies 4C7, ab85302, and C-20 that respectively target the Dyst N-terminus, central rod domain, and C-terminus, I could establish the simultaneous fluorescence labeling of different domains of the Dyst protein in VM. This approach shall here be referred to as "Dyst intra-protein labeling" which yielded two-color and three-color immunofluorescence samples for STED microscopy.
In a first step to investigate the mutual assembly of the Dyst N-terminus, central rod domain and C-terminus, two-color fluorescence stains were prepared. This yielded the following three combinations:

i. Samples of fixed VM simultaneously labeled for the Dyst N-terminus and the Dyst C-terminus; referred to as (N)/(C).

ii. Samples of fixed VM simultaneously labeled for the Dyst N-terminus and the Dyst central rod domain; referred to as (N)/(Rod).

iii. Samples of fixed VM simultaneously labeled for the Dyst C-terminus and the Dyst central rod domain; referred to as (C)/(Rod).

Fig. 3.39 shows two-color STED images of these three types of samples. For details regarding the sample preparation, the used antibodies and dyes, and the image acquisition, please refer to section 2.3.3, Appendix A.3, Appendix A.4, and Appendix B.

Fig. 3.39 **B** shows the two-color STED image of the combination i.: (N)/(C). Most of the (N) signal (displayed in cyan) is highly clustered and reproduces the cardiac costamere structure that shows even stripes along the transverse cell axis spaced at a distance of about 1.8-2.0 µm (i.e. one sarcomere length, see also Fig. 3.36). In addition, some (N) signal structures are not assembled in higher-order clusters but appear to be single domains. The (C) signal (displayed in magenta) is almost entirely dispersed and shows clusters only seldom. It is predominantly composed of smaller, circular single domains. Regions of colocalization are seldom seen and mostly confined to the large (N) signal clusters.

In Fig. 3.39 **D**, the spatial arrangement of the signals from the combination ii.: (N)/(Rod) is presented. Again, like in Fig. 3.39 **A**, the (N) signal (cyan) mainly shows elongated clustered structures and a few solitary single domains. The (Rod) signal (in magenta) is in seemingly equal parts composed of both clusters that are of no distinct shape - i.e. reproducing the pattern of bunchy clusters of various shapes that have been described in e.g. Fig. 3.32 - and single domains. Spatial overlap is observed to a larger extent between clustered structures of the (N) and the (Rod) signal, while little to no colocalization between (N) and (Rod) single domains is observable. The (Rod) single domains are distributed irregularly between clusters of both the (N) and the (Rod) signal.

The combination iii. (C)/(Rod) is displayed in Fig. 3.39 F. Here, both the (Rod) and the (C) signal patterns (in cyan and magenta, respectively) are predominantly composed of single domains. However, the (Rod) signal shows a profoundly higher degree of clustering than the (C) signal which is consistent with the data shown in Fig. 3.39 **B** and **D**. Almost all clusters of the (C) signal that are observed colocalize with (Rod) clusters. Further, the extent of colocal-

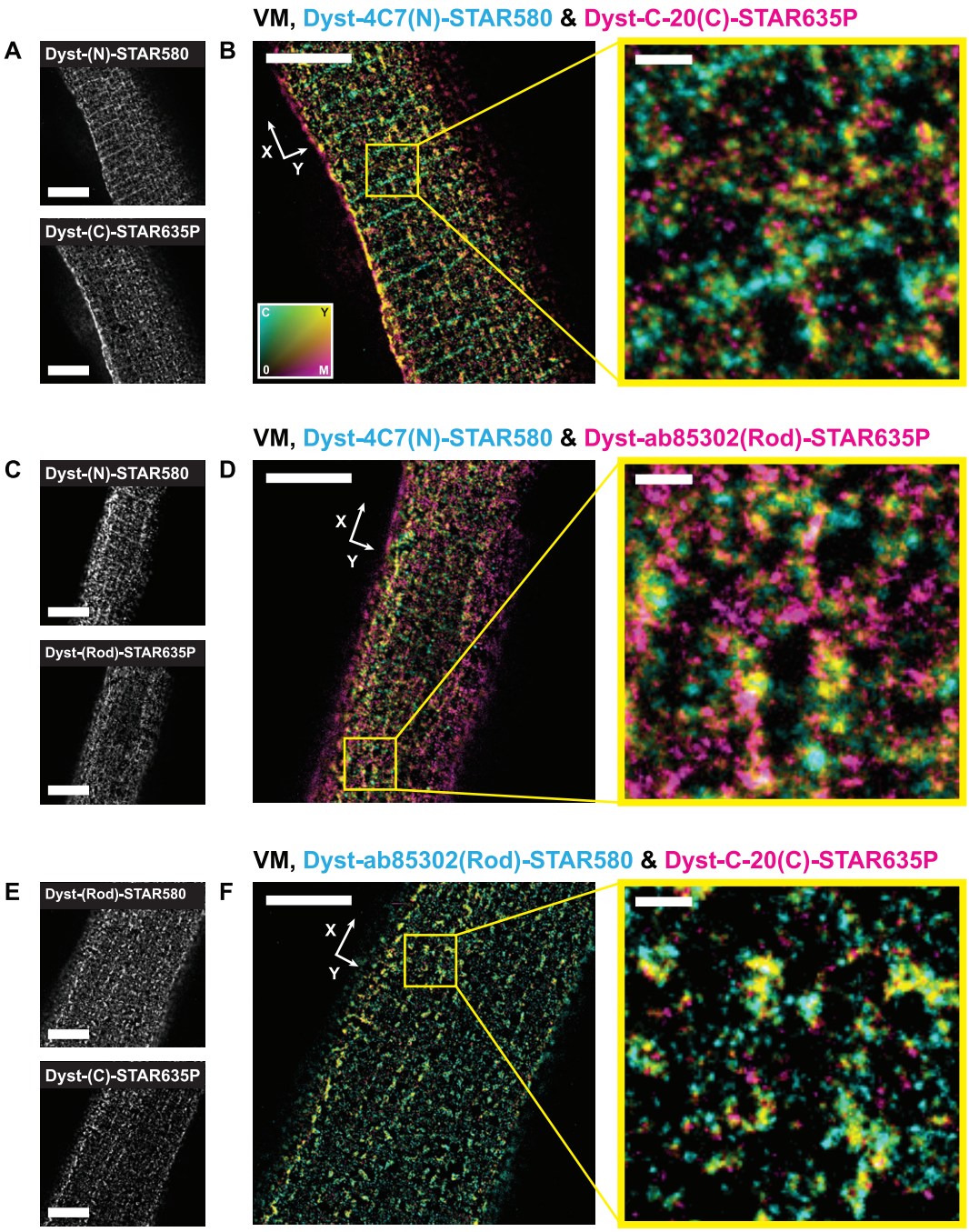

Figure 3.39.: Intra-protein two-color STED images of Dystrophin (Dyst) at the sarcolemma of mouse ventricular cardiomyocytes (VM). Dyst was respectively labeled at its N-terminus (N), central rod domain (Rod), and C-terminus (C) using the primary antibodies 4C7, ab85302, and C-20, decorated with one of the two dye compounds STAR580 or STAR635P. For detailed information about the used antibodies and dye compounds, please refer to Appendix A.3 and Appendix A.4. **A**, **C** and **E** Single color channel images of the particularly labeled Dyst protein domains (see corresponding image captions). **B**, **D**, and **F** Two-color overview images of Dyst labeled at different protein domains (see corresponding image captions). Image magnifications corresponding to the yellow boxed regions. Images were smoothed using a two-dimensional Gaussian filter with a width of 1.5 pixels and converted to the color map displayed in **B** as described in section 2.6.1.The color map corresponds to the captions of the two-color overlay images. White arrows indicate the longitudinal (X) and the transverse (Y) cell axes, respectively. Scale bar in overview image: 5 µm; scale bar in magnification: 500 nm.

ization of the (Rod) and the (C) signal seems to be of the same order as that for the (N) and the (Rod) signal (see Fig. 3.39 **D**).
Note that for all three two-color combinations, sarcolemmal regions devoid of any Dyst signal can be seen. These regions often resemble circular "openings" at the sarcolemma, yet the specific nature of these openings remains unclear. One could reckon they are Transverse Tubule (TT) openings, however, they are generally not evenly distributed along the sarcolemma at the typical sarcomere distance, as it would be expected for TT.
Based on the observations made in Fig. 3.39 **B**, **D**, and **F**, the qualitative comparison of the spatial association of the combinations (N)/(C), (N)/(Rod), and (Rod)/(C) leads to the following findings and possible interpretations:

1.) (N) shows the largest signal clusters. While these (N) clusters form stripes parallel to the transverse axis of the VM and are spaced about one sarcomere length apart, (Rod) and (C) clusters appear to be more bunchy and rounded and neither show a distinct orientation nor a regular positioning along the sarcolemma. This could mean that the Dyst N-termini are arranged in higher-order complexes at the cardiac costameres, while the (Rod) and the (C) domains that are in closer proximity to the sarcolemma are less interconnected and might thus be able to move more freely. Such an arrangement might provide stability at the attachment point between Dyst and the cytoskeleton while allowing for a certain flexibility and mobility of the sarcolemma-associated domains of the Dyst protein.

2.) The majority of both the (Rod) and the (C) signal is composed of small, circular single domains. The (N) signal consists of fewer of such single domains in comparison to the fraction of total (N) signal that is arranged in clustered assemblies. This finding is in agreement with 1.) and would support the assumption that the attachment points between Dyst and the sarcolemma are more dispersed while the attachment points between Dyst and the cytoskeleton are more concentrated.

3.) Colocalization is predominantly observed between clustered signal structures of the respective Dyst signals and not in regions that show higher densities of single domain structures. This suggests that the spatial arrangement between single Dyst proteins could be mediated by protein

regions that are preferably assembled in larger complexes (e.g. interconnected or cross-linked regions) and unconnected regions that would rather avoid potential oligomerization.

4.) The degree of colocalization seems to be larger for the two combinations (C)/(Rod) and (N)/(Rod) than for the combination (N)/(C). This motivates the models of Dyst as an elongated protein that have been discussed in the introduction of this thesis (see section 1.1.4) and that are based on biochemical studies and protein sequencing analyses. If Dyst was of a more rounded or coiled shape, one would expect a higher degree of colocalization between the particular protein domains and a more isotropic signal distribution along the sarcolemma.

In an attempt to quantify the above findings, I assessed many of the standard figures that are typically used to determine spatial correlation and colocalization. A variety of these figures has been presented in this thesis, e.g. the pixel-based signal overlap (see section 2.7) and the peak-to-peak nearest neighbor distance (see section 2.8). However, extracting these quantities from the obtained two-color micrographs did not yield definite results regarding the assembly between individual Dyst domains along the sarcolemma. This is because several factors complicate the quantitative analysis of the here presented two-color intra-protein stains.

First, it cannot be readily assumed that two signal peaks that stem from different color channels belong to the same protein. This would require the Dyst protein to be distributed only sparsely across the sarcolemma which is obviously not the case when looking at the microscopy data. In consequence, the determination of the nearest neighbor distance is intrinsically unreliable: if multiple proteins are closer together than the approximate length of a single protein, the fluorescence signal cannot be precisely assigned to one particular protein.

Second, while the assessment of the degree of colocalization between two distinct protein domains is very valuable for a qualitative estimate of the possible protein orientation or structural arrangement, concise quantitative figures such as the number of proteins within the region of colocalization cannot be derived from it. This is e.g. because of the inaccuracy of the thresholding procedure used to define the spatial extent of a signal.

Still, there are other potentially promising approaches to quantitatively evaluate the here established intra-protein Dyst stains. Some of these approaches will be touched upon in section 4.

Nevertheless, despite the difficulties to extract definite quantitative figures from the here presented two-color intra-protein STED micrographs, the prospect of achieving three-color subdiffraction intra-protein imaging is very tempting. Using the combination of all three anti-Dyst primary antibodies, three-color samples were prepared and imaged.
Fig. 3.40 shows the obtained three-color image data obtained at the sarcolemma of two different VM (**A** and **B**, and **C** and **D**, respectively). Here, the (N) signal is displayed in blue, the (Rod) signal is displayed in red, and the (C) signal is displayed in green. I chose to use this color map (i.e. different from the one previously used for two-color images) in order to illustrate sarcolemmal regions that show either single channel signal stemming from a particular Dyst domain (in red, green, or blue), spatial overlap of two color channels (magenta, yellow, or cyan), or overlap of all three color channels (white).
Upon first sight, a general principle of arrangement of the domain signal cannot be derived from the three-color images. When looking at the single color channel images of the (N) signal (Fig. 3.40 **A** and **C**) the assembly parallel to the transverse cell axis and resembling costameric structures can be identified. Yet, the (Rod) and (C) signals do not necessarily follow this striated pattern, although Fig. 3.40 **D** might suggest such a preferential transverse orientation of all three Dyst domains. But despite the difficulties to infer the concise molecular orientation of the Dyst protein along the sarcolemma from the image data, two structural peculiarities of the sarcolemmal Dyst arrangement can be extracted:

1.) Signal colocalization and para-localization predominantly happens between clusters of individual Dyst domain signals. The resulting signal complexes are of various sizes and shapes and do neither show a clearly identifiable local orientation or positioning with respect to each other nor a global positioning with respect to the cell axes. Further, the clusters are seldom surrounded by single signal domains but are rather embedded within regions that are devoid of any Dyst signal (see also 2.)). Typically, there is no smooth transition between Dyst clusters and regions without

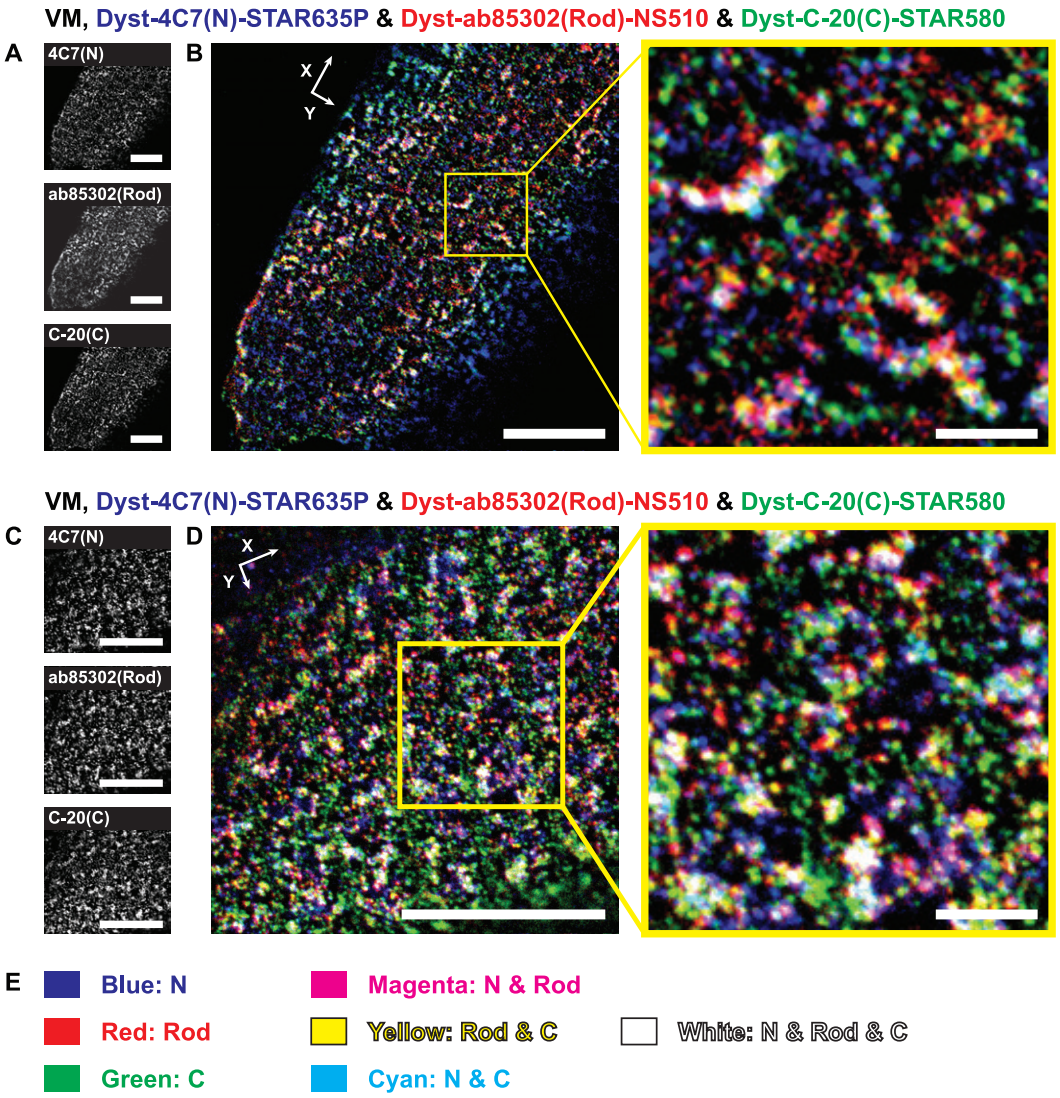

Figure 3.40.: Intra-protein three-color STED images of the Dystrophin (Dyst) protein N-terminus (N), central rod domain (Rod), and C-terminus at the sarcolemma of mouse ventricular cardiomyocytes (VM). Image data from two different cells is displayed (**A** and **B**, and **C** and **D**, respectively). **A** Single color overview images of the three labeled Dyst domains (N), (Rod), and (C) (see image captions). **B** Three-color overlay image of the (N), (Rod), and (C) signal shown in **A**. Image magnification corresponding to the yellow boxed region. **C** Single color overview images of the three labeled Dyst domains (N), (Rod), and (C) (see image captions). **D** Three-color overlay image of the (N), (Rod), and (C) signal shown in **C**. Image magnification corresponding to the yellow boxed region. **E** The color key indicates regions of single channel signal, and signal overlap of two or all three color channels. White arrows indicate the longitudinal (X) and the transverse (Y) cell axes. Images were smoothed using a two-dimensional Gaussian filter with a width of 1.5 pixels. For detailed information about the used antibodies and fluorescent dyes, please refer to Appendix A.3 and Appendix A.4. Scale bar in overview images: 5 µm; scale bar in magnifications: 1 µm.

Dyst signal; the two domains are mostly definitive and form a membrane mosaic.

2.) Although the density of the fluorescence signal stemming from the labeled Dyst domains is very high, the sarcolemma is not entirely covered

with Dyst signal. There are sarcolemmal regions in the images that are completely black - i.e. devoid of any Dyst signal. Such empty regions have been observed in the two-color images of Cav-3 co-labeled with the particular Dyst domains (see Fig. 3.37) and in the two-color images of the combinations of two simultaneously Dyst domains (see Fig. 3.39) and were there referred to as "openings".

Again, the question remains: what could these openings be? Are they the regions where Transverse Tubules (TT) bud from the sarcolemma? If so, the high density of Dyst at the TT openings might indicate that these openings could dynamically change their diameter, probably depending on the degree of cellular contraction (i.e. depending on the momentary membrane tension). However, the openings reach diameter sizes of more than 800 nm - much too big for the typical diameter of TT, unless one assumes that the invaginating membrane that eventually forms the TT shows only a small curvature which would result in the TT having the shape of a funnel at the sarcolemma and thus an increased diameter. Alternatively, these openings could be sarcolemmal regions that are independent of the cellular cytoskeleton (i.e. not directly mechanically associated with the myofibrils). They could thus represent membrane regions that provide cellular elasticity. Undoubtedly, there is much room for speculation.

In a last step, to most instructively visualize how densely the sarcolemma is packed with Dyst - and how characteristically - all three Dyst domains (N), (Rod), and (C) were decorated with the same fluorescent dye and their signal recorded simultaneously in a single sample scan. This sample preparation protocol was chosen to rule out any effects of chromatic aberrations or dye dependent differences in image resolution.
Assuming that in the resulting samples, the full-length Dyst protein and thus the entire sarcolemmal Dyst population is fluorescently tagged, Fig. 3.41 reflects that membrane regions devoid of Dyst signal are a distinct property of the sarcolemmal Dyst arrangement.
The question about the nature of the Dyst-negative sarcolemmal regions shall be the final - and unanswered - question in this thesis. Strategies to approach an answer will be presented in section 4. For now, the images shall have a merely qualitative purpose and might perhaps serve as an inspiration.

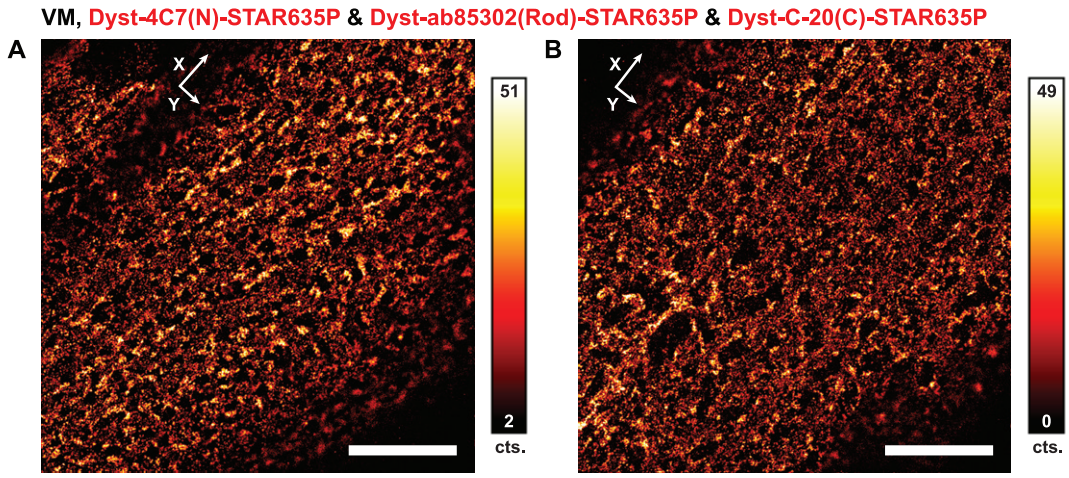

Figure 3.41.: STED images of the sarcolemma of two individual mouse ventricular cardiomyocytes (VM, **A** and **B**, respectively) labeled for the protein Dystrophin (Dyst) via indirect immunofluorescence. Dyst was labeled along its full length by decorating the specifically targeted protein N-terminus (N), central rod domain (Rod), and the C-terminus (C) with the same fluorescent dye STAR635P. For detailed information about the labeling procedure, the used antibodies, and the used dye compounds, please refer to section 2.3.3, Appendix A.3, and Appendix A.4. Color bars indicate the respective image brightness in photon counts (cts.). White arrows indicate the longitudinal (X) and the transverse (Y) cell axes. Images were smoothed using a two-dimensional Gaussian filter with a width of 1.5 pixels. Scale bars: 5 µm.

In summary, the here presented subdiffraction image based findings about the localization and orientation of Dyst with respect to Cav-3 and the cardiac sarcolemma are in agreement with the cardiac membrane model proposed in section 1.4. Dyst is an elongated protein whose N-terminus is located further away from Cav-3 rich membrane domains (and thus potentially the sarcolemma) than its central rod domain and its C-terminus. The Dyst N-terminus forms regularly spaced striated structures that resemble the myocyte costameres. These costamere-like signal structures confirm the F-Actin binding domain located at the Dyst N-terminus. Chol depletion does not alter the signal distribution of the Dyst central rod domain which indicates that Dyst does not directly interact with caveolae along this domain. And, last but not least, there are two distinct Dyst populations observable with respect to their spatial association with Cav-3. The functional properties of these two populations remain yet to be uncovered.

4. Conclusion and outlook

In this thesis, experimental and analytical methods were developed and applied to investigate cardiac membrane nanodomains with STED microscopy.
Comprehensive studies using single- and multicolor, one- and two-photon-excitation STED microscopy were performed on living and fixed isolated mouse ventricular cardiomyocytes (VM).
Special emphasis was laid on the visualization of the three-dimensional (3D) nanoscopic structure of the cardiac Transverse-Axial Tubular System (TATS) because alterations of the TATS topology are correlated to many cardiovascular pathologies.
Further, the spatial arrangement of the two sarcolemmal lipids Cholesterol (Chol) and Ganglioside GM1 (GM1) and of the two sarcolemma-associated proteins Caveolin-3 (Cav-3) and Dystrophin (Dyst) was investigated in detail. These molecules play an important role in maintaining membrane integrity, in cellular signaling processes, and in disease mechanisms and their specific sarcolemmal topology crucially determines their proper physiological functionality.
The essential milestones that were reached in this thesis and the key findings that could be derived therefrom shall here be summarized:

1.) A novel class of fluorescent Cholesterol (Chol) analogs was established as a live-cell membrane label for STED microscopy. The compound Chol-KK114 yielded an unprecedented lateral resolution of $\leq 35\,\mathrm{nm}$ in living VM. Chol-KK114 is superior to standard fluorescent membrane markers in many regards and allows both membrane bulk staining and labeling Chol rich membrane compartments (see section 3.1).

2.) A Two-Photon-Excitation-CW-STED (2P-Exc-CWSTED) microscope was built (see section 3.4.1) and a comprehensive quantitative study to identify and characterize organic fluorophores suitable for 2P-Exc-CWSTED

imaging was conducted focusing on fluorescence switch-off and bleaching behavior (see section 3.4.2). Chol-OG488 was found to be the most suitable fluorescent Chol analog for 2P-Exc-CWSTED live-cell imaging and enabled the acquisition of 3D images of the TATS of living VM. These 3D images revealed that (a) Transverse Tubules bud from Chol rich sarcolemmal patches and (b) Chol rich nanoscopic sarcolemmal patches form shallow membrane invaginations which were assumed to be caveolae (see section 3.4.3).

3.) Chol and Cav-3 were found to form similar sarcolemmal signal patterns comprised of three reoccurring motifs: 1. single domains of ≈ 70 nm diameter, 2. ring structures of ≈ 240 nm diameter and 3. bunchy clusters of various sizes (see section 3.5). Chol depletion substantially altered the sarcolemmal Cav-3 signal distribution and led to the quantifiable dissociation of Cav-3 clusters (see section 3.5.1). The use of GM1 for two-color STED imaging together with each Cav-3 and Chol demonstrated the spatial association of Chol and Cav-3 and their probable localization to the same sarcolemmal membrane domains (see section 3.6).

4.) Dyst was simultaneously labeled at its N-terminus (N), central rod domain (Rod), and C-terminus (C) in a newly established "intra-protein" labeling protocol for multicolor STED imaging. This yielded image based evidence that Dyst is an elongated protein attached to the cardiac costameres via (N) and associated with the sarcolemma via (Rod) and (C) (see section 3.9). Two-color images of Cav-3 and the particular Dyst protein domains showed distinctly different mutual signal pattern arrangements. The spatial association between Dyst and Cav-3 was found to be closer for each (N) and (Rod) than for (C) (see section 3.8). Chol depletion did not alter the sarcolemmal signal pattern of (Rod) which indicated that the possible connection between (Rod) and the sarcolemma might be mediated by Cav-3 but is not dependent on it (see section 3.7.1).

5.) A cardiac membrane nanodomain model summarizing the findings of this thesis was proposed and validated and is recapitulated in Fig. 4.1 (see also section 1.4).

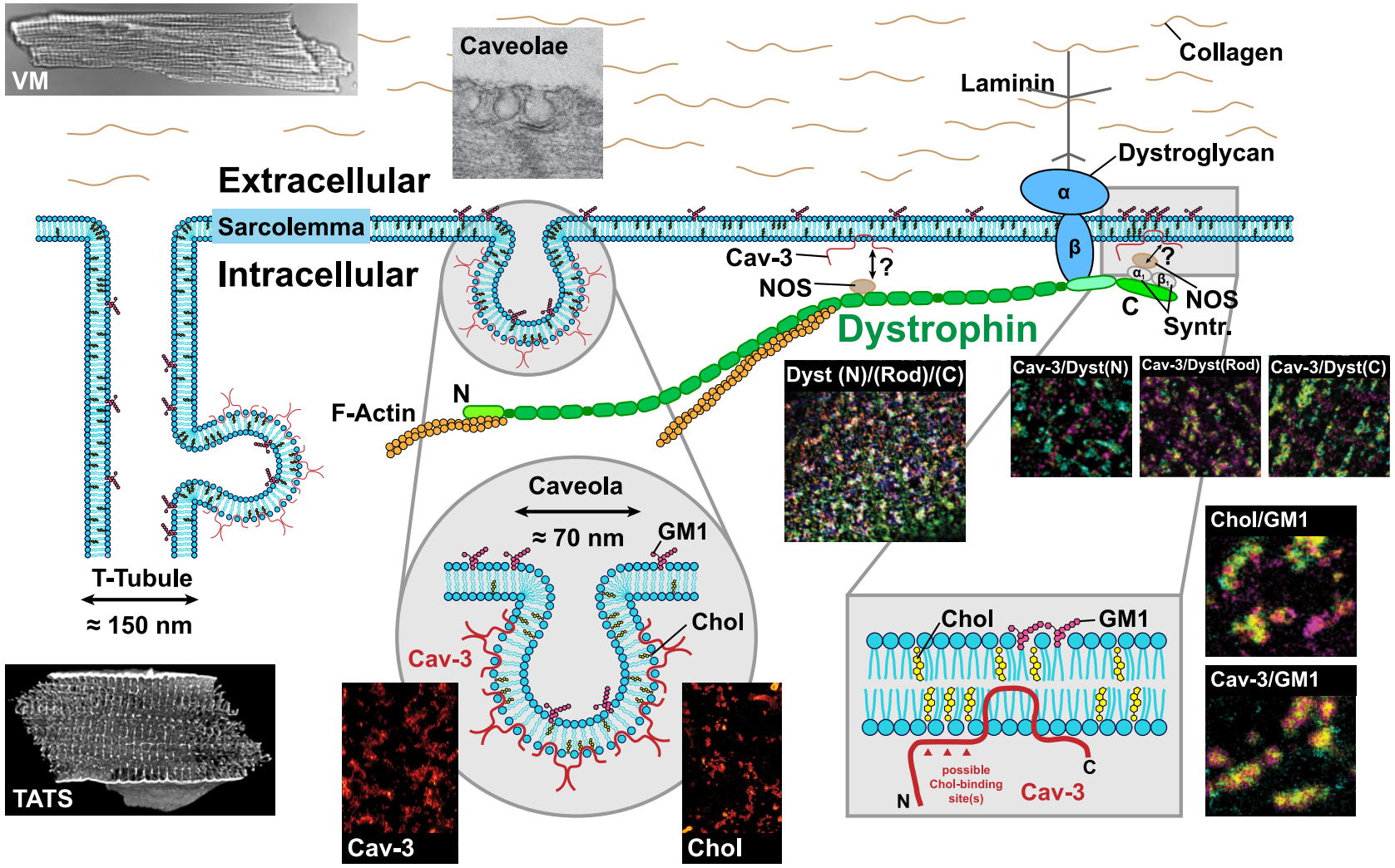

Figure 4.1.: The cardiac membrane nanodomain model proposed in this work. This membrane model is focusing on the two sarcolemmal lipids Cholesterol (Chol) and Ganglioside GM1 (GM1) and on the two sarcolemma-associated proteins Caveolin-3 (Cav-3) and Dystrophin (Dyst). Inserted micrographs were obtained in this thesis and summarize the gained insights. Question marks indicate so far unknown association or interaction. Additional abbreviations: C - Dyst C-terminus; F-Actin - Filamentous Actin; N - Dyst N-terminus; NOS - Nitric Oxide Synthase; Syntr. - Syntrophins (α_1 and β_1, respectively); T-Tubule - Transverse Tubule. Neither drawn to actual proportions nor with correct stoichiometry. See also section 1.4

In conclusion, this thesis visualizes for the first time the arrangement of specific sarcolemmal lipid/protein nanodomains in healthy cardiomyocytes and demonstrates their association with the characteristic cardiac membrane topology.

The established experimental and analytical methods and the therewith obtained results offer plenty of possibilities for further explorations.

Future directions: the great potential of fluorescent Chol analogs
The identification and establishment of the versatile class of fluorescent Chol analogs featuring organic fluorophores linked to the Chol molecule via PEG as highly suitable membrane labels for STED microscopy of living VM enables a variety of customized applications.
For one, the experimenter can freely choose the fluorophore that is coupled to Chol and thus freely adjust the spectral properties of the membrane label according to their specific experimental setup. This would for example allow the simultaneous subdiffraction imaging of the cardiac membrane architecture and of Calcium signals along the membrane using established Calcium marker dyes such as Fluo-4 or Oregon Green 488 BAPTA-1 [560, 439].
Further, using the Chol-PEG labels at high concentrations as non-toxic membrane bulk labels to thoroughly stain the entire TATS of the VM allows real-time live-cell studies of the potential alterations of the TATS during mechanical stretching of VM, upon administration of drugs, or upon induced membrane damage. Experiments of stretching cardiomyocytes with control over the applied stretching force and while imaging Calcium sparks has so far yielded many novel findings regarding excitation-contraction coupling [561, 562]. The application of STED microscopy to localize Calcium sparks along the cardiac membrane system during cellular stretching would open up a fantastic and exciting field of research. Here, one of the first experiments that would come to mind is investigating whether there is a spatial correlation between Calcium sparks and Chol rich sarcolemmal patches.
As another interesting application, one could think of monitoring the effect of pharmaceuticals on the cardiac membrane system in real time and with nanometric resolution. For example, the "membrane sealant" Poloxamer P188 has been shown to stabilize the dystrophic cell membrane and provide for mem-

brane integrity [563, 564]. 3D 2P-Exc-CWSTED microscopy of the Chol-OG488 labeled TATS of dystrophic VM during the administration of P188 (and maybe during cell stretch or after induced damage to the cell) would be a wonderful experimental system to study the mode of action of P188 and potential membrane repair mechanisms. Other interesting processes to record would for example be the possible alteration of membrane structures upon incubation of VM with Latrunculin A which disrupts cytoskeletal structures [565, 566].
Note that the fluorescent Chol analogs that have proven ideal labels for STED imaging of the VM membrane were originally designed for STED-FCS measurements [100]. Regarding the specific nature of the sarcolemmal Chol nanodomains, STED-FCS experiments studying their diffusivity or the effects that these domains have on the movement of a diffusing lipid or protein could be set up fast and would provide valuable insights.
Finally, the successful use of the fluorescent Chol analogs in many different cell systems as demonstrated in this thesis motivates the application of these membrane labels for fluorescence nanoscopy of basically any cell system of interest. As an example, the dye Chol-STAR580 proved to be feasible for imaging membrane structures in skeletal muscle cells (data not shown).

Future directions: two-color lipid/protein labeling in living VM
An unfortunate shortcoming of the attempt to associate sarcolemmal Chol and Cav-3 signal was the incompatibility of Chol-KK114 with cell permeabilization and of Cav-3 immunofluorescence labeling with live-cell STED microscopy. Apart from various fluorescent labels that are membrane-specific, there are not many protein-specific organic dye based fluorescence tags available for live-cell imaging. An exciting addition to the family of fluorescent live-cell labels are the cell permeable and fluorogenic Silicon Rhodamine (SiR) dyes SiR and SiR700 that can be used to target e.g. cellular F-Actin or Tubulin when coupled to cell toxins [345]. Although in this thesis, these labels have been tested to visualize cytoskeletal structures in living VM, the attempts were not successful, yielding unspecific signal probably due to a large degree of fluorophore uptake by mitochondria (data not shown). Also, it would be of much greater interest to be able to simultaneously label Chol and Cav-3 or Dyst structures in living VM.
A promising possibility to achieve two-color STED imaging of sarcolemmal

Chol and e.g. Cav-3 structures would be the generation and utilization of transgenic animals that express the protein of interest coupled to a fluorescent protein with the appropriate spectral properties (for example the green fluorescent protein for the combination with Chol-KK114). Unfortunately, such animals were not readily available in this thesis. The correlative investigations of lipid/protein nanodomains at the cardiac sarcolemma would in any case greatly benefit from transgenic animal models.

Future directions: STED combined with near-field microscopy techniques
Since the heart is essentially a pump, the biomechanical properties of cardiomyocytes also deserve a closer look.
Regarding the assessment of biophysical properties of cardiomyocytes (e.g. Young's modulus), Atomic Force Microscopy (AFM) is the method of choice [567]. In addition, AFM can be used to map the texture of the cellular surface. The combined application of AFM and STED microscopy has already been shown [364, 365]. And together with the membrane-specific fluorescent Chol analogs, the simultaneous assessment of cardiac surface texture and the nanopattern of Chol domains would be possible. Since Chol enriched membrane domains such as caveolae are supposed to provide additional surface area to ensure cellular elasticity, it would be of great interest to find out whether the sarcolemmal Chol nanodomains shown in this thesis indicate negatively curved membrane regions.
Further, the circular regions devoid of Dyst and Cav-3 signal that were demonstrated in section 3.9 are an interesting feature. As speculated, these "openings" could be the regions where Transverse Tubules (TT) bud from the sarcolemma, i.e. membrane regions with a large negative curvature. A combination of near-field scanning microscopy techniques such as Scanning Ion Conductance Microscopy (SICM) or AFM and STED microscopy would be valuable to elucidate the nature of these peculiar openings. Since the observed openings strongly vary in diameter (see Fig. 3.41), they could - apart from being TT openings - also be different membrane structures, potentially serving the purpose of providing cellular elasticity since they may not be linked directly to the cytoskeleton via Dyst. Cardiac surface texture mapping using SICM has been successful at identifying both TT and caveolae at the cardiac sarcolemma [568, 569, 570]. The possibility of simultaneously assessing cardiomyocyte sur-

face texture and protein distribution on the nanoscale would open up a vast field of correlative studies - also extendable to disease models. One caveat exists, however: to adequately map the cardiac surface, the membrane has to be intact, i.e. cells cannot be labeled via immunofluorescence. Here again, the generation and use of transgenic animals that express protein variants coupled to fluorescent proteins would be a feasible alternative. It has been reported that the diameter of TT remains unchanged upon cellular contraction [571]. Thus, if the Dyst negative membrane openings coincide with TT openings, this would mean that TT are flanked by sarcolemmal Dyst but that they are not directly associated with it.
The observed openings might also be related to cellular focal adhesion points - the sites along the cellular membrane that mediate the attachment to the extracellular matrix [572, 558]. Multicolor labeling of Dyst and focal adhesion point marker proteins such as Vinculin, Paxillin, or the extracellular matrix protein Laminin could elucidate the possible structural importance of the Dyst negative membrane regions.

Future directions: strategies for quantitative data analyses
The quantitative analysis of three-color STED images of different Dyst protein domains (see Fig. 3.40) is complicated by the high fluorescence signal density and the impossibility of determining whether two signal peaks from different color channels label the same or two different Dyst proteins.
Potential approaches to still extract information about the molecular orientation from the data could for example involve the determination of a preferred directionality of the vectors connecting two labeled protein domains with respect to the longitudinal or transverse cell axes. Since the striated arrangement of the Dyst N-terminus signal is approximately parallel to the transverse cell axis, it could likewise be used as an internal reference for the orientation of the Dyst C-terminus and the Dyst central rod domain along the sarcolemma.
Further, the signal peaks from the three individual color channels could be treated as "moving" signal peaks from a single channel that were recorded at three points in time. Based on this abstraction, a correlative image analysis method - e.g. SpatioTemporal Image Correlation Spectroscopy (STICS, [573]) - could be used to determine the predominant orientation of the different Dyst domains with respect to each other and with respect to the sarcolemma.

Future directions: expansion of the established multicolor immunofluorescence labeling protocols

The multicolor immunofluorescence labeling protocols for STED that were established in section 3.8 enable very versatile applications. Interesting further experiments regarding two-color imaging of Cav-3 and different Dyst domains would comprise studying the effect of Chol depletion on the mutual spatial arrangement between Cav-3 and the Dyst N-terminus or, primarily, the Dyst C-terminus. Since the spatial association between Dyst and Cav-3 seems to be closest at the Dyst C-terminus, Chol depletion might lead to a significant signal redistribution.

The combination of the three fluorophores NS510 (i.e. STAR520), STAR580, and STAR635P for STED microscopy with a single STED beam at 775 nm, allows three-color STED imaging without the need for post-acquisition color channel registration because the use of only one STED laser intrinsically aligns all three color channels with subdiffraction precision. Within this labeling scheme, there are in principle no limits to the choice of the proteins of interest to answer specific biological questions. Very interesting proteins for three-color STED imaging would be Cav-3, Dyst and eNOS (see also Fig. 4.1). Their mutual spatial arrangement could further elucidate the molecular orientation of Dyst along the cardiac sarcolemma.

Future directions: cardiac membrane nanodomains in disease models

Plenty of published studies using a variety of experimental techniques have confirmed that cardiac pathologies are closely linked to structural alterations of the cardiac membrane architecture (see section 1.1). In a side project of this thesis, the nanoscopic arrangement of Cav-3 and Dyst structures was investigated in a mouse model of proliferative cardiac hypertrophy induced by Transverse Aortic Constriction (TAC) - but no structural changes were observed (data not shown). Nevertheless, the specific 3D distribution of membrane Chol domains in VM has so far not been assessed in disease models. Possible and promising investigations would for example comprise the visualization of Chol nanopatterns in disease models of hypertrophy or myocardial infarction. There, one would expect a decrease in density of the sarcolemmal Chol signal and possibly a dilatation of the observed ring structures formed by Chol.

Further, the Chol nanopattern and the 3D TATS topology in living VM derived

from Cav-3 knockout mice would be of great interest. Such experiments could supply valuable information about the interdependence between Cav-3 and the content and arrangement of Chol within the extracellular membrane leaflet. In this thesis, I could show that Chol extraction has a profound impact on the sarcolemmal Cav-3 signal pattern - one would expect that VM devoid of Cav-3 are also devoid of those sarcolemmal Chol nanodomains that are visualized by Chol-KK114.
Finally, 3D 2P-Exc-CWSTED microscopy of the Chol-OG488 labeled TATS of *mdx* or even Dyst knockout mice also enables exciting new experiments. Although it was shown in this thesis that Chol depletion has no effect on the sarcolemmal signal pattern of the Dyst central rod domain, the 3D structure of the cardiac membrane system in *mdx 5cv* mice was not characterized using a fluorescent Chol analog and the potential importance of Dyst expression for the specific distribution of membrane Chol remains to be clarified.

Of course, there are many more imaginable future directions to continue the fascinating studies of the intricate protein and lipid structures and their interactions that allow heart cells to accomplish their demanding and amazing tasks. Concluding, I can confidently confirm that the heart is an expressive symbol, an impressive organ - and a huge adventure playground for biophysics.

Bibliography

[1] D. Tirziu, F. J. Giordano, and M. Simons, "Cell communications in the heart," *Circulation*, vol. 122, no. 9, pp. 928–937, Aug. 2010.

[2] A. Katz, *Physiology of the Heart*. Wolters Kluwer Health/Lippincott Williams & Wilkins Health, 2010. [Online]. Available: https://books.google.de/books?id=24CcilHdzC4C

[3] J. A. Fay and N. Sonwalkar, *A fluid mechanics hypercourse*. The MIT Press, 1996.

[4] D. J. Duncker and R. J. Bache, "Regulation of coronary blood flow during exercise," *Physiol Rev*, vol. 88, no. 3, pp. 1009–1086, Jul. 2008.

[5] N. C. C. for Chronic Conditions (Great Britain) and R. C. of Physicians of London, "Chronic heart failure: National clinical guideline for diagnosis and management in primary and secondary care." Royal College of Physicians, 2003.

[6] D. Mozaffarian, E. J. Benjamin, A. S. Go, D. K. Arnett, M. J. Blaha, M. Cushman, S. R. Das, S. de Ferranti, J.-P. Després, H. J. Fullerton, V. J. Howard, M. D. Huffman, C. R. Isasi, M. C. Jiménez, S. E. Judd, B. M. Kissela, J. H. Lichtman, L. D. Lisabeth, S. Liu, R. H. Mackey, D. J. Magid, D. K. McGuire, E. R. Mohler, C. S. Moy, P. Muntner, M. E. Mussolino, K. Nasir, R. W. Neumar, G. Nichol, L. Palaniappan, D. K. Pandey, M. J. Reeves, C. J. Rodriguez, W. Rosamond, P. D. Sorlie, J. Stein, A. Towfighi, T. N. Turan, S. S. Virani, D. Woo, R. W. Yeh, and M. B. Turner, "Executive summary: Heart disease and stroke statistics - 2016 update," *Circulation*, vol. 133, no. 4, pp. 447–772, Jan. 2016.

[7] C. J. Schwiening, "A brief historical perspective: Hodgkin and Huxley," *The Journal of Physiology*, vol. 590, no. Pt 11, pp. 2571–2575, May 2012.

[8] M. E. Mangoni and J. Nargeot, "Genesis and regulation of the heart automaticity," *Physiol Rev*, vol. 88, no. 3, pp. 919–982, Jul. 2008.

[9] T. Tahin and G. Széplaki, in *Cardiac Arrhythmias: From Basic Mechanism to State-of-the-Art Management*. Springer-Verlag London Ltd, 2014, ch. 24.

[10] J. Z. Zhang, H. M. Waddell, and P. P. Jones, "Regulation of RYR2 by sarcoplasmic reticulum Ca^{2+}," *Clinical and Experimental Pharmacology and Physiology*, vol. 42, no. 6, pp. 720–726, 2015.

[11] M. Endo, "Calcium release from the sarcoplasmic reticulum," *Physiol Rev*, vol. 57, no. 1, pp. 71–108, Jan. 1977.

[12] A. Fabiato, "Calcium-induced release of Calcium from the cardiac sarcoplasmic reticulum," *American Journal of Physiology-Cell Physiology*, vol. 245, no. 1, pp. 1–14, 1983.

[13] A. Fabiato, "Time and Calcium dependence of activation and inactivation of Calcium-induced release of Calcium from the sarcoplasmic reticulum of a skinned canine cardiac Purkinje cell." *J Gen Physiol*, vol. 85, no. 2, pp. 247–289, Feb. 1985.

[14] M. Cannell, Berlin, and W. Lederer, "Effect of membrane potential changes on the Calcium transient in single rat cardiac muscle cells," *Science*, vol. 238, no. 4832, pp. 1419–1423, Dec. 1987.

[15] M. A. Geeves and K. C. Holmes, "Structural mechanism of muscle contraction," *Annu. Rev. Biochem.*, vol. 68, no. 1, pp. 687–728, Jun. 1999.

[16] A. Berk, S. Zipursky, and H. Lodish, *Molecular Cell Biology 4th edition*, 4th ed. W. H. Freeman, New York, 2000.

[17] R. Milo and R. Phillips, *Cell Biology by the Numbers*. Garland Science, Taylor & Francis Group, 2015.

[18] M. J. Kushmerick and R. J. Podolsky, "Ionic mobility in muscle cells," *Science*, vol. 166, no. 3910, pp. 1297–1298, Dec. 1969.

[19] A. Einstein, "Über die von der molekularkinetischen Theorie der Wärme geforderte Bewegung von in ruhenden Flüssigkeiten suspendierten Teilchen," *Annalen der Physik*, vol. 322, no. 8, pp. 549–560, 1905.

[20] M. S. Forbes, L. A. Hawkey, and N. Sperelakis, "The Transverse-Axial Tubular System (TATS) of mouse myocardium: Its morphology in the developing and adult animal," *American Journal of Anatomy*, vol. 170, no. 2, pp. 143–162, 1984.

[21] C. Soeller and M. B. Cannell, "Examination of the transverse tubular system in living cardiac rat myocytes by 2-photon microscopy and digital image–processing techniques," *Circulation Research*, vol. 84, no. 3, pp. 266–275, 1999.

[22] E. Wagner, M. A. Lauterbach, T. Kohl, V. Westphal, G. S. Williams, J. H. Steinbrecher, J.-H. Streich, B. Korff, H.-T. M. Tuan, B. Hagen, S. Luther, G. Hasenfuss, U. Parlitz, M. S. Jafri, S. W. Hell, W. J. Lederer, and S. E. Lehnart, "Stimulated emission depletion live-cell super-resolution imaging shows proliferative remodeling of T-Tubule membrane structures after myocardial infarction," *Circulation Research*, vol. 111, no. 4, pp. 402–414, 2012.

[23] E. Wagner, "Cardiac T-Tubule Membranes - Nanostructure and Remodeling Mechanisms in Disease," Ph.D. dissertation, Georg-August-Universität zu Göttingen, 2012.

[24] T. Ogata and Y. Yamasaki, "High-resolution scanning electron microscopic studies on the three-dimensional structure of the Transverse-Axial Tubular System, sarcoplasmic reticulum and intercalated disc of the rat myocardium," *The Anatomical Record*, vol. 228, no. 3, pp. 277–287, 1990.

[25] R. B. Clark, A. Tremblay, P. Melnyk, B. G. Allen, W. R. Giles, and C. Fiset, "T-Tubule localization of the inward-rectifier K^+ channel in mouse ventricular myocytes: a role in K^+ accumulation," *The Journal of Physiology*, vol. 537, no. 3, pp. 979–992, 2001.

[26] F. Brette and C. Orchard, "T-Tubule function in mammalian cardiac myocytes," *Circ Res*, vol. 92, no. 11, pp. 1182–1192, Jun. 2003.

[27] L.-S. Song, S. Guatimosim, L. Gómez-Viquez, E. A. Sobie, A. Ziman, H. Hartmann, and W. J. Lederer, "Calcium Biology of the Transverse

Tubules in heart," *Annals of the New York Academy of Sciences*, vol. 1047, no. 1, pp. 99–111, 2005.

[28] M. Pásek, J. Šimurda, G. Christé, and C. Orchard, "Modelling the cardiac Transverse-Axial Tubular System," *Progress in Biophysics and Molecular Biology*, vol. 96, no. 1â€"3, pp. 226–243, Jan. 2008.

[29] F. Brette, P. Rodriguez, K. Komukai, J. Colyer, and C. Orchard, "β-adrenergic stimulation restores the Ca transient of ventricular myocytes lacking T-Tubules," *Journal of Molecular and Cellular Cardiology*, vol. 36, no. 2, pp. 265–275, Feb. 2004.

[30] F. Brette and C. Orchard, "Resurgence of cardiac T-Tubule research," *Physiology*, vol. 22, no. 3, pp. 167–173, Jun. 2007.

[31] R. S. Velagaleti, P. Gona, M. J. Pencina, J. Aragam, T. J. Wang, D. Levy, R. B. D'Agostino, D. S. Lee, W. B. Kannel, E. J. Benjamin, and R. S. Vasan, "Left ventricular hypertrophy patterns and incidence of heart failure with preserved versus reduced ejection fraction," *The American Journal of Cardiology*, vol. 113, no. 1, pp. 117–122, Jan. 2014.

[32] A. R. Lyon, K. T. MacLeod, Y. Zhang, E. Garcia, G. K. Kanda, M. J. Lab, Y. E. Korchev, S. E. Harding, and J. Gorelik, "Loss of T-Tubules and other changes to surface topography in ventricular myocytes from failing human and rat heart," *Proceedings of the National Academy of Sciences*, vol. 106, no. 16, pp. 6854–6859, Apr. 2009.

[33] J. Gorelik, L. Q. Yang, Y. Zhang, M. Lab, Y. Korchev, and S. E. Harding, "A novel Z-groove index characterizing myocardial surface structure," *Cardiovasc Res*, vol. 72, no. 3, pp. 422–429, Dec. 2006.

[34] E. Dague, G. Genet, V. Lachaize, C. Guilbeau-Frugier, J. Fauconnier, C. Mias, B. Payré, L. Chopinet, D. Alsteens, S. Kasas, C. Severac, J. Thireau, C. Heymes, B. Honton, A. Lacampagne, A. Pathak, J.-M. Sénard, and C. Galés, "Atomic force and electron microscopic-based study of sarcolemmal surface of living cardiomyocytes unveils unexpected mitochondrial shift in heart failure," *Journal of Molecular and Cellular Cardiology*, vol. 74, pp. 162–172, Sep. 2014.

[35] R. C. Balijepalli, A. J. Lokuta, N. A. Maertz, J. M. Buck, R. A. Haworth, H. H. Valdivia, and T. J. Kamp, "Depletion of T-Tubules and specific subcellular changes in sarcolemmal proteins in tachycardia-induced heart failure," *Cardiovasc Res*, vol. 59, no. 1, pp. 67–77, Jul. 2003.

[36] S. Wei, A. Guo, B. Chen, W. Kutschke, Y.-P. Xie, K. Zimmerman, R. M. Weiss, M. E. Anderson, H. Cheng, and L.-S. Song, "T-Tubule remodeling during transition from hypertrophy to heart failure," *Circ Res*, vol. 107, no. 4, pp. 520–531, Aug. 2010.

[37] J.-Q. He, M. W. Conklin, J. D. Foell, M. R. Wolff, R. A. Haworth, R. Coronado, and T. J. Kamp, "Reduction in density of transverse tubules and L-type Ca^{2+} channels in canine tachycardia-induced heart failure," *Cardiovascular Research*, vol. 49, no. 2, pp. 298–307, 2001.

[38] F. R. Quinn, S. Currie, A. M. Duncan, S. Miller, R. Sayeed, S. M. Cobbe, and G. L. Smith, "Myocardial infarction causes increased expression but decreased activity of the myocardial Na^{+}-Ca^{+} exchanger in the rabbit," *The Journal of Physiology*, vol. 553, no. 1, pp. 229–242, 2003.

[39] L. Sacconi, C. Ferrantini, J. Lotti, R. Coppini, P. Yan, L. M. Loew, C. Tesi, E. Cerbai, C. Poggesi, and F. S. Pavone, "Action potential propagation in Transverse-Axial Tubular System is impaired in heart failure," *Proceedings of the National Academy of Sciences*, vol. 109, no. 15, pp. 5815–5819, Apr. 2012.

[40] M. B. Cannell, D. J. Crossman, and C. Soeller, "Effect of changes in action potential spike configuration, junctional sarcoplasmic reticulum micro-architecture and altered T-Tubule structure in human heart failure," *Journal of Muscle Research & Cell Motility*, vol. 27, no. 5, pp. 297–306, 2006.

[41] A. Guo, C. Zhang, S. Wei, B. Chen, and L.-S. Song, "Emerging mechanisms of T-Tubule remodelling in heart failure," *Cardiovascular Research*, vol. 98, no. 2, pp. 204–215, Jan. 2013.

[42] M. Pásek, F. Brette, A. Nelson, C. Pearce, A. Qaiser, G. Christé, and C. Orchard, "Quantification of T-Tubule area and protein distribution

in rat cardiac ventricular myocytes," *Progress in Biophysics and Molecular Biology*, vol. 96, no. 1â€“3, pp. 244–257, Jan. 2008.

[43] M. Pásek, J. Simurda, C. H. Orchard, and G. Christé, "A model of the guinea-pig ventricular cardiac myocyte incorporating a transverse-axial tubular system," *Progress in Biophysics and Molecular Biology*, vol. 96, pp. 258–280, Jan. 2008.

[44] R. Hooke, *Micrographia: Or some Physiological Descriptions of Minute Bodies made by Magnifying Glasses with Observations and Inquiries thereupon*. J. Martyn, J. Allestry, Printers to the Royal Society, 1665.

[45] G. Ourisson and Y. Nakatani, "The terpenoid theory of the origin of cellular life: the evolution of terpenoids to cholesterol," *Chemistry & biology*, vol. 1, no. 1, 1994.

[46] X. Wang, W. Xie, Y. Zhang, P. Lin, L. Han, P. Han, Y. Wang, Z. Chen, G. Ji, M. Zheng, N. Weisleder, R.-P. Xiao, H. Takeshima, J. Ma, and H. Cheng, "Cardioprotection of ischemia/reperfusion injury by cholesterol-dependent MG53-mediated membrane repair," *Circ Res*, vol. 107, no. 1, pp. 76–83, Jul. 2010.

[47] K. B. Pasumarthi and L. J. Field, "Cardiomyocyte cell cycle regulation," *Circ Res*, vol. 90, no. 10, pp. 1044–1054, May 2002.

[48] P. Janmey and P. Kinnunen, "Biophysical properties of lipids and dynamic membranes," *Trends in Cell Biology*, vol. 16, no. 10, pp. 538–546, Oct. 2006.

[49] A. J. Kosmalska, L. Casares, A. Elosegui-Artola, J. J. Thottacherry, R. Moreno-Vicente, V. González-Tarragó, M. n. del Pozo, S. Mayor, M. Arroyo, D. Navajas, X. Trepat, N. C. Gauthier, and P. Roca-Cusachs, "Physical principles of membrane remodelling during cell mechanoadaptation," *Nature Communications*, vol. 6, p. 7292, Jun. 2015.

[50] M. S. Bretscher, "Membrane structure: Some general principles," *Science*, vol. 181, no. 4100, pp. 622–629, Aug. 1973.

[51] S. Sigismund, S. Confalonieri, A. Ciliberto, S. Polo, G. Scita, and P. P. Di Fiore, "Endocytosis and signaling: Cell logistics shape the eukaryotic cell plan," *Physiol Rev*, vol. 92, no. 1, pp. 273–366, Jan. 2012.

[52] M. RaafetAmmar, N. Kassas, S. Chasserot-Golaz, M.-F. Bader, and N. Vitale, "Lipids in regulated exocytosis: what are they doing?" *The regulated secretory pathway in neuroendocrine cells*, p. 71, 2014.

[53] R. G. W. Anderson, "The caveolae membrane system," *Annu. Rev. Biochem.*, vol. 67, no. 1, pp. 199–225, Jun. 1998.

[54] R. G. Parton and M. A. del Pozo, "Caveolae as plasma membrane sensors, protectors and organizers," *Nat Rev Mol Cell Biol*, vol. 14, no. 2, pp. 98–112, Feb. 2013.

[55] H. T. McMahon and E. Boucrot, "Molecular mechanism and physiological functions of clathrin-mediated endocytosis," *Nat Rev Mol Cell Biol*, vol. 12, no. 8, pp. 517–533, Aug. 2011.

[56] H. T. McMahon and J. L. Gallop, "Membrane curvature and mechanisms of dynamic cell membrane remodelling," *Nature*, vol. 438, no. 7068, pp. 590–596, Dec. 2005.

[57] H. T. McMahon and E. Boucrot, "Membrane curvature at a glance," *J. Cell Sci.*, vol. 128, no. 6, pp. 1065–1070, Mar. 2015.

[58] R. Rohatgi and W. J. Snell, "The ciliary membrane," *Current Opinion in Cell Biology*, vol. 22, no. 4, pp. 541–546, Aug. 2010.

[59] R. Bloodgood, *Ciliary and flagellar membranes*. Springer Science & Business Media, 2013.

[60] G. Jacquemet, H. Hamidi, and J. Ivaska, "Filopodia in cell adhesion, 3D migration and cancer cell invasion," *Current Opinion in Cell Biology*, vol. 36, pp. 23–31, Oct. 2015.

[61] W. R. Loewenstein, "Junctional intercellular communication: the cell-to-cell membrane channel." *Physiol Rev*, vol. 61, no. 4, pp. 829–913, Oct. 1981.

[62] E. Balse, D. F. Steele, H. Abriel, A. Coulombe, D. Fedida, and S. N. Hatem, "Dynamic of ion channel expression at the plasma membrane of cardiomyocytes," *Physiol Rev*, vol. 92, no. 3, pp. 1317–1358, Jul. 2012.

[63] C. Fahlke and B. Nilius, "Molecular physiology of anion channels: dual function proteins and new structural motifs - a special issue," *Pflügers Archiv - European Journal of Physiology*, vol. 468, no. 3, pp. 369–370, 2016.

[64] K. Simons, "Cell membranes: A subjective perspective," *Biochimica et Biophysica Acta (BBA) - Biomembranes*, vol. 1858, no. 10, pp. 2569–2572, Oct. 2016.

[65] R. E. Pagano and R. G. Sleight, "Emerging problems in the cell biology of lipids," *Trends in Biochemical Sciences*, vol. 10, no. 11, pp. 421–425, 1985.

[66] M. J. Berridge, "Inositol trisphosphate and diacylglycerol: two interacting second messengers," *Annual review of biochemistry*, vol. 56, no. 1, pp. 159–193, 1987.

[67] G. A. Cross, "Eukaryotic protein modification and membrane attachment via phosphatidylinositol," *Cell*, vol. 48, no. 2, pp. 179–181, 1987.

[68] K. Simons and G. Van Meer, "Lipid sorting in epithelial cells," *Biochemistry*, vol. 27, no. 17, pp. 6197–6202, 1988.

[69] K. Simons and E. Ikonen, "Functional rafts in cell membranes," *Nature*, vol. 387, no. 6633, pp. 569–572, Jun. 1997.

[70] D. M. Engelman, "Membranes are more mosaic than fluid," *Nature*, vol. 438, no. 7068, pp. 578–580, Dec. 2005.

[71] L. J. Pike, "The challenge of lipid rafts," *Journal of Lipid Research*, vol. 50, no. Supplement, pp. S323–S328, Apr. 2009.

[72] I. Levental and S. L. Veatch, "The continuing mystery of lipid rafts," *Journal of Molecular Biology*, 2016.

[73] L. J. Pike, "Rafts defined: a report on the keystone symposium on lipid rafts and cell function," *Journal of Lipid Research*, vol. 47, no. 7, pp. 1597–1598, Jul. 2006.

[74] X. Xu and E. London, "The effect of sterol structure on membrane lipid domains reveals how Cholesterol can induce lipid domain formation," *Biochemistry*, vol. 39, no. 5, pp. 843–849, Feb. 2000.

[75] N. P. Barrera, M. Zhou, and C. V. Robinson, "The role of lipids in defining membrane protein interactions: insights from mass spectrometry," *Trends in Cell Biology*, vol. 23, no. 1, pp. 1–8, Jan. 2013.

[76] M. C. Rheinstädter and O. G. Mouritsen, "Small-scale structure in fluid cholesterol - lipid bilayers," *Current Opinion in Colloid & Interface Science*, vol. 18, no. 5, pp. 440–447, Oct. 2013.

[77] H. Heerklotz, "Triton promotes domain formation in lipid raft mixtures," *Biophysical Journal*, vol. 83, no. 5, pp. 2693–2701, Nov. 2002.

[78] S. Munro, "Lipid rafts: Elusive or illusive?" *Cell*, vol. 115, no. 4, pp. 377–388, Nov. 2003.

[79] T. M. Stulnig, M. Berger, T. Sigmund, D. Raederstorff, H. Stockinger, and W. Waldhäusl, "Polyunsaturated fatty acids inhibit T cell signal transduction by modification of detergent-insoluble membrane domains," *J Cell Biol*, vol. 143, no. 3, pp. 637–644, Nov. 1998.

[80] E. D. Sheets, D. Holowka, and B. Baird, "Critical role for Cholesterol in Lyn-mediated Tyrosine phosphorylation of FcϵRI and their association with detergent-resistant membranes," *J Cell Biol*, vol. 145, no. 4, pp. 877–887, May 1999.

[81] E. Ikonen, "Roles of lipid rafts in membrane transport," *Current Opinion in Cell Biology*, vol. 13, no. 4, pp. 470–477, Aug. 2001.

[82] N. T. Watt, H. H. Griffiths, and N. M. Hooper, "Lipid rafts: linking prion protein to zinc transport and amyloid-β toxicity in Alzheimer's disease," *Promiscuous Functions of the Prion Protein Gene Family*, p. 92, 2015.

[83] R. Schroeder, E. London, and D. Brown, "Interactions between saturated acyl chains confer detergent resistance on lipids and GPI-anchored proteins: GPI-anchored proteins in liposomes and cells show similar behavior," *Proc. Natl. Acad. Sci. USA*, vol. 91, pp. 12 130–12 134, 1994.

[84] R. G. Parton and K. Simons, "Digging into caveolae," *Science*, vol. 269, no. 5229, p. 1398, Sep 1995.

[85] T. Harder and K. Simons, "Caveolae, DIGs, and the dynamics of sphingolipid-cholesterol microdomains," *Current Opinion in Cell Biology*, vol. 9, no. 4, pp. 534–542, 1997.

[86] T. V. Kurzchalia, E. Hartmann, and P. Dupree, "Guilty by insolubility - does a protein's detergent insolubility reflect a caveolar location?" *Trends in Cell Biology*, vol. 5, no. 5, pp. 187–189, 1995.

[87] J. E. Schnitzer, D. P. McIntosh, A. M. Dvorak, J. Liu, and P. Oh, "Separation of caveolae from associated microdomains of GPI-anchored proteins," *Science*, vol. 269, no. 5229, p. 1435, Sep 1995.

[88] M. W. Peters and C. W. Grant, "Freeze-etch study of an unmodified lectin interacting with its receptors in model membranes," *Biochimica et Biophysica Acta (BBA) - Biomembranes*, vol. 775, no. 3, pp. 273–282, 1984.

[89] C. Yuan and L. J. Johnston, "Atomic force microscopy studies of ganglioside GM1 domains in phosphatidylcholine and phosphatidylcholine/cholesterol bilayers," *Biophysical Journal*, vol. 81, no. 2, pp. 1059–1069, Aug. 2001.

[90] C. Yuan, J. Furlong, P. Burgos, and L. J. Johnston, "The size of lipid rafts: An atomic force microscopy study of ganglioside GM1 domains in sphingomyelin/DOPC/cholesterol membranes," *Biophysical Journal*, vol. 82, no. 5, pp. 2526–2535, May 2002.

[91] T. Harder, P. Scheiffele, P. Verkade, and K. Simons, "Lipid domain structure of the plasma membrane revealed by patching of membrane components," *The Journal of Cell Biology*, vol. 141, no. 4, pp. 929–942, 1998.

[92] C. Dietrich, L. Bagatolli, Z. Volovyk, N. Thompson, M. Levi, K. Jacobson, and E. Gratton, "Lipid rafts reconstituted in model membranes," *Biophysical Journal*, vol. 80, no. 3, pp. 1417–1428, Mar. 2001.

[93] N. Kahya, D. Scherfeld, K. Bacia, B. Poolman, and P. Schwille, "Probing lipid mobility of raft-exhibiting model membranes by fluorescence correlation spectroscopy," *Journal of Biological Chemistry*, vol. 278, no. 30, pp. 28 109–28 115, Jul. 2003.

[94] K. Simons and M. J. Gerl, "Revitalizing membrane rafts: new tools and insights," *Nat Rev Mol Cell Biol*, vol. 11, no. 10, pp. 688–699, Oct. 2010.

[95] K. Bacia, P. Schwille, and T. Kurzchalia, "Sterol structure determines the separation of phases and the curvature of the liquid-ordered phase in model membranes," *Proceedings of the National Academy of Sciences of the United States of America*, vol. 102, no. 9, pp. 3272–3277, Mar. 2005.

[96] O. Coban, M. Burger, M. Laliberte, A. Ianoul, and L. J. Johnston, "Ganglioside partitioning and aggregation in phase-separated monolayers characterized by BODIPY GM1 monomer/dimer emission," *Langmuir*, vol. 23, no. 12, pp. 6704–6711, Jun. 2007.

[97] L. Mrowczynska, C. Lindqvist, A. Iglis, and H. Hägerstrand, "Spontaneous curvature of ganglioside GM1 — effect of cross-linking," *Biochemical and Biophysical Research Communications*, vol. 422, no. 4, pp. 776–779, Jun. 2012.

[98] C. Eggeling, C. Ringemann, R. Medda, G. Schwarzmann, K. Sandhoff, S. Polyakova, V. N. Belov, B. Hein, C. von Middendorff, A. Schonle, and S. W. Hell, "Direct observation of the nanoscale dynamics of membrane lipids in a living cell," *Nature*, vol. 457, no. 7233, pp. 1159–1162, Feb. 2009.

[99] V. Mueller, C. Ringemann, A. Honigmann, G. Schwarzmann, R. Medda, M. Leutenegger, S. Polyakova, V. Belov, S. Hell, and C. Eggeling, "STED nanoscopy reveals molecular details of Cholesterol- and cytoskeleton-modulated lipid interactions in living cells," *Biophysical Journal*, vol. 101, no. 7, pp. 1651–1660, Oct. 2011.

[100] A. Honigmann, V. Mueller, H. Ta, A. Schönle, E. Sezgin, S. W. Hell, and C. Eggeling, "Scanning STED-FCS reveals spatiotemporal heterogeneity

of lipid interaction in the plasma membrane of living cells," *Nature Communications*, vol. 5, p. 5412, Nov. 2014.

[101] A. Honigmann, S. Sadeghi, J. Keller, S. W. Hell, C. Eggeling, and R. Vink, "A lipid bound actin meshwork organizes liquid phase separation in model membranes," *eLife*, vol. 3, p. e01671, mar 2014.

[102] P. H. Lommerse, K. Vastenhoud, N. J. Pirinen, A. I. Magee, H. P. Spaink, and T. Schmidt, "Single-molecule diffusion reveals similar mobility for the Lck, H-Ras, and K-Ras membrane anchors," *Biophysical Journal*, vol. 91, no. 3, pp. 1090–1097, Aug. 2006.

[103] M. D. Wilson and L. L. Rudel, "Review of Cholesterol absorption with emphasis on dietary and biliary cholesterol," *Journal of Lipid Research*, vol. 35, pp. 943–955, 1994.

[104] F. R. Kapourchali, G. Surendiran, A. Goulet, and M. H. Moghadasian, "The role of dietary Cholesterol in lipoprotein metabolism and related metabolic abnormalities: A mini-review," *Critical Reviews in Food Science and Nutrition*, vol. 56, no. 14, pp. 2408–2415, Oct. 2016.

[105] J. M. Berg, J. L. Tymoczko, and L. Stryer, *Important Derivatives of Cholesterol Include Bile Salts and Steroid Hormones*. WH Freeman, 2002.

[106] A. H. Payne and D. B. Hales, "Overview of steroidogenic enzymes in the pathway from cholesterol to active steroid hormones," *Endocrine Reviews*, vol. 25, no. 6, pp. 947–970, Dec. 2004.

[107] W. L. Miller and R. J. Auchus, "The molecular biology, biochemistry, and physiology of human steroidogenesis and its disorders," *Endocrine Reviews*, vol. 32, no. 1, pp. 81–151, Nov. 2010.

[108] G. Gibbons, K. Mitropoulos, and N. B. Myant, *Biochemistry of cholesterol*. Elsevier Biomedical Press, 1982.

[109] M. S. Brown and J. L. Goldstein, "Heart attacks: Gone with the century?" *Science*, vol. 272, no. 5262, p. 629, May 1996.

[110] S. Berger, G. Raman, R. Vishwanathan, P. F. Jacques, and E. J. Johnson, "Dietary cholesterol and cardiovascular disease: a systematic review and meta-analysis," *The American Journal of Clinical Nutrition*, Jun. 2015.

[111] S. M. Grundy, "Does dietary cholesterol matter?" *Current Atherosclerosis Reports*, vol. 18, no. 11, p. 68, 2016.

[112] R. A. Cooper, M. H. Leslie, S. Fischkoff, M. Shinitzky, and S. J. Shattil, "Factors influencing the lipid composition and fluidity of red cell membranes in vitro: production of red cells possessing more than two cholesterols per phospholipid," *Biochemistry*, vol. 17, no. 2, pp. 327–331, Jan. 1978.

[113] B. Alberts, D. Bray, J. Lewis, M. Raff, K. Roberts, and J. Watson, *Molecular Biology of the Cell (3rd edn.)*. Garland Science, Taylor & Francis Group, 1994.

[114] D. E. Vance and H. Van den Bosch, "Cholesterol in the year 2000," *Biochimica et Biophysica Acta (BBA) - Molecular and Cell Biology of Lipids*, vol. 1529, pp. 1–8, Dec. 2000.

[115] K. E. Bloch, "Speculations on the evolution of sterol structure and function," *Critical Reviews in Biochemistry*, vol. 7, no. 1, pp. 1–5, Jan. 1979.

[116] K. E. Bloch, "Sterol, structure and membrane function," *Critical Reviews in Biochemistry*, vol. 14, no. 1, pp. 47–92, Jan. 1983.

[117] L. Miao, M. Nielsen, J. Thewalt, J. H. Ipsen, M. Bloom, M. J. Zuckermann, and O. G. Mouritsen, "From lanosterol to cholesterol: Structural evolution and differential effects on lipid bilayers," *Biophysical Journal*, vol. 82, no. 3, pp. 1429–1444, Mar. 2002.

[118] M. A. Churchward, T. Rogasevskaia, D. M. Brandman, H. Khosravani, P. Nava, J. K. Atkinson, and J. R. Coorssen, "Specific lipids supply critical negative spontaneous curvature - an essential component of native Ca^{2+}-triggered membrane fusion," *Biophysical Journal*, vol. 94, no. 10, pp. 3976–3986, May 2008.

[119] J. Fantini and F. J. Barrantes, "How cholesterol interacts with membrane proteins: an exploration of cholesterol-binding sites including CRAC, CARC, and tilted domains," *Frontiers in Physiology*, vol. 4, pp. 31–39, Feb. 2013.

[120] W. B. Huttner and J. Zimmerberg, "Implications of lipid microdomains for membrane curvature, budding and fission: Commentary," *Current Opinion in Cell Biology*, vol. 13, no. 4, pp. 478–484, Aug. 2001.

[121] M. E. Johnson, D. A. Berk, D. Blankschtein, D. E. Golan, R. K. Jain, and R. S. Langer, "Lateral diffusion of small compounds in human stratum corneum and model lipid bilayer systems." *Biophysical Journal*, vol. 71, no. 5, pp. 2656–2668, Nov. 1996.

[122] T. Hianik, M. Haburcák, K. Lohner, E. Prenner, F. Paltauf, and A. Hermetter, "Compressibility and density of lipid bilayers composed of polyunsaturated phospholipids and cholesterol," *Colloids and Surfaces A: Physicochemical and Engineering Aspects*, vol. 139, no. 2, pp. 189–197, Aug. 1998.

[123] D. Wüstner and K. Solanko, "How Cholesterol interacts with proteins and lipids during its intracellular transport," *Biochimica et Biophysica Acta (BBA) - Biomembranes*, vol. 1848, no. 9, pp. 1908–1926, Sep. 2015.

[124] P. S. Kabouridis, J. Janzen, A. L. Magee, and S. C. Ley, "Cholesterol depletion disrupts lipid rafts and modulates the activity of multiple signaling pathways in T lymphocytes," *European journal of immunology*, vol. 30, no. 3, pp. 954–963, 2000.

[125] A. R. Tall and L. Yvan-Charvet, "Cholesterol, inflammation and innate immunity," *Nat Rev Immunol*, vol. 15, no. 2, pp. 104–116, Feb. 2015.

[126] P. A. Edwards and J. Ericsson, "Sterols and isoprenoids: Signaling molecules derived from the Cholesterol biosynthetic pathway," *Annu. Rev. Biochem.*, vol. 68, no. 1, pp. 157–185, Jun. 1999.

[127] S. Cao, M. E. Fernandez-Zapico, D. Jin, V. Puri, T. A. Cook, L. O. Lerman, X.-Y. Zhu, R. Urrutia, and V. Shah, "KLF11-mediated repression

antagonizes Sp1/sterol-responsive element-binding protein-induced transcriptional activation of Caveolin-1 in response to Cholesterol signaling," *Journal of Biological Chemistry*, vol. 280, no. 3, pp. 1901–1910, Jan. 2005.

[128] R. P. Cook, *Cholesterol: chemistry, biochemistry, and pathology*. Elsevier, 2015.

[129] F. Maxfield and G. van Meer, "Cholesterol, the central lipid of mammalian cells," *Current Opinion in Cell Biology*, vol. 22, no. 4, pp. 422–429, 2010.

[130] T. L. Steck and Y. Lange, "Cell cholesterol homeostasis: Mediation by active Cholesterol," *Trends in Cell Biology*, vol. 20, no. 11, pp. 680–687, Nov. 2010.

[131] A. Reboulleau, V. Robert, B. Vedie, A. Doublet, A. Grynberg, J.-L. Paul, and N. Fournier, "Involvement of cholesterol efflux pathway in the control of cardiomyocytes cholesterol homeostasis," *Journal of Molecular and Cellular Cardiology*, vol. 53, no. 2, pp. 196–205, Aug. 2012.

[132] A. Radhakrishnan, T. G. Anderson, and H. M. McConnell, "Condensed complexes, rafts, and the chemical activity of cholesterol in membranes," *Proceedings of the National Academy of Sciences*, vol. 97, no. 23, pp. 12 422–12 427, Nov. 2000.

[133] P. L. Chong, "Evidence for regular distribution of sterols in liquid crystalline phosphatidylcholine bilayers," *Proceedings of the National Academy of Sciences*, vol. 91, no. 21, pp. 10 069–10 073, Oct. 1994.

[134] M. R. Ali, K. H. Cheng, and J. Huang, "Assess the nature of cholesterol–lipid interactions through the chemical potential of cholesterol in phosphatidylcholine bilayers," *Proceedings of the National Academy of Sciences*, vol. 104, no. 13, pp. 5372–5377, Mar. 2007.

[135] J. Dai, M. Alwarawrah, and J. Huang, "Instability of Cholesterol clusters in lipid bilayers and the Cholesterol's umbrella effect," *J. Phys. Chem. B*, vol. 114, no. 2, pp. 840–848, Jan. 2010.

[136] R. J. Alsop and M. C. Rheinstädter, "Lipid rafts in binary lipid/cholesterol bilayers," in *Cell Biology Research Progress;17-42*. Nova, 2016.

[137] Z. Chen and R. P. Rand, "The influence of cholesterol on phospholipid membrane curvature and bending elasticity." *Biophysical Journal*, vol. 73, no. 1, pp. 267–276, Jul. 1997.

[138] M. A. Churchward, T. Rogasevskaia, J. Höfgen, J. Bau, and J. R. Coorssen, "Cholesterol facilitates the native mechanism of Ca^{2+}-triggered membrane fusion," *J. Cell Sci.*, vol. 118, no. 20, pp. 4833–4848, Oct. 2005.

[139] B. Kollmitzer, P. Heftberger, M. Rappolt, and G. Pabst, "Monolayer spontaneous curvature of raft-forming membrane lipids," *Soft Matter*, vol. 9, no. 45, pp. 10 877–10 884, 2013.

[140] R. G. Parton and K. Simons, "The multiple faces of caveolae," *Nat Rev Mol Cell Biol*, vol. 8, no. 3, pp. 185–194, Mar. 2007.

[141] B. Sinha, D. Köster, R. Ruez, P. Gonnord, M. Bastiani, D. Abankwa, R. V. Stan, G. Butler-Browne, B. Vedie, L. Johannes, N. Morone, R. G. Parton, G. Raposo, P. Sens, C. Lamaze, and P. Nassoy, "Cells respond to mechanical stress by rapid disassembly of caveolae," *Cell*, vol. 144, no. 3, pp. 402–413, Feb. 2011.

[142] E. Pfeiffer, A. Wright, A. Edwards, J. Stowe, K. McNall, J. Tan, I. Niesman, H. Patel, D. Roth, J. Omens, and A. McCulloch, "Caveolae in ventricular myocytes are required for stretch-dependent conduction slowing," *Journal of Molecular and Cellular Cardiology*, vol. 76, pp. 265 – 274, 2014.

[143] Y. Lange and T. L. Steck, "Active membrane Cholesterol as a physiological effector," *Chemistry and Physics of Lipids*, vol. 199, pp. 74–93, Sep. 2016.

[144] E. Bastiaanse, D. Atsma, M. Kuijpers, and A. Vanderlaarse, "The effect of sarcolemmal Cholesterol content on intracellular Calcium ion

concentration in cultured cardiomyocytes," *Archives of Biochemistry and Biophysics*, vol. 313, no. 1, pp. 58–63, 1994.

[145] G. E. Sumnicht and R. A. Sabbadini, "Lipid composition of transverse tubular membranes from normal and dystrophic skeletal muscle," *Archives of Biochemistry and Biophysics*, vol. 215, no. 2, pp. 628–637, 1982.

[146] Y. Hasin, Y. Shimoni, O. Stein, and Y. Stein, "Effect of cholesterol depletion on the electrical activity of rat heart myocytes in culture," *Journal of Molecular and Cellular Cardiology*, vol. 12, no. 7, pp. 675–683, Jul. 1980.

[147] H. Satoh, L. Delbridge, L. Blatter, and D. Bers, "Surface:volume relationship in cardiac myocytes studied with confocal microscopy and membrane capacitance measurements: species-dependence and developmental effects," *Biophysical Journal*, vol. 70, no. 3, pp. 1494–1504, 1996.

[148] S. Calaghan and E. White, "Caveolae modulate excitation-contraction coupling and β2-adrenergic signalling in adult rat ventricular myocytes," *Cardiovascular Research*, vol. 69, no. 4, pp. 816–824, 2006.

[149] M. Z. Haque, V. J. McIntosh, A. B. Abou Samra, R. M. Mohammad, and R. D. Lasley, "Cholesterol depletion alters cardiomyocyte subcellular signaling and increases contractility," *PLoS ONE*, vol. 11, no. 7, pp. e0 154 151–, Jul. 2016.

[150] Y. Zhu, C. Zhang, B. Chen, R. Chen, A. Guo, J. Hong, and L.-S. Song, "Cholesterol is required for maintaining T-Tubule integrity and intercellular connections at intercalated discs in cardiomyocytes," *Journal of Molecular and Cellular Cardiology*, vol. 97, pp. 204–212, Aug. 2016.

[151] G. Christé, "Localization of K^+ channels in the T-Tubules of cardiomyocytes as suggested by the parallel decay of membrane capacitance, IK_1 and IK_{ATP} during culture and by delayed IK_1 response to Barium," *Journal of Molecular and Cellular Cardiology*, vol. 31, no. 12, pp. 2207–2213, Dec. 1999.

[152] W. E. Louch, V. Bito, F. R. Heinzel, R. Macianskiene, J. Vanhaecke, W. Flameng, K. Mubagwa, and K. R. Sipido, "Reduced synchrony of Ca^{2+} release with loss of T-Tubules - a comparison to Ca^{2+} release in human failing cardiomyocytes," *Cardiovasc Res*, vol. 62, no. 1, pp. 63–73, Apr. 2004.

[153] T. Banyasz, I. Lozinskiy, C. E. Payne, S. Edelmann, B. Norton, B. Chen, Y. Chen-Izu, L. T. Izu, and C. W. Balke, "Transformation of adult rat cardiac myocytes in primary culture," *Experimental Physiology*, vol. 93, no. 3, pp. 370–382, 2008.

[154] J. Perk, G. De Backer, H. Gohlke, I. Graham, Ž. Reiner, M. Verschuren, C. Albus, P. Benlian, G. Boysen, R. Cifkova *et al.*, "European guidelines on cardiovascular disease prevention in clinical practice (version 2012)," *European heart journal*, vol. 33, no. 13, pp. 1635–1701, 2012.

[155] T. B. Horwich, M. A. Hamilton, W. MacLellan, and G. C. Fonarow, "Low serum total cholesterol is associated with marked increase in mortality in advanced heart failure," *Journal of Cardiac Failure*, vol. 8, no. 4, pp. 216–224, Aug. 2002.

[156] M. Rauchhaus, A. L. Clark, W. Doehner, C. Davos, A. Bolger, R. Sharma, A. J. Coats, and S. D. Anker, "The relationship between Cholesterol and survival in patients with chronic heart failure," *Journal of the American College of Cardiology*, vol. 42, no. 11, pp. 1933–1940, Dec. 2003.

[157] T. V. Kurzchalia, P. Dupree, R. G. Parton, R. Kellner, H. Virta, M. Lehnert, and K. Simons, "VIP21, a 21-kD membrane protein is an integral component of *trans*-Golgi-network-derived transport vesicles." *J Cell Biol*, vol. 118, no. 5, pp. 1003–1014, Sep. 1992.

[158] M. Way and R. G. Parton, "M-Caveolin, a muscle-specific caveolin-related protein," *FEBS Letters*, vol. 376, no. 1-2, pp. 108–112, 1995.

[159] Z. Tang, P. E. Scherer, T. Okamoto, K. Song, C. Chu, D. S. Kohtz, I. Nishimoto, H. F. Lodish, and M. P. Lisanti, "Molecular cloning of Caveolin-3, a novel member of the caveolin gene family expressed

predominantly in muscle," *Journal of Biological Chemistry*, vol. 271, no. 4, pp. 2255–2261, Jan. 1996.

[160] C. J. Fielding and P. E. Fielding, "Cholesterol and caveolae: structural and functional relationships," *Biochimica et Biophysica Acta (BBA) - Molecular and Cell Biology of Lipids*, vol. 1529, pp. 210–222, Dec. 2000.

[161] R. G. Parton, "Caveolae and caveolins," *Current Opinion in Cell Biology*, vol. 8, no. 4, pp. 542–548, 1996.

[162] A. Schlegel, R. B. Schwab, P. E. Scherer, and M. P. Lisanti, "A role for the caveolin scaffolding domain in mediating the membrane attachment of Caveolin-1: The caveolin scaffolding domain is both necessary and sufficient for membrane binding in vitro," *Journal of Biological Chemistry*, vol. 274, no. 32, pp. 22 660–22 667, Aug. 1999.

[163] A. Schlegel and M. P. Lisanti, "A molecular dissection of Caveolin-1 membrane attachment and oligomerization: Two separate regions of the Caveolin-1 C-terminal domain mediate membrane binding and oligomer/oligomer interactions in vivo," *Journal of Biological Chemistry*, vol. 275, no. 28, pp. 21 605–21 617, Jul. 2000.

[164] G. Whiteley, R. F. Collins, and A. Kitmitto, "Characterization of the molecular architecture of human Caveolin-3 and interaction with the skeletal muscle ryanodine receptor," *Journal of Biological Chemistry*, vol. 287, no. 48, pp. 40 302–40 316, Nov. 2012.

[165] C. Boscher and I. R. Nabi, "Caveolin-1: role in cell signaling," in *Caveolins and Caveolae*. Springer, 2012, pp. 29–50.

[166] J.-H. Kim, D. Peng, J. P. Schlebach, A. Hadziselimovic, and C. R. Sanders, "Modest effects of lipid modifications on the structure of Caveolin-3," *Biochemistry*, vol. 53, no. 27, pp. 4320–4322, Jul. 2014.

[167] A. Arbuzova, L. Wang, J. Wang, G. Hangyás-Mihályné, D. Murray, B. Honig, and S. McLaughlin, "Membrane binding of peptides containing both basic and aromatic residues. experimental studies with peptides corresponding to the scaffolding region of caveolin and

the effector region of MARCKS," *Biochemistry*, vol. 39, no. 33, pp. 10 330–10 339, Aug. 2000.

[168] T. M. Williams and M. P. Lisanti, "The caveolin proteins," *Genome Biology*, vol. 5, no. 3, p. 214, 2004.

[169] G. Frühbeck, M. López, and C. Diéguez, "Role of caveolins in body weight and insulin resistance regulation," *Trends in Endocrinology & Metabolism*, vol. 18, no. 5, pp. 177 – 182, 2007.

[170] R. G. Parton, M. Hanzal-Bayer, and J. F. Hancock, "Biogenesis of caveolae: a structural model for caveolin-induced domain formation," *J. Cell Sci.*, vol. 119, no. 5, pp. 787–796, Feb. 2006.

[171] M. Murata, J. Peränen, R. Schreiner, F. Wieland, T. V. Kurzchalia, and K. Simons, "Vip21/caveolin is a cholesterol-binding protein," *Proceedings of the National Academy of Sciences*, vol. 92, no. 22, pp. 10 339–10 343, Oct. 1995.

[172] C. Thiele, M. J. Hannah, F. Fahrenholz, and W. B. Huttner, "Cholesterol binds to synaptophysin and is required for biogenesis of synaptic vesicles," *Nat Cell Biol*, vol. 2, no. 1, pp. 42–49, Jan. 2000.

[173] L. J. Pike, X. Han, K.-N. Chung, and R. W. Gross, "Lipid rafts are enriched in arachidonic acid and plasmenylethanolamine and their composition is independent of caveolin-1 expression: A quantitative electrospray ionization/mass spectrometric analysis," *Biochemistry*, vol. 41, no. 6, pp. 2075–2088, Feb. 2002.

[174] P. Dupree, R. G. Parton, G. Raposo, T. V. Kurzchalia, and K. Simons, "Caveolae and sorting in the *trans*-Golgi network of epithelial cells." *The EMBO Journal*, vol. 12, no. 4, pp. 1597–1605, Apr. 1993.

[175] L. Pelkmans and M. Zerial, "Kinase-regulated quantal assemblies and kiss-and-run recycling of caveolae," *Nature*, vol. 436, no. 7047, pp. 128–133, Jul. 2005.

[176] G. E. Palade, "Fine structure of blood capillaries," *J Appl phys*, vol. 24, no. 1, pp. 1424–1436, 1953.

[177] E. Yamada, "The fine structure of the gall bladder epithelium of the mouse," *The Journal of Biophysical and Biochemical Cytology*, vol. 1, no. 5, pp. 445–458, Jun. 1955.

[178] A. Tagawa, A. Mezzacasa, A. Hayer, A. Longatti, L. Pelkmans, and A. Helenius, "Assembly and trafficking of caveolar domains in the cell," *J Cell Biol*, vol. 170, no. 5, pp. 769–779, Aug. 2005.

[179] M. M. Hill, M. Bastiani, R. Luetterforst, M. Kirkham, A. Kirkham, S. J. Nixon, P. Walser, D. Abankwa, V. M. Oorschot, S. Martin, J. F. Hancock, and R. G. Parton, "PTRF-Cavin, a conserved cytoplasmic protein required for caveola formation and function," *Cell*, vol. 132, no. 1, pp. 113–124, Jan. 2008.

[180] A. Hayer, M. Stoeber, C. Bissig, and A. Helenius, "Biogenesis of caveolae: Stepwise assembly of large caveolin and cavin complexes," *Traffic*, vol. 11, no. 3, pp. 361–382, 2010.

[181] R. G. Parton, M. Way, N. Zorzi, and E. Stang, "Caveolin-3 associates with developing T-Tubules during muscle differentiation," *J Cell Biol*, vol. 136, no. 1, pp. 137–154, Jan. 1997.

[182] E. Ralston and T. Ploug, "Caveolin-3 is associated with the T-Tubules of mature skeletal muscle fibers," *Experimental Cell Research*, vol. 246, no. 2, pp. 510–515, Feb. 1999.

[183] R. M. Murphy, J. P. Mollica, and G. D. Lamb, "Plasma membrane removal in rat skeletal muscle fibers reveals Caveolin-3 hot-spots at the necks of transverse tubules," *Experimental Cell Research*, vol. 315, no. 6, pp. 1015–1028, Apr. 2009.

[184] X.-L. Wang, D. Ye, T. E. Peterson, S. Cao, V. H. Shah, Z. S. Katusic, G. C. Sieck, and H.-C. Lee, "Caveolae targeting and regulation of large conductance Ca^{2+}-activated K^+ channels in vascular endothelial cells," *Journal of Biological Chemistry*, vol. 280, no. 12, pp. 11 656–11 664, Mar. 2005.

[185] X. Cheng and J. H. Jaggar, "Genetic ablation of caveolin-1 modifies Ca^{2+} spark coupling in murine arterial smooth muscle cells," *Am J Physiol Heart Circ Physiol*, vol. 290, no. 6, pp. H2309–H2319, May 2006.

[186] Y.-Y. Zhao, Y. Liu, R.-V. Stan, L. Fan, Y. Gu, N. Dalton, P.-H. Chu, K. Peterson, J. Ross, and K. R. Chien, "Defects in Caveolin-1 cause dilated cardiomyopathy and pulmonary hypertension in knockout mice," *Proceedings of the National Academy of Sciences*, vol. 99, no. 17, pp. 11 375–11 380, Aug. 2002.

[187] Y.-Y. Zhao, Y. D. Zhao, M. K. Mirza, J. H. Huang, H.-H. S. Potula, S. M. Vogel, V. Brovkovych, J. X.-J. Yuan, J. Wharton, and A. B. Malik, "Persistent eNOS activation secondary to Caveolin-1 deficiency induces pulmonary hypertension in mice and humans through PKG nitration," *J Clin Invest*, vol. 119, no. 7, pp. 2009–2018, 2009.

[188] J. P. Cheng and B. J. Nichols, "Caveolae: One function or many?" *Trends in Cell Biology*, vol. 26, no. 3, pp. 177–189, Mar. 2016.

[189] M. Awasthi-Kalia, P. P. Schnetkamp, and J. P. Deans, "Differential effects of Filipin and Methyl-β-Cyclodextrin on B Cell Receptor signaling," *Biochemical and Biophysical Research Communications*, vol. 287, no. 1, pp. 77–82, 2001.

[190] U. Geumann, C. Schäfer, D. Riedel, R. Jahn, and S. O. Rizzoli, "Synaptic membrane proteins form stable microdomains in early endosomes," *Microscopy Research and Technique*, vol. 73, no. 6, pp. 606–617, 2010.

[191] E. J. Smart and R. G. Anderson, "Alterations in membrane cholesterol that affect structure and function of caveolae," in *Redox Cell Biology and Genetics Part B*, C. K. Sen and L. Packer, Eds. Academic Press, 2002, vol. Volume 353, pp. 131–139. [Online]. Available: http://www.sciencedirect.com/science/article/pii/S0076687902530433

[192] S. K. Rodal, G. Skretting, Ø. Garred, F. Vilhardt, B. Van Deurs, and K. Sandvig, "Extraction of cholesterol with methyl-β-cyclodextrin perturbs formation of clathrin-coated endocytic vesicles," *Molecular biology of the cell*, vol. 10, no. 4, pp. 961–974, 1999.

[193] K. Dreja, M. Voldstedlund, J. Vinten, J. Tranum-Jensen, P. Hellstrand, and K. Swärd, "Cholesterol depletion disrupts caveolae and differentially impairs agonist-induced arterial contraction," *Arterioscler Thromb Vasc Bio*, vol. 22, no. 8, pp. 1267–1272, Aug. 2002.

[194] M. Westermann, F. Steiniger, and W. Richter, "Belt-like localisation of caveolin in deep caveolae and its re-distribution after cholesterol depletion," *Histochemistry and Cell Biology*, vol. 123, no. 6, pp. 613–620, 2005.

[195] A. F. Dulhunty and C. Franzini-Armstrong, "The relative contributions of the folds and caveolae to the surface membrane of frog skeletal muscle fibres at different sarcomere lengths." *The Journal of Physiology*, vol. 250, no. 3, pp. 513–539, Sep. 1975.

[196] V. Vogel and M. Sheetz, "Local force and geometry sensing regulate cell functions," *Nat Rev Mol Cell Biol*, vol. 7, no. 4, pp. 265–275, Apr. 2006.

[197] N. W. Andrews, P. E. Almeida, and M. Corrotte, "Damage control: cellular mechanisms of plasma membrane repair," *Trends in Cell Biology*, vol. 24, no. 12, pp. 734–742, Dec. 2014.

[198] V. Idone, C. Tam, J. W. Goss, D. Toomre, M. Pypaert, and N. W. Andrews, "Repair of injured plasma membrane by rapid Ca^{2+}-dependent endocytosis," *J Cell Biol*, vol. 180, no. 5, pp. 905–914, Mar. 2008.

[199] M. Corrotte, P. E. Almeida, C. Tam, T. Castro-Gomes, M. C. Fernandes, B. A. Millis, M. Cortez, H. Miller, W. Song, T. K. Maugel, and N. W. Andrews, "Caveolae internalization repairs wounded cells and muscle fibers," *eLife*, vol. 2, p. e00926, sep 2013.

[200] M. Vatta, M. J. Ackerman, B. Ye, J. C. Makielski, E. E. Ughanze, E. W. Taylor, D. J. Tester, R. C. Balijepalli, J. D. Foell, Z. Li, T. J. Kamp, and J. A. Towbin, "Mutant Caveolin-3 induces persistent late Sodium current and is associated with Long-QT Syndrome," *Circulation*, vol. 114, no. 20, pp. 2104–2112, Nov. 2006.

[201] L. B. Cronk, B. Ye, T. Kaku, D. J. Tester, M. Vatta, J. C. Makielski, and M. J. Ackerman, "Novel mechanism for sudden infant death syndrome: persistent late Sodium current secondary to mutations in Caveolin-3," *Heart Rhythm*, vol. 4, no. 2, pp. 161–166, 2007.

[202] A. Koga, N. Oka, T. Kikuchi, H. Miyazaki, S. Kato, and T. Imaizumi, "Adenovirus-mediated overexpression of Caveolin-3 inhibits rat cardiomyocyte hypertrophy," *Hypertension*, vol. 42, no. 2, pp. 213–219, Jul. 2003.

[203] Y. M. Tsutsumi, Y. T. Horikawa, M. M. Jennings, M. W. Kidd, I. R. Niesman, U. Yokoyama, B. P. Head, Y. Hagiwara, Y. Ishikawa, A. Miyanohara, P. M. Patel, P. A. Insel, H. H. Patel, and D. M. Roth, "Cardiac-specific overexpression of Caveolin-3 induces endogenous cardiac protection by mimicking ischemic preconditioning," *Circulation*, vol. 118, no. 19, pp. 1979–1988, Nov. 2008.

[204] E. M. McNally, E. de Sá Moreira, D. J. Duggan, C. G. Bönnemann, M. P. Lisanti, H. G. Lidov, M. Vainzof, M. Rita Passos-Bueno, E. P. Hoffman, M. Zatz, and L. M. Kunkel, "Caveolin-3 in muscular dystrophy," *Human Molecular Genetics*, vol. 7, no. 5, pp. 871–877, May 1998.

[205] F. Galbiati, B. Razani, and M. P. Lisanti, "Caveolae and Caveolin-3 in muscular dystrophy," *Trends in Molecular Medicine*, vol. 7, no. 10, pp. 435–441, Oct. 2001.

[206] P. Nassoy and C. Lamaze, "Stressing caveolae new role in cell mechanics," *Trends in Cell Biology*, vol. 22, no. 7, pp. 381–389, Jul. 2012.

[207] E. Bonilla, K. Fischbeck, and D. L. Schotland, "Freeze-fracture studies of muscle caveolae in human muscular dystrophy." *The American Journal of Pathology*, vol. 104, no. 2, pp. 167–173, Aug. 1981.

[208] K. Song, P. Scherer, Z. Tang, T. Okamoto, S. Li, M. Chafel, C. Chu, D. Kohtz, and M. Lisanti, "Expression of Caveolin-3 in skeletal, cardiac, and smooth muscle cells: Caveolin-3 is a component of the sarcolemma and co-fractionates with Dystrophin and Dystrophin-

associated glycoproteins," *Journal of Biological Chemistry*, vol. 271, no. 25, pp. 15 160–15 165, 1996, cited By 511.

[209] S. Repetto, M. Bado, P. Broda, G. Lucania, E. Masetti, F. Sotgia, I. Carbone, A. Pavan, E. Bonilla, G. Cordone, M. P. Lisanti, and C. Minetti, "Increased number of caveolae and Caveolin-3 overexpression in Duchenne Muscular Dystrophy," *Biochemical and Biophysical Research Communications*, vol. 261, no. 3, pp. 547–550, 1999.

[210] V. Leonhard, V. Alasino, I. Bianco, and D. Beltramo, "Water-soluble pharmaceutical composition comprising at least one therapeutically active substance having hydrophobic properties and at least one compound selected from among sialoglycosphingolipids, glycosphingolipids or a mixture of sialoglycosphingolipids and glycosphingolipids," U.S. American Patent US20 130 195 924 A1, Aug. 1, 2013, uS Patent App. 13/635,595. [Online]. Available: https://www.google.ch/patents/US20130195924

[211] H. Carter, P. Johnson, and E. Weber, "Glycolipids," *Annual review of biochemistry*, vol. 34, no. 1, pp. 109–142, 1965.

[212] T. Kolter, "Ganglioside biochemistry," *ISRN biochemistry*, vol. 2012, 2012.

[213] R. W. Ledeen, "Ganglioside structures and distribution: Are they localized at the nerve ending?" *Journal of Supramolecular Structure*, vol. 8, no. 1, pp. 1–17, 1978.

[214] R. W. Ledeen and G. Wu, "The multi-tasked life of GM1 ganglioside, a true factotum of nature," *Trends in Biochemical Sciences*, vol. 40, no. 7, pp. 407–418, Jul. 2015.

[215] M. Aureli, L. Mauri, M. G. Ciampa, A. Prinetti, G. Toffano, C. Secchieri, and S. Sonnino, "GM1 ganglioside: Past studies and future potential," *Molecular Neurobiology*, vol. 53, no. 3, pp. 1824–1842, 2016.

[216] L. Svennerholm, "Chromatographic separation of human brain gangliosides," *Journal of Neurochemistry*, vol. 10, no. 9, pp. 613–623, 1963.

[217] I. Mocchetti, "Exogenous gangliosides, neuronal plasticity and repair, and the neurotrophins," *Cellular and Molecular Life Sciences CMLS*, vol. 62, no. 19, pp. 2283–2294, 2005.

[218] P. Rock, M. Allietta, W. W. Young, T. E. Thompson, and T. W. Tillack, "Ganglioside GM1 and Asialo-GM1 at low concentration are preferentially incorporated into the gel phase in two-component, two-phase phosphatidylcholine bilayers," *Biochemistry*, vol. 30, no. 1, pp. 19–25, Jan. 1991.

[219] A. V. Samsonov, I. Mihalyov, and F. S. Cohen, "Characterization of cholesterol-sphingomyelin domains and their dynamics in bilayer membranes," *Biophysical Journal*, vol. 81, no. 3, pp. 1486–1500, Sep. 2001.

[220] S. Prioni, L. Mauri, N. Loberto, R. Casellato, V. Chigorno, D. Karagogeos, A. Prinetti, and S. Sonnino, "Interactions between gangliosides and proteins in the exoplasmic leaflet of neuronal plasma membranes: A study performed with a Tritium-labeled GM1 derivative containing a photoactivable group linked to the oligosaccharide chain," *Glycoconjugate Journal*, vol. 21, no. 8, pp. 461–470, 2004.

[221] H. Sun, L. Chen, L. Gao, and W. Fang, "Nanodomain formation of ganglioside GM1 in lipid membrane: Effects of Cholera toxin-mediated cross-linking," *Langmuir*, vol. 31, no. 33, pp. 9105–9114, Aug. 2015.

[222] R. V. McDaniel, A. McLaughlin, A. P. Winiski, M. Eisenberg, and S. McLaughlin, "Bilayer membranes containing the ganglioside GM1: models for electrostatic potentials adjacent to biological membranes," *Biochemistry*, vol. 23, no. 20, pp. 4618–4624, Sep. 1984.

[223] R. V. McDaniel, K. Sharp, D. Brooks, A. C. McLaughlin, A. P. Winiski, D. Cafiso, and S. McLaughlin, "Electrokinetic and electrostatic properties of bilayers containing gangliosides GM1, GD1a, or GT1. comparison with a nonlinear theory." *Biophysical Journal*, vol. 49, no. 3, pp. 741–752, Mar. 1986.

[224] S.-I. Hakomori, "Glycosphingolipids in cellular interaction, differentiation, and oncogenesis," *Annual review of biochemistry*, vol. 50, no. 1, pp. 733–764, 1981.

[225] E. G. Bremer, S. Hakomori, D. F. Bowen-Pope, E. Raines, and R. Ross, "Ganglioside-mediated modulation of cell growth, growth factor binding, and receptor phosphorylation." *Journal of Biological Chemistry*, vol. 259, no. 11, pp. 6818–6825, Jun. 1984.

[226] M. W. Peters, I. E. Mehlhorn, K. R. Barber, and C. W. Grant, "Evidence of a distribution difference between two gangliosides in bilayer membranes," *Biochimica et Biophysica Acta (BBA) - Biomembranes*, vol. 778, no. 3, pp. 419–428, 1984.

[227] D. Cheresh, R. Reisfeld, and A. Varki, "O-acetylation of disialoganglioside gd3 by human melanoma cells creates a unique antigenic determinant," *Science*, vol. 225, no. 4664, pp. 844–846, Aug. 1984.

[228] A. Uncini, "A common mechanism and a new categorization for anti-ganglioside antibody-mediated neuropathies," *Experimental Neurology*, vol. 235, no. 2, pp. 513–516, Jun. 2012.

[229] Y. S. Tsao and L. Huang, "Sendai virus induced leakage of liposomes containing gangliosides," *Biochemistry*, vol. 24, no. 5, pp. 1092–1098, Feb. 1985.

[230] P. H. Fishman, "Role of membrane gangliosides in the binding and action of bacterial toxins," *The Journal of Membrane Biology*, vol. 69, no. 2, pp. 85–97, 1982.

[231] J. Sánchez and J. Holmgren, "Cholera toxin - a foe & a friend," *Indian J Med Res*, vol. 133, no. 2, pp. 153–163, Feb. 2011.

[232] G. M. Kuziemko, M. Stroh, and R. C. Stevens, "Cholera toxin binding affinity and specificity for gangliosides determined by surface plasmon resonance," *Biochemistry*, vol. 35, no. 20, pp. 6375–6384, Jan. 1996.

[233] G. Margheri, R. D'Agostino, S. Trigari, S. Sottini, and M. Del Rosso, "The β-subunit of Cholera toxin has a high affinity for Ganglioside GM1

embedded into solid supported lipid membranes with a lipid raft-like composition," *Lipids*, vol. 49, no. 2, pp. 203–206, 2014.

[234] P. H. Fishman, J. Moss, and J. C. Osborne, "Interaction of choleragen with the oligosaccharide of ganglioside GM1: evidence for multiple oligosaccharide binding sites," *Biochemistry*, vol. 17, no. 4, pp. 711–716, Feb. 1978.

[235] E. A. Merritt, S. Sarfaty, F. V. D. Akker, C. L'Hoir, J. A. Martial, and W. G. Hol, "Crystal structure of Cholera toxin B-pentamer bound to receptor GM1 pentasaccharide," *Protein Science*, vol. 3, no. 2, pp. 166–175, 1994.

[236] W. B. Turnbull, B. L. Precious, and S. W. Homans, "Dissecting the Cholera toxin - ganglioside GM1 interaction by isothermal titration calorimetry," *J. Am. Chem. Soc.*, vol. 126, no. 4, pp. 1047–1054, Feb. 2004.

[237] H.-A. Hansson, J. Holmgren, and L. Svennerholm, "Ultrastructural localization of cell membrane GM1 ganglioside by Cholera toxin," *Proceedings of the National Academy of Sciences*, vol. 74, no. 9, pp. 3782–3786, Sep. 1977.

[238] L. Kalvodova, N. Kahya, P. Schwille, R. Ehehalt, P. Verkade, D. Drechsel, and K. Simons, "Lipids as modulators of proteolytic activity of BACE: Involvement of cholesterol, glycosphingolipids, and anionic phospholipids in vitro," *Journal of Biological Chemistry*, vol. 280, no. 44, pp. 36 815–36 823, Nov. 2005.

[239] D. Lingwood, J. Ries, P. Schwille, and K. Simons, "Plasma membranes are poised for activation of raft phase coalescence at physiological temperature," *Proceedings of the National Academy of Sciences*, vol. 105, no. 29, pp. 10 005–10 010, Jul. 2008.

[240] R.-X. Gu, H. I. Ingólfsson, A. H. de Vries, S. J. Marrink, and D. P. Tieleman, "Ganglioside-lipid and ganglioside-protein interactions revealed by coarse-grained and atomistic molecular dynamics simulations," *J. Phys. Chem. B*, Sep. 2016.

[241] R. G. Parton, "Ultrastructural localization of gangliosides; GM1 is concentrated in caveolae." *Journal of Histochemistry & Cytochemistry*, vol. 42, no. 2, pp. 155–66, 1994.

[242] T. Fujimoto, "GPI-anchored proteins, glycosphingolipids, and sphingomyelin are sequestered to caveolae only after crosslinking." *Journal of Histochemistry & Cytochemistry*, vol. 44, no. 8, pp. 929–941, Aug. 1996.

[243] E. Shvets, V. Bitsikas, G. Howard, C. G. Hansen, and B. J. Nichols, "Dynamic caveolae exclude bulk membrane proteins and are required for sorting of excess glycosphingolipids," *Nature Communications*, vol. 6, p. 6867, Apr. 2015.

[244] E. P. Hoffman, R. H. Brown, and L. M. Kunkel, "Dystrophin: The protein product of the Duchenne Muscular Dystrophy locus," *Cell*, vol. 51, no. 6, pp. 919–928, 1987.

[245] M. Koenig, A. Monaco, and L. Kunkel, "The complete sequence of Dystrophin predicts a rod-shaped cytoskeletal protein," *Cell*, vol. 53, no. 2, pp. 219–228, 1988.

[246] M. Koenig, E. Hoffman, C. Bertelson, A. Monaco, C. Feener, and L. Kunkel, "Complete cloning of the Duchenne Muscular Dystrophy (DMD) cDNA and preliminary genomic organization of the DMD gene in normal and affected individuals," *Cell*, vol. 50, no. 3, pp. 509–517, 1987.

[247] E. Le Rumeur, S. J. Winder, and J.-F. Hubert, "Dystrophin: More than just the sum of its parts," *Biochimica et Biophysica Acta (BBA) - Proteins and Proteomics*, vol. 1804, no. 9, pp. 1713–1722, Sep. 2010.

[248] N. Bhasin, R. Law, G. Liao, D. Safer, J. Ellmer, B. M. Discher, H. L. Sweeney, and D. E. Discher, "Molecular extensibility of Mini-dystrophins and a Dystrophin rod construct," *Journal of Molecular Biology*, vol. 352, no. 4, pp. 795 – 806, 2005.

[249] A. H. Ahn and L. M. Kunkel, "The structural and functional diversity of Dystrophin," *Nature genetics*, vol. 3, no. 4, pp. 283–291, 1993.

[250] I. N. Rybakova, K. J. Amann, and J. M. Ervasti, "A new model for the interaction of Dystrophin with F-actin." *J Cell Biol*, vol. 135, no. 3, pp. 661–672, Nov. 1996.

[251] J. M. Ervasti, "Dystrophin, its interactions with other proteins, and implications for muscular dystrophy," *Biochimica et Biophysica Acta (BBA) - Molecular Basis of Disease*, vol. 1772, no. 2, pp. 108–117, Feb. 2007.

[252] R. J. Fairclough, M. J. Wood, and K. E. Davies, "Therapy for Duchenne Muscular Dystrophy: renewed optimism from genetic approaches," *Nat Rev Genet*, vol. 14, no. 6, pp. 373–378, Jun. 2013.

[253] J. W. McGreevy, C. H. Hakim, M. A. McIntosh, and D. Duan, "Animal models of Duchenne Muscular Dystrophy: from basic mechanisms to gene therapy," *Dis Models Mech*, vol. 8, no. 3, pp. 195–213, Mar. 2015.

[254] S. Guiraud, A. Aartsma-Rus, N. M. Vieira, K. E. Davies, G.-J. B. van Ommen, and L. M. Kunkel, "The pathogenesis and therapy of muscular dystrophies," *Annu. Rev. Genom. Hum. Genet.*, vol. 16, no. 1, pp. 281–308, Aug. 2015.

[255] R. G. Hammonds Jr, "Protein sequence of DMD gene is related to Actin-binding domain of α-Actinin," *Cell*, vol. 51, no. 1, 1987.

[256] M. Koenig and L. M. Kunkel, "Detailed analysis of the repeat domain of Dystrophin reveals four potential hinge segments that may confer flexibility." *Journal of Biological Chemistry*, vol. 265, no. 8, pp. 4560–4566, 1990.

[257] I. N. Rybakova, J. L. Humston, K. J. Sonnemann, and J. M. Ervasti, "Dystrophin and Utrophin bind Actin through distinct modes of contact," *Journal of Biological Chemistry*, vol. 281, no. 15, pp. 9996–10 001, Apr. 2006.

[258] Y. Lai, G. D. Thomas, Y. Yue, H. T. Yang, D. Li, C. Long, L. Judge, B. Bostick, J. S. Chamberlain, R. L. Terjung, and D. Duan, "Dystrophins carrying Spectrin-like repeats 16 and 17 anchor nNOS to the sarcolemma and enhance exercise performance in a mouse model of muscular dystrophy," *J Clin Invest*, vol. 119, no. 3, pp. 624–635, 2009.

[259] V. J. Venema, H. Ju, R. Zou, and R. C. Venema, "Interaction of neuronal Nitric-Oxide Synthase with Caveolin-3 in skeletal muscle: Identification of a novel Caveolin scaffolding/inhibitory domain," *Journal of Biological Chemistry*, vol. 272, no. 45, pp. 28 187–28 190, Nov. 1997.

[260] G. García-Cardeña, P. Martasek, B. S. S. Masters, P. M. Skidd, J. Couet, S. Li, M. P. Lisanti, and W. C. Sessa, "Dissecting the interaction between Nitric Oxide Synthase (NOS) and caveolin: Functional significance of the NOS caveolin binding domainin vivo," *Journal of Biological Chemistry*, vol. 272, no. 41, pp. 25 437–25 440, Oct. 1997.

[261] A. E. Trane, D. Pavlov, A. Sharma, U. Saqib, K. Lau, F. van Petegem, R. D. Minshall, L. J. Roman, and P. N. Bernatchez, "Deciphering the binding of Caveolin-1 to client protein endothelial Nitric-Oxide Synthase (eNOS): Scaffolding subdomain identification, interaction modeling, and biological significance," *The Journal of Biological Chemistry*, vol. 289, no. 19, pp. 13 273–13 283, Mar. 2014.

[262] J.-L. Balligand and P. J. Cannon, "Nitric Oxide Synthases and cardiac muscle," *Arterioscler Thromb Vasc Bio*, vol. 17, no. 10, p. 1846, Oct. 1997.

[263] M. Seddon, A. M. Shah, and B. Casadei, "Cardiomyocytes as effectors of nitric oxide signalling," *Cardiovasc Res*, vol. 75, no. 2, pp. 315–326, Jul. 2007.

[264] K. W. Prins, J. L. Humston, A. Mehta, V. Tate, E. Ralston, and J. M. Ervasti, "Dystrophin is a microtubule-associated protein," *J Cell Biol*, vol. 186, no. 3, pp. 363–369, Aug. 2009.

[265] J. J. Belanto, T. L. Mader, M. D. Eckhoff, D. M. Strandjord, G. B. Banks, M. K. Gardner, D. A. Lowe, and J. M. Ervasti, "Microtubule binding distinguishes Dystrophin from Utrophin," *Proceedings of the National Academy of Sciences*, vol. 111, no. 15, pp. 5723–5728, Apr. 2014.

[266] J. J. Belanto, J. T. Olthoff, T. L. Mader, C. M. Chamberlain, D. M. Nelson, P. M. McCourt, D. M. Talsness, G. G. Gundersen, D. A. Lowe, and J. M. Ervasti, "Independent variability of microtubule perturbations

associated with dystrophinopathy," *Human Molecular Genetics*, pp. 1–11, Sep. 2016.

[267] S. Rentschler, H. Linn, K. Deininger, M. T. Bedford, X. Espanel, and M. Sudol, "The WW domain of Dystrophin requires EF-hands region to interact with β-Dystroglycan," *Biological chemistry*, vol. 380, no. 4, pp. 431–442, 1999.

[268] A. Aartsma-Rus, J. C. T. Van Deutekom, I. F. Fokkema, G.-J. B. Van Ommen, and J. T. Den Dunnen, "Entries in the Leiden Duchenne Muscular Dystrophy mutation database: An overview of mutation types and paradoxical cases that confirm the reading-frame rule," *Muscle & Nerve*, vol. 34, no. 2, pp. 135–144, 2006.

[269] D. J. Blake, A. Weir, S. E. Newey, and K. E. Davies, "Function and genetics of Dystrophin and Dystrophin-related proteins in muscle," *Physiol Rev*, vol. 82, no. 2, pp. 291–329, Apr. 2002.

[270] I. N. Mungrue and D. S. Bredt, "nNOS at a glance: implications for brain and brawn," *J. Cell Sci.*, vol. 117, no. 13, pp. 2627–2629, May 2004.

[271] B. Nichols, S. Takeda, and T. Yokota, "Nonmechanical roles of Dystrophin and associated proteins in exercise, neuromuscular junctions, and brains," *Brain sciences*, vol. 5, no. 3, pp. 275–298, 2015.

[272] V. Straub, R. E. Bittner, J. J. Léger, and T. Voit, "Direct visualization of the Dystrophin network on skeletal muscle fiber membrane." *J Cell Biol*, vol. 119, no. 5, pp. 1183–1191, Dec. 1992.

[273] K. Ohlendieck, "Towards an understanding of the Dystrophin-Glycoprotein complex: linkage between the extracellular matrix and the membrane cytoskeleton in muscle fibers." *European journal of cell biology*, vol. 69, no. 1, pp. 1–10, 1996.

[274] O. Jaka, L. Casas-Fraile, A. López de Munain, and A. Sáenz, "Costamere proteins and their involvement in myopathic processes," *Expert Reviews in Molecular Medicine*, vol. 17, pp. 1–11, 2015.

[275] H. Moser, "Duchenne Muscular Dystrophy: Pathogenetic aspects and genetic prevention," *Human Genetics*, vol. 66, no. 1, pp. 17–40, 1984.

[276] A. Emery and F. Muntoni, *Duchenne Muscular Dystrophy*. Oxford University Press, 1993.

[277] L. Passamano, A. Taglia, A. Palladino, E. Viggiano, P. D'Ambrosio, M. Scutifero, M. Rosaria Cecio, V. Torre, F. De Luca, E. Picillo, O. Paciello, G. Piluso, G. Nigro, and L. Politano, "Improvement of survival in Duchenne Muscular Dystrophy: retrospective analysis of 835 patients," *Acta Myologica*, vol. 31, no. 2, pp. 121–125, Oct. 2012.

[278] M. Mosqueira, U. Zeiger, M. Förderer, H. Brinkmeier, and R. H. A. Fink, "Cardiac and respiratory dysfunction in Duchenne Muscular Dystrophy and the role of second messengers," *Medicinal Research Reviews*, vol. 33, no. 5, pp. 1174–1213, 2013.

[279] S. B. England, L. V. B. Nicholson, M. A. Johnson, S. M. Forrest, D. R. Love, E. E. Zubrzycka-Gaarn, D. E. Bulman, J. B. Harris, and K. Davies, "Very mild muscular dystrophy associated with the deletion of 46% of Dystrophin," *Nature*, vol. 343, no. 6254, pp. 180–182, Jan. 1990.

[280] A. E. Emery, "The muscular dystrophies," *The Lancet*, vol. 359, no. 9307, pp. 687–695, Feb. 2002.

[281] E. Hoogerwaard, E. Bakker, P. Ippel, J. Oosterwijk, D. Majoor-Krakauer, N. Leschot, A. Van Essen, H. Brunner, P. van der Wouw, A. Wilde, and M. de Visser, "Signs and symptoms of Duchenne Muscular Dystrophy and Becker Muscular Dystrophy among carriers in the Netherlands: a cohort study," *The Lancet*, vol. 353, no. 9170, pp. 2116–2119, Jun. 1999.

[282] E. Hoogerwaard, P. van der Wouw, A. Wilde, E. Bakker, P. Ippel, J. Oosterwijk, D. Majoor-Krakauer, A. van Essen, N. Leschot, and M. de Visser, "Cardiac involvement in carriers of Duchenne and Becker Muscular Dystrophy," *Neuromuscular Disorders*, vol. 9, no. 5, pp. 347–351, Jul. 1999.

[283] L. Grain, M. Cortina-Borja, C. Forfar, D. Hilton-Jones, J. Hopkin, and M. Burch, "Cardiac abnormalities and skeletal muscle weakness in

carriers of duchenne and becker muscular dystrophies and controls," *Neuromuscular Disorders*, vol. 11, no. 2, pp. 186–191, Mar. 2001.

[284] M. Nolan, O. Jones, R. Pedersen, and H. Johnston, "Cardiac assessment in childhood carriers of Duchenne and Becker Muscular Dystrophies," *Neuromuscular Disorders*, vol. 13, no. 2, pp. 129–132, Feb. 2003.

[285] K. R. Wagner, N. Lechtzin, and D. P. Judge, "Current treatment of adult Duchenne Muscular Dystrophy," *Biochimica et Biophysica Acta (BBA) - Molecular Basis of Disease*, vol. 1772, no. 2, pp. 229–237, Feb. 2007.

[286] M. Koenig, A. H. Beggs, M. Moyer, S. Scherpf, K. Heindrich, T. Bettecken, G. Meng, C. R. Müller, M. Lindlöf, H. Kaariainen, A. de la Chapelle, A. Kiuru, M.-L. Savontaus, H. Gilgenkrantz, D. Récan, J. Chelly, J.-C. Kaplan, A. E. Covone, N. Archidiacono, G. Romeo, S. Liechti-Gallati, V. Schneider, S. Braga, H. Moser, B. T. Darras, P. Murphy, U. Francke, J. D. Chen, G. Morgan, M. Denton, C. R. Greenberg, K. Wrogemann, L. A. J. Blonden, H. M. B. van Paassen, G. J. B. van Ommen, and L. M. Kunkel, "The molecular basis for Duchenne versus Becker Muscular Dystrophy: Correlation of severity with type of deletion," *American Journal of Human Genetics*, vol. 45, no. 4, pp. 498–506, Oct. 1989.

[287] J. N. Robinson-Hamm and C. A. Gersbach, "Gene therapies that restore Dystrophin expression for the treatment of Duchenne Muscular Dystrophy," *Human Genetics*, vol. 135, no. 9, pp. 1029–1040, 2016.

[288] V. M. Chapman, D. R. Miller, D. Armstrong, and C. T. Caskey, "Recovery of induced mutations for X chromosome-linked muscular dystrophy in mice." *Proceedings of the National Academy of Sciences of the United States of America*, vol. 86, no. 4, pp. 1292–1296, Feb. 1989.

[289] N. Deconinck, J. Tinsley, F. D. Backer, R. Fisher, D. Kahn, S. Phelps, K. Davies, and J.-M. Gillis, "Expression of truncated utrophin leads to major functional improvements in Dystrophin-deficient muscles of mice," *Nat Med*, vol. 3, no. 11, pp. 1216–1221, Nov. 1997.

[290] S. Q. Harper, M. A. Hauser, C. DelloRusso, D. Duan, R. W. Crawford, S. F. Phelps, H. A. Harper, A. S. Robinson, J. F. Engelhardt, S. V. Brooks,

and J. S. Chamberlain, "Modular flexibility of Dystrophin: Implications for gene therapy of Duchenne Muscular Dystrophy," *Nat Med*, vol. 8, no. 3, pp. 253–261, Mar. 2002.

[291] E. Bachrach, S. Li, A. L. Perez, J. Schienda, K. Liadaki, J. Volinski, A. Flint, J. Chamberlain, and L. M. Kunkel, "Systemic delivery of human microdystrophin to regenerating mouse dystrophic muscle by muscle progenitor cells," *Proceedings of the National Academy of Sciences of the United States of America*, vol. 101, no. 10, pp. 3581–3586, Mar. 2004.

[292] G. Cossu and M. Sampaolesi, "New therapies for Duchenne Muscular Dystrophy: challenges, prospects and clinical trials," *Trends in Molecular Medicine*, vol. 13, no. 12, pp. 520–526, Dec. 2007.

[293] Z. Wang, C. S. Kuhr, J. M. Allen, M. Blankinship, P. Gregorevic, J. S. Chamberlain, S. J. Tapscott, and R. Storb, "Sustained AAV-mediated Dystrophin expression in a canine model of Duchenne Muscular Dystrophy with a brief course of immunosuppression," *Molecular Therapy*, vol. 15, no. 6, pp. 1160–1166, 2007.

[294] K. R. Wagner, S. Hamed, D. W. Hadley, A. L. Gropman, A. H. Burstein, D. M. Escolar, E. P. Hoffman, and K. H. Fischbeck, "Gentamicin treatment of Duchenne and Becker Muscular Dystrophy due to nonsense mutations," *Annals of Neurology*, vol. 49, no. 6, pp. 706–711, 2001.

[295] H. Radley, A. De Luca, G. Lynch, and M. Grounds, "Duchenne Muscular Dystrophy: Focus on pharmaceutical and nutritional interventions," *The International Journal of Biochemistry & Cell Biology*, vol. 39, no. 3, pp. 469–477, 2007.

[296] P. L. Vaghy, J. Fang, W. Wu, and L. P. Vaghy, "Increased Caveolin-3 levels in *mdx* mouse muscles," *FEBS Letters*, vol. 431, no. 1, pp. 125–127, Jul. 1998.

[297] C. Minetti, F. Sotgia, C. Bruno, P. Scartezzini, P. Broda, M. Bado, E. Masetti, M. Mazzocco, A. Egeo, M. Donati, F. Galbiati, G. Cordone, F. Bricarelli, M. Lisanti, and F. Zara, "Mutations in the Caveolin-3 gene

cause autosomal dominant limb-girdle muscular dystrophy," *Nat. Genet*, vol. 18, pp. 365–368, 1998.

[298] S. Woodman, F. Sotgia, F. Galbiati, C. Minetti, and M. Lisanti, "Caveolinopathies mutations in Caveolin-3 cause four distinct autosomal dominant muscle diseases," *Neurology*, vol. 62, no. 4, pp. 538–543, 2004.

[299] F. Sotgia, J. K. Lee, K. Das, M. Bedford, T. C. Petrucci, P. Macioce, M. Sargiacomo, F. D. Bricarelli, C. Minetti, M. Sudol *et al.*, "Caveolin-3 directly interacts with the C-terminal tail of β-Dystroglycan identification of a central WW-like domain within caveolin family members," *Journal of Biological Chemistry*, vol. 275, no. 48, pp. 38 048–38 058, 2000.

[300] F. Muntoni and T. Voit, "The congenital muscular dystrophies in 2004: a century of exciting progress," *Neuromuscular Disorders*, vol. 14, no. 10, pp. 635–649, Oct. 2004.

[301] S. Ong, B. Blagoev, I. Kratchmarova, D. B. Kristensen, H. Steen, A. Pandey, and M. Mann, "Stable isotope labeling by amino acids in cell culture, silac, as a simple and accurate approach to expression proteomics," *Molecular & Cellular Proteomics*, vol. 1, no. 5, pp. 376–386, May 2002.

[302] C. Giordani, C. Wakai, E. Okamura, N. Matubayasi, and M. Nakahara, "Dynamic and 2D NMR studies on hydrogen-bonding aggregates of cholesterol in low-polarity organic solvents," *J. Phys. Chem. B*, vol. 110, no. 31, pp. 15 205–15 211, Aug. 2006.

[303] F. Aussenac, M. Tavares, and E. J. Dufourc, "Cholesterol dynamics in membranes of raft composition - a molecular point of view from ^{2}H and ^{31}P solid-state NMR," *Biochemistry*, vol. 42, no. 6, pp. 1383–1390, Feb. 2003.

[304] A. M. Smondyrev and M. L. Berkowitz, "Structure of dipalmitoylphosphatidylcholine/cholesterol bilayer at low and high cholesterol concentrations: Molecular dynamics simulation," *Biophysical Journal*, vol. 77, no. 4, pp. 2075–2089, Oct. 1999.

[305] M. Corti, V. Degiorgio, R. Ghidoni, S. Sonnino, and G. Tettamanti, "Laser-light scattering investigation of the micellar properties of gangliosides," *Chemistry and Physics of Lipids*, vol. 26, no. 3, pp. 225–238, 1980.

[306] M. Corti, V. DeGiorgio, S. Sonnino, R. Ghidoni, M. Masserini, and G. Tettamanti, "GM1-ganglioside-Triton X-100 mixed micelles: Changes of micellar properties studied by laser-light scattering and enzymatic methods," *Chemistry and Physics of Lipids*, vol. 28, no. 3, pp. 197–214, 1981.

[307] K. J. Nowak and K. E. Davies, "Duchenne Muscular Dystrophy and Dystrophin: pathogenesis and opportunities for treatment," *EMBO Reports*, vol. 5, no. 9, pp. 872–876, Jul. 2004.

[308] B. E. Saleh, M. C. Teich, and B. E. Saleh, *Fundamentals of photonics*. Wiley New York, 2008, vol. 22.

[309] L. F. Rayleigh, "Investigations in optics, with special reference to the spectroscope," *Philosophical Magazine Series 5*, vol. 8, no. 49, pp. 261–274, Oct. 1879.

[310] S. Inoué, "Foundations of confocal scanned imaging in light microscopy," in *Handbook of biological confocal microscopy*. Springer, 2006, pp. 1–19.

[311] E. Abbe, "Beiträge zur Theorie des Mikroskops und der mikroskopischen Wahrnehmung," *Archiv für mikroskopische Anatomie*, vol. 9, no. 1, pp. 413–418, 1873.

[312] J. Wittig, *Ernst Abbe*, ser. Biographien hervorragender Naturwissenschaftler, Techniker und Mediziner. Vieweg+Teubner Verlag, 2013. [Online]. Available: https://books.google.de/books?id=RA3MBgAAQBAJ

[313] S. Hell, "Doppelkonfokales Rastermikroskop," German Patent DE 4 040 441 A1, Jul. 2, 1992, dE Patent App. DE19,904,040,441. [Online]. Available: https://www.google.com/patents/DE4040441A1?cl=en

[314] J. J. Bozzola and L. D. Russell, *Electron microscopy: principles and techniques for biologists*. Jones & Bartlett Learning, 1999.

[315] R. F. Egerton, *Physical principles of electron microscopy: an introduction to TEM, SEM, and AEM*. Springer Science & Business Media, 2006.

[316] S. D. Schwartzbach and T. Osafune, *Immunoelectron microscopy: methods and protocols*. Humana PressInc, 2010, vol. 657.

[317] A. H. Coons, H. Creech, R. Jones, and E. Berliner, "The demonstration of pneumococcal antigen in tissues by the use of fluorescent antibody," *J. Immunol*, vol. 45, no. 3, pp. 159–70, 1942.

[318] A. H. Coons, "The beginnings of immunofluorescence," *The Journal of Immunology*, vol. 87, no. 5, pp. 499–503, Nov. 1961.

[319] M. Minsky, "Microscopy apparatus," US American Patent 3 013 467, 1957.

[320] M. Minsky, "Memoir on inventing the confocal scanning microscope," *Scanning*, vol. 10, no. 4, pp. 128–138, 1988.

[321] A. Einstein, "Strahlungsemission und -absorption nach der Quantentheorie," *Deutsche Physikalische Gesellschaft, Verhandlungen*, vol. 18, pp. 318–323, 1916.

[322] G. Donnert, "Dual-color STED-microscopy on the Nanoscale," Ph.D. dissertation, Ruprecht-Karls-Universität Heidelberg, 2007.

[323] J. R. Lakowicz, *Principles of fluorescence spectroscopy*. Springer Science & Business Media, 2013.

[324] L. Song, E. J. Hennink, I. T. Young, and H. J. Tanke, "Photobleaching kinetics of Fluorescein in quantitative fluorescence microscopy." *Biophysical Journal*, vol. 68, no. 6, pp. 2588–2600, Jun. 1995.

[325] S. W. Hell and J. Wichmann, "Breaking the diffraction resolution limit by stimulated emission: stimulated-emission-depletion fluorescence microscopy," *Opt. Lett.*, vol. 19, no. 11, pp. 780–782, Jun 1994.

[326] S. W. Hell, "Toward fluorescence nanoscopy," *Nat Biotech*, vol. 21, no. 11, pp. 1347–1355, Nov. 2003.

[327] S. W. Hell, K. I. Willig, M. Dyba, S. Jakobs, L. Kastrup, and V. Westphal, "Nanoscale resolution with focused light: STED and other RESOLFT microscopy concepts," *Handbook of biological confocal microscopy*, pp. 571–579, 2006.

[328] M. Hofmann, C. Eggeling, S. Jakobs, and S. W. Hell, "Breaking the diffraction barrier in fluorescence microscopy at low light intensities by using reversibly photoswitchable proteins," *Proceedings of the National Academy of Sciences of the United States of America*, vol. 102, no. 49, pp. 17 565–17 569, Dec. 2005.

[329] E. Rittweger, B. Rankin, V. Westphal, and S. Hell, "Fluorescence depletion mechanisms in super-resolving STED microscopy," *Chemical Physics Letters*, vol. 442, pp. 483 – 487, 2007.

[330] V. Westphal, S. O. Rizzoli, M. A. Lauterbach, D. Kamin, R. Jahn, and S. W. Hell, "Video-rate far-field optical nanoscopy dissects synaptic vesicle movement," *Science*, vol. 320, no. 5873, pp. 246–249, 2008.

[331] D. Wildanger, J. R. Maze, and S. W. Hell, "Diffraction unlimited all-optical recording of electron spin resonances," *Phys. Rev. Lett.*, vol. 107, p. 017601, Jul 2011.

[332] I. Testa, E. D'Este, N. T. Urban, F. Balzarotti, and S. W. Hell, "Dual channel RESOLFT nanoscopy by using fluorescent state kinetics," *Nano Lett.*, vol. 15, no. 1, pp. 103–106, Jan. 2015.

[333] M. G. L. Gustafsson, "Nonlinear structured-illumination microscopy: Wide-field fluorescence imaging with theoretically unlimited resolution," *Proceedings of the National Academy of Sciences of the United States of America*, vol. 102, no. 37, pp. 13 081–13 086, Sep. 2005.

[334] E. Rittweger, D. Wildanger, and S. W. Hell, "Far-field fluorescence nanoscopy of diamond color centers by ground state depletion," *EPL (Europhysics Letters)*, vol. 86, no. 1, p. 14001, 2009.

[335] B. Harke, J. Keller, C. K. Ullal, V. Westphal, A. Schönle, and S. W. Hell, "Resolution scaling in STED microscopy," *Opt. Express*, vol. 16, no. 6, pp. 4154–4162, Mar 2008.

[336] F. Göttfert, C. Wurm, V. Mueller, S. Berning, V. Cordes, A. Honigmann, and S. Hell, "Coaligned dual-channel STED nanoscopy and molecular diffusion analysis at 20 nm resolution," *Biophysical Journal*, vol. 105, no. 1, pp. L01 – L03, 2013.

[337] K. I. Willig, B. Harke, R. Medda, and S. W. Hell, "STED microscopy with continuous wave beams," *Nat Meth*, vol. 4, no. 11, pp. 915–918, Nov. 2007.

[338] G. Vicidomini, G. Moneron, K. Y. Han, V. Westphal, H. Ta, M. Reuss, J. Engelhardt, C. Eggeling, and S. W. Hell, "Sharper low-power STED nanoscopy by time gating," *Nat Meth*, vol. 8, no. 7, pp. 571–573, Jul. 2011.

[339] B. Harke, "3D STED Microscopy with Pulsed and Continuous Wave Lasers," Ph.D. dissertation, Georg-August-Universität Göttingen, 2008.

[340] M. Leutenegger, C. Eggeling, and S. W. Hell, "Analytical description of STED microscopy performance," *Opt. Express*, vol. 18, no. 25, pp. 26 417–26 429, Dec 2010.

[341] G. Vicidomini, I. C. Hernández, M. d'Amora, F. C. Zanacchi, P. Bianchini, and A. Diaspro, "Gated CW-STED microscopy: A versatile tool for biological nanometer scale investigation," *Methods*, vol. 66, no. 2, pp. 124 – 130, 2014, advanced Light Microscopy.

[342] J. G. Danzl, S. C. Sidenstein, C. Gregor, N. T. Urban, P. Ilgen, S. Jakobs, and S. W. Hell, "Coordinate-targeted fluorescence nanoscopy with multiple off states," *Nat Photon*, vol. 10, no. 2, pp. 122–128, Feb. 2016.

[343] S. Nizamov, M. V. Sednev, M. L. Bossi, E. Hebisch, H. Frauendorf, S. E. Lehnart, V. N. Belov, and S. W. Hell, ""Reduced" Coumarin Dyes with an O-Phosphorylated 2,2-Dimethyl-4-(hydroxymethyl)-1,2,3,4-tetrahydroquinoline Fragment: Synthesis, Spectra, and STED Microscopy," *Chemistry – A European Journal*, vol. 22, no. 33, pp. 11 631–11 642, 2016.

[344] A. N. Butkevich, G. Y. Mitronova, S. C. Sidenstein, J. L. Klocke, D. Kamin, D. N. H. Meineke, E. D'Este, P.-T. Kraemer, J. G. Danzl, V. N. Belov, and S. W. Hell, "Fluorescent rhodamines and fluorogenic carbopyronines for super-resolution STED microscopy in living cells," *Angewandte Chemie International Edition*, vol. 55, no. 10, pp. 3290–3294, 2016.

[345] G. Lukinavicius, L. Reymond, E. D'Este, A. Masharina, F. Gottfert, H. Ta, A. Guther, M. Fournier, S. Rizzo, H. Waldmann, C. Blaukopf, C. Sommer, D. W. Gerlich, H.-D. Arndt, S. W. Hell, and K. Johnsson, "Fluorogenic probes for live-cell imaging of the cytoskeleton," *Nat Meth*, vol. 11, no. 7, pp. 731–733, Jul. 2014.

[346] D. Wildanger, R. Medda, L. Kastrup, and S. Hell, "A compact STED microscope providing 3D nanoscale resolution," *Journal of Microscopy*, vol. 236, no. 1, pp. 35–43, 2009.

[347] C. Osseforth, J. R. Moffitt, L. Schermelleh, and J. Michaelis, "Simultaneous dual-color 3D STED microscopy," *Opt. Express*, vol. 22, no. 6, pp. 7028–7039, Mar 2014.

[348] J. Keller, "Optimal de-excitation patterns for RESOLFT-microscopy," Ph.D. dissertation, Georg-August-Universität Göttingen, 2006.

[349] T. J. Gould, D. Burke, J. Bewersdorf, and M. J. Booth, "Adaptive optics enables 3D STED microscopy in aberrating specimens," *Opt. Express*, vol. 20, no. 19, pp. 20 998–21 009, Sep 2012.

[350] E. Betzig, G. H. Patterson, R. Sougrat, O. W. Lindwasser, S. Olenych, J. S. Bonifacino, M. W. Davidson, J. Lippincott-Schwartz, and H. F. Hess, "Imaging intracellular fluorescent proteins at nanometer resolution," *Science*, vol. 313, no. 5793, pp. 1642–1645, Sep. 2006.

[351] M. J. Rust, M. Bates, and X. Zhuang, "Sub-diffraction-limit imaging by stochastic optical reconstruction microscopy (STORM)," *Nat Meth*, vol. 3, no. 10, pp. 793–796, Oct. 2006.

[352] S. W. Hell and M. Kroug, "Ground-state-depletion fluorscence microscopy: A concept for breaking the diffraction resolution limit," *Applied Physics B*, vol. 60, no. 5, pp. 495–497, 1995.

[353] J. Fölling, M. Bossi, H. Bock, R. Medda, C. A. Wurm, B. Hein, S. Jakobs, C. Eggeling, and S. W. Hell, "Fluorescence nanoscopy by ground-state depletion and single-molecule return," *Nat Meth*, vol. 5, no. 11, pp. 943–945, Nov. 2008.

[354] J. Chojnacki, T. Staudt, B. Glass, P. Bingen, J. Engelhardt, M. Anders, J. Schneider, B. Müller, S. W. Hell, and H.-G. Kräusslich, "Maturation-dependent HIV-1 surface protein redistribution revealed by fluorescence nanoscopy," *Science*, vol. 338, no. 6106, pp. 524–, Oct. 2012.

[355] M. Beck, F. Förster, M. Ecke, J. M. Plitzko, F. Melchior, G. Gerisch, W. Baumeister, and O. Medalia, "Nuclear pore complex structure and dynamics revealed by cryoelectron tomography," *Science*, vol. 306, no. 5700, pp. 1387–, Nov. 2004.

[356] A. von Appen, J. Kosinski, L. Sparks, A. Ori, A. L. DiGuilio, B. Vollmer, M.-T. Mackmull, N. Banterle, L. Parca, P. Kastritis, K. Buczak, S. Mosalaganti, W. Hagen, A. Andres-Pons, E. A. Lemke, P. Bork, W. Antonin, J. S. Glavy, K. H. Bui, and M. Beck, "In situ structural analysis of the human nuclear pore complex," *Nature*, vol. 526, no. 7571, pp. 140–143, Oct. 2015.

[357] E. Hurt and M. Beck, "Towards understanding nuclear pore complex architecture and dynamics in the age of integrative structural analysis," *Current Opinion in Cell Biology*, vol. 34, pp. 31–38, Jun. 2015.

[358] E. D'Este, D. Kamin, F. Göttfert, A. El-Hady, and S. W. Hell, "STED nanoscopy reveals the ubiquity of subcortical cytoskeleton periodicity in living neurons," *Cell Reports*, vol. 10, no. 8, pp. 1246–1251, Mar. 2015.

[359] K. Xu, G. Zhong, and X. Zhuang, "Actin, Spectrin, and associated proteins form a periodic cytoskeletal structure in axons," *Science*, vol. 339, no. 6118, pp. 452–456, Jan. 2013.

[360] F. Korobova and T. Svitkina, "Molecular architecture of synaptic actin cytoskeleton in hippocampal neurons reveals a mechanism of dendritic spine morphogenesis," *Molecular Biology of the Cell*, vol. 21, no. 1, pp. 165–176, Jan. 2010.

[361] N. T. Urban, K. Willig, S. Hell, and U. Nägerl, "STED nanoscopy of actin dynamics in synapses deep inside living brain slices," *Biophysical Journal*, vol. 101, no. 5, pp. 1277–1284, Sep. 2011.

[362] S. Berning, K. I. Willig, H. Steffens, P. Dibaj, and S. W. Hell, "Nanoscopy in a living mouse brain," *Science*, vol. 335, no. 6068, p. 551, Feb. 2012.

[363] K. Willig, H. Steffens, C. Gregor, A. Herholt, M. Rossner, and S. Hell, "Nanoscopy of filamentous actin in cortical dendrites of a living mouse," *Biophysical Journal*, vol. 106, no. 1, pp. L01–L03, Jan. 2014.

[364] B. Harke, J. V. Chacko, H. Haschke, C. Canale, and A. Diaspro, "A novel nanoscopic tool by combining AFM with STED microscopy," *Optical Nanoscopy*, vol. 1, no. 1, pp. 3–6, 2012.

[365] J. V. Chacko, F. C. Zanacchi, and A. Diaspro, "Probing cytoskeletal structures by coupling optical superresolution and AFM techniques for a correlative approach," *Cytoskeleton*, vol. 70, no. 11, pp. 729–740, 2013.

[366] S. Watanabe, A. Punge, G. Hollopeter, K. I. Willig, R. J. Hobson, M. W. Davis, S. W. Hell, and E. M. Jorgensen, "Protein localization in electron micrographs using fluorescence nanoscopy," *Nat Meth*, vol. 8, no. 1, pp. 80–84, Jan. 2011.

[367] C. Eggeling, "STED-FCS nanoscopy of membrane dynamics," in *Fluorescent methods to study biological membranes*. Springer, 2012, pp. 291–309.

[368] G. Moneron and S. W. Hell, "Two-photon excitation STED microscopy," *Opt. Express*, vol. 17, no. 17, pp. 14 567–14 573, Aug 2009.

[369] J. B. Ding, K. T. Takasaki, and B. L. Sabatini, "Supraresolution imaging in brain slices using stimulated-emission depletion two-photon laser scanning microscopy," *Neuron*, vol. 63, no. 4, pp. 429–437, Aug. 2009.

[370] M. Göppert-Mayer, "Über Elementarakte mit zwei Quantensprüngen," *Annalen der Physik*, vol. 401, no. 3, pp. 273–294, 1931.

[371] W. Denk, J. H. Strickler, W. W. Webb *et al.*, "Two-photon laser scanning fluorescence microscopy," *Science*, vol. 248, no. 4951, pp. 73–76, 1990.

[372] P. T. C. So, C. Y. Dong, B. R. Masters, and K. M. Berland, "Two-photon excitation fluorescence microscopy," *Annual Review of Biomedical Engineering*, vol. 2, no. 1, pp. 399–429, 2000, pMID: 11701518.

[373] R. K. Benninger and D. W. Piston, "Two-photon excitation microscopy for the study of living cells and tissues," *Current protocols in cell biology*, vol. 0 4, pp. Unit–4.1124, Jun. 2013.

[374] B. R. Masters and P. So, *Handbook of biomedical nonlinear optical microscopy*. Oxford University Press on Demand, 2008.

[375] J. Hodak, Z. Chen, S. Wu, and R. Etchenique, "Multiphoton excitation of upconverting nanoparticles in pulsed regime," *Anal. Chem.*, vol. 88, no. 2, pp. 1468–1475, Jan. 2016.

[376] W. Denk and K. Svoboda, "Photon upmanship: Why multiphoton imaging is more than a gimmick," *Neuron*, vol. 18, no. 3, pp. 351–357, Mar. 1997.

[377] S. Maiti, J. B. Shear, R. M. Williams, W. R. Zipfel, and W. W. Webb, "Measuring serotonin distribution in live cells with three-photon excitation," *Science*, vol. 275, no. 5299, pp. 530–, Jan. 1997.

[378] N. G. Horton, K. Wang, D. Kobat, C. G. Clark, F. W. Wise, C. B. Schaffer, and C. Xu, "In vivo three-photon microscopy of subcortical structures within an intact mouse brain," *Nat Photon*, vol. 7, no. 3, pp. 205–209, Mar. 2013.

[379] S.-W. Chu, M.-C. Chan, S.-P. Tai, S. Keller, S. P. DenBaars, and C.-K. Sun, "Simultaneous four-photon luminescence, third-harmonic generation, and second-harmonic generation microscopy of gan," *Opt. Lett.*, vol. 30, no. 18, pp. 2463–2465, Sep 2005.

[380] W. Denk, D. W. Piston, and W. W. Webb, *Two-Photon Molecular Excitation in Laser-Scanning Microscopy*. Boston, MA: Springer US, 1995, pp. 445–458. [Online]. Available: http://dx.doi.org/10.1007/978-1-4757-5348-6_28

[381] F. Bestvater, E. Spiess, G. Stobrawa, M. Hacker, T. Feurer, T. Porwol, U. Berchner-Pfannschmidt, C. Wotzlaw, and H. Acker, "Two-photon fluorescence absorption and emission spectra of dyes relevant for cell imaging," *Journal of Microscopy*, vol. 208, no. 2, pp. 108–115, 2002.

[382] M. G. M. Velasco, E. S. Allgeyer, P. Yuan, J. Grutzendler, and J. Bewersdorf, "Absolute two-photon excitation spectra of red and far-red fluorescent probes," *Opt. Lett.*, vol. 40, no. 21, pp. 4915–4918, Nov 2015.

[383] W. R. Zipfel, R. M. Williams, and W. W. Webb, "Nonlinear magic: multiphoton microscopy in the biosciences," *Nat Biotech*, vol. 21, no. 11, pp. 1369–1377, Nov. 2003.

[384] R. Benninger, M. Hao, and D. Piston, "Multi-photon excitation imaging of dynamic processes in living cells and tissues," in *Reviews of Physiology Biochemistry and Pharmacology*. Springer, 2008, pp. 71–92.

[385] F. Helmchen, M. S. Fee, D. W. Tank, and W. Denk, "A miniature head-mounted two-photon microscope: High-resolution brain imaging in freely moving animals," *Neuron*, vol. 31, no. 6, pp. 903–912, Sep. 2001.

[386] K. Svoboda and R. Yasuda, "Principles of two-photon excitation microscopy and its applications to neuroscience," *Neuron*, vol. 50, no. 6, pp. 823–839, Jun. 2006.

[387] F. Helmchen, W. Denk, and J. N. Kerr, "Miniaturization of two-photon microscopy for imaging in freely moving animals," *Cold Spring Harbor Protocols*, vol. 2013, no. 10, pp. 904–913, Oct. 2013.

[388] T. B. Krasieva, J. Ehren, T. O'Sullivan, B. J. Tromberg, and P. Maher, "Cell and brain tissue imaging of the flavonoid fisetin using label-free two-photon microscopy," *Neurochemistry International*, vol. 89, pp. 243–248, Oct. 2015.

[389] W. Supatto, T. V. Truong, D. Débarre, and E. Beaurepaire, "Advances in multiphoton microscopy for imaging embryos," *Current Opinion in Genetics & Development*, vol. 21, no. 5, pp. 538–548, Oct. 2011.

[390] S. Adjili, A. Favier, G. Fargier, A. Thomas, J. Massin, K. Monier, C. Favard, C. Vanbelle, S. Bruneau, N. Peyriéras, C. Andraud, D. Muriaux, and M.-T. Charreyre, "Biocompatible photoresistant far-red emitting, fluorescent polymer probes, with near-infrared two-photon absorption, for living cell and zebrafish embryo imaging," *Biomaterials*, vol. 46, pp. 70–81, Apr. 2015.

[391] J. Ripoll, B. Koberstein-Schwarz, and V. Ntziachristos, "Unleashing optics and optoacoustics for developmental biology," *Trends in Biotechnology*, vol. 33, no. 11, pp. 679–691, Nov. 2015.

[392] B. H. Cumpston, S. P. Ananthavel, S. Barlow, D. L. Dyer, J. E. Ehrlich, L. L. Erskine, A. A. Heikal, S. M. Kuebler, I.-Y. S. Lee, D. McCord-Maughon, J. Qin, H. Röckel, M. Rumi, X.-L. Wu, S. R. Marder, and J. W. Perry, "Two-photon polymerization initiators for three-dimensional optical data storage and microfabrication," *Nature*, vol. 398, no. 6722, pp. 51–54, Mar. 1999.

[393] A. Kanevce, D. Kuciauskas, D. H. Levi, A. M. Allende Motz, and S. W. Johnston, "Two dimensional numerical simulations of carrier dynamics during time-resolved photoluminescence decays in two-photon microscopy measurements in semiconductors," *Journal of Applied Physics*, vol. 118, no. 4, 2015.

[394] B. Gaury and P. M. Haney, "Probing surface recombination velocities in semiconductors using two-photon microscopy," *Journal of Applied Physics*, vol. 119, no. 12, 2016.

[395] J. M. Squirrell, D. L. Wokosin, J. G. White, and B. D. Bavister, "Long-term two-photon fluorescence imaging of mammalian embryos without compromising viability," *Nat Biotech*, vol. 17, no. 8, pp. 763–767, Aug. 1999.

[396] B. D. Bennett, T. L. Jetton, G. Ying, M. A. Magnuson, and D. W. Piston, "Quantitative subcellular imaging of glucose metabolism within intact pancreatic islets," *Journal of Biological Chemistry*, vol. 271, no. 7, pp. 3647–3651, Feb. 1996.

[397] K. König, P. T. C. So, W. W. Mantulin, B. J. Tromberg, and E. Gratton, "Two-photon excited lifetime imaging of autofluorescence in cells during UVA and NIR photostress," *Journal of Microscopy*, vol. 183, no. 3, pp. 197–204, 1996.

[398] H. J. Koester, D. Baur, R. Uhl, and S. W. Hell, "Ca^{2+} fluorescence imaging with pico- and femtosecond two-photon excitation: Signal and photodamage," *Biophysical Journal*, vol. 77, no. 4, pp. 2226–2236, Oct. 1999.

[399] A. Hopt and E. Neher, "Highly nonlinear photodamage in two-photon fluorescence microscopy," *Biophysical Journal*, vol. 80, no. 4, pp. 2029–2036, Apr. 2001.

[400] B. E. Urban, J. Yi, S. Chen, B. Dong, Y. Zhu, S. H. DeVries, V. Backman, and H. F. Zhang, "Super-resolution two-photon microscopy via scanning patterned illumination," *Phys. Rev. E*, vol. 91, p. 042703, Apr 2015.

[401] Q. Li, S. S. Wu, and K. C. Chou, "Subdiffraction-limit two-photon fluorescence microscopy for GFP-tagged cell imaging," *Biophysical Journal*, vol. 97, no. 12, pp. 3224–3228, Dec. 2009.

[402] P. Bethge, R. Chéreau, E. Avignone, G. Marsicano, and U. Nägerl, "Two-photon excitation STED microscopy in two colors in acute brain slices," *Biophysical Journal*, vol. 104, no. 4, pp. 778 – 785, 2013.

[403] K. Takasaki, J. Ding, and B. Sabatini, "Live-cell superresolution imaging by pulsed STED two-photon excitation microscopy," *Biophysical Journal*, vol. 104, no. 4, pp. 770 – 777, 2013.

[404] R. Chéreau, J. Tönnesen, and U. V. Nägerl, "STED microscopy for nanoscale imaging in living brain slices," *Methods*, vol. 88, pp. 57–66, Oct. 2015.

[405] J. R. Moffitt, C. Osseforth, and J. Michaelis, "Time-gating improves the spatial resolution of STED microscopy," *Opt. Express*, vol. 19, no. 5, pp. 4242–4254, Feb 2011.

[406] G. Vicidomini, A. Schönle, H. Ta, K. Y. Han, G. Moneron, C. Eggeling, and S. W. Hell, "STED nanoscopy with time-gated detection: Theoretical and experimental aspects," *PLoS ONE*, vol. 8, no. 1, pp. 1–12, Jan. 2013.

[407] I. Coto Hernández, M. Castello, L. Lanzanò, M. d'Amora, P. Bianchini, A. Diaspro, and G. Vicidomini, "Two-photon excitation STED microscopy with time-gated detection," *Scientific Reports*, vol. 6, Jan. 2016.

[408] V. Westphal, M. A. Lauterbach, A. D. Nicola, and S. W. Hell, "Dynamic far-field fluorescence nanoscopy," *New Journal of Physics*, vol. 9, no. 12, p. 435, 2007.

[409] M. Lauterbach, "Fast STED microscopy," Ph.D. dissertation, Georg-August-Universität Göttingen, 2009.

[410] J. Bückers, D. Wildanger, G. Vicidomini, L. Kastrup, and S. W. Hell, "Simultaneous multi-lifetime multi-color STED imaging for colocalization analyses," *Opt. Express*, vol. 19, no. 4, pp. 3130–3143, Feb 2011.

[411] E. Wagner, S. Brandenburg, T. Kohl, and S. E. Lehnart, "Analysis of tubular membrane networks in cardiac myocytes from atria and ventricles," *JoVE*, vol. 92, no. 92, p. e51823, 2014.

[412] M. Skrzypiec-Spring, B. Grotthus, A. Szelag, and R. Schulz, "Isolated heart perfusion according to Langendorff - still viable in the new millennium," *Journal of Pharmacological and Toxicological Methods*, vol. 55, no. 2, pp. 113 – 126, 2007.

[413] E. Fluhler, V. G. Burnham, and L. M. Loew, "Spectra, membrane binding, and potentiometric responses of new charge shift probes," *Biochemistry*, vol. 24, no. 21, pp. 5749–5755, 1985.

[414] R. Bedlack, M. Wei, and L. Loew, "Localized membrane depolarizations and localized calcium influx during electric field-guided neurite growth," *Neuron*, vol. 9, no. 3, pp. 393 – 403, 1992.

[415] B. Hein, K. I. Willig, C. A. Wurm, V. Westphal, S. Jakobs, and S. W. Hell, "Stimulated emission depletion nanoscopy of living cells using SNAP-Tag fusion proteins," *Biophysical Journal*, vol. 98, no. 1, pp. 158 – 163, 2010.

[416] I. Testa, C. A. Wurm, R. Medda, E. Rothermel, C. von Middendorf, J. Fölling, S. Jakobs, A. Schönle, S. W. Hell, and C. Eggeling, "Multicolor fluorescence nanoscopy in fixed and living cells by exciting conventional fluorophores with a single wavelength," *Biophysical Journal*, vol. 99, no. 8, pp. 2686–2694, Aug. 2010.

[417] G. J. Hausman, J. E. Novakofski, R. J. Martin, and G. B. Thomas, "The development of adipocytes in primary stromal-vascular culture of fetal pig adipose tissue," *Cell and Tissue Research*, vol. 236, no. 2, pp. 459–464, 1984.

[418] I. Nakajima, H. Aso, T. Yamaguchi, and K. Ozutsumi, "Adipose tissue extracellular matrix: newly organized by adipocytes during differentiation," *Differentiation*, vol. 63, no. 4, pp. 193 – 200, 1998.

[419] L. G. Luna and A. F. I. of Pathology (U.S.), *Manual of histologic staining methods of the Armed Forces Institute of Pathology*. New York: Blakiston Division, McGraw-Hill, 1968.

[420] J. L. Ramírez-Zacarías, F. Castro-Muñozledo, and W. Kuri-Harcuch, "Quantitation of adipose conversion and triglycerides by staining intracytoplasmic lipids with oil red O," *Histochemistry*, vol. 97, no. 6, pp. 493–497, 1992.

[421] A. Mehlem, C. E. Hagberg, L. Muhl, U. Eriksson, and A. Falkevall, "Imaging of neutral lipids by oil red O for analyzing the metabolic status in health and disease," *Nat. Protocols*, vol. 8, no. 6, pp. 1149–1154, Jun. 2013.

[422] A. Schönle, "Imspector image acquisition & analysis software, v0.1," 2006. [Online]. Available: http://www.imspector.de

[423] J. Schindelin, I. Arganda-Carreras, E. Frise, V. Kaynig, M. Longair, T. Pietzsch, S. Preibisch, C. Rueden, S. Saalfeld, B. Schmid, J.-Y. Tinevez, D. J. White, V. Hartenstein, K. Eliceiri, P. Tomancak, and A. Cardona, "Fiji: an open-source platform for biological image analysis," *Nat Meth*, vol. 9, no. 7, pp. 676–682, Jul. 2012.

[424] W. H. Richardson, "Bayesian-based iterative method of image restoration," *J. Opt. Soc. Am.*, vol. 62, no. 1, pp. 55–59, Jan 1972.

[425] L. B. Lucy, "An iterative technique for the rectification of observed distributions," *The astronomical journal*, vol. 79, pp. 745–754, 1974.

[426] V. N. Belov, G. Y. Mitronova, M. L. Bossi, V. P. Boyarskiy, E. Hebisch, C. Geisler, K. Kolmakov, C. A. Wurm, K. I. Willig, and S. W. Hell, "Masked rhodamine dyes of five principal colors revealed by photolysis of a 2-diazo-1-indanone caging group: Synthesis, photophysics, and light microscopy applications," *Chemistry – A European Journal*, vol. 20, no. 41, pp. 13 162–13 173, 2014.

[427] K. Kolmakov, E. Hebisch, T. Wolfram, L. A. Nordwig, C. A. Wurm, H. Ta, V. Westphal, V. N. Belov, and S. W. Hell, "Far-red emitting fluorescent dyes for optical nanoscopy: Fluorinated silicon–rhodamines (SiRF dyes) and phosphorylated oxazines," *Chemistry – A European Journal*, vol. 21, no. 38, pp. 13 344–13 356, 2015.

[428] H. B. Mann and D. R. Whitney, "On a test of whether one of two random variables is stochastically larger than the other," *The annals of mathematical statistics*, pp. 50–60, 1947.

[429] M. P. Fay and M. A. Proschan, "Wilcoxon-Mann-Whitney or t-test? on assumptions for hypothesis tests and multiple interpretations of decision rules," *Statistics surveys*, vol. 4, pp. 1–39, 2010.

[430] G. Cardillo. (2009) mwwtest: Mann-Whitney-Wilcoxon nonparametric test for two unpaired samples. [Online]. Available: http://www.mathworks.com/matlabcentral/fileexchange/25830

[431] R. Saetzler, J. Jallo, H. Lehr, C. Philips, U. Vasthare, K. Arfors, and R. Tuma, "Intravital fluorescence microscopy: Impact of light-induced phototoxicity on adhesion of fluorescently labeled leukocytes," *Journal of Histochemistry & Cytochemistry*, vol. 45, no. 4, pp. 505–513, 1997.

[432] R. A. Hoebe, C. H. Van Oven, T. W. J. Gadella, P. B. Dhonukshe, C. J. F. Van Noorden, and E. M. M. Manders, "Controlled light-exposure microscopy reduces photobleaching and phototoxicity in fluorescence live-cell imaging," *Nat Biotech*, vol. 25, no. 2, pp. 249–253, Feb. 2007.

[433] M. Steinbauer, G. A. Harris, C. Abels, and K. Messmer, "Characterization and prevention of phototoxic effects in intravital fluorescence microscopy in the hamster dorsal skinfold model," *Langenbeck's Archives of Surgery*, vol. 385, no. 4, pp. 290–298, 2000.

[434] D. S. Rosenbaum, D. T. Kaplan, A. Kanai, L. Jackson, H. Garan, R. J. Cohen, and G. Salama, "Repolarization inhomogeneities in ventricular myocardium change dynamically with abrupt cycle length shortening." *Circulation*, vol. 84, no. 3, pp. 1333–1345, 1991.

[435] L. M. Loew, L. B. Cohen, J. Dix, E. N. Fluhler, V. Montana, G. Salama, and W. Jian-young, "A naphthyl analog of the aminostyryl pyridinium class of potentiometric membrane dyes shows consistent sensitivity in a variety of tissue, cell, and model membrane preparations," *The Journal of Membrane Biology*, vol. 130, no. 1, pp. 1–10, 1992.

[436] L. Pereira, H. Rehmann, D. H. Lao, J. R. Erickson, J. Bossuyt, J. Chen, and D. M. Bers, "Novel Epac fluorescent ligand reveals distinct Epac1 vs. Epac2 distribution and function in cardiomyocytes," *Proceedings of the National Academy of Sciences*, vol. 112, no. 13, pp. 3991–3996, 2015.

[437] T. Georgiev, B. Zapiec, M. Förderer, R. H. Fink, and M. Vogel, "Colocalization properties of elementary Ca^{2+} release signals with structures specific to the contractile filaments and the tubular system of intact mouse skeletal muscle fibers," *Journal of Structural Biology*, vol. 192, no. 3, pp. 366 – 375, 2015.

[438] C. Manno, L. Figueroa, R. Fitts, and E. Ríos, "Confocal imaging of transmembrane voltage by SEER of Di-8-ANEPPS," *The Journal of General Physiology*, vol. 141, no. 3, pp. 371–387, 2013.

[439] Q. Tian, S. Pahlavan, K. Oleinikow, J. Jung, S. Ruppenthal, A. Scholz, C. Schumann, A. Kraegeloh, M. Oberhofer, P. Lipp, and L. Kaestner, "Functional and morphological preservation of adult ventricular myocytes in culture by sub-micromolar cytochalasin D supplement," *Journal of Molecular and Cellular Cardiology*, vol. 52, no. 1, pp. 113 – 124, 2012.

[440] W. E. Louch, H. K. Mørk, J. Sexton, T. A. Strømme, P. Laake, I. Sjaastad, and O. M. Sejersted, "T-Tubule disorganization and reduced synchrony of Ca^{2+} release in murine cardiomyocytes following myocardial infarction," *The Journal of Physiology*, vol. 574, no. 2, pp. 519–533, 2006.

[441] J. Hüser, P. Lipp, and E. Niggli, "Confocal microscopic detection of potential-sensitive dyes used to reveal loss of voltage control during patch-clamp experiments," *Pflügers Archiv*, vol. 433, no. 1, pp. 194–199, 1996.

[442] A. Obaid, L. Loew, J. Wuskell, and B. Salzberg, "Novel naphthylstyryl-pyridinium potentiometric dyes offer advantages for neural network analysis," *Journal of Neuroscience Methods*, vol. 134, no. 2, pp. 179 – 190, 2004.

[443] S. Rohr and B. Salzberg, "Multiple site optical recording of transmembrane voltage (MSORTV) in patterned growth heart cell cultures: assessing electrical behavior, with microsecond resolution, on a cellular and subcellular scale," *Biophysical Journal*, vol. 67, no. 3, pp. 1301 – 1315, 1994.

[444] "ThermoFisher Scientific, Di-8-ANEPPS, order number D3167," https://www.thermofisher.com/order/catalog/product/D3167, accessed: August 2016.

[445] G. L. Goff, M. F. Vitha, and R. J. Clarke, "Orientational polarisability of lipid membrane surfaces," *Biochimica et Biophysica Acta (BBA) - Biomembranes*, vol. 1768, no. 3, pp. 562 – 570, 2007.

[446] R. W. Sabnis, *Handbook of Biological Dyes and Stains - Synthesis and Industrial Applications*. John Wiley & Sons, Inc., 2010.

[447] R. Y. Tsien, "The green fluorescent protein," *Annual Review of Biochemistry*, vol. 67, no. 1, pp. 509–544, 1998, pMID: 9759496.

[448] R. Heim, D. C. Prasher, and R. Y. Tsien, "Wavelength mutations and posttranslational autoxidation of green fluorescent protein." *Proceedings of the National Academy of Sciences of the United States of America*, vol. 91, no. 26, pp. 12 501–12 504, Dec. 1994.

[449] T. Ehrig, D. J. O'Kane, and F. G. Prendergast, "Green-fluorescent protein mutants with altered fluorescence excitation spectra," *FEBS Letters*, vol. 367, no. 2, pp. 163–166, 1995.

[450] B. Rankin, G. Moneron, C. Wurm, J. Nelson, A. Walter, D. Schwarzer, J. Schroeder, D. Colón-Ramos, and S. Hell, "Nanoscopy in a living multicellular organism expressing GFP," *Biophysical Journal*, vol. 100, no. 12, pp. L63 – L65, 2011.

[451] J. Hotta, E. Fron, P. Dedecker, K. P. F. Janssen, C. Li, K. Müllen, B. Harke, J. Bückers, S. W. Hell, and J. Hofkens, "Spectroscopic rationale for efficient stimulated-emission depletion microscopy fluorophores," *Journal of the American Chemical Society*, vol. 132, no. 14, pp. 5021–5023, 2010.

[452] J. L. Wong, D. E. Koppel, A. E. Cowan, and G. M. Wessel, "Membrane hemifusion is a stable intermediate of exocytosis," *Developmental Cell*, vol. 12, no. 4, pp. 653 – 659, 2007.

[453] J. S. Oghalai, H.-B. Zhao, J. W. Kutz, and W. E. Brownell, "Voltage- and tension-dependent lipid mobility in the outer hair cell plasma membrane," *Science*, vol. 287, no. 5453, pp. 658–661, 2000.

[454] S. K. Saka, A. Honigmann, C. Eggeling, S. W. Hell, T. Lang, and S. O. Rizzoli, "Multi-protein assemblies underlie the mesoscale organization of the plasma membrane," *Nature Communications*, vol. 5(4509), Jul. 2014.

[455] O. Steshenko, D. Andrade, A. Honigmann, V. Mueller, F. Schneider, E. Sezgin, S. Hell, M. Simons, and C. Eggeling, "Reorganization of lipid diffusion by myelin basic protein as revealed by STED nanoscopy," *Biophysical Journal*, vol. 110, no. 11, pp. 2441 – 2450, 2016.

[456] E. Sevcsik, M. Brameshuber, M. Fölser, J. Weghuber, A. Honigmann, and G. J. Schütz, "GPI-anchored proteins do not reside in ordered domains in the live cell plasma membrane," *Nature Communications*, vol. 6, p. 6969, Apr. 2015.

[457] D. Wüstner, M. Modzel, F. W. Lund, and M. A. Lomholt, "Imaging approaches for analysis of cholesterol distribution and dynamics in the plasma membrane," *Chemistry and Physics of Lipids*, vol. 199, pp. 106 – 135, 2016.

[458] K. Kolmakov, V. N. Belov, J. Bierwagen, C. Ringemann, V. Müller, C. Eggeling, and S. W. Hell, "Red-emitting rhodamine dyes for fluorescence microscopy and nanoscopy," *Chemistry – A European Journal*, vol. 16, no. 1, pp. 158–166, 2010.

[459] S. B. Sato, K. Ishii, A. Makino, K. Iwabuchi, A. Yamaji-Hasegawa, Y. Senoh, I. Nagaoka, H. Sakuraba, and T. Kobayashi, "Distribution and transport of cholesterol-rich membrane domains monitored by a membrane-impermeant fluorescent polyethylene glycol-derivatized cholesterol," *Journal of Biological Chemistry*, vol. 279, no. 22, pp. 23 790–23 796, 2004.

[460] E. Sezgin, F. B. Can, F. Schneider, M. P. Clausen, S. Galiani, T. A. Stanly, D. Waithe, A. Colaco, A. Honigmann, D. Wüstner, F. Platt, and C. Eggeling, "A comparative study on fluorescent cholesterol analogs as versatile cellular reporters," *Journal of Lipid Research*, vol. 57, no. 2, pp. 299–309, 2016.

[461] R. Smith and C. Green, "The rate of cholesterol 'flip-flop' in lipid bilayers and its relation to membrane sterol pools," *FEBS Letters*, vol. 42, no. 1, pp. 108–111, 1974.

[462] T. Róg, L. M. Stimson, M. Pasenkiewicz-Gierula, I. Vattulainen, and M. Karttunen, "Replacing the cholesterol hydroxyl group with the ketone group facilitates sterol flip-flop and promotes membrane fluidity," *The Journal of Physical Chemistry B*, vol. 112, no. 7, pp. 1946–1952, 2008.

[463] J. A. Hamilton, "Fast flip-flop of cholesterol and fatty acids in membranes: implications for membrane transport proteins," *Current Opinion in Lipidology*, vol. 14, no. 3, 2003.

[464] F. R. Maxfield and D. Wüstner, "Intracellular cholesterol transport," *The Journal of Clinical Investigation*, vol. 110, no. 7, pp. 891–898, 10 2002.

[465] W. J. Johnson, F. H. Mahlberg, G. H. Rothblat, and M. C. Phillips, "Cholesterol transport between cells and high-density lipoproteins," *Biochimica et Biophysica Acta (BBA) - Lipids and Lipid Metabolism*, vol. 1085, no. 3, pp. 273 – 298, 1991.

[466] E. Sezgin, I. Levental, M. Grzybek, G. Schwarzmann, V. Mueller, A. Honigmann, V. N. Belov, C. Eggeling, Ünal Coskun, K. Simons, and P. Schwille, "Partitioning, diffusion, and ligand binding of raft lipid analogs in model and cellular plasma membranes," *Biochimica et Biophysica Acta (BBA) - Biomembranes*, vol. 1818, no. 7, pp. 1777 – 1784, 2012.

[467] T. Fujiwara, K. Ritchie, H. Murakoshi, K. Jacobson, and A. Kusumi, "Phospholipids undergo hop diffusion in compartmentalized cell membrane," *The Journal of Cell Biology*, vol. 157, no. 6, pp. 1071–1082, 2002.

[468] P. K. Mattila and P. Lappalainen, "Filopodia: molecular architecture and cellular functions," *Nat Rev Mol Cell Biol*, vol. 9, no. 6, pp. 446–454, Jun. 2008.

[469] J. Faix and K. Rottner, "The making of filopodia," *Current Opinion in Cell Biology*, vol. 18, no. 1, pp. 18 – 25, 2006.

[470] S. T. Christensen and C. M. Ott, "A ciliary signaling switch," *Science*, vol. 317, no. 5836, pp. 330–331, Jul. 2007.

[471] C. Schwan, T. Nölke, A. S. Kruppke, D. M. Schubert, A. E. Lang, and K. Aktories, "Cholesterol- and sphingolipid-rich microdomains are essential for microtubule-based membrane protrusions induced by Clostridium Difficile Transferase (CDT)," *Journal of Biological Chemistry*, vol. 286, no. 33, pp. 29 356–29 365, 2011.

[472] W. Möbius, Y. Ohno-Iwashita, E. G. v. Donselaar, V. M. Oorschot, Y. Shimada, T. Fujimoto, H. F. Heijnen, H. J. Geuze, and J. W. Slot, "Immunoelectron microscopic localization of Cholesterol using biotinylated and non-cytolytic Perfringolysin O," *Journal of Histochemistry & Cytochemistry*, vol. 50, no. 1, pp. 43–55, 2002.

[473] H. Mizuno, M. Abe, P. Dedecker, A. Makino, S. Rocha, Y. Ohno-Iwashita, J. Hofkens, T. Kobayashi, and A. Miyawaki, "Fluorescent probes for superresolution imaging of lipid domains on the plasma membrane," *Chem. Sci.*, vol. 2, no. 8, pp. 1548–1553, 2011.

[474] C.-C. Ho, P.-H. Huang, H.-Y. Huang, Y.-H. Chen, P.-C. Yang, and S.-M. Hsu, "Up-regulated Caveolin-1 accentuates the metastasis capability of lung adenocarcinoma by inducing filopodia formation," *The American Journal of Pathology*, vol. 161, no. 5, pp. 1647 – 1656, 2002.

[475] Y.-R. Liou, W. Torng, Y.-C. Kao, K.-B. Sung, C.-H. Lee, and P.-L. Kuo, "Substrate stiffness regulates filopodial activities in lung cancer cells," *PLoS ONE*, vol. 9, no. 2, pp. 1–11, 02 2014.

[476] H. Yamada, T. Takeda, H. Michiue, T. Abe, and K. Takei, "Actin bundling by Dynamin 2 and Cortactin is implicated in cell migration by stabilizing filopodia in human non-small cell lung carcinoma cells," *International Journal of Oncology*, vol. 49, no. 3, pp. 877–886, 2016.

[477] J. C. Fiala, J. Spacek, and K. M. Harris, "Dendritic spine pathology: Cause or consequence of neurological disorders?" *Brain Research Reviews*, vol. 39, no. 1, pp. 29 – 54, 2002.

[478] X. Chen, J. Hu, L. Jiang, S. Xu, B. Zheng, C. Wang, J. Zhang, X. Wei, L. Chang, and Q. Wang, "Brilliant Blue G improves cognition in an animal model of Alzheimer's disease and inhibits amyloid-β-induced loss of filopodia and dendrite spines in hippocampal neurons," *Neuroscience*, vol. 279, pp. 94 – 101, 2014.

[479] M. Yazawa, B. Hsueh, X. Jia, A. M. Pasca, J. A. Bernstein, J. Hallmayer, and R. E. Dolmetsch, "Using induced pluripotent stem cells to investigate cardiac phenotypes in Timothy syndrome," *Nature*, vol. 471, no. 7337, pp. 230–234, Mar. 2011.

[480] M. Hoekstra, C. L. Mummery, A. A. M. Wilde, C. R. Bezzina, and A. O. Verkerk, "Induced pluripotent stem cell derived cardiomyocytes as models for cardiac arrhythmias," *Frontiers in Physiology*, vol. 3, no. 346, Aug. 2012.

[481] G. Narazaki, H. Uosaki, M. Teranishi, K. Okita, B. Kim, S. Matsuoka, S. Yamanaka, and J. K. Yamashita, "Directed and systematic differentiation of cardiovascular cells from mouse induced pluripotent stem cells," *Circulation*, vol. 118, no. 5, pp. 498–506, 2008.

[482] C. Mauritz, K. Schwanke, M. Reppel, S. Neef, K. Katsirntaki, L. S. Maier, F. Nguemo, S. Menke, M. Haustein, J. Hescheler, G. Hasenfuss, and U. Martin, "Generation of functional murine cardiac myocytes from induced pluripotent stem cells," *Circulation*, vol. 118, no. 5, pp. 507–517, 2008.

[483] J. Zhang, G. F. Wilson, A. G. Soerens, C. H. Koonce, J. Yu, S. P. Palecek, J. A. Thomson, and T. J. Kamp, "Functional cardiomyocytes derived from human induced pluripotent stem cells," *Circulation Research*, vol. 104, no. 4, pp. e30–e41, 2009.

[484] F. Weinberger, K. Breckwoldt, S. Pecha, A. Kelly, B. Geertz, J. Starbatty, T. Yorgan, K.-H. Cheng, K. Lessmann, T. Stolen, M. Scherrer-Crosbie,

G. Smith, H. Reichenspurner, A. Hansen, and T. Eschenhagen, "Cardiac repair in guinea pigs with human engineered heart tissue from induced pluripotent stem cells," *Science Translational Medicine*, vol. 8, no. 363, Nov. 2016.

[485] B. C. Knollmann, "Controversies in cardiovascular research: Induced pluripotent stem cell-derived cardiomyocytes - boutique science or valuable arrhythmia model?" *Circulation research*, vol. 112, no. 6, pp. 969–976, Mar. 2013.

[486] D. Sinnecker, A. Goedel, K.-L. Laugwitz, and A. Moretti, "Induced pluripotent stem cell-derived cardiomyocytes," *Circulation Research*, vol. 112, no. 6, pp. 961–968, 2013.

[487] T. G. Melo, D. S. Almeida, M. N. S. L. Meirelles, and M. C. S. Pereira, "Disarray of sarcomeric alpha-Actinin in cardiomyocytes infected by Trypanosoma cruzi," *Parasitology*, vol. 133, pp. 171–178, Aug. 2006.

[488] N. Cao, Y. Huang, J. Zheng, C. I. Spencer, Y. Zhang, J.-D. Fu, B. Nie, M. Xie, M. Zhang, H. Wang, T. Ma, T. Xu, G. Shi, D. Srivastava, and S. Ding, "Conversion of human fibroblasts into functional cardiomyocytes by small molecules," *Science*, pp. 1–9, 2016.

[489] S. Martin and R. G. Parton, "Lipid droplets: a unified view of a dynamic organelle," *Nat Rev Mol Cell Biol*, vol. 7, no. 5, pp. 373–378, May 2006.

[490] D. J. Murphy, "The biogenesis and functions of lipid bodies in animals, plants and microorganisms," *Progress in Lipid Research*, vol. 40, no. 5, pp. 325–438, Sep. 2001.

[491] A. H. Berg and P. E. Scherer, "Adipose tissue, inflammation, and cardiovascular disease," *Circ Res*, vol. 96, no. 9, pp. 939–949, May 2005.

[492] T. P. Fitzgibbons and M. P. Czech, "Epicardial and perivascular adipose tissues and their influence on cardiovascular disease: Basic mechanisms and clinical associations," *Journal of the American Heart Association*, vol. 3, no. 2, Apr. 2014.

[493] S. Chung, H. Cuffe, S. M. Marshall, A. L. McDaniel, J.-H. Ha, K. Kavanagh, C. Hong, P. Tontonoz, R. E. Temel, and J. S. Parks, "Dietary cholesterol promotes adipocyte hypertrophy and adipose tissue inflammation in visceral, but not in subcutaneous, fat in monkeys," *Arteriosclerosis, Thrombosis, and Vascular Biology*, vol. 34, no. 9, pp. 1880–1887, 2014.

[494] M. Bastien, P. Poirier, I. Lemieux, and J.-P. Després, "Overview of epidemiology and contribution of obesity to cardiovascular disease," *Progress in Cardiovascular Diseases*, vol. 56, no. 4, pp. 369–381, Jan. 2014.

[495] M. Blüher, "Adipose tissue dysfunction contributes to obesity related metabolic diseases," *Best Practice & Research Clinical Endocrinology & Metabolism*, vol. 27, no. 2, pp. 163–177, Apr. 2013.

[496] S. Prattes, G. Horl, A. Hammer, A. Blaschitz, W. Graier, W. Sattler, R. Zechner, and E. Steyrer, "Intracellular distribution and mobilization of unesterified cholesterol in adipocytes: triglyceride droplets are surrounded by cholesterol-rich ER-like surface layer structures," *J. Cell Sci.*, vol. 113, no. 17, pp. 2977–2989, Sep. 2000.

[497] G. Dagher, N. Donne, C. Klein, P. Ferré, and I. Dugail, "HDL-mediated cholesterol uptake and targeting to lipid droplets in adipocytes," *Journal of Lipid Research*, vol. 44, no. 10, pp. 1811–1820, 2003.

[498] Z. Li, E. Mintzer, and R. Bittman, "First synthesis of free cholesterol-BODIPY conjugates," *J. Org. Chem.*, vol. 71, no. 4, pp. 1718–1721, Feb. 2006.

[499] F. S. Ariola, Z. Li, C. Cornejo, R. Bittman, and A. A. Heikal, "Membrane fluidity and lipid order in ternary giant unilamellar vesicles using a new BODIPY-cholesterol derivative," *Biophysical Journal*, vol. 96, no. 7, pp. 2696–2708, Apr. 2009.

[500] S. Milles, T. Meyer, H. A. Scheidt, R. Schwarzer, L. Thomas, M. Marek, L. Szente, R. Bittman, A. Herrmann, T. Günther Pomorski, D. Huster, and P. Müller, "Organization of fluorescent cholesterol analogs in lipid

bilayers - lessons from cyclodextrin extraction," *Biochimica et Biophysica Acta (BBA) - Biomembranes*, vol. 1828, no. 8, pp. 1822–1828, Aug. 2013.

[501] E. Ikonen, "Cellular cholesterol trafficking and compartmentalization," *Nat Rev Mol Cell Biol*, vol. 9, no. 2, pp. 125–138, Feb. 2008.

[502] D. Lingwood and K. Simons, "Lipid rafts as a membrane-organizing principle," *Science*, vol. 327, no. 5961, pp. 46–50, 2009.

[503] M. Maekawa and G. D. Fairn, "Complementary probes reveal that phosphatidylserine is required for the proper transbilayer distribution of cholesterol," *Journal of Cell Science*, vol. 128, no. 7, pp. 1422–1433, 2015.

[504] P. J. Campagnola, M. de Wei, A. Lewis, and L. M. Loew, "High-resolution nonlinear optical imaging of live cells by second harmonic generation," *Biophysical Journal*, vol. 77, no. 6, pp. 3341 – 3349, 1999.

[505] O. J. Kemi, M. A. Hoydal, N. MacQuaide, P. M. Haram, L. G. Koch, S. L. Britton, O. Ellingsen, G. L. Smith, and U. Wisloff, "The effect of exercise training on transverse tubules in normal, remodeled, and reverse remodeled hearts," *Journal of Cellular Physiology*, vol. 226, no. 9, pp. 2235–2243, 2011.

[506] W. Becker, "Fluorescence lifetime imaging – techniques and applications," *Journal of Microscopy*, vol. 247, no. 2, pp. 119–136, 2012.

[507] J. R. Lakowicz, *Principles of Fluorescence Spectroscopy*. Springer Science+Business Media, 2010.

[508] D. Axelrod, D. E. Koppel, J. Schlessinger, E. Elson, and W. W. Webb, "Mobility measurement by analysis of fluorescence photobleaching recovery kinetics." *Biophysical Journal*, vol. 16, no. 9, pp. 1055–1069, Sep. 1976.

[509] E. F. F. da Silva, F. M. Pimenta, B. W. Pedersen, F. H. Blaikie, G. N. Bosio, T. Breitenbach, M. Westberg, M. Bregnhoj, M. Etzerodt, L. G. Arnaut, and P. R. Ogilby, "Intracellular singlet oxygen photosensitizers: on the road to solving the problems of sensitizer degradation, bleaching and relocalization," *Integr. Biol.*, vol. 8, pp. 177–193, 2016.

[510] S.-W. Chu, T.-M. Liu, C.-K. Sun, C.-Y. Lin, and H.-J. Tsai, "Real-time second-harmonic-generation microscopy based on a 2-GHz repetition rate Ti:Sapphire laser," *Opt. Express*, vol. 11, no. 8, pp. 933–938, Apr 2003.

[511] A. Ehlers, I. Riemann, S. Martin, R. Le Harzic, A. Bartels, C. Janke, and K. König, "High (1GHz) repetition rate compact femtosecond laser: A powerful multiphoton tool for nanomedicine and nanobiotechnology," *Journal of Applied Physics*, vol. 102, no. 1, 2007.

[512] G. J. Brakenhoff, J. Squier, T. Norris, A. C. Bliton, M. H. Wade, and B. Athey, "Real-time two-photon confocal microscopy using a femtosecond, amplified Ti:Sapphire system," *Journal of Microscopy*, vol. 181, no. 3, pp. 253–259, 1996.

[513] C. Eggeling, J. Widengren, R. Rigler, and C. A. M. Seidel, "Photobleaching of fluorescent dyes under conditions used for single-molecule detection: Evidence of two-step photolysis," *Analytical Chemistry*, vol. 70, no. 13, pp. 2651–2659, 1998.

[514] J. Widengren and R. Rigler, "Mechanisms of photobleaching investigated by fluorescence correlation spectroscopy," *Bioimaging*, vol. 4, no. 3, pp. 149–157, 1996.

[515] P. Dittrich and P. Schwille, "Photobleaching and stabilization of fluorophores used for single-molecule analysis with one- and two-photon excitation," *Applied Physics B*, vol. 73, no. 8, pp. 829–837, 2001.

[516] G. H. Patterson and D. W. Piston, "Photobleaching in two-photon excitation microscopy," *Biophysical Journal*, vol. 78, no. 4, pp. 2159 – 2162, 2000.

[517] E. Spiess, F. Bestvater, A. Heckel-Pompey, K. Toth, M. Hacker, G. Stobrawa, T. Feurer, C. Wotzlaw, U. Berchner-Pfannschmidt, T. Porwol, and H. Acker, "Two-photon excitation and emission spectra of the green fluorescent protein variants ECFP, EGFP and EYFP," *Journal of Microscopy*, vol. 217, no. 3, pp. 200–204, 2005.

[518] C. Xu and W. W. Webb, "Measurement of two-photon excitation cross sections of molecular fluorophores with data from 690 to 1050 nm," *J. Opt. Soc. Am. B*, vol. 13, no. 3, pp. 481–491, Mar 1996.

[519] V. Danilov, Y. Mazurenko, and S. Vorontsova, "Anti-stokes excitation of luminescence of dyes by high-power radiation," *Optics Communications*, vol. 9, no. 3, pp. 283 – 286, 1973.

[520] G. Vicidomini, G. Moneron, C. Eggeling, E. Rittweger, and S. W. Hell, "STED with wavelengths closer to the emission maximum," *Opt. Express*, vol. 20, no. 5, pp. 5225–5236, Feb 2012.

[521] M. D. Bordenave, F. Balzarotti, F. D. Stefani, and S. W. Hell, "STED nanoscopy with wavelengths at the emission maximum," *Journal of Physics D: Applied Physics*, vol. 49, no. 36, p. 365102, 2016.

[522] T. A. Klar, S. Jakobs, M. Dyba, A. Egner, and S. W. Hell, "Fluorescence microscopy with diffraction resolution barrier broken by stimulated emission," *Proceedings of the National Academy of Sciences*, vol. 97, no. 15, pp. 8206–8210, 2000.

[523] E. J. Sánchez, L. Novotny, G. R. Holtom, and S. X. Xie, "Room-temperature fluorescence imaging and spectroscopy of single molecules by two-photon excitation," *The Journal of Physical Chemistry A*, vol. 101, no. 38, pp. 7019–7023, 1997.

[524] G. Donnert, J. Keller, R. Medda, M. A. Andrei, S. O. Rizzoli, R. Lührmann, R. Jahn, C. Eggeling, and S. W. Hell, "Macromolecular-scale resolution in biological fluorescence microscopy," *Proceedings of the National Academy of Sciences*, vol. 103, no. 31, pp. 11 440–11 445, 2006.

[525] Q. Li, Y. Wang, D. Chen, and S. S. H. Wu, "2PE-STED microscopy with a single Ti:Sapphire laser for reduced illumination," *PLoS ONE*, vol. 9, no. 2, pp. 1–5, 02 2014.

[526] S. Krishnamurthy, P. Bhattacharya, , P. E. Phelan, and R. S. Prasher, "Enhanced mass transport in nanofluids," *Nano Letters*, vol. 6, no. 3, pp. 419–423, 2006.

[527] N. G. Zhegalova, S. He, H. Zhou, D. M. Kim, and M. Y. Berezin, "Minimization of self-quenching fluorescence on dyes conjugated to biomolecules with multiple labeling sites via asymmetrically charged NIR fluorophores," *Contrast media & molecular imaging*, vol. 9, no. 5, pp. 355–362, Apr. 2014.

[528] S. Hamann, J. F. Kiilgaard, T. Litman, F. J. Alvarez-Leefmans, B. R. Winther, and T. Zeuthen, "Measurement of cell volume changes by fluorescence self-quenching," *Journal of Fluorescence*, vol. 12, no. 2, pp. 139–145, 2002.

[529] D. Wildanger, E. Rittweger, L. Kastrup, and S. W. Hell, "STED microscopy with a supercontinuum laser source," *Opt. Express*, vol. 16, no. 13, pp. 9614–9621, Jun 2008.

[530] P. Bianchini, C. Peres, M. Oneto, S. Galiani, G. Vicidomini, and A. Diaspro, "STED nanoscopy: a glimpse into the future," *Cell and Tissue Research*, vol. 360, no. 1, pp. 143–150, 2015.

[531] P. Bingen, M. Reuss, J. Engelhardt, and S. W. Hell, "Parallelized STED fluorescence nanoscopy," *Opt. Express*, vol. 19, no. 24, pp. 23 716–23 726, Nov 2011.

[532] E. Savio-Galimberti, J. Frank, M. Inoue, J. I. Goldhaber, M. B. Cannell, J. H. Bridge, and F. B. Sachse, "Novel features of the rabbit transverse tubular system revealed by quantitative analysis of three-dimensional reconstructions from confocal images," *Biophysical Journal*, vol. 95, no. 4, pp. 2053–2062, Aug. 2008.

[533] J. Zimmerberg and M. M. Kozlov, "How proteins produce cellular membrane curvature," *Nat Rev Mol Cell Biol*, vol. 7, no. 1, pp. 9–19, Jan. 2006.

[534] T. Lang and S. O. Rizzoli, "Membrane protein clusters at nanoscale resolution: More than pretty pictures," *Physiology*, vol. 25, no. 2, pp. 116–124, Apr. 2010.

[535] M. Dyba, S. Jakobs, and S. W. Hell, "Immunofluorescence stimulated emission depletion microscopy," *Nat Biotech*, vol. 21, no. 11, pp. 1303–1304, Nov. 2003.

[536] S. Yu, K. Matsusue, P. Kashireddy, W.-Q. Cao, V. Yeldandi, A. V. Yeldandi, M. S. Rao, F. J. Gonzalez, and J. K. Reddy, "Adipocyte-specific gene expression and adipogenic steatosis in the mouse liver due to peroxisome proliferator-activated receptor γ1 (PPARγ1) overexpression," *Journal of Biological Chemistry*, vol. 278, no. 1, pp. 498–505, Jan. 2003.

[537] A. W. Cohen, B. Razani, W. Schubert, T. M. Williams, X. B. Wang, P. Iyengar, D. L. Brasaemle, P. E. Scherer, and M. P. Lisanti, "Role of Caveolin-1 in the modulation of lipolysis and lipid droplet formation," *Diabetes*, vol. 53, no. 5, pp. 1261–1270, Apr. 2004.

[538] M. G. Qaddoumi, H. J. Gukasyan, J. Davda, V. Labhasetwar, K.-J. Kim, and V. Lee, "Clathrin and Caveolin-1 expression in primary pigmented rabbit conjunctival epithelial cells: role in PLGA nanoparticle endocytosis," *Mol Vis*, vol. 9, pp. 559–568, 2003.

[539] A. Keppler, S. Gendreizig, T. Gronemeyer, H. Pick, H. Vogel, and K. Johnsson, "A general method for the covalent labeling of fusion proteins with small molecules in vivo," *Nat Biotech*, vol. 21, no. 1, pp. 86–89, Jan. 2003.

[540] G. Lukinavicius, K. Umezawa, N. Olivier, A. Honigmann, G. Yang, T. Plass, V. Mueller, L. Reymond, I. R. Correa Jr, Z.-G. Luo, C. Schultz, E. A. Lemke, P. Heppenstall, C. Eggeling, S. Manley, and K. Johnsson, "A near-infrared fluorophore for live-cell super-resolution microscopy of cellular proteins," *Nat Chem*, vol. 5, no. 2, pp. 132–139, Feb. 2013.

[541] A. Kuga, Y. Ohsawa, T. Okada, F. Kanda, M. Kanagawa, T. Toda, and Y. Sunada, "Endoplasmic reticulum stress response in P104L mutant Caveolin-3 transgenic mice," *Human Molecular Genetics*, vol. 20, no. 15, pp. 2975–2983, May 2011.

[542] P. L. Yeagle, "Non-covalent binding of membrane lipids to membrane proteins," *Biochimica et Biophysica Acta (BBA) - Biomembranes*, vol. 1838, no. 6, pp. 1548–1559, Jun. 2014.

[543] R. G. W. Anderson and K. Jacobson, "A role for lipid shells in targeting proteins to caveolae, rafts, and other lipid domains," *Science*, vol. 296, no. 5574, pp. 1821–1825, 2002.

[544] R. M. Epand, "Cholesterol and the interaction of proteins with membrane domains," *Progress in Lipid Research*, vol. 45, no. 4, pp. 279–294, Jul. 2006.

[545] K. Simons and D. Toomre, "Lipid rafts and signal transduction," *Nat Rev Mol Cell Biol*, vol. 1, no. 1, pp. 31–39, Oct. 2000.

[546] S. Y. Nishimura, M. Vrljic, L. O. Klein, H. M. McConnell, and W. E. Moerner, "Cholesterol depletion induces solid-like regions in the plasma membrane," *Biophysical Journal*, vol. 90, no. 3, pp. 927–938, Feb. 2006.

[547] C. A. López, A. H. de Vries, and S. J. Marrink, "Molecular mechanism of cyclodextrin mediated cholesterol extraction," *PLoS Comput Biol*, vol. 7, no. 3, p. e1002020, Mar. 2011.

[548] S. Ilangumaran and D. C. Hoessli, "Effects of cholesterol depletion by cyclodextrin on the sphingolipid microdomains of the plasma membrane," *Biochem J*, vol. 335, no. 2, pp. 433–440, Oct. 1998.

[549] R. Onodera, K. Motoyama, A. Okamatsu, T. Higashi, R. Kariya, S. Okada, and H. Arima, "Involvement of cholesterol depletion from lipid rafts in apoptosis induced by methyl-β-cyclodextrin," *International journal of pharmaceutics*, vol. 452, no. 1, pp. 116–123, 2013.

[550] H. Sprong, P. van der Sluijs, and G. van Meer, "How proteins move lipids and lipids move proteins," *Nat Rev Mol Cell Biol*, vol. 2, no. 7, pp. 504–513, Jul. 2001.

[551] D. A. Brown and E. London, "Structure and function of sphingolipid- and cholesterol-rich membrane rafts," *Journal of Biological Chemistry*, vol. 275, no. 23, pp. 17 221–17 224, Jun. 2000.

[552] D. A. Zacharias, J. D. Violin, A. C. Newton, and R. Y. Tsien, "Partitioning of lipid-modified monomeric GFPs into membrane microdomains of live cells," *Science*, vol. 296, no. 5569, pp. 913–916, May 2002.

[553] E. Lachmanovich, D. E. Shvartsman, Y. Malka, C. Botvin, Y. I. Henis, and A. M. Weiss, "Co-localization analysis of complex formation among membrane proteins by computerized fluorescence microscopy: application to immunofluorescence co-patching studies," *Journal of Microscopy*, vol. 212, no. 2, pp. 122–131, 2003.

[554] L. Gilboa, R. G. Wells, H. F. Lodish, and Y. I. Henis, "Oligomeric structure of type I and type II transforming growth factor β receptors: Homodimers form in the ER and persist at the plasma membrane," *J Cell Biol*, vol. 140, no. 4, pp. 767–777, Feb. 1998.

[555] H. W. Favoreel, T. C. Mettenleiter, and H. J. Nauwynck, "Copatching and lipid raft association of different viral glycoproteins expressed on the surfaces of pseudorabies virus-infected cells," *Journal of Virology*, vol. 78, no. 10, pp. 5279–5287, May 2004.

[556] T. Hirschhorn, N. di Clemente, A. R. Amsalem, R. B. Pepinsky, J.-Y. Picard, N. I. Smorodinsky, R. L. Cate, and M. Ehrlich, "Constitutive negative regulation in the processing of the anti-Müllerian hormone receptor II," *J. Cell Sci.*, vol. 128, no. 7, pp. 1352–1364, Mar. 2015.

[557] J. V. Pardo, J. D. Siliciano, and S. W. Craig, "A Vinculin-containing cortical lattice in skeletal muscle: transverse lattice elements ("costameres") mark sites of attachment between myofibrils and sarcolemma," *Proceedings of the National Academy of Sciences*, vol. 80, no. 4, pp. 1008–1012, Feb. 1983.

[558] A. M. Samarel, "Costameres, focal adhesions, and cardiomyocyte mechanotransduction," *Am J Physiol Heart Circ Physiol*, vol. 289, no. 6, pp. H2291–H2301, Nov. 2005.

[559] W. B. Im, S. F. Phelps, E. H. Copen, E. G. Adams, J. L. Slightom, and J. S. Chamberlain, "Differential expression of Dystrophin isoforms in strains

of *mdx* mice with different mutations," *Human molecular genetics*, vol. 5, no. 8, pp. 1149–1153, 1996.

[560] D. A. Rusakov, K. Zheng, and C. Henneberger, "Astrocytes as regulators of synaptic function: A quest for the Ca^{2+} master key," *The Neuroscientist*, pp. 1–11, May 2011.

[561] G. Iribe, C. W. Ward, P. Camelliti, C. Bollensdorff, F. Mason, R. A. Burton, A. Garny, M. K. Morphew, A. Hoenger, W. J. Lederer, and P. Kohl, "Axial stretch of rat single ventricular cardiomyocytes causes an acute and transient increase in Ca^{2+} spark rate," *Circ Res*, vol. 104, no. 6, pp. 787–795, Mar. 2009.

[562] B. L. Prosser, C. W. Ward, and W. J. Lederer, "X-ROS signalling is enhanced and graded by cyclic cardiomyocyte stretch," *Cardiovasc Res*, vol. 98, no. 2, pp. 307–, Apr. 2013.

[563] S. Yasuda, D. Townsend, D. E. Michele, E. G. Favre, S. M. Day, and J. M. Metzger, "Dystrophic heart failure blocked by membrane sealant poloxamer," *Nature*, vol. 436, no. 7053, pp. 1025–1029, Aug. 2005.

[564] D. Townsend, S. Yasuda, and J. Metzger, "Cardiomyopathy of Duchenne Muscular Dystrophy: pathogenesis and prospect of membrane sealants as a new therapeutic approach," *Expert Review of Cardiovascular Therapy*, vol. 5, no. 1, pp. 99–109, Jan. 2007.

[565] E. Y. Davani, D. R. Dorscheid, C.-H. Lee, C. van Breemen, and K. R. Walley, "Novel regulatory mechanism of cardiomyocyte contractility involving ICAM-1 and the cytoskeleton," *Am J Physiol Heart Circ Physiol*, vol. 287, no. 3, pp. H1013–H1022, Aug. 2004.

[566] J. Wang, J. M. Sanger, and J. W. Sanger, "Differential effects of Latrunculin-A on myofibrils in cultures of skeletal muscle cells: Insights into mechanisms of myofibrillogenesis," *Cell Motility and the Cytoskeleton*, vol. 62, no. 1, pp. 35–47, 2005.

[567] T. G. Kuznetsova, M. N. Starodubtseva, N. I. Yegorenkov, S. A. Chizhik, and R. I. Zhdanov, "Atomic force microscopy probing of cell elasticity," *Micron*, vol. 38, no. 8, pp. 824–833, Dec. 2007.

[568] V. O. Nikolaev, A. Moshkov, A. R. Lyon, M. Miragoli, P. Novak, H. Paur, M. J. Lohse, Y. E. Korchev, S. E. Harding, and J. Gorelik, "β_2-Adrenergic receptor redistribution in heart failure changes cAMP compartmentation," *Science*, vol. 327, no. 5973, pp. 1653–1657, Mar. 2010.

[569] P. T. Wright, V. O. Nikolaev, T. O'Hara, I. Diakonov, A. Bhargava, S. Tokar, S. Schobesberger, A. I. Shevchuk, M. B. Sikkel, R. Wilkinson, N. A. Trayanova, A. R. Lyon, S. E. Harding, and J. Gorelik, "Caveolin-3 regulates compartmentation of cardiomyocyte beta2-adrenergic receptor-mediated cAMP signaling," *Journal of Molecular and Cellular Cardiology*, vol. 67, pp. 38–48, Feb. 2014.

[570] M. Miragoli, J. Sanchez-Alonso, A. Bhargava, P. Wright, M. Sikkel, S. Schobesberger, I. Diakonov, P. Novak, A. Castaldi, P. Cattaneo, A. Lyon, M. Lab, and J. Gorelik, "Microtubule-dependent mitochondria alignment regulates calcium release in response to nanomechanical stimulus in heart myocytes," *Cell Reports*, vol. 14, no. 1, pp. 140–151, Jan. 2016.

[571] S. Kostin, D. Scholz, T. Shimada, Y. Maeno, H. Mollnau, S. Hein, and J. Schaper, "The internal and external protein scaffold of the T-Tubular system in cardiomyocytes," *Cell and Tissue Research*, vol. 294, no. 3, pp. 449–460, 1998.

[572] N. Q. Balaban, U. S. Schwarz, D. Riveline, P. Goichberg, G. Tzur, I. Sabanay, D. Mahalu, S. Safran, A. Bershadsky, L. Addadi, and B. Geiger, "Force and focal adhesion assembly: a close relationship studied using elastic micropatterned substrates," *Nat Cell Biol*, vol. 3, no. 5, pp. 466–472, May 2001.

[573] B. Hebert, S. Costantino, and P. W. Wiseman, "Spatiotemporal Image Correlation Spectroscopy (STICS) – theory, verification, and application to protein velocity mapping in living CHO cells," *Biophysical Journal*, vol. 88, no. 5, pp. 3601–3614, May 2005.

[574] P. Lamesch, N. Li, S. Milstein, C. Fan, T. Hao, G. Szabo, Z. Hu, K. Venkatesan, G. Bethel, P. Martin, J. Rogers, S. Lawlor, S. McLaren,

A. Dricot, H. Borick, M. E. Cusick, J. Vandenhaute, I. Dunham, D. E. Hill, and M. Vidal, "hORFeome v3.1: A resource of human open reading frames representing over 10,000 human genes," *Genomics*, vol. 89, no. 3, pp. 307 – 315, 2007.

[575] M. Rabe, H. R. Zope, and A. Kros, "Interplay between lipid interaction and homo-coiling of membrane-tethered coiled-coil peptides," *Langmuir*, vol. 31, no. 36, pp. 9953–9964, 2015.

[576] F. Bergström, I. Mikhalyov, P. Hägglöf, R. Wortmann, T. Ny, and L. B.-Å. Johansson, "Dimers of dipyrrometheneboron difluoride (BODIPY) with light spectroscopic applications in chemistry and biology," *J. Am. Chem. Soc.*, vol. 124, no. 2, pp. 196–204, Jan. 2002.

[577] D. L. Marks, R. D. Singh, A. Choudhury, C. L. Wheatley, and R. E. Pagano, "Use of fluorescent sphingolipid analogs to study lipid transport along the endocytic pathway," *Methods*, vol. 36, no. 2, pp. 186–195, Jun. 2005.

[578] D. Li, L. Shao, B.-C. Chen, X. Zhang, M. Zhang, B. Moses, D. E. Milkie, J. R. Beach, J. A. Hammer, M. Pasham, T. Kirchhausen, M. A. Baird, M. W. Davidson, P. Xu, and E. Betzig, "Extended-resolution structured illumination imaging of endocytic and cytoskeletal dynamics," *Science*, vol. 349, no. 6251, 2015.

Appendices

A. Lists of materials

A.1. Used chemicals

Chemical/Product	Company	Order number	Application
2, 3-Butanedione monoxime (BDM)	Sigma-Aldrich, Munich, Germany	B0753	VM sample prep.; section 2.3
Bovine Calf Serum (BCS)	HyClone via ThermoFisher Scientific, Dreieich, Germany	SH30073	VM sample prep.; section 2.3
Butanol	Merck Chemicals GmbH, Darmstadt, Germany	K40272688	Western blots; section 2.10.2
$CaCl_2$	Sigma-Aldrich, Munich, Germany	C2661	VM sample prep.; section 2.3
Collagenase type II	Worthington via Cell Systems, Troisdorf, Germany	on request	VM sample prep.; section 2.3
cOmplete (protease inhibitor cocktail)	Roche, Grenzach, Germany	11836170001	Western blots; section 2.10.2
Ethylene Glycol-Tetraacetic Acid (EGTA)	Sigma-Aldrich, Munich, Germany	E3889	Western blots; section 2.10.2
Glucose	Carl Roth, Karlsruhe, Germany	HN06.1	VM sample prep.; section 2.3
Glycine	Carl Roth, Karlsruhe, Germany	3908.3	Western blots; section 2.10.2
HEPES	Carl Roth, Karlsruhe, Germany	9105.4	VM sample prep.; section 2.3

Chemical/Product	Company	Order number	Application
KCl	Carl Roth, Karlsruhe, Germany	6781.3	VM sample prep.; section 2.3
KH_2PO_4	Carl Roth, Karlsruhe, Germany	3904.2	VM sample prep.; section 2.3
Laminin (2 mg/ml)	BD Biosciences, Heidelberg, Germany	354232	VM sample prep.; section 2.3
Methanol	Carl Roth, Karlsruhe, Germany	8388.6	Western blots; section 2.10.2
$MgCl_2 \cdot 6\,H_2O$	Carl Roth, Karlsruhe, Germany	2189.2	VM sample prep.; section 2.3
$MgSO_4 \cdot 7\,H_2O$	Carl Roth, Karlsruhe, Germany	8283.2	VM sample prep.; section 2.3
Milk powder	Carl Roth, Karlsruhe, Germany	T145.2	Western blots; section 2.10.2
$Na_2HPO_4 \cdot 2\,H_2O$	Carl Roth, Karlsruhe, Germany	4984.2	VM sample prep.; section 2.3
NaCl	Carl Roth, Karlsruhe, Germany	HN00.2	VM sample prep.; section 2.3
$NaHCO_3$	Carl Roth, Karlsruhe, Germany	HN01.1	VM sample prep.; section 2.3
Paraformaldehyde (PFA)	Sigma-Aldrich, Munich, Germany	158127	VM sample prep.; section 2.3
Phosphate Buffered Saline (PBS, pH 7.4, w/o Ca^{2+} and Mg^{2+}	Life Technologies via ThermoFisher Scientific, Dreieich, Germany	10010	VM sample prep.; section 2.3
PhosSTOP (phosphatase inhibitor cocktail)	Roche, Grenzach, Germany	4906837001	Western blots; section 2.10.2
Ponceau solution	Carl Roth, Karlsruhe, Germany	5938.2	Western blots; section 2.10.2
Sodium Dodecyl Sulfate (SDS)	Carl Roth, Karlsruhe, Germany	1057.1	Western blots; section 2.10.2
Taurin	Carl Roth, Karlsruhe, Germany	4721.2	VM sample prep.; section 2.3

Chemical/Product	Company	Order number	Application
Tetramethylethylene-diamine (TEMED)	Carl Roth, Karlsruhe, Germany	2367.3	Western blots; section 2.10.2
Tris	Carl Roth, Karlsruhe, Germany	4855.2	Western blots; section 2.10.2
Trisphosphine (TCEP)	Carl Roth, Karlsruhe, Germany	HN95.1	Western blots; section 2.10.2
Triton X-100	Sigma-Aldrich, Munich, Germany	T9284	VM sample prep.; section 2.3 and Western blots; section 2.10.2
Tween 20	Sigma-Aldrich, Munich, Germany	P1379	Western blots; section 2.10.2

Table A.1.: Overview of the chemicals used for the experiments within this PhD work; see also section 2.

A.2. Consumables

Product	Company	Order number	Application
BCA Protein Assay Kit	ThermoFisher Scientific, Dreieich, Germany	#23227	Western blots; section 2.10.2
Chemiluminescent substrate	Merck Chemicals GmbH, Darmstadt, Germany	WKBLSO100	Western blots; section 2.10.2
Protein-Marker V	Peqlab via VWR International GmbH, Darmstadt, Germany	27-2210	Western blots; section 2.10.2
PVDF Immobilon-FL transfer membrane	Merck Chemicals GmbH, Darmstadt, Germany	IPFL00010	Western blots; section 2.10.2

Table A.2.: Overview of the consumables used for the experiments within this PhD work; see also section 2.

A.3. Used antibodies

Primary antibodies

Table A.3 gives an overview over the primary antibodies used for the experiments in this thesis. The column "Name" denotes the abbreviation of the specific antibody as it is referred to in this thesis (mostly in the figure captions); the column typically reproduces the antibody order number. For staining protocols, see also sections 2.3.3 and 2.4.

Secondary antibodies

Table A.4 gives an overview over the secondary antibodies used for the experiments in this thesis. Note that most of the compounds of fluorescent dyes conjugated to secondary antibodies were performed in-house at the MPIBPC (thanks to Ellen Rothermel) and thus whole compounds were not purchased. Therefore, the table denotes the species specific secondary antibodies (unlabeled) that were purchased for conjugation. In combination with the Tables A.3 and A.5, the possible permutations for the fluorescence labels that were ultimately used for STED imaging can be derived. For staining protocols, see also sections 2.3.3 and 2.4.

Species reactivity	Host species	Clonality	Company	Order number
Mouse	Goat	polyclonal	Dianova GmbH, Hamburg, Germany	115-005-003
Mouse	Sheep	polyclonal	Dianova GmbH, Hamburg, Germany	515-005-003
Rabbit	Goat	polyclonal	Dianova GmbH, Hamburg, Germany	111-005-003
Rabbit	Sheep	polyclonal	Dianova GmbH, Hamburg, Germany	DAB-87967
Goat	Donkey	polyclonal	Dianova GmbH, Hamburg, Germany	705-005-147

Table A.4.: Overview of the secondary antibodies used for the experiments within this PhD work; for staining protocols, see also sections 2.3.3 and 2.4. Note that most of the compounds of fluorescent dyes conjugated to secondary antibodies were performed in-house at the MPIBPC (thanks to Ellen Rothermel) and thus whole compounds were not purchased. Therefore, the table denotes the species specific secondary antibodies (unlabeled) that were purchased for conjugation. In combination with the Tables A.3 and A.5, the possible permutations for the fluorescence labels that were ultimately used for STED imaging can be derived.

Protein	Name	Host species	Company	Order number	Application
α-Actinin	–	Mouse (monoclonal)	Sigma-Aldrich GmbH, Munich, Germany	A7811	ViPSC differentiation controls; Appendix D.1
Caveolin-1	–	Rabbit (polyclonal)	GeneTex, Inc., Irvine, CA, USA	GTX 100 205	Labeling of Cav-1 in HAd; see section 3.5
Caveolin-3	ab2912	Rabbit (polyclonal)	Abcam, Cambridge, UK	ab2912	Standard labeling of Cav-3; see e.g. section 3.5
Caveolin-3	BD#610421	Mouse (monoclonal)	BD Biosciences, Heidelberg, Germany	610421	Two-color STED labeling of Cav-3 in conjunction with Dyst; see section 3.8
Choleratoxin subunit B	CtB-AF594	–	Molecular Probes via ThermoFisher Scientific, Dreieich, Germany	C34777	GM1 labeling in VM; see section 3.6
Dystrophin (N)	4C7	Mouse (monoclonal)	Santa Cruz Biotechnology, Inc., Heidelberg, Germany	sc-33697	N-specific Dyst labeling; see section 3.8
Dystrophin (Rod)	ab85302	Rabbit (polyclonal)	Abcam, Cambridge, UK	ab85302	Rod-specific Dyst labeling; see section 3.8
Dystrophin (Rod)	ab7163 [MANDYS8]	Mouse (monoclonal)	Abcam, Cambridge, UK	ab7163	Rod-specific Dyst labeling, see section 3.8
Dystrophin (C)	C-20	Goat (polyclonal)	Santa Cruz Biotechnology, Inc., Heidelberg, Germany	sc7461	C-specific Dyst labeling; see section 3.8
Dystrophin (C)	ab15277	Rabbit (polyclonal)	Abcam, Cambridge, UK	ab15277	C-specific Dyst labeling; see section 3.8
Dystrophin (C)	ab7164 [MANDRA1]	Mouse (monoclonal)	Abcam, Cambridge, UK	ab7164	C-specific Dyst labeling; see section 3.8
Dystrophin (C)	7A10	Mouse (monoclonal)	Santa Cruz Biotechnology, Inc., Heidelberg, Germany	sc-47760	C-specific Dyst labeling; see section 3.8
α-Tubulin	Tubulin	Rabbit (polyclonal)	Abcam, Cambridge, UK	ab18251	Labeling of Tub in Vero cells; see e.g. section 3.4.2

Table A.3.: Overview of the primary antibodies used for the experiments within this PhD work; for staining protocols, see also sections 2.3.3 and 2.4. Abbreviations: C - Carboxy terminus (C-terminus); Cav-1 - Caveolin-1; Cav-3 - Caveolin-3; Dyst - Dystrophin; GM1 - Ganglioside GM1; HAd - Human adipocytes; N - Amino terminus (N-terminus); Rod - Rod domain (of the Dyst protein); VM - mouse ventricular cardiomyocytes.

A.4. Used fluorescent dyes and dye compounds

Dye (abbreviation)	Company	Order number	Application
Alexa Fluor 488 (AF488)	ThermoFisher Scientific, Dreieich, Germany	A20000	2P-Exc-STED; section 3.4
Alexa Fluor 532 (AF532)	ThermoFisher Scientific, Dreieich, Germany	A20001	2P-Exc-STED; section 3.4
ATTO 390	ATTO-TEC, Siegen, Germany	AD 390-31	2P-Exc-STED; section 3.4
ATTO 425	ATTO-TEC, Siegen, Germany	AD 425-31	2P-Exc-STED; section 3.4
ATTO 465	ATTO-TEC, Siegen, Germany	AD 465-31	2P-Exc-STED; section 3.4
ATTO 488	ATTO-TEC, Siegen, Germany	AD 488-31	2P-Exc-STED; section 3.4
ATTO 495	ATTO-TEC, Siegen, Germany	AD 495-31	2P-Exc-STED; section 3.4
ATTO 430LS	ATTO-TEC, Siegen, Germany	AD 430LS-31	2P-Exc-STED; section 3.4
ATTO 532	ATTO-TEC, Siegen, Germany	AD 532-31	2P-Exc-STED; section 3.4
Chromeo 488	Active Motif Inc., Carlsbad, CA, USA	15511	2P-Exc-STED; section 3.4
Cholesterol-BODIPY	Avanti Polar Lipids, Inc., Alabaster, AL, USA	810255	775 nm STED; e.g. section 3.3
Di-8-ANEPPS	Molecular Probes, Life Technologies, Darmstadt, Germany	D-3167	775 nm STED; e.g. section 2.1.3
DY 380XL	Dyomics GmbH, Jena, Germany	380XL-01	2P-Exc-STED; section 3.4
DY 505	Dyomics GmbH, Jena, Germany	505-01	2P-Exc-STED; section 3.4

Dye	Company	Order number	Application
DY 500XL	Dyomics GmbH, Jena, Germany	On request	2P-Exc-STED; section 3.4
DY 490XL	Dyomics GmbH, Jena, Germany	On request	2P-Exc-STED; section 3.4
NS510 [343]	Abberior GmbH, Goettingen, Germany (distributed as STAR520SXP)	1-0101-009-0	Two-color STED; section 3.7
Oregon Green 488 (OG 488)	ThermoFisher Scientific, Dreieich, Germany	O6149	2P-Exc-STED; section 3.4
STAR 440SXP	Abberior GmbH, Goettingen, Germany	1-0101-003-8	2P-Exc-STED; section 3.4
STAR 488	Abberior GmbH, Goettingen, Germany	1-0101-006-9	2P-Exc-STED; section 3.4
STAR 512	Abberior GmbH, Goettingen, Germany	1-0101-001-4	2P-Exc-STED; section 3.4
STAR 520SXP	Abberior GmbH, Goettingen, Germany	1-0101-009-0	775 nm STED; e.g. section 2.1.2
STAR 635P	Abberior GmbH, Goettingen, Germany	1-0101-007-6	775 nm STED; e.g. section 2.1.2
STAR RED (KK114)	Abberior GmbH, Goettingen, Germany	1-0101-011-3	775 nm STED; e.g. section 2.1.2

Table A.5.: Overview of the fluorescent dye compounds tested and used for the experiments within this PhD work; see also section 2.

B. Imaging specifications for the presented fluorescence micrographs

Table B.1 lists in detail the following image acquisition parameters for every fluorescence micrograph obtained and presented in the main text of this thesis:

1.) The microscope used for image acquisition (column "Microscope"): the custom-built Two-Photon-Excitation-CW-STED (2P-Exc-CWSTED) microscope (see section 2.1.1), the custom-built fast scanning STED (F-Scan STED) microscope (see section 2.1.2), the commercially available Leica TCS SP8 STED 3X (Leica STED) STED microscope (see section 2.1.3), or the commercially available Abberior 2C STED 775 QUAD Scan (Abberior STED) STED microscope (see section 2.1.4).

2.) The used excitation wavelength (in nm) including the reference to the corresponding used fluorescent dye or dye compound, and the set laser power (in µW or mW) in the backfocal plane of the objective, denoted as λ_{Exc} [nm] (dye), $\mathrm{P}_{\mathrm{Exc}}$. For the commercial STED systems (Leica STED and Abberior STED), the excitation power can only be stated in % of the total laser output power because this is the standard information about the set laser power given by the microscope control software. For information about the used dye compounds, please refer to Appendix A.4.

3.) The used STED wavelength (in nm) and the set laser power (in mW) in the backfocal plane of the objective, denoted as λ_{STED} [nm], $\mathrm{P}_{\mathrm{STED}}$. For the commercial STED systems (Leica STED and Abberior STED), the STED laser power can only be stated in % of the total laser output power because this is the standard information about the set laser power given by

the microscope control software. If the image was obtained in the confocal (Conf.) mode or in the Two-Photon-Excitation (2P-Exc) mode, i.e. if no STED laser was used, it is stated explicitly.

4.) The used fluorescence detection window (in nm), denoted as "Det. [nm]".

5.) The set pixel dwell time (in ms), denoted as "px DT [ms]".

6.) The set pixel size (in nm), denoted as "px size [nm]". For two-dimensional images, the pixel size is given in (X×Y) direction; for three-dimensional images, the pixel size is given in (X×Y×Z) direction, i.e. for simplicity, here, pixels can be both two- and three-dimensional containers, depending on the type of image for which they are defined.

Figure	1.)	2.)	3.)	4.)	5.)	6.)
Fig. 1.1 **B**	2P-Exc-CWSTED	760 (Chol-OG488), 10 mW	2P-Exc	(530 ± 20)	0.02	(40 × 40 × 200)
Fig. 3.3	Abberior STED	640 (Chol-KK114), 2 %	775, 80 %	(675 ± 25)	0.04	(20 × 20)
Fig. 3.4	Abberior STED	640 (Chol-KK114), 2 %	775, 80 %	(675 ± 25)	0.04	(20 × 20)
Fig. 3.5	Leica STED	640 (Chol-KK114), 1 %	775, 60 %	(670-740)	0.017	(20 × 20)
Fig. 3.6 **B**	F-Scan STED	638 (Chol-KK114), 5 µW	750, 300 mW	(675 ± 30)	0.02	(20 × 20)
Fig. 3.8	Leica STED	490/640 (Chol-BODIPY/Chol-KK114), 5 %/1 %	Conf.	(505-570)/(670-740)	0.017	(20 × 20)
Fig. 3.9	Leica STED	490/640 (Di-8-ANEPPS/Chol-KK114), 10 %/1 %	775, 80 %	(510-620)/(670-740)	0.017	(20 × 20)
Fig. 3.10	F-Scan STED	638 (Chol-KK114), 5 µW	750, 300 mW	(675 ± 30)	0.02	(20 × 20)
Fig. 3.11	F-Scan STED	638 (Chol-KK114), 5 µW	750, 300 mW	(675 ± 30)	0.02	(20 × 20)
Fig. 3.13 **A**	2P-Exc-CWSTED	757 (YG FluoBeads), 20 mW	2P-Exc	(525 ± 25)	0.02	(20 × 20)
Fig. 3.13 **B**	2P-Exc-CWSTED	757 (YG FluoBeads), 20 mW	592, 240 mW	(525 ± 25)	0.05	(20 × 20)

Figure	1.)	2.)	3.)	4.)	5.)	6.)
Fig. 3.15	2P-Exc-CWSTED	cf. Table 3.2	592, cf. Table 3.2	cf. Table 3.2	0.05	(20 × 20)
Fig. 3.16	2P-Exc-CWSTED	760 (Chol-OG488), 10 mW	2P-Exc	(530 ± 20)	0.02	(40 × 40 × 200)
Fig. 3.17	2P-Exc-CWSTED	760 (Chol-OG488), 10 mW	2P-Exc	(530 ± 20)	0.02	(40 × 40 × 200)
Fig. 3.18	2P-Exc-CWSTED	760 (Chol-OG488), 10 mW	592, 240 mW	(530 ± 20)	0.05	(20 × 20)
Fig. 3.19	2P-Exc-STED	760 (Chol-OG488), 10 mW	592, 240 mW	(530 ± 20)	0.05	(20 × 20 × 200)
Fig. 3.20	2P-Exc-STED	760 (Chol-OG488), 10 mW	592, 240 mW	(530 ± 20)	0.05	(20 × 20 × 200)
Fig. 3.21	2P-Exc-CWSTED	760 (Chol-OG488), 10 mW	592, 240 mW	(530 ± 20)	0.05	(20 × 20)
Fig. 3.22	F-Scan STED	638 (Chol-KK114, STAR635P), 5 µW	750, 300 mW	(675 ± 30)	0.02	(20 × 20)
Fig. 3.24	Leica STED	640 (Chol-KK114, STAR635P), 1 %, 0.8 %	775, 70 %, 100 %	(670-740)	0.017	(20 × 20)
Fig. 3.25	Abberior STED	640 (Chol-KK114, SiR), 5 %, 12 %	775, 70 %, 80 %	(675 ± 25)	0.04	(20 × 20)
Fig. 3.26	Abberior STED	561/640 (580CP-BG(SNAP)/Chol-KK114), 20 %/5 %	775, 60 %	(620 ± 10)/(675 ± 25)	0.04	(20 × 20)
Fig. 3.27	F-Scan STED	638 (STAR635P), 5 µW	750, 300 mW	(675 ± 30)	0.02	(20 × 20)
Fig. 3.29	Abberior STED	561/640 (CtB-AF594/Chol-KK114), 20 %/10 %	775, 50 %	(620 ± 10)/(675 ± 25)	0.05	(20 × 20)
Fig. 3.30	Abberior STED	561/640 (CtB-AF594/Chol-KK114), 20 %/5 %	775, 70 %	(620 ± 10)/(675 ± 25)	0.04	(20 × 20)
Fig. 3.32	F-Scan STED	638 (STAR635P), 5 µW	750, 300 mW	(675 ± 30)	0.02	(20 × 20)
Fig. 3.33	F-Scan STED	532/638 (NS510/STAR635P), 20 µW/5 µW	750, 300 mW	(620 ± 30)/(675 ± 30)	0.02	(20 × 20)
Fig. 3.34	F-Scan STED	532/638 (NS510/STAR635P), 20 µW/5 µW	750, 300 mW	(620 ± 30)/(675 ± 30)	0.02	(20 × 20)
Fig. 3.36 **A**	Leica STED	640 (STAR635P), 1 %	775, 80 %	(670-740)	0.017	(20 × 20)
Fig. 3.36 **B**	Leica STED	530 (NS510), 40 %	775, 40 %	(550-650)	0.017	(20 × 20)

Figure	1.)	2.)	3.)	4.)	5.)	6.)
Fig. 3.36 **C**	Leica STED	580 (STAR580), 5 %	775, 100 %	(600-650)	0.017	(20×20)
Fig. 3.37 **A**-**F**	Leica STED	580/640 (STAR580/STAR635P), 4 %/2 %	775, 100 %	(600-630)/(670-740)	0.017	(20×20)
Fig. 3.39 **A**-**F**	Leica STED	580/640 (STAR580/STAR635P), 5 %/5 %	775, 80 %	(600-630)/(670-740)	0.017	(20×20)
Fig. 3.41	Leica STED	640 (STAR635P), 5 %/5 %	775, 80 %	(600-630)/(670-740)	0.017	(20×20)

Table B.1.: Overview of all fluorescence micrographs that are presented in the main text of this thesis and detailed information about the corresponding image acquisition procedures. Please refer to the main text of this section (Appendix B) for the description and explanation of the given parameters and used abbreviations.

C. Plasmid construction for transfection of living culture cells

Fluorescence imaging of living cultured cells overexpressing human Caveolin-3 was achieved by transfecting cells with the expression plasmid pSEMS-CAV3-SNAP. This expression plasmid was constructed by Gateway vector conversion from the donor vector pDONR223-Cav3 ([574]) and the empty destination vector pSEMS-GATEWAY-SNAP26m (Covalys Biosciences, Witterswil, Switzerland) [415, 416]. Cell transfection of living cultured cells with this plasmid, fluorescent tagging, and imaging was performed as described in section 2.4.1.

D. Control experiments

D.1. Differentiation of ventricular induced pluripotent stem cells

To validate that the ventricular induced pluripotent stem cells (ViPSC) stained with the novel cell-specific membrane marker Cholesterol-PEG-KK114 (Chol-KK114, see section 3.1) were fully and properly differentiated, a portion of the cells was stained for α-Actinin via indirect immunofluorescence as described in section 2.4.2. I chose the indirect immunofluorescence stain of α-Actinin in fixed ViPSC to motivate the successful differentiation protocol and the structural similarities between ventricular mouse cardiomyocytes (VM). α-Actinin, an Actin-binding protein involved in the formation of Z-lines, is widely used in the literature as a cardiomyocyte marker protein to validate the proper physiological state of cardiomyocytes [487] and the proper differentiation of other cells types induced to be cardiomyocytes [488, 482]. Surely, some of the ViPSC in a cell culture have features which distinguish them from fully differentiated, mature VM: they are of a smaller size, they do not show the characteristic rod-like shape of mature VM, they lack transverse tubules and have other structural and functional differences from VM as summarized for example in [480, 485]. Yet, the stain against α-Actinin presented in Figure D.1 for both ViPSC and VM show that the striated pattern of the cells is well-developed and widespread over almost all ViPSC in the sample which hints towards a global cytoskeletal scaffolding comparable to mature VM. Additionally to this control for appropriately developed striations in ViPSC, we paid special attention to select only those ViPSC for image analysis of the nanopatterns of Cholesterol domains at the basement membrane, as presented in section 3.2, that were of the approximate same cell size as VM and that had the same rod-shaped appearance. For example, the ViPSC marked with the yellow box in Figure D.1 **A** would be

a candidate for display and analysis of a Chol-KK114 surface signal. Images were obtained in confocal mode using the Leica TCS SP8 STED 3X (see section 2.1.3). Samples were excited at 635 nm at 2 % laser power and their fluorescence signal recorded within a detection window of $(650 - 750)$ nm.

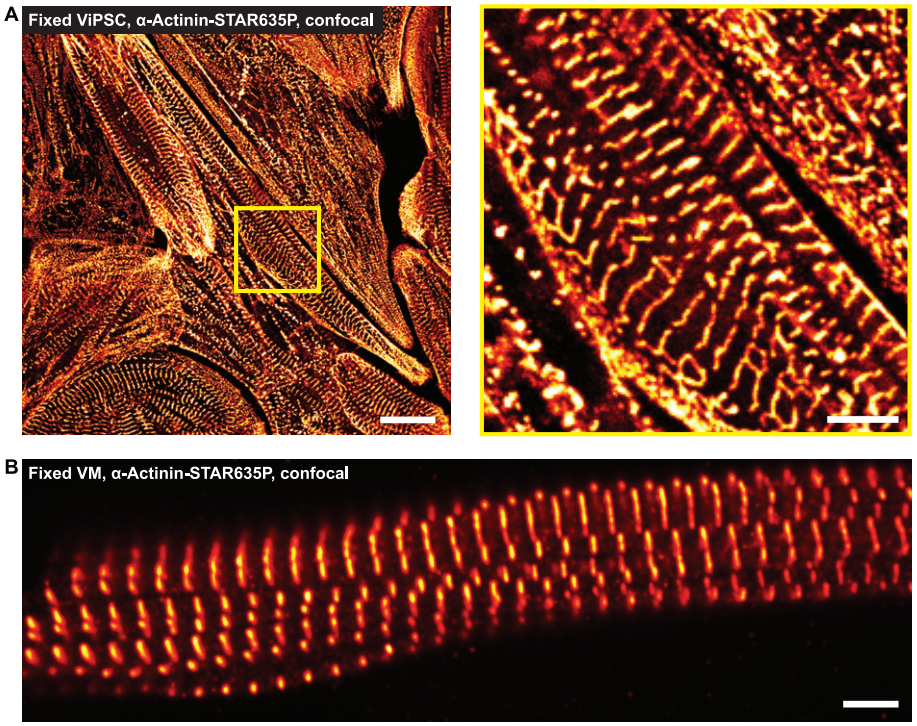

Figure D.1.: Verification of the full and proper differentiation of ventricular induced pluripotent stem cells (ViPSC). Confocal immunofluorescence images of fixed ViPSC and fixed ventricular mouse cardiomyocytes (VM) stained for α-Actinin. **A** Confocal immunofluorescence images of ViPSC stained for α-Actinin. Cell line: iWT.D2.1o; differentiation for 120 days. Primary antibody: monoclonal mouse anti-α-Actinin (A7811, Sigma-Aldrich GmbH, Munich, Germany); secondary antibody: goat anti-mouse-STAR635P (2-0002-00705, Abberior GmbH, Goettingen, Germany). Left panel: overview scan (field of view: (150×150) μm^2) demonstrating the extent of cell differentiation using the striated α-Actinin signal as a control; scale bar: 20 µm. Right panel: zoom-in to the yellow boxed region of interest in the overview scan; field of view: (30×30) μm^2; scale bar: 5 µm. **B** Confocal image of one VM stained for α-Actinin; field of view: (80×23) μm^2; primary and secondary antibodies as in **A**; scale bar: 5 µm.

D.2. Differentiation of human adipocytes

To validate that the human adipocytes stained with the novel cell-specific membrane marker Chol-KK114 (see sections 3.2 and 3.5) were fully and properly differentiated, a portion of the cells was stained with the lipid marker Oil Red O (ORO) as described in section 2.4.3. Figure D.2 displays the ORO signal in undifferentiated human preadipocytes (HPAd, derived from adult heart adipose tissue) versus the ORO signal in differentiated human adipocytes (HAd).

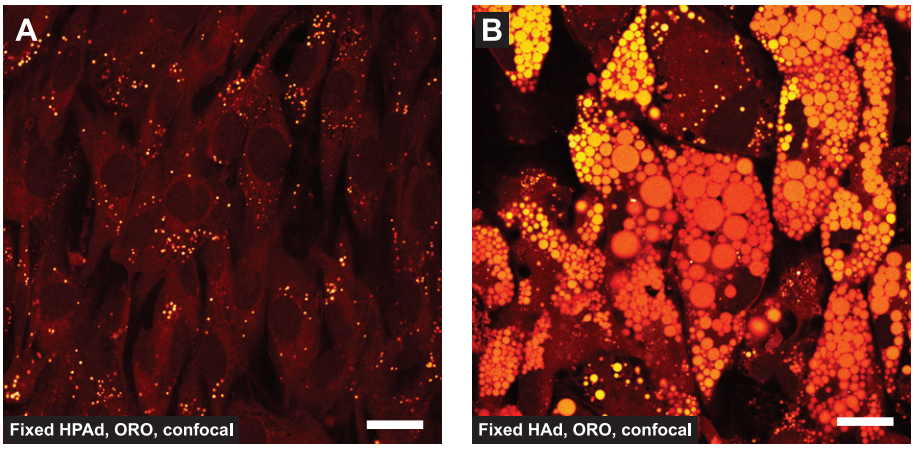

Figure D.2.: Verification of the full and proper differentiation of human adipocytes. Human preadipocytes (HPAd, i.e. undifferentiated) and fully differentiated human adipocytes (HAd, see section 2.4.3) were stained with the lipid marker Oil Red O (ORO) as described in section 2.4.3 to detect lipid droplets. Scale bars: 20 µm. **A** Confocal image of fixed human preadipocytes (HPAd) from adult heart adipose tissue, stained with ORO. Accumulations of ORO signal are visible but lipid droplets cannot be identified. **B** Confocal image of fixed human adipocytes (HAd) stained with ORO after differentiation following the protocol described in section 2.4.3. Clearly visible lipid droplets validate the full differentiation of HPAd to HAd.

Images were obtained in confocal mode using the Leica TCS SP8 STED 3X (see section 2.1.3). Samples were excited at 560 nm at 11 % laser power and their fluorescence signal recorded within a detection window of $(605 - 720)$ nm. There was also an attempt to record the ORO signal in STED imaging mode, yet it did not yield feasible results (data not shown).

E. Comparison of fluorescent lipids for membrane labeling

Several fluorescent lipids were screened and tested in search of membrane labeling techniques of living mouse ventricular cardiomyocytes (VM) for high-quality STED imaging. As presented in the main text (cf. section 3.3), Cholesterol-PEG-KK114 (Chol-KK114) proved to be a superior live-cell membrane label. Here, an overview of additionally tested fluorescent lipids is presented. VM were labeled with the respective lipids in a protocol similar to the one described for Chol-KK114 (see section 2.3.2). Fig. E.1 displays the resulting confocal (Conf.) and STED images of stained VM.

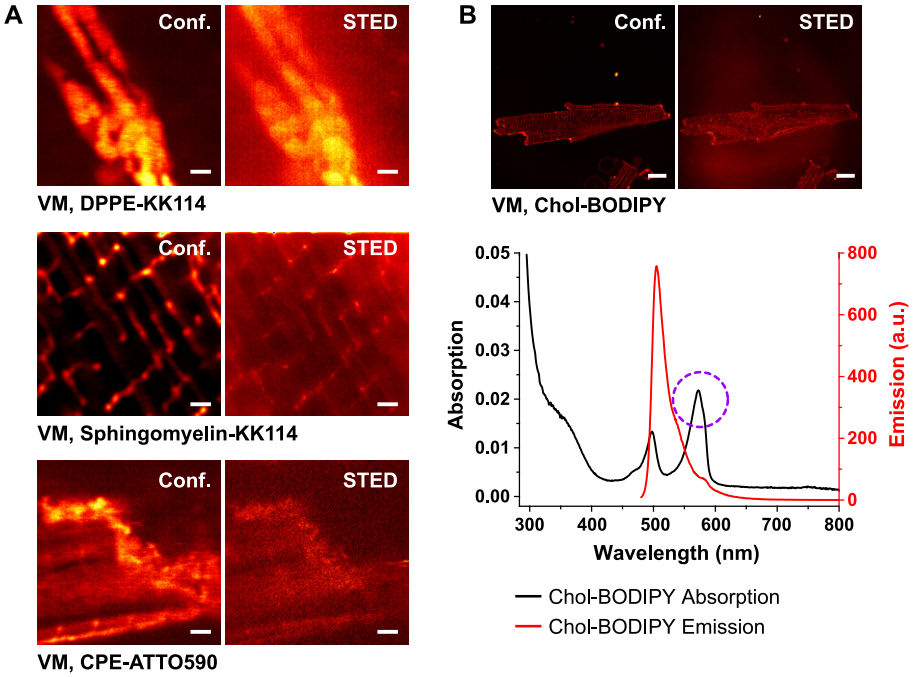

Figure E.1.: Additionally investigated fluorescent lipids for membrane labeling in living mouse ventricular cardiomyocytes (VM). **A** Top row: Confocal (Conf.) and STED images of a living VM labeled with DPPE-KK114. Middle row: Conf. and STED images of a living VM labeled with Sphingomyelin-KK114. Bottom row: Conf. and STED images of a living VM labeled with CPE-ATTO590. Scale bars: 1 µm. **B** Top: Conf. and STED images of a living VM labeled with Cholesterol-BODIPY (Chol-BODIPY); scale bars: 10 µm. Bottom: Absorption (black line) and emission (red line) spectra of the fluorescent lipid Chol-BODIPY.

Fig. E.1 **A** shows VM labeled with 1,2-Dipalmitoyl-sn-glycero-3-phosphoethanolamine linked to the dye KK114 (DPPE-KK114, top row), with Sphingomyelin linked to the dye KK114 (middle row), and with lipopeptide CPE [575] linked to the dye ATTO590 (CPE-ATTO590, bottom row), respectively. All three fluorescent lipid compounds were prepared at the Max Planck Institute for Biophysical Chemistry (the dye ATTO590 was obtained as carboxylic acid from Atto-tec GmbH, Siegen, Germany) and were used in a STED imaging scheme employing a STED laser wavelength of 750 nm (KK114 and ATTO590 were excited at 635 nm and 532 nm, respectively. DPPE-KK114 shows a very high degree of cellular internalization which makes the identification of a membrane-specific signal impossible for both the confocal as well as the STED image. Sphingomyelin-KK114 shows a low degree of cellular internalization and a membrane-specific signal (i.e. T-Tubule structures) are visible. However, the fluorescence images show a nonspecific background signal which is especially pronounced in the STED image, rendering it unsuitable for nanoscopic studies of cardiac membrane patterns. CPE-ATTO590 shows insufficient membrane penetration, cannot access intracellular membrane structures and seems to be exclusively confined to the sarcolemma.
Fig. E.1 **B** shows a VM labeled with Cholesterol linked to the dye BODIPY (Chol-BODIPY, top row). Chol-BODIPY was purchased from Avanti Polar Lipids, Inc., Alabaster, AL, USA (order number: 810255) and used in STED imaging scheme with excitation at 490 nm and a CW-STED laser at 592 nm. Although the dye compound seems suitable for confocal imaging, the STED images show an unfortunate artefact due to the STED laser illumination which manifests itself as "ripple" around the labeled structures. A more in-depth investigation of the absorption and emission spectrum of Chol-BODIPY (see Fig. E.1 **B**, bottom row) revealed a profound absorption peak at $\approx$ 580 nm, i.e. very close to the STED laser wavelength (marked with a dotted purple circle). Although the reasons for this additional, red-shifted absorption peak of Chol-BODIPY is not clear, there have been studies reporting the concentration dependent appearance of an additional red-shifted emission peak of BODIPY both in its free form [576], and when coupled to membrane lipids [577]. This additonal, redder emission peak has been attributed to the formation of BODIPY dimers. A red-shifted absorption peak of BODIPY has not yet been re-

ported, yet dimerization of the compound might play a role in this observed effect. All in all, labeling VM with Chol-BODIPY is not compatible with CW-STED imaging at 592 nm. Using a pulsed STED laser 775 nm, however, did not switch off the dye molecules efficiently enough for a visible increase in image resolution.

F. Visualization of surface density determination

Here, in Fig. F.1, the procedure of image thresholding and binarization that is described in section 2.6.4 to determine the density of different fluorescence signal structures at the basement membrane and/or in filopodia of various cell types (discussed in sections 3.2, 3.3, and 3.5) is illustrated. The obtained surface signal density is generally denoted as ρ and given in % of the total area of a specific region of interest (ROI) extracted from a recorded image. Fig. F.1 **A** exemplarily shows a raw data STED image of the sarcolemmal Cholesterol-PEG-KK114 (Chol-KK114) signal in a living mouse ventricular cardiomyocyte (VM) and the binarized image extracted from it after the pixel based thresholding procedure described in section 2.6.4. Fig. F.1 **B** illustrates the image processing steps to arrive at the necessary for the determination of the surface signal density in filopodia (ρ_{Filo}, here, for the Chol-KK114 signal). These steps include: 1.) the manual identification and selection of filopodial structures (Fig. F.1, **B**, top row), 2.) the determination of the area of the Chol-KK114 signal within the filopodial structure (Fig. F.1, **B**, middle row), and 3.) the determination of the total area of the respetive filopodial structure (Fig. F.1, **B**, bottom row). ρ_{Filo} is then calculated as the ratio of the Chol-KK114 signal within the filopodial structure divided by the total area of that filopodial structure. Fig. F.1 **C** and **D** demonstrate the profound increase in accuracy regarding the determination of ρdue to the much higher object resolution that is achievable with subdiffraction STED microscopy opposed to diffraction limited confocal microscopy. Fig. F.1 **C** displays the raw data confocal (conf., top row) and STED (bottom row) image of a fixed VM labeled for Caveolin-3 (Cav-3) via indirect immunofluorescence, respectively, and their corresponding binarized image analogs. From many such (conf. and STED) binarized images, ρ was determined and its derived arithmetic mean $\pm$ standard deviation displayed in the bar graphs in

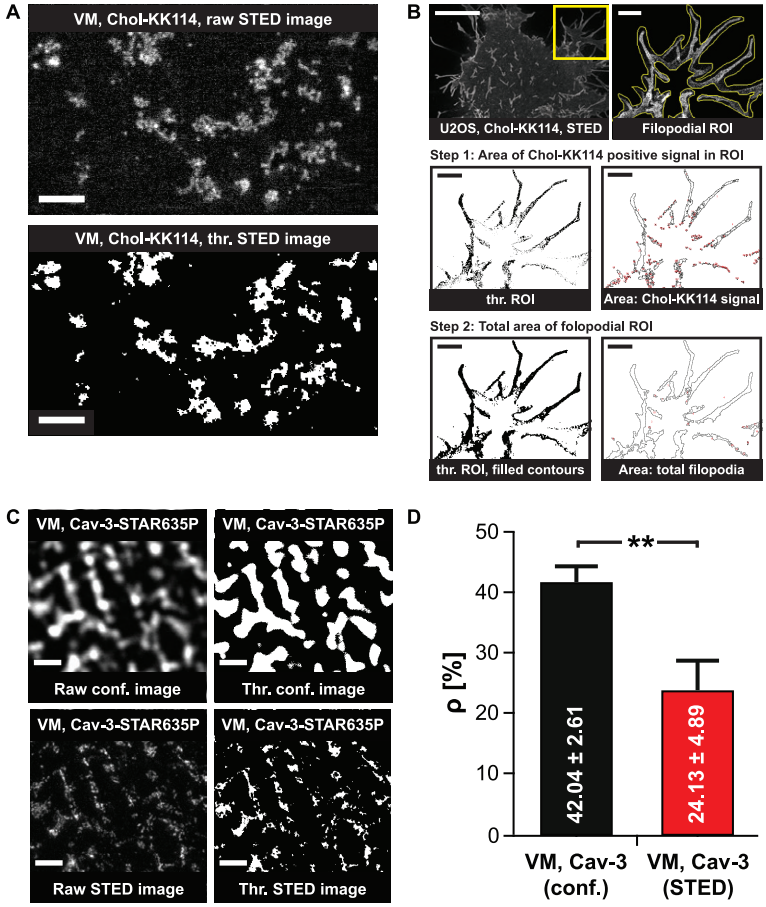

Figure F.1.: Schematic of the image thresholding procedure applied for the determination of the surface signal density ρ (see section 2.6.4) both at the basement membrane and in filopodia of selected cell types, and comparison between the values of ρ extracted from confocal images and their analogous STED images. **A** Exemplary STED image of the sarcolemma of a living primary mouse ventricular cardiomyocyte (VM) stained with the membrane label Cholesterol-PEG-KK114 (Chol-KK114). The upper panel shows the raw image; the lower panel shows the corresponding image after performing the thresholding (thr.) procedure described in section 2.6.4. Scale bars: 1 µm. **B** Exemplary STED images of filopodial structures in U2OS cells stained with Chol-KK114 and schematic illustration of the procedure for the determination of ρ in filopodia. Top row: raw STED overview image of the Chol-KK114 signal in U2OS cells and magnified view of a selected filopodial region of interest (ROI) marked by the yellow box. The filopodial structures in the ROI are manually cropped along the marked yellow line in the inset as described in section 2.6.4 Middle row: schematic illustration of the determination of the area of Chol-KK114 signal (in black in the thresholded image). Bottom row: schematic illustration of the determination of the total area of filopodia within the selected ROI. Scale bar in U2OS-Chol-KK114 overview STED image: 10 µm; scale bars in all ROI images: 2 µm. **C** Exemplary images of a fixed VM stained for Caveolin-3 (Cav-3) via indirect immunofluorescence (see section 2.3.3). The two panels on the left show the confocal and the corresponding STED image of a region of interest extracted for the determination of ρ. The two panels on the right show the confocal and STED image after signal thresholding. All scale bars: 1 µm. **D** Bar graph representation of the Cav-3 surface signal density ρ in VM determined from confocal images (in black) vs. STED images (in red). The density ρ is given in % of the total sarcolemmal cell area and is presented as mean ± standard deviation. Statistical significance of the variation of ρ was determined by a two-sided Mann-Whitney-Wilcoxon U test (MWW, see section 2.9) and is displayed as: (**) - very significant ($p \leq 0.001$). Number of analyzed cells in confocal imaging mode: 10; number of analyzed cells in STED mode: 44 (MWW U statistic: $U_{confocal} = 0$; $U_{STED} = 710$; p-value: 3.59 ± 10^{-7}).

Fig. F.1 **D**. As can be seen from the results shown in Fig. F.1 **D**, while the confocal images suggest that about 42 % of the sarcolemma of a living VM is covered with Chol rich clusters, the STED images reveal that a mere 24 % of the

sarcolemma is covered with Chol rich clusters - i.e. only about half of the Chol-KK114 surface signal density that would be extracted from confocal images. This demonstrates that only about one quarter of the sarcolemmal of a living VM features regions with a high Chol content, meaning that the sarcolemma is probably more heterogeneous regarding its specific lipid content and probably less curved than it would be expected from purely confocal studies of the distribution of Chol rich cardiac membrane regions.

G. Custom-built 2P-Exc-CWSTED microscope and suitable fluorescent labels

Please refer to sections 3.4.1 and 3.4.2 for a detailed description and characterization of the custom-built Two-Photon-Excitation-CW-STED (2P-Exc-CW-STED) microscope, its performance and capabilities as well as the results and the discussion of the identification and investigation of fluorescent labels suitable for 2P-Exc-CWSTED, specifically for the generation of fluorescent Cholesterol analogs to label membrane structures in living mouse ventricular myocytes.

G.1. Gated vs. un-gated Two-Photon-Excitation-CW-STED microscopy

The importance of fluorescence signal time gating in two-photon-excitation-CW-STED (2P-Exc-CWSTED) microscopy is demonstrated in Figure G.1 based on recording yellow-green fluorescent beads (40 nm diameter) in the following three configurations: ungated two-photon-excitation (2P-Exc), ungated 2P-Exc-CWSTED, and gated 2P-Exc-CWSTED. Images were obtained using the custom-built 2P-Exc-CWSTED microscope described in section 2.1.1 with the 2P-Exc wavelength set to 760 nm and fluorescence detection within a range of (530 $\pm$ 20 nm). For the gated detection of the fluorescence 2P-Exc-CWSTED signal, the gate delay was set to 3.74 ns, the gate width was set to 9.88 ns with respect to the incoming 2P-Exc laser pulses. The image resolution of individual beads was determined by curve fitting of summed signal intensity profiles with Gaussian curve fitting for the 2P-Exc case and Lorentzian curve fitting for

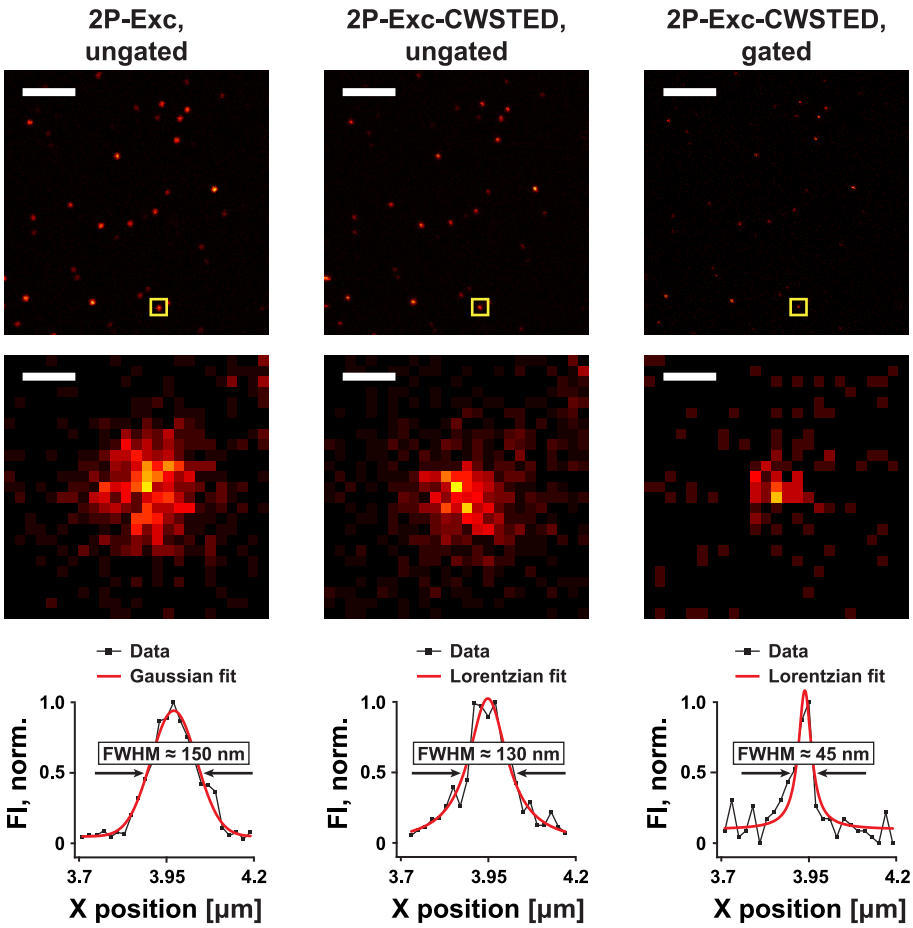

Figure G.1.: Comparison of image resolution for the following three imaging modes: ungated 2P-Exc (left column); ungated 2P-Exc-CWSTED (middle column); gated 2P-Exc-CWSTED (right column). Images show overview scans of the same field of view (top row, scale bars: 2 µm) and exemplary magnifications to individual fluorescent beads (middle row, scale bars: 100 nm). The graphs of normalized fluorescence intensity (FI, norm.) profiles below the corresponding image were obtained from the summation of pixel intensity counts within the yellow boxes indicated in the overview images; profiles were summed over 25 pixels, corresponding to 500 nm, in the x direction. Image resolutions were determined as the full width at half maximum from either Gaussian (in the 2P-Exc case) or Lorentzian (in the 2P-Exc-CWSTED case) curve fitting (see section 2.6.2) and are explicitly stated in the graphs.

the 2P-Exc-CWSTED case (see section 2.6.2). The image resolution was then determined as the FWHM of the fitted PSFs. Comparing the resulting FWHM of the ungated 2P-Exc-CWSTED PSF (FWHM $\approx$ 130 nm) with that of the 2P-Exc PSF (FWHM $\approx$ 150 nm) brings about only a small increase in image resolution while by fluorescence time gating the 2P-Exc-CWSTED PSF can be reduced by a factor of three (FWHM $\approx$ 45 nm).

G.2. 2P-Exc-STED at a 1 GHz 2P-Exc repetition rate

To evaluate the achievable image resolution employing a two-photon-excitation (2P-Exc) laser with a repetition rate of 1 GHz (GigaJet TWIN 20c/20c, Laser Quantum, Konstanz, Germany) for (two-photon-Excitation-CW-STED) 2P-Exc-CWSTED applications, I recorded images of fixed Vero cells immunofluorescently labeled for the cytoskeletal protein Tubulin with the dye compound DY 380XL (see Appendix A.4) in both 2P-Exc as well as 2P-Exc-STED mode. It has to be kept in mind, that due to the lack of appropriate electronics, it was not possible to set up a time gate for the fluorescence signal detected by the APD with respect to the incoming 2P-Exc laser pulses (i.e. laser pulses of about 300 fs pulse width at a frequency of 1 pulse per nanosecond). Figure G.2 **A** compares the 2P-Exc image and the 2P-Exc-STED image obtained at a 2P-Exc repetition rate of 1 GHz. The obtained intensity profile in 2P-Exc mode was fitted to a Gaussian function; the intensity profile in 2P-Exc-STED mode was fitted to a Lorentzian function (see section 2.6.2). The image resolution was determined as the full width at half maximum (FWHM) of the respective fit curve. Using the GigaJet Twin 20c/20c laser for 2P-Exc with a repetition rate of 1 GHz - and thus no fluorescence signal time gating - yielded the following results for the image resolution: 2P-Exc image - 190 nm; 2P-Exc-STED image - 140 nm (Fig. G.2 **A**). On the other hand, for comparison, Fig. G.2 **B** shows an analogous spot in a different cell, yet in the same sample, employing a 2P-Exc laser with a repetition rate of 80 MHz (Mai Tai, Newport Spectra-Physics, Darmstadt, Germany), see also Appendix G.1. The panels in Fig. G.2 **B** show, from left to right, the 2P-Exc image, the ungated 2P-Exc-STED image, and the gated 2P-Exc-STED image with a time gate delay of 0.86 ns and a time gate width of 9.92 ns. Below each respective panel, the obtained image resolution from curve fitting analogously to Fig. G.2 **A** is displayed and amounts to: 2P-Exc image - 190 nm; ungated 2P-Exc-STED image - 100 nm; gated 2P-Exc-STED image - 45 nm. This demonstrates the non-applicability of a 2P-Exc laser operating at a repetition rate of 1 GHz which is most likely entirely due to the unrealizable time gating of the detected fluorescence signal.

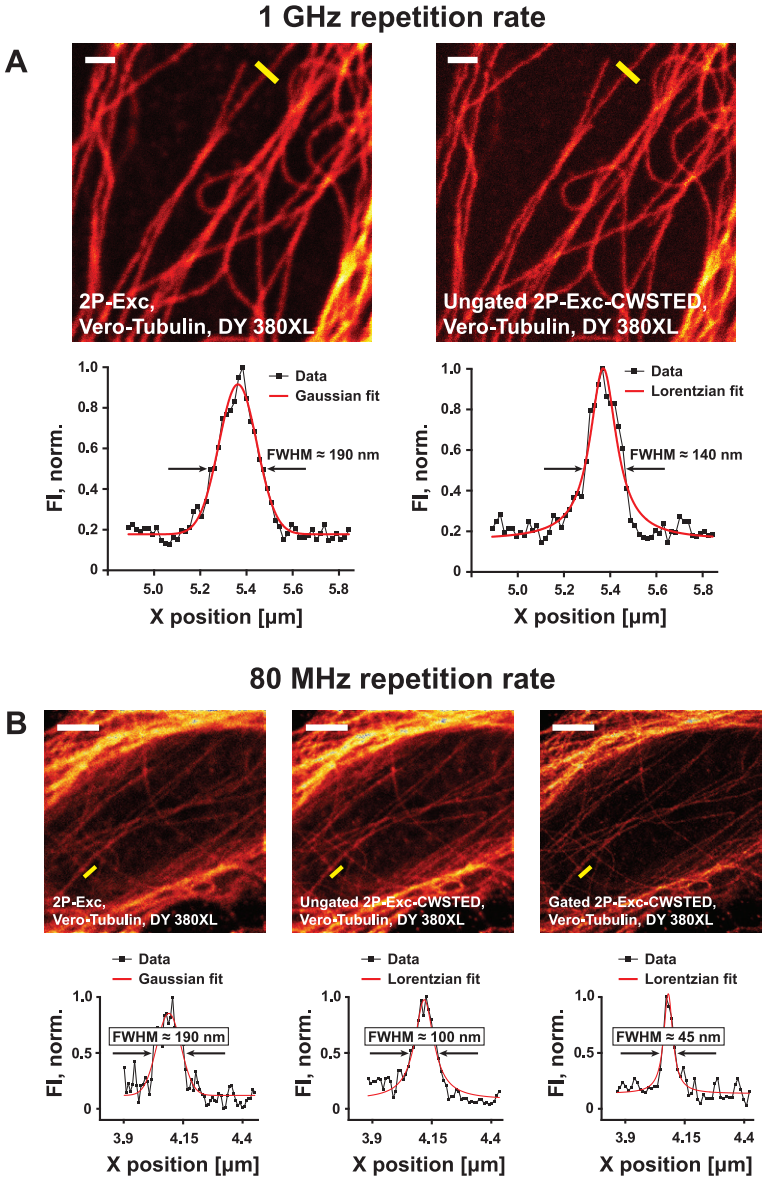

Figure G.2.: Comparison of image resolution for the following 5 imaging modes: 2P-Exc at a laser repetition rate of 1 GHz (**A**, left panel); ungated 2P-Exc-CWSTED at a laser repetition rate of 1 GHz (**A**, right panel); 2P-Exc at a laser repetition rate of 80 MHz (**B**, left panel); ungated 2P-Exc-CWSTED at a laser repetition rate of 80 MHz (**B**, middle panel); gated 2P-Exc-CWSTED at laser repetition rate of 80 MHz and with a time gate delay of 0.86 ns and a time gate width of 9.92 ns (**B**, right panel). The graphs of normalized intensity profiles below the corresponding images were obtained from line profiles along the indicated yellow lines in the image; line profiles were averaged over 5 pixels, corresponding to 100 nm. Image resolutions were determined as the full width at half maximum from either Gaussian (in the 2P-Exc case) or Lorentzian (in the 2P-Exc-CWSTED case) curve fitting (see section 2.6.2) and are explicitly stated in the graphs. Scale bars (in white): 1 µm.

G.3. Characterization of 2P-Exc-STED bleaching curves

The bleaching curves of different antibody-conjugated dye compounds, shown in section 3.4.2, were fit with mono-, bi-, and triexponential decay functions, respectively in order to assess which model would best describe the photobleaching behavior. Curve fitting based on the Levenberg-Marquardt algorithm was performed in Origin using the standardly built-in exponential decay functions. Here, the resulting curve fits and the corresponding regular residuals are exemplarily shown for the dye DY 380XL in Fig. G.3. The investigation of different fit functions was analogously performed for the dyes ATTO 488, AF 488, and STAR 488 and yielded the same qualitative results. While the use of a bi-exponential decay function (Fig. G.3 **B**) is clearly more adequate to model the bleaching behavior than a mono-exponential decay function (Fig. G.3 **A**), the introduction of a third exponential term for curve fitting (Fig. G.3 **C**) does not notably increase the goodness of fit and would only add unnecessary complexity. Conclusively, the bleaching behavior of dyes under 2P-Exc-STED conditions is most comprehensively described by a bi-exponential decay.

G.4. ATTO 390 and ATTO 425 for 2P-Exc-CWSTED

Figure G.4 demonstrates the unsuitability of the antibody-coupled dye compounds ATTO 390 and ATTO 425 for 2P-Exc-CWSTED applications based on labeling Tubulin structures in fixed Vero cells via indirect immunofluorescence. Although the two dyes seemed promising regarding their spectral properties and their photostability (see section 3.4.2), they did not yield convincing images. ATTO 390 (Fig. G.4 **A**) showed a relatively high background signal and rather blurred structures in 2P-Exc mode. No profound increase in image resolution in 2P-Exc-CWSTED mode was observable. ATTO 425 (Fig. G.4 **B**) showed highly unspecific structure labeling and both 2P-Exc images and 2P-Exc-CWSTED images had a low signal-to-noise ratio and were badly resolved.

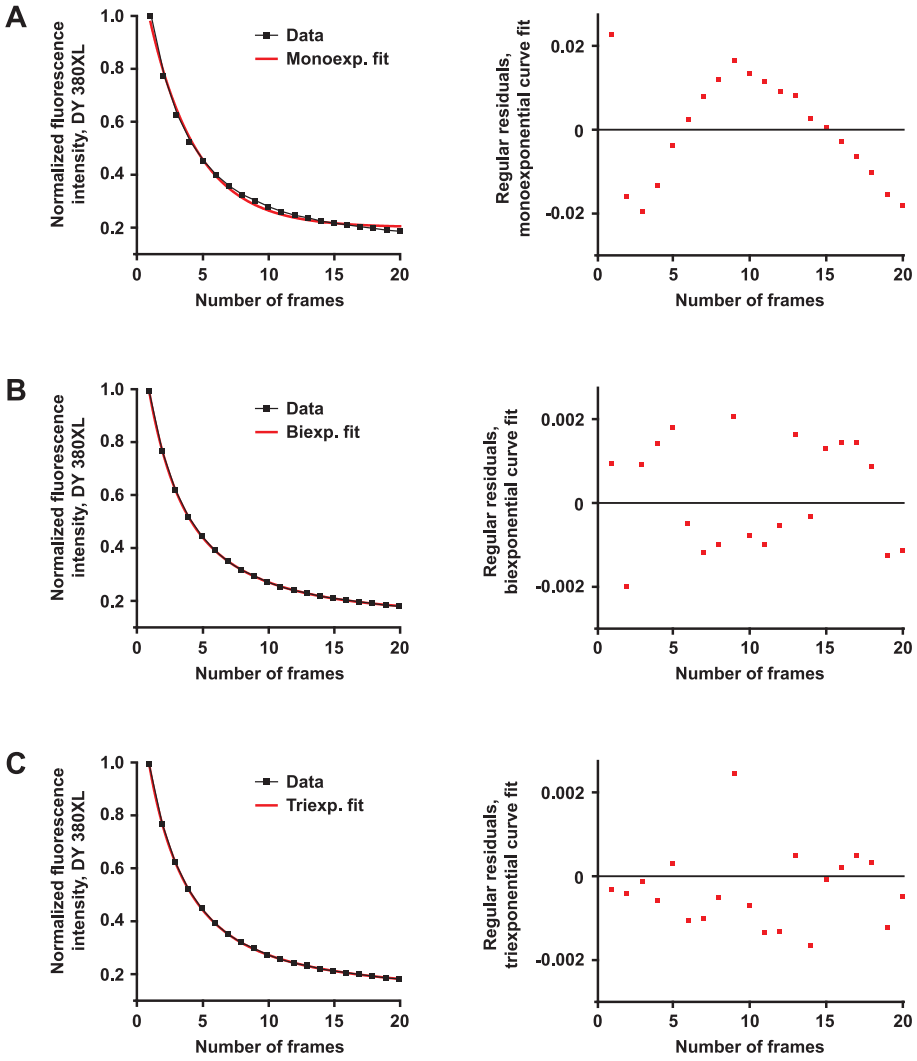

Figure G.3.: Comparison mono-, bi- and triexponential curve fits to model the bleaching behavior of the exemplary antibody-conjugated dye DY 380XL. Bleaching curves were obtained from successively scanning 20 image frames of immunofluorescence labeled Vero cells under two-photon-excitation-STED conditions, see section 3.4.2. **A** Mono-exponential curve fit (left, red line) and corresponding residuals (right). **B** Bi-exponential curve fit (left, red line) and corresponding residuals (right). **C** Triexponential curve fit (left, red line) and corresponding residuals (right). The smaller the residuals, the higher the goodness of the respective curve fit.

G.5. Performance of the alternative fluorescent Cholesterol analogs Chol-DY380XL, Chol-AF488, and Chol-STAR488

The dyes DY 380XL, AF 488, STAR 488, and OG 488 all showed high potential for membrane labeling of living cardiomyocytes for 2P-Exc-CWSTED - at least based on their spectroscopic properties, bleaching behavior and performance

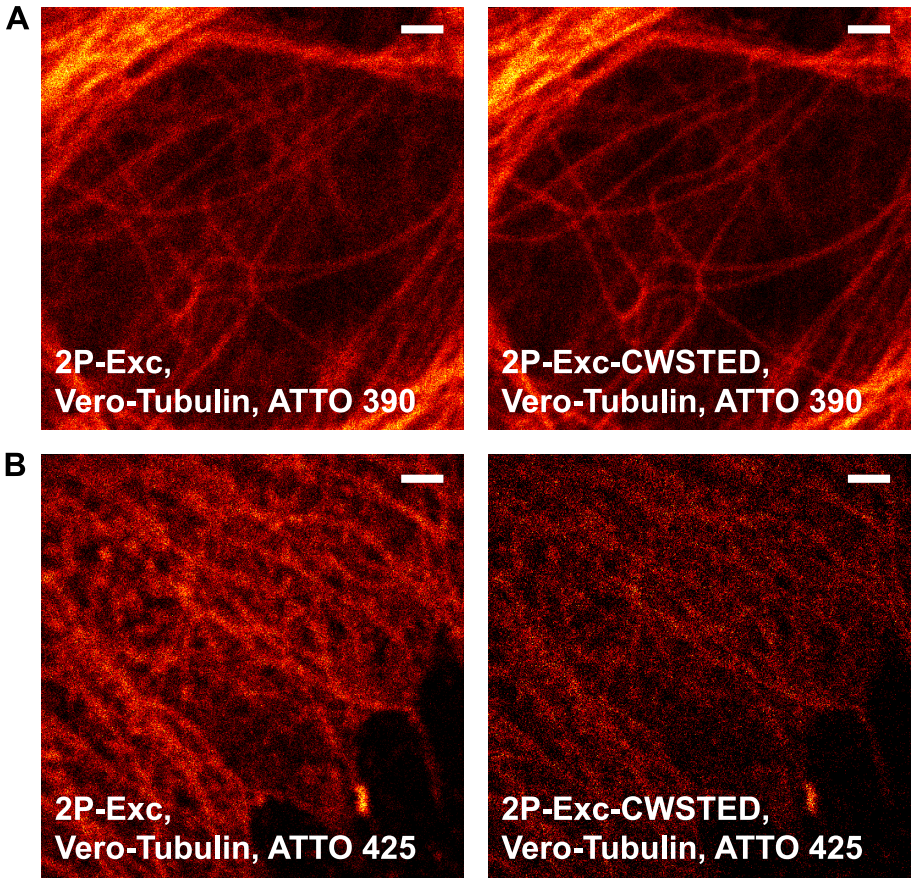

Figure G.4.: Fixed Vero cells stained for the cytoskeletal protein Tubulin via indirect immunofluorescence with the dye compounds ATTO 390 and ATTO 425. Comparison of images obtained in two-photon-excitation (2P-Exc) mode and two-photon-excitation-CW-STED (2P-Exc-CWSTED) mode to demonstrate the unsuitability of the respective dye compounds for 2P-Exc-CWSTED applications. All images show raw data; images were obtained at the apical cell membrane imaging through the cell nucleus. Scale bars: 1 µm. **A** 2P-Exc image (left panel) and 2P-Exc-CWSTED image (right panel) of Tubulin decorated with ATTO 390. There is no noticeable gain in image resolution in the 2P-Exc-CWSTED image. **B** 2P-Exc image (left panel) and 2P-Exc-CWSTED image (right panel) of Tubulin decorated with ATTO 425. The 2P-Exc image is diffuse and labeling seems to be unspecific. The 2P-Exc-CWSTED image brings about no gain in neither information nor image resolution.

when imaging fixed cell samples (see section 3.4.2). However, after having coupled these dyes to Cholesterol-PEG derivatives, I could identify the resulting Chol-OG488 as the most suitable membrane label based on image quality and cell compatibility. Here, Figure G.5 gives an exemplary overview of the images membrane structures in living mouse ventricular cardiomyocytes (VM) I obtained with 2P-Exc-CWSTED microscopy when using Chol-DY380XL, Chol-AF488, and Chol-STAR488, respectively. These images illustrate why I chose Chol-OG488 for further investigations (see section 3.4.3). Labeling VM with Chol-DY380XL (Fig. G.5, upper row) resulted in a diffuse, unspecific signal which is probably due to a fast cellular internalization of the label, and/or due

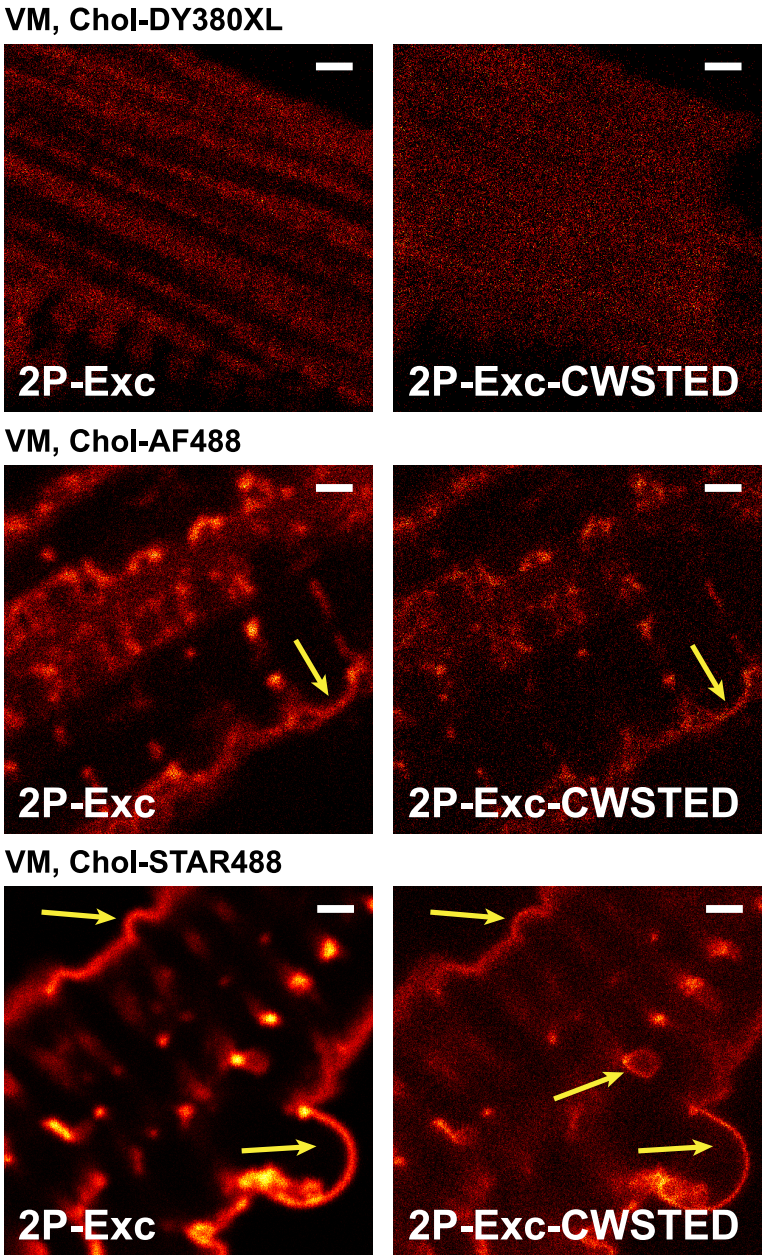

Figure G.5.: Performance of the fluorescent Cholesterol analogs Chol-DY380L, Chol-AF488, and Chol-STAR488 in two-photon-excitation (2P-Exc) and two-photon-excitation-CW-STED (2P-Exc-CWSTED) microscopy of membrane structures in living mouse ventricular cardiomyocytes (VM). VM were stained with 5 µM of the respective fluorescent Cholesterol analog according to the protocol described in section 2.3.2. Images show unprocessed data; scale bars: 1 µm. Chol-DY380XL (upper row) shows a diffuse and unspecific signal in both 2P-Exc as well as 2P-Exc-CWSTED mode. Chol-AF488 and Chol-STAR488 (middle and bottom row, respectively), albeit showing a good switch-off behavior and image resolution in 2P-Exc-CWSTED mode, both membrane labels subject the VM to substantial stress, resulting in membrane blebbing and vesicle formation (yellow arrows) soon after cell staining.

to a high affinity of Chol-DY380XL to the cardiac mitochondria. Chol-AF488 (Fig. G.5, middle row) and Chol-STAR488 (Fig. G.5, bottom row) both show a very bright and membrane-specific signal in 2P-Exc mode. In 2P-Exc-CWSTED

mode, Chol-AF488 shows a good switch-off behavior and high signal-to-noise ratio resulting in a profound increase in image resolution. Chol-STAR488, on the other hand, is less suitable for 2P-Exc-CWSTED microscopy as it shows a poor signal-to-noise ratio with a high amount of unspecific background fluorescence. Both Chol-AF488 and Chol-STAR488 exhibit the living cells to a high degree of cellular stress which results in membrane blebbing (as marked by the yellow arrows in the respective images) and cell contraction (not visible in the images) within a short time after staining, typically within 10 min. Additionally, Chol-AF488 had a seemingly high potential for phototoxicity as cells could neither sustain extended laser illumination nor an increase in illumination intensity when they were stained with Chol-AF488. Similar illumination protocols were far less critical for the cells when being stained with the other prepared fluorescent Cholesterol analogs.

H. Supporting material: 2P-Exc-CWSTED of Chol-OG488 labeled living VM

Please refer to section 3.4.3 for a detailed description of the results and the discussion of Two-Photon-Excitation-CW-STED (2P-Exc-CWSTED) imaging of living mouse ventricular cardiomyocytes (VM) labeled with the fluorescent Cholesterol (Chol) analog Chol-PEG-OregonGreen488 (Chol-OG488).

H.1. 2P-Exc-CWSTED of Chol-OG in live VM - raw data image stack at different depths in the cell

Figure H.1 shows the raw data of Two-Photon-Excitation-CW-STED (2P-Exc-CWSTED) images of a living mouse ventricular cardiomyocytes (VM) stained with Cholesterol-PEG-OregonGreen488 (Chol-OG488) and recorded at different depths within the cell. The images are the raw data analogs to the smoothed images presented in section 3.4.3, Fig. 3.18. The imaging depths are given in µm beneath the sarcolemma and range from -0.4 µm to -2.0 µm. VM were stained with Chol-OG488 as described in section 2.3.2 at a concentration of 5 µM of Chol-OG488. 2P-Exc at a wavelength of 760 nm was performed at 10 mW and STED at a wavelength of 592 nm was performed at 50 mW (measured in a back focal plane of the objective, respectively). The fluorescence signal was time gated with a delay of 2.42 ns and a gate width of 9.80 ns. The lateral pixel size was set to 20 nm in the X- and Y-direction, respectively and 200 nm for the Z-direction; the pixel dwell time was set to 0.05 ms. The resolution of transverse tubular membrane structures (see also section 2.6.2) was determined by first extracting the summed up fluorescence intensity along the yellow line and

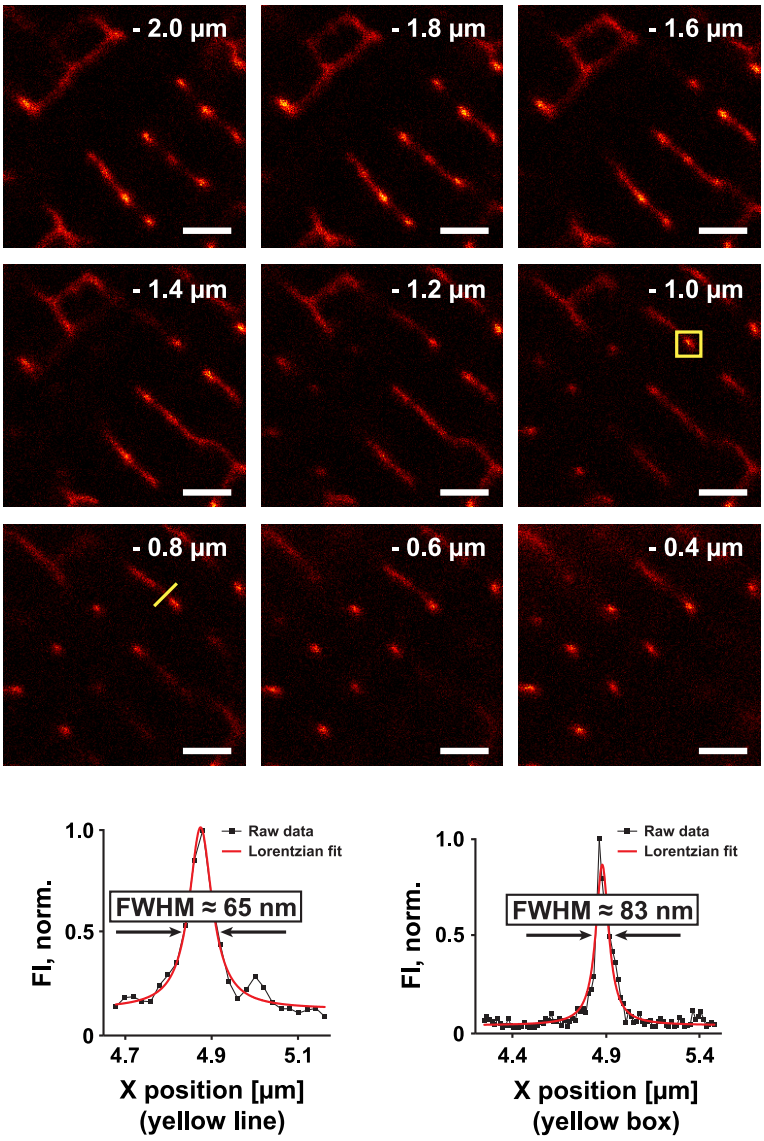

Figure H.1.: Two-Photon-Excitation-CW-STED (2P-Exc-CWSTED) raw data images of a living mouse ventricular cardiomyocyte (VM) stained with Cholesterol-PEG-OregonGreen488 (Chol-OG488), see also section 3.4.3. VM were stained as described in section 2.3.2 and successively imaged at different depths within the cell. The depth is indicated in the image frames, refers to µm beneath the sarcolemma and ranges from -0.4 µm to -2.0 µm. The imaging parameters are given in this section. Scale bars: 1 µm. Graphs below the image frames show normalized fluorescence intensity profiles (FI, norm.) obtained from the yellow line (for the left graph) and yellow box (for the right graph) indicated in the respective image frames and marking transverse tubular cross sections. The resolution of transverse tubule structures is denoted as the full width at half maximum (FWHM) extracted from fitting the intensity data to a Lorentzian curve (see also section 2.6.2).

within the yellow box, respectively, indicated in the respective image frames. Then, a Lorentzian curve was fit to the normalized fluorescence intensity distribution, and the resolution denoted as the full width at half maximum (FWHM) of the curve fit.

H.2. Quantification of the size of Chol rich sarcolemmal patches

In section 3.4.3, using Two-Photon-Excitation-CW-STED (2P-Exc-CWSTED) microscopy of living mouse ventricular cardiomyocytes (VM) labeled with the fluorescent Cholesterol (Chol) analog Chol-PEG-OregonGreen488 (Chol-OG-488), I could show that Chol rich patches at the sarcolemma of VM could be categorized into two populations. One population of Chol rich sarcolemmal patches buds into Transverse Tubules (TT) eventually forming the complex Transverse-Axial Tubular System (TATS) which is the membrane structure typical of VM. The other population of Chol rich sarcolemmal patches does not bud into TT but forms shallow membrane invaginations that do not extend deeper than about 500 nm into the VM interior. To investigate whether the area size of the observed Chol rich sarcolemmal patches influences if a Chol patch buds into a TT or not, I determined the distribution of area sizes of Chol patches classified to belong to one of the two specific populations (i.e. associated to TT or associated to shallow membrane invaginations), respectively. To this end, VM were labeled as described in section 2.3.2. Sample imaging was performed using the custom-built 2P-Exc-CWSTED microscope (see section 2.1.1) and with the settings specified in section 3.4.3. Chol rich sarcolemmal patches were classified as associated with Tranverse Tubules (TT) or as associated with shallow membrane invaginations as described in section 3.4.3. 2P-Exc-CWSTED images of sarcolemmal Chol-OG488 signals were binarized and the areas of selected Chol rich patches determined using the "Analyze Particles" plugin within the FiJi image analysis software (see also sections 2.6.1 and 3.4.3). Fig. H.2 summarizes the area size distribution of Chol rich sarcolemmal patches that are either associated to TT (displayed in pink) or associated to shallow membrane invaginations (displayed in yellow), respectively. As can be seen from the shown bar graph representation, the area size distributions do not vary significantly between the two populations of Chol rich sarcolemmal patches. Both populations show a broad distribution of patch area sizes ranging from 1600 nm^2 up to about 150,000 nm^2. Further, both populations feature a typical area size of about 4500 nm^2, corresponding to a patch diameter of about 75 nm (thereby assuming the Chol patches to be circular). Conclusively, a gen-

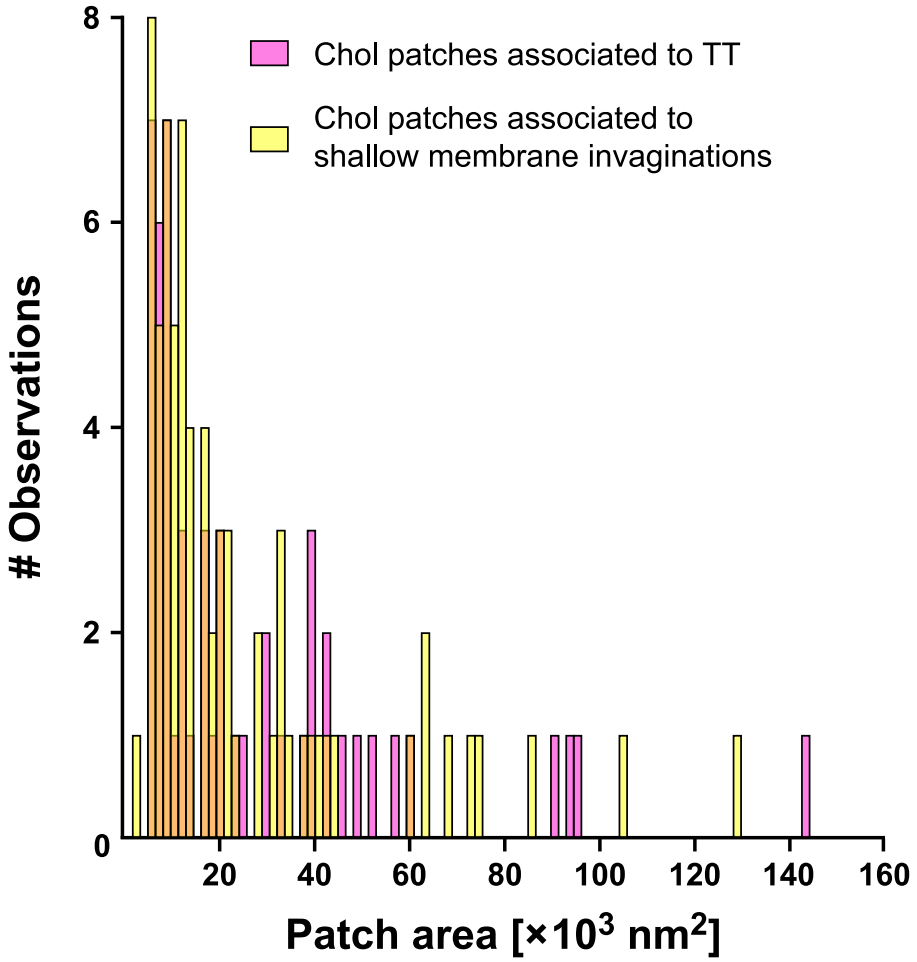

Figure H.2.: Area size distribution of Cholesterol (Chol) rich patches at the sarcolemma of living mouse ventricular cardiomyocytes (VM) labeled with the fluorescent Chol analog Chol-PEG-OregonGreen488 (Chol-OG488) and imaged in Two-Photon-Excitation-CW-STED (2P-Exc-CWSTED) mode. The here displayed bar graph representation with a bin size of 1600 nm² (i.e. corresponding to an area of 2 × 2 px shows the areas of Chol patches associated with Transverse Tubules (TT) in pink and the areas of Chol patches associated with shallow membrane invaginations in yellow, respectively. To facilitate the visibility of the area size distribution, the bars were shaded with a color transparency of 50 % resulting in an orange hue where pink and yellow bars overlap. The y-axis ("# Observations") denotes the frequency with which a Chol patch with a certain area was observed. Number of evaluated Chol rich sarcolemmal patches: patches associated with TT - 52; patches associated with shallow membrane invaginations - 71. See section H.2 for further details regarding data acquisition and interpretation.

eral principle that would allow for the inference if a Chol rich sarcolemmal patch is either associated to TT or associated to shallow membrane invaginations could not be derived based on the determination of the distribution of the area sizes of the sarcolemmal Chol patches.

I. Statistical significance testing

Statistical significance testing for the data presented throughout this PhD work was performed using the two-sided Mann-Whitney-Wilcoxon U test (MWW) as described in section 2.9. The tables in the following summarize and display the explicit MWW U statistics for the data sets presented in the main text.

Cell line	U2OS	HeLa	HEK	Vero
U2OS	—	$\rho_{U2OS} = (47.34 \pm 10.17)\,\%$ $\rho_{HeLa} = (37.81 \pm 8.04)\,\%$ $n_{U2OS} = 61$; $U_{U2OS} = 718$ $n_{HeLa} = 52$; $U_{HeLa} = 2454$ $p = 5.81 \times 10^{-7}$ $(**)$	$\rho_{U2OS} = (47.34 \pm 10.17)\,\%$ $\rho_{HEK} = (39.91 \pm 7.71)\,\%$ $n_{U2OS} = 61$; $U_{U2OS} = 1421$ $n_{HEK} = 85$; $U_{HEK} = 3764$ $p = 3.38 \times 10^{-6}$ $(**)$	$\rho_{U2OS} = (47.34 \pm 10.17)\,\%$ $\rho_{Vero} = (41.32 \pm 8.20)\,\%$ $n_{U2OS} = 61$; $U_{U2OS} = 700$ $n_{Vero} = 36$; $U_{Vero} = 1496$ $p = 3.00 \times 10^{-3}$ $(*)$
HeLa	$\rho_{HeLa} = (37.81 \pm 8.04)\,\%$ $\rho_{U2OS} = (47.34 \pm 10.17)\,\%$ $n_{HeLa} = 52$; $U_{HeLa} = 2454$ $n_{U2OS} = 61$; $U_{U2OS} = 718$ $p = 5.81 \times 10^{-7}$ $(**)$	—	$\rho_{HeLa} = (37.81 \pm 8.04)\,\%$ $\rho_{HEK} = (39.91 \pm 7.71)\,\%$ $n_{HeLa} = 52$; $U_{HeLa} = 2480$ $n_{HEK} = 85$; $U_{HEK} = 1940$ $p = 0.232$ (n.s.)	$\rho_{HeLa} = (37.81 \pm 8.04)\,\%$ $\rho_{Vero} = (41.32 \pm 8.20)\,\%$ $n_{HeLa} = 52$; $U_{HeLa} = 1160$ $n_{Vero} = 36$; $U_{Vero} = 712$ $p = 0.058$ (n.s.)
HEK	$\rho_{HEK} = (39.91 \pm 7.71)\,\%$ $\rho_{U2OS} = (47.34 \pm 10.17)\,\%$ $n_{HEK} = 85$; $U_{HEK} = 3764$ $n_{U2OS} = 61$; $U_{U2OS} = 1421$ $p = 3.38 \times 10^{-6}$ $(**)$	$\rho_{HEK} = (39.91 \pm 7.71)\,\%$ $\rho_{HeLa} = (37.81 \pm 8.04)\,\%$ $n_{HEK} = 85$; $U_{HEK} = 1940$ $n_{HeLa} = 52$; $U_{HeLa} = 2480$ $p = 0.232$ (n.s.)	—	$\rho_{HEK} = (39.91 \pm 7.71)\,\%$ $\rho_{Vero} = (41.32 \pm 8.20)\,\%$ $n_{HEK} = 85$; $U_{HEK} = 1718$ $n_{Vero} = 36$; $U_{Vero} = 1342$ $p = 0.288$ (n.s.)
Vero	$\rho_{Vero} = (41.32 \pm 8.20)\,\%$ $\rho_{U2OS} = (47.34 \pm 10.17)\,\%$ $n_{Vero} = 36$; $U_{Vero} = 1496$ $n_{U2OS} = 61$; $U_{U2OS} = 700$ $p = 3.00 \times 10^{-3}$ $(*)$	$\rho_{Vero} = (41.32 \pm 8.20)\,\%$ $\rho_{HeLa} = (37.81 \pm 8.04)\,\%$ $n_{Vero} = 36$; $U_{Vero} = 712$ $n_{HeLa} = 52$; $U_{HeLa} = 1160$ $p = 0.058$ (n.s.)	$\rho_{Vero} = (41.32 \pm 8.20)\,\%$ $\rho_{HEK} = (39.91 \pm 7.71)\,\%$ $n_{Vero} = 36$; $U_{Vero} = 1342$ $n_{HEK} = 85$; $U_{HEK} = 1718$ $p = 0.288$ (n.s.)	—

Table I.1.: MWW U statistics for Chol-KK114 surface signal densities ρ in filopodia of cultured cell lines. This table corresponds to the data presented in Fig. 3.4 in the main text. ρ was determined as described in section 2.6.4 and is presented as mean $\pm$ standard deviation. The parameters defining the MWW distribution are presented in the table as n_i: the sample size of the respective cell line i and U_i: the MWW statistic U of the respective cell line i. Further, the p-value of the two-sided MWW is denoted in the table and, in parenthesis, evaluated as (n.s.): not significant, $p > 0.01$; $(*)$: significant, $p < 0.01$; $(**)$: very significant, $p < 0.001$.

Cell line	U2OS	HeLa	HEK	Vero	V-IPSC	HAd	VM
U2OS	—	$\rho_{U2OS} = (0.52 \pm 0.21)\,\%$ $\rho_{HeLa} = (0.53 \pm 0.29)\,\%$ $n_{U2OS} = 28$; $U_{U2OS} = 441$ $n_{HeLa} = 33$; $U_{HeLa} = 483$ $p = 0.767$ (n.s.)	$\rho_{U2OS} = (0.52 \pm 0.21)\,\%$ $\rho_{HEK} = (0.37 \pm 0.19)\,\%$ $n_{U2OS} = 28$; $U_{U2OS} = 440$ $n_{HEK} = 55$; $U_{HEK} = 1100$ $p = 0.0015$ $(*)$	$\rho_{U2OS} = (0.52 \pm 0.21)\,\%$ $\rho_{Vero} = (0.43 \pm 0.24)\,\%$ $n_{U2OS} = 28$; $U_{U2OS} = 186$ $n_{Vero} = 18$; $U_{Vero} = 318$ $p = 0.140$ (n.s.)	$\rho_{U2OS} = (0.52 \pm 0.21)\,\%$ $\rho_{V\text{-}IPSC} = (18.07 \pm 3.96)\,\%$ $n_{U2OS} = 28$; $U_{U2OS} = 1008$ $n_{V\text{-}IPSC} = 36$; $U_{V\text{-}IPSC} = 0$ $p = 9.49 \times 10^{-12}$ $(**)$	$\rho_{U2OS} = (0.52 \pm 0.21)\,\%$ $\rho_{HAd} = (18.86 \pm 2.54)\,\%$ $n_{U2OS} = 28$; $U_{U2OS} = 1400$ $n_{HAd} = 50$; $U_{HAd} = 0$ $p = 3.19 \times 10^{-13}$ $(**)$	$\rho_{U2OS} = (0.52 \pm 0.21)\,\%$ $\rho_{VM} = (16.93 \pm 4.36)\,\%$ $n_{U2OS} = 28$; $U_{U2OS} = 3500$ $n_{VM} = 125$; $U_{VM} = 0$ $p = 1.52 \times 10^{-16}$ $(**)$
HeLa	$\rho_{HeLa} = (0.53 \pm 0.29)\,\%$ $\rho_{U2OS} = (0.52 \pm 0.21)\,\%$ $n_{HeLa} = 33$; $U_{HeLa} = 483$ $n_{U2OS} = 28$; $U_{U2OS} = 440$ $p = 0.767$ (n.s.)	—	$\rho_{HeLa} = (0.53 \pm 0.29)\,\%$ $\rho_{HEK} = (0.37 \pm 0.19)\,\%$ $n_{HeLa} = 33$; $U_{HeLa} = 578$ $n_{HEK} = 55$; $U_{HEK} = 1237$ $p = 0.0046$ $(*)$	$\rho_{HeLa} = (0.53 \pm 0.29)\,\%$ $\rho_{Vero} = (0.43 \pm 0.24)\,\%$ $n_{HeLa} = 33$; $U_{HeLa} = 243$ $n_{Vero} = 18$; $U_{Vero} = 351$ $p = 0.292$ $(n.s.)$	$\rho_{HeLa} = (0.53 \pm 0.29)\,\%$ $\rho_{V\text{-}IPSC} = (18.07 \pm 3.96)\,\%$ $n_{HeLa} = 33$; $U_{HeLa} = 1188$ $n_{V\text{-}IPSC} = 36$; $U_{V\text{-}IPSC} = 0$ $p = 1.01 \times 10^{-12}$ $(**)$	$\rho_{HeLa} = (0.53 \pm 0.29)\,\%$ $\rho_{HAd} = (18.86 \pm 2.54)\,\%$ $n_{HeLa} = 33$; $U_{HeLa} = 1650$ $n_{HAd} = 50$; $U_{HAd} = 0$ $p = 1.70 \times 10^{-14}$ $(**)$	$\rho_{HeLa} = (0.53 \pm 0.29)\,\%$ $\rho_{VM} = (16.93 \pm 4.36)\,\%$ $n_{HeLa} = 33$; $U_{HeLa} = 4125$ $n_{VM} = 125$; $U_{VM} = 0$ $p = 1.14 \times 10^{-18}$ $(**)$
HEK	$\rho_{HEK} = (0.37 \pm 0.19)\,\%$ $\rho_{U2OS} = (0.52 \pm 0.21)\,\%$ $n_{HEK} = 55$; $U_{HEK} = 1100$ $n_{U2OS} = 28$; $U_{U2OS} = 440$ $p = 0.0015$ $(*)$	$\rho_{HEK} = (0.37 \pm 0.19)\,\%$ $\rho_{HeLa} = (0.53 \pm 0.29)\,\%$ $n_{HEK} = 55$; $U_{HEK} = 1237$ $n_{HeLa} = 33$; $U_{HeLa} = 578$ $p = 0.0046$ $(*)$	—	$\rho_{HEK} = (0.37 \pm 0.19)\,\%$ $\rho_{Vero} = (0.43 \pm 0.24)\,\%$ $n_{HEK} = 55$; $U_{HEK} = 569$ $n_{Vero} = 18$; $U_{Vero} = 421$ $p = 0.347$ (n.s.)	$\rho_{HEK} = (0.37 \pm 0.19)\,\%$ $\rho_{V\text{-}IPSC} = (18.07 \pm 3.96)\,\%$ $n_{HEK} = 55$; $U_{HEK} = 1980$ $n_{V\text{-}IPSC} = 36$; $U_{V\text{-}IPSC} = 0$ $p = 9.65 \times 10^{-16}$ $(**)$	$\rho_{HEK} = (0.37 \pm 0.19)\,\%$ $\rho_{HAd} = (18.86 \pm 2.54)\,\%$ $n_{HEK} = 55$; $U_{HEK} = 2750$ $n_{HAd} = 50$; $U_{HAd} = 0$ $p = 1.16 \times 10^{-18}$ $(**)$	$\rho_{HEK} = (0.37 \pm 0.19)\,\%$ $\rho_{VM} = (16.93 \pm 4.36)\,\%$ $n_{HEK} = 55$; $U_{HEK} = 6875$ $n_{VM} = 125$; $U_{VM} = 0$ $p = 1.36 \times 10^{-26}$ $(**)$
Vero	$\rho_{Vero} = (0.43 \pm 0.24)\,\%$ $\rho_{U2OS} = (0.52 \pm 0.21)\,\%$ $n_{Vero} = 18$; $U_{Vero} = 318$ $n_{U2OS} = 28$; $U_{U2OS} = 186$ $p = 0.140$ (n.s.)	$\rho_{Vero} = (0.43 \pm 0.24)\,\%$ $\rho_{HeLa} = (0.53 \pm 0.29)\,\%$ $n_{Vero} = 18$; $U_{Vero} = 351$ $n_{HeLa} = 33$; $U_{HeLa} = 243$ $p = 0.292$ (n.s.)	$\rho_{Vero} = (0.43 \pm 0.24)\,\%$ $\rho_{HEK} = (0.37 \pm 0.19)\,\%$ $n_{Vero} = 18$; $U_{Vero} = 421$ $n_{HEK} = 55$; $U_{HEK} = 569$ $p = 0.347$ (n.s.)	—	$\rho_{Vero} = (0.43 \pm 0.24)\,\%$ $\rho_{V\text{-}IPSC} = (18.07 \pm 3.96)\,\%$ $n_{Vero} = 18$; $U_{Vero} = 648$ $n_{V\text{-}IPSC} = 36$; $U_{V\text{-}IPSC} = 0$ $p = 2.92 \times 10^{-9}$ $(**)$	$\rho_{Vero} = (0.43 \pm 0.24)\,\%$ $\rho_{HAd} = (18.86 \pm 2.54)\,\%$ $n_{Vero} = 18$; $U_{Vero} = 900$ $n_{HAd} = 50$; $U_{HAd} = 0$ $p = 4.14 \times 10^{-10}$ $(**)$	$\rho_{Vero} = (0.43 \pm 0.24)\,\%$ $\rho_{VM} = (16.93 \pm 4.36)\,\%$ $n_{Vero} = 18$; $U_{Vero} = 2250$ $n_{VM} = 125$; $U_{VM} = 0$ $p = 7.73 \times 10^{-12}$ $(**)$
V-IPSC	$\rho_{V\text{-}IPSC} = (18.07 \pm 3.96)\,\%$ $\rho_{U2OS} = (0.52 \pm 0.21)\,\%$ $n_{V\text{-}IPSC} = 36$; $U_{V\text{-}IPSC} = 0$ $n_{U2OS} = 28$; $U_{U2OS} = 1008$ $p = 9.49 \times 10^{-12}$ $(**)$	$\rho_{V\text{-}IPSC} = (18.07 \pm 3.96)\,\%$ $\rho_{HeLa} = (0.53 \pm 0.29)\,\%$ $n_{V\text{-}IPSC} = 36$; $U_{V\text{-}IPSC} = 0$ $n_{HeLa} = 28$; $U_{HeLa} = 1008$ $p = 1.01 \times 10^{-12}$ $(**)$	$\rho_{V\text{-}IPSC} = (18.07 \pm 3.96)\,\%$ $\rho_{HEK} = (0.37 \pm 0.19)\,\%$ $n_{V\text{-}IPSC} = 36$; $U_{V\text{-}IPSC} = 0$ $n_{HEK} = 55$; $U_{HEK} = 1980$ $p = 9.65 \times 10^{-16}$ $(**)$	$\rho_{V\text{-}IPSC} = (18.07 \pm 3.96)\,\%$ $\rho_{Vero} = (0.43 \pm 0.24)\,\%$ $n_{V\text{-}IPSC} = 36$; $U_{V\text{-}IPSC} = 0$ $n_{Vero} = 18$; $U_{Vero} = 648$ $p = 2.92 \times 10^{-9}$ $(**)$	—	$\rho_{V\text{-}IPSC} = (18.07 \pm 3.96)\,\%$ $\rho_{HAd} = (18.86 \pm 2.54)\,\%$ $n_{V\text{-}IPSC} = 36$; $U_{V\text{-}IPSC} = 1041$ $n_{HAd} = 50$; $U_{HAd} = 759$ $p = 0.219$ (n.s.)	$\rho_{V\text{-}IPSC} = (18.07 \pm 3.96)\,\%$ $\rho_{VM} = (16.93 \pm 4.36)\,\%$ $n_{V\text{-}IPSC} = 36$; $U_{V\text{-}IPSC} = 1991$ $n_{VM} = 125$; $U_{VM} = 2509$ $p = 0.294$ (n.s.)
HAd	$\rho_{HAd} = (18.86 \pm 2.54)\,\%$ $\rho_{U2OS} = (0.52 \pm 0.21)\,\%$ $n_{HAd} = 50$; $U_{HAd} = 0$ $n_{U2OS} = 28$; $U_{U2OS} = 1400$ $p = 3.99 \times 10^{-13}$ $(**)$	$\rho_{HAd} = (18.86 \pm 2.54)\,\%$ $\rho_{HeLa} = (0.53 \pm 0.29)\,\%$ $n_{HAd} = 50$; $U_{HAd} = 0$ $n_{HeLa} = 33$; $U_{HeLa} = 1650$ $p = 1.70 \times 10^{-14}$ $(**)$	$\rho_{HAd} = (18.86 \pm 2.54)\,\%$ $\rho_{HEK} = (0.37 \pm 0.19)\,\%$ $n_{HAd} = 50$; $U_{HAd} = 0$ $n_{HEK} = 55$; $U_{HEK} = 2750$ $p = 1.16 \times 10^{-18}$ $(**)$	$\rho_{HAd} = (18.86 \pm 2.54)\,\%$ $\rho_{Vero} = (0.43, \pm 0.24)\,\%$ $n_{HAd} = 50$; $U_{HAd} = 0$ $n_{Vero} = 18$; $U_{Vero} = 900$ $p = 4.14 \times 10^{-10}$ $(**)$	$\rho_{HAd} = (18.86 \pm 2.54)\,\%$ $\rho_{V\text{-}IPSC} = (18.07 \pm 3.96)\,\%$ $n_{HAd} = 50$; $U_{HAd} = 759$ $n_{V\text{-}IPSC} = 36$; $U_{V\text{-}IPSC} = 1041$ $p = 0.219$ (n.s.)	—	$\rho_{HAd} = (18.86 \pm 2.54)\,\%$ $\rho_{VM} = (16.93 \pm 4.36)\,\%$ $n_{HAd} = 50$; $U_{HAd} = 2440$ $n_{VM} = 125$; $U_{VM} = 3810$ $p = 0.024$ (n.s.)
VM	$\rho_{VM} = (16.93 \pm 4.36)\,\%$ $\rho_{U2OS} = (0.52 \pm 0.21)\,\%$ $n_{VM} = 125$; $U_{VM} = 0$ $n_{U2OS} = 28$; $U_{U2OS} = 3500$ $p = 1.52 \times 10^{-16}$ $(**)$	$\rho_{VM} = (16.93 \pm 4.36)\,\%$ $\rho_{HeLa} = (0.53 \pm 0.29)\,\%$ $n_{VM} = 125$; $U_{VM} = 0$ $n_{HeLa} = 33$; $U_{HeLa} = 4125$ $p = 1.14 \times 10^{-18}$ $(**)$	$\rho_{VM} = (16.93 \pm 4.36)\,\%$ $\rho_{HEK} = (0.52 \pm 0.21)\,\%$ $n_{VM} = 125$; $U_{VM} = 0$ $n_{HEK} = 55$; $U_{HEK} = 6875$ $p = 1.36 \times 10^{-26}$ $(**)$	$\rho_{VM} = (16.93 \pm 4.36)\,\%$ $\rho_{Vero} = (0.43 \pm 0.24)\,\%$ $n_{VM} = 125$; $U_{VM} = 0$ $n_{Vero} = 18$; $U_{Vero} = 2250$ $p = 7.73 \times 10^{-12}$ $(**)$	$\rho_{VM} = (16.93 \pm 4.36)\,\%$ $\rho_{VM} = (18.07 \pm 3.96)\,\%$ $n_{VM} = 125$; $U_{VM} = 2509$ $n_{V\text{-}IPSC} = 36$; $U_{V\text{-}IPSC} = 1991$ $p = 0.294$ (n.s.)	$\rho_{VM} = (16.93 \pm 4.36)\,\%$ $\rho_{VM} = (18.86 \pm 2.54)\,\%$ $n_{VM} = 125$; $U_{VM} = 3810$ $n_{HAd} = 50$; $U_{HAd} = 2440$ $p = 0.024$ (n.s.)	—

Table I.2.: MWW U statistics for Chol-KK114 surface signal densities ρ at the basement membrane of cultured cell lines and primary ventricular mouse cardiomyocytes (VM). This table corresponds to the data presented in Fig. 3.7 in the main text. ρ was determined as described in section 2.6.4 and is presented as mean $\pm$ standard deviation. The parameters defining the MWW distribution are presented in the table as n_i: the sample size of the respective cell line i and U_i: the MWW statistic U of the respective cell line i. Further, the p-value of the two-sided MWW is denoted in the table and, in parenthesis, evaluated as (n.s.): not significant, $p > 0.01$; $(*)$: significant, $p < 0.01$; $(**)$: very significant, $p < 0.001$.

Cell type and labeled structure	VM, Cav-3
VM, Chol	$\rho_{\text{VM, Chol}} = (16.93 \pm 4.36)\,\%$ $\rho_{\text{VM, Cav-3}} = (24.13 \pm 4.89)\,\%$ $n_{\text{VM, Chol}} = 125$; $U_{\text{VM, Chol}} = 7634$ $n_{\text{VM, Cav-3}} = 71$; $U_{\text{VM, Cav-3}} = 1241$ $p = 5.62 \times 10^{-17}$ $(**)$

Table I.3.: MWW U statistics for surface signal densities ρ of the Cholesterol-PEG-KK114 (Chol-KK114) signal at the sarcolemma of living primary ventricular mouse cardiomyocytes (VM, Chol) and of the Caveolin-3 (Cav-3) signal at the sarcolemma of fixed VM (VM, Cav-3). This table corresponds to the data presented in Fig. 3.23 in the main text. ρ was determined as described in section 2.6.4, is given in % of the total basement membrane area and is presented as mean $\pm$ standard deviation. The parameters defining the MWW distribution are presented in the table as n_i: the sample size of the respective sample i and U_i: the MWW statistic U of the respective sample i. Further, the p-value from the two-tailed MWW is denoted in the table and, in parenthesis, evaluated as $(**)$: very significant, $p < 0.001$.

Cell type and labeled structure	VM, Cav-3
VM, Chol	$\varnothing_{\text{VM, Chol}} = (74 \pm 20)\,\text{nm}$ $\varnothing_{\text{VM, Cav-3}} = (68 \pm 24)\,\text{nm}$ $n_{\text{VM, Chol}} = 129$; $U_{\text{VM, Chol}} = 134812$ $n_{\text{VM, Cav-3}} = 2397$; $U_{\text{VM, Cav-3}} = 174401$ $p = 0.0142$ (n.s.)

Table I.4.: MWW U statistics for the diameter $\varnothing$ of single domains of the Cholesterol-PEG-KK114 (Chol-KK114) signal at the sarcolemma of living primary ventricular mouse cardiomyocytes (VM, Chol) and of the Caveolin-3 (Cav-3) signal at the sarcolemma of fixed VM (VM, Cav-3). This table corresponds to the data presented in Fig. 3.23 in the main text. The diameter of single domains was determined as described in section 2.6.5, is given in nm and is presented as mean $\pm$ standard deviation. The parameters defining the MWW distribution are presented in the table as n_i: the sample size of the respective sample i and U_i: the MWW statistic U of the respective sample i. Further, the p-value from the two-tailed MWW is denoted in the table and, in parenthesis, evaluated as (n.s.): not significant, $p > 0.01$.

Cell type and labeled structure	VM, Cav-3
VM, Chol	$\varnothing_{\text{VM, Chol}} = (226 \pm 86)\,\text{nm}$ $\varnothing_{\text{VM, Cav-3}} = (253 \pm 58)\,\text{nm}$ $n_{\text{VM, Chol}} = 404$; $U_{\text{VM, Chol}} = 20253$ $n_{\text{VM, Cav-3}} = 77$; $U_{\text{VM, Cav-3}} = 10855$ $p = 2.63 \times 10^{-5}$ $(**)$

Table I.5.: MWW U statistics for the diameter $\varnothing$ of ring structures of the Cholesterol-PEG-KK114 (Chol-KK114) signal at the sarcolemma of living primary ventricular mouse cardiomyocytes (VM, Chol) and of the Caveolin-3 (Cav-3) signal at the sarcolemma of fixed VM (VM, Cav-3). This table corresponds to the data presented in Fig. 3.23 in the main text. The diameter of ring structures was determined as described in section 2.6.6, is given in nm and is presented as mean $\pm$ standard deviation. The parameters defining the MWW distribution are presented in the table as n_i: the sample size of the respective sample i and U_i: the MWW statistic U of the respective sample i. Further, the p-value from the two-tailed MWW is denoted in the table and, in parenthesis, evaluated as $(**)$: very significant, $p < 0.001$.

Cell type, condition, and labeled structure	HeLa, Chol	HeLa OE, Cav-3	HeLa OE, Chol
HeLa, Chol	—	$\rho_{\text{HeLa, Chol}} = (0.53 \pm 0.29)\,\%$ $\rho_{\text{HeLa OE, Cav-3}} = (8.92 \pm 2.51)\,\%$ $n_{\text{HeLa, Chol}} = 33$; $U_{\text{HeLa, Chol}} = 957$ $n_{\text{HeLa OE, Cav-3}} = 29$; $U_{\text{HeLa OE, Cav-3}} = 0$ $p = 1.55 \times 10^{-11}$ $(**)$	$\rho_{\text{HeLa, Chol}} = (0.53 \pm 0.29)\,\%$ $\rho_{\text{HeLa OE, Chol}} = (5.79 \pm 1.24)\,\%$ $n_{\text{HeLa, Chol}} = 33$; $U_{\text{HeLa, Chol}} = 2277$ $n_{\text{HeLa OE, Chol}} = 39$; $U_{\text{HeLa OE, Chol}} = 0$ $p = 3.95 \times 10^{-16}$ $(**)$
HeLa OE, Cav-3	$\rho_{\text{HeLa OE, Cav-3}} = (8.92 \pm 2.51)\,\%$ $\rho_{\text{HeLa, Chol}} = (0.53 \pm 0.29)\,\%$ $n_{\text{HeLa OE, Cav-3}} = 29$; $U_{\text{HeLa OE, Cav-3}} = 0$ $n_{\text{HeLa, Chol}} = 33$; $U_{\text{HeLa, Chol}} = 957$ $p = 1.55 \times 10^{-11}$ $(**)$	—	$\rho_{\text{HeLa OE, Cav-3}} = (8.92 \pm 2.51)\,\%$ $\rho_{\text{HeLa OE, Chol}} = (5.79 \pm 1.24)\,\%$ $n_{\text{HeLa OE, Cav-3}} = 29$; $U_{\text{HeLa OE, Cav-3}} = 276$ $n_{\text{HeLa OE, Chol}} = 39$; $U_{\text{HeLa OE, Chol}} = 1725$ $p = 1.75 \times 10^{-8}$ $(**)$
HeLa OE, Chol	$\rho_{\text{HeLa OE, Chol}} = (5.79 \pm 1.24)\,\%$ $\rho_{\text{HeLa, Chol}} = (0.53 \pm 0.29)\,\%$ $n_{\text{HeLa OE, Chol}} = 39$; $U_{\text{HeLa OE, Chol}} = 0$ $n_{\text{HeLa, Chol}} = 33$; $U_{\text{HeLa, Chol}} = 2277$ $p = 3.95 \times 10^{-16}$ $(**)$	$\rho_{\text{HeLa OE, Chol}} = (5.79 \pm 1.24)\,\%$ $\rho_{\text{HeLa OE, Cav-3}} = (8.92 \pm 2.51)\,\%$ $n_{\text{HeLa OE, Chol}} = 39$; $U_{\text{HeLa OE, Chol}} = 1725$ $n_{\text{HeLa OE, Cav-3}} = 29$; $U_{\text{HeLa OE, Cav-3}} = 276$ $p = 1.75 \times 10^{-8}$ $(**)$	—

Table I.6.: MWW U statistics for the surface signal density ρ of the Cholesterol-PEG-KK114 (Chol-KK114) signal and the Caveolin-3 (Cav-3) signal at the basement membrane of control vs. Cav-3 overexpressing HeLa cells. This table corresponds to the data presented in Fig. 3.25 in the main text. In the table, the data for control HeLa cells stained with Chol-KK114 is denoted as "HeLa, Chol"; the data for Cav-3 overexpressing HeLa cells labeled for Cav-3 is denoted as "HeLa OE, Cav-3"; the data for Cav-3 overexpressing HeLa cells stained with Chol-KK114 is denoted as "HeLa OE, Chol". ρ was determined as described in section 2.6.4, is given in % of the total basement membrane area and is presented as mean $\pm$ standard deviation. The parameters defining the MWW distribution are presented in the table as n_i: the sample size of the respective sample i and U_i: the MWW statistic U of the respective sample i. Further, the p-value from the two-tailed MWW is denoted in the table and, in parenthesis, evaluated as $(**)$: very significant, $p < 0.001$.

Cell type, condition, and labeled structure	HeLa OE, Chol
HeLa OE, Cav-3	$\varnothing_{\text{HeLa OE, Cav-3}} = (78 \pm 19)\,\text{nm}$ $\varnothing_{\text{HeLa OE, Chol}} = (76 \pm 23)\,\text{nm}$ $n_{\text{HeLa OE, Cav-3}} = 426$; $U_{\text{HeLa OE, Cav-3}} = 61364$ $n_{\text{HeLa OE, Chol}} = 319$; $U_{\text{HeLa OE, Chol}} = 74530$ $p = 0.0235$ (n.s.)

Table I.7.: MWW U statistics for the diameter $\varnothing$ of single domains of the Cholesterol-PEG-KK114 (Chol-KK114) signal and the Caveolin-3 (Cav-3) signal at the basement membrane of Cav-3 overexpressing HeLa cells (HeLa OE). This table corresponds to the data presented in Fig. 3.25 in the main text. $\varnothing$ was determined as described in section 2.6.5, is given in nm and is presented as mean $\pm$ standard deviation. The parameters defining the MWW distribution are presented in the table as n_i: the sample size of the respective sample i and U_i: the MWW statistic U of the respective sample i. Further, the p-value from the two-tailed MWW is denoted in the table and, in parenthesis, evaluated as (n.s.): not significant, $p > 0.01$.

Cell type, condition, and labeled structure	HeLa OE, Chol
HeLa OE, Cav-3	$\varnothing_{\text{HeLa OE, Cav-3}} = (201 \pm 80)\,\text{nm}$ $\varnothing_{\text{HeLa OE, Chol}} = (218 \pm 89)\,\text{nm}$ $n_{\text{HeLa OE, Cav-3}} = 179$; $U_{\text{HeLa, Cav-3}} = 17689$ $n_{\text{HeLa OE, Chol}} = 152$; $U_{\text{HeLa OE, Chol}} = 9519$ $p = 2.50 \times 10^{-6}$ $(**)$

Table I.8.: MWW U statistics for the diameter $\varnothing$ of ring structures of the Cholesterol-PEG-KK114 (Chol-KK114) signal and the Caveolin-3 (Cav-3) signal at the basement membrane of Cav-3 overexpressing HeLa cells (HeLa OE). This table corresponds to the data presented in Fig. 3.25 in the main text. $\varnothing$ was determined as described in section 2.6.6, is given in nm and is presented as mean $\pm$ standard deviation. The parameters defining the MWW distribution are presented in the table as n_i: the sample size of the respective sample i and U_i: the MWW statistic U of the respective sample i. Further, the p-value from the two-tailed MWW is denoted in the table and, in parenthesis, evaluated as $(**)$: very significant, $p < 0.001$.

Cell type and condition (labeled structure: Cav-3)	VM, Control
VM, Chol depl.	$\varnothing_{\text{VM, Control}} = (68 \pm 24)\,\text{nm}$ $\varnothing_{\text{VM, Chol depl.}} = (66 \pm 23)\,\text{nm}$ $n_{\text{VM, Control}} = 2397$; $U_{\text{VM, Control}} = 2730318$ $n_{\text{VM, Chol depl.}} = 2360$; $U_{\text{VM, Chol depl.}} = 2926602$ $p = 0.0382$ (n.s.)

Table I.9.: MWW U statistics for the diameter $\varnothing$ of single domains of the Caveolin-3 (Cav-3) signal at the sarcolemma of control vs. Chol depleted (Chol depl.) mouse ventricular cardiomyocytes (VM). Chol depletion was performed as described in section 2.3.3. This table corresponds to the data presented in Fig. 3.27 in the main text. $\varnothing$ was determined as described in section 2.6.5, is given in nm and is presented as mean $\pm$ standard deviation. The parameters defining the MWW distribution are presented in the table as n_i: the sample size of the respective sample i and U_i: the MWW statistic U of the respective sample i. The p-value from the two-tailed MWW is denoted in the table and, in parenthesis, evaluated as (n.s.): not significant, $p > 0.01$.

Cell type and condition (labeled structure: Cav-3)	VM, Control
VM, Chol depl.	$\Gamma_{\text{VM, Control}} = (3.37 \pm 0.55)\,\%$ $\Gamma_{\text{VM, Chol depl.}} = (7.85 \pm 1.04)\,\%$ $n_{\text{VM, Control}} = 44$; $U_{\text{VM, Control}} = 1672$ $n_{\text{VM, Chol depl.}} = 38$; $U_{\text{VM, Chol depl.}} = 0$ $p = 7.89 \times 10^{-5}$ $(**)$

Table I.10.: MWW U statistics for the contour density Γ of the Caveolin-3 (Cav-3) signal at the sarcolemma of control vs. Chol depleted (Chol depl.) mouse ventricular cardiomyocytes (VM). Chol depletion was performed as described in section 2.3.3. This table corresponds to the data presented in Fig. 3.27 in the main text. Γ was determined as described in section 2.6.7, is given in % and is presented as mean $\pm$ standard deviation. The parameters defining the MWW distribution are presented in the table as n_i: the sample size of the respective sample i and U_i: the MWW statistic U of the respective sample i. The p-value from the two-tailed MWW is denoted in the table and, in parenthesis, evaluated as $(**)$: very significant, $p < 0.001$.

Cell type and condition (labeled structure: Cav-3)	VM, Control
VM, Chol depl.	$\rho_{\text{VM, Control}} = (24.13 \pm 4.89)\,\%$ $\rho_{\text{VM, Chol depl.}} = (50.55 \pm 4.67)\,\%$ $n_{\text{VM, Control}} = 44$; $U_{\text{VM, Control}} = 1665$ $n_{\text{VM, Chol depl.}} = 38$; $U_{\text{VM, Chol depl.}} = 0$ $p = 8.98 \times 10^{-15}$ $(**)$

Table I.11.: MWW U statistics for the surface signal density ρ of the Caveolin-3 (Cav-3) signal at the sarcolemma of control vs. Chol depleted (Chol depl.) mouse ventricular cardiomyocytes (VM). Chol depletion was performed as described in section 2.3.3. This table corresponds to the data presented in Fig. 3.27 in the main text. ρ was determined as described in section 2.6.4, is given in % and is presented as mean ± standard deviation. The parameters defining the MWW distribution are presented in the table as n_i: the sample size of the respective sample *i* and U_i: the MWW statistic U of the respective sample *i*. The p-value from the two-tailed MWW is denoted in the table and, in parenthesis, evaluated as $(**)$: very significant, $p < 0.001$.

Cell type and labeled structure	VM, Cav-3
VM, Dyst	$\varnothing_{\text{VM, Dyst}} = (67 \pm 27)\,\text{nm}$ $\varnothing_{\text{VM, Cav-3}} = (74 \pm 20)\,\text{nm}$ $n_{\text{VM, Dyst}} = 2947$; $U_{\text{VM, Dyst}} = 4367022$ $n_{\text{VM, Cav-3}} = 2397$; $U_{\text{VM, Cav-3}} = 4317787$ $p = 0.706$ (n.s.)

Table I.12.: MWW U statistics for the diameter ⌀ of single domains of the Dystrophin (Dyst) and Caveolin-3 (Cav-3) signal at the sarcolemma of mouse ventricular cardiomyocytes (VM). This table corresponds to the data presented in Fig. 3.32 in the main text. ⌀ was determined as described in section 2.6.5, is given in nm and is presented as mean ± standard deviation. The parameters defining the MWW distribution are presented in the table as n_i: the sample size of the respective sample *i* and U_i: the MWW statistic U of the respective sample *i*. The p-value from the two-tailed MWW is denoted in the table and, in parenthesis, evaluated as (n.s.): not significant, $p > 0.01$.

Cell type and labeled structure	VM, Cav-3
VM, Dyst	$\varnothing_{\text{VM, Dyst}} = (211 \pm 60)\,\text{nm}$ $\varnothing_{\text{VM, Cav-3}} = (253 \pm 58)\,\text{nm}$ $n_{\text{VM, Dyst}} = 121$; $U_{\text{VM, Dyst}} = 78068$ $n_{\text{VM, Cav-3}} = 80$; $U_{\text{VM, Cav-3}} = 11594$ $p = 8.03 \times 10^{-55}$ $(**)$

Table I.13.: MWW U statistics for the diameter ⌀ of ring structures of the Dystrophin (Dyst) and Caveolin-3 (Cav-3) signal at the sarcolemma of mouse ventricular cardiomyocytes (VM). This table corresponds to the data presented in Fig. 3.32 in the main text. ⌀ was determined as described in section 2.6.6, is given in nm and is presented as mean ± standard deviation. The parameters defining the MWW distribution are presented in the table as n_i: the sample size of the respective sample *i* and U_i: the MWW statistic U of the respective sample *i*. The p-value from the two-tailed MWW is denoted in the table and, in parenthesis, evaluated as $(**)$: very significant, $p < 0.001$.

Relative colocalization (RC) between A and B (A⟶B), cell condition	Cav-3⟶Dyst, Chol depl.
Cav-3⟶Dyst, Control	$RC_{\text{Cav-3}\longrightarrow\text{Dyst, Control}} = (32 \pm 2.7)\,\%$ $RC_{\text{Cav-3}\longrightarrow\text{Dyst, Chol depl.}} = (29 \pm 1.9)\,\%$ $n_{\text{Cav-3}\longrightarrow\text{Dyst, Control}} = 57$; $U_{\text{Cav-3}\longrightarrow\text{Dyst, Control}} = 1009$ $n_{\text{Cav-3}\longrightarrow\text{Dyst, Chol depl.}} = 41$; $U_{\text{Cav-3}\longrightarrow\text{Dyst, Chol depl.}} = 1328$ $p = 0.252$ (n.s.)

Table I.14.: MWW U statistics for the relative colocalization (RC, in %) between the sarcolemmal Caveolin-3 (Cav-3) and Dystrophin (Dyst) signal in control vs. Cholesterol depleted (Chol depl.) fixed mouse ventricular cardiomyocytes (VM). Chol depletion was performed as described in section 2.3.3. This table corresponds to the data presented in Fig. 3.34 in the main text. RC was determined as described in section 2.7, is given in % of the total sarcolemmal Cav-3 signal and is presented as mean ± standard deviation. The parameters defining the MWW distribution are presented in the table as n_i: the sample size of the respective sample i and U_i: the MWW statistic U of the respective sample i. Further, the p-value from the two-tailed MWW is denoted in the table and, in parenthesis, evaluated as (n.s.): not significant, $p > 0.01$.

Relative colocalization (RC) between A and B (A⟶B), cell condition	Dyst⟶Cav-3, Chol depl.
Dyst⟶Cav-3, Control	$RC_{\text{Dyst}\longrightarrow\text{Cav-3, Control}} = (7.2 \pm 0.7)\,\%$ $RC_{\text{Dyst}\longrightarrow\text{Cav-3, Chol depl.}} = (15 \pm 1.2)\,\%$ $n_{\text{Dyst}\longrightarrow\text{Cav-3, Control}} = 57$; $U_{\text{Dyst}\longrightarrow\text{Cav-3, Control}} = 2255$ $n_{\text{Dyst}\longrightarrow\text{Cav-3, Chol depl.}} = 41$; $U_{\text{Dyst}\longrightarrow\text{Cav-3, Chol depl.}} = 0$ $p = 6.97 \times 10^{-17}$ (n.s.)

Table I.15.: MWW U statistics for the relative colocalization (RC, in %) between the sarcolemmal Dystrophin (Dyst) and Caveolin-3 (Cav-3) signal in control vs. Cholesterol depleted (Chol depl.) fixed mouse ventricular cardiomyocytes (VM). Chol depletion was performed as described in section 2.3.3. This table corresponds to the data presented in Fig. 3.34 in the main text. RC was determined as described in section 2.7, is given in % of the total sarcolemmal Cav-3 signal and is presented as mean ± standard deviation. The parameters defining the MWW distribution are presented in the table as n_i: the sample size of the respective sample i and U_i: the MWW statistic U of the respective sample i. Further, the p-value from the two-tailed MWW is denoted in the table and, in parenthesis, evaluated as $(**)$: very significant, $p < 0.001$.

Peak-to-peak nearest neighbor distance (NND) between A and B (A⟶B)	Cav-3⟶Dyst(N)	Cav-3⟶Dyst(Rod)	Cav-3⟶Dyst(C)
Cav-3⟶Dyst(N)	—	$NND_{Cav\text{-}3\longrightarrow Dyst(N)} = (167 \pm 37)\,nm$ $NND_{Cav\text{-}3\longrightarrow Dyst(Rod)} = (83 \pm 51)\,nm$ $n_{Cav\text{-}3\longrightarrow Dyst(N)} = 47$; $U_{Cav\text{-}3\longrightarrow Dyst(N)} = 0$ $n_{Cav\text{-}3\longrightarrow Dyst(Rod)} = 43$; $U_{Cav\text{-}3\longrightarrow Dyst(Rod)} = 2021$ $p = 3.39 \times 10^{-16}$ $(**)$	$NND_{Cav\text{-}3\longrightarrow Dyst(N)} = (167 \pm 37)\,nm$ $NND_{Cav\text{-}3\longrightarrow Dyst(C)} = (70 \pm 27)\,nm$ $n_{Cav\text{-}3\longrightarrow Dyst(N)} = 47$; $U_{Cav\text{-}3\longrightarrow Dyst(N)} = 0$ $n_{Cav\text{-}3\longrightarrow Dyst(C)} = 51$; $U_{Cav\text{-}3\longrightarrow Dyst(C)} = 2397$ $p = 1.61 \times 10^{-17}$ $(**)$
Cav-3⟶Dyst(Rod)	$NND_{Cav\text{-}3\longrightarrow Dyst(Rod)} = (83 \pm 51)\,nm$ $NND_{Cav\text{-}3\longrightarrow Dyst(N)} = (167 \pm 37)\,nm$ $n_{Cav\text{-}3\longrightarrow Dyst(Rod)} = 43$; $U_{Cav\text{-}3\longrightarrow Dyst(Rod)} = 2021$ $n_{Cav\text{-}3\longrightarrow Dyst(N)} = 47$; $U_{Cav\text{-}3\longrightarrow Dyst(N)} = 0$ $p = 3.39 \times 10^{-16}$ $(**)$	—	$NND_{Cav\text{-}3\longrightarrow Dyst(Rod)} = (83 \pm 51)\,nm$ $NND_{Cav\text{-}3\longrightarrow Dyst(C)} = (70 \pm 27)\,nm$ $n_{Cav\text{-}3\longrightarrow Dyst(Rod)} = 43$; $U_{Cav\text{-}3\longrightarrow Dyst(Rod)} = 1023$ $n_{Cav\text{-}3\longrightarrow Dyst(C)} = 51$; $U_{Cav\text{-}3\longrightarrow Dyst(C)} = 1170$ $p = 0.580$ (n.s.)
Cav-3⟶Dyst(C)	$NND_{Cav\text{-}3\longrightarrow Dyst(C)} = (70 \pm 27)\,nm$ $NND_{Cav\text{-}3\longrightarrow Dyst(N)} = (167 \pm 37)\,nm$ $n_{Cav\text{-}3\longrightarrow Dyst(C)} = 51$; $U_{Cav\text{-}3\longrightarrow Dyst(C)} = 2397$ $n_{Cav\text{-}3\longrightarrow Dyst(N)} = 47$; $U_{Cav\text{-}3\longrightarrow Dyst(N)} = 0$ $p = 1.61 \times 10^{-17}$ $(**)$	$NND_{Cav\text{-}3\longrightarrow Dyst(C)} = (70 \pm 27)\,nm$ $NND_{Cav\text{-}3\longrightarrow Dyst(Rod)} = (83 \pm 51)\,nm$ $n_{Cav\text{-}3\longrightarrow Dyst(C)} = 51$; $U_{Cav\text{-}3\longrightarrow Dyst(C)} = 1170$ $n_{Cav\text{-}3\longrightarrow Dyst(Rod)} = 43$; $U_{Cav\text{-}3\longrightarrow Dyst(Rod)} = 1023$ $p = 0.580$ (n.s.)	—

Table I.16.: MWW U statistics for the peak-to-peak nearest neighbor distance NND (in nm) between the sarcolemmal Caveolin-3 (Cav-3) signal and the signal of different Dystrophin (Dyst) domains in fixed mouse ventricular cardiomyocytes (VM). The different Dyst domains are: the N-terminus (Dyst(N)), the central rod domain (Dyst(Rod)), and the C-terminus (Dyst(C)). This table corresponds to the data presented in Fig. 3.38 **A** in the main text. NND was determined as described in section 2.8, is given in nm and is presented as mean $\pm$ standard deviation. The parameters defining the MWW distribution are presented in the table as n_i: the sample size of the respective sample i and U_i: the MWW statistic U of the respective sample i. Further, the p-value from the two-tailed MWW is denoted in the table and, in parenthesis, evaluated as $(**)$: very significant, $p < 0.001$ and (n.s.): not significant, $p > 0.01$.

Relative colocalization (RC) between A and B (A⟶B)	Cav-3⟶Dyst(N)	Cav-3⟶Dyst(Rod)	Cav-3⟶Dyst(C)
Cav-3⟶Dyst(N)	—	$RC_{Cav\text{-}3\longrightarrow Dyst(N)} = (15 \pm 2.5)\,\%$ $RC_{Cav\text{-}3\longrightarrow Dyst(Rod)} = (32 \pm 2.7)\,\%$ $n_{Cav\text{-}3\longrightarrow Dyst(N)} = 47$; $U_{Cav\text{-}3\longrightarrow Dyst(N)} = 1927$ $n_{Cav\text{-}3\longrightarrow Dyst(Rod)} = 43$; $U_{Cav\text{-}3\longrightarrow Dyst(Rod)} = 0$ $p = 7.93 \times 10^{-16}$ $(**)$	$RC_{Cav\text{-}3\longrightarrow Dyst(N)} = (15 \pm 2.5)\,\%$ $RC_{Cav\text{-}3\longrightarrow Dyst(C)} = (39 \pm 3.1)\,\%$ $n_{Cav\text{-}3\longrightarrow Dyst(N)} = 47$; $U_{Cav\text{-}3\longrightarrow Dyst(N)} = 2350$ $n_{Cav\text{-}3\longrightarrow Dyst(C)} = 51$; $U_{Cav\text{-}3\longrightarrow Dyst(C)} = 0$ $p = 2.29 \times 10^{-17}$ $(**)$
Cav-3⟶Dyst(Rod)	$RC_{Cav\text{-}3\longrightarrow Dyst(Rod)} = (32 \pm 2.7)\,\%$ $RC_{Cav\text{-}3\longrightarrow Dyst(N)} = (15 \pm 2.5)\,\%$ $n_{Cav\text{-}3\longrightarrow Dyst(Rod)} = 43$; $U_{Cav\text{-}3\longrightarrow Dyst(Rod)} = 0$ $n_{Cav\text{-}3\longrightarrow Dyst(N)} = 47$; $U_{Cav\text{-}3\longrightarrow Dyst(N)} = 1927$ $p = 7.93 \times 10^{-16}$ $(**)$	—	$RC_{Cav\text{-}3\longrightarrow Dyst(Rod)} = (32 \pm 2.7)\,\%$ $RC_{Cav\text{-}3\longrightarrow Dyst(C)} = (39 \pm 3.1)\,\%$ $n_{Cav\text{-}3\longrightarrow Dyst(Rod)} = 43$; $U_{Cav\text{-}3\longrightarrow Dyst(Rod)} = 250$ $n_{Cav\text{-}3\longrightarrow Dyst(C)} = 51$; $U_{Cav\text{-}3\longrightarrow Dyst(C)} = 0$ $p = 3.03 \times 10^{-16}$ $(**)$
Cav-3⟶Dyst(C)	$RC_{Cav\text{-}3\longrightarrow Dyst(C)} = (39 \pm 3.1)\,\%$ $RC_{Cav\text{-}3\longrightarrow Dyst(N)} = (15 \pm 2.5)\,\%$ $n_{Cav\text{-}3\longrightarrow Dyst(C)} = 51$; $U_{Cav\text{-}3\longrightarrow Dyst(C)} = 0$ $n_{Cav\text{-}3\longrightarrow Dyst(N)} = 47$; $U_{Cav\text{-}3\longrightarrow Dyst(N)} = 2350$ $p = 2.29 \times 10^{-17}$ $(**)$	$RC_{Cav\text{-}3\longrightarrow Dyst(C)} = (39 \pm 3.1)\,\%$ $RC_{Cav\text{-}3\longrightarrow Dyst(Rod)} = (32 \pm 2.7)\,\%$ $n_{Cav\text{-}3\longrightarrow Dyst(C)} = 51$; $U_{Cav\text{-}3\longrightarrow Dyst(C)} = 0$ $n_{Cav\text{-}3\longrightarrow Dyst(Rod)} = 43$; $U_{Cav\text{-}3\longrightarrow Dyst(Rod)} = 250$ $p = 3.03 \times 10^{-16}$ $(**)$	—

Table I.17.: MWW U statistics for the relative colocalization (RC, in %) between the sarcolemmal Caveolin-3 (Cav-3) signal and the signal of different Dystrophin (Dyst) domains in fixed mouse ventricular cardiomyocytes (VM). The different Dyst domains are: the N-terminus (Dyst(N)), the central rod domain (Dyst(Rod)), and the C-terminus (Dyst(C)). This table corresponds to the data presented in Fig. 3.38 **B** in the main text. RC was determined as described in section 2.7, is given in % of the total sarcolemmal Cav-3 signal and is presented as mean $\pm$ standard deviation. The parameters defining the MWW distribution are presented in the table as n_i: the sample size of the respective sample i and U_i: the MWW statistic U of the respective sample i. Further, the p-value from the two-tailed MWW is denoted in the table and, in parenthesis, evaluated as $(**)$: very significant, $p < 0.001$.

J. Sarcolemmal Cav-3 in fixed cardiomyocytes labeled with a fluorescent Fab fragment

As a control that the sarcolemmal Caveolin-3 (Cav-3) signal in fixed and immunofluorescently labeled mouse ventricular cardiomyocytes (VM) that was observed and described in section 3.5 was not an artifact attributable to the possible clustering of the used secondary antibodies, samples were prepared of VM labeled for Cav-3 using the fluorescent dye STAR635P conjugated to a Fragment antigen-binding (Fab) fragment as the secondary antibody (instead of a full length secondary antibody). STED images of the samples were acquired with the STED microscope system Leica TCS SP8 STED 3X (see section 2.1.3) and using the same imaging parameters as for the standardly prepared fluorescent samples of fixed VM immunolabeled for Cav-3 using a full length secondary antibody. Fig. J.1 exemplarily shows the sarcolemmal Cav-3 signal structure of the Fab fragment labeled fixed VM.
Sarcolemmal Cav-3 clusters could be observed and the same nanoscopic Cav-3 membrane motifs as the ones described in section 3.5 could be identified: 1. single domains of about 70 nm in diameter, 2. ring structures of about 240 nm in diameter, and 3. bunchy clusters of various sizes. Specifically, the single domains were not smaller than the ones observed in the samples with the full length secondary antibody. If the clustered Cav-3 signal shown in section 3.5 would be due to the clustering of the used antibodies, a reduction in the diameter of the single domains would have been expected in the samples decorated with the Fab fragment. Since this was not the case, the observed clustered Cav-3 signal at the sarcolemma of VM is in fact attributable to protein clustering.

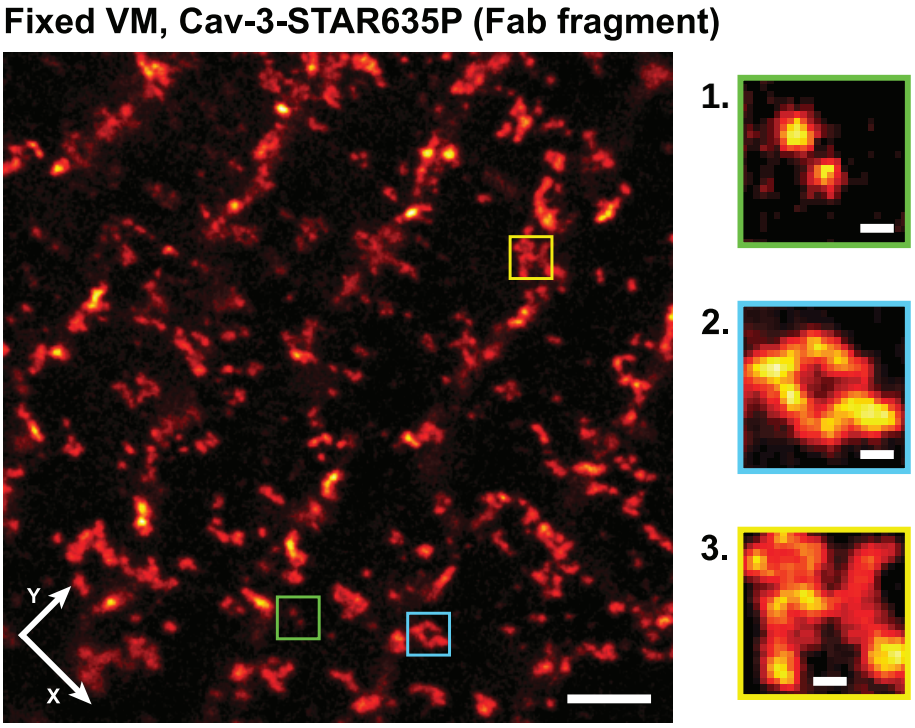

Figure J.1.: STED image of the sarcolemmal Caveolin-3 (Cav-3) signal pattern in a fixed mouse ventricular cardiomyocyte (VM) labeled via indirect immunofluorescence using the fluorescent dye STAR635P conjugated to a Fragment antigen-binding (Fab) fragment as the secondary antibody (instead of a full length secondary antibody). For the preparation of the fluorescent samples, please refer to section 2.3.3. Image magnifications display distinct reoccurring Cav-3 membrane motifs: 1. single domains, 2. ring structures, and 3. bunchy clusters. The imaged region of the cell did not lie completely flat on the cover slip, hence the signal along the image diagonal from top left to bottom right stems from a subsarcolemmal region in the cell where striated Cav-3 signal patterns can be observed. Therefore, special attention was paid to only select those Cav-3 membrane motifs for the image magnifications that were located at the sarcolemma, i.e. in regions not showing striated Cav-3 signals. Images were smoothed using a two-dimensional Gaussian filter with a width of 1.5 pixels. White arrows indicate the longitudinal (X) and the transverse (Y) cell axes, respectively. Scale bar in the overview image: 1 µm; scale bars in the magnifications: 100 nm.

K. Electron microscopy of caveolae in differently prepared heart samples

In section 3.5, using STED microscopy, a distinct membrane motif typical to both the Cav-3 and the Chol-KK114 signal seen at the sarcolemma of mouse ventricular cardiomyocytes (VM) is introduced and characterized: bunchy clusters of various sizes that are composed of several single domains in close proximity that assemble to form botryoidal (i.e. "grape like") superstructures. These superstructures are likely composed of individual neighboring caveolae or even of caveolae that have fused, forming intricate structural complexes along the sarcolemma - similar to the burrow system of moles and rabbits. These sarcolemmal caveolar complexes have been proposed based on imaging of caveolae using Electron Microscopy (EM) [140]. To confirm the observation of caveolar superstructures in VM, I prepared samples of VM for investigation using EM. The generated samples comprised VM under three different cellular conditions: 1.) single, isolated VM, 2.) VM in a loose cell complex (cell pellet), and 3.) tissue sections from excised papillary muscle. The preparation of the respective samples for EM is described in detail in section 2.10.3. Specifically, the three different cellular conditions 1.), 2.), and 3.) represent a respective increase in physiological accurateness. Fig. K.1 summarizes exemplary EM images of caveolar structures in VM samples under each of the above mentioned three conditions: 1.) single VM (Fig. K.1 **A**), 2.) cell pellets (Fig. K.1 **B**), and 3.) tissue sections (Fig. K.1 **C**). While the arrangement of caveolae in close proximity to each other could be observed for each of the three sample preparations, the fusing of caveolae was most often observed in the tissue sections (Fig. K.1 **C**). With the additional presence of e.g. connective tissue and blood vessels in the tissue sections, these sample preparations represent the

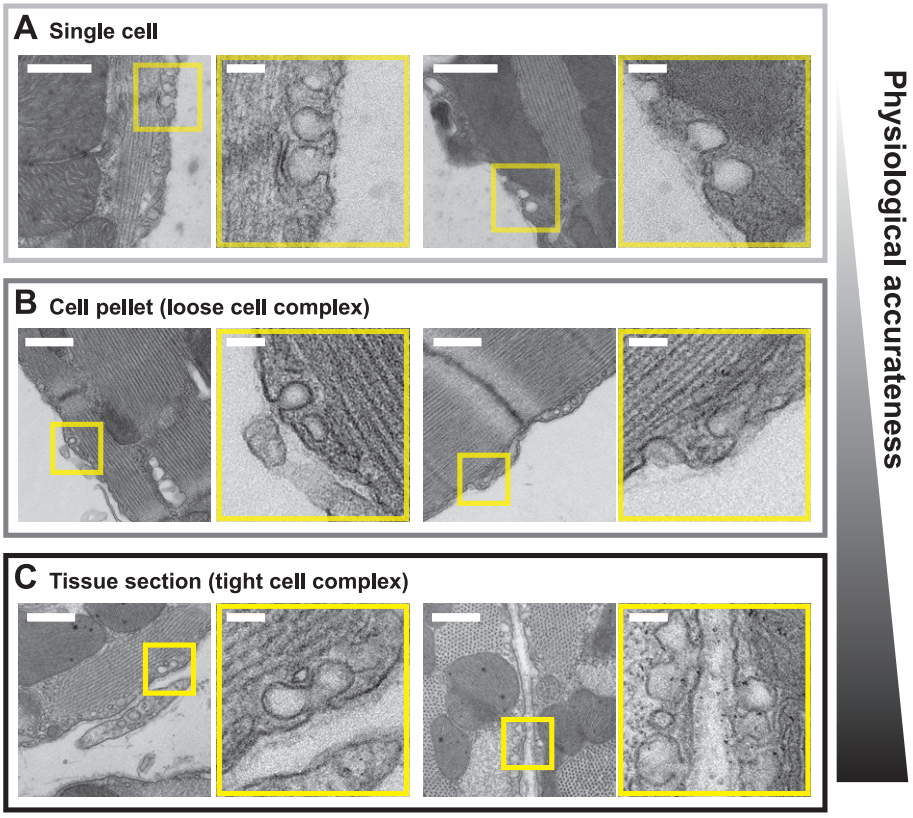

Figure K.1.: Electron micrographs of caveolar structures along the sarcolemma of primary mouse ventricular cardiomyocytes (VM) obtained from the following three different sample preparations: single cells, cell pellets, and tissue sections (see section 2.10.3). The increase in physiological accurateness of these three preparations is qualitatively demonstrated by the gradient bar to the right of the panels. Overview images and magnified insets (yellow boxes) showing omega-shaped caveolae along the sarcolemma and opened towards the extracellular space. Scale bars in overview images: 500 nm; scale bars in magnified insets: 100 nm. **A** Electron micrographs of two exemplary single VM plated after isolation. **B** Electron micrographs of two exemplary regions of interest (ROI) within slices of a cell pellet of isolated VM. **C** Electron micrographs of two exemplary ROI within perpendicularly cut sections of the papillary muscles from the left ventricle.

most physiological condition under which the EM images of caveolae could be obtained. Thus, the EM images of the cardiac tissue sections seem to be most comparable to a snap shot of an intact, physiological state (of course, it has to be kept in mind that the sample preparation for EM includes several very harsh steps that possibly very strongly influence the real physiological state of intact caveolar structures). Conclusively, EM images of caveolae at the cardiac sarcolemma under the - comparatively - most physiological conditions show the highest incidence of fused caveolae. This probably indicates that the formation of caveolar superstructures is a characteristic feature of intact VM. Given that the bunchy clusters that were observed for the sarcolemmal Cav-3 and Chol-KK114 signal using STED microscopy (see e.g. Fig. 3.22 in section 3.5) correspond to caveolar superstructures, the abundance of complex caveolar

assemblies is even higher in living VM. Such a distinct and often-seen formation of caveolae at the sarcolemma almost begs for the hypothesis of serving an underlying specific function. Such a specific function could e.g. be the adjustable provision of a reservoir of additional membrane surface area (see e.g. [188]) - this could be a big advantage for cells like VM that undergo constant mechanical stress. STED microscopy using fluorescent Cholesterol analogs to image caveolar structures in living VM seems to be very well suited to study the sarcolemmal membrane nanopattern and the functions that it may serve. Such studies could include the dynamic tracking of nanoscopic changes at the sarcolemma of living VM under different experimental conditions, e.g. during mechanical stress or following the administration of drugs that specifically alter cellular membrane properties (see also section 4).

L. Additional information: Western blot analysis

For the determination of protein expression levels by Western blotting, protein concentrations in individual samples were assessed using a standard protein detection kit (see section 2.10.2). The obtained protein concentrations per sample are displayed in Table L.1. For statistical significance of the Caveolin-

Sample ID	Protein concentration [µg/µl]
Samples from mouse left ventricle homogenates	
C57Bl/6N #1	11.6
C57Bl/6N #2	10.4
C57Bl/6N #3	10.0
C57Bl/6N #4	11.4
Samples from HeLa cell homogenates	
HeLa T- #1	3.28
HeLa T- #2	2.86
HeLa T- #3	2.78
HeLa T- #4	3.06
HeLa C	3.96

Table L.1.: Protein concentrations in samples for Western blot analysis. See section 2.10.2 for details on sample preparation and specification of buffers. Samples contained a final concentration of 2 µg/µl protein in a final sample volume of 45 µl (i.e. protein content was brought to 90 g per sample). Abbreviations: C57Bl/6N ## - respective identification of mouse left ventricle samples; HeLa T- ## - respective identification of samples of HeLa cells transfected with the Cav-3-SNAP construct (see section 2.4.1); HeLa C - Control sample of untransfected HeLa cells; HP - Homogenization buffer.

3 (Cav-3) protein expression levels determined by Western blotting, a total of two Western blots with four individual samples from both left ventricle homogenates and transfected HeLa cell homogenates, respectively, were prepared. The complete set of prepared Western blots is displayed in Fig. L.1 **A.1** and **B.1**, wherein the signal was adjusted in brightness so as to be able

to make out the molecular marker bands. The protein marker bands were labeled manually according to their molecular weight in kDa. For explanatory purposes, Fig. L.1 **A.2** and **B.2** show the same Western blots as Fig. L.1 **A.1** and **B.1**, respectively, but with the lanes in the gel and the protein bands labeled in yellow according to the nomenclature explained in the following (for sample preparation, please refer to section 2.10.2). Lanes 01 to 04 (L01 to L04) contain the samples from left ventricle homogenates C57Bl/6N mice #1 to #4, respectively. Lanes 05 to 08 (L05 to L08) contain the samples from homogenates of HeLa cells transfected with the Cav-3-SNAP construct. Lane 09 (L09) contains the control sample from untransfected HeLa cells. Cav-3 protein bands (at $\approx$ 20 kDa) and Cav-3-SNAP bands (at $\approx$ 40 kDa) are shown in green and labeled as B01 in the respective lane and with a green underscore. The loading control protein GAPDH bands (at $\approx$ 36 kDa are shown in red and labeled as B01 in the respective lane and with a red underscore.

Complete set of Western blots for protein level determination

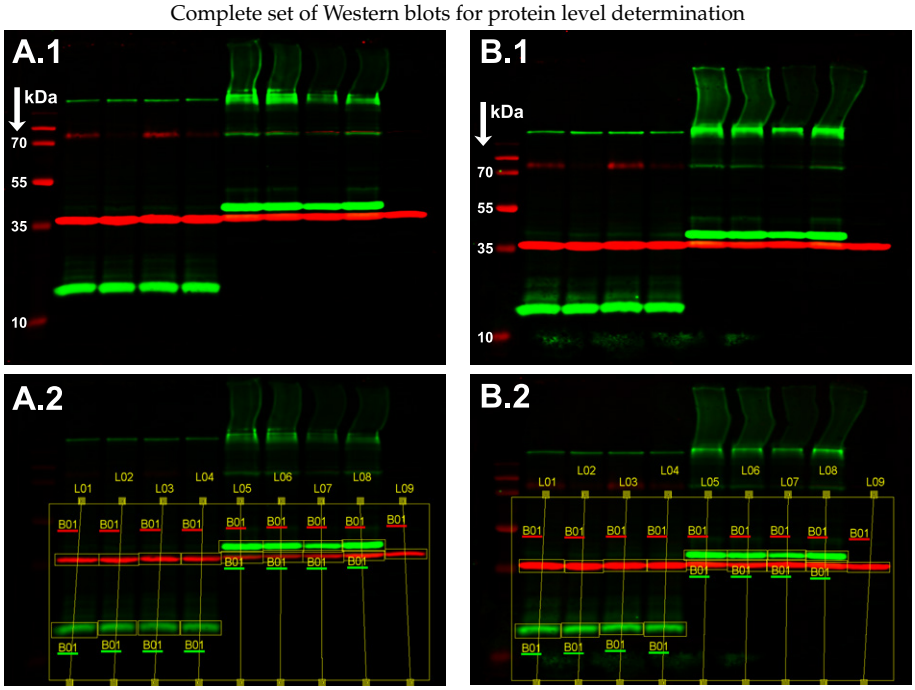

Figure L.1.: Determination of Caveolin-3 (Cav-3) protein expression by western blotting and presented in section 3.5. Western blots were prepared following the protocol described in section 2.10.2 and contained four samples from left ventricle homogenates and transfected HeLa cell homogenates, respectively, as well as one control sample from untransfected HeLa cells. Please refer to the text for further details on sample preparation and description of the Western blots.

M. Cholesterol depletion does not change the TATS topology

Control experiments were conducted to confirm that sarcolemmal Cholesterol (Chol) depletion by Methyl-β-Cyclodextrin (M-β-CD) only affects the degree of sarcolemmal membrane protein clustering - specifically, the clustering of Caveolin-3 (Cav-3) - but does not alter the basic architectural structure of the Transverse-Axial Tubular System (TATS). To this end, living mouse ventricular cardiomyocytes (VM) were incubated with 5 mM M-β-CD (for 1 h, at 37°C, see section 2.3.3), stained with the potentiometric membrane dye Di-8-ANEPPS (see section 2.3.2) and imaged in confocal mode using the STED microscope system Leica TCS SP8 STED 3X (see section 2.1.3). The obtained images of the membrane structures were qualitatively compared to Di-8-ANEPPS labeled control cells (i.e. no treatment with M-β-CD). Fig. M.1 **A** exemplarily shows the confocal (conf.) images of the Di-8-ANEPPS signal of the TATS of control VM (Control) vs. VM incubated with M-β-CD (+ 5 mM M-β-CD). Qualitatively, no difference between the TATS of control and M-β-CD treated cells regarding the signal brightness, the amount of detectable tubular structures, their interconnectedness, and their regularity was observed. Further, to validate that after Chol depletion by M-β-CD, the reintroduction of Chol to the TATS membrane would lead to a Chol signal that showed a similar arrangement as the Chol signal in control VM, M-β-CD treated cells were labeled with 5 µM of Chol-KK114 (see section 2.3.2) and STED images obtained using the STED microscope system Leica TCS SP8 STED 3X. The acquired images were qualitatively compared to Chol-KK114 labeled control cells (i.e. no treatment with M-β-CD). Fig. M.1 **B** exemplarily shows the signal structure of Chol-KK114 labeled control vs. M-β-CD treated VM. No difference between control vs. M-β-CD treated cells could be observed; the TATS showed no alterations in structure and regularity. This confirms that Chol depletion is a reversible effect as Chol rich regions along

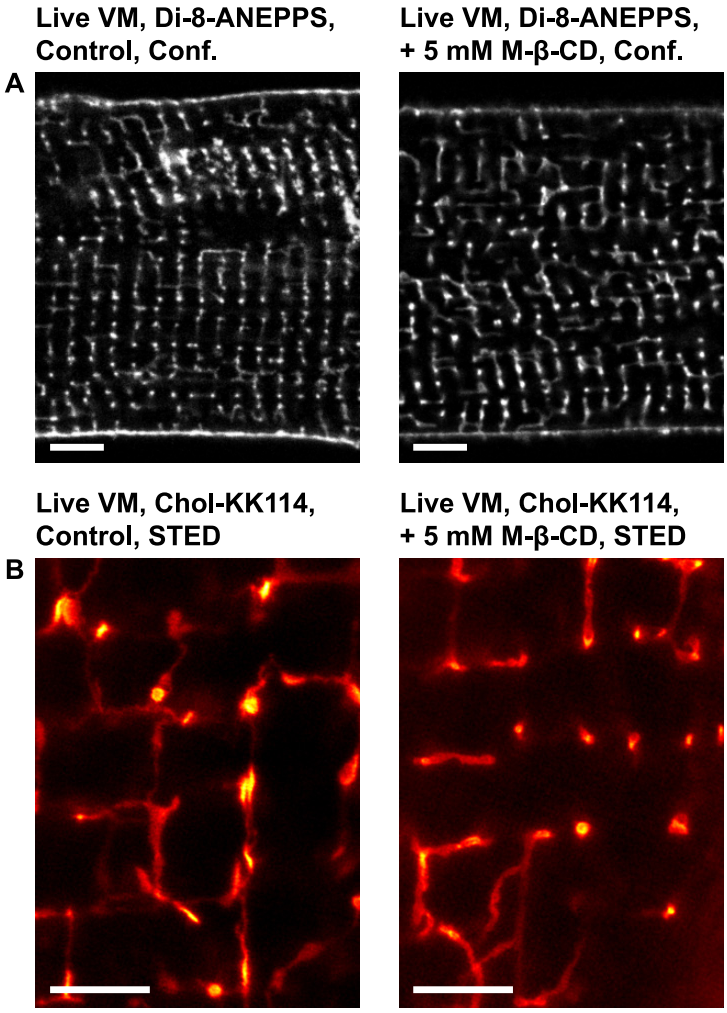

Figure M.1.: Fluorescent stains of living mouse ventricular cardiomyocytes (VM) before and after Cholesterol depletion (Chol depletion) show that the principal VM membrane architecture remains unaltered upon Chol depletion. **A** Confocal images of living VM stained with 50 µM Di-8-ANEPPS (see section 2.3.2) for the two scenarios: 1. Untreated cells, no Chol depletion (left panel, "Control"); 2. Chol depleted cells via incubation with 5 mM Methyl-β-Cyclodextrin (M-β-CD, see section 2.3.3; right panel, "+ 5 mM M-β-CD"). Scale bars: 5 µm. **B** STED images of living VM stained with 5 µM Chol-KK114 for the two scenarios: 1. Untreated cells, no Chol depletion (left panel, "Control"); 2. Chol depleted cells via incubation with 5 mM M-β-CD (right panel, "5 mM M-β-CD"). Scale bars: 2 µm.

the membrane reform when Chol is added back. This could also mean that the disruption of caveolae that occurs upon Chol depletion (see section 3.5.1) is reversible and that the Chol content along the sarcolemma influences the degree of caveolar clustering in an adjustable fashion.

N. Dystrophin antibody control stains in *mdx 5cv* cardiomyocytes

This appendix provides an overview over the control experiments for the specificity of the anti-Dystrophin (Dyst) primary antibodies that are used in this thesis (see section 3.7). For these controls, two-color immunofluorescence stains of mouse ventricular cardiomyocytes (VM) from the Dyst deficient mouse strain *mdx 5cv* were prepared (see sections 2.3.4 and 2.3.3). VM were labeled for Dyst using the different primary antibodies that are presented in the following and that target specific epitopes of the Dyst protein. The targeted amino acids (aa) are denoted in the following figures. VM were additionally stained for the membrane associated protein Caveolin-3 (Cav-3) to provide an internal control for the cell quality.
The two-color STED images were obtained using the STED microscope system Leica TCS SP8 STED 3X (see section 2.1.3). For the image acquisition settings, please refer to the overview given in Appendix B. For the two respective color channels, the two dyes STAR635P and STAR580 were chosen (see section A.4). To control that there is no effect of the respective dye compound chosen for labeling on the protein signal distribution, Dyst and Cav-3 were labeled using STAR635P and STAR580 and vice versa.

Fig. N.1 shows STED images of the sarcolemma of *mdx 5cv* VM labeled for Dyst using the amino-terminus (N-terminus) specific primary antibody 4C7 (Santa Cruz Biotechnology, see section A.3) that targets aa 1-68. Note that a distinct Dyst signal can be observed in both color channels despite the fact that the VM stem from the Dyst deficient *mdx 5cv* mouse line (and the Cav-3 signal is as expected and not a possible source of spectral cross talk, as seen in the overlay images of the two color channels). The presence of a visible N-terminal Dyst signal stems from the specific mutation of the Dyst gene in the *mdx 5cv* mouse

model that causes a truncation of the Dyst protein starting at aa 282 [288, 253]. Thus, the Dyst N-terminus is still expressed in the *mdx 5cv* mouse and can be recognized by the 4C7 antibody, thus leading to a Dyst pos signal. The specific Dyst signal pattern that is seen when using the 4C7 antibody is also discussed in section 3.8.

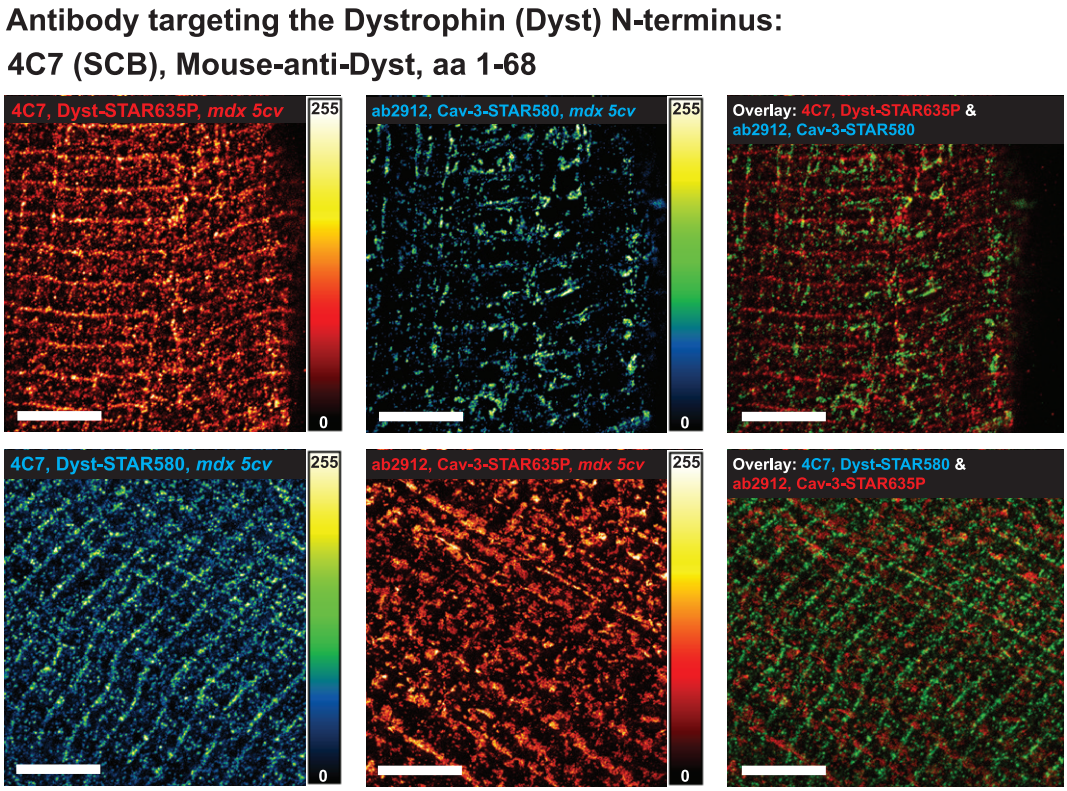

Figure N.1.: Two-color STED images of Dystrophin (Dyst) and Caveolin-3 (Cav-3) in *mdx 5cv*, i.e. Dystrophin deficient, mouse ventricular cardiomyocytes (VM). Dyst was immunofluorescence labeled via the N-terminus specific antibody 4C7 (Mouse-anti-Dyst, Santa Cruz Biotechnology, see also section A.3) which is directed against the amino acids (aa) 1-68 of the Dyst molecule. Dyst was decorated with the fluorophores STAR635P or STAR580 (see section A.4). Cav-3 was immunofluorescence labeled with the antibody ab2912 (Rabbit-anti-Cav-3, abcam, see also section A.3) and decorated with the fluorophores STAR635P or STAR580 (see section A.4). Color bars indicate the respective image intensity value (RGB scale). Scale bars: 5 µm.

Fig. N.2 shows STED images of the sarcolemma of *mdx 5cv* VM labeled for Dyst using the rod domain specific primary antibodies ab85302 (Fig. N.2 **A**, from abcam, see also section A.3) and ab7163 (Fig. N.2 **B**, from abcam, see also section A.3). The antibody ab85302 recognizes the sequence of the Dyst aa 1850-1950 (ab85302 is also used for the imaging protocols presented in section 3.8). The antibody ab7163 recognizes the sequence of the Dyst aa 1400-1505. As expected, for both antibodies the sarcolemmal Dyst signal is negative in *mdx 5cv* VM while the Cav-3 signal looks normal.

Figs. N.3 and N.4 respectively show STED images of the sarcolemma of *mdx 5cv* VM labeled for Dyst using the carboxyl-terminus (C-terminus) specific primary antibodies C-20 (Fig. N.3 **A-1**, Santa Cruz Biotechnology), ab15277 (Fig. N.3 **A-2**, abcam), ab7164 (Fig. N.4 **A-2**, abcam), and 7A10 (Fig. N.4 **B-2**, Santa Cruz Biotechnology). For detailed information on the used Dyst primary antibodies, please refer to section A.3. The antibody C-20 recognizes the sequence of the Dyst aa 3361-3685; the antibody ab15277 recognizes the sequence of the Dyst aa 3661-3677; the antibody ab7164 recognizes the sequence of the Dyst aa 3558-3684, and the antibody 7A10 recognizes the sequence of the Dyst aa 3200-3684.The antibody C-20 was also used for the imaging protocols presented in section 3.8. As expected, none of the C-terminus specific anti-Dyst primary antibodies yields a significant Dyst signal in VM of the *mdx 5cv* mouse strain while the Cav-3 signal looks normal.

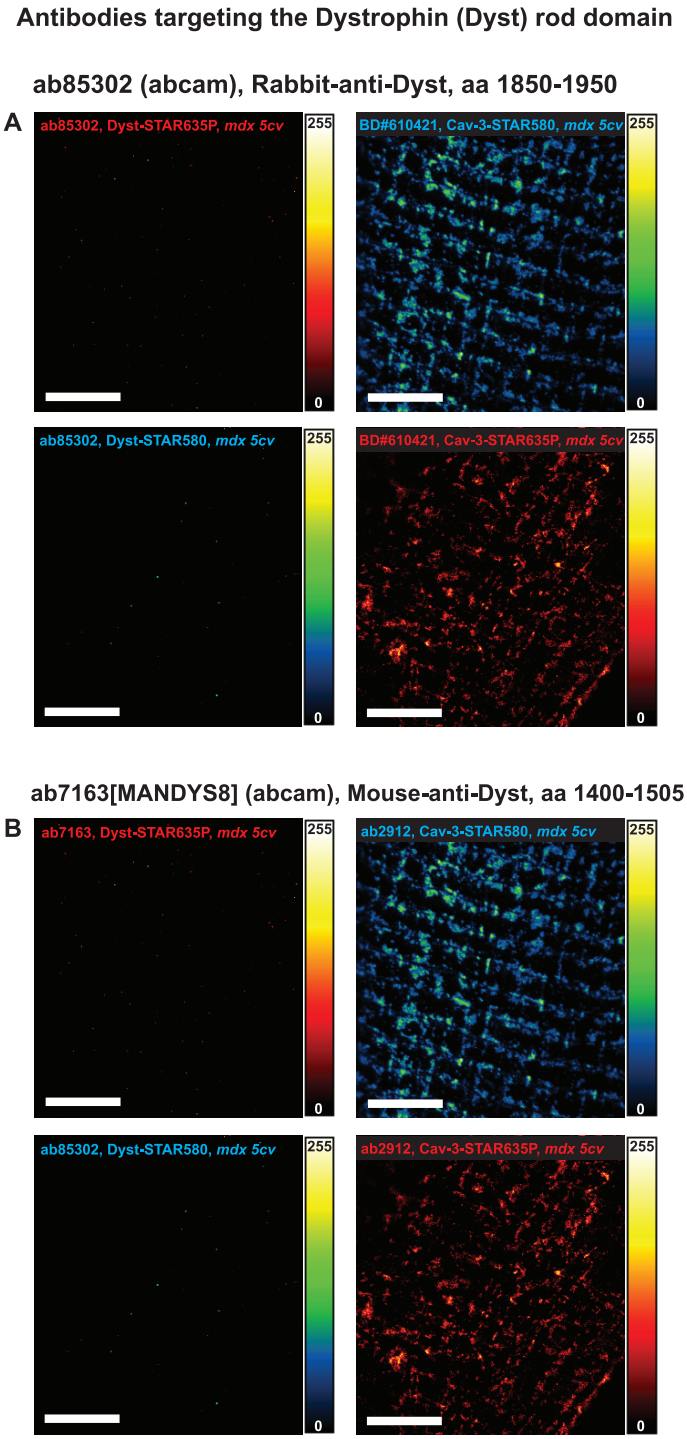

Figure N.2.: Two-color STED images of Dystrophin (Dyst) and Caveolin-3 (Cav-3) in *mdx 5cv*, i.e. Dystrophin deficient, mouse ventricular cardiomyocytes (VM). **A** Immunofluorescence labeled Dyst via the rod domain specific antibody ab85302 (Rabbit-anti-Dyst, abcam, see section A.3) which is directed against the amino acids (aa) 1850-1950 of the Dyst molecule. Immunofluorescence labeled Cav-3 via the antibody BD#610421 (Mouse-anti-Cav-3, BD Biosciences, see section A.3). *B* Immunofluorescence labeled Dyst via the rod domain specific antibody ab7163 (Mouse-anti-Dyst, abcam, see section A.3) directed against aa 1400-1505. Immunofluorescence labeled Cav-3 via the antibody ab2912 (Rabbit-anti-Cav-3, abcam, see section A.3). Dyst and Cav-3 were respectively decorated with the dyes STAR 635P or STAR 580 (see section A.4). Color bars indicate the respective image intensity value (RGB scale). Scale bars: 5 µm.

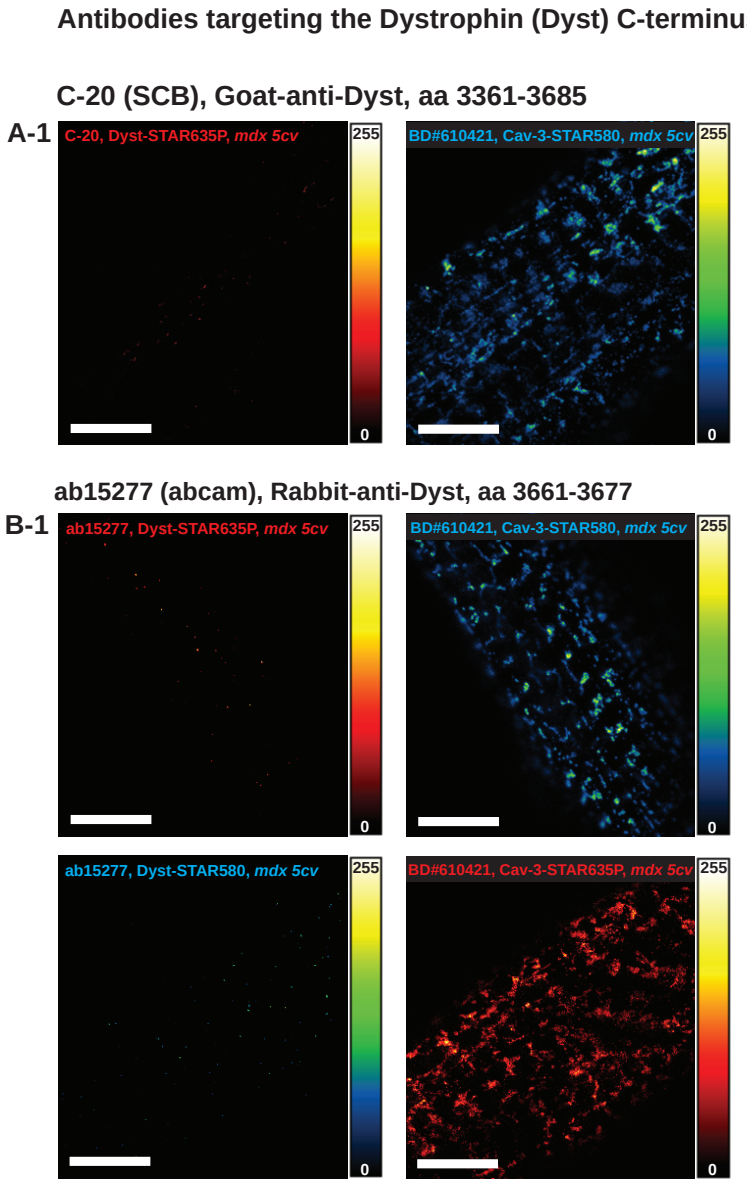

Figure N.3.: Two-color STED images of Dystrophin (Dyst) and Caveolin-3 (Cav-3) in *mdx 5cv*, i.e. Dystrophin deficient, mouse ventricular cardiomyocytes (VM). **A-1** Immunofluorescence labeled Dyst via the C-terminus specific antibody C-20 (Goat-anti-Dyst, Santa Cruz Biotechnology, see section A.3) which is directed against the amino acids (aa) 3361-3685 of the Dyst molecule. Immunofluorescence labeled Cav-3 via the antibody BD#610421 (Mouse-anti-Cav-3, BD Biosciences, see section A.3). *B-1* Immunofluorescence labeled Dyst via the C-terminus specific antibody ab15277 (Rabbit-anti-Dyst, abcam, see section A.3) directed against aa 3661-3677. Immunofluorescence labeled Cav-3 via the antibody BD#610421 (Mouse-anti-Cav-3, BD Biosciences, see section A.3). Dyst and Cav-3 were respectively decorated with the dyes STAR 635P or STAR 580 (see section A.4). Color bars indicate the respective image intensity value (RGB scale). Scale bars: 5 µm.

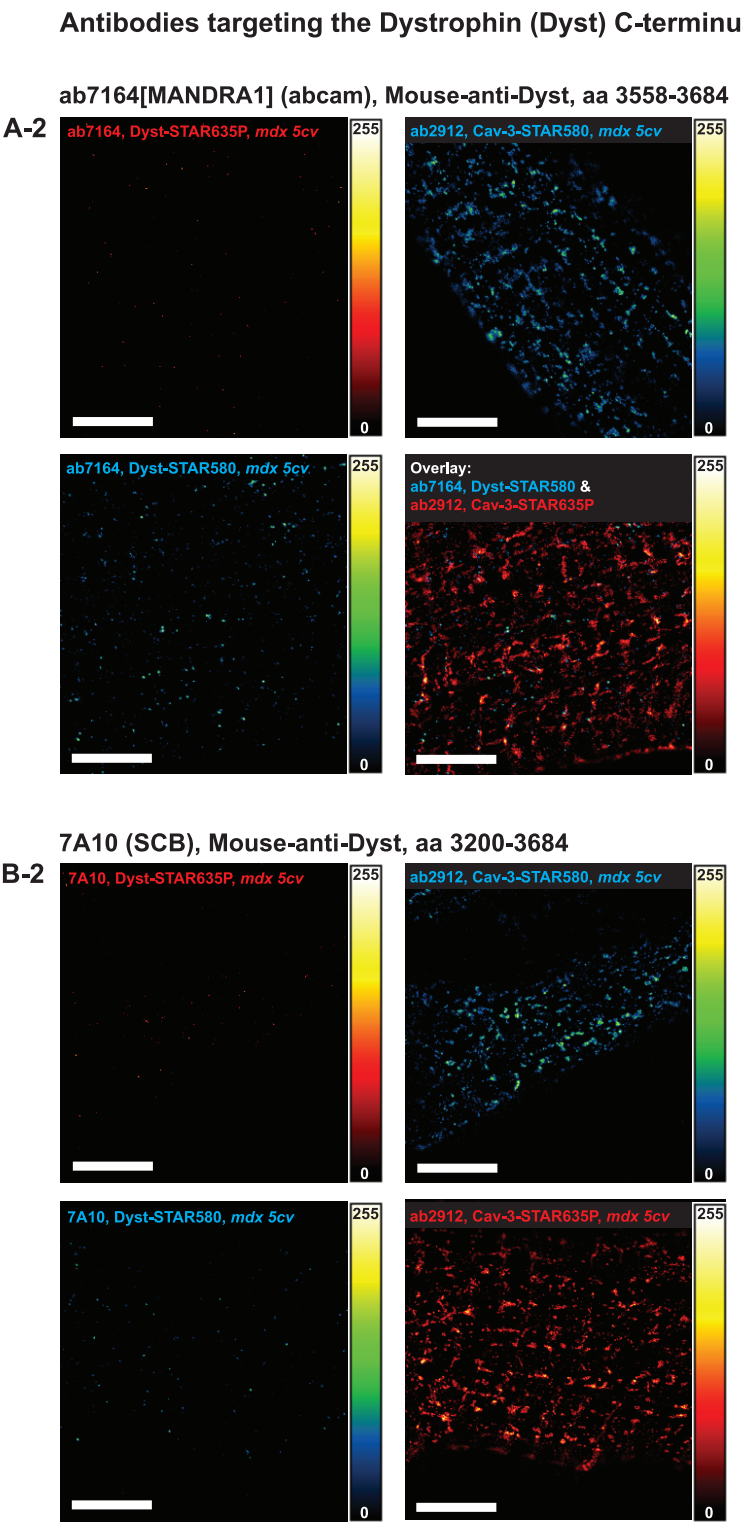

Figure N.4.: Two-color STED images of Dystrophin (Dyst) and Caveolin-3 (Cav-3) in *mdx 5cv*, i.e. Dystrophin deficient, mouse ventricular cardiomyocytes (VM). **A-2** Immunofluorescence labeled Dyst via the C-terminus specific antibody ab7164 (Mouse-anti-Dyst, abcam, see section A.3) which is directed against the amino acids (aa) 3558-3684 of the Dyst molecule. Immunofluorescence labeled Cav-3 via the antibody ab2912 (Rabbit-anti-Cav-3, BD Biosciences, see section A.3). The panel marked as "Overlay" shows the overlaid color channels to indicate that the Dyst signal in the *mdx 5cv* VM is not caused by spectral cross talk with the Cav-3 signal. *B-2* Immunofluorescence labeled Dyst via the C-terminus specific antibody 7A10 (Mouse-anti-Dyst, Santa Cruz Biotechnology, see section A.3) directed against aa 3200-3684. Immunofluorescence labeled Cav-3 via the antibody ab2912 (Rabbit-anti-Cav-3, BD Biosciences, see section A.3). Dyst and Cav-3 were respectively decorated with the dyes STAR 635P or STAR 580 (see section A.4). Color bars indicate the respective image intensity value (RGB scale). Scale bars: 5 µm.

O. Funding

This doctoral thesis was supported by the Deutsche Forschungsgemeinschaft through the SFB 1002 project A05.

P. Curriculum vitae

Personal data

Name:	Elke Hebisch
Date of birth:	March 17, 1987
Place of birth:	Berlin, Germany
Current address:	Zimmermannstr. 9, App. 9.204
	D-37075 Goettingen
	Germany
Email address (work):	elke.hebisch@mpibpc.mpg.de
Email address (private):	elke.hebisch@gmail.com
Telephone (work):	+49 (0)551 201 2513
Telephone (private, landline):	+49 (0)551 49 255 922
Telephone (private, mobile):	+49 (0)177 870 38 13

Education

September 2012 - February 2017: Employment as a doctoral student in the group of Prof. Dr. Stefan Hell at the Max Planck Institute for Biophysical Chemistry in Goettingen, Germany, with research focus on the development of STED microscopes and fluorescence labeling techniques for STED microscopy, and their application to isolated mouse cardiomyocytes to study cardiac membrane nanopatterns. This research was funded by the German Research Foundation (SFB 1002, project A05).

October 2009 - March 2012: Successful participation in the physics master program at the Ludwig Maximilian University of Munich. Obtainment

of the degree "Master of Science" in physics with an additional focus on biophysics in March 2012. The master thesis titled "Bacterial Interactions: Visualization - Characterization - Manipulation" (graded 1.3) was written at the Chair for Experimental Physics of Prof. Dr. J. O. Raedler under the supervision of Dr. M. Optiz (née Leisner).

October 2006 - August 2009: Successful participation in the physics bachelor program at the Ludwig Maximilian University of Munich. Obtainment of the degree "Bachelor of Science" in physics in July 2009. The bachelor thesis title "Analysis of the force field of glycine dipeptide by means of density functional theory" (graded 1.0) was written at the Chair for BioMolecular Optics at LMU Munich in the group on "theoretical molecular biophysics" of Prof. Dr. P. Tavan.

1997 - 2006: High school education at the Pestalozzi-Gymnasium Unna, Germany. Obtainment of the German Abitur in June 2006 (grade: 1.0).

2003/2004: Stay abroad in Excelsior Springs, Missouri, USA. Obtainment of the high school diploma from Excelsior Springs High School in May 2004.

Research/Teaching Experience

September 2012 - February 2017: Employment as a doctoral student in the group of Prof. Dr. Stefan Hell at the Max Planck Institute for Biophysical Chemistry in Goettingen, Germany.

September 9-20, 2013: Supervision of the practical course on physics for student of physics at the University of Heidelberg, Germany, corresponding to one teaching load.

June 1-3, 2012: Academic employment as a scientific associate at the chair of Prof. Dr. J. O. Raedler (LMU Munich) in the group of Dr. Madeleine Opitz (née Leisner) on a project about fluorescent protein maturation times in bacteria. The resulting paper "High variation of fluorescence protein maturation times in closely related *Escherichia coli* strains" has been published in the journal *PLoS ONE* in October 2013.

2009 - 2012: Tutorage of the course "T0 - Rechenmethoden (Introduction to Theoretical Physics)" at LMU Munich.

Winter semester 2011/2012: Supervision of the practical lab course on physics for students of physics, and medicine, respectively, at LMU Munich (in the times from April 15, 2009 - August 14, 2009; October 15, 2009 - February 2, 2010; April 15, 2010 - August 14, 2010; October 18, 2010 - February 14, 2011; May 1, 2011 - August 31, 2011; October 15, 2011 - February 2, 2012).

Scientific/Laboratory Skills

Optical engineering (design and construction of an open system two-photon-excitation STED microscope).

Familiarity with various commercially avaiblabe confocal and STED microscope systems.

Authorization to carry out experimental and other scientific procedures on living animals (holder of a FELASA B certificate).

Laboratory experience in tissue and organ harvesting and preparation for fluorescence imaging applications. Extended experience in cardiomyocyte isolation.

Laboratory experience in fluorescence staining of living and fixed cell samples for fluorescence imaging applications.

Laboratory experience in the field of basic microbiology, working with bacteria. Extended experience in working with fluorescence labeled *E. coli* bacteria and their quantitative examination by spectrometry, flow cytometry and fluorescence microscopy on the single-cell and colony level.

Experience in theoretical modeling of protein conformations by employment of molecular dynamics (especially density functional theory).

Experience in theoretical simulations of morphogenic and regulatory genetic systems by employment of reaction-diffusion-models.

Computer Skills

Programming skills in Matlab, Python, Mathematica, C++, and C.

Foreign Language Skills

Excellent knowledge of English
Good knowledge of French
Basic knowledge of Dutch
Basic knowledge of Spanish

Personal Interests

Various sports (fitness training, long distance running, triathlon; holder of a group fitness instructor certificate).
Foreign languages and cultures, traveling.
Current events, especially in interdisciplinary sciences.

Q. Publications

Publications in peer-reviewed journals

E. Hebisch, E. Wagner, V. Westphal, J. J. Sieber, and S. E. Lehnart. A protocol for registration and correction of multi-color STED superresolution images. *Journal of Microscopy*, 2016, in revision.

S. Brandenburg, T. Kohl, G. S. B. Williams, K. Gusev, E. Wagner, E. A. Rog-Zielinska, **E. Hebisch**, M. Dura, M. Didié, M. Gotthardt, V. O. Nikolaev, G. Hasenfuss, P. Kohl, C. W. Ward, W. J. Lederer, and S. E. Lehnart. Axial tubule junctions control rapid calcium signaling in atria. *The Journal of Clinical Investigation*, 126, 2016.

S. Nizamov, M. V. Sednev, M. L. Bossi, **E. Hebisch**, H. Frauendorf, S. E. Lehnart, V. N. Belov, and S. W. Hell. "Reduced" coumarin dyes with an O-phosphorylated 2,2-dimethyl-4-(hydroxymethyl)-1,2,3,4-tetrahydroquinoline fragment: Synthesis, spectra, and STED microscopy. *Chemistry - A European Journal*, 22(33): 11631-11642, 2016.

K. Kolmakov, **E. Hebisch**, T. Wolfram, L. A. Nordwig, C. A. Wurm, H. Ta, V. Westphal, V. N. Belov, and S. W. Hell. Far-Red emitting fluorescent dyes for optical nanoscopy: Fluorinated Silicon-Rhodamines (SiRF Dyes) and phosphorylated oxazines. *Chemistry A European Journal*, 21(38): 13344-13356, 2015.

V. N. Belov, G. Y. Mitronova, M. L. Bossi, V. P. Boyarskiy, **E. Hebisch**, C. Geisler, K. Kolmakov, C. A. Wurm, K. I. Willig, and S. W. Hell. Masked rhodamine dyes of five principal colors revealed by photolysis of a 2-diazo-1-indanone caging group: Synthesis, photophysics, and light microscopy applications. *Chemistry A European Journal*, 20(41): 13162-13173, 2014.

M. F. Weber, G. Poxleitner, **E. Hebisch**, E. Frey, and M. Opitz. Chemical warfare and survival strategies in bacterial range expansions. *Journal of the Royal Society Interface*, 11(96), 2014.

E. Hebisch, J. Knebel, J. Landsberg, E. Frey, and M. Leisner. High variation of fluorescence protein maturation times in closely related *Escherichia coli* strains. *PLoS ONE*, 8(10): 1-9, 2013.

Contributions to scientific symposia

80th Annual Meeting of the German Physical Society (DPG) in Regensburg, Germany, March 6-11, 2016. Session BP 8: Bioimaging and Spectroscopy I; Presentation BP 8.3 (conference talk). **E. Hebisch**, S. E. Lehnart, and S. W. Hell. A novel membrane label for STED nanoscopy of living cardiomyocytes. E. Hebisch was recipient of a generous travel grant from the German Centre for Cardiovascular Research (DZHK) covering the entire business trip expenses (in the amount of about €500).

60th Annual Meeting of the Biophysical Society in Los Angeles, USA, February 27 - March 2, 2016. Abstract number 1320-Pos, Board B297 (conference poster). S. Brandenburg, T. Kohl, G. S. B. Williams, K. Gusev, E. Wagner, **E. Hebisch**, C. W. Ward, W. J. Lederer, and S. E. Lehnart. Axial membrane tubules in atrial cardiomyocytes confine ultrarapid intracellular Calcium signals through a new super-hub mechanism. *Biophysical Journal*, 110: 267a, February 2016.

Volkswagen Foundation, international kick-off conference "Life? - A fresh scientific approach to the basic principles of life" in Hannover, Germany, December 17-18, 2015. Conference poster. **E. Hebisch**, S. E. Lehnart, and S. W. Hell. A novel membrane label for STED nanoscopy of living cardiomyocytes. E. Hebisch was recipient of a generous travel grant from the Volkswagen Foundation in the amount of €200.

10th EBSA European Biophysics Congress in Dresden, Germany, July 18-22, 2015. Abstract number L-843, section 7. Membrane Structure and Domains

(conference poster). **E. Hebisch**, T. Kohl, S. E. Lehnart, and S. W. Hell. A novel membrane label for STED nanoscopy of living cardiomyocytes.

28th Focus on Microscopy conference in Goettingen, Germany, March 29 - April 1, 2015. Session TU-MO-PAR-A, Super Resolution III: STED (conference talk), Tuesday, March 31, 2015. **E. Hebisch**, T. Kohl, S. E. Lehnart, and S. W. Hell. A novel membrane label for STED nanoscopy of living cardiomyocytes. Abstract available at `http://www.focusonmicroscopy.org/2015/index.html`

1st Labeling & Nanoscopy Conference in Heidelberg, Germany, September 24-26, 2014. Poster Session I (conference poster). **E. Hebisch**, T. Kohl, V. Westphal, S. E. Lehnart, and S. W. Hell. Characterization of Caveolin-3 domains and their association to Cholesterol in cardiomyocytes.

European Society of Cardiology Congress 2014 in Barcelona, Spain, August 30 - September 3, 2014. Abstract number P677 (conference poster). E. Wagner, **E. Hebisch**, J. H. Steinbrecher, V. Westphal, G. Hasenfuss, S. W. Hell, and S. E. Lehnart. P677* Superresolution microscopy reveals proliferative T-Tubule remodeling as general disease mechanism in early stages of heart failure development. *Cardiovascular Research*, 103(suppl 1): S123-S123, 2014

Additional scientific contributions

Within the German Centre for Cardiovascular Research (DZHK) **E. Hebisch** is member of the extended Young DZHK committee at the partner site Goettingen, Germany.

E. Hebisch was invited speaker to the regularly organized talk series "Cardio-Lunch" at the University Medicine Goettingen (UMG), Germany, on April 26, 2016. Title of the talk: "Cardiac membrane nanodomains".

Science Online Commentary, October 8, 2015. `http://comments.sciencemag.org/content/10.1126/science.aab3500` **E. Hebisch**, T. Kohl, E. Wagner, V. Westphal, G. Hasenfuss, W. J. Lederer, and S. E. Lehnart. This online commentary published online is referring to the article by Li et al. [578].

1st Network meeting of the International Research Training Group (IRTG) 1816 established by the German Research Foundation (DFG) and the King's College London British Heart Foundation Centre of Research Excellence in Wernigerode, Germany, September 6-8, 2015. Invited speaker (together with E. Wagner). **E. Hebisch**, and E. Wagner. Title of the talk: "STED microscopy".

SFB 1002 Symposium 2015 in Goettingen, Germany, June 4-5, 2015.
E. Hebisch was invited speaker within the category "Presentation of SFB Graduate Student". Title of the presentation: "Cardiac membrane nanodomains and the Dystrophin-Associated Membrane Protein Complex (DAMP)", given on June 5, 2015.

TAMPting Seminar II: The Physiology of Membrane Proteins; held in Goettingen, Germany, September 28-30, 2014 and organized by Prof. Blanche Schwappach, Director of Biochemistry at the University Medical center Goettingen. **E. Hebisch** was invited lecturer leading the seminar "Automated microscope and STED microscope' on September 30, 2014.

Acknowledgments

I would like to thank everyone who was involved and contributed to the success of this project and thesis - be it directly or indirectly.

Prof. Dr. Stefan W. Hell to whom my special thanks and gratitude go out for letting me develop freely as a scientist, for letting me find my niche in research, and for creating an inspiring working environment. I am also thankful for his guidance and his constant support of this project.

Prof. Dr. Stephan E. Lehnart for his valuable ideas, for welcoming me to his research group, and for always making the time for lively scientific exchange.

Prof. Dr. Rainer H. A. Fink for agreeing to be the second referee of this thesis.

Dr. Eva Wagner for her impressive cleverness and for teaching a physicist biological procedures that the certain physicist would have never thought she'd be doing one day. Also for being such a warmhearted, kind, and extremely fun person who made work and life much more amazing: running, crawling through mud, triathlon, hanging out - thank you!

Dr. Volker Westphal for teaching me everything about optics, for his time and support, for fruitful discussions and for proofreading of manuscripts (and "prooflistening" to talks).

Dr. Jan Keller-Findeisen for all his kind and patient support with programming and for critically proofreading this thesis (and for being the caveman who would manufacture the most pointy spear!).

Dr. Alf Honigmann for the design of the dye compound Cholesterol-PEG-KK114, for kindly letting me use it and showing me how to prepare it.

Dr. Vladimir Belov, Dr. Kirill Kolmakov, Dr. Shamil Nizamov, and Dr. Alexey Butkevich for being such extremely talented chemists and for creating the dyes that made most of the - admittedly - very beautiful images in this thesis possible.

Jaydev Jethwa for knowing where to find everything, for knowing everything about lasers, for being the backbone of the group - and for critically proofreading paper manuscripts and this thesis.

Birgit Schumann for her constant support regarding laboratory tasks, the many cell isolations, her amazing organisational skills, and her cheerful soul. Also for all the nice email conversations and chats.

Brigitte Korff for taking care of the mouse order at the University Medicine Göttingen, for all of the Western blots she performed, and for all the chats that we had.

Tanja Gilat, Ellen Rothermel, Patricia Mannheim, and the whole staff in the labs at both the MPIBPC and the UMG for the countless cell samples, transfections, cell isolations, cell differentiation.

Dr. Dietmar Riedel, Gudrun Heim, and Dirk Wenzel from the electron microscopy facility at the MPIBPC for making "my" heart cell samples ready for electron microscopy and for taking beautiful, picture-perfect, textbook example images.

Marco Roose and Björn Thiel for their help with hardware, software, Imspector, all the organic honey, and for many nice and fun conversations.

Stefanie Kruse, Sarah Leondarakis, Sylvia Löbermann, Rita Schmitz-Salue, Maria Sermond, and Rainer Pick for all their organization efforts and making things happen.

Rainer Schürkötter, Mario Lengauer, Thomas Kantelhardt, Frank Grüneklee, Andreas Pucher-Diehl, Marc Rosenthal, and the whole team of the mechanics workshop at the MPIBPC for their amazing talent, for turning my scribbled designs into actual, real-life things (and for doing that so fast!), and for their constant cheerfulness.

Peter Böttcher and Bodo Schneider from the woodwork shop at the MPIBPC for helping me create an optics lab that was veritably inviting me to efficient and comfortable (long) working hours.

Wolfgang Kluge and Matthias Kleinhans from the optics workshop of the department for NanoBiophotonics for their skill at creating all the (sometimes almost bizarre) optics components with which my mind came up, for working with such admirable precision, and for their heartiness.

Frank Meyer, Udo Gemm, and the whole team from the electronics workshop at the MPIBPC for the design and construction of various electronic components and for being able to repair so many gadgets without the need for any manual.

Dr. Ulrike Teichmann, Kirsten Kiel, Christiane Heuchel, and the whole team of the MPIBPC animal facility for teaching me the proper conduct with laboratory animals and for taking good care of all the mice that were sacrificed in this project (and to whom I am also thankful!).

Hartmut Sebesse, Irene Böttcher-Gajewski, Peter Goldmann, and the whole team of the media service at the MPIBPC for printing various posters and this thesis, and for running the world's fastest printer.

My office mates: Franziska Winter, Maria Loidolt, Débora Machado Andrade, Jasmin Pape ("the girls") and Sebastian Schubert and Yvan Eilers ("the boys") for creating a comfortable and pleasant atmosphere and for all the discussions, the emotional support, and tolerating my day-to-day quirkiness.

All the cool, fun, nice, friendly, decent - in short: amazing! - people in the group of NanoBiophotonics, in the group of Translational Cardiology, and beyond whom I have not mentioned yet; for good times in and outside the lab, for hanging out (Willie-Platz!), for going out, for chatting, watching movies, enjoying the Göttingen night life, cooking together, eating together, drinking together. I will list them in alphabetical order but they are all equally fantastic: Philipp Alt, Francisco Balzarotti, Federico Barabas, Christian Brüser, Fabian Göttfert, Lena Große, Klaus Gwosch, Moritz Heuser, Peter Ilgen, Daniel Jans, Isabelle Jansen, Nickels Jensen, Maria Kamper, Timo Konen, Matthias Krüger, Steffi Lehnertz, Jennifer Masch, Jason Martineau, Dirk Meineke, Sebastian Pasch, Sebastian Schnorrenberg, Till Stephan, Stefan Stoldt, Nicolai Urban.

Basically, the whole Translational Cardiology research group at the University Medicine Göttingen and everyone associated with them. Go Team "Herzrasen"!

All my precious old time friends who would even come to Göttingen to pay good old me a visit: Charlotte Hanses, Johannes Müller-Seidlitz, Philipp Heß, Tibor Klüver, Johannes Frohnmayer.

Mein größter Dank aus tiefstem Herzen geht an meine Eltern und meinen Bruder. Ich bin so froh, dass es Euch gibt und dass Ihr mich immer unterstützt. Ihr seid die wichtigsten Menschen in meinem Leben und ich liebe Euch sehr!

Ich habe sehr viel gelernt.